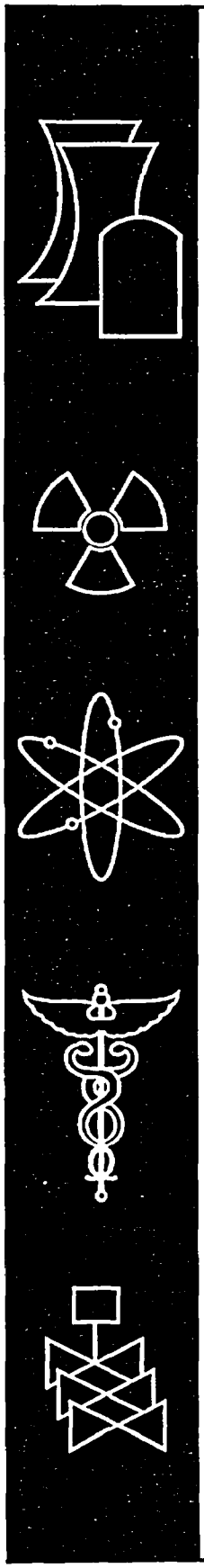

The Battelle Integrity of Nuclear Piping (BINP) Program Final Report

Appendices

U.S. Nuclear Regulatory Commission
Office of Nuclear Regulatory Research
Washington, DC 20555-0001

AVAILABILITY OF REFERENCE MATERIALS IN NRC PUBLICATIONS

NRC Reference Material

As of November 1999, you may electronically access NUREG-series publications and other NRC records at NRC's Public Electronic Reading Room at http://www.nrc.gov/reading-rm.html. Publicly released records include, to name a few, NUREG-series publications; *Federal Register* notices; applicant, licensee, and vendor documents and correspondence; NRC correspondence and internal memoranda; bulletins and information notices; inspection and investigative reports; licensee event reports; and Commission papers and their attachments.

NRC publications in the NUREG series, NRC regulations, and *Title 10, Energy*, in the Code of *Federal Regulations* may also be purchased from one of these two sources.

1. The Superintendent of Documents
   U.S. Government Printing Office
   Mail Stop SSOP
   Washington, DC 20402–0001
   Internet: bookstore.gpo.gov
   Telephone: 202-512-1800
   Fax: 202-512-2250
2. The National Technical Information Service
   Springfield, VA 22161–0002
   www.ntis.gov
   1–800–553–6847 or, locally, 703–605–6000

A single copy of each NRC draft report for comment is available free, to the extent of supply, upon written request as follows:

Address: Office of the Chief Information Officer,
Reproduction and Distribution
Services Section
U.S. Nuclear Regulatory Commission
Washington, DC 20555-0001
E-mail: DISTRIBUTION@nrc.gov
Facsimile: 301–415–2289

Some publications in the NUREG series that are posted at NRC's Web site address http://www.nrc.gov/reading-rm/doc-collections/nuregs are updated periodically and may differ from the last printed version. Although references to material found on a Web site bear the date the material was accessed, the material available on the date cited may subsequently be removed from the site.

Non-NRC Reference Material

Documents available from public and special technical libraries include all open literature items, such as books, journal articles, and transactions, *Federal Register* notices, Federal and State legislation, and congressional reports. Such documents as theses, dissertations, foreign reports and translations, and non-NRC conference proceedings may be purchased from their sponsoring organization.

Copies of industry codes and standards used in a substantive manner in the NRC regulatory process are maintained at—

The NRC Technical Library
Two White Flint North
11545 Rockville Pike
Rockville, MD 20852–2738

These standards are available in the library for reference use by the public. Codes and standards are usually copyrighted and may be purchased from the originating organization or, if they are American National Standards, from—

American National Standards Institute
11 West 42nd Street
New York, NY 10036–8002
www.ansi.org
212–642–4900

Legally binding regulatory requirements are stated only in laws; NRC regulations; licenses, including technical specifications; or orders, not in NUREG-series publications. The views expressed in contractor-prepared publications in this series are not necessarily those of the NRC.

The NUREG series comprises (1) technical and administrative reports and books prepared by the staff (NUREG–XXXX) or agency contractors (NUREG/CR–XXXX), (2) proceedings of conferences (NUREG/CP–XXXX), (3) reports resulting from international agreements (NUREG/IA–XXXX), (4) brochures (NUREG/BR–XXXX), and (5) compilations of legal decisions and orders of the Commission and Atomic and Safety Licensing Boards and of Directors' decisions under Section 2.206 of NRC's regulations (NUREG–0750).

NUREG/CR-6837, Vol. 2

The Battelle Integrity of Nuclear Piping (BINP) Program Final Report

Appendices

Manuscript Completed: September 2003
Date Published: June 2005

Prepared by
P.Scott[1], R.Olson[1], J.Bockbrader[1], M.Wilson[1], B.Gruen[1],
R.Morbitzer[1], Y.Yang[1], C.Williams[1], F.Brust[1], L.Fredette[1],
N.Ghadiali[1]

G.Wilkowski[2], D.Rudland[2], Z.Feng[2], R.Wolterman[2]

[1]Battelle
505 King Avenue
Columbus, OH 43201

Subcontractor:
[2]Engineering Mechanics Corporation of Columbus
3518 Riverside Drive
Suite 202
Columbus, OH 43221-1735

C. Greene, NRC Project Manager

Prepared for
Division of Engineering Technology
Office of Nuclear Regulatory Research
U.S. Nuclear Regulatory Commission
Washington, DC 20555-0001
NRC Job Code W6775

NUREG/CR-6837, Volume 2, has been reproduced from the best available copy.

ABSTRACT

Volume I of the final report for the Battelle Integrity of Nuclear Piping (BINP) program provided a summary of the results from this program and a discussion of the implications of those results. This volume (Volume II - Appendices) provides the details from the various technical tasks conducted as part of this program. Each individual appendix provides the details of a specific task conducted as part of the BINP program.

FOREWORD

Since 1965, the U.S. Nuclear Regulatory Commission (NRC) has been involved in research on various aspects of pipe fracture in nuclear power plant piping systems. The most recent programs are the Degraded Piping Program, Short Cracks in Piping and Piping Welds Program, and two International Piping Integrity Research Group programs. These programs have developed and validated "state-of-the-art" structural analysis methods and data for nuclear piping systems.

This report describes the results of the Battelle Integrity of Nuclear Piping (BINP) program, which was performed by Battelle Columbus Laboratories. The objective of the BINP program was to address the most important unresolved technical issues from the earlier research programs. The BINP program was initiated as an international program to enable fiscal leveraging and an expanded scope of work. Technical direction for the program was provided by a Technical Advisory Group composed of representatives from the funding organizations.

The BINP program was divided into eight independent tasks, each of which examined one of the unresolved technical issues. These eight tasks included both experimental and analytical efforts. The two pipe-system experiments examined the effects of secondary stresses (such as thermal expansion) and cyclic loading (such as during a seismic event) on the load-carrying capacity of flawed piping. For these experiments, the pipe system had large flaws or cracks. The remaining six tasks were "best-estimate" analyses to examine the effects of other factors, such as pipe system boundary conditions, and weld residual stresses on the behavior of flawed pipes. Many of these analyses involved the use of finite element modeling techniques. One of these analytical tasks was to examine the actual margins that may exist in flawed pipe evaluations as a result of non-linear behavior. While the magnitude of these margins would vary on a case-by-case basis, the results of this task show that a potential for significant margins does exist.

In addition to developing a technical basis for more advanced inservice flaw evaluation procedures for use with Class 1 piping, as defined by the American Society of Mechanical Engineers (ASME), the BINP program considered the development of flaw evaluation procedures for ASME Class 2 and 3 piping and balance-of-plant piping.

This research supports the NRC's goal to improve the effectiveness and realism of the agency's regulatory actions.

Charles J. Miller for

Carl Paperiello, Director
Office of Nuclear Regulatory Research
U.S. Nuclear Regulatory Commission

Table of Contents

List of Figures

List of Tables

APPENDIX A

EVALUATION OF PROCEDURES FOR THE TREATMENT OF SECONDARY STRESSES IN PIPE FRACTURE ANALYSES

A.1 BACKGROUND

Currently, the flaw evaluation procedures embodied in ASME Section XI specify different safety factors for global secondary stresses, such as thermal expansion and seismic anchor motion (SAM) stresses, than they do for primary stresses, such as primary membrane or primary bending stresses. The ASME Code specifies a safety factor of 2.77 for Service Levels A and B, and 1.39 for Service Levels C and D for primary stresses. For cracks in ferritic materials (base metal and welds) and austenitic flux welds (submerge-arc and shielded-metal-arc welds), the Section XI procedures indicate that the thermal expansion stresses should be included, but with a safety factor of only 1.0. In addition, for cracks in austenitic base metals, the ASME Code indicates that thermal expansion stresses need not be considered. Furthermore, the current ASME Section XI procedures do not explicitly require SAM stresses to be considered, regardless of the material.

The R6 analysis classifies certain secondary stresses, such as thermal expansion and other displacement-induced stresses (SAM), as effectively being primary stresses if there is significant elastic follow-up at the crack section. These stresses will not generally be self-equilibrating as is typically assumed for secondary stresses, such as weld residual stresses.

In a similar view, the LBB procedures specified in draft Standard Review Plan (SRP) 3.6.3 have an option that allows the thermal expansion stresses to be considered in the stability analysis of cracks in austenitic submerge-arc and shielded-metal-arc welds, but not in the stability analysis of cracks in austenitic wrought base metals and TIG welds. For ferritic materials, this option is not given so that secondary and primary stresses are combined.

A.2 RESULTS OF PRIOR PIPE-SYSTEM EXPERIMENTS

The results from the IPIRG pipe-system experiments indicate that for large cracks, where the failure stresses are below the general yield strength of the uncracked pipe, the thermal expansion and SAM stresses contributed just as much to fracture as did the primary stresses, see Figure A.1. Figure A.1 shows a plot of the maximum experimental stress normalized by the Net-Section-Collapse (NSC) stress for five quasi-static bend and five pipe-system experiments conducted as part of the IPIRG (Refs. A.1 and A.2) and related programs (Refs. A.3 and A.4). The crack sizes in each of these experiments were relatively large, such that the failure moments were low enough that plasticity was restricted to the crack section. The maximum experimental stresses have been normalized by the NSC stress to account for slight differences in pipe size and crack size. For each experiment, the maximum stress has been broken down into its various stress components, i.e., primary membrane, primary bending (inertial), seismic anchor motion, and thermal expansion (For the quasi-static bend companion experiments, the only stress components applicable are primary membrane and primary bending [quasi-static bending]). From Figure A.1 it can be seen that if the thermal expansion and SAM stresses are ignored in the stress terms for the pipe-system experiments, then the normalized failure stresses for the pipe-system experiments would only be 40 to 50 percent of normalized failure stresses for the quasi-static bend experiments. Consequently, it appears from these results that secondary stresses do contribute to fracture, at least for the case of large surface cracks where plasticity is limited.

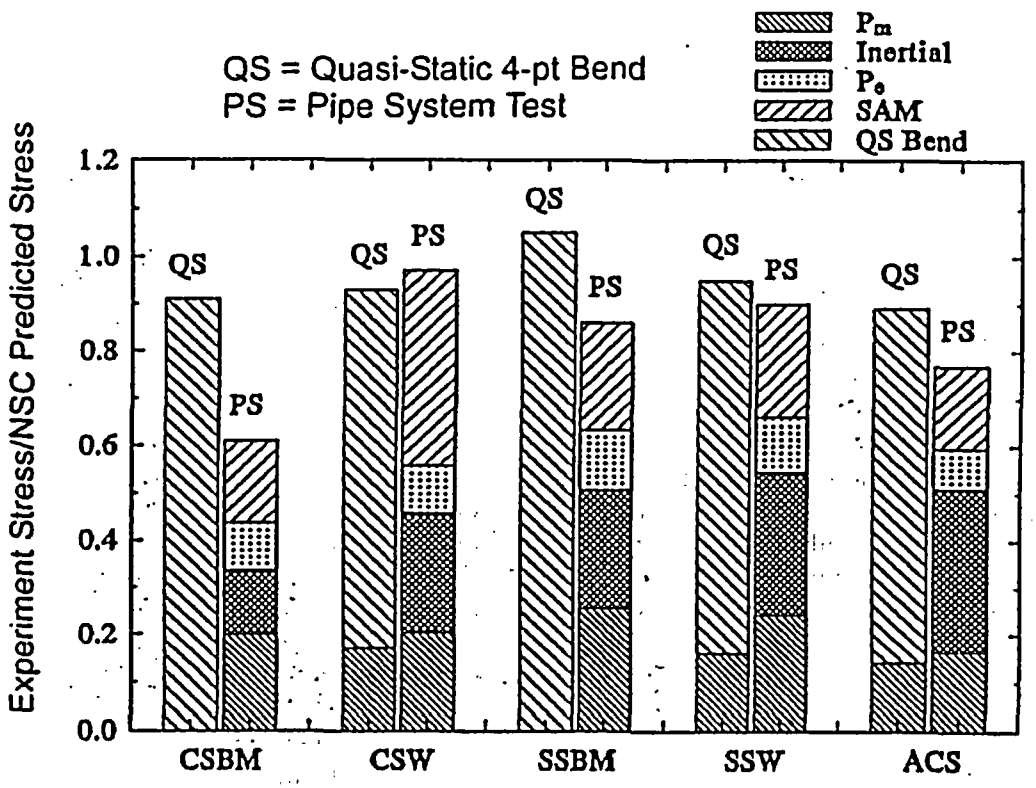

Figure A.1 Comparison of the results from the IPIRG-1 pipe-system experiments with companion quasi-static, four-point bend experiments demonstrating how global secondary stresses, such as thermal expansion and seismic anchor motion stresses, contribute to fracture

A.3 BINP TASK 1 EXPERIMENT

As part of this effort in the BINP program, another pipe-system experiment (BINP Experiment 1) was conducted. For this experiment the actuator was intentionally offset at the beginning of the experiment, prior to the application of the dynamic cyclic load history, to simulate a larger thermal expansion stress. Figure A.2 is a plot of the actuator time history for this experiment along with the actuator time history for its companion pipe-system experiment from the First IPIRG program, i.e., Experiment 1.3-5. The crack for both of these pipe-system experiments (1.3-5 from IPIRG-1 and BINP Experiment 1) was located in the center of a stainless steel submerge-arc weld. The crack sizes for both experiments were nominally the same, i.e., 50 percent of the pipe circumference in length and 66 percent of the pipe wall thickness in depth. From Figure A.2 it can be seen that the actuator for the BINP experiment was offset an additional 56 mm (2.2 inches) at the start of the experiment with respect to the actuator displacement for the IPIRG-1 experiment. This additional static offset in displacement resulted in an additional 255 kN-m (2,257 in-kips) of static moment at the crack section.

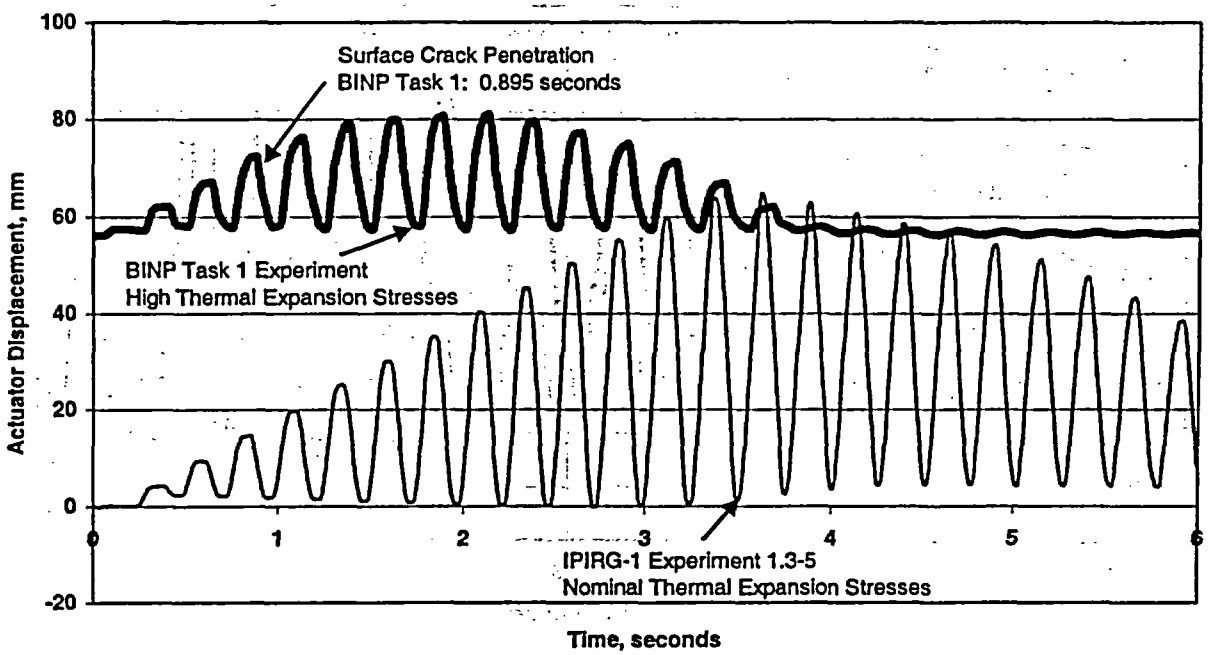

Figure A.2 Actuator time history for BINP Task 1 experiment and IPIRG-1 Experiment 1.3-5

Figure A.3 is a plot of the crack section moment as a function of time for these two pipe-system experiments up to the instant when the surface crack penetrated the pipe wall thickness. From this figure it can be seen that the total moment at the crack section at the instant of surface crack penetration was comparable for the two experiments. This further supports the contention that these global secondary stresses (thermal expansion and SAM stresses) contribute just as much to fracture as do the primary stresses, at least for the case where the stresses in the uncracked pipe are below the yield strength of the pipe. From Figure A.4, which is a similar plot as Figure A.1, except it shows the results for the four stainless steel weld experiments (Experiment 4141-4 from the Degraded Piping Program, Experiment 1.3-5 from IPIRG-1, Experiment 1-5 from IPIRG-2, and the BINP Task 1 experiment), it can be seen that the primary stresses for the BINP Task 1 experiment represented only 35 percent of the total stress at maximum load.

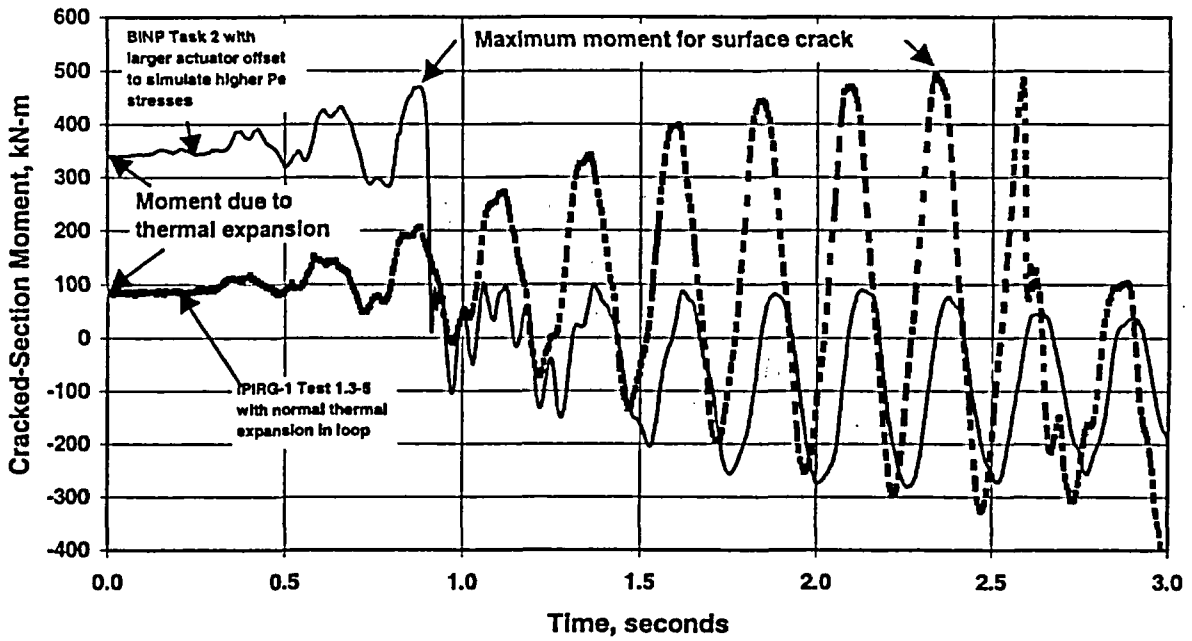

Figure A.3 Plot of crack section moment as function of time for BINP Task 1 experiment and IPIRG-1 Experiment 1.3-5

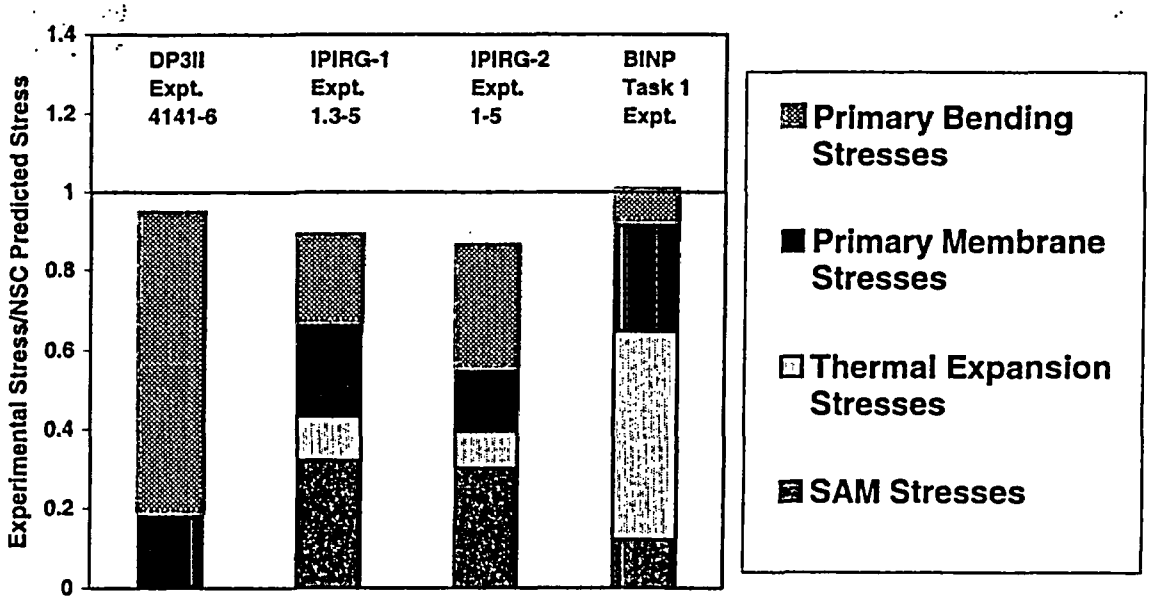

Figure A.4 Comparison of the results from four stainless steel weld experiments showing the contributions of the various stress components to pipe fracture

These findings support the contention that the thermal expansion and seismic anchor motion (SAM) stresses (secondary stresses) are as detrimental as the primary stresses, at least for these test conditions for which the stresses at failure for the uncracked pipe were less than the yield strength of the material.

For such conditions, there is the potential for elastic follow-up. Section III of the ASME code recognizes this potential in its local overstrain criteria in paragraph NC-3672.6(b). This paragraph implies that global secondary stresses, such as thermal expansion and seismic anchor motion stresses, can act as primary stresses under certain conditions, such as when the weaker or higher stressed portions of the piping system are subjected to strain concentrations due to elastic follow-up of the stiffer or lower stressed portions. One such obvious example of this is the IPIRG pipe system in which a large crack is introduced into a weaker material (lower yield strength) than the surrounding materials. Consequently, the resultant stresses for the uncracked pipe sections were less than the yield strength at the time of failure of the cracked section. The implication is that the safety margins for secondary stresses may be a function of the ratio of the failure stress to the yield strength. If the failure/yield stress ratio is less than 1.0, then global secondary stresses should probably be treated the same as primary stresses for fracture in the stability/critical crack size analyses. If the opposite holds true, then the global secondary stresses may become less important with some nonlinear function.

A.4 REFERENCES

A.1 Scott, P., Olson, R., and Wilkowski, G. Marschall, C., and Schmidt, R., "Crack Stability in a Representative Piping System Under Combined Inertial and Seismic/Dynamic Displacement-Controlled Stresses – Subtask 1.3 Final Report," NUREG/CR-6233, Vol. 3, June 1997.

A.2 Scott, P., Olson, R., Marschall, C., Rudland, D., Francini, R., Wolterman, R., Hopper, A., and Wilkowski, G., "IPIRG-2 Task 1 – Pipe System Experiments with Circumferential Cracks in Straight-Pipe Locations," NUREG/CR-6389, February 1997.

A.3 Wilkowski, G., and others, "Degraded Piping Program – Phase II, Summary of Technical Results and Their Significance to Leak-Before-Break and In-Service Flaw Acceptance Criteria – March 1993 – December 1994," NUREG/CR-4599, Vol. 8, March 1989.

A.4 Kanninen, M., and others, "Instability Predictions for Circumferentially Cracked Type 304 Stainless Steel Pipes Under Dynamic Loadings," EPRI Report NP-2347, April 1982.

APPENDIX B

PIPE-SYSTEM EXPERIMENT WITH AN ALTERNATIVE SIMULATED SEISMIC LOAD HISTORY

In the IPIRG-2 program two surface-cracked pipe-system experiments were conducted using a simulated seismic load history for the forcing function. For both experiments the test specimens contained internal circumferential surface cracks located at the same location as the cracks for the previously conducted IPIRG-1 pipe-system experiments. The cracked test specimens for these two IPIRG-2 pipe-system experiments were sections of A106 Grade B carbon steel and Type 304 stainless steel.

Of note from the analysis of these experiments was the fact that the load-carrying capacities of the simulated seismic experiments were higher than anticipated. There did not seem to be much of an effect of the cyclic history on the load-carrying capacity of the cracked section. One possible explanation for this observation was that the seismic history applied had a large cycle earlier in the time history, see Figure B.1, which resulted in a large moment cycle to occur at the crack section early in the experiment. It was during this large moment cycle that the crack initiated and began to grow. Consequently, the resultant moment-time history for the crack section looked very much like a dynamic-monotonic load history, see Figure B.2. As can be seen in this figure there were a number of small elastic cycles, very early in the time history, then the one large plastic cycle, during which the crack initiated, followed by another series of elastic cycles.

As a result, it was thought that the effects of cyclic loading due to a seismic loading event may not have been properly evaluated in these experiments. As such, it was decided to conduct a third surface-cracked simulated seismic pipe-system experiment as part of the BINP program with an alternative simulated seismic forcing function. The alternative seismic history would be designed such that there were more plastic cycles prior to crack initiation. This appendix describes the design of this alternative seismic history as well as presents the results and the analysis of this experiment.

B.1 DESIGN OF ALTERNATIVE SIMULATED SEISMIC FORCING FUNCTION

B.1.1 Background

Design of the forcing function used in the IPIRG-2 experiments was a well-considered process (Ref. B.1) using the following design criteria:

- Used accepted nuclear plant seismic design procedures
- Met various seismic regulatory guideline performance criteria
- Met TAG desires for percentage of inertial loading and stress ratio
- Seemed rational when compared with other seismic "floor" excitations
- Fit within the loading capabilities of the IPIRG pipe loop test system
- Was suitable for all of the IPIRG-2 simulated seismic experiments.

Although the IPIRG-2 forcing function met all of the design criteria, it did have the one previously mentioned deficiency that was not recognized until after all the experiments had been completed: the forcing function was not very challenging in terms of cyclic damage effects.

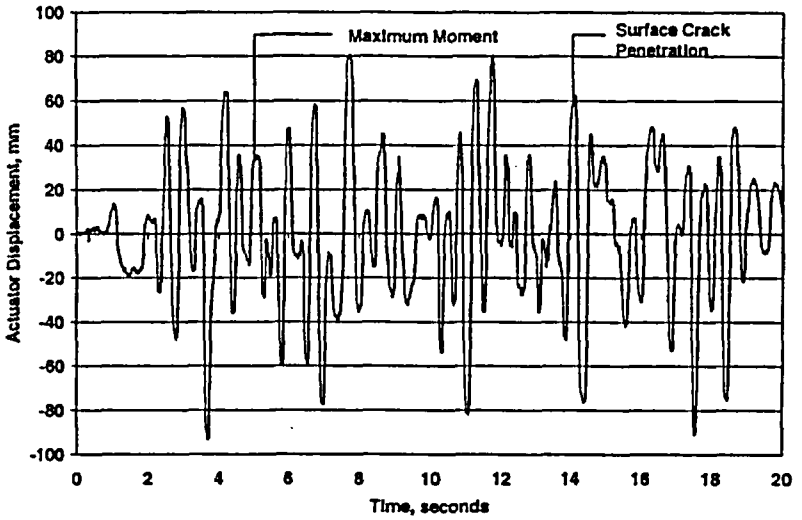

Figure B.1 Actuator displacement-time history for IPIRG-2 simulated seismic forcing function for stainless steel base metal experiment (Experiment 1-1)

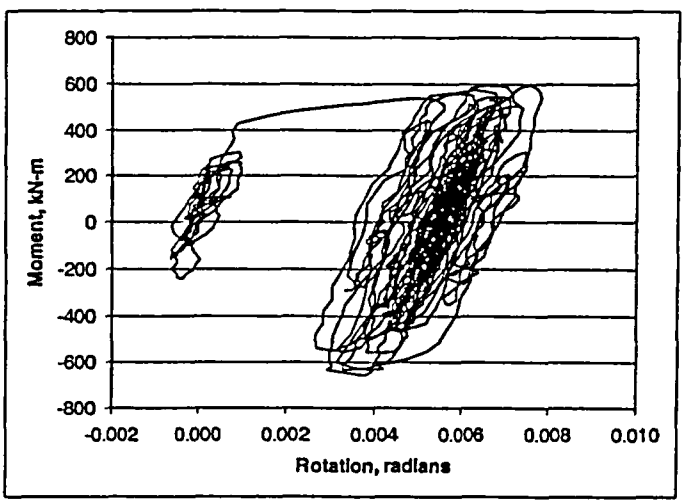

Figure B.2 Moment-rotation response for IPIRG-2 simulated seismic forcing function for stainless steel base metal experiment (Experiment 1-1)

Task 2 of the Battelle Integrity of Nuclear Piping (BINP) Program provided an opportunity to revisit the issue of the effects of cyclic, variable-amplitude, multi-frequency loading on the behavior of cracked pipe. Thus, in light of the understanding of cyclic and dynamic damage mechanisms that eventually existed at the end of the IPIRG-2 program, the BINP TAG members decided to conduct another simulated-seismic loading test in the IPIRG pipe-loop facility with a seismic forcing function that would be more challenging to the crack.

B.1.2 Design Issues for the BINP Seismic Forcing Function

The design of a seismic forcing function involves two distinct elements: 1) the selection of the loading and, 2) the analysis of the effect of the seismic loading on the cracked pipe. Because cracked pipe behavior is nonlinear, the

analysis must be done in the time domain to capture all of the load history effects and this, in turn, requires that the loading be defined in terms of a time history. Thus, the objective for the design of the BINP simulated-seismic forcing function was to find a "seismically inspired" time history of the pipe-loop system actuator motion that was potentially more damaging to a cracked pipe than the IPIRG-2 seismic time history.

Within this rather broad prescription for the design process, there are three basic issues that need to be considered:

1. The approach used to design the loading,
2. Material response issues, and
3. The implementation of the material response in the nonlinear analysis.

Each of these issues played a significant role in coming up with the final design for the BINP seismic forcing function and thus, deserves to be documented.

B.1.2.1 Design Approaches - There are a number of different approaches that can be used to design a seismic time history. Among the approaches, three good candidates are:

1. Use traditional seismic design procedures; ground motion developed from design response spectra – time history applied to a building – building motion applied to the pipe,
2. Design a "bounding" time history of excitation, and
3. Synthesize a time history from a floor response spectrum.

Consideration was given to using all three of these approaches in this effort before the third method was selected.

The first approach was the one that was used to design the IPIRG-2 seismic forcing function. In this approach, five basic steps were followed:

1. The NRC Regulatory Guide 1.60 ground acceleration response spectrum provided the basic description of the seismic input.
2. An artificial time-history of ground acceleration was generated that was spectrum-consistent with Step 1.
3. A simple model of a pressurized water reactor (PWR) plant was used as a transfer function between the time-history ground acceleration and an assumed location for the pipe system.
4. The relative motion between two "floors" in the PWR model and the inertial loading represented the loading to be applied to the pipe system.
5. The time-history of actuator motion for the pipe loop was defined by finding a displacement-time history that would give the same moment-time response at the crack location as the multi-point excitation defined in Step 4.

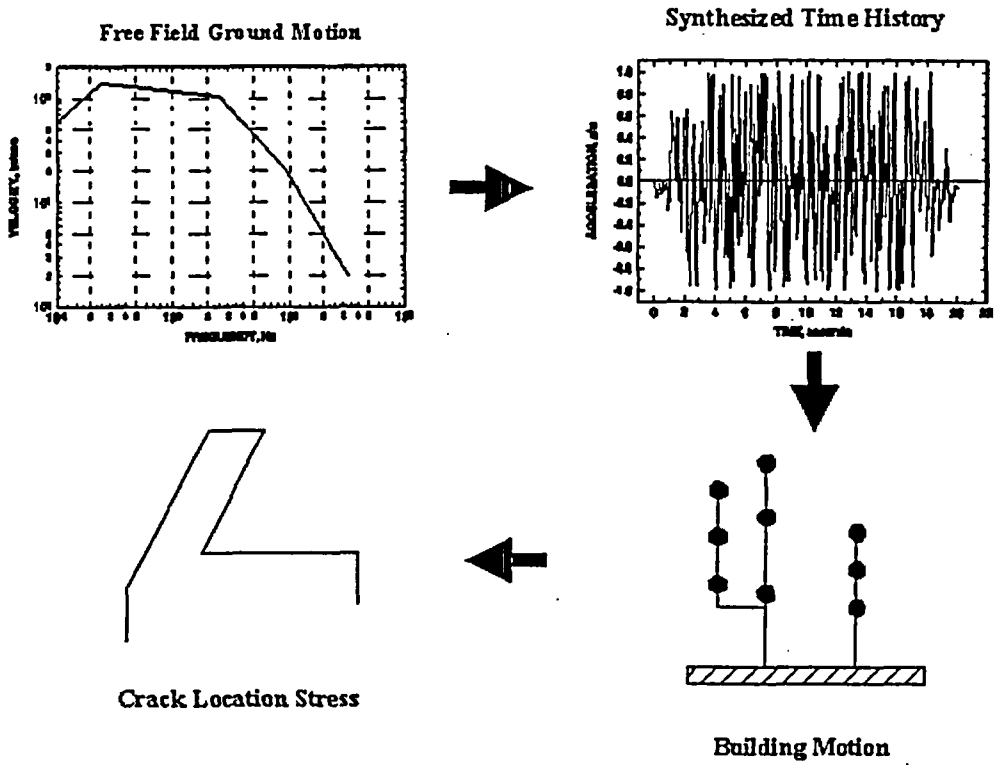

Figure B.3 Traditional seismic design process

Figure B.3 shows a pictorial representation of this seismic design process. This approach is not particularly difficult, but is quite tedious because many synthetic time histories must be considered. First, time histories must be qualified in terms of passing the seismic design rule prescriptions, and secondly, they must meet the BINP experiment requirements.

The second approach to designing a seismic time history was to use a "bounding" case type of loading. Based on the data available at the close of the IPIRG-2 program from C(T) specimen testing and the IPIRG pipe-system experiments, a worst case cyclic damage seismic time history was hypothesized to be as follows: single frequency excitation near the natural frequency of the pipe system, rise time of 3 to 5 seconds with increasing amplitude, strong motion duration of 4 to 15 seconds, and loading that makes the stress ratio less than -0.3 (i.e., significant compressive stresses at the crack location). Figure B.4 shows a conceptual idea of the "bounding case" forcing function. Assuming a 4 Hz natural frequency for a pipe system, 12 to 20 cycles of loading would occur in the build-up phase of the time history with 16 to 60 additional cycles that would continue to grow the crack after it has initiated. Such a time history would definitely invoke both cyclic and dynamic effects.

A third possible approach for designing the BINP seismic time history is to synthesize a time history from a floor response spectrum, see Figure B.5. This approach involves many of the same basic ideas as the first approach, but it is not quite as involved, given a target floor response. Unlike the second approach, this method has a solid foundation in seismic analysis techniques. It is, however, like the first approach, a trial and error process to find the right solution for the BINP program.

All three approaches for designing the BINP seismic time history were considered. The second method, the "bounding case" method, was very quickly dropped because it did not have enough of a seismic flavor. The first method, the IPIRG-2 design approach, was initially thought to be the best alternative since it already had good technical credentials. Unfortunately, the non-deterministic nature of the design process was judged to be a serious impediment. Regarding the last alternative, the floor response spectrum-based design, an IPIRG-2 Round Robin (Ref. B.2) conveniently was conducted on this very subject and thus, there was already a good body of basic data available for guiding the BINP seismic design. Because the round-robin results greatly simplified the design process, and because of the direct tie to the IPIRG-2 seismic forcing function, the floor-response spectrum analysis approach was selected for the BINP seismic forcing function design.

B.1.2.2 Material Property Issues - The test specimen to be used in the BINP simulated-seismic experiment was a nominal 16-inch diameter Schedule 100 TP304 stainless steel pipe, denoted as DP2-A8 in the Battelle material property library. This pipe has been used for a large number of the Degraded Piping Program and IPIRG experiments, and has been very well characterized in terms of stress-strain behavior and fracture toughness. Issues involved in the use of the TP304 base metal for the BINP test that have an impact on the seismic forcing function design include, which heat of TP304 is to be used in the experiment (high or low sulfur content) and which J-resistance behavior (quasi-static, dynamic, cyclic, monotonic) is most appropriate.

The pipe designated as A8 can have one of two different chemistries as documented in Reference B.3. Although both meet the TP304 specifications, eventually it was discovered in the IPIRG-2 program that the two different chemistries have very different fracture toughness levels, and different susceptibility to dynamic and cyclic loading effects, Figures B.6 and B.7. Not recognizing that all pipes delivered from the same lot and initially labeled as DP2-A8 are different can, in fact, disguise the role of cyclic and dynamic effects in pipe fracture experiments. Thus, it was important for the design of the BINP seismic forcing function to know which heat of TP304, A8i or A8ii, was going to be used in the experiment.

A second material property issue that impacts the design of the BINP seismic forcing function is the choice/selection of what kind of J-resistance curve to use: dynamic or quasi-static loading rates, at what stress ratio, and what cyclic plastic displacement. Clearly, the selection is based on the results of the pipe system stress analysis, which in turn is based on the selection of the J-resistance curve, i.e., it is a circular proposition.

The decision about A8i and A8ii was easily resolved by a chemical analysis, i.e., the BINP test specimen was from heat A8ii (the higher sulfur content, lower toughness heat). Likewise, the decision about whether to use dynamic or quasi-static data was quite easy, because the loading is dynamic. The appropriate stress ratio and cyclic plastic displacement increment to use was an iterative process driven by the dynamics and scaling of the forcing function.

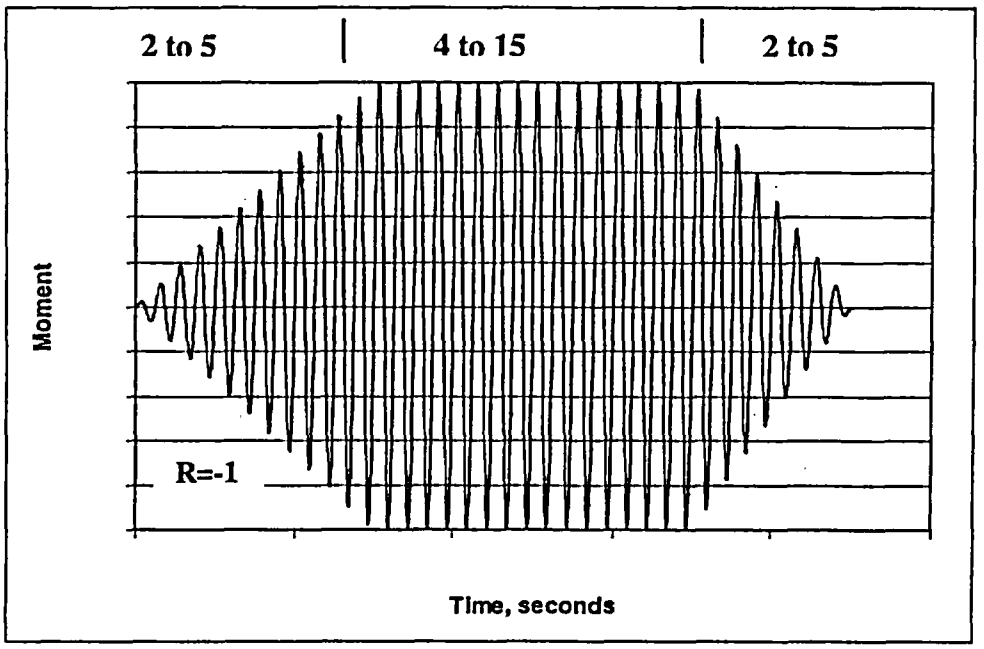

Figure B.4 Hypothesized worst case seismic loading

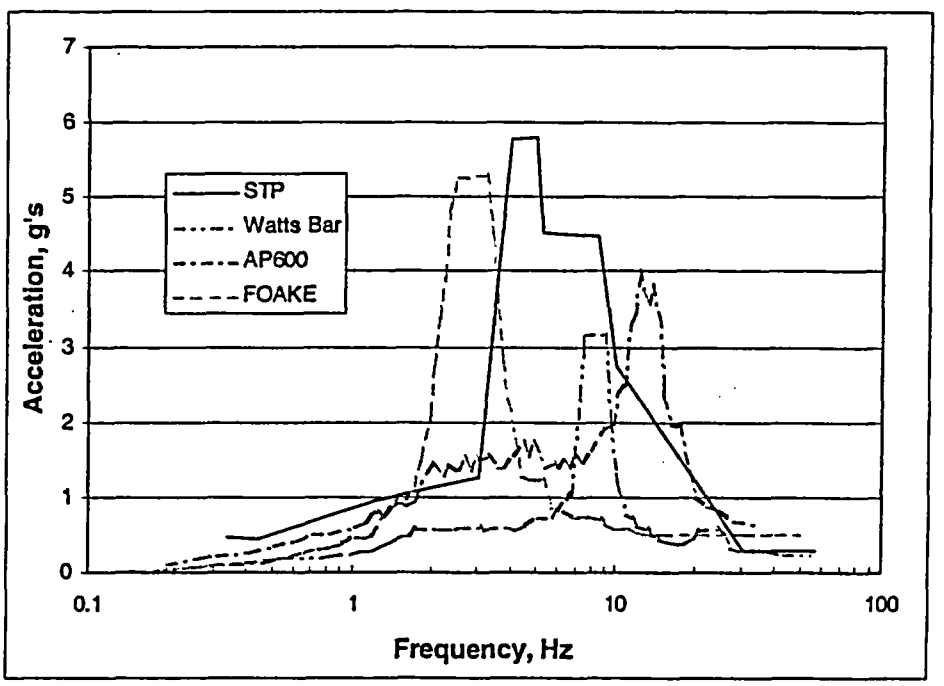

Figure B.5 Typical SSE seismic floor-response spectra

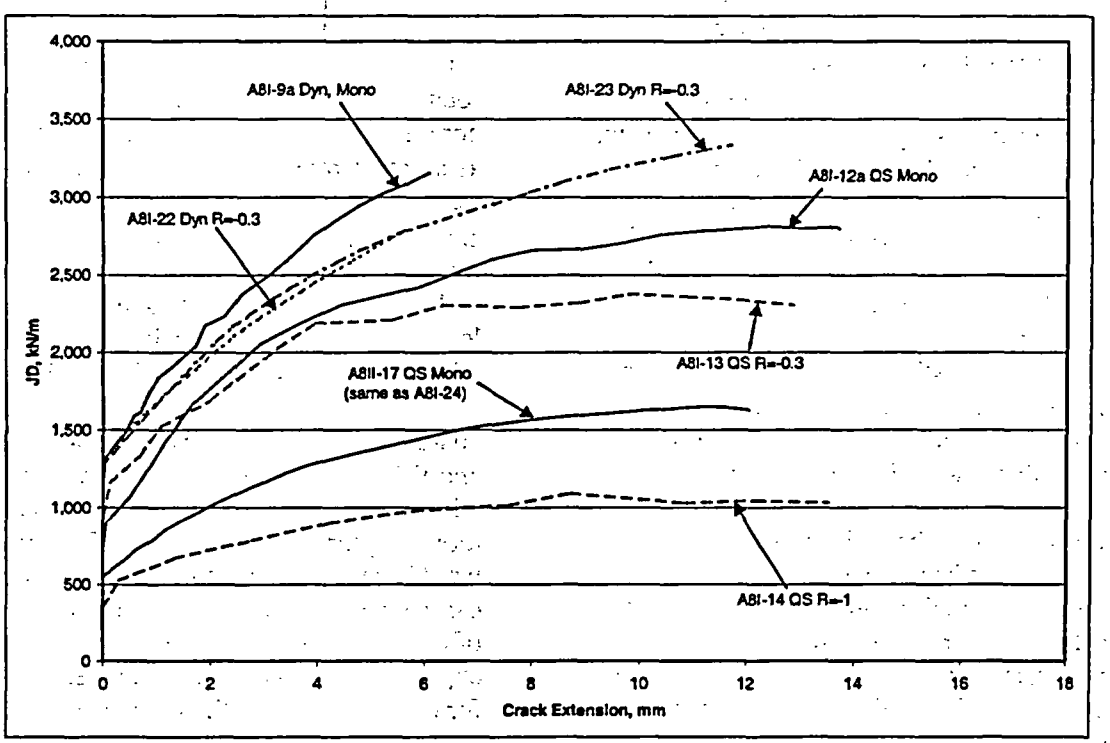

Figure B.6 Fracture toughness properties from pipe DP2-A8i

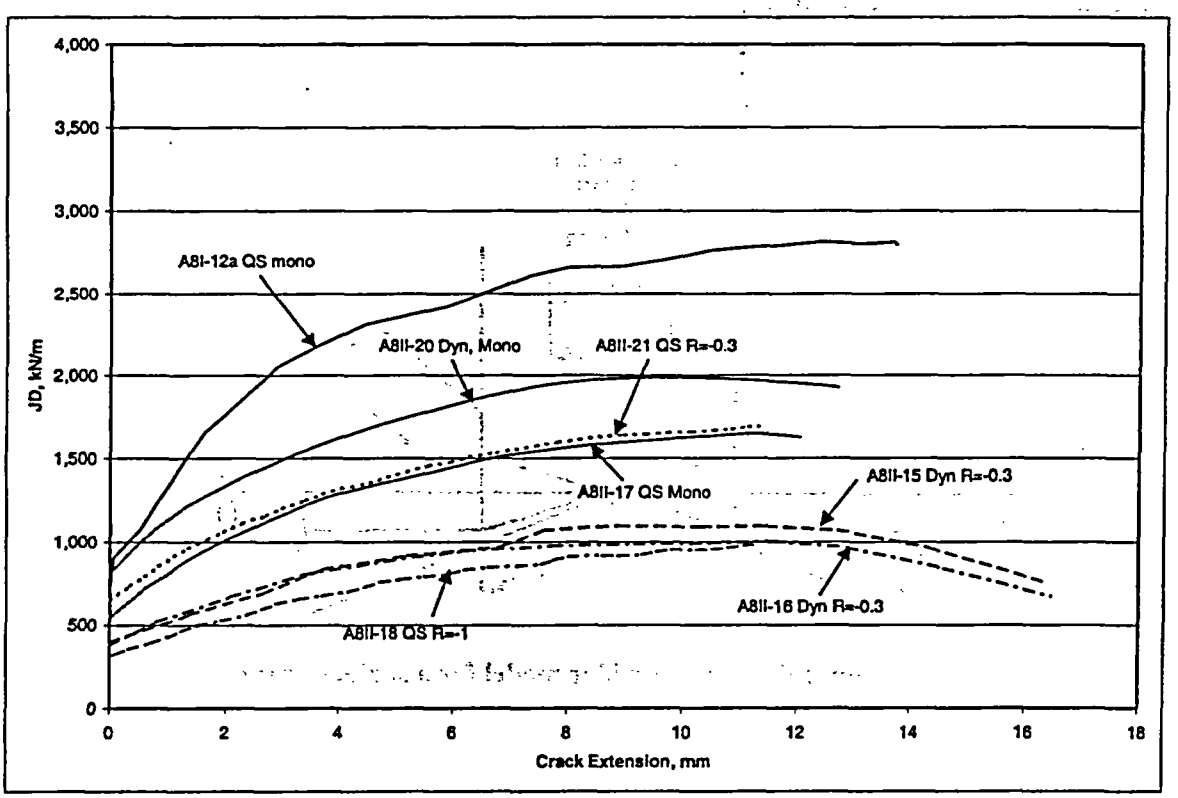

Figure B.7 Fracture toughness properties from pipe DP2-A8ii

B.1.2.3 ANSYS Implementation Issues - In all of the design exercises for the IPIRG pipe-system experiments, dynamic, nonlinear spring, time-history finite element analysis have been successfully used with analysis tools that have evolved to a fairly sophisticated level, Ref. B.4. In these previous analyses, the best available data have been used to define the crack nonlinear response – quasi-static pipe tests at first, moving to J-estimation scheme analyses with quasi-static J-R curves and stress-strain data, and finally ending with J-estimation scheme analyses with dynamic J-R curves.

The nonlinear crack behavior in the finite element analyses has been characterized as crack moment versus crack rotation and, for surface cracks, has been implemented as a set of three elastic-perfectly plastic springs in parallel, see Figure B.8. Implicit with the nonlinear spring formulation is the assumption of kinematic hardening, i.e., yielding in the compressive direction occurs at $2\sigma_y$ below a plastic unloading point, Figure B.9. This is equivalent to saying that the compressive moment-rotation response is the mirror image of the tension moment-rotation response. Furthermore, because the nonlinear behavior of the crack is modeled only as moment-rotation, effects such as axial loading, which affects the state of stress at the crack tip, must be "built into" the moment-rotation curve. That is, a crack with pressure and moment loading will have an apparently lower moment-rotation resistance than a crack with moment only loading, Figure B.10.

Historically, all of the analyses for the IPIRG-1 and IPIRG-2 programs have been conducted with moment-rotation curves developed for moment plus pressure loading. Intuitively, this would seem to be the correct thing to do and, for cases where the unloading is limited, i.e., most of the IPIRG single frequency loading experiments, it is quite reasonable. However, for cases where significant reverse loading is expected, i.e., seismic loading, compressive yielding will occur far too early if a pressure-corrected moment rotation curve is used.

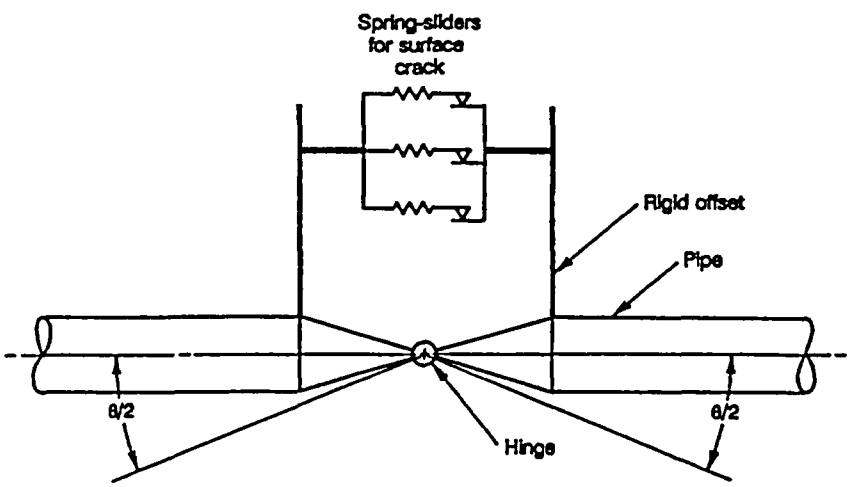

Figure B.8 Spring-slider model for a surface crack

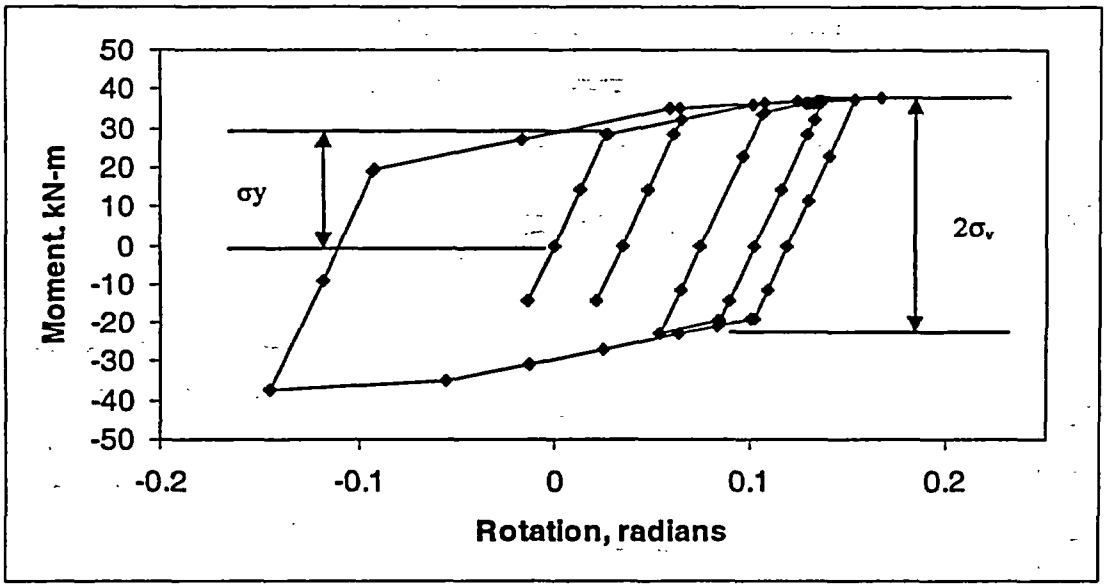

Figure B.9 Kinematic hardening assumption under unloading conditions

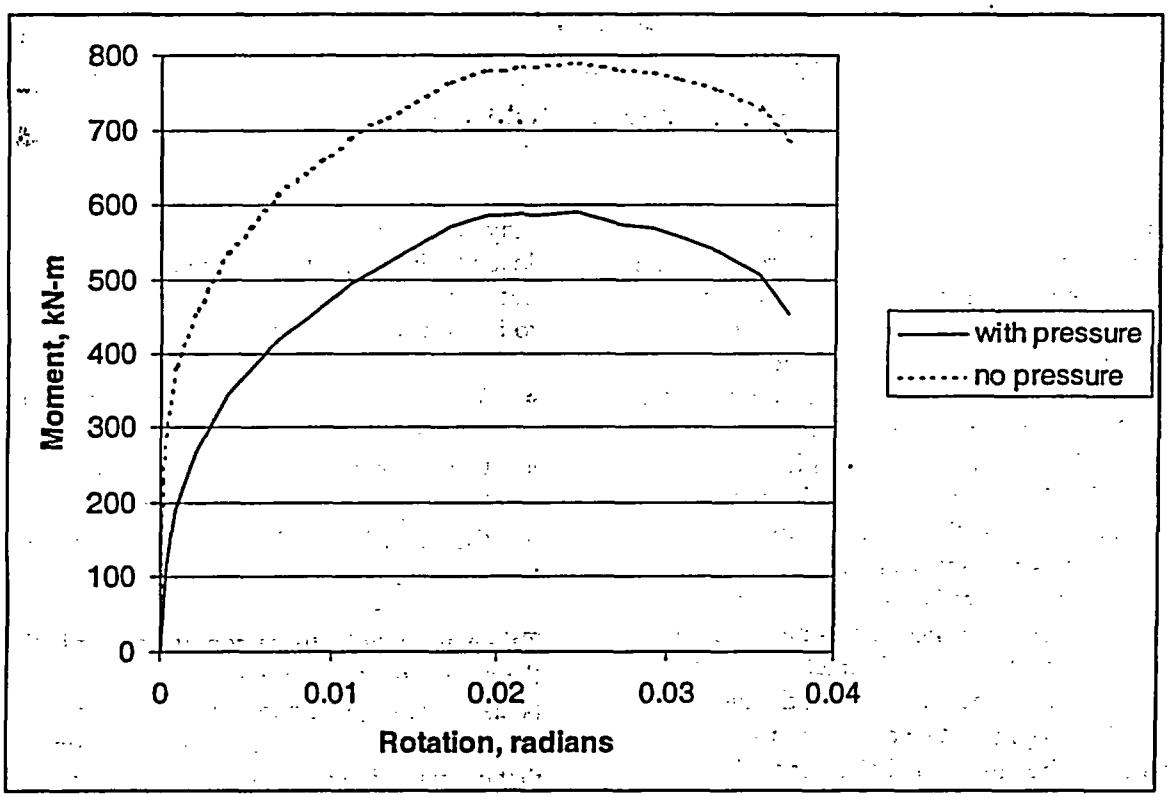

Figure B.10 The effect of pressure on crack moment-rotation behavior (BINP Task 2 flaw, A8ii-20 dynamic monotonic J-resistance)

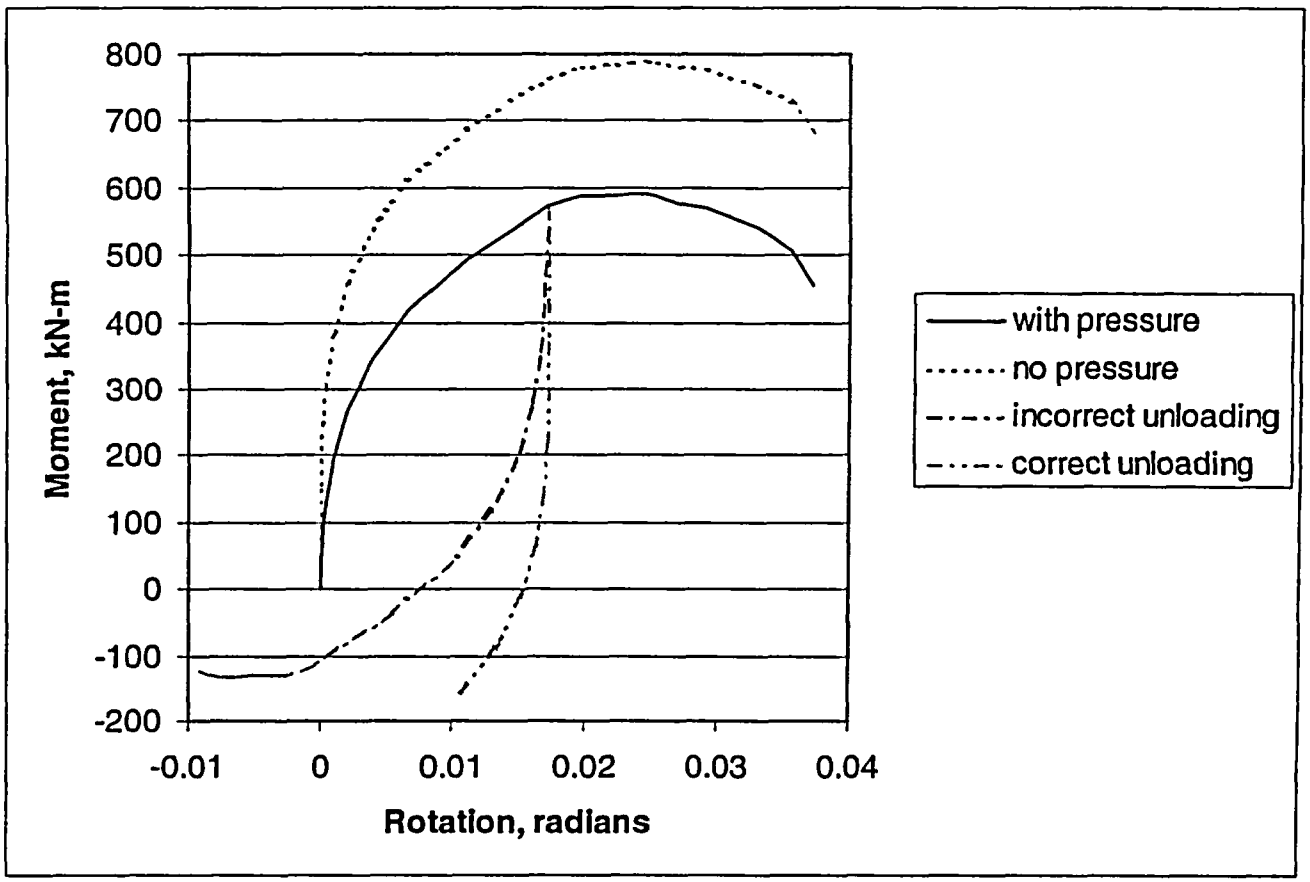

Figure B.11 Crack unloading behavior

Basically, because the pressure-corrected moment-rotation curve is the mirror image of the tensile moment-rotation curve, it is as if the stress at the crack tip, caused by pressure, changes sign when the crack is unloaded, a totally inappropriate response. The crack should unload elastically much further before it yields in compression, Figure B.11. This is quite important for the design of a seismic forcing function because it is the unloading that determines the stress ratio and hence, the amount of cyclic degradation that will occur. Like the fact that the IPIRG-2 seismic loading was not very challenging, this crack modeling deficiency was not recognized until the close of the IPIRG-2 program. Overcoming this deficiency in the unloading behavior of the nonlinear spring model requires that a slightly different approach be used to model the nonlinear behavior of cracks.

Any new modeling approach for surface cracks loaded with pressure and bending to better define the compressive loading behavior needs to include the following:

- Tensile loading failure based on pressure plus bending,
- Consistency with kinematic hardening rules, i.e., $2\sigma_y$ yielding behavior, and
- Compressive loading to account for the pressure effect.

Taken as a whole, these conditions imply that the moment-rotation response of the crack must be asymmetric, i.e., compression is not a mirror image of tension. The last two conditions imply that compressive yielding in moment-rotation coordinates must occur at twice the tensile yield moment (including the pressure effect) plus twice the pressure-induced moment effect.

Figure B.11 provides a pictorial representation of the desired behavior.

Implementation of asymmetry in the moment-rotation response in the finite element model would, in general, require a special constitutive model or a special element that ANSYS does not have in its standard element library. The desired response, however, can be achieved with the current elements as follows:

1. Define the expected tensile crack moment-rotation behavior using a J-estimation scheme analysis that includes pressure,
2. Define the pressure contribution to the tensile failure by running a J-estimation scheme analysis identical to the first one, but without pressure,
3. Use the data from the second analysis to define the "springs" and "sliders" for the nonlinear crack model,
4. Apply + and - crack opening moments at the two nodes of the spring-sliders equal to the moment difference between the results from Step 1 and Step 2, and
5. Conduct the analysis as usual.

The net effect of this process is to make the crack moment-rotation response appear asymmetric as far as tensile and compressive yielding of the crack is concerned. However, as far as the pipe system is concerned, everything is as it should be:

- The stresses in the pipe will be calculated correctly because the moments applied in Step 4 sum to zero.
- The incremental tensile moment that the crack can stand will be correct because the moments applied in Step 4 make up the difference between the moments the spring sliders in the model will permit and the real failure moment calculated in Step 1.

Validation Analyses - To provide some level of comfort that the new surface crack modeling approach is rational, an analysis of IPIRG-2 Experiment 1-1 was conducted to see how well the analysis compares with an experiment. (Experiment 1-1 is the "companion" IPIRG-2 seismic loading experiment to the present BINP experiment.) Figures B.12 and B.13 show the measured pipe response from the experiment up to surface-crack penetration.

IPIRG-2 Experiment 1-1 used Battelle pipe DP2-A8i. (Note: this is not the same material as used in the BINP experiment.) Available J-resistance curve data for DP2-A8i include quasi-static data (A8i-12a: monotonic, A8i-13: R = -0.3, A8i-14: R = -1.0), and dynamic data (A8i-9a: monotonic, A8i-22 and A8i-23: R = -0.3, A8i-24: R = -1.0). Stress-strain data at a variety of testing rates are also available, although no significant rate dependence has been observed for either DP2-A8i or DP2-A8ii. Obviously, the dynamic J-R data are most appropriate for this analysis.

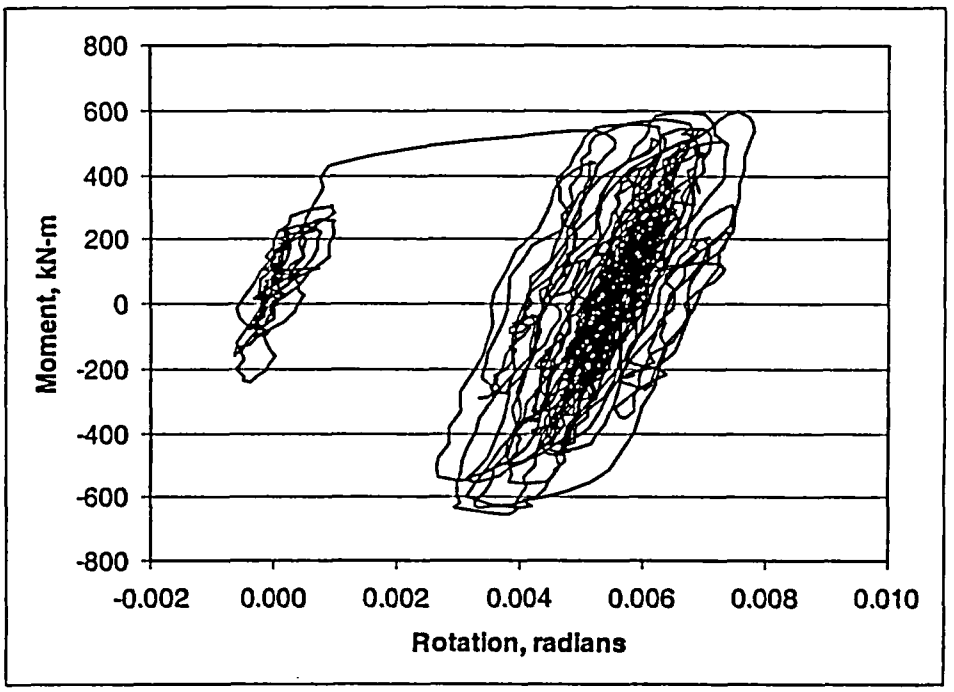

Figure B.12 IPIRG-2 Experiment 1-1 cracked-section moment-rotation response

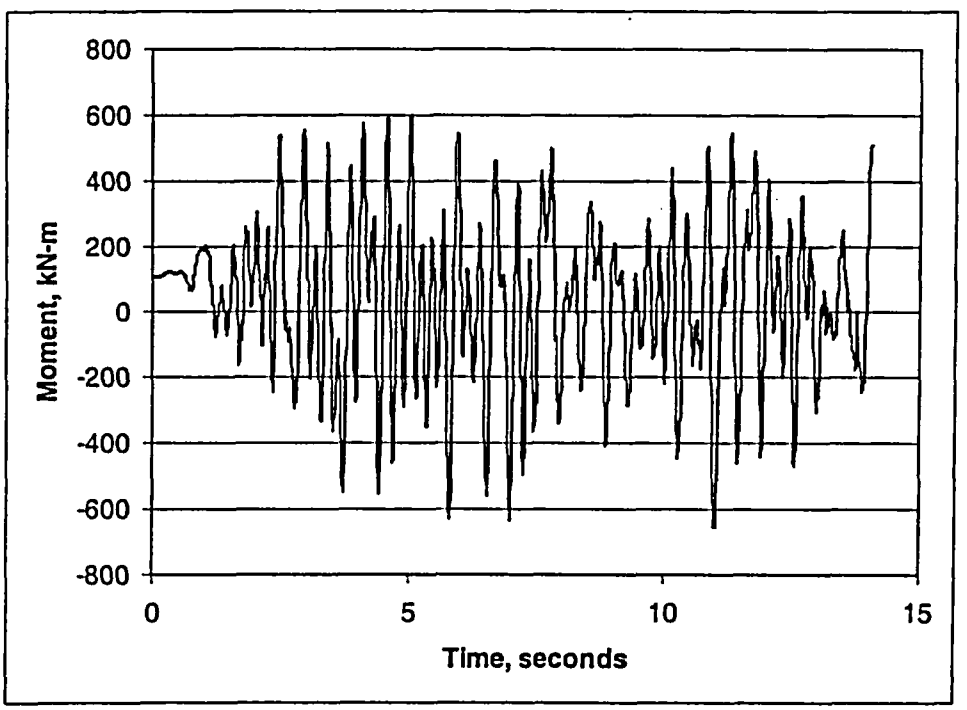

Figure B.13 IPIRG-2 Experiment 1-1 cracked-section moment-time history

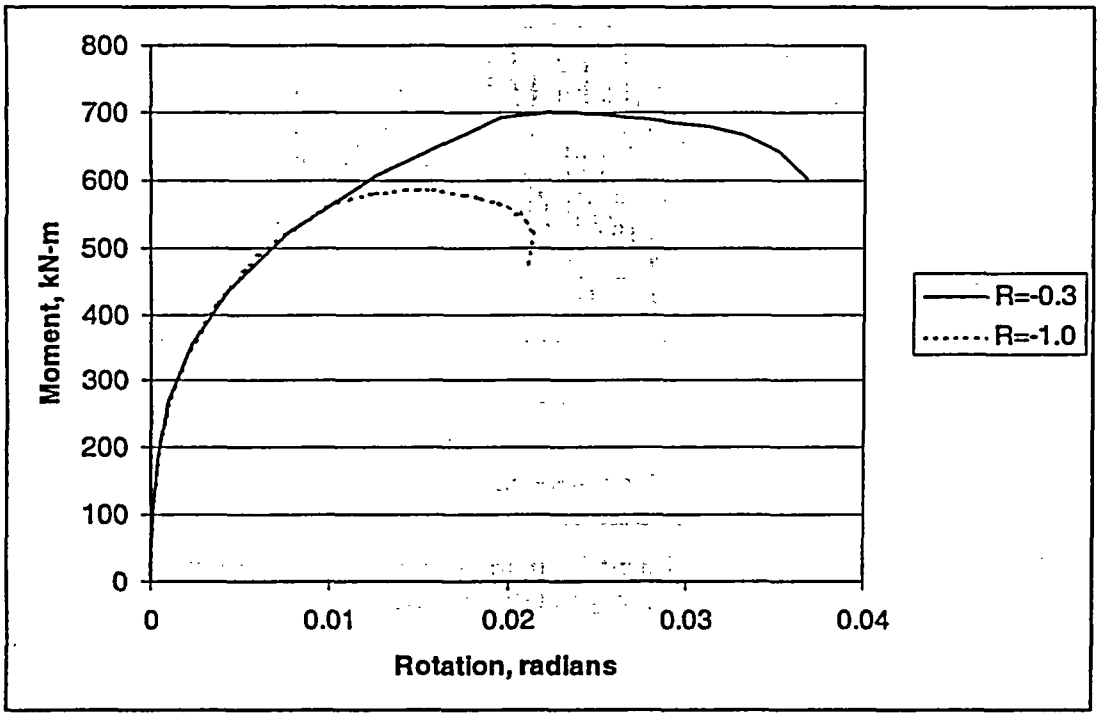

Figure B.14 IPIRG-2 Experiment 1-1 predicted cracked-section upper envelop moment-rotation from the SC.TNP1 J-estimation scheme

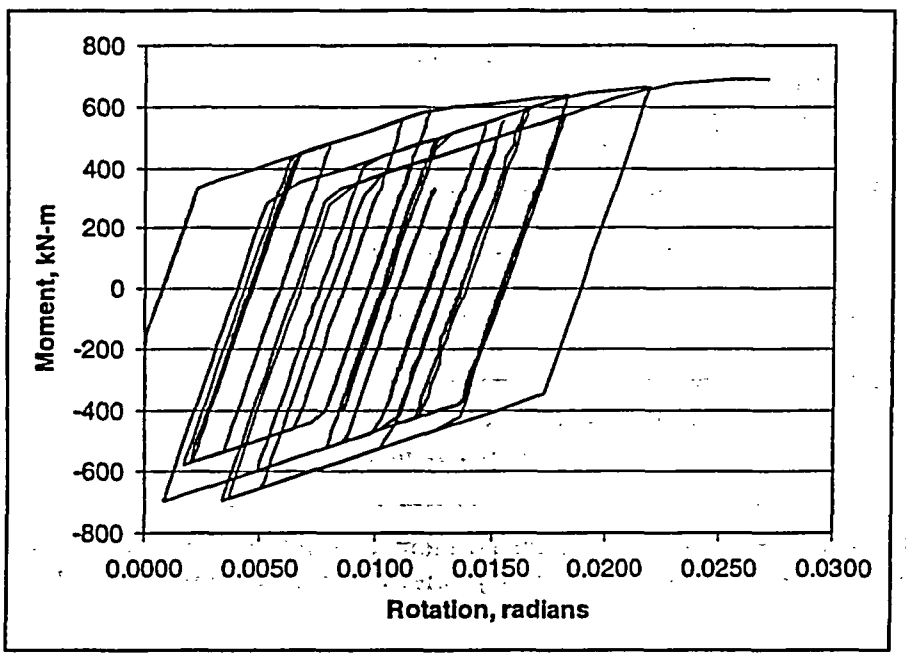

Figure B.15 Predicted IPIRG-2 Experiment 1-1 moment-rotation history using the dynamic R = -0.3 J-R curve with the new asymmetric moment-rotation model

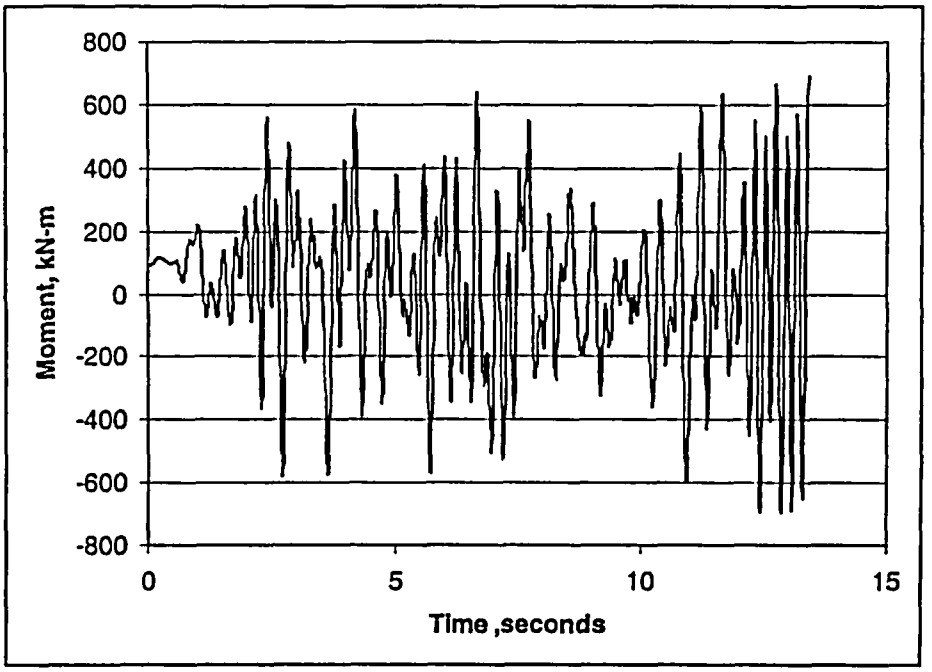

Figure B.16 Predicted IPIRG-2 Experiment 1-1 moment-time history with the dynamic R = -0.3 J-R curve with the new asymmetric moment-rotation model

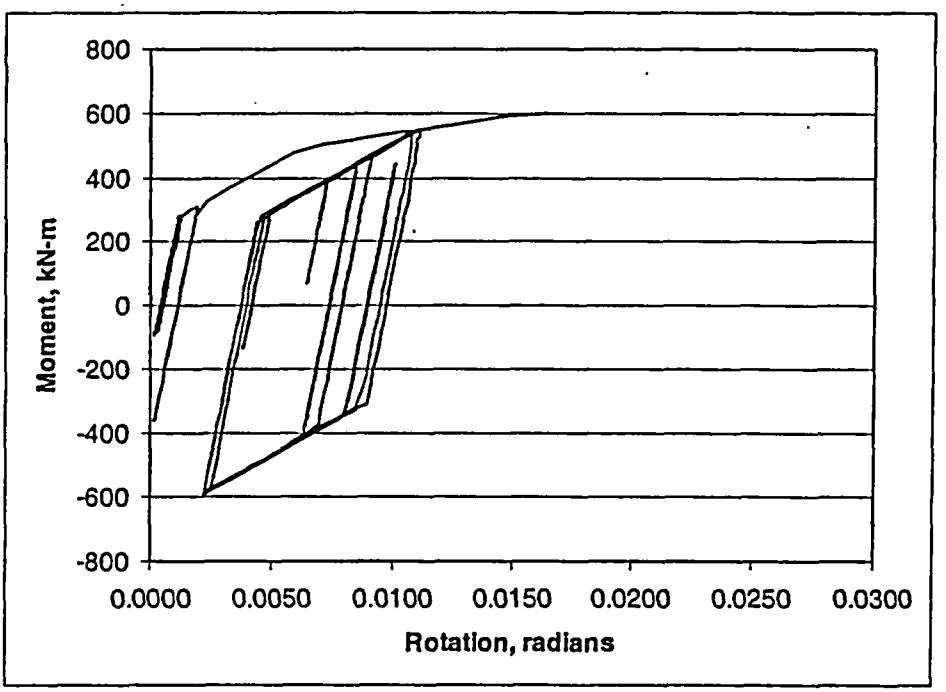

Figure B.17 Predicted IPIRG-2 Experiment 1-1 moment-rotation history with the dynamic R = -1.0 J-R curve with the new asymmetric moment-rotation model

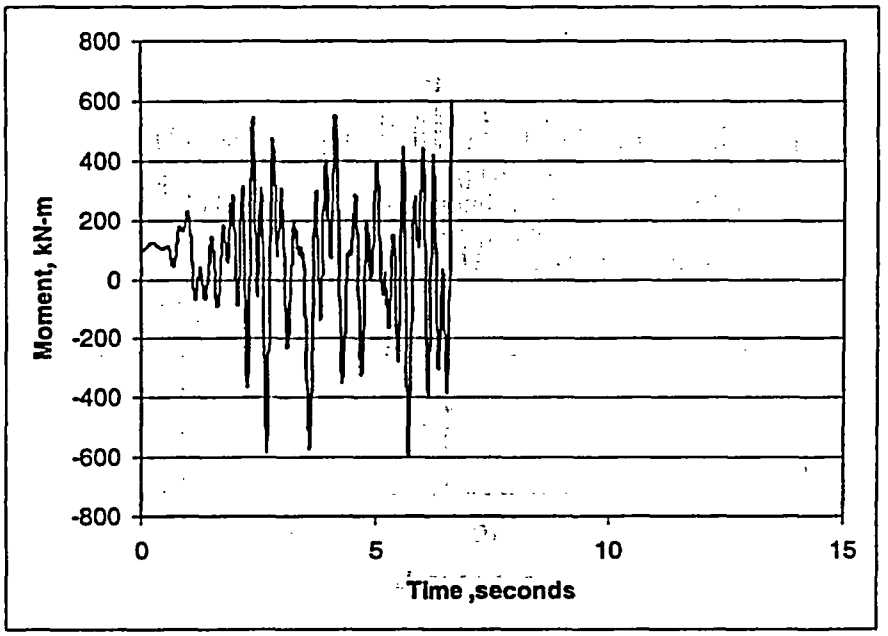

Figure B.18 Predicted IPIRG-2 Experiment 1-1 moment-time history with the dynamic R = -1.0 J-R curve with the new asymmetric moment-rotation model

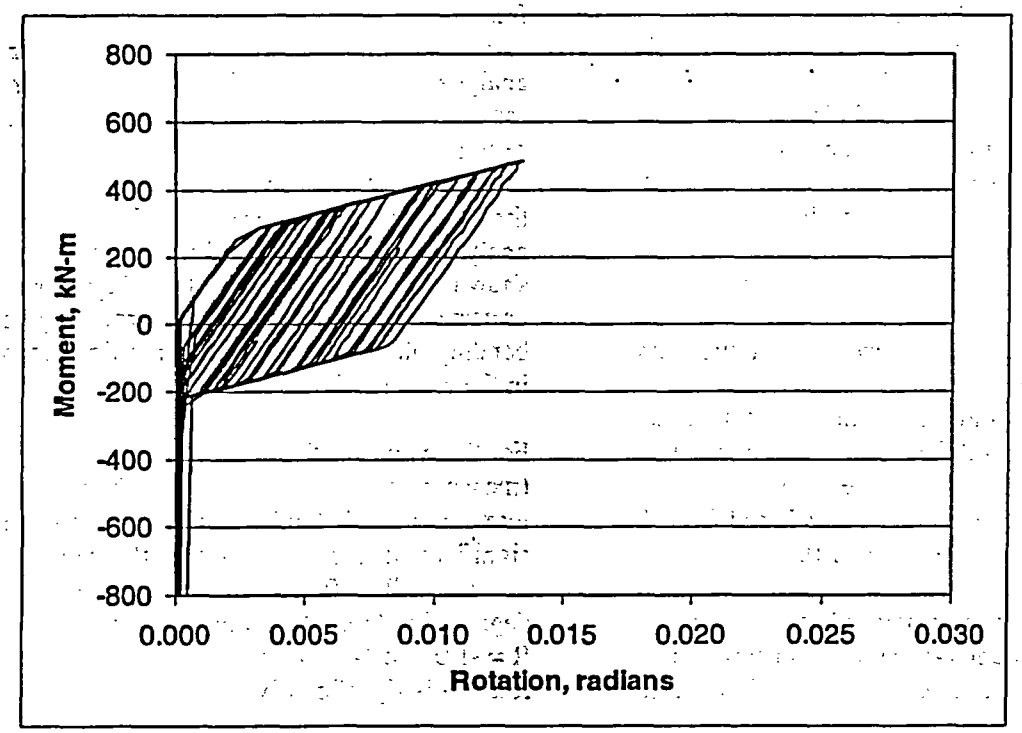

Figure B.19 Old (1993) IPIRG-2 Experiment 1-1 pretest design analysis moment-rotation history results

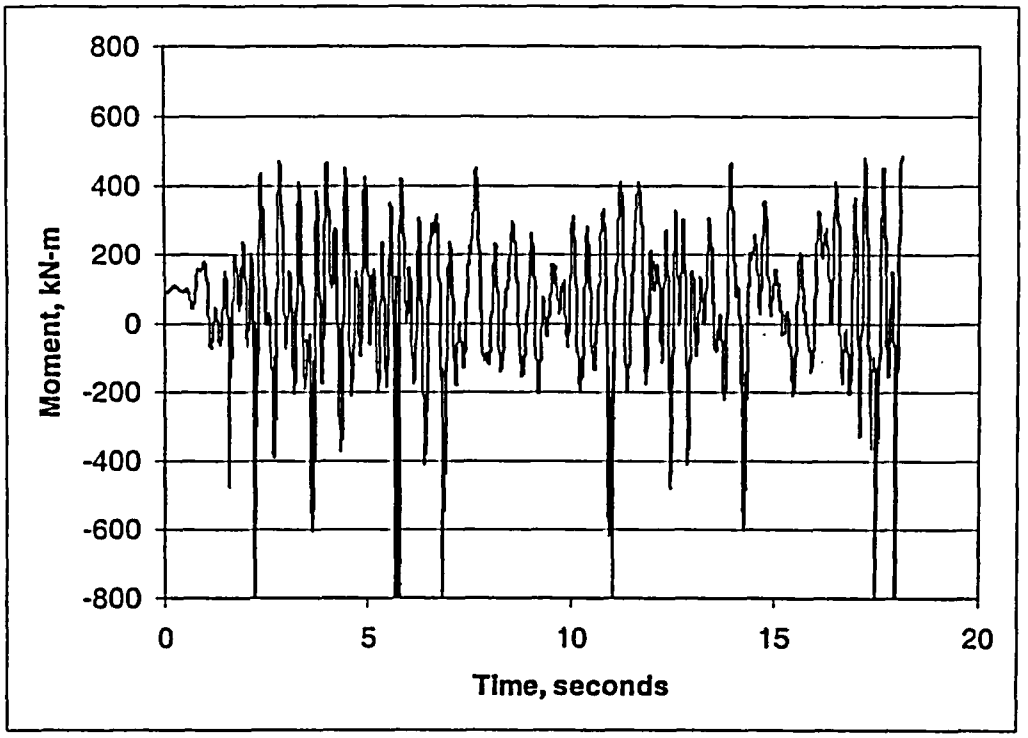

Figure B.20 Old (1993) IPIRG-2 Experiment 1-1 pretest design analysis moment-time results

The result of any analysis is driven by the selection of the moment-rotation response. This, in turn, is a function of the J-R curve, which is a function of the stress ratio and plastic displacement increments. In general, the stress ratio and plastic increments are not known until an analysis has been completed. In this case, however, because the results of the experiment are available, the "best" J-R curve can be immediately selected. Inspection of the experimental results of Experiment 1-1 suggests that the effective stress ratio (a function of the actual stress ratio and plastic increments) varies between R = -0.3 and R = -0.6. To bound the expected behavior, analyses were conducted using moment-rotation curves developed from J-R curves for R = -0.3 and R = -1.0.

The predicted moment-rotation behavior for the IPIRG-2 Experiment 1-1, generated using the SC.TNP1 analysis in NRCPIPES Version 3.0, is shown in Figure B.14.

Using the design seismic forcing function (there is virtually no difference between the designed function and the experimentally measured actuator response), ANSYS nonlinear-spring analyses were conducted to the point of maximum load, i.e., presumed surface-crack penetration, using the new compressive unloading behavior model. Figures B.15 through B.18 show the results of the "bounding" analyses. For reference, Figures B.19 and B.20 show the results of the IPIRG-2 Experiment 1-1 pretest analysis that used the mirror image of the bending plus tension moment-rotation response in the compressive regime.

For these curves, the equivalent crack length (measured crack area divided by the measured maximum crack depth) was used. There are significant differences between these curves because at R = -0.3, there is very little degradation from the monotonic case, whereas at R = -1.0, the J-R curve, and hence moment-rotation is significantly affected.

Comparing Figures B.12, B.15, B.17, and B.19, qualitatively, the new analyses are much closer to the experiment than the "old" analysis in two

regards: 1) the new analyses do not show the severe crack closures that the old analysis did, and 2) the new analyses show evidence of the large monotonic load cycle that the old analysis did not predict. Quantitatively, the new analyses bracket the experimentally observed failure moment, whereas the old analysis is low, although there is a good reason for this – the old analysis was a pretest prediction that used the best pretest estimate of the flaw size, whereas the new analyses used the measured flaw size. Quantitatively, it is also important to note that the rotations in the new analyses are very much larger than the experimentally observed rotations. This is a J-estimation scheme problem – the ANSYS nonlinear spring analysis is only as good as the input from the J-estimation scheme. As a final observation, in the experiment, surface-crack penetration occurred long after maximum moment.

Within the bounds of the ANSYS nonlinear spring analysis, this just cannot be predicted because surface-crack penetration is defined to happen at maximum moment. From an experimental perspective, what this implies is that there was either cyclic or fatigue damage that contributed to the eventual failure.

In general, the new analysis appears to be an improvement upon the previous method. The crack closures that are a part of the old technique would profoundly bias a seismic design analysis because it would suggest that the stress ratio was much more negative than it really is. Since stress ratio is one of the principal governing factors in cyclic damage, it is important to calculate it correctly. The new analysis technique, although not perfect, is a distinct improvement over the old technique and should lead to a better design for the BINP simulated-seismic experiment.

B.1.3 Design Details for the Simulated-Seismic Forcing Function

B.1.3.1 Design Process - The BINP seismic forcing function design process, as noted earlier, was based on developing a time history from a floor-response spectrum. In particular, the design was based on the results of IPIRG-2 Round-Robin Problem C.1, "Spectrum-Compatible Time-Histories". In this round robin, the participants were given a peak-broadened IPIRG-2 SSE actuator acceleration response spectrum at 2-percent damping, Figure B.21, and were asked to provide a spectrum-compatible displacement-time history of actuator motion. The resulting motion was then applied to a linear elastic finite element model of the IPIRG pipe loop by Battelle to see the effect of different "equivalent" time histories on applied crack bending moment.

Four solutions to the round-robin problem were submitted and all solutions were based on the same methodology: acceleration was assumed to be the sum of a number of sine functions with variable amplitudes and random phase angles, sine amplitudes were fixed using an iterative process, "raw" accelerations were somehow filtered to meet target maximum displacement prescriptions.

The key feature of this round-robin problem that led it to be considered for the design of the BINP seismic forcing function was that two of the submitted solutions, F-3a and D, show a nice build-up of moment at the early part of the solutions for linear analysis, Figures B.22 and B.23. Figures B.24 and B.25 show the corresponding actuator time histories from Solutions F-3a and D at an SSE scaled level. Given the two candidate time histories of actuator motion, the BINP seismic forcing function design process reduced to finding the best scaling and "tuning" factors for one of the histories so that it would meet the BINP seismic forcing function design goals. As suggested earlier, the scaling and tuning process is iterative, involving a significant number of nonlinear analyses. The guiding principles for the design were a desire to have significant cyclic degradation (stress ratio at or below R=-0.3, see Figure B.25), a desire to have gradual build-up of stress amplitude with about 10 plastic displacement (rotation) cycles, and a desire to have failure occur in the range of 5 to 10 seconds.

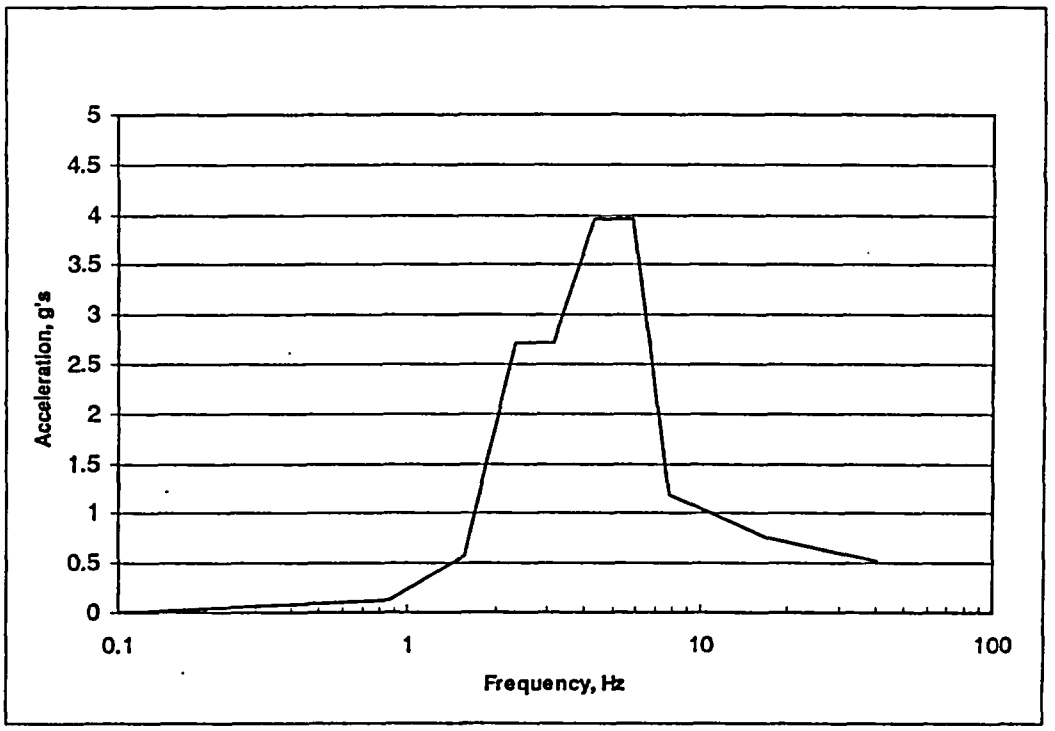

Figure B.21 The IPIRG-2 Round-Robin Problem C.1 floor-response spectrum (IPIRG-2 simulated-seismic forcing function actuator acceleration at SSE loading)

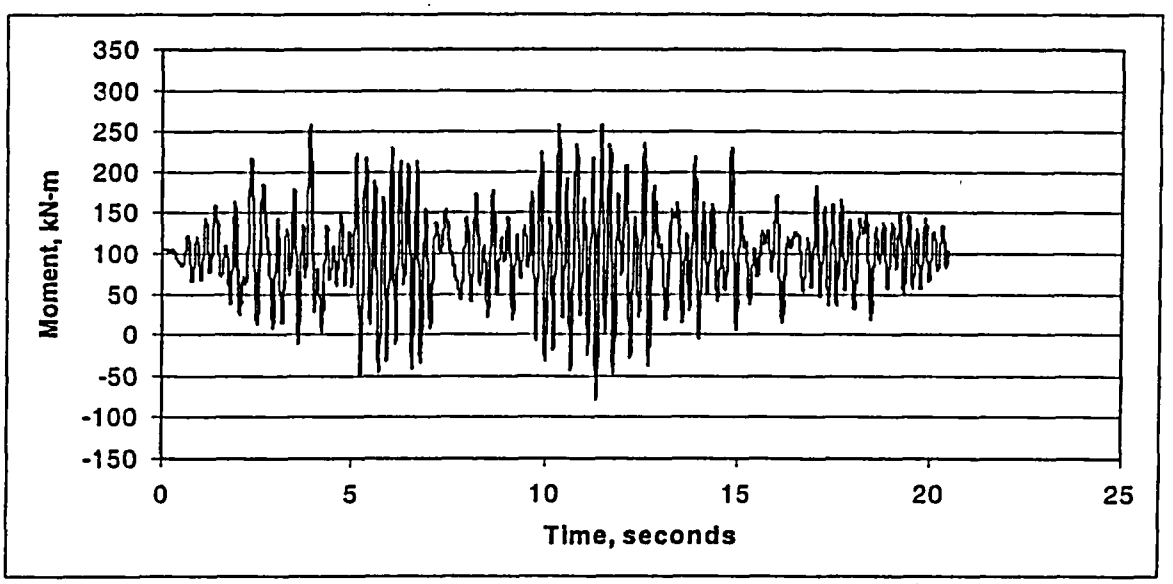

Figure B.22 IPIRG-2 Round-Robin Problem C.1 predicted linear moment response from Solution F-3a

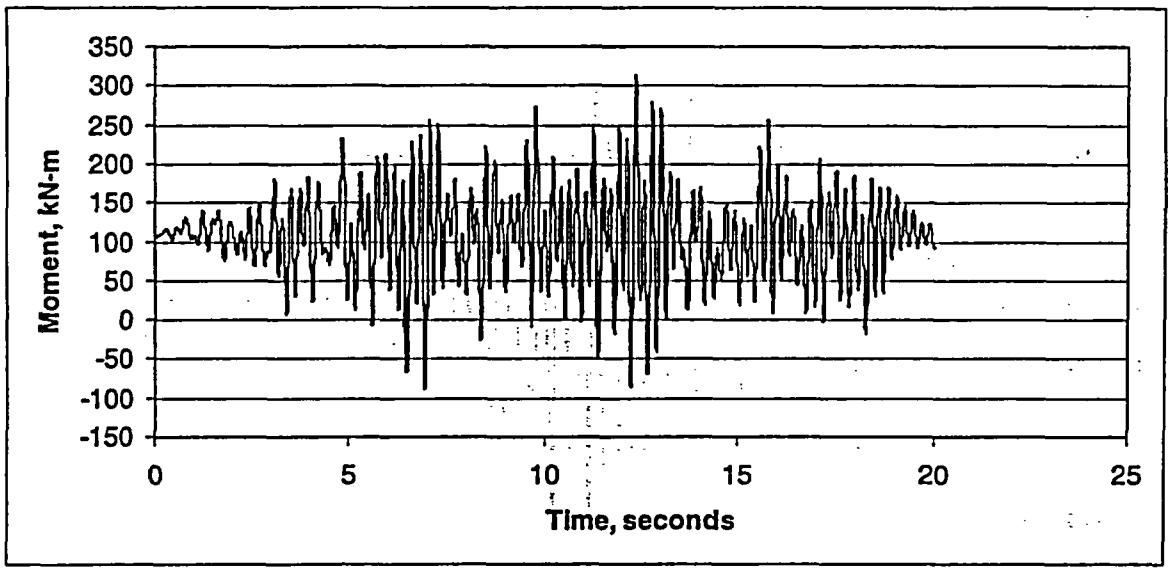

Figure B.23 IPIRG-2 Round-Robin Problem C.1 predicted linear moment response from Solution D

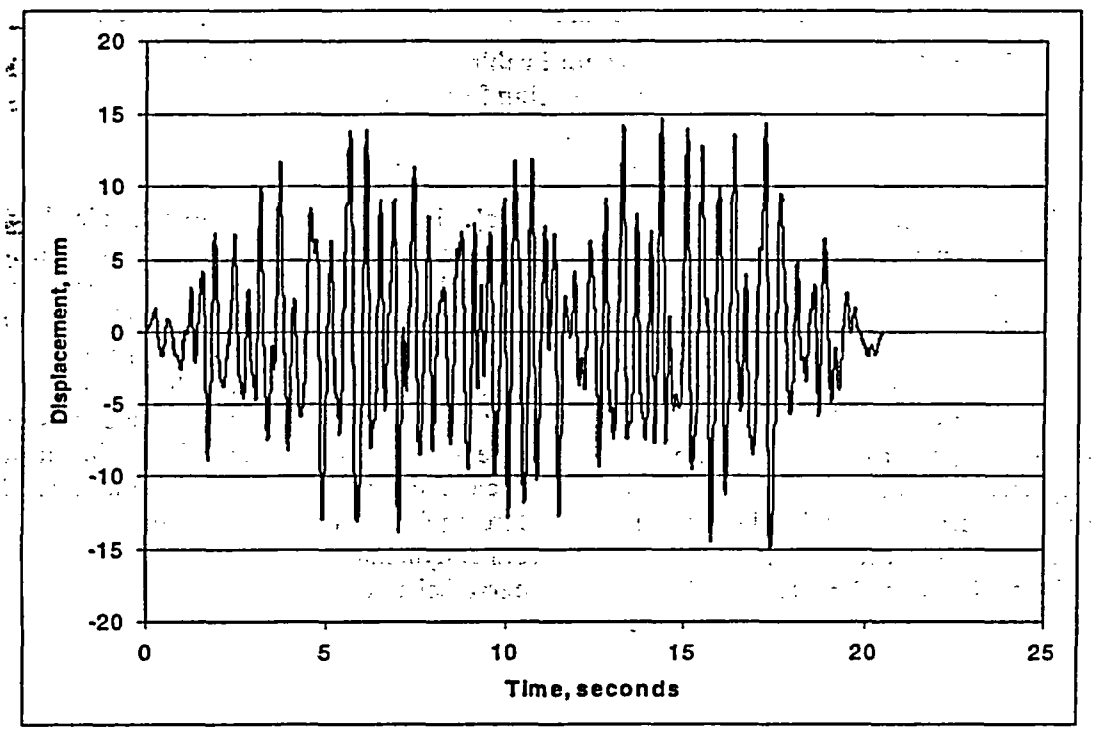

Figure B.24 IPIRG-2 Round-Robin Problem C.1 Solution F-3a actuator displacement forcing function

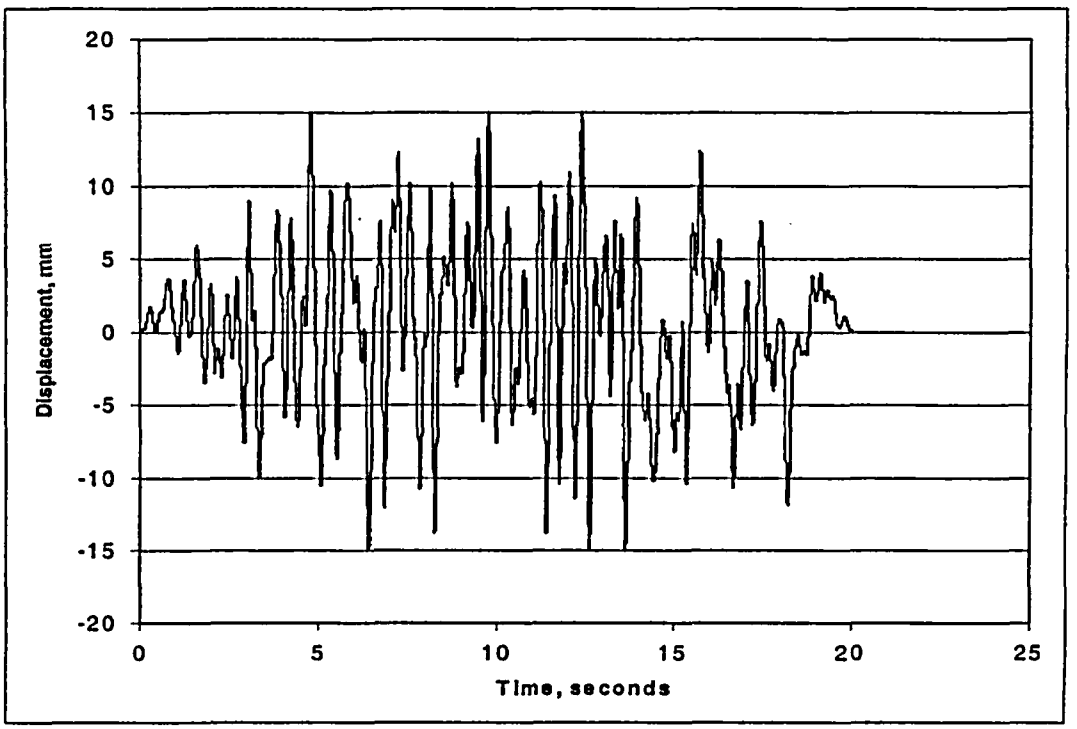

Figure B.25 IPIRG-2 Round-Robin Problem C.1 Solution D actuator displacement forcing function

The predicted pipe-system response is a function of the moment-rotation curve used in the analysis. It is expected that the BINP Task 2 crack will behave according to the response dictated by the dynamic, R = -0.3 J-resistance curve. In the extreme, however, the behavior might be as good as if the pipe had quasi-static, R = -0.3 J-resistance properties. Figure B.26 shows the expected extremes in moment-rotation behavior for the experiment calculated using the SC.TNP1 analysis in NRCPIPES Version 3.0 using the A8ii-15 (dynamic, R = -0.3) and A8ii-21 (quasi-static, R = -0.3) J-R curves. [Note: the cyclic J-R curves had a ratio of cyclic plastic displacement to monotonic plastic displacement at crack initiation of 0.1. That is, 10 plastic displacement cycles were required before crack initiation.] For reference, the dynamic monotonic behavior is also shown. To be certain that the chosen forcing function will be able to fail the pipe in a single loading, it was decided that it would be good if the selected forcing function was able to fail cracks with either dynamic or quasi-static, R = -0.3 J-R curve behavior.

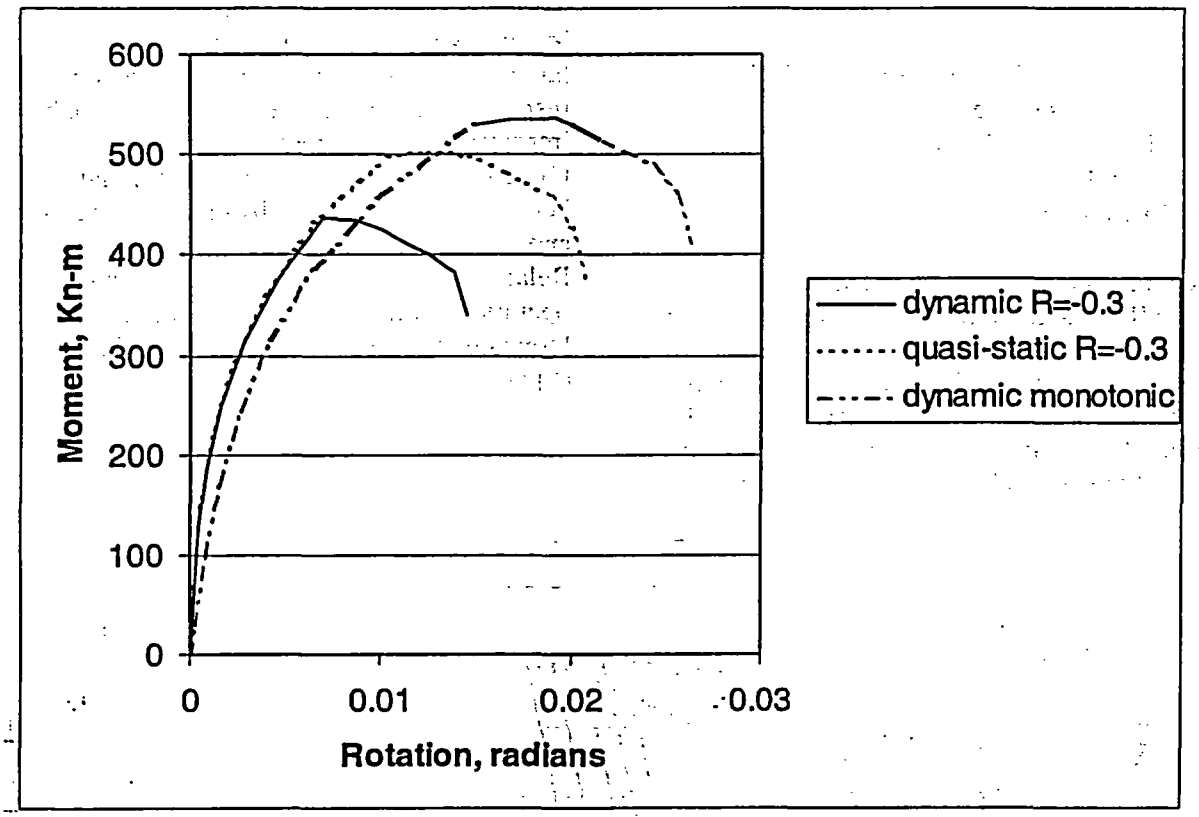

Figure B.26 BINP Task 2 predicted cracked-section upper envelop moment-rotation from the SC.TNP1 J-estimation scheme

B.1.3.2 Selection and Scaling - Initially it was felt that the F-3a solution was the most promising. However, subsequently it was discovered that nonlinear behavior at 4 SSE, at least with dynamic monotonic crack behavior, substantially modifies the Solution F-3a response. Fundamentally, the nonlinear crack acts like damping, phase shifting the system response. Initial analysis with Solution D using dynamic monotonic crack behavior at 4 SSE looked very promising, so a process of scaling and "tuning" the Solution D forcing function was undertaken.

Scaling and "tuning" of the Solution D forcing function to eventually settle on the BINP forcing function involved three inter-related processes:

1. Changing of the initial static actuator offset to decrease the stress ratio,
2. Scaling the amplitude of the SSE level forcing function up so that maximum moment is achieved, and
3. Modifying one of the displacement peaks in the original forcing function to get a better amplitude build up.

This process is an iterative one involving a significant number of nonlinear pipe-system analyses. The new surface-crack analysis methodology (asymmetric tension and compression), as described in Section B.1.2.3, is necessary for these analyses.

Figures B.27 through B.30 show the final results of analyses with the scaled and "tuned" Round-Robin Solution D forcing function with the BINP Task 2 bounding case crack moment-rotation curves. Figure B.31 shows the forcing function used to generate these results. For

either moment-rotation response assumption, the forcing function meets all of the BINP seismic forcing function design goals:

- Significant cyclic damage potential (the stress ratio (R) is between – 0.3 and – 1.0),
- 5 to 10 plastic cycles (there are 7 or 9), and
- Reasonable time to failure (it is 6.775 or 9.770 seconds).

The scaling and "tuning" amounted to scaling the basic Round-Robin Solution D up by a factor of 3, limiting the amplitude of the large actuator displacement at time 4.790 seconds to 8.89 mm (0.35 inch) [it was 15.01 mm (0.591 inch)], and offsetting the actuator by -12.7 mm (0.5 inch) at the start of the test. The scaling up is necessary to get a failure. (In the light of the IPIRG simulated-seismic test results from the SSE loading, it would be very surprising if SSE loading would cause a failure). Reducing the large amplitude has no dramatic effect on the response spectrum of the actuator motion, but it improves the cyclic moment build up. Offsetting the actuator reduces the initial bending moment caused by thermal expansion and makes the stress ratio more negative. Relating this actuator offset to real plant operations, it merely means that the expansion loop is more effective in controlling thermal expansion stresses.

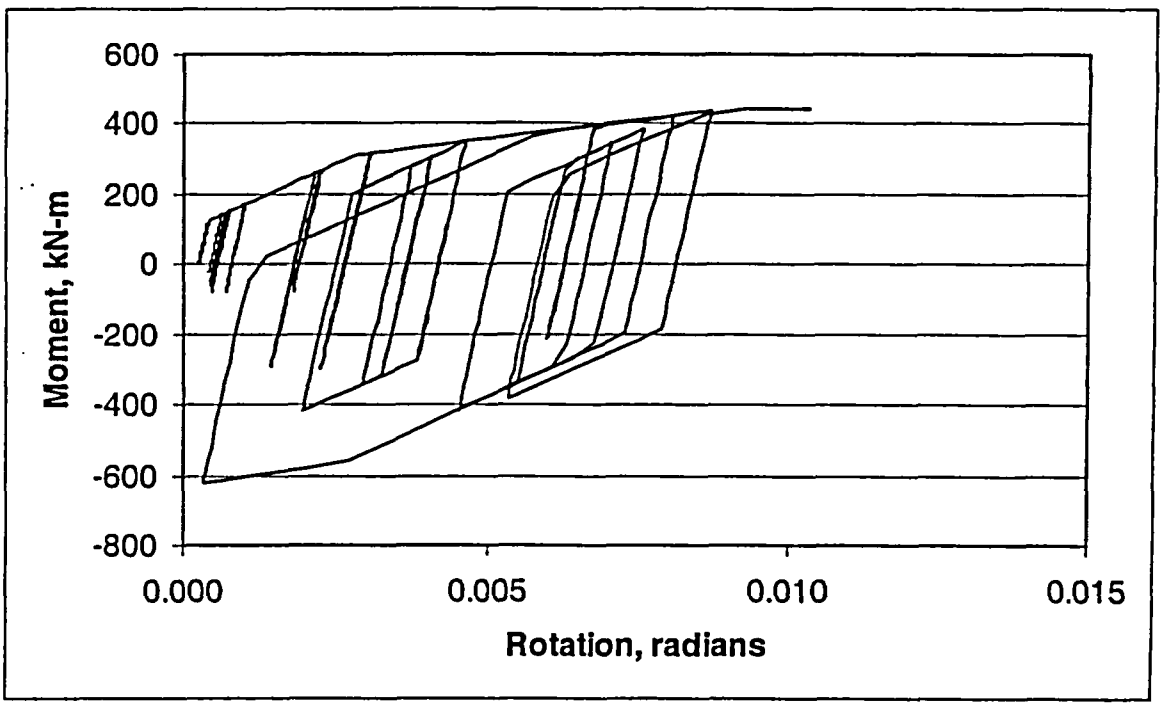

Figure B.27 Predicted BINP Task 2 cracked-section moment-rotation behavior using the dynamic R = -0.3 J-R curve

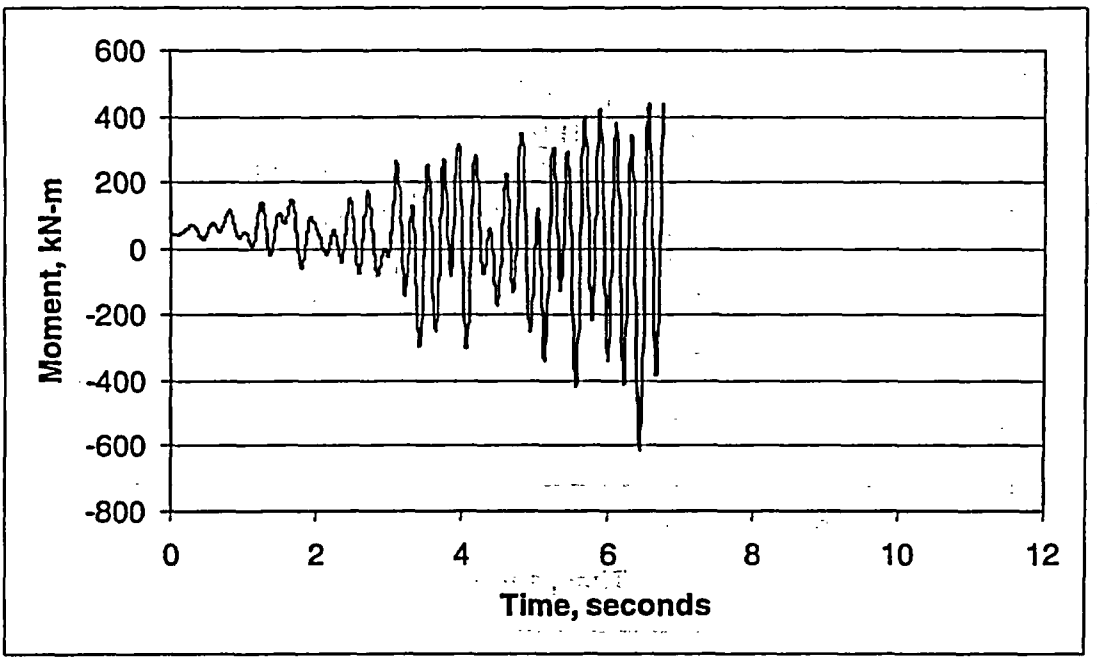

Figure B.28 Predicted BINP Task 2 moment-time behavior using the dynamic R = -0.3 J-R curve

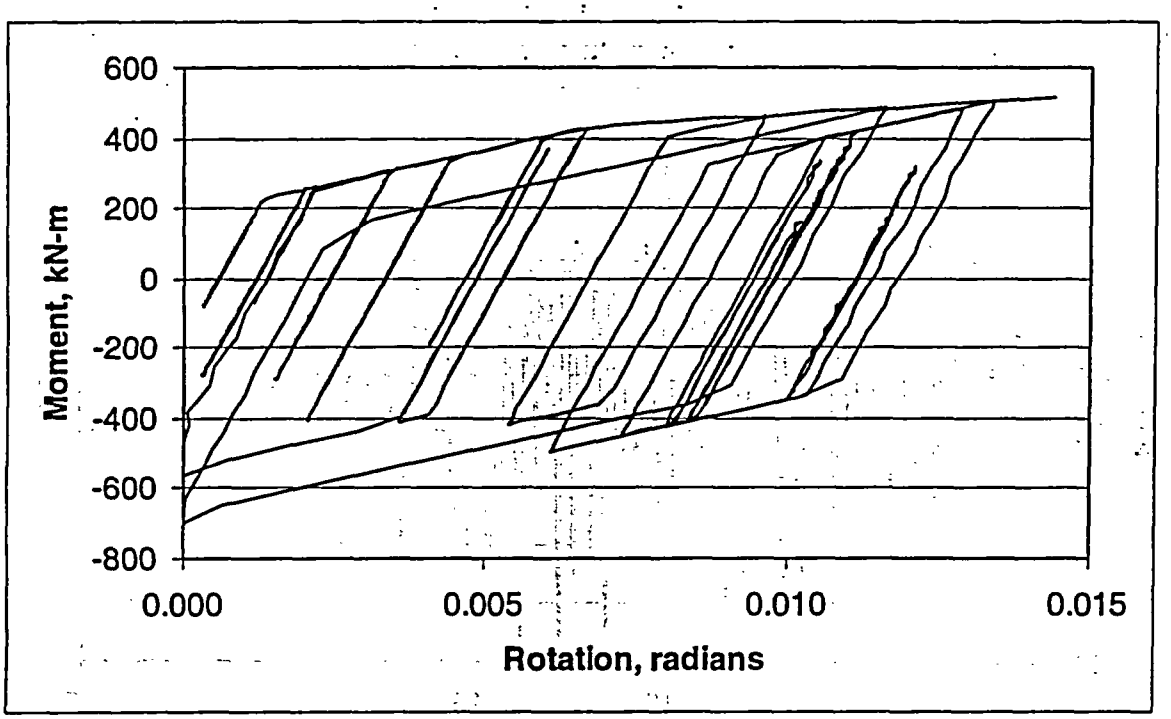

Figure B.29 Predicted BINP Task 2 cracked-section moment-rotation behavior using the quasi-static R = -0.3 J-R curve

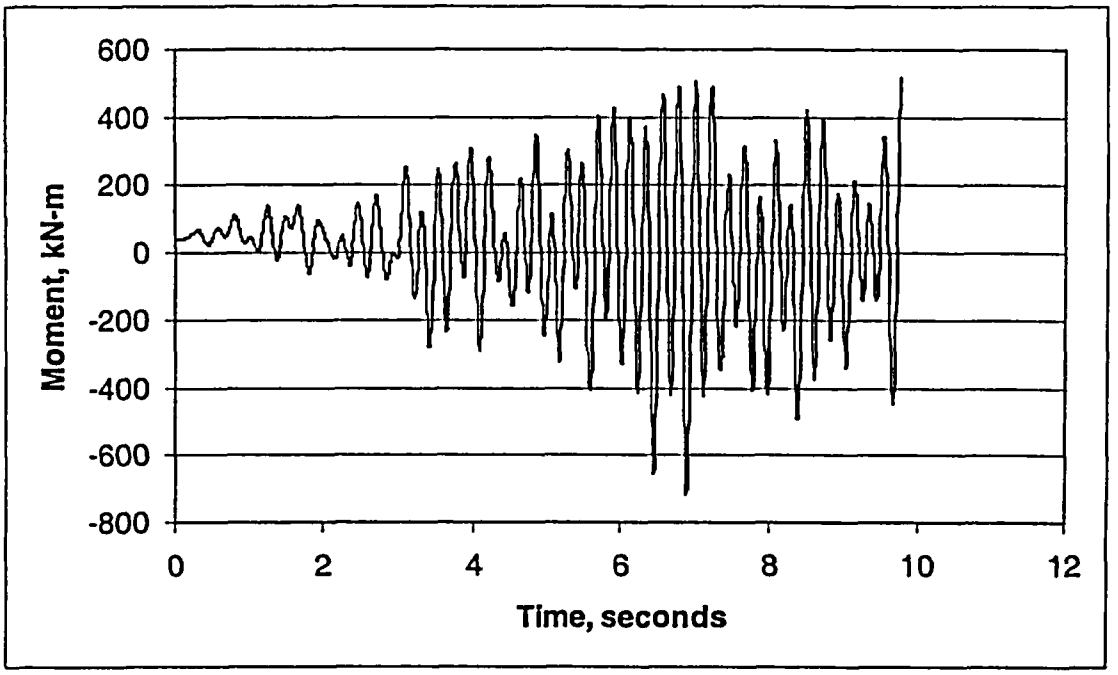

Figure B.30 Predicted BINP Task 2 moment-time behavior using the quasi-static R = -0.3 J-R curve

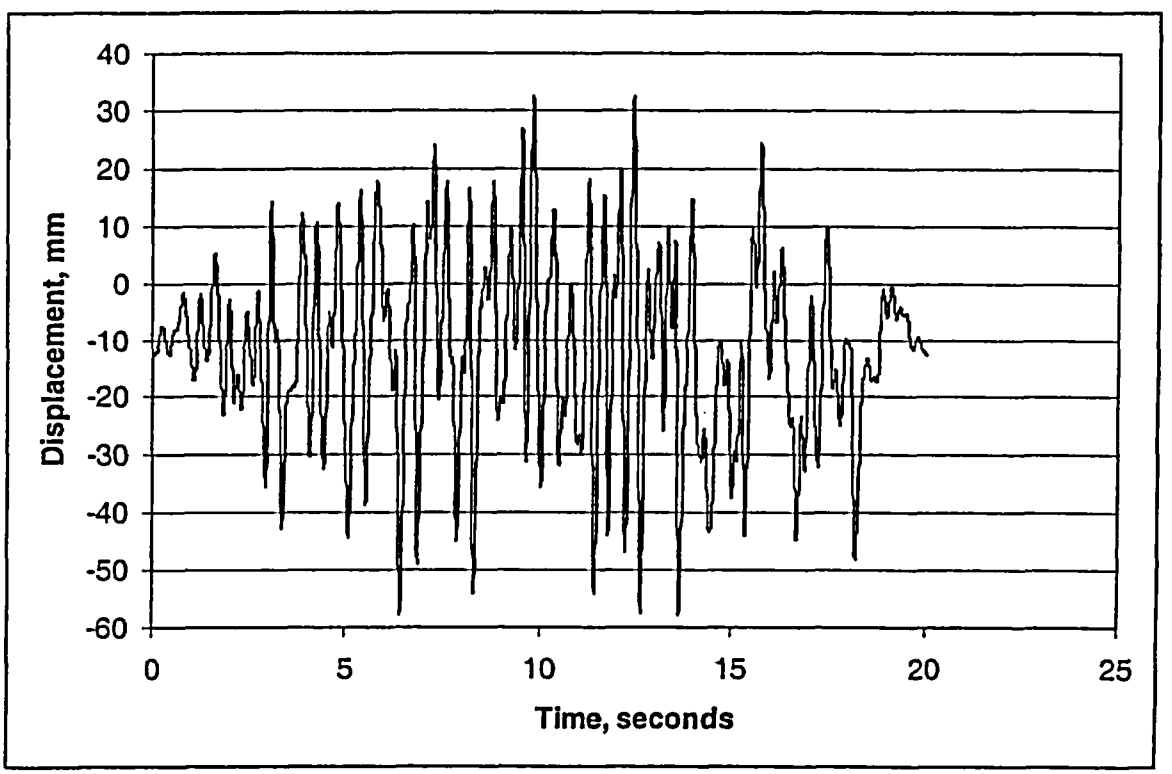

Figure B.31 The BINP simulated-seismic forcing function actuator displacement

B.1.4 Conclusions from Seismic Design Analysis

In terms of its character, the BINP seismic forcing function is similar to the IPIRG-2 seismic forcing function. Scaled to 3 SSE and respecting the fact that there is a -12.7 mm (0.5 inch) initial offset in the BINP forcing function, it is very difficult to tell the two functions apart, Figures B.31 and B.32. At the 3 SSE level, the IPIRG-2 seismic forcing function has a maximum displacement amplitude of 40.59 mm (1.6 inches) while the BINP forcing function has a maximum displacement amplitude of 45.03 mm (1.77 inches). Both forcing functions have the same "floor response" spectrum at the SSE level loading and 2-percent damping. Thus, at least superficially, they should have the same nominal potential for crack-driving force. Nonlinear analysis suggests otherwise.

As documented in this appendix, the BINP seismic forcing function was expected to have a significantly different effect on the cracked pipe than the IPIRG-2 seismic forcing function. By design, it had a much more negative stress ratio and thus, it should have induced more cyclic damage. Fortuitously, the BINP Task 2 test specimen used pipe DP2-A8ii, a heat of TP304 that has significantly more susceptibility to dynamic and cyclic effects than other heats tested in the IPIRG-2 program. The BINP Task 2 seismic loading, as it has been designed, should bring out these effects so that if the laboratory property J-resistance data translates into cracked pipe system fracture resistance degradation, it should be evident.

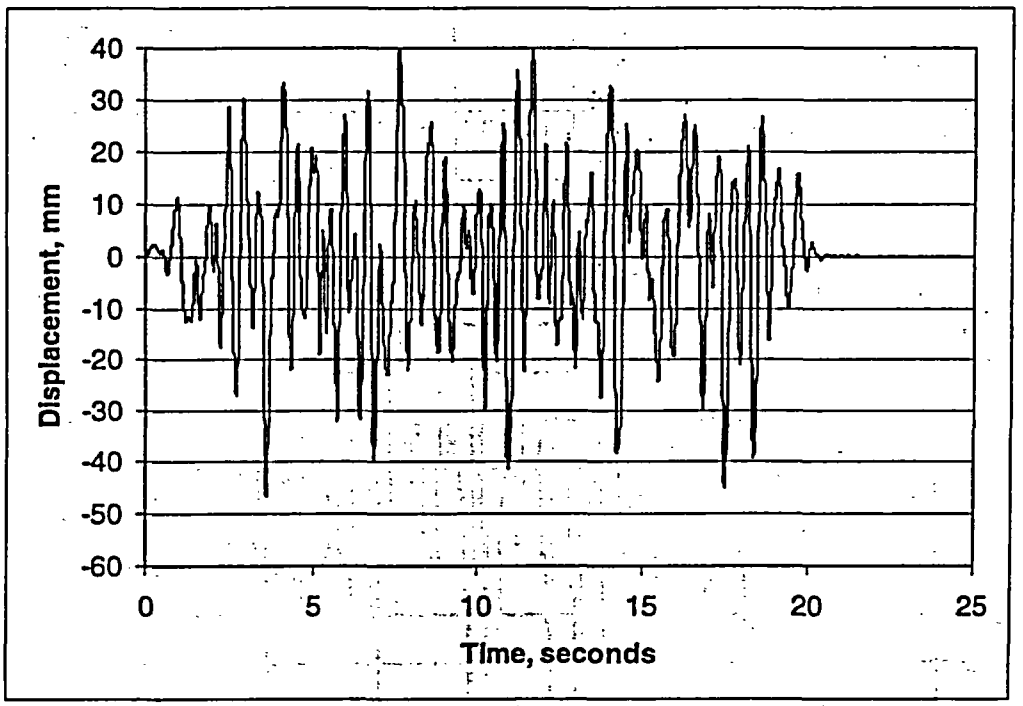

Figure B.32 The IPIRG-2 simulated-seismic forcing function actuator displacement at 3 SSE

B.2 RESULTS OF BINP SIMULATED SEISMIC PIPE-SYSTEM EXPERIMENT

The key results from the BINP simulated seismic pipe-system experiment are presented next. Table B.1 presents the test conditions, e.g., test pressure and temperature and test specimen and crack dimensions, for this experiment. Also included in Table B.1 is the maximum moment for the experiment.

Figure B.33 shows the actual actuator-time history from the experiment. Comparing the actual displacement-time history with the design displacement history in Figure B.31, one can see that the two forcing functions are very similar except the actual displacement-time history from the experiment does not reflect the initial static offset of –12.7 mm (0.5 inch) that was applied. The static offset was applied in the experiment, but the time = zero displacement value from the experimental record has been set to zero.

Figures B.34 and B.35 show the moment-time and moment-CMOD (crack-mouth-opening displacement) response for the experiment. Of particular note from Figure B.35 is the fact that there were significantly more plastic cycles in the early portion of the loading for this experiment than there were for the IPIRG-2 1-1 experiment, compare Figure B.35 with Figure B.2. Thus, it appears that the new BINP simulated seismic forcing function developed as part of this effort satisfied the basic objective of this task in that the forcing function resulted in a more cyclic damaging load history. The stress ratio, based on moment from Figure B.35, is -1.2 while the stress ratio, based on stress and accounting for the membrane stress due to the internal pressure, is –0.73. Consequently, the new BINP Task 2 seismic forcing function also satisfied the objective of creating the proper conditions for a forcing function with a significantly negative stress ratio.

Table B.1 Test conditions for BINP Task 2 simulated seismic pipe-system experiment

Mat'l	Outside Diameter, mm (inch)	Wall Thickness, mm (inch)	Crack Depth, mm (inch)	a/t	2c/πD	Test Temp., C (F)	Pipe Pressure, MPa (psi)	Max. Moment, kN-m (in-kips)
TP304	415.3 (16.35)	25.8 (1.016)	13.11 (0.516)	0.508	0.534	288 (550)	15.5 (2,250)	590 (5,220)

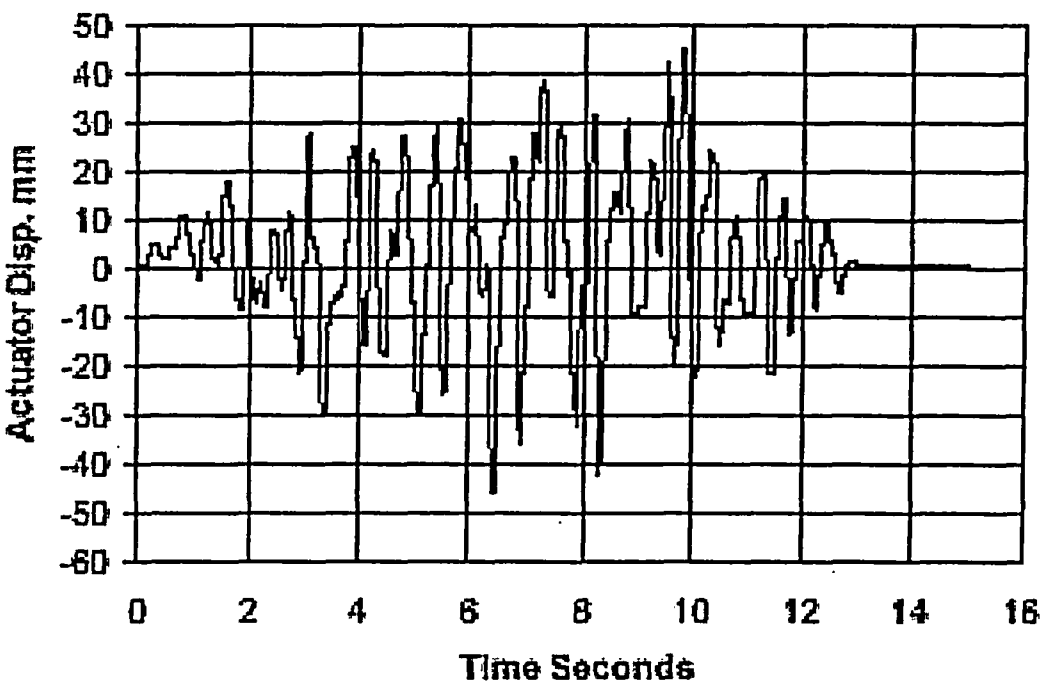

Figure B.33 Actuator displacement-time history for BINP Task 2 experiment

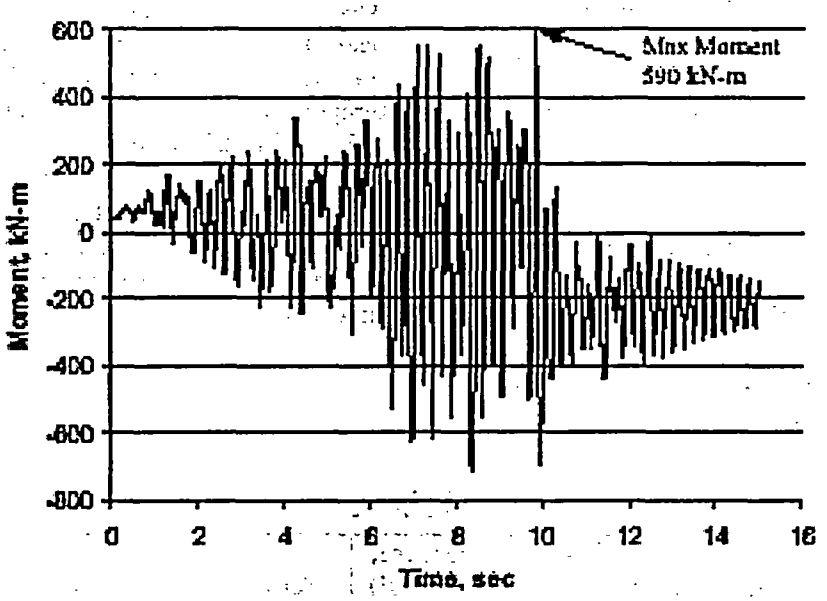

Figure B.34 Crack section moment-time response for BINP Task 2 experiment

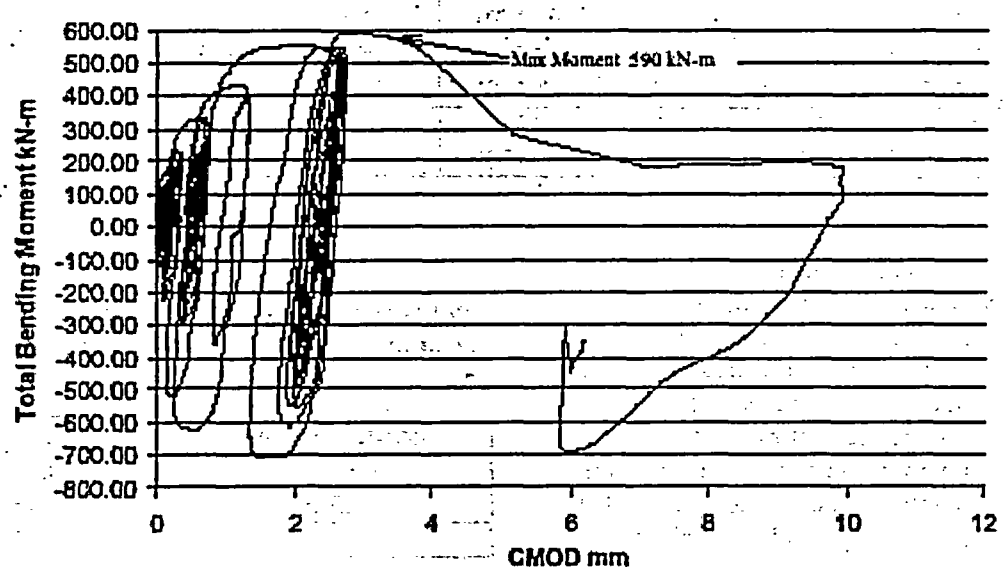

Figure B.35 Crack section moment-CMOD response for BINP Task 2 experiment

B.3 ANALYSIS OF RESULTS FROM BINP PIPE-SYSTEM EXPERIMENT WITH AN ALTERNATIVE SEISMIC LOAD HISTORY

To ascertain the impact of this alternative seismic forcing function on the fracture behavior of surface-cracked pipe-system experiments, comparisons with the other companion TP304 stainless steel surface-cracked pipe-system experiments conducted as part of the two IPIRG programs had to be made. The two companion stainless steel base metal pipe-system experiments were Experiment 1.3-3 from the

IPIRG-1 program and Experiment 1-1 from the IPIRG-2 program. The forcing function for Experiment 1.3-3 was a single frequency excitation superimposed over top an increasing displacement ramp, see Figure B.36. The forcing function for Experiment 1-1 was the IPIRG simulated seismic forcing function as shown in Figure B.1.

Table B.2 summaries the test conditions for the BINP Task 2 experiment as well as the two companion stainless steel pipe-system experiments. The test specimens for Experiments 1.3-3 from IPIRG-1 and the BINP Task 2 experiment were fabricated from the higher sulfur content heat of A8 (A8ii) while the test specimen for Experiment 1-1 from IPIRG-2 was fabricated from the lower sulfur content heat of A8 (A8i). The test conditions for each of the experiments were comparable (same test temperature [288 C (550F)], same test pressure [15.5 MPa (2,250 psi)], and nominally the same flaw size [50 percent of the pipe circumference in length and 66 percent of the pipe wall thickness in depth]). The major discriminator between the three experiments being the forcing function.

Table B.2 Test conditions for three stainless steel pipe-system experiments

Expt. Number	Mat'l Heat	OD, mm (inch)	Wall thickness, mm (inch)	Pressure, MPa (psi)	Test Temp., C (F)	a/t	2c/πD	Max. Moment, kN-m (in-kips)
BINP2	A8ii (high S)	415.3 (16.35)	25.8 (1.016)	15.5 (2,250)	288 (550)	0.508	0.534	590 (5,220)
1.3-3	A8ii (high S)	415.8 (16.37)	26.2 (1.031)	15.5 (2,250)	288 (550)	0.647	0.552	426 (3,770)
1-1	A8i (low S)	417.1 (16.42)	25.5 (1.005)	15.5 (2,250)	288 (550)	0.632	0.527	598 (5,290)

Table B.3 summaries the results from these experiments by presenting the maximum moment-carrying capacities in terms of the fracture ratios, i.e., the maximum stress from the experiments normalized by the Net-Section-Collapse (NSC) stress, accounting for the pressure induced membrane stress, see Equation B.1. This normalization process accounts for the slight differences in the pipe and crack sizes.

$$FR = \frac{\left(\sigma_m + \sigma_{b\_expt}\right)}{\left(\sigma_m + \sigma_{b\_NSC}\right)} \qquad \text{(B.1)}$$

where,

FR = Fracture Ratio
σ_m = membrane stress due to pressure
σ_{b_expt} = experimental bending stress
σ_{b_NSC} = Net-Section-Collapse predicted bending stress

Table B.3 Test results from three stainless steel pipe-system experiments in terms of fracture ratios

Expt. Number	Fracture Ratio
BINP2	0.906
1.3-3	0.936
1-1	1.158

In can be seen from Table B.3 that the moment-carrying capacity of the IPIRG-1 simulated seismic experiment (Experiment 1-1) is about 25 percent higher than the moment-carrying capacity of the other two stainless steel surface-cracked pipe-system experiments. One may want to immediately believe that this entire 25 percent reduction in moment-carrying capacity for the BINP Task 2 and the IPIRG-1 single-frequency experiments is due to cyclic effects

since the cyclic component of the moment-CMOD or rotation response is much more evident in Figure B.35 for BINP2 and Figure B.37 for Experiment 1.3-3 than it is for IPIRG-2 Experiment 1-1, see Figure B.2. However, the difference due to cyclic behavior is only half the story. As alluded to earlier, the test specimen for Experiment 1-1 was fabricated from the lower sulfur content, higher toughness heat of A8 (A8i) while the test specimens for the other two experiments were fabricated from higher sulfur content, lower toughness heat of A8 (A8ii), see Figure B.38. Sensitivity studies conducted as part of Reference B.5 showed that this difference in toughness may account for about a 15 percent difference in moment-carrying capacity. Consequently, the higher moment-carrying capacity of IPIRG-1 Experiment 1-1 is probably an artifact of both phenomena.

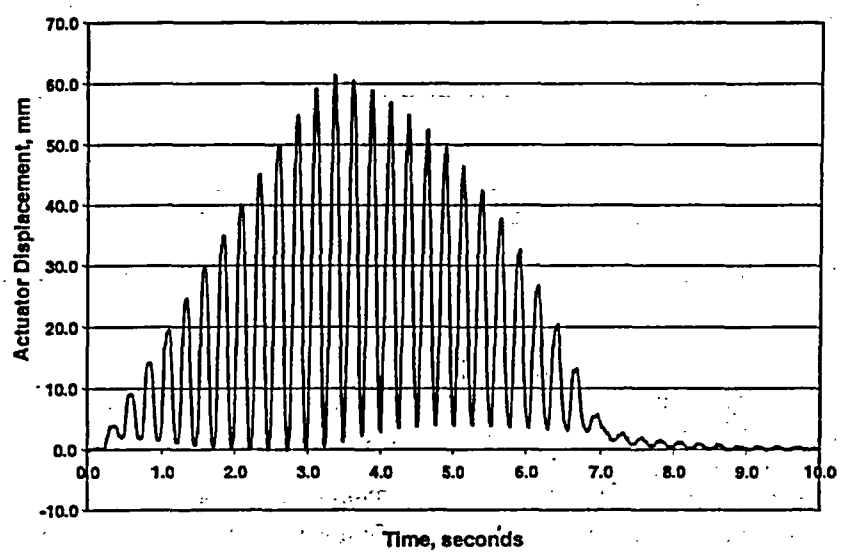

Figure B.36 Actuator displacement-time history for IPIRG-1 Experiment 1.3-3

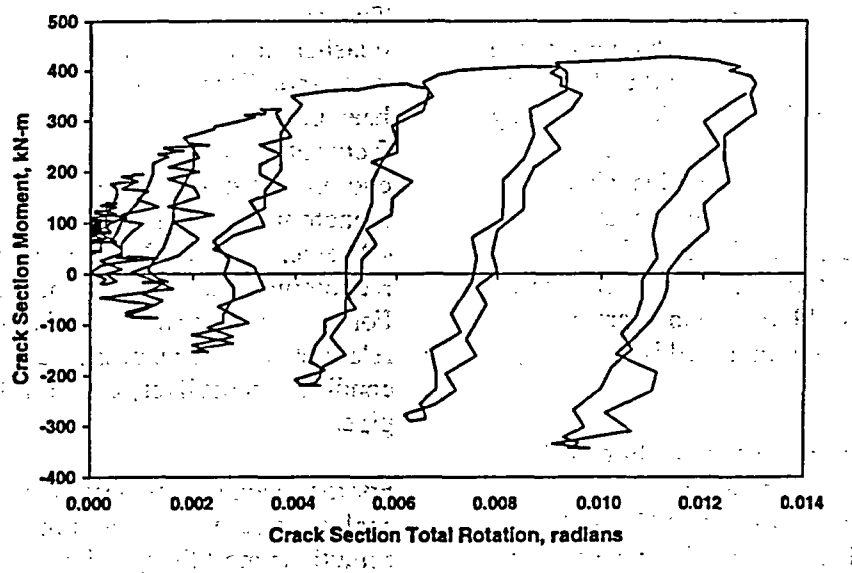

Figure B.37 Crack section moment-rotation response for IPIRG-1 Experiment 1.3-3

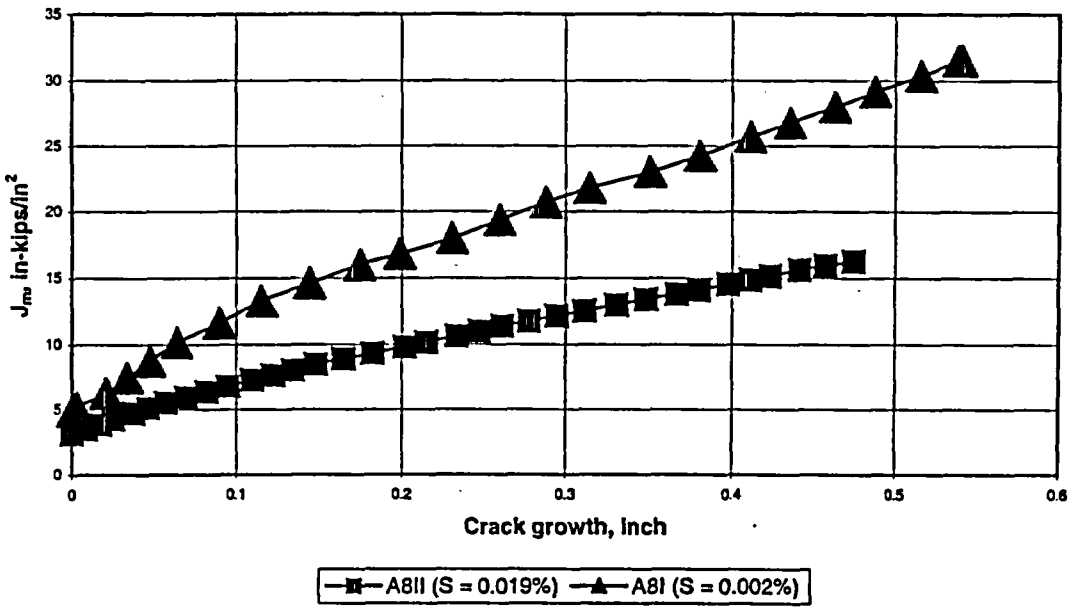

Figure B.38 Comparison of J-R curves for two heats of DP2-A8 stainless steel

Consequently the effect of cyclic loading on the moment-carrying capacity of these stainless steel base metal pipe-system experiments may result in only a 10 to 15 percent reduction. This does not seem to be that important of an effect, especially in light of the large factors of safety applied by such standards as ASME Section XI. However, the experiments conducted and analyzed so far have been for the case where the surface cracks were in rather high toughness stainless steel pipe materials for which limit load conditions probably prevailed and the effects of toughness degradation due to cyclic loading may not be that significant. Consequently, the question that needs to be answered is what would be the effect if these experiments and analyses had been conducted using a lower toughness ferritic material or a lower toughness stainless steel flux weld, maybe in a larger diameter pipe for which limit load is less likely to occur.

In order to address this question, additional J-estimation scheme analyses were conducted. For these additional analyses, the SC.TNP1 method was used since past studies have shown that this method is the most accurate predictor of the moment-carrying capacity of surface-cracked pipe.

Two sets of analyses were conducted. For the first set, J-estimation scheme analyses were conducted for a 16-inch diameter, Schedule 100 stainless steel pipe, with a crack in the base metal 25 percent of the pipe circumference long and 50 percent of the pipe wall thickness deep. Two analyses were conducted. For one, the quasi-static, monotonic J-R curve for Heat A8i was used. For the other, a J-R curve that had been uniformly reduced for all values of Δa by a factor of 2.5 was used. This factor of 2.5 was chosen in that the J-R curve for A8i for the monotonic, R = -1 loading condition was only 40 percent of the J-R curve for the quasi-static, monotonic loading condition, see Figure B.39. For this stainless steel material, with its relatively high toughness level, limit-load conditions most likely exist for this diameter pipe.

For the second set of J-estimation scheme analyses a case was chosen for which limit-load conditions most likely did not exist. For these analyses, 32-inch diameter main steam line was

chosen for analysis. In this case, the crack was in a lower toughness ferritic weld. Both quasi-static, monotonic J-R curve data and quasi-static, cyclic (R = -1) J-R curve data were used in the SC.TNP1 analyses. The quasi-static data were obtained from weld material DP2-F29W, a ferritic pipe weld used in a number of past pipe experiments. The cyclic J-R curve data were obtained by multiplying each of the J values in the quasi-static, monotonic J-R curve file by 0.4. In this manner, it will be possible to ascertain if the reduction in moment-carrying capacity is different for the case where limit-load conditions exist and for the case where elastic-plastic fracture governs.

Figure B.40 is a plot of the resultant moment-rotation curves from the SC.TNP1 analyses for the stainless steel case where limit-load conditions most likely exists. As can be seen, the maximum moment for the cyclic case was about 81 percent of the maximum moment for the monotonic case. Figure B.41 is a plot of the resultant moment-rotation curves from the SC.TNP1 analyses for the larger diameter, ferritic weld case where EPFM most likely governs. For this case, the maximum moment when using the cyclic J-R curve was only about 66 percent of the maximum moment when using the monotonic J-R curve. Thus, it appears cyclic loading may be a more important factor to consider for cases where EPFM governs.

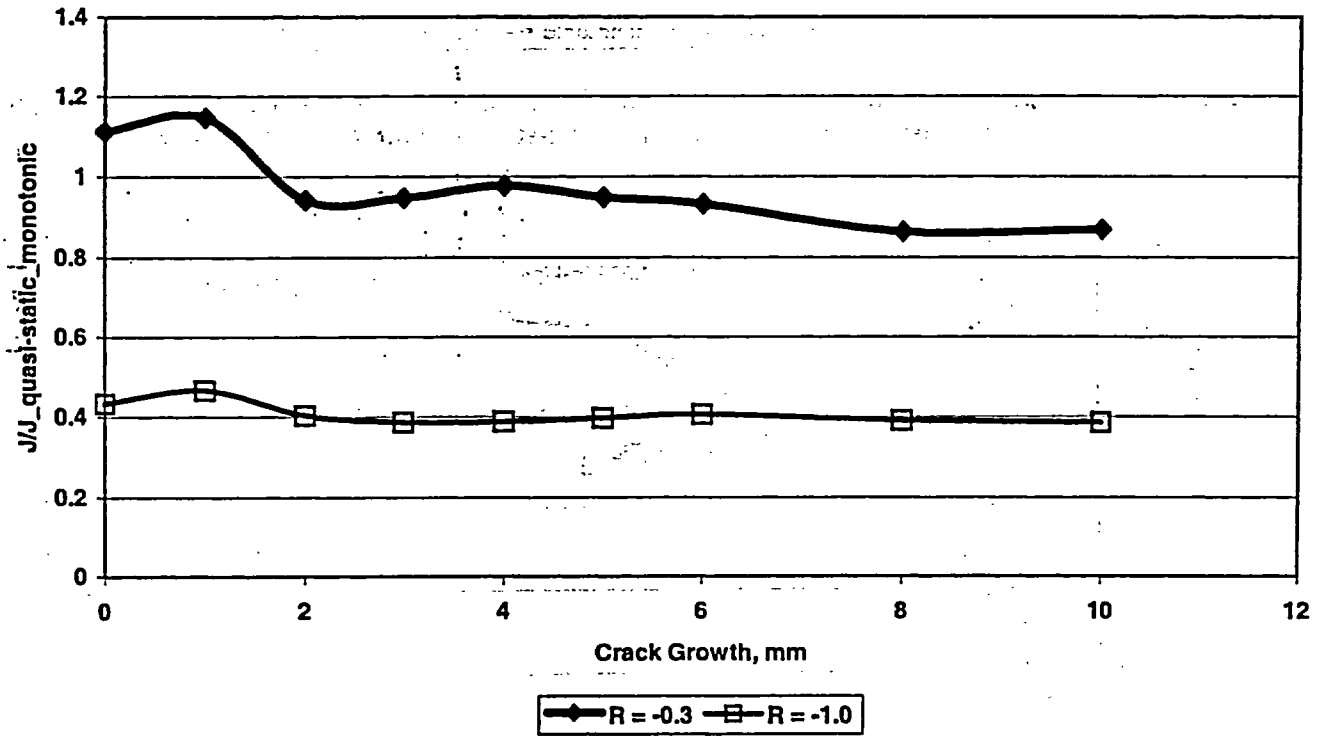

Figure B.39 Ratio of quasi-static cyclic J values to J for quasi-static monotonic loading as a function of crack growth (Δa)

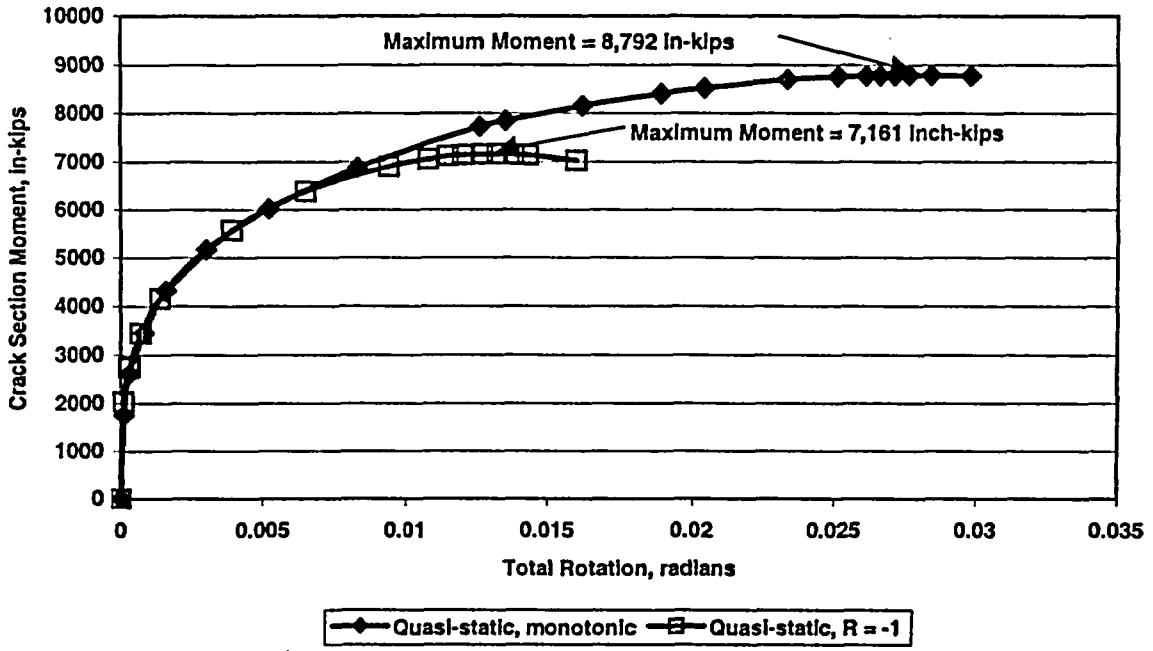

Figure B.40 Predicted moment-rotation behavior for 16-inch diameter schedule 100 stainless steel pipe for quasi-static monotonic and quasi-static cyclic (R = -1) J-R curves

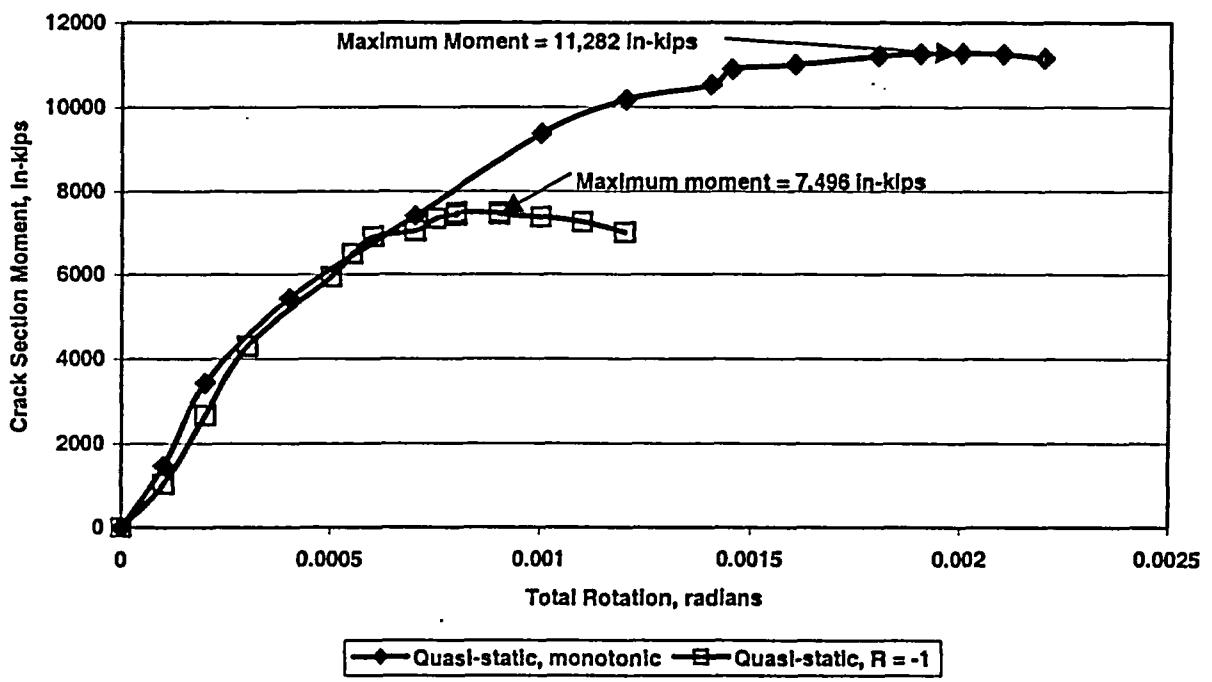

Figure B.41 Predicted moment-rotation behavior for 32-inch diameter carbon steel pipe for quasi-static monotonic and quasi-static cyclic (R = -1) J-R curves

B.4 REFERENCES

B.1 Olson, R., Scott, P., and Wilkowski, G., "Design of the IPIRG-2 Simulated Seismic Forcing Function," NUREG/CR-6439, February 1996.

B.2 Rahman, S., Olson, R., Rosenfield, A., and Wilkowski, G., "Summary of Results From the IPIRG-2 Round-Robin Analyses," NUREG/CR-6337, January 1996.

B.3 Rudland, D., Brust, F., and Wilkowski, G., "Fracture Toughness Evaluations of TP304 Stainless Steel Pipes," NUREG/CR-6446, February 1997.

B.4 Olson, R., Wolterman, R., Wilkowski, G., and Kot, C., "Validation of Analysis Methods for Assessing Flawed Piping Subjected to Dynamic Loading," NUREG/CR-6234, August 1994.

B.5 Scott, P., Olson, R., and Wilkowski, G., "Development of Technical Basis for Leak-Before-Break Evaluation Procedures," NUREG/CR-6765 May 2002.

APPENDIX C

BINP TASK 3 – DETERMINATION OF ACTUAL MARGINS IN PLANT PIPING

BINP Task 3 – Determination of Actual Margins in Plant Piping

C. 1 Introduction

Traditional plant piping flaw evaluation procedures use an uncoupled stress analysis and flaw evaluation procedure. The stress analysis typically does not include any feature to account for the degradation at the flawed section, it is traditionally performed using a linear elastic analysis, and it usually is done using a response spectrum analysis that provides only peak loads. Traditional flaw evaluation procedures do include plasticity effects, but they generally assume that the peak load obtained from the stress analysis is load-controlled, they ignore low-cycle fatigue during the seismic event as a crack extension mechanism, and use quasi-static material properties. In fact, real piping and real cracks behave in a nonlinear manner. The presence of the crack can influence the behavior of the rest of the piping, sections remote from the crack can yield and absorb some of the seismic energy that could grow the crack, seismic loads are never sustained, cracks can extend by fatigue even for the few load cycles a crack may experience during a seismic event, and the toughness of the materials is affected by dynamic and cyclic loads. Hence, a traditional flaw evaluation analysis may not accurately reflect the ability of the flaw to sustain seismic loads.

Results of analyses and experiments conducted in the IPIRG-1 and IPIRG-2 programs provided a strong indication that flawed plant piping can withstand far greater loads without failure than traditional flaw evaluation methods suggest. Comparing measured experimental moments and calculated moments for the IPIRG-1 pipe-system experiments, the linear-elastic moments were as much as 40 percent higher than the measured moments (Ref. C.1). Thus, the crack driving force is grossly overestimated. For the IPIRG-1 pipe-system experiments, the R6 Revision 3 Option 1 method under-predicted the flaw stress capacity by as much as 88 percent (Ref. C.1). This happened in spite of the fact that the IPIRG-1 flaws were large and none of the pipe remote from the crack experienced plasticity. Analyses done for the U.S. Department of Energy's New Production Reactor program (Refs. C.2 and C.3) suggested that the differences between traditional flaw evaluation procedures and analyses incorporating nonlinear crack behavior support elimination of an instantaneous double-ended pipe break as the system design basis for this particular reactor design. For the case of a 360-degree internal surface flaw 75-percent deep with a 41-percent of the circumference leaking through-wall crack in 406-mm (16-inch) diameter Schedule 40 TP304 stainless steel pipe at 3 SSE seismic loading, nonlinear analysis indicated that the crack remained stable, whereas a traditional LBB flaw evaluation (linear stress analysis and Net-Section-Collapse fracture analysis) suggested that the flaw would fail because the linearly calculated applied moment of 192.6 kN-m (1,705 in-kips) exceeded the calculated flaw capacity of 38.9 kN-m, (344 in-kips) see Figure C.1, by almost a factor of 5. Based on moment, there was a margin in excess of 5 between the traditional LBB analysis and the more realistic nonlinear analysis for the DOE case.

Prior to the BINP program, there had been no systematic effort to determine whether the margins suggested above can be realized in broad classes of real plant piping systems, flaw locations, and loadings. The lack of any significant failures of nuclear power plant piping, such as loss-of-coolant accidents, indicates that margins on piping design and flaw evaluation may be able to be reduced with a consequent reduction in operating costs, and without compromising plant safety. Clearly, flaw nonlinearity, interaction between the crack and the pipe system, plasticity remote from the crack, and the transient nature of seismic loads all could contribute to margins against piping failure that traditional analyses cannot capture. Conversely, low cycle fatigue in a seismic event, which is generally ignored, may reduce margins. For advanced reactor design, more realistic LBB assessments, plant life extension, and more accurate flaw evaluation procedures, the actual margins in plant piping needed to be quantified.

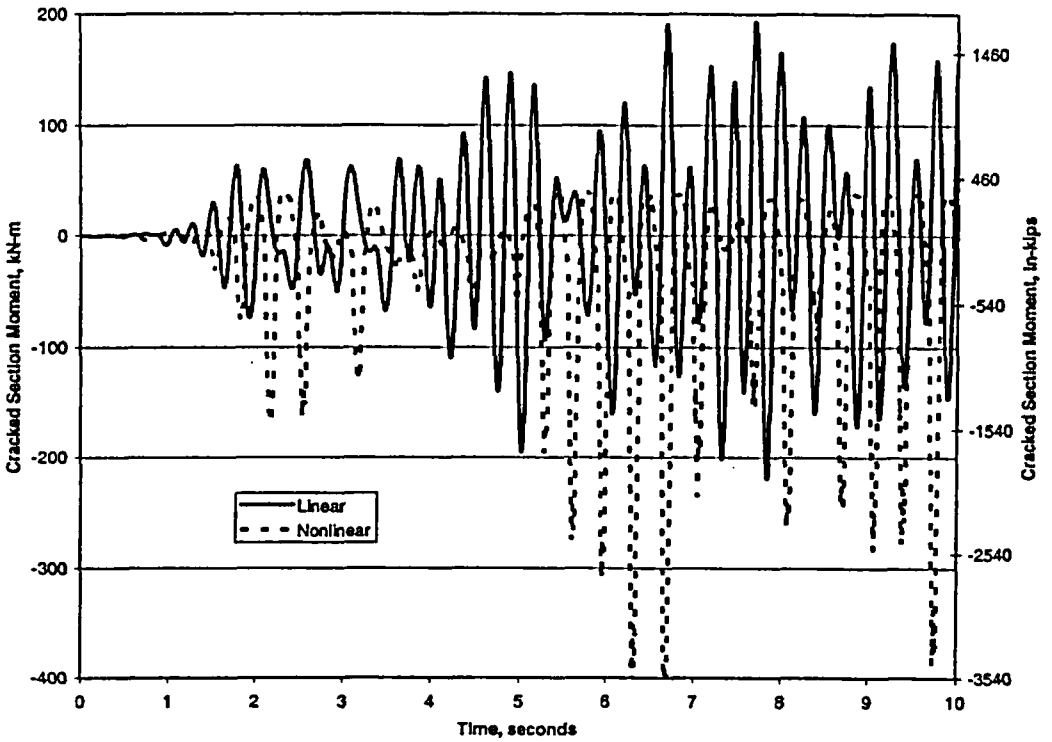

Figure C.1 New Production Reactor moment-time history from both a linear and nonlinear analysis: a large margin exists between these two analyses

C.1.1 Historical Perspective

The original BINP proposal from November 1996 offered an analytical approach to conducting the Actual Margins task. This was to be accomplished by contrasting the results from traditional and advanced nonlinear piping stress analyses on actual plant piping systems submitted for evaluation to Battelle by the TAG. In a subsequent July 1998 meeting of parties interested in participating in the BINP program, it was decided that it would be better if the Actual Margins task was conducted experimentally. Accordingly, a revised statement of work was submitted and accepted wherein two IPIRG cracked pipe system experiments were to be conduced: A single frequency excitation experiment with the high-strength IPIRG pipe replaced by A106 Grade B carbon steel pipe and a second similar experiment using TP304 stainless pipe.

As the BINP program moved forward, there was an evolution of technical interests that, eventually, led to eliminating one of the Actual Margins experiments in favor of some other technical activities. This happened in August 2000. Moving forward with the design of the remaining Actual Margins experiment, it became apparent by January 2001 that it was going to be difficult to conduct a meaningful experiment: The allocated budget was insufficient to conduct an all stainless steel pipe loop experiment and it was virtually impossible to find a carbon steel pipe with a sufficiently low strength to fulfill the task objective of demonstrating margin. In light of this, a decision was made in May 2001 to return to the original concept of doing the Actual Margins task analytically.

C.2 Task Objective and Approach

The objective of the Actual Margins task was to make a systematic assessment of the margin between the load capacity of flawed pipe based on traditional elastic stress analyses of plant pip-

ing and the load capacity based on more realistic nonlinear analyses under seismic loads. The aim was to provide a rational basis for relaxing plant piping stress limitations or simplifying the flaw acceptance criteria in piping design codes.

The work conducted in this task was strictly analytical in nature, although the procedures were experimentally validated in IPIRG-1 (Ref. C.1), IPIRG-2 (Ref. C.4), and a program conducted by Battelle for Argonne National Laboratory (Ref. C.5). Using these previously developed analytical tools, which were supplemented by a few analytical refinements developed during the course of the BINP program, linear and nonlinear analyses were conducted for two classes of problems:

- The IPIRG pipe loop
- Actual plant piping.

The IPIRG pipe loop analyses addressed the question of what we might have learned had the task been done experimentally, while the plant piping analyses addressed real-world practical applications.

Within the two classes of problems, IPIRG pipe loop and plant piping, several different margins were considered:

- The margin between a linear analysis and an analysis that considers nonlinearity due only to a crack in the pipe,
- The margin between a linear analysis and an analysis that considers nonlinearity caused by plasticity remote from the crack, i.e., general yielding in the pipe, and
- The margin between a linear analysis and an analysis that considers the combined nonlinearity of a crack and remote yielding.

The principal output of these analyses was data to determine whether or not the margins from any of the nonlinear analyses are large enough to warrant conducting such a relatively sophisticated analysis for flaw evaluation or LBB applications.

C.3 Preliminary Technical Considerations

Prior to considering the Actual Margins problem, some preliminary technical issues need to be addressed:

- Validation of the ANSYS piping plasticity model
- Moment-rotation of cracks during unloading
- Crack orientation issues.

Although these issues are peripheral to the main focus of the Actual Margins task, they are important elements that enhance the credibility of the results or they are technical details that are required to complete the analyses.

C.3.1 ANSYS Nonlinear Validation

In work previously done at Battelle some years prior to the BINP program, there was some evidence that the ANSYS computer program's pipe elements were too stiff compared with results from the ABAQUS computer program when general plasticity was involved. Because two of the calculated margins of interest from the nonlinear analyses are based on remote yielding, it is important to be sure that the ANSYS program piping elements accurately predicts plastic behavior. Accordingly, a closed-form test problem that would exercise the ANSYS pipe elements in the plastic regime was developed. Identical analyses were performed with ANSYS and ABAQUS and the results compared.

C.3.1.1 Closed-Form Pipe Plasticity Solution

Under the kinematic assumption that plane sections remain plane, radius of curvature, curvature, and strain in a beam bending problem are related to each other by:

$$\frac{1}{\rho} = \kappa = \frac{\varepsilon}{y} \qquad \text{(C.1)}$$

where ρ and y are defined in Figure C.2. This relationship applies independent of the material of the beam, whether or not the beam yields, and what type of constitutive model the beam follows. The stress distribution in the beam is determined by the constitutive model relationship between strain and stress with the strains defined by Equation C.1. The bending moment needed to attain the radius of curvature is simply the integral of the stresses across the cross-section.

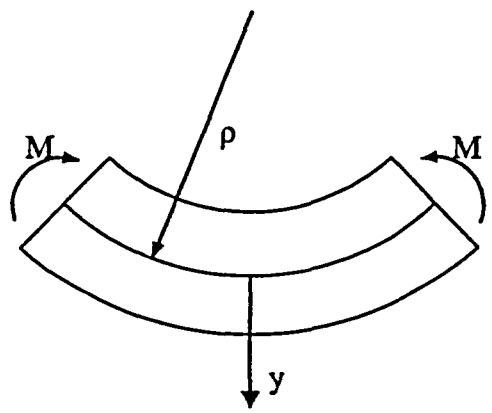

Figure C.2 Plasticity validation bend geometry nomenclature

Using the relationship between curvature and strain for pure bending, a simple closed-form solution for checking finite element beam plasticity formulations can be developed:

1. Pick a cross-sectional shape for the beam
2. Assume a stress-strain constitutive behavior
3. Pick a radius of curvature
4. Calculate the strains throughout the beam cross-section using Equation C.1
5. Using the constitutive model, calculate the stresses in the cross-section
6. Integrate the calculated stresses to find the theoretical moment
7. Integrate the calculated stresses to find the axial force
8. Calculate the theoretical end deflection of the cantilever beam of length as:

$$\theta = \frac{2\, l_0}{\rho} \qquad \text{(C.2)}$$

$$y = \rho\left(1 - \cos\frac{\theta}{2}\right) \qquad \text{(C.3)}$$

9. Build a finite element model of the cantilever beam
10. Apply the calculated moment to the finite element model
11. Compare the finite element stresses and strains at various locations in the cross-section to the corresponding theoretical values
12. Compare the theoretical and finite element end deflections.

For the case of bending plus tension, the procedure is altered slightly:

1. An initial axial strain is assumed, ε_0
2. The "stretch" of the beam is found from the definition of axial strain

$$\Delta l = l_o \varepsilon_0 \qquad \text{(C.4)}$$

3. The axial strain is added to the bending strain, the beam elongation is added to the beam length, and the solution proceeds as above.

C.3.1.2 Closed-Form Solution Details

Hutchinson's stress-strain relationship (Ref. C.6), which is represented by the two-segment curve defined in Equations C.5a and C.5b, was used as the constitutive relationship to generate the closed-form solutions:

$$\sigma = E\varepsilon \quad , \quad \varepsilon \le \varepsilon_o \qquad \text{(C.5a)}$$

$$\sigma = \sigma_o\left[\frac{n\varepsilon}{\varepsilon_o} + 1 - n\right]^{\frac{1}{n}} \quad , \quad \varepsilon > \varepsilon_o \qquad \text{(C.5b)}$$

where

ε = strain, in/in
σ = stress, psi
E = Young's modulus, psi
σ_o = stress at proportional limit, psi

ε_o = strain at proportional limit, in/in

$= E / \varepsilon_0$

n = dimensionless exponent greater than 1.0

Inverting this relationship,

$$\varepsilon = \frac{\sigma}{E} \qquad , \varepsilon \le \varepsilon_0 \qquad \text{(C.6a)}$$

$$\varepsilon = \frac{\sigma_0}{E}\left[\frac{1}{n}\left(\frac{\sigma}{\sigma_0}\right)^n + 1 - \frac{1}{n}\right] \quad , \varepsilon > \varepsilon_0 \qquad \text{(C.6b)}$$

With reference to Figure C.3 and under the plane sections remain plane during bending assumption, the strain at any point in a pipe cross-section can be found:

$$\varepsilon = \frac{y}{\rho} + \varepsilon_t = \frac{r\sin\theta}{\rho} + \varepsilon_t \qquad \text{(C.7)}$$

The moment is given by

$$M = \int_A \sigma y \, dA \qquad \text{(C.8)}$$

$$= 2\int_{-\pi/2}^{\pi/2}\int_a^b \sigma(r,\theta,\rho)\, r^2 \sin\theta \; dr \; d\theta \qquad \text{(C.9a)}$$

or, equivalently,

$$M = \int_0^{2\pi}\int_{\varepsilon_b}^{\varepsilon_a} \frac{\sigma\varepsilon^2\rho^3}{(\sin\theta)^3} \, d\varepsilon \; d\theta \qquad \text{(C.9b)}$$

The axial force is given by

$$F = \int_A \sigma \, dA \qquad \text{(C.10)}$$

$$= 2\int_{-\pi/2}^{\pi/2}\int_a^b \sigma(r,\theta,\rho)\, r \; dr \; d\theta \qquad \text{(C.11a)}$$

or, equivalently,

$$M = \int_0^{2\pi}\int_{\varepsilon_b}^{\varepsilon_a} \frac{\sigma\varepsilon\rho^2}{(\sin\theta)^2} \, d\varepsilon \; d\theta \qquad \text{(C.11b)}$$

The integrals in Equations C.9 and C.11 are not amenable to a closed-from solution. Accordingly, Guass quadrature was used to approximate the integrals. For a single integral,

$$\int_a^b f(y)dy \cong \left(\frac{b-a}{2}\right)\sum_{i=1}^{n} w_i f(y_i) \qquad \text{(C.12a)}$$

$$y_i = \left(\frac{b-a}{2}\right)x_i + \left(\frac{b+a}{2}\right) \qquad \text{(C.12b)}$$

where x_i, w_i are tabulated abscissas and weight factors that can be found in reference texts on numerical methods. For double integrals, as shown in Equations C.9 and C.11, two successive applications of Equation C.12 are required.

C.3.1.2 Plasticity Validation Results

The validation analysis was conducted using the parameters shown in Table C.1. Tables C.2 and C.4 list the theoretical values for the pure bending and bending plus tension load cases, respectively, and Tables C.3 and C.5 list deviations from these theoretical values for the various finite element analyses. Values for listed strains are at theta = 90 degrees at the mid-thickness of the pipe wall.

The ANSYS finite element model solution consisted of 20 PIPE20 elements fixed at one end with a moment applied to the free end. The moment was varied to produce different curvatures in the pipe and, accordingly, different strains. An axial force was applied to the free end of the cantilevered pipe followed by various moments to produce the bending with axial load results. Multi-linear isotropic hardening

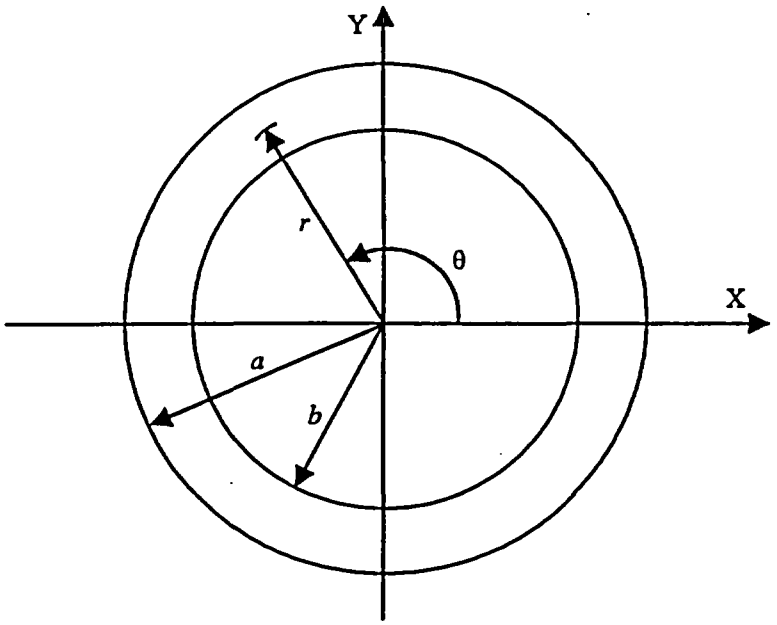

Figure C.3 Plasticity validation pipe cross-section nomenclature

Table C.1 Plasticity validation analysis parameters

Constant	Value
a	203.2 mm (8.00 inch)
b	172.2 mm (6.781 inch)
E	206.85 GPa ($30x10^6$ psi)
σ_o	206.85 MPa ($30x10^3$ psi)
ε_o	0.001 mm/mm (inch/inch)
n	7.0
ε_t	0.0006 mm/mm (inch/inch)
l_0	508 mm (20 inch)

Table C.2 Plasticity validation theoretical values for pure bending

Radius of Curvature, m (in)	Moment, kN-m (in-kips)	Strain, mm/mm (in/in)	Stress, MPa (psi)	Deflection, mm (inch)
177.80 (7000)	750.835 (6645.731)	0.001056	216.825 (31447)	0.73 (0.029)
170.18 (6700)	780.535 (6908.615)	0.001103	223.539 (32420)	0.76 (0.030)
165.10 (6500)	800.470 (7085.059)	0.001137	227.706 (33025)	0.78 (0.031)
152.40 (6000)	850.358 (7526.621)	0.001232	237.392 (34430)	0.85 (0.033)
139.70 (5500)	900.226 (7968.008)	0.001344	246.429 (35740)	0.92 (0.036)
132.08 (5200)	930.199 (8233.309)	0.001421	251.689 (36503)	0.98 (0.038)
127.00 (5000)	950.244 (8410.726)	0.001478	255.165 (37007)	1.02 (0.040)
114.30 (4500)	1000.768 (8857.920)	0.001642	263.864 (38269)	1.13 (0.044)
101.60 (4000)	1052.319 (9314.210)	0.001848	272.766 (39560)	1.27 (0.050)
88.90 (3500)	1105.644 (9786.189)	0.002112	282.129 (40918)	1.45 (0.057)
76.20 (3000)	1161.842 (10283.604)	0.002464	292.274 (42389)	1.69 (0.067)
63.50 (2500)	1222.643 (10821.764)	0.002956	303.660 (44041)	2.03 (0.080)

Table C.3 Plasticity validation deviation from theoretical values for pure bending

Radius of Curvature, m (in)	Strain Error, %			Stress, %			Displacement, %		
		ABAQUS			ABAQUS			ABAQUS	
	ANSYS	PIPE31	ELBOW31	ANSYS	PIPE31	ELBOW31	ANSYS	PIPE31	ELBOW31
177.80 (7000)	0.74	2.01	1.25	0.56	-0.68	-1.09	0.74	2.01	1.28
170.18 (6700)	0.97	2.70	1.84	0.62	-1.07	-1.51	0.97	2.69	1.87
165.10 (6500)	1.10	2.97	2.23	0.64	-1.22	-1.60	1.10	2.97	2.26
152.40 (6000)	0.88	2.91	3.14	0.41	-1.42	-1.33	0.88	2.91	3.17
139.70 (5500)	-0.04	1.71	3.85	-0.01	-1.56	-0.61	-0.04	1.71	3.89
132.08 (5200)	-0.94	0.89	3.87	-0.34	-1.44	-0.15	-0.94	0.89	3.90
127.00 (5000)	-1.66	1.20	3.64	-0.57	-0.90	0.13	-1.66	1.21	3.68
114.30 (4500)	-2.30	1.39	2.43	-0.68	0.42	0.84	-2.30	1.39	2.48
101.60 (4000)	-1.74	0.60	0.78	-0.45	1.65	1.71	-1.74	0.60	0.83
88.90 (3500)	0.43	-1.28	-1.71	0.11	2.77	2.58	0.43	-1.28	-1.66
76.20 (3000)	3.52	-4.37	-5.58	0.76	3.74	3.25	3.52	-4.37	-5.52
63.50 (2500)	7.54	-8.82	-10.98	1.46	4.52	3.68	7.54	-8.82	-10.93

Table C.4 Plasticity validation theoretical values for tension plus bending

Radius of Curvature, m (in)	Moment, kN-m (in-kips)	Tension, N (lb)	Strain, mm/mm (in/in)	Stress, MPa (psi)	Deflection, mm (inch)
177.80 (7000)	647.414 (5730.342)	3902 (877168)	0.001656	264.505 (38362)	0.73 (0.029)
170.18 (6700)	669.373 (5924.700)	3829 (860793)	0.001703	266.687 (38678)	0.76 (0.030)
165.10 (6500)	684.982 (6062.857)	3776 (848775)	0.001737	268.190 (38896)	0.78 (0.031)
152.40 (6000)	727.946 (6443.136)	3622 (814195)	0.001832	272.137 (39469)	0.85 (0.033)
139.70 (5500)	777.730 (6883.781)	3432 (771628)	0.001944	276.399 (40087)	0.92 (0.036)
132.08 (5200)	811.668 (7184.170)	3297 (741241)	0.002021	279.133 (40483)	0.98 (0.039)
127.00 (5000)	836.317 (7402.346)	3196 (718537)	0.002078	281.041 (40760)	1.02 (0.040)
114.30 (4500)	905.097 (8011.129)	2904 (652899)	0.002242	286.154 (41502)	1.13 (0.044)
101.60 (4000)	978.159 (8657.807)	2586 (581437)	0.002448	291.859 (42329)	1.27 (0.050)
88.90 (3500)	1049.926 (9293.023)	2276 (511581)	0.002712	298.332 (43268)	1.45 (0.057)
76.20 (3000)	1121.281 (9924.594)	1972 (443418)	0.003064	305.830 (44355)	1.70 (0.067)
63.50 (2500)	1194.443 (10572.160)	1673 (376048)	0.003556	314.764 (45651)	2.03 (0.080)

Table C.5 Plasticity validation deviation from theoretical values for tension plus bending

Radius of Curvature, m (in)	Strain Error, %			Stress, %			Displacement, %		
		ABAQUS			ABAQUS			ABAQUS	
	ANSYS	PIPE31	ELBOW31	ANSYS	PIPE31	ELBOW31	ANSYS	PIPE31	ELBOW31
177.80 (7000)	0.66	4.70	3.26	0.19	0.77	0.15	0.62	4.39	2.65
170.18 (6700)	0.41	4.51	3.03	0.12	0.99	0.35	0.41	4.14	2.35
165.10 (6500)	0.75	4.36	2.88	0.38	1.14	0.50	0.68	3.94	2.14
152.40 (6000)	0.91	3.86	2.42	0.24	1.54	0.90	0.81	3.38	1.60
139.70 (5500)	0.99	3.19	1.86	0.25	1.98	1.36	0.86	2.70	1.00
132.08 (5200)	1.46	2.70	1.44	0.36	2.27	1.67	1.25	2.22	0.59
127.00 (5000)	1.85	2.32	1.13	0.44	2.47	1.88	1.58	1.89	0.29
114.30 (4500)	2.04	1.13	0.10	0.46	2.97	2.44	1.74	0.77	-0.60
101.60 (4000)	2.32	0.00	-1.43	0.53	3.75	3.08	2.15	0.17	-1.76
88.90 (3500)	2.88	-2.61	-3.84	0.60	4.20	3.65	2.28	-2.55	-3.90
76.20 (3000)	1.30	-6.94	-7.28	0.26	4.26	4.16	0.06	-7.53	-7.14
63.50 (2500)	3.15	-11.83	-12.19	-0.84	4.61	4.39	2.81	-11.89	-12.22

(ANSYS MISO model) was used to model the stress-strain behavior using 86 points to define the curve. Default convergence criteria were used. The analyses were conducted with ANSYS/ED 5.7 running on a desktop PC.

The ABAQUS solution used PIPE31 or ELBOW31 elements. Again, 20 elements were used along the length of a cantilever beam. The same 86 points were used to define the stress-strain curve, and default convergence criteria were used. ABAQUS 5.8 running on a Sun UltraSparc was used to generate the solutions.

All of the models used in the plasticity evaluation are listed in section C.6.1.

C.3.1.3 Plasticity Validation Summary

The results of the analyses show that both ANSYS and ABAQUS give results in reasonably good agreement with the theoretical solutions. General observations, based on the cases considered include: 1) the finite element solutions are within about 10 percent of the theoretical solutions, 2) both programs have some solutions that are above and some solutions that are below the theoretical values, depending on the load level, 3) higher loads tend to have greater absolute errors, 4) the ANSYS solution for combined tension and bending is better than the pure bending solution while the opposite is true for the ABAQUS solutions, and 5) the largest absolute errors occur with ABAQUS ELBOW31 elements.

In terms of the Actual Margins task, the results of this study indicate that the ANSYS pipe plasticity model is perfectly acceptable for the analyses that consider plasticity remote from the crack.

C.3.2 Moment-Rotation Behavior of Cracks During Unloading

The behavior of a crack undergoing unloading needs to be carefully considered in a nonlinear finite element analysis. Crack behavior is inherently asymmetric—pressure reduces the moment carrying capacity during loading, but it certainly does not promote compressive yielding. Because the nonlinear crack will usually follow some sort of standard plasticity hardening rule and these rules are generally symmetric in their behavior, crack models based on elements that use these hardening rules may not unload correctly after yielding unless special precautions are taken.

An approach to crack unloading, developed during the BINP program is presented in the following discussion. Although the work as presented is focused on circumferential surface cracks, extension to the case of circumferential through-wall and axial cracks is not difficult.

C.3.2.1 Moment-Rotation General Considerations

Nonlinear crack behavior of a circumferential crack in a finite element analyses can be characterized as crack moment versus crack rotation and can be implemented as a set of three elastic-perfectly plastic springs in series, see Figure C.4. Implicit with the elastic-plastic spring formulation is the assumption of kinematic hardening, i.e., yielding in the compressive direction occurs at $2\sigma_y$ below a plastic unloading point, Figure C.5. This is equivalent to saying that the compressive moment-rotation response is the mirror image of the tension moment-rotation response. Furthermore, because the nonlinear behavior of the crack is modeled only as moment-rotation, effects such as axial loading, which affects the state of stress at the crack tip, must be "built into" the moment-rotation curve. That is, a crack with pressure and moment loading will have an apparently lower moment-rotation resistance than a crack with moment only loading, Figure C.6.

For cases where crack loading is always tensile and reverse yielding never occurs, a kinematic hardening model using the pressure-corrected case is perfectly suitable. However, if significant reverse loading is expected, i.e., seismic loading, compressive yielding will occur far too early if a pressure-corrected moment rotation curve is used as the basis of the crack model. Basically, because the pressure-corrected moment-rotation curve is the mirror image of the tensile moment-rotation curve, it is as if the

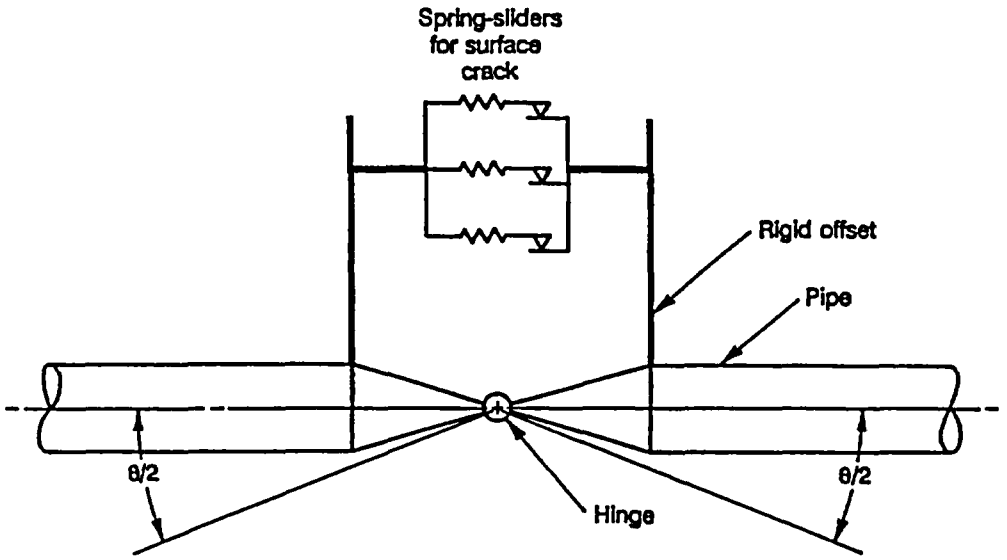

Figure C.4 Spring-slider model for a surface crack (or a through-wall crack)

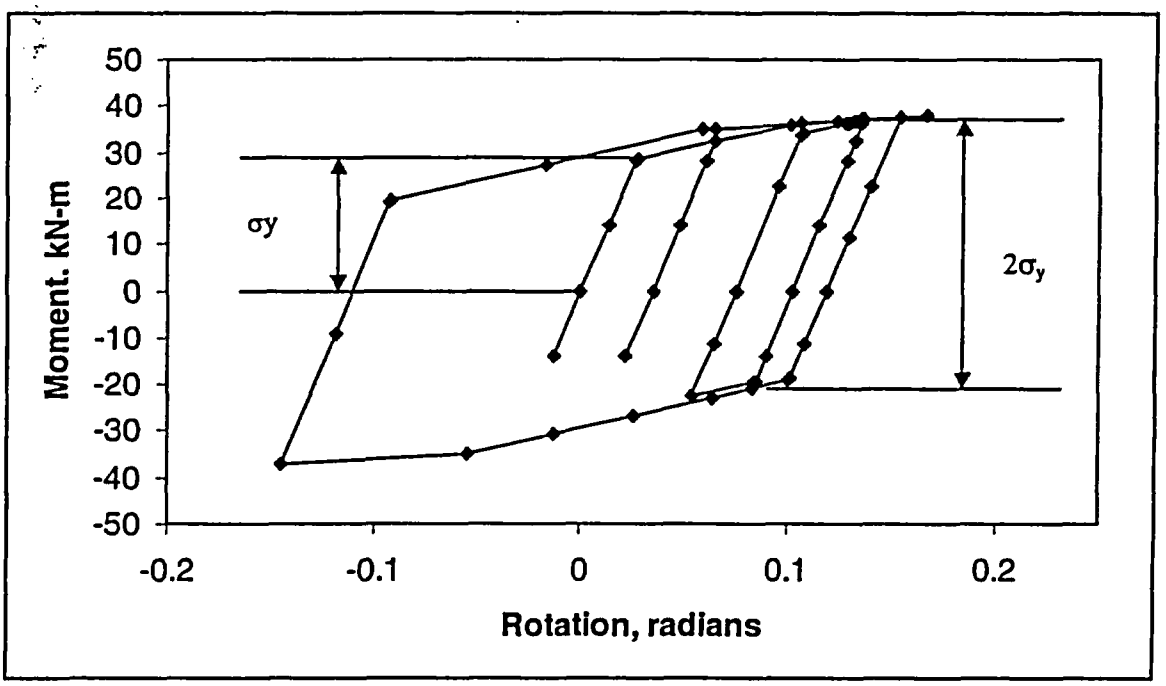

Figure C.5 Kinematic hardening assumption under unloading conditions

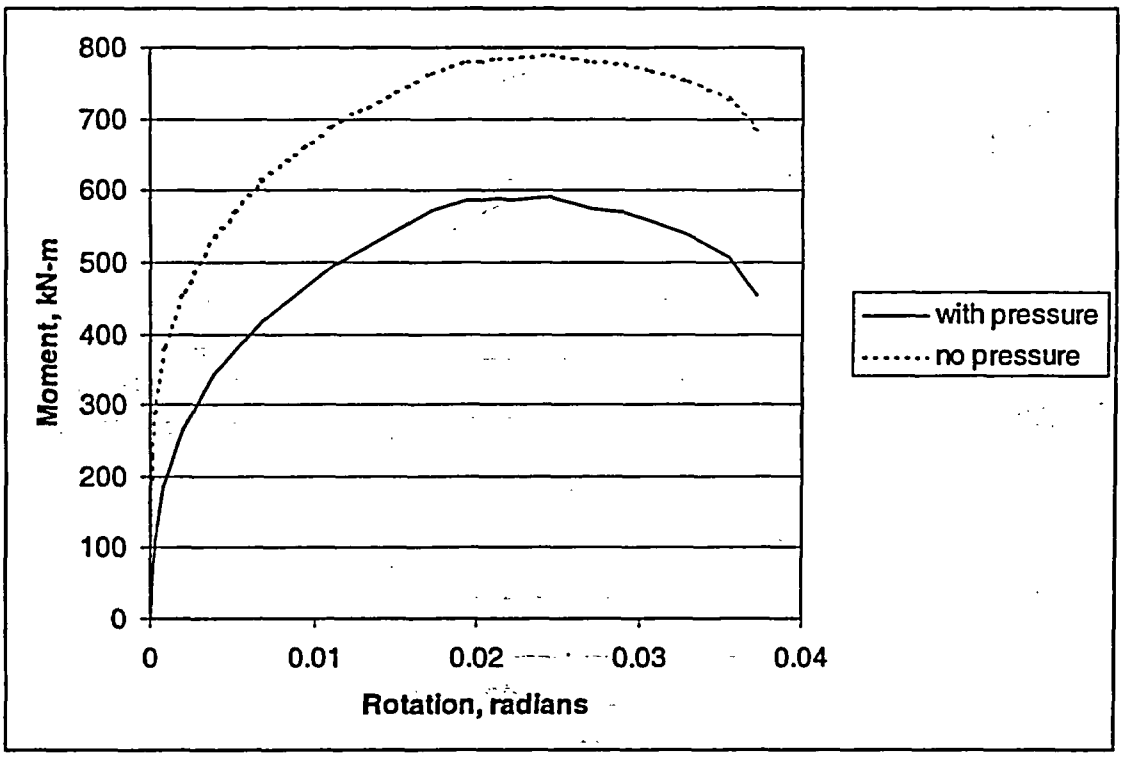

Figure C.6 The effect of pressure on crack moment-rotation behavior (BINP Task 2 flaw, A8ii-20 dynamic monotonic J-resistance)

stress at the crack tip caused by pressure changes sign when the crack is unloaded: A totally inappropriate response. The crack should unload elastically much further before it yields in compression, Figure C.7. This is quite important for an LBB analysis or a flaw evaluation analysis where one is trying to find margin, because it is the unloading and subsequent compressive yielding that takes energy away from driving the crack.

C.3.2.2 Model for Crack Unloading

Any new modeling approach for circumferential cracks loaded with pressure and bending to better define the compressive loading behavior needs to include the following:

- Tensile loading failure based on pressure plus bending,
- Consistency with kinematic hardening rules, i.e., $2\sigma_y$ yielding behavior, and
- Compressive loading must account for the pressure effect.

Taken as a whole, these conditions imply that the moment-rotation response of the crack must be asymmetric, i.e., compression is not a mirror image of tension. The last two conditions imply that compressive yielding in moment-rotation coordinates must occur at twice the tensile yield moment (including the pressure effect) plus twice the pressure-induced moment effect. Figure C.7 provides a pictorial representation of the desired behavior.

Implementation of asymmetry in the moment-rotation response in the finite element model would, in general, require a special constitutive model or a special element that is not likely in a standard finite element library. The desired response, however, can be achieved with kinematic hardening elements as follows:

1. Define the expected tensile crack moment-rotation behavior using a J-estimation scheme analysis that includes pressure,

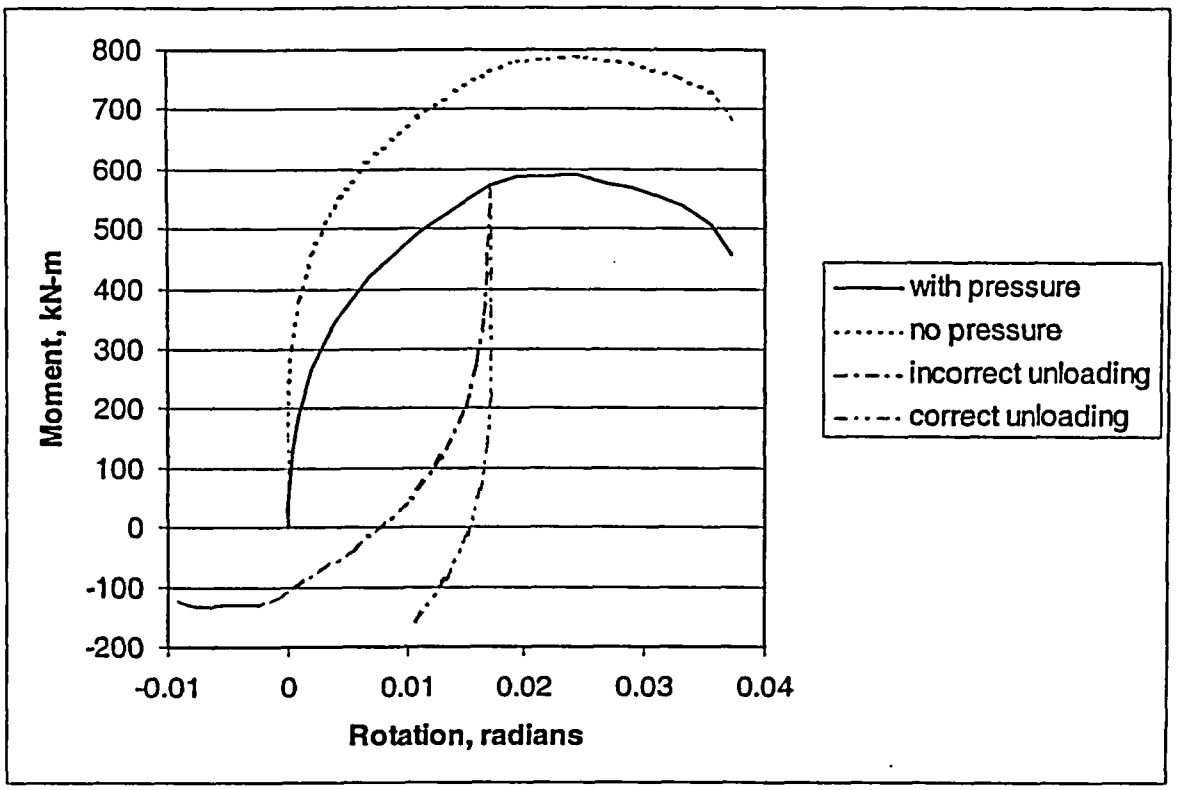

Figure C.7 Crack unloading behavior

2. Define the pressure contribution to the tensile failure by running a J-estimation scheme analysis identical to the first one but without pressure,
3. Use the data from the second analysis to define the "springs" and "sliders" for the nonlinear crack model,
4. Apply + and - crack opening moments at the two nodes of the spring-sliders equal to the moment difference between the results from Step 1 and Step 2, and
5. Conduct the analysis as usual.

The net effect of this process is to make the crack moment-rotation response appear asymmetric as far as tensile and compressive yielding of the crack is concerned. However, as far as the pipe system is concerned the correct crack response is modeled:

- The stresses in the pipe will be calculated correctly because the moments applied in Step 4 sum to zero.
- The incremental tensile moment that the crack can stand will be correct because the moments applied in Step 4 make up the difference between the moments the spring sliders in the model will permit and the real failure moment calculated in Step 1.

One does have to be careful about recovering and reporting moments at the crack because the apparent moment in the spring sliders will be too large by the offset moment.

C.3.2.3 Crack Unloading Model Validation

To provide some level of comfort that the proposed crack unloading model is rational, an analysis of the IPIRG-2 Experiment 1-1 (Ref. C.4) surface crack experiment was conducted to see how well the analysis compares with an experiment. Figures C.8 and C.9 show the measured pipe response from the experiment up to surface-crack penetration.

The result of the cracked pipe analysis is driven by the input moment-rotation response, which, in turn, is determined by the J-estimation scheme crack growth analysis. To bound the

expected behavior, analyses were conducted using moment-rotation curves developed from J-R curves for R = -0.3 and R = 1.0, because the stress ratio for the experiment is about R = -0.6. The predicted moment-rotation behavior for the IPIRG-2 1-1 experiment, generated using the SC.TNP1 analysis in NRCPIPES Version 3.0, is shown in Figure C.10. For these curves, the equivalent crack length (measured crack area divided by the measured maximum depth) was used. There are significant differences between these curves because at R = -0.3 there is very little degradation from the monotonic J-R curve case, whereas at R = -1.0 the J-R curve, and hence moment-rotation is significantly affected by crack closure.

Using the design seismic forcing function for IPIRG-2 Experiment 1-1 (there is virtually no difference between the designed function and the experimentally measured actuator response), ANSYS nonlinear-spring analyses were conducted to the point of maximum load, i.e., presumed surface-crack penetration, using the new compressive unloading behavior model. Figures C.11 through C.14 show the results of the "bounding" analyses. For reference, Figures C.15 and C.16 show the results of the IPIRG-2 1-1 pretest analysis that used the mirror image of the bending plus tension moment-rotation response in the compressive regime.

Comparing Figures C.8, C.11, C.13 and C.15, qualitatively, the new analyses are much closer to the experiment than the "old" analysis in two regards: 1) the new analyses do not show the severe crack closures that the old analysis did, and 2) the new analyses show evidence of the large monotonic load cycle that the old analysis did not predict. Quantitatively, the new R = -0.3 and R = -1.0 analyses bracket the experimentally observed R = -0.6 failure moment, whereas the old analysis is low, although there is a good reason for this—the old analysis was a pretest prediction that used the best pretest estimate of the flaw size, whereas the new analyses used the measured flaw size. Quantitatively, it is also important to note that the rotations in the new analyses are very much larger than the experimentally observed rotations. This is a J-estimation scheme problem—the ANSYS nonlinear spring analysis is only as good as the input from the J-estimation scheme. As a final observation, in the experiment, surface-crack penetration occurred long after maximum moment. Within the bounds of the ANSYS nonlinear spring analysis, this just cannot be predicted because surface-crack penetration is defined to happen at maximum moment. From an experimental perspective, what this implies is that there was either cyclic or fatigue damage that contributed to the eventual failure.

C3.2.4 Crack Unloading Model Summary

The new technique for modeling a crack as it unloads accounts for the expected asymmetric behavior of a crack using a simple hardening rule-based plasticity model. Although there is not a way to rigorously prove that the model is correct because there is not enough quality experimental data available, from a heuristic perspective, it makes sense to use such a model for all plant piping analyses. The issue of which J-R curve to use, R = 0, or R = -?, will always be a question, but the basic mechanics of defining the springs is not in question.

C.3.3 Crack Orientation

In a general finite element analysis of plant piping, some arbitrary global reference coordinate system is used to define the location of all piping system features. Except for a few fortuitous instances, the global coordinate system rarely is aligned orthogonally with the orientation of cracks that may be hypothesized in the piping. Thus, the job of putting nonlinear springs with constraint equations to model cracks at arbitrary orientations becomes a bit of a challenge.

A brute-force approach to putting a spring or constraint at an arbitrary orientation would involve specification of the orientation in terms of Euler angles and applying a series of coordinate transformations to spring stiffnesses and constraint equations. Fortunately, most finite element programs have a far more elegant and simple way to define orientations: Local coordinate systems. The notion of using local coordinates is not revolutionary or new, but it is

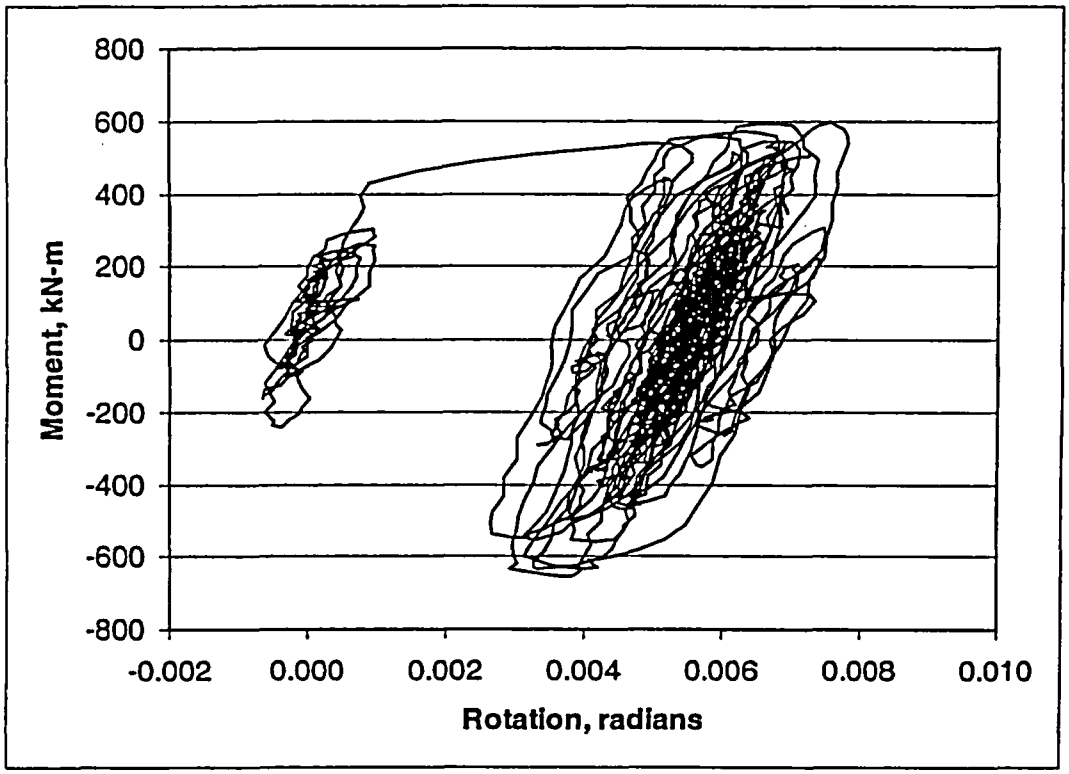

Figure C.8 IPIRG-2 Experiment 1-1 cracked-section moment-rotation response

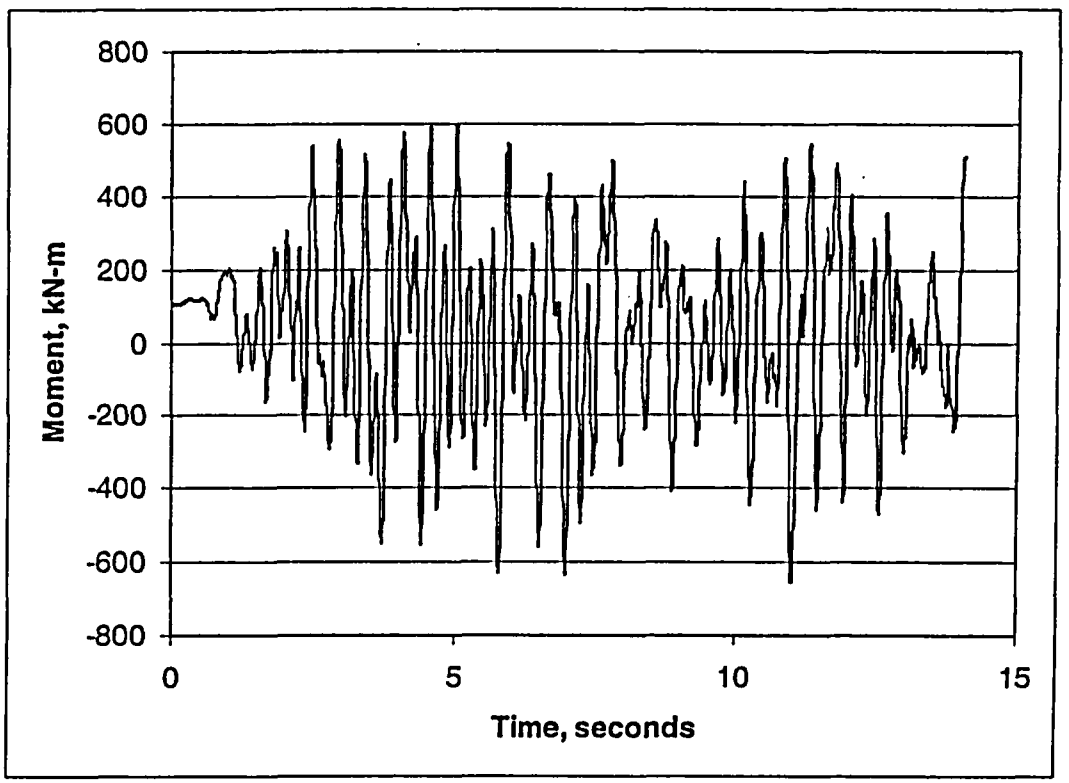

Figure C.9 IPIRG-2 Experiment 1-1 cracked-section moment-time history

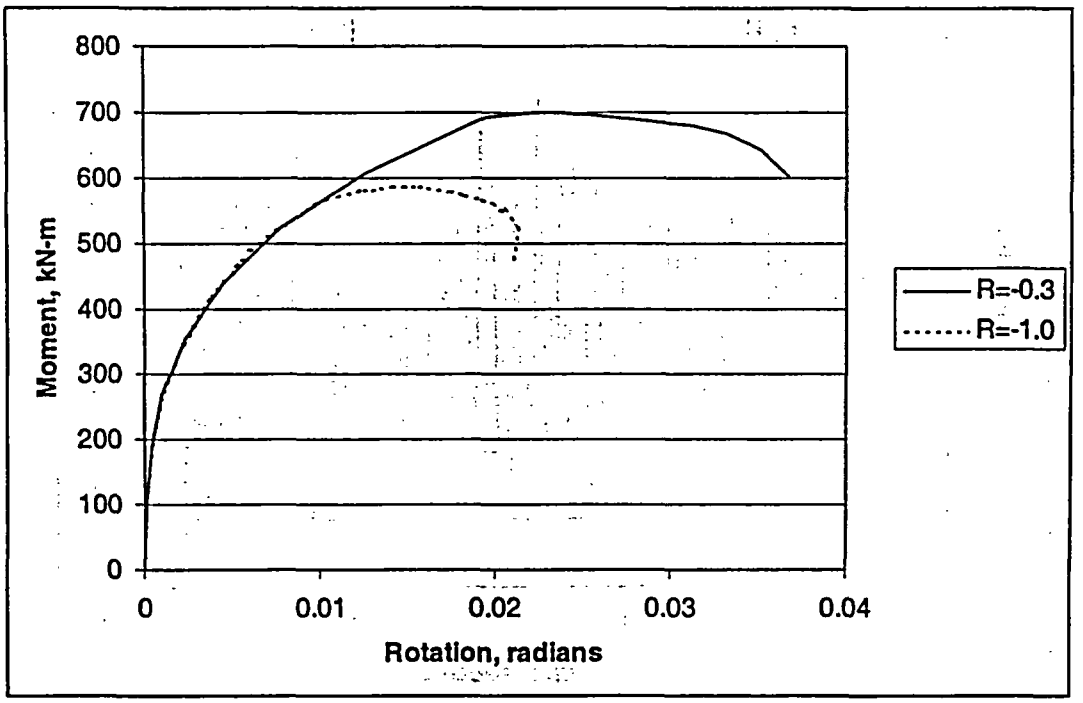

Figure C.10 IPIRG-2 Experiment 1-1 predicted cracked-section upper envelop moment-rotation from the SC.TNP1 J-estimation scheme

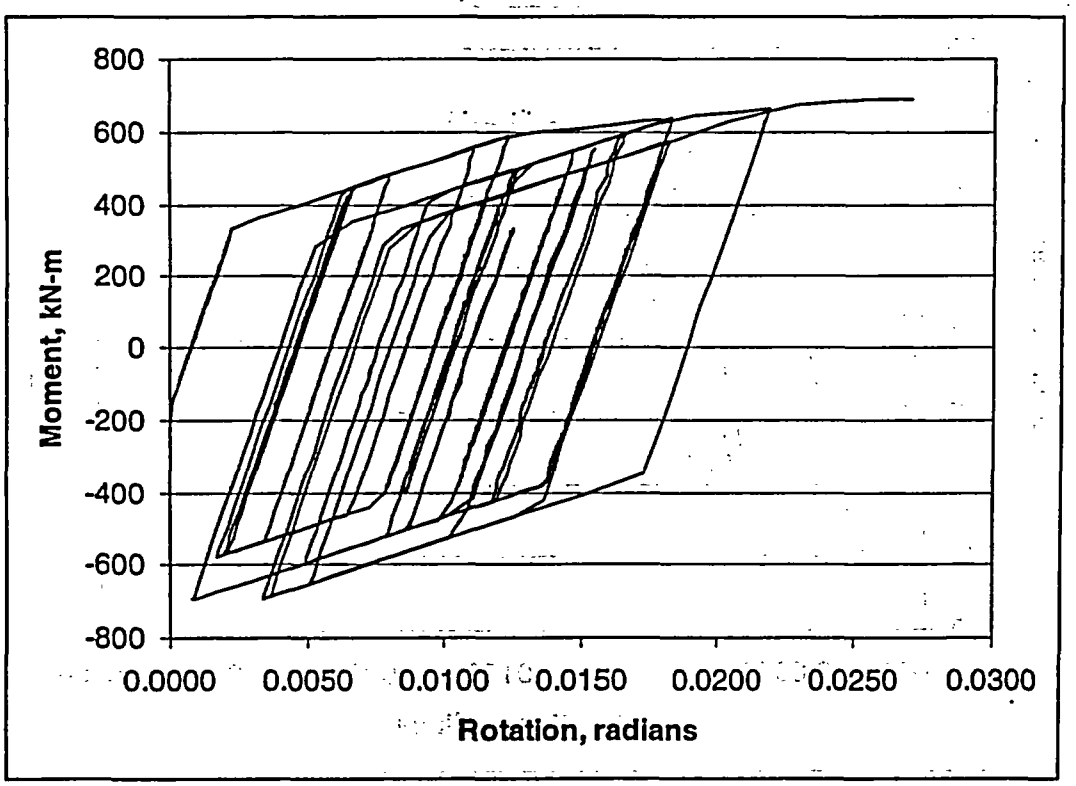

Figure C.11 Predicted IPIRG-2 Experiment 1-1 moment-rotation history using the dynamic R=-0.3 J-R curve with the new asymmetric moment-rotation model

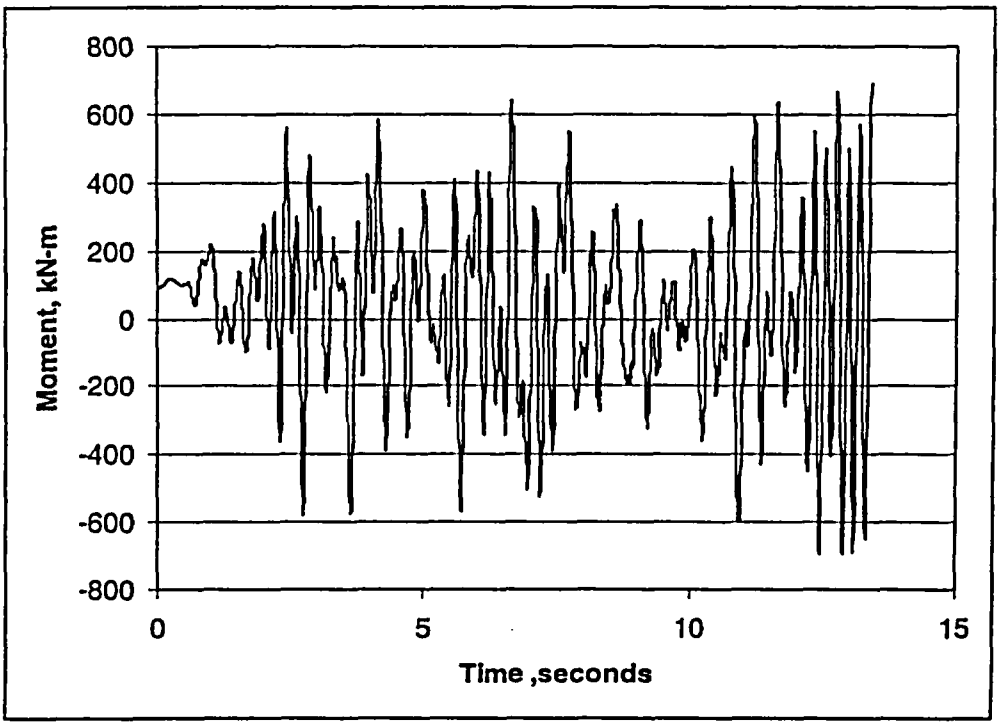

Figure C.12 Predicted IPIRG-2 Experiment 1-1 moment-time history with the dynamic R=-0.3 J-R curve with the new asymmetric moment-rotation model

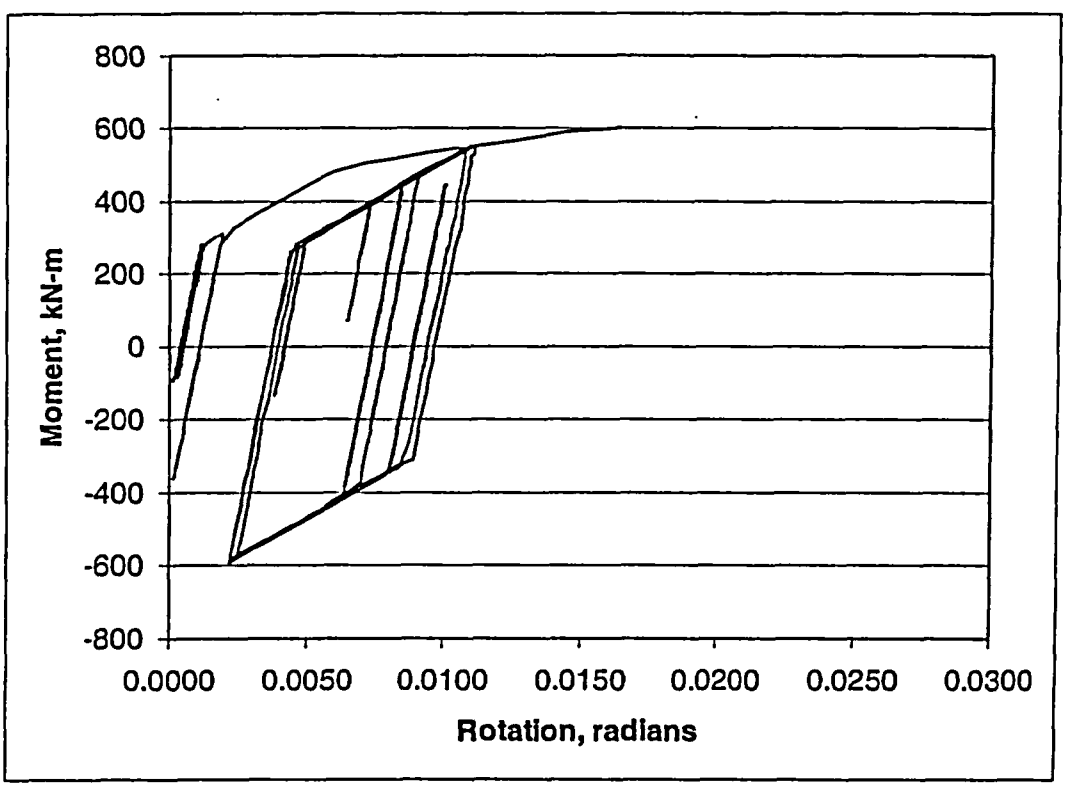

Figure C.13 Predicted IPIRG-2 Experiment 1-1 moment-time history with the dynamic R=-1.0 J-R curve with the new asymmetric moment-rotation model

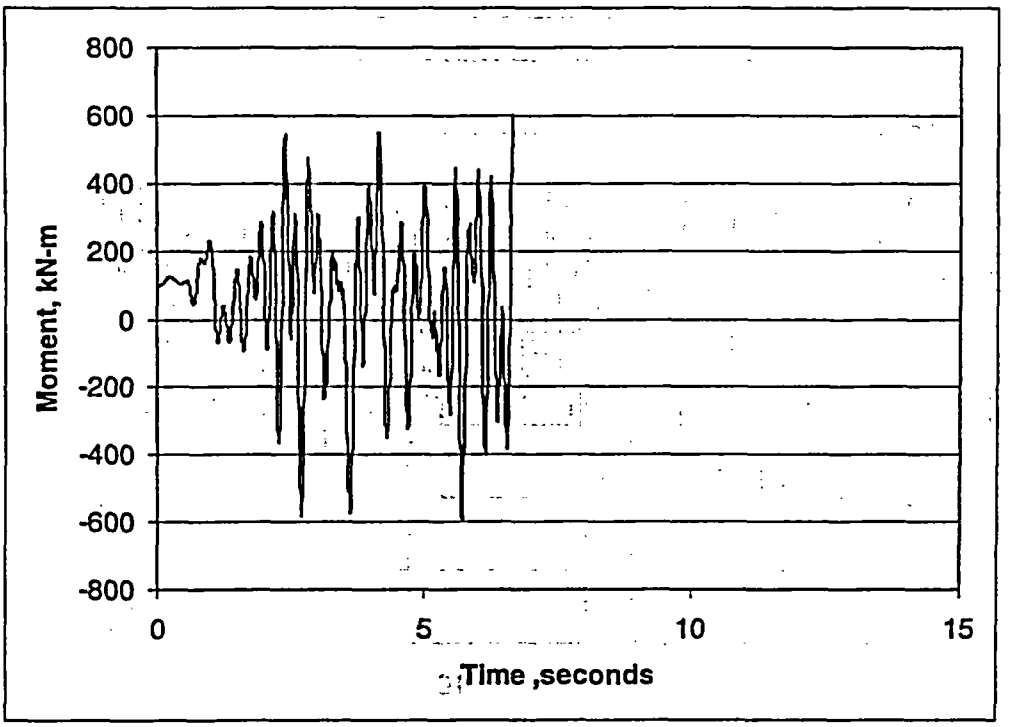

Figure C.14 Predicted IPIRG-2 Experiment 1-1 moment-time history with the dynamic R=-1.0 J-R curve with the new asymmetric moment-rotation model

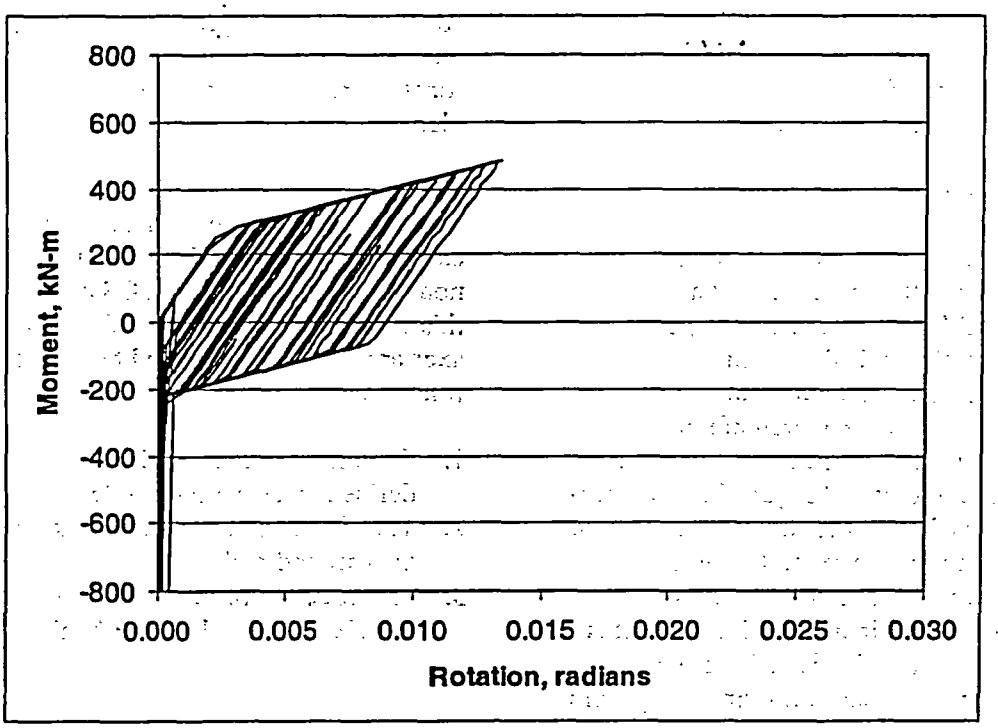

Figure C.15 Old (1993) IPIRG-2 Experiment 1-1 pretest design analysis moment-rotation history results

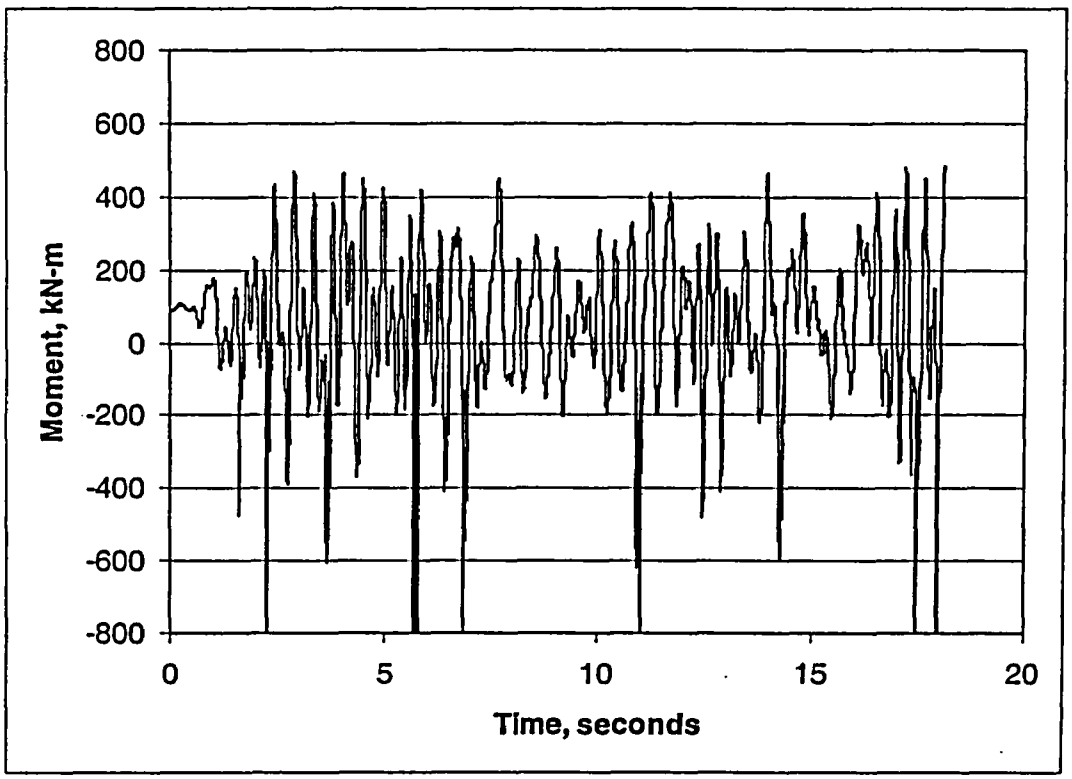

Figure C.16 Old (1993) IPIRG-2 Experiment 1-1 pretest design analysis moment-time results

worthwhile to document their use for the cracked pipe problem, because without them, generating solutions for arbitrarily oriented cracks may appear to be intractable.

C.3.3.1 Defining Crack Orientation

Figure C.17 shows a surge line running from the hot leg to the pressurizer of a Westinghouse 3-loop PWR plant in a perspective view. Also shown is the steam generator and the global reference coordinate system. Considering a case where a circumferential crack is to be analyzed at the hot leg to surge line intersection, looking at Figure C.17, it nominally appears as though the surge line is aligned with the global reference axes. However, looking at the system with orthogonal views aligned with the global axes, Figures C.18 to C.20, it is apparent that the surge line is definitely not aligned with the global axes: Moving away from the hot leg along the axis of the surge line, it drops down in Z, and it moves toward –X. Describing the directions associated with this geometry via Euler angles and coordinate rotations would be prone to mistakes, if not extremely difficult, whereas using the built-in local coordinate system capabilities of the finite element program is, comparatively, trivial.

ANSYS has a number of methods that can be used to define local coordinate systems, but the easiest one to use for illustration purposes is the node-based definition, i.e., CS command. Using this style of local coordinate definition, the local axes are completely defined by specifying the following:

1. The origin of the coordinate system is defined by selecting a node
2. The direction of the local X axis is defined by a second node
3. The direction of the Y axis is then defined by selecting a node in the X-Y plane.

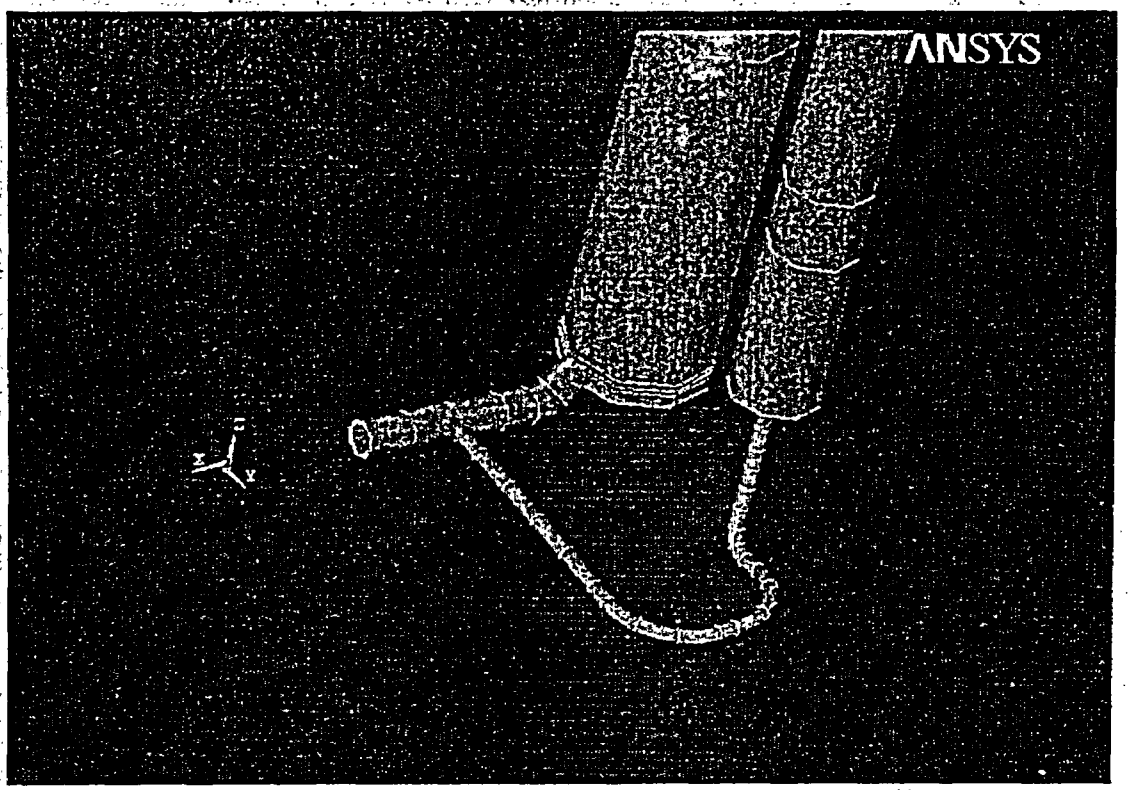

Figure C.17 PWR model surge line with global reference axes

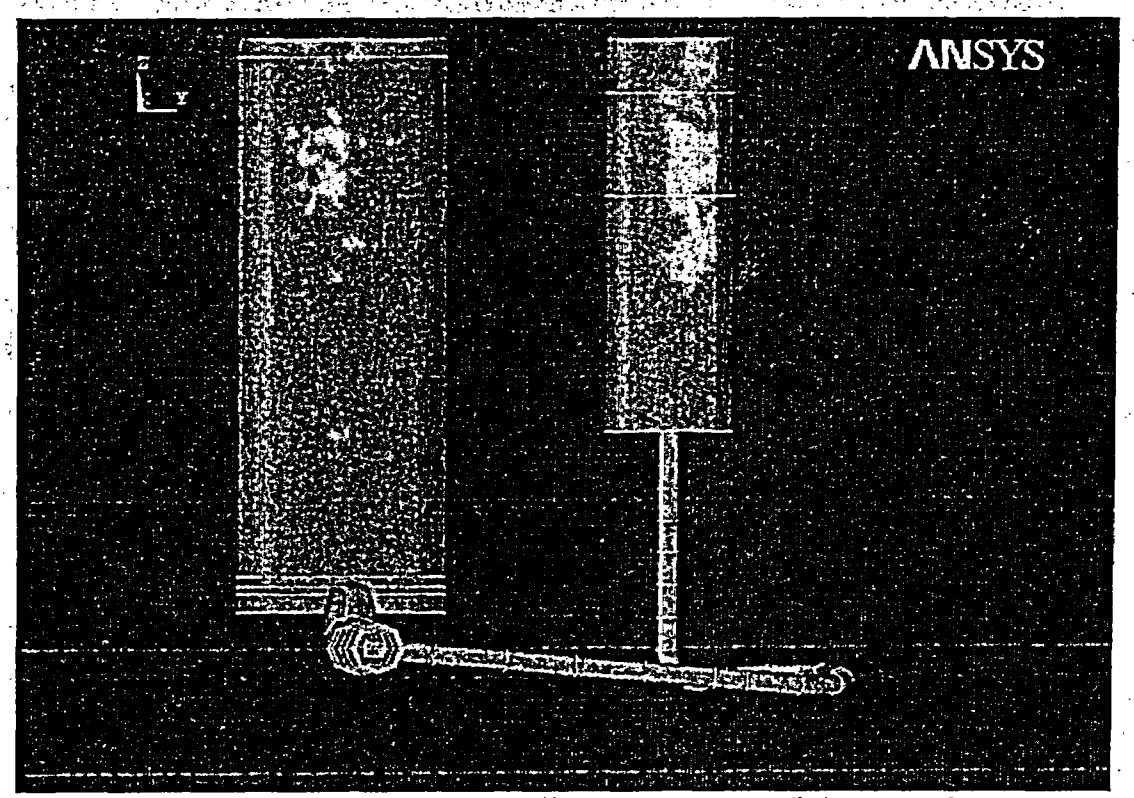

Figure C.18 Side view of the surge line

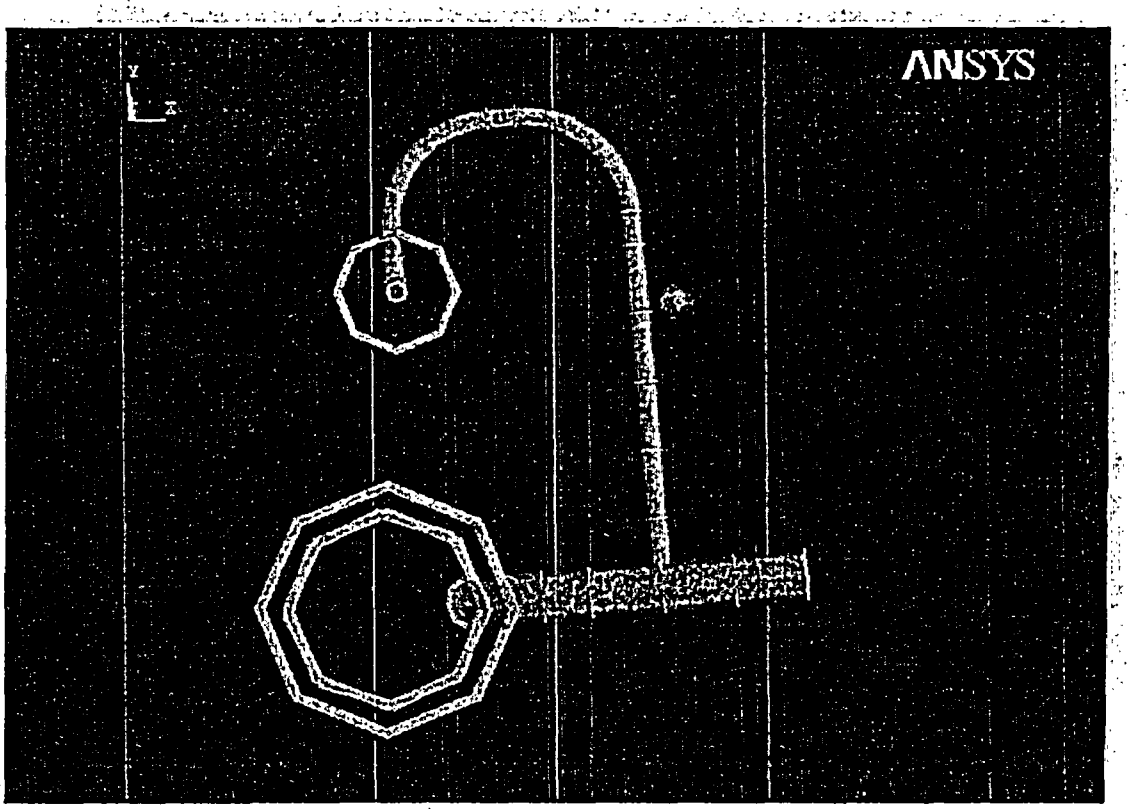

Figure C.19 Top view of the surge line

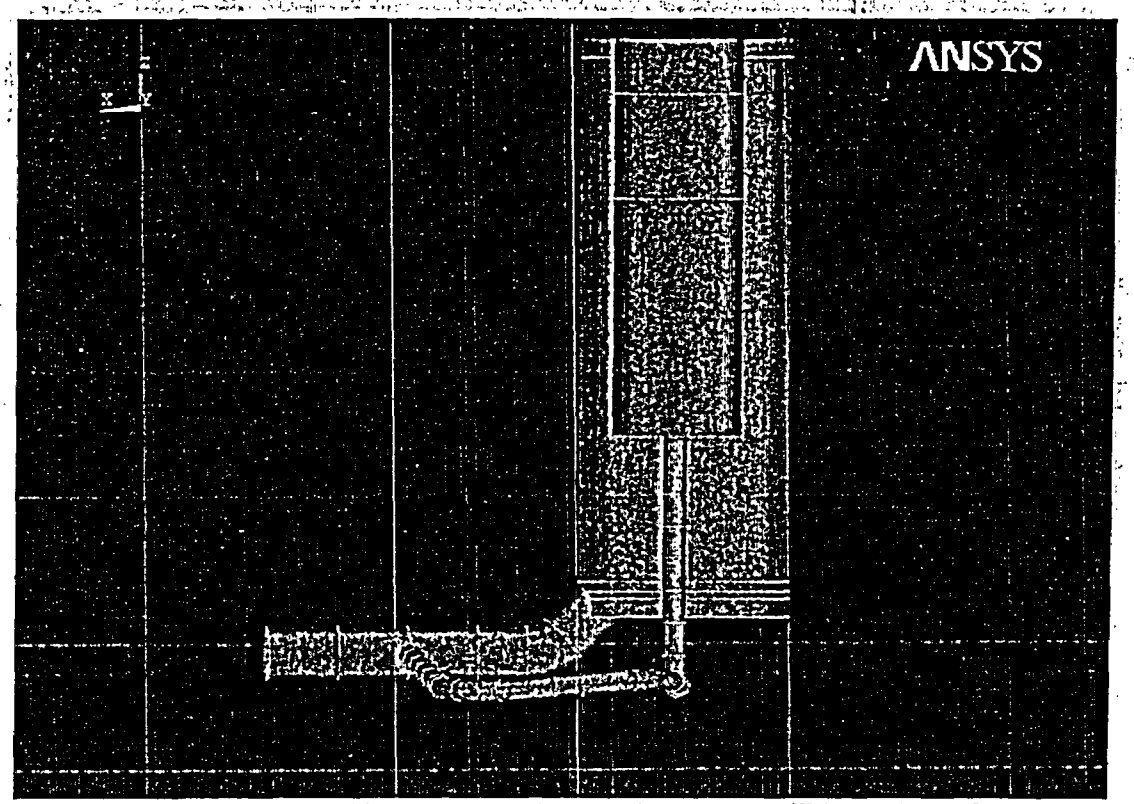

Figure C.20 Front view of the surge line

Given these three bits of information, a local coordinate system, with the X-axis directed along the axis of pipe can easily be defined, Figures C.21 and C.22. (Note: To define these axes, a dummy node was inserted at the X-Y coordinates of the end of the surge line but with a greater Z elevation.) To complete the local axis definition, the local coordinate system can be rotated about its own X axis with a CLOCAL command, compare Figures C.21 and C.23.

Given the local coordinate system, the coincident finite element nodes associated with the crack can be rotated into the local coordinate system (NROTAT command) and the crack springs and constraints defined in the local system just as though they were in the global reference system. Care must be taken when recovering crack rotations and moments to be sure which coordinate system they are in, but usually, these can be forced to be output in the local coordinate system.

C.3.3.2 Crack Orientation Summary

Being able to define the orientation of a crack oriented in any direction, relative to a global reference coordinate system, is essential to conducting nonlinear cracked pipe analyses. There are well-defined brute-force methods that can be applied, but the use of local coordinates greatly simplifies the work for the piping stress analyst.

Although the present discussion has focused on the local coordinate system facilities of ANSYS, any contemporary general purpose finite element program should have similar capabilities that a piping analyst needs to use to his/her advantage.

C.4 Analytical Study of Margins

There is a sense that nuclear power plant piping is far more tolerant of defects than the traditionally used linear analyses suggest. Heretofore, no systematic effort had been spent to determine just how much margin really exists in plant piping. The BINP Actual Margins task addressed this deficiency. By way of example, some idea of the margins that might be seen in plant piping was explored by looking at the margins that exist in two piping systems, namely the IPIRG pipe loop and the primary piping in a PWR plant. The conclusions from these examples can, by no means, be extrapolated to every plant piping situation, but they do provide a justification for continued consideration of the use of the nonlinear methods that are used to calculate these margins.

C.4.1 Analysis of IPIRG Pipe Loop Experiment Scenarios

As a preliminary to considering the margins in real plant piping, margins were calculated for the IPIRG pipe test system. The interest in the IPIRG pipe system was driven by a desire to know what might have been observed had the Actual Margins task had been conducted experimentally. To make the margins most apparent, the analyses were conducted assuming that the whole IPIRG pipe loop was made out of TP304 stainless steel and single frequency excitation loading was used.

C.4.1.1 IPIRG Analysis Model

Figure C.24 is an artist's rendition of the IPIRG pipe loop and Figure C.25 shows the physical dimensions of the pipe loop. Unlike the actual IPIRG pipe loop, all of the Actual Margins pipe, except for the cracked section, was assumed to be 406-mm (16-inch) nominal diameter Schedule 100 pipe. Also unlike the actual IPIRG pipe loop which had high-strength carbon steel elbows and straight pipe, the configuration analyzed assumed that all of the pipe was TP304 stainless steel.

Four different cracks were analyzed as shown in Table C.6. In every case, the cracks were assumed to be in base metal TP304 stainless steel pipe of the same size as tested in IPIRG-1 Experiment 1.3-3 (Refs. C.7 and C.8), i.e., 415.8-mm (16.37-inch) OD by 26.2-mm (1.031-inch) wall thickness. The cracks, as well as the rest of the pipe loop, were assumed to be at PWR conditions, i.e. 288°C (550°F) and 15.5 MPa (2250 psi). For the leak rate calculations, the through-wall cracks were assumed to be fatigue cracks, with an assumed nominal

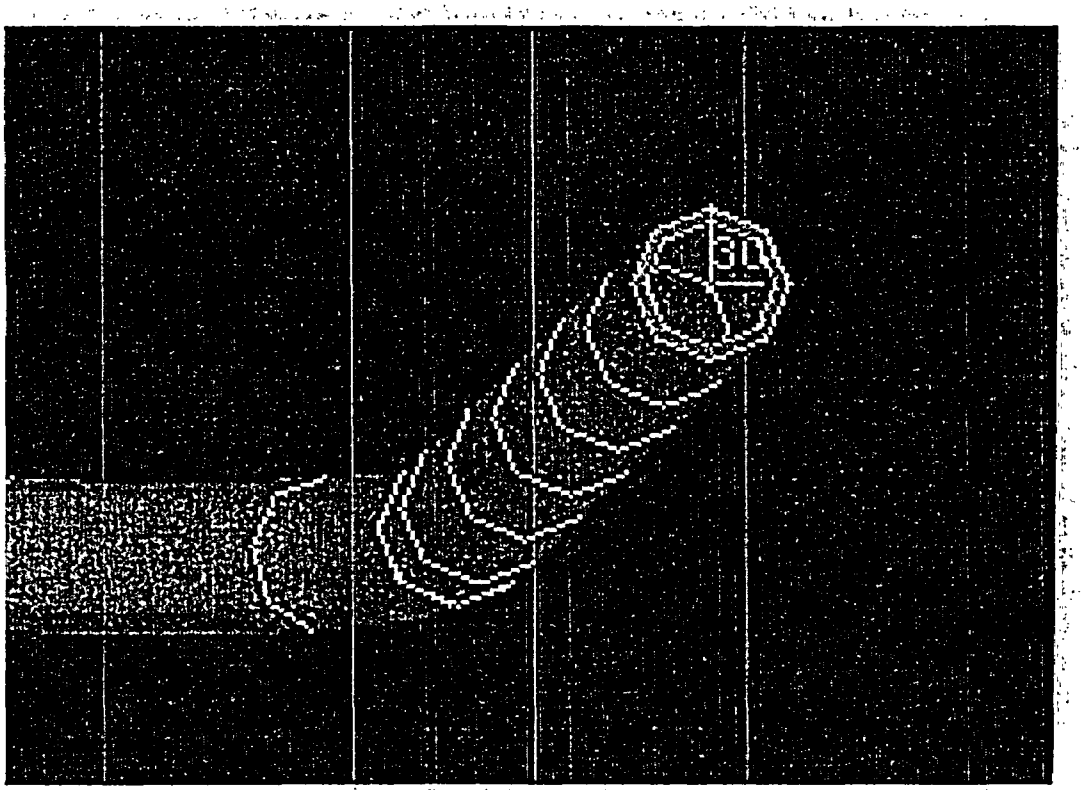

Figure C.21 View looking down the surge line, more or less along the #30 local coordinate system X axis

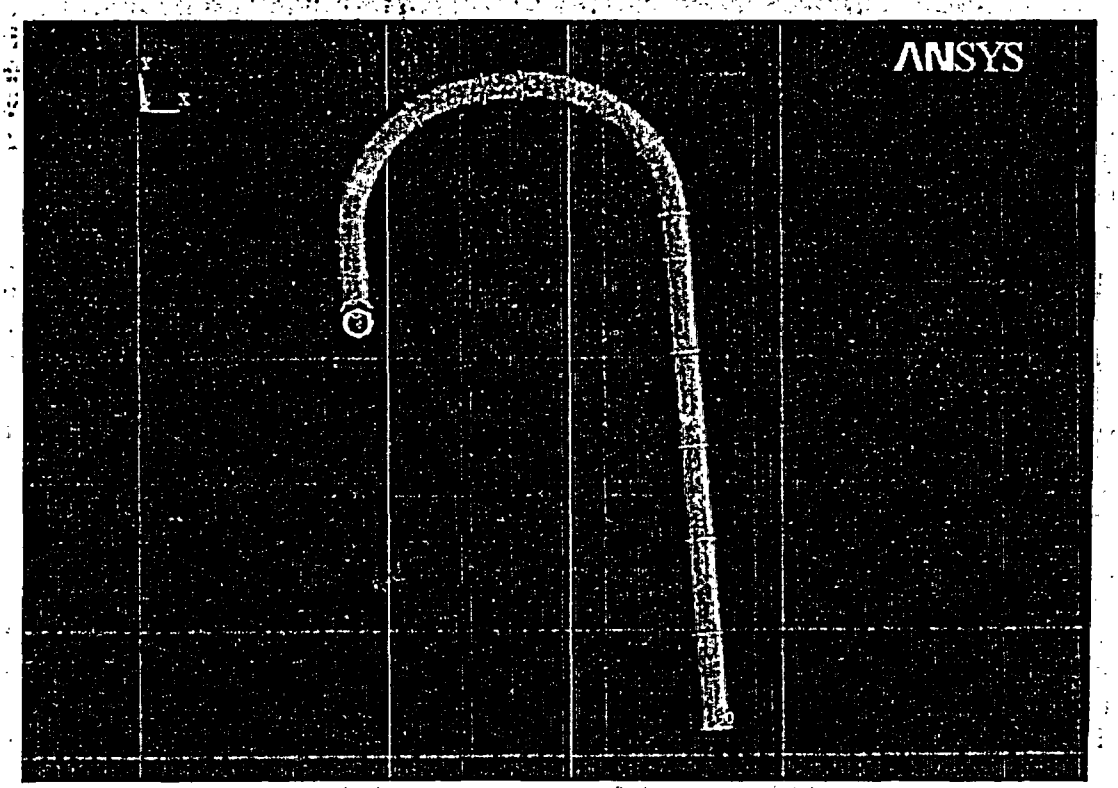

Figure C.22 Top view of the surge line showing local coordinate system #30

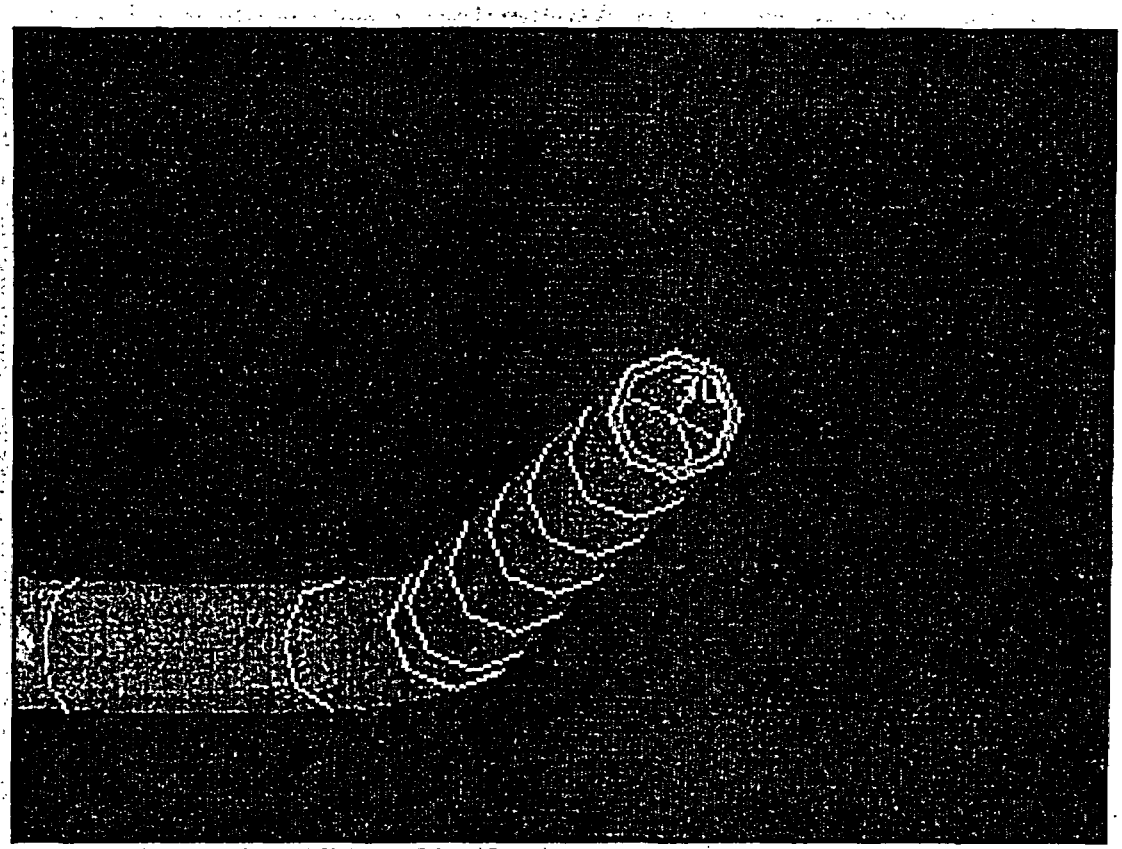

Figure C.23 View looking down the surge line, more or less along the rotated #30 local coordinate system X axis

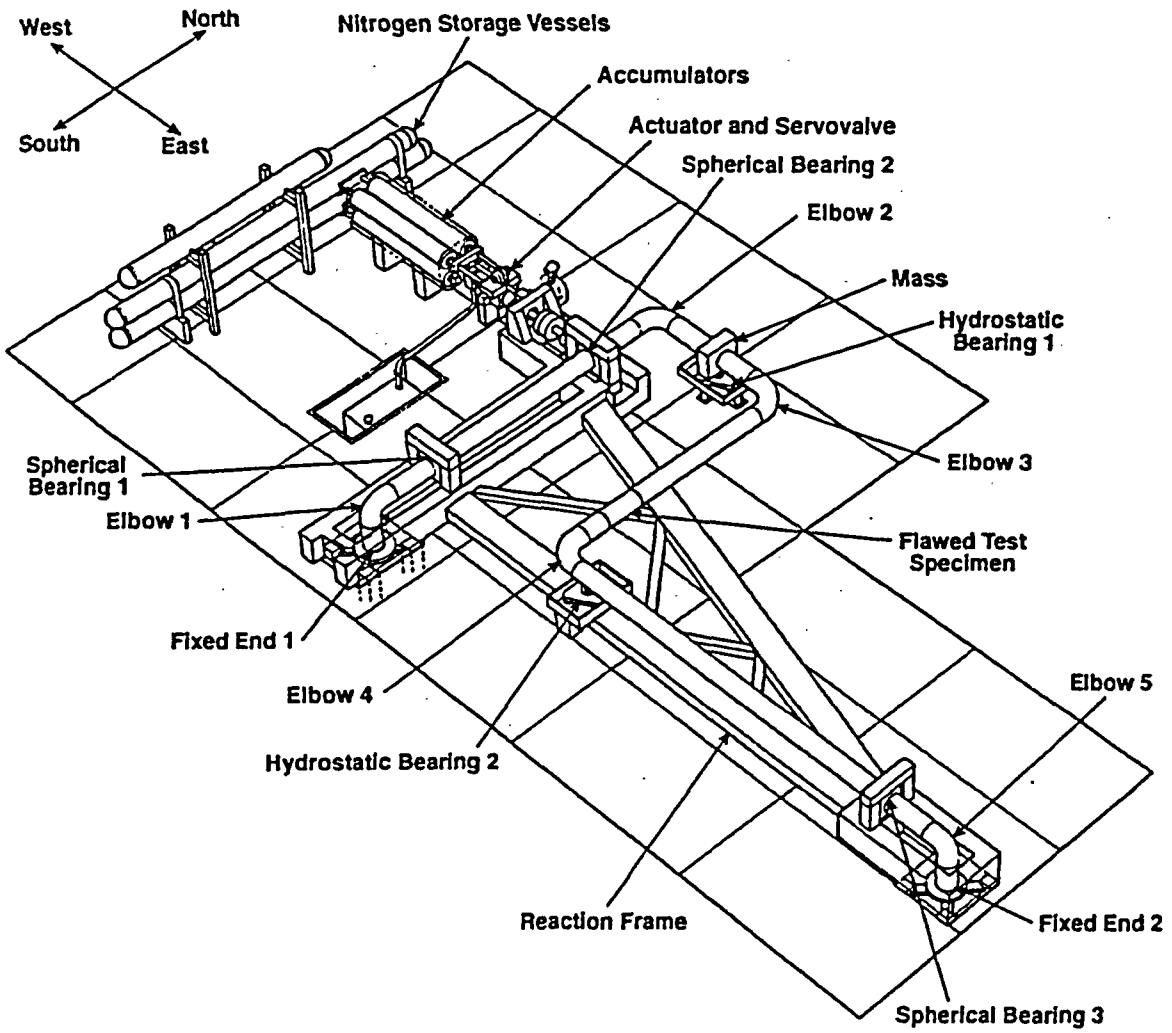

Figure C.24 Artist's rendition of the IPIRG pipe test facility

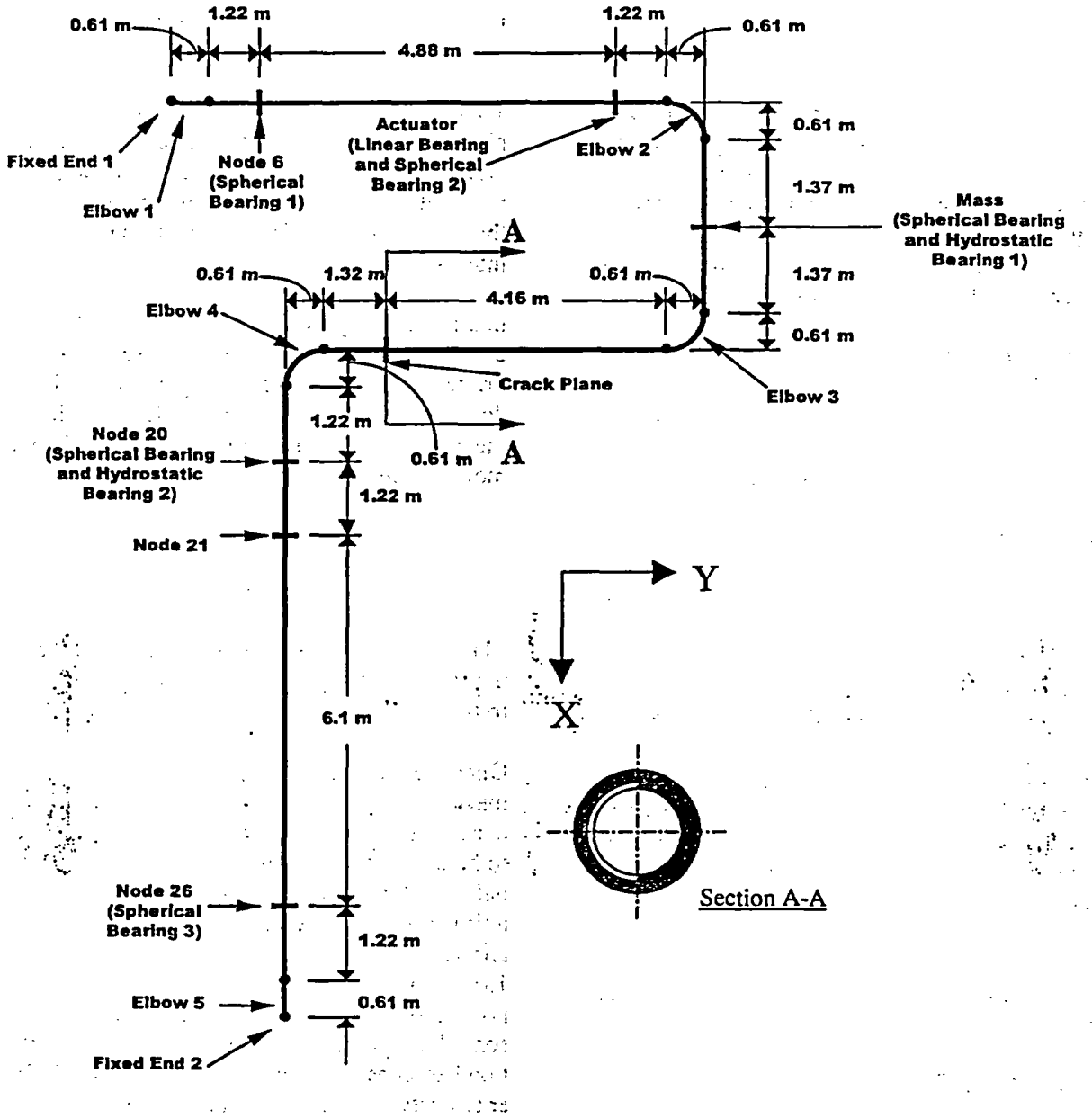

Figure C.25 Dimensions of the IPIRG pipe loop

Table C.6 IPIRG pipe loop system Actual Margins task cracks

Crack Description	Leak Rate liter/min (gpm)	Crack Size		Load Capacity kN-m (in-kip)
		Depth, d/t	Length, L/(πD)	
Large SC	-	0.66	0.50	459.2 (4064.4)
Small SC	-	0.48	0.50	651.5 (5766.1)
Large TWC	189.27 (50)	1.0	0.19	452.2 (4000.4)
Small TWC	18.9 (5)	1.0	0.09	679.6 (6015.5)

operating stress of S_m [116.9 MPa (16.95 ksi)]. Material properties for the cracks and the pipe remote from the crack were assumed to match A8ii-17 (Ref. C.9). NRCPIPE (Ref. C.10) was used to calculate the moment carrying capacity of the through-wall cracks and NRCPIPES (Ref. C.11) was used to calculate the moment carrying capacity for the surface cracks. SQUIRT (Ref. C.12) was used to do the though-wall crack leak rate calculations.

The applied load for these analyses were assumed to be the same single frequency, growing amplitude forcing function used in experiment IPIRG-1 1.3-3, see Figure C.26. In equation form, the applied displacement is:

$$\text{disp} = 0.375t + 9.5(1 - e^{-0.04042t})\sin 24.819t \quad \text{inches} \quad \text{(C.13)}$$

This excitation is at about 90-percent of first resonance for the pipe loop, so it provides a great deal of dynamic amplification. Single frequency excitation was selected for the Actual Margins calculations so that attention could be focused solely on margin issues and not on crack closure behavior and ordering of load peaks in a seismic time history—the moment will be monotonically increasing, at least for a linear analysis.

A complete listing of the geometry for the model is given in section C.6.2.

C.4.1.2 IPIRG Cases

Four analyses were conducted for each of the four flaws as shown in Table C.7. These four cases consider all of the possible sources of margin from nonlinearities: plasticity due the crack, plasticity due to remote yielding, and the combined effect. Comparing each of the nonlinear cases with the linear case provides a sense of margin that each of the separate effects contributes to the total actual margin.

C.4.1.3 Calculation of Margins in the IPIRG Analyses

There are many ways to quantify margin in a piping stress analysis: Stresses can be compared, crack sizes that can sustain a certain applied moment, or a comparison of moments are a few that come to mind. In any event, the margin of interest comes from a comparison of what happens in a nonlinear analysis with what happens in a linear analysis. For the purposes of this discussion, comparison of moments seems appropriate. Furthermore, the comparison can be done several ways, but the simplest is to look at the ratio of the nonlinear moment to the linear moment, i.e.,

$$\text{margin} = \frac{M_{elast}}{M_{nl}} \quad \text{(C.14)}$$

Margins greater than one imply that that the nonlinearity has mitigated the moment applied to the crack so that it is less likely to "fail."

Once a commitment has been made to discuss margin in terms of moment, the details of exactly how the margin is to be calculated have to be prescribed, because the margin is a continually evolving thing in time: For some portion of a time history of moment, a nonlinear and linear analysis will be identical so the margin will be 1.0, i.e., plasticity has not developed so there is no benefit from doing the nonlinear analysis. At some later point in time, however, if the excitation becomes large enough, there will be differences between the linear and nonlinear analyses that, presumably, should lead to margin. Issues such as time phasing of response will manifest themselves in the analysis results because nonlinearities look like damping to the rest of the pipe system. Because of the evolving nature of margin, one has to set "rules" for how the margin is to be calculated so that the comparisons are reasonable and fair.

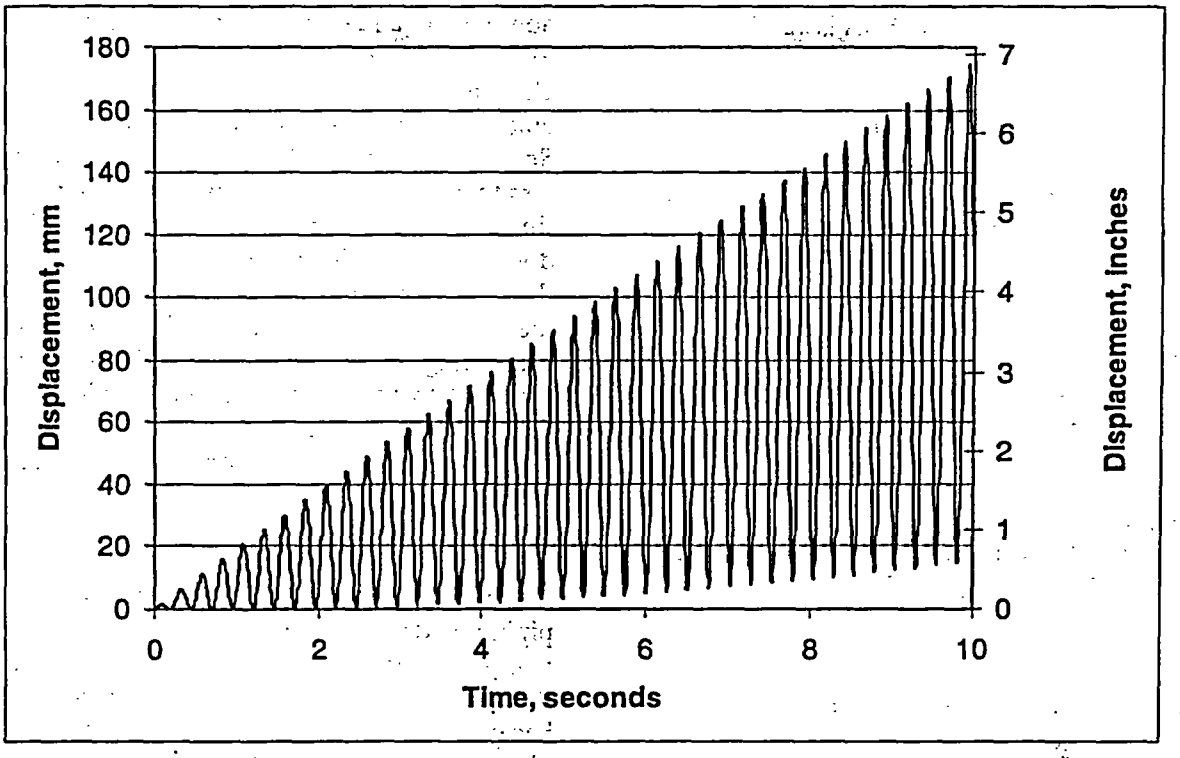

Figure C.26 Actual Margins forcing function used for IPIRG pipe loop analyses

Table C.7 IPIRG pipe loop system Actual Margins runs

Analysis	Crack	Remote Pipe Condition
1	No	Elastic
2	Yes	Elastic
3	No	Nonlinear
4	Yes	Nonlinear

For the purposes of this discussion the following rules were followed to calculate margins:

1. The maximum moment capacity for the crack, as calculated using the J–estimation schemes in NRCPIPE (Ref. C.10) or NRCPIPES (Ref. C.11), is the reference moment, M_{ref}.
2. A nonlinear analysis with a crack as the only nonlinearity is conducted to the time when the crack reaches its maximum moment carrying capacity.
3. The time at which maximum moment is attained is taken as reference time, $t1_{ref}$.
4. A nonlinear analysis with remote plasticity as the only nonlinearity is conducted to the time when the applied moment at the crack location reaches the reference moment defined in Step 1.
5. The time at which maximum moment is attained is taken as reference time, $t2_{ref}$.
6. A nonlinear analysis with a crack and remote plasticity is conducted to the time when the crack reaches its moment carrying capacity.
7. The time at which maximum moment is attained is taken as reference time, $t3_{ref}$.

8. A completely elastic analysis is conducted out to the maximum of $t1_{ref}$, $t2_{ref}$, or $t3_{ref}$ times.
9. Margins are calculated as follows:

$$\text{margin}_{\text{Crack}} = \frac{M_{elast}(\max \text{ from } t = 0 \text{ to } t1_{ref})}{M_{nl}(t1_{ref})} \quad \text{(C.15a)}$$

$$\text{margin}_{\text{Remote Plasticity}} = \frac{M_{elast}(\max \text{ from } t = 0 \text{ to } t2_{ref})}{M_{nl}(t2_{ref})} \quad \text{(C.15b)}$$

$$\text{margin}_{\text{Plasticity+Crack}} = \frac{M_{elast}(\max \text{ from } t = 0 \text{ to } t3_{ref})}{M_{nl}(t3_{ref})} \quad \text{(C.15c)}$$

C.4.1.4 IPIRG Analysis Results

Analyses were conducted for the four flaws described in C.4.1.1 in accordance with the "rules" defined in C.4.1.3 for an all stainless steel IPIRG pipe system geometry with a single frequency, increasing amplitude forcing function. Figures C.27 through C.31 show the moment-time plots for all of the runs. As expected, the moment grows monotonically with time for the linear analysis. For the plasticity only case, the moment reaches a plateau in approximately two seconds that is almost never exceeded. In this case, plasticity initiates in elbow 2 and subsequently appears in elbow 3 and at the actuator location, as well as a slight amount at the hanger near fixed end 2 (see Figures C.24 and C.25). For several of the cases with remote plasticity, the crack location never reaches the "failure" moment.

Table C.8 summarizes the margins that are implied by Figures C.27 though C.31.

C.4.1.5 Conclusions From the IPIRG Pipe System Margin Analyses

Inspection of the margins listed in Table C.8 shows that virtually all of the margin from these analyses comes from plasticity remote from the crack and that the margin effects of the crack nonlinearity and remote plasticity are not additive. Furthermore, it is apparent that these conclusions are true, independent of the whether the crack is a through-wall crack or a surface crack. Some of the crack-only cases yielded margins less than one, but these cases have "failure times" very early on, when transient behavior is dominating the pipe response. For several cases, the reference moment was never attained within the time frame of the analysis. Remote plasticity was taking so much energy away from driving the crack that the crack was never loaded to failure in a ductile tearing episode. Low cycle fatigue would need to be considered in these cases.

The results of these calculations suggest that it is not terribly important to have a crack in the piping model, because the vast majority of the margin comes from remote plasticity. Indeed, this is an unexpected, but positive result, because it makes a nonlinear analysis much simpler to conduct: The issues related to defining crack springs, crack unloading, and crack orientation become moot—there is no need to put a crack in the model.

C.4.2 Analysis of PWR Plant Piping

The results presented in C.4.1 provide a tantalizing view of the margins that may be available in flawed plant piping. Clearly, in a situation where linear analysis shows that a flaw evaluation or LBB assessment has inadequate margin, adequate margin may in fact actually exist if the effort is made to do a nonlinear analysis. The results from the previous section seem to indicate that a cost-benefit may be there, if there is a compelling need to find additional margin.

The analyses presented in C.4.1 are rather idealized: The IPIRG pipe system has unrealistic boundary conditions and the loading was monotonically increasing. To see if the margins observed in C.4.1 can be realized in real plant piping, analyses consistent with what was done in C.4.1 but using real geometry, boundary conditions, and real seismic loading were performed.

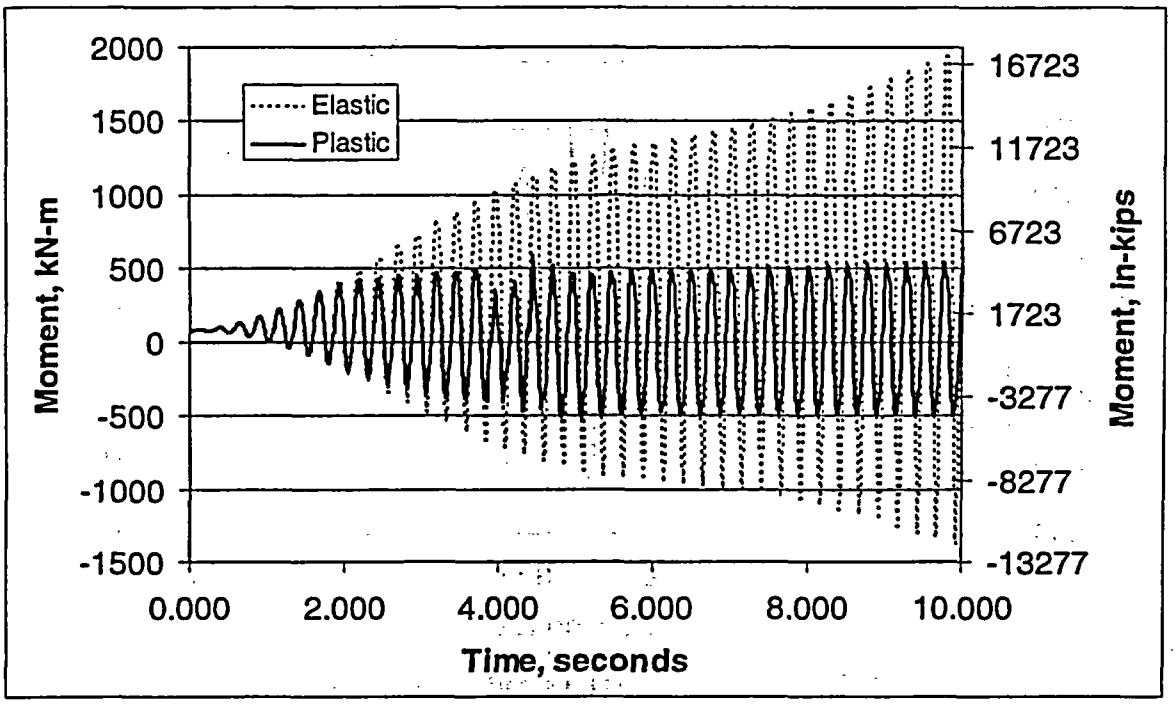

Figure C.27 IPIRG pipe system reference moments

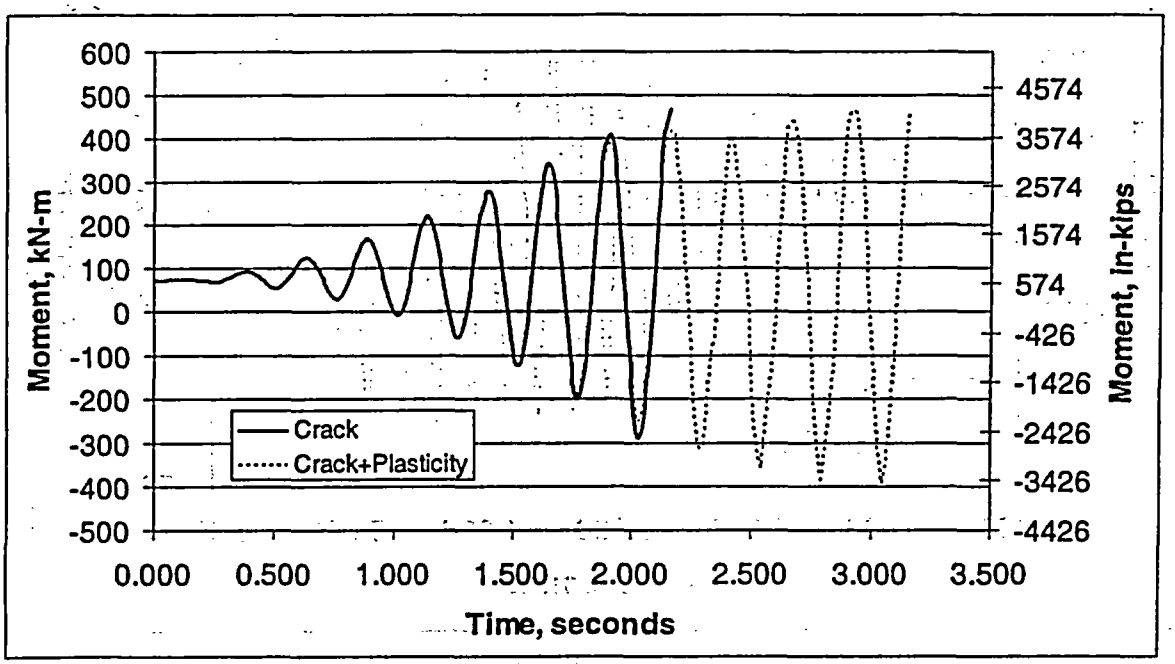

Figure C.28 IPIRG pipe system large surface crack results

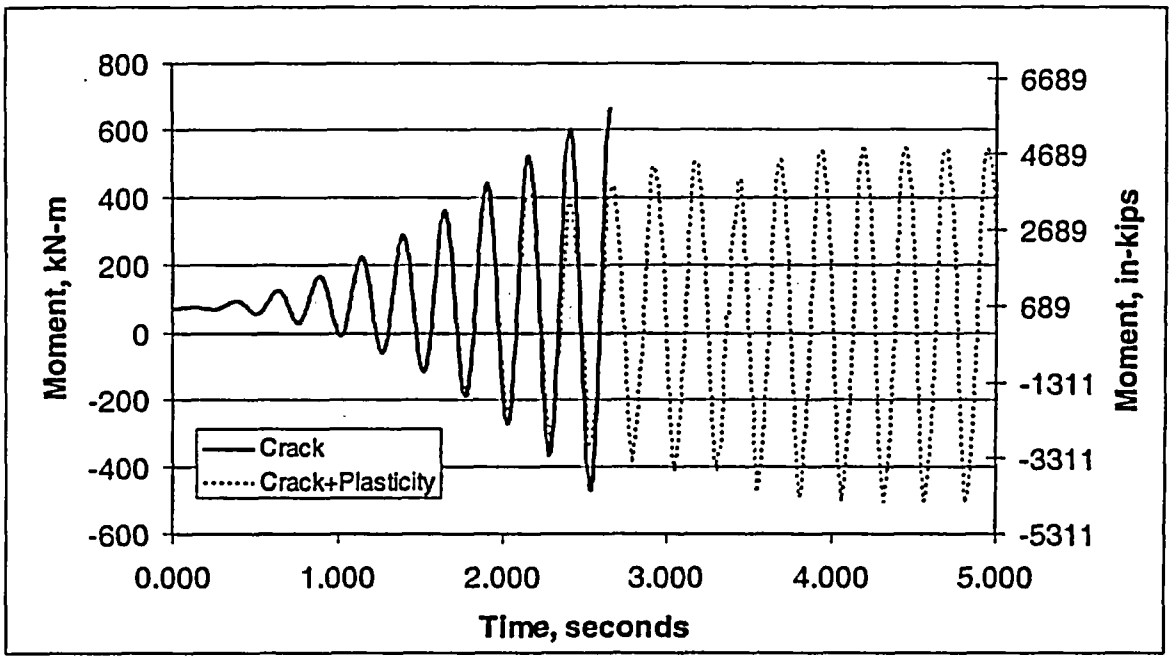

Figure C.29 IPIRG pipe system small surface crack results

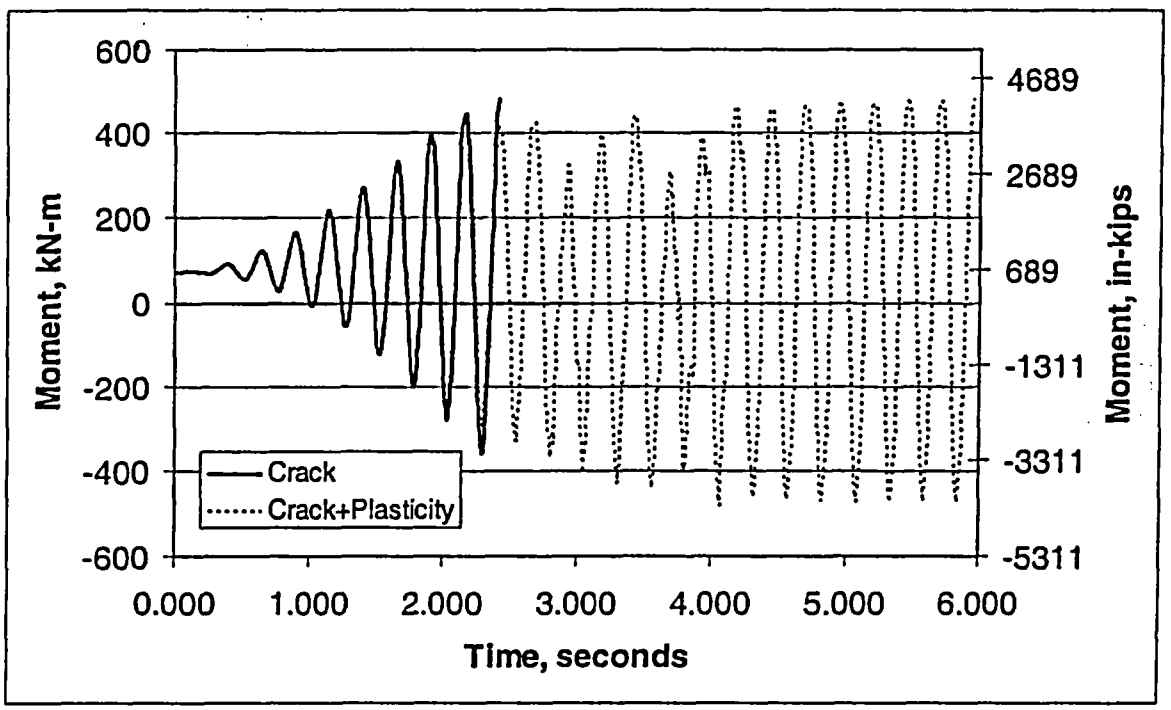

Figure C.30 IPIRG pipe system large through-wall crack results

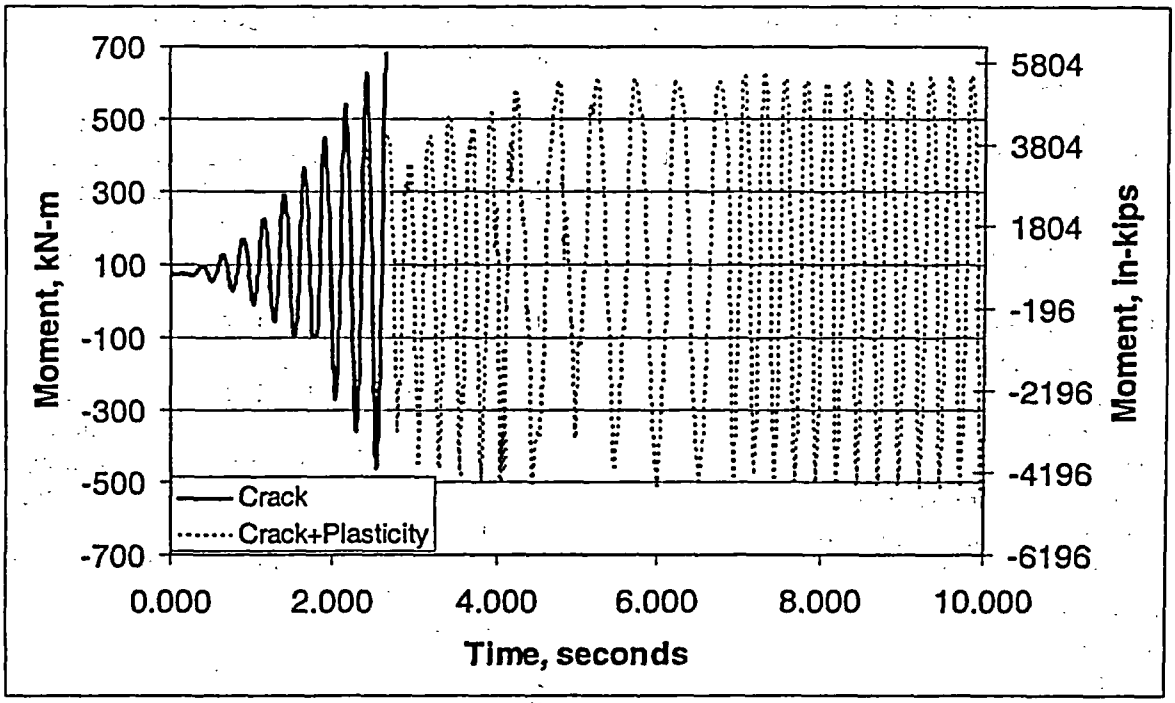

Figure C.31 IPIRG pipe system small through-wall crack results

Table C.8 IPIRG pipe system analysis margins

Condition	Crack		Large SC	Small SC	Large TWC	Small TWC
	M_{ref}	kN-m	459.2	651.5	452.2	679.6
		(in-kips)	(4064.4)	(5766.1)	(4002.4)	(6015.5)
Crack Only	$t1_{ref}$,sec		2.155	2.660	2.410	2.655
	M_{elast}	kN-m	438.0	572.1	500.5	571.7
		(in-kips)	(3876.5)	(5064.0)	(4430.0)	(5060.0)
	margin1		0.95	0.88	1.11	0.84
Remote Plasticity Only	$t2_{ref}$, sec		3.185	DNF*@5	2.685	DNF*@10
	M_{elast}	kN-m	759.3	1218.3	648.5	1943.3
		(in-kips)	(6720.4)	(10782.9)	(5740.0)	(17200.0)
	margin2		1.65	2.08	1.43	3.31
Crack+Plasticity	$t3_{ref}$, sec		2.920	DNF*@5	5.955	DNF*@10
	M_{elast}	kN-m	651.5	1218.3	1333.2	1943.3
		(in-kips)	(5766.6)	(10782.9)	(11800.0)	(17200.0)
	margin3		1.42	1.75	2.95	2.71

DNF = did not "fail"

C.4.2.1 Development of a Plant Piping Model

In order to perform margin calculations for plant piping, a plant piping model that includes all of the features relevant to loading of the pipe must be available or developed. Features that were judged to be of first order significance in the dynamic behavior of PWR plant piping are:

- All primary loops:
  - The piping
  - Coolant pumps and support
  - Steam generator and support
- The reactor
- The surge line with hangers
- The pressurizer and its support
- Concrete inside containment
- The containment
- The plant base mat
- The soil

For each of these features, detailed geometry, properties including mass, section properties, and material properties, as well as boundary conditions (supports and applied SSE loading) must be known.

When the Actual Margins task was originally proposed, the hope was that one of the participants would be able to supply some or all of the plant data listed above. The reality was that the model had to be developed from scratch from publically available documents and some reasonable engineering guesses. Specifically, the data sources available for building the model were limited to US NRC Final Safety Analysis Reports (FSAR's), several internet web sites, NUREG reports, some soil-structure interaction software user's manuals, and conversations with NRC staff (Refs. C.13 through C.17). After some preliminary investigations, a three-loop Westinghouse PWR was selected for analysis because there appeared to be a wealth of the required information contained in some of the FSAR's. In addition, internet searches for information on nuclear plant construction details turned up a great deal of useful information for Westinghouse 3-loop plants.

The basic premise for developing the model was as follows:

1. The model was to be built from simple beam-type elements and springs/dampers
2. Consideration would only be given to analyzing the 3 primary loops, the surge line, and one safety injection system (SIS) line
3. The structural detail of the piping would be as precise as the available data would permit
4. The structural detail of the reactor foundation, containment, and internal concrete supports would only need to be good enough to adequately represent the mass and gross stiffness
5. In most cases, details of the piping hanger and other piping attachments to the building would be unknown and would have to be modeled as rigid connections
6. A simple linear spring and damper soil model would be used
7. If precise data for mass and stiffness of certain features was not available, informed engineering guesses would be made based on the best available information and/or scaled from pictures and artist's renditions.

The overriding consideration in developing the model was to do a very good job modeling the piping of interest and to make the rest of the model representative enough that it could be judged to have provided reasonable boundary conditions for the piping. Every attempt was made to rationalize mass and stiffness properties with other publically available data.

C.4.2.2 Plant Model and Loading Details

Figures C.32 to C.40 show various features in the plant and how they were modeled in the finite element model. In most cases, features were modeled with circular cross-section beams. Mass properties of the beams were adjusted to give the correct total mass and mass distribution.

Linear soil springs and dampers (Ref. C.18 and C.19) were selected to model a rock foundation. Consistent with the stiff, rock foundation assumption, the natural frequencies for the

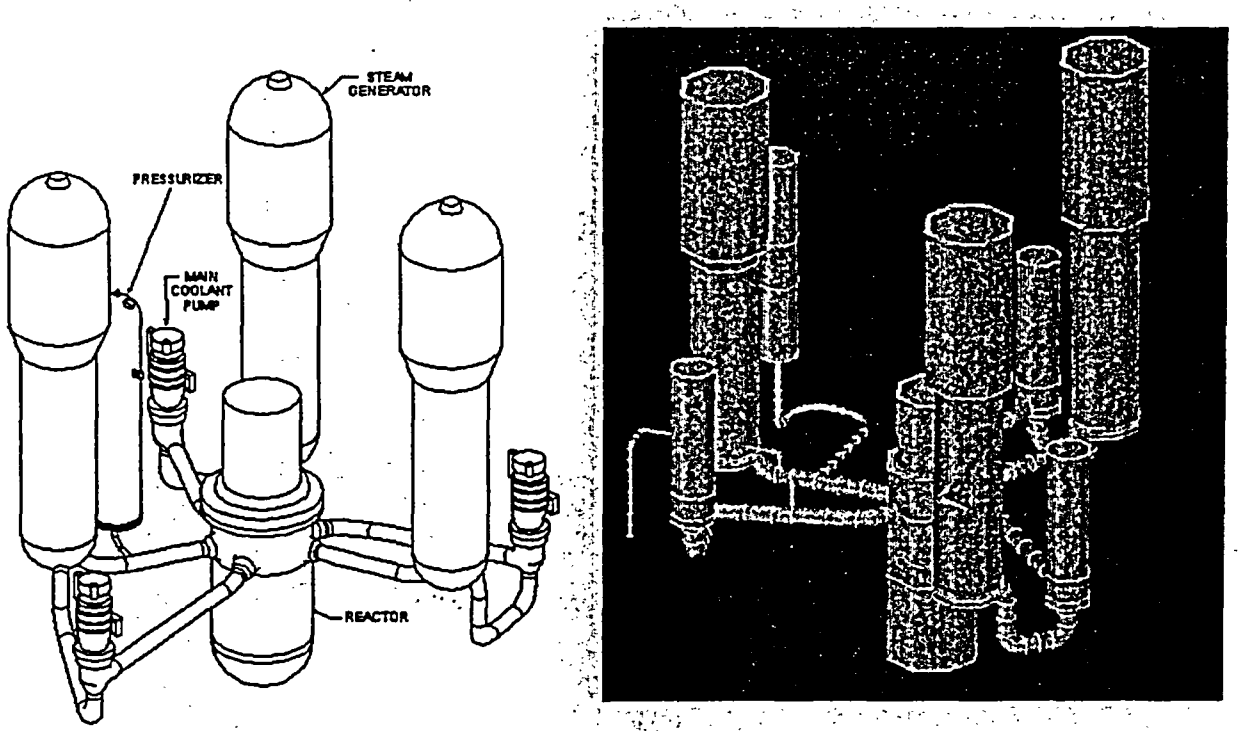

Figure C.32 PWR system model piping

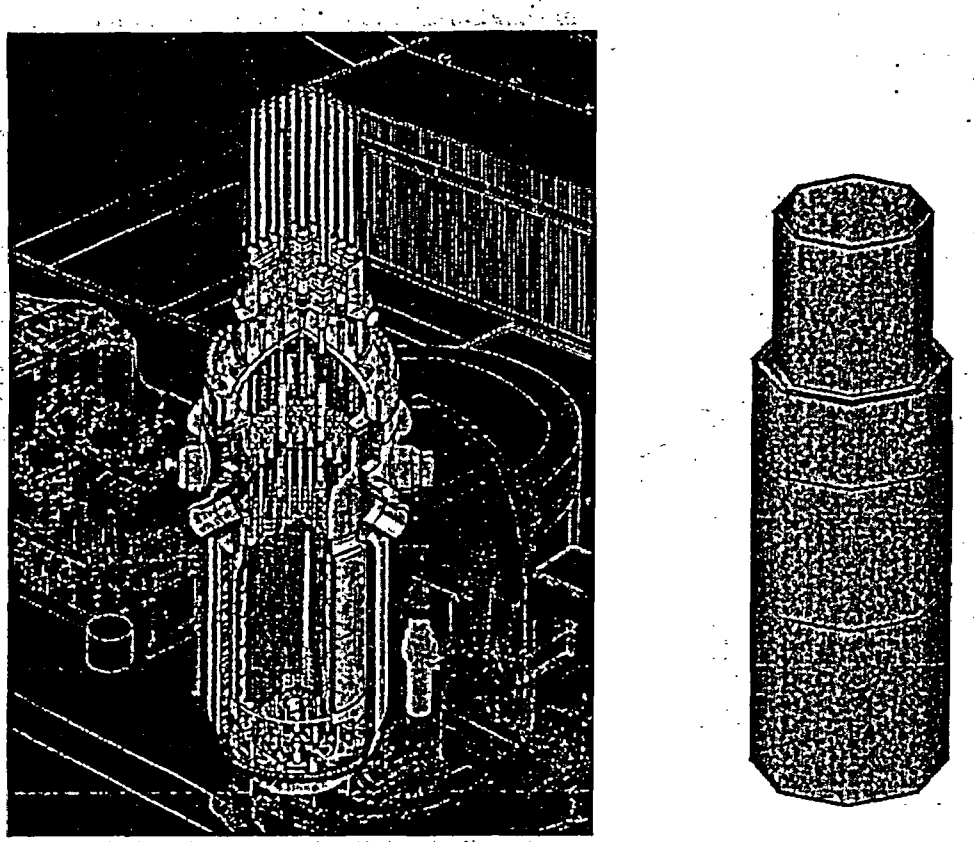

Figure C.33 PWR System Model Reactor

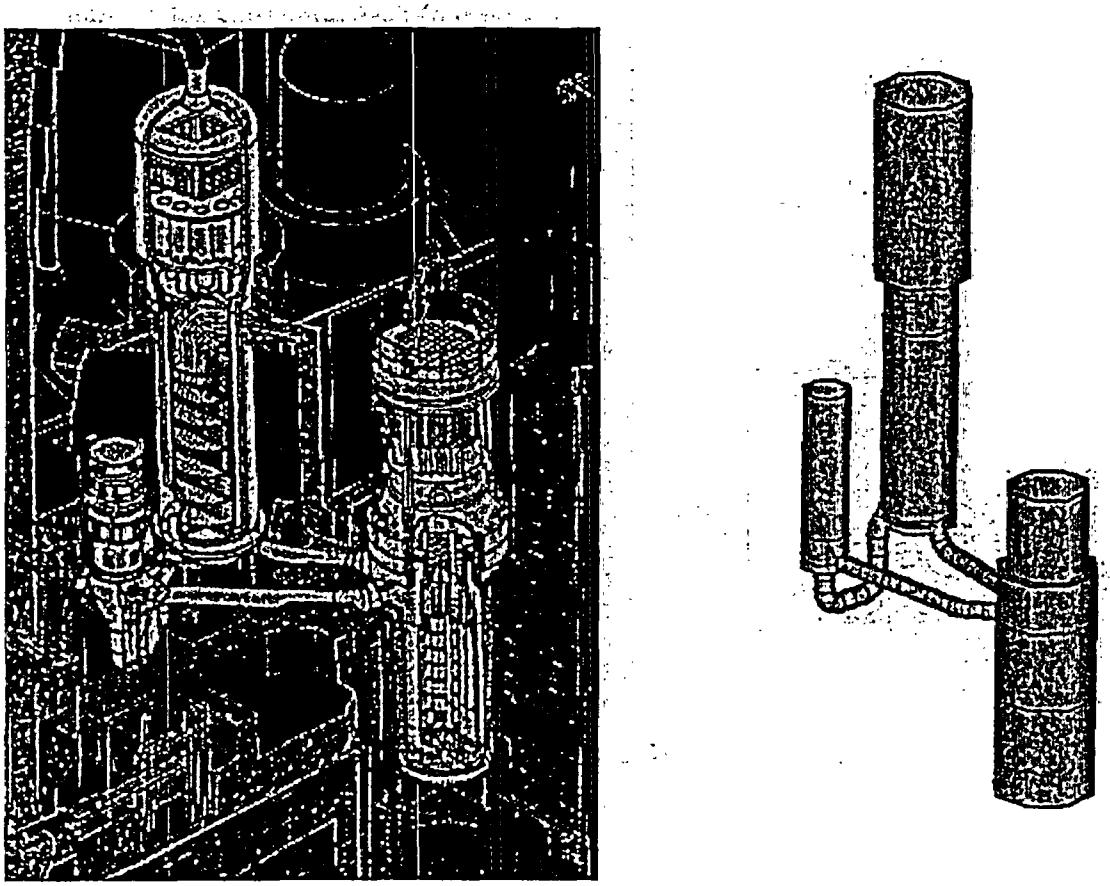

Figure C.34 PWR system model primary loop (one of three)

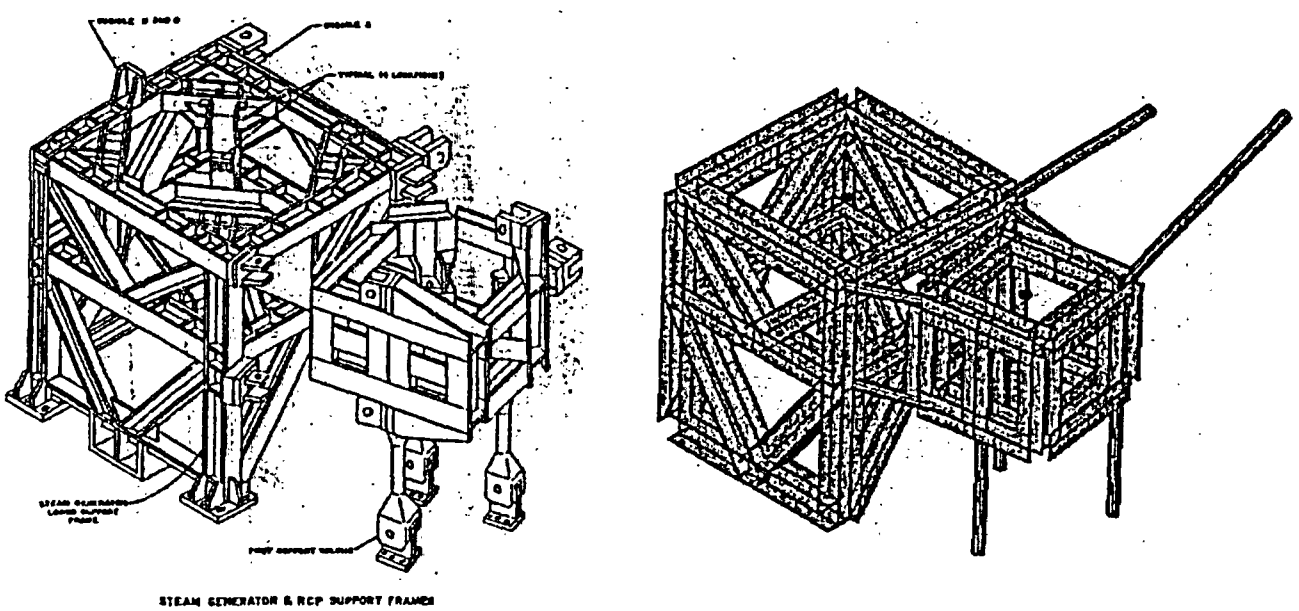

Figure C.35 PWR plant model stream generator and coolant pump support

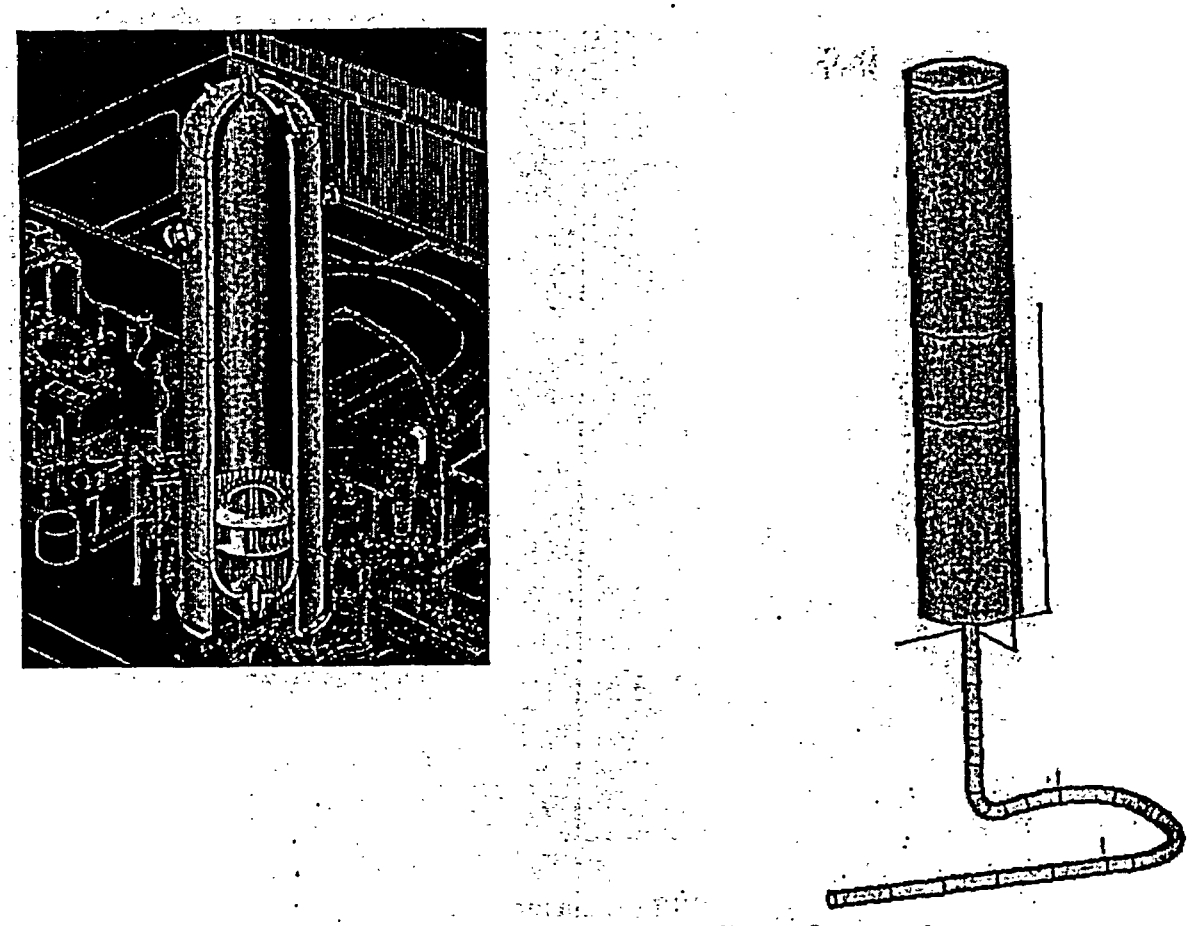

Figure C.36 PWR plant model surge line and pressurizer

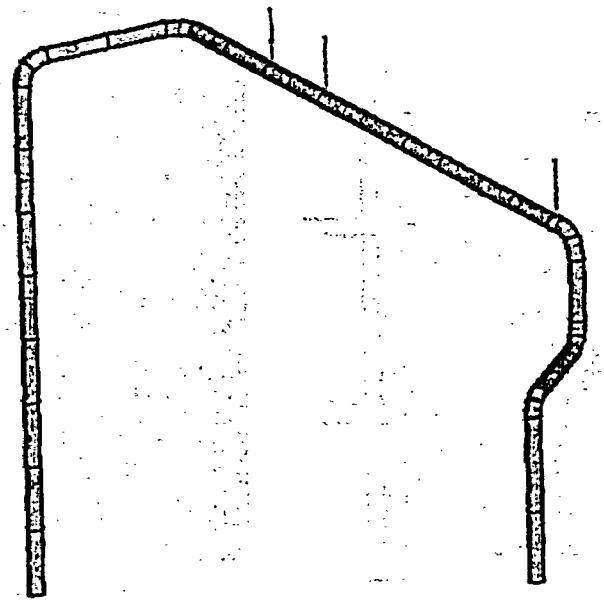

Figure C.37 PWR system model safety injection system (SIS) line

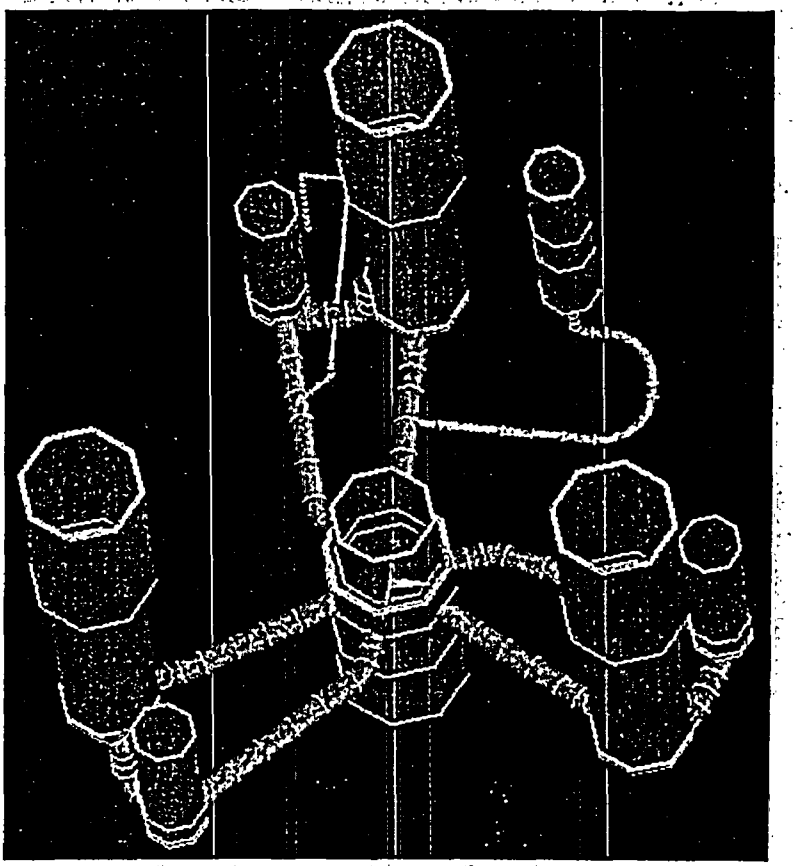

Figure C.38 PWR system model piping

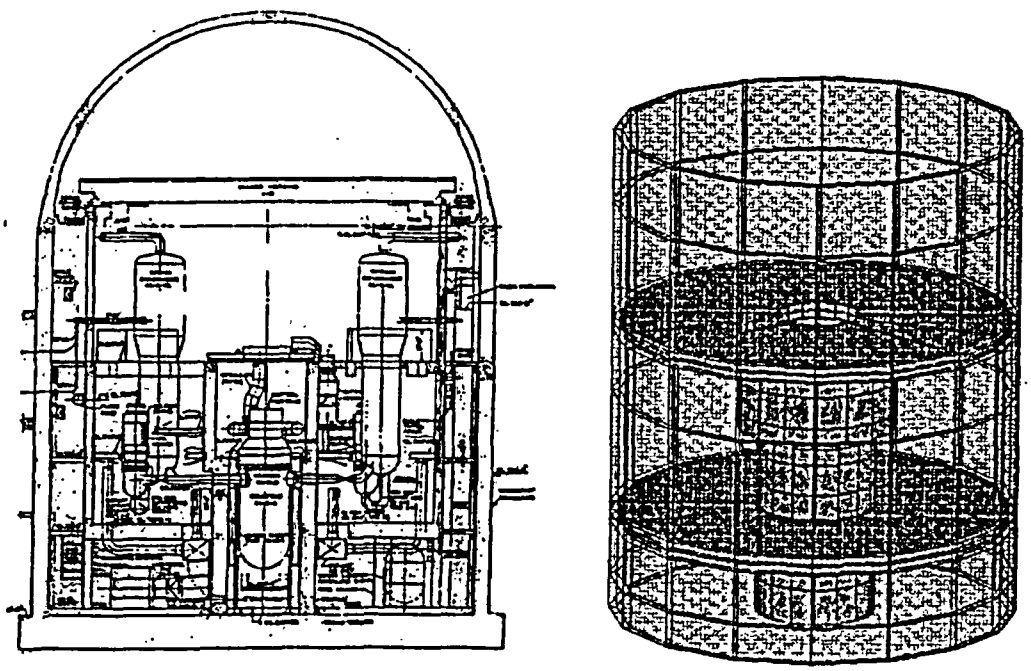

Figure C.39 PWR system model containment building internal concrete

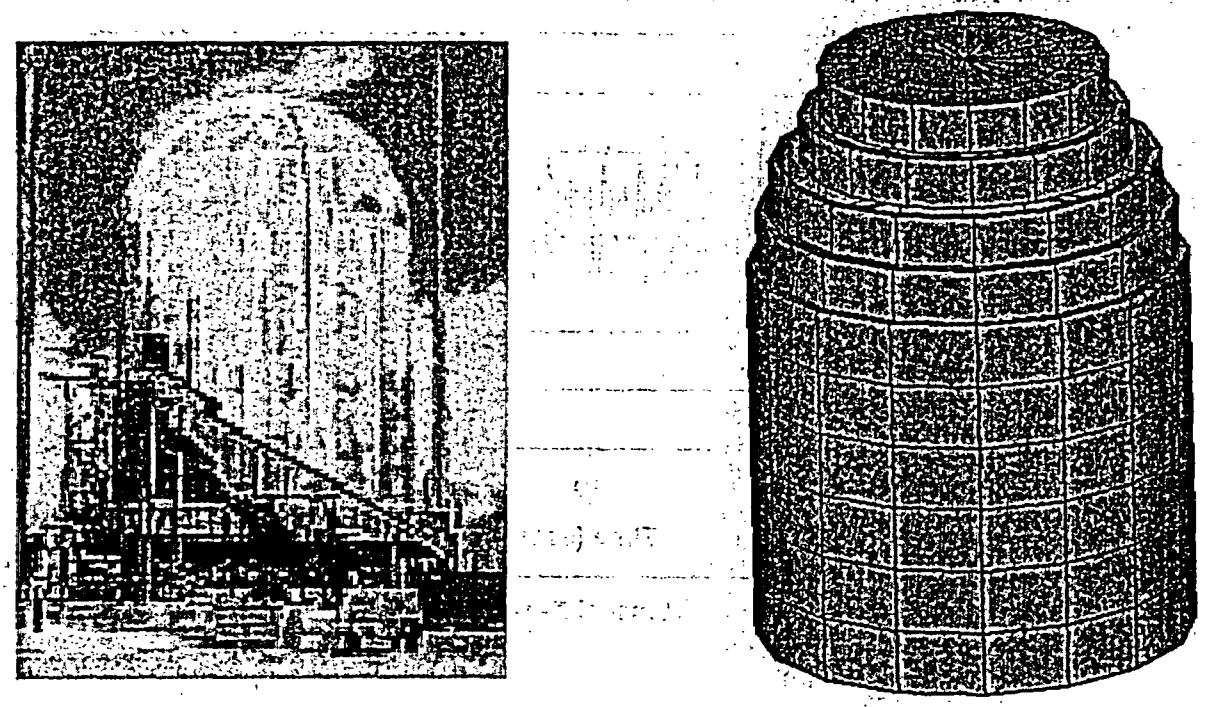

Figure C.40 PWR system model containment

reactor base mat, containment, and internal concrete, reactor core and piping are as follows:

- F_1=3.096 Hz, synchronized rocking of the containment and internals about the base mat
- F_2=3.980 Hz, rocking of the containment about the base mat with the internals relatively stationary
- F_3=5.151 Hz, a mode very similar to mode 2
- F_4=5.206 Hz, out of phase rocking of the containment and the internals about the base mat
- F_5=8.654 Hz, rocking of the internals about the base mat with the containment relatively stationary
- F_6=9.681 Hz, vertical in-phase motion of the containment and internals.

These frequencies are consistent with other published data for nuclear plant building natural frequencies (Refs. C.20 through C.22).

The input loading to the plant model was a scaled earthquake applied as acceleration loading in the global X and Y direction. The basic ground motion records, obtained from References C.23 and C.24, are derived from the 1988 Saguenay earthquake and represent a 5.9 magnitude earthquake at a distance of 96 km (60 miles) from the epicenter. This earthquake is characterized as having a 2-percent chance of exceedance in 50 years for the Boston, USA area, and has a peak acceleration of 0.57 g in the X direction and 0.78 g in the Y direction, see Figures C.41 and C.42. To put this excitation in perspective, Figure C.43 shows the SSE earthquake for the Beaver Valley PWR (a 3-loop Westinghouse design), taken from the Beaver Valley FSAR (0.13 g peak acceleration). The 2-percent in 50 years in Boston excitation is similar in duration and basic character, but is substantially more severe in magnitude. The two orthogonal components of the earthquake excitation were applied aligned with the global model reference axes. The decision to orient the earthquake in this direction is completely arbitrary and may have had some impact on the stresses generated in the piping.

The model has 1446 degrees-of-freedom and the seismic loading was applied at time steps of 0.005 second.

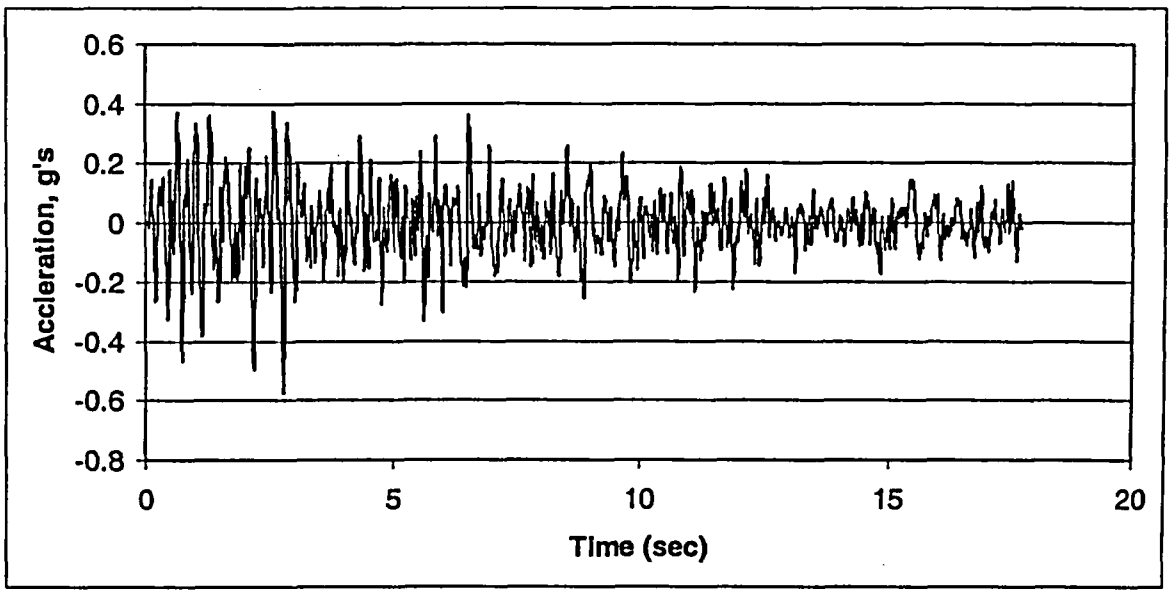

Figure C.41 PWR model X-axis loading

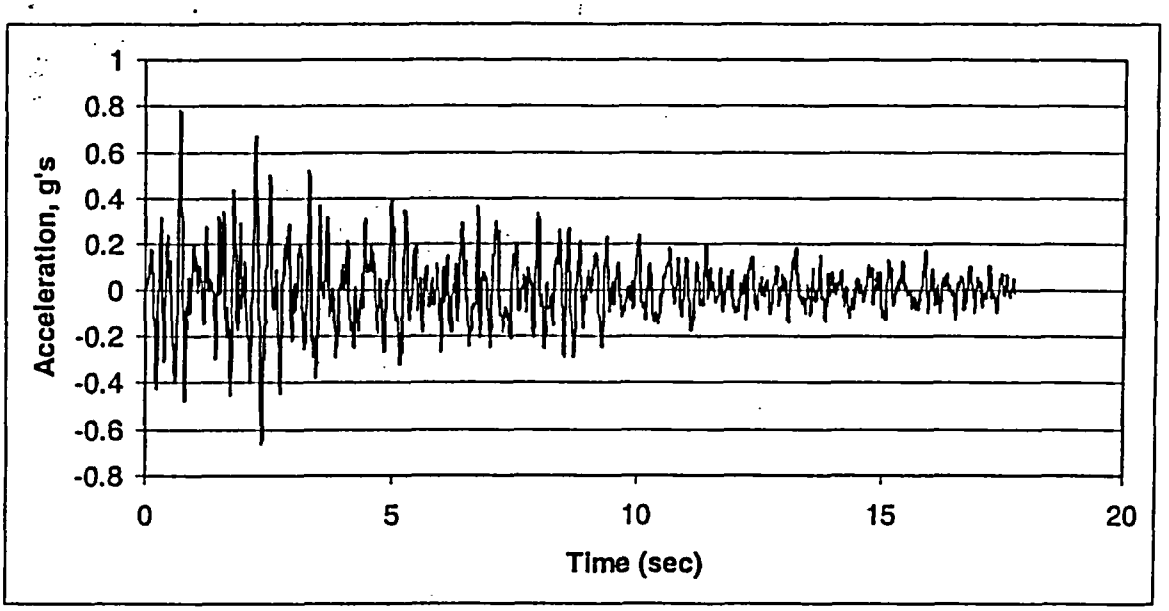

Figure C.42 PWR model Y-axis loading

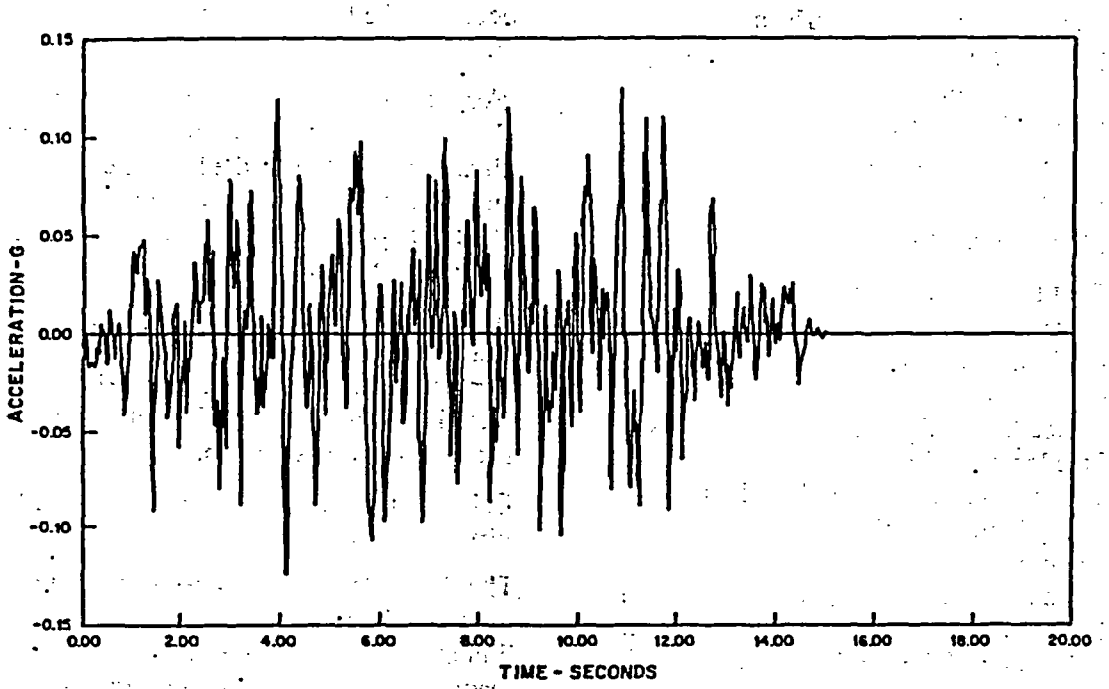

Figure C.43 Beaver Valley PWR artificial time history horizontal SSE (Ref. C.16)

C.4.2.3 Calculation of Margin for the PWR Piping System

The IPIRG pipe system margin calculations compared nonlinear moments with elastic moments over a window of time from t= 0 to the time when the hypothesized cracks reached maximum moment carrying capacity. Based on the conclusions of these analyses, it was determined that the crack does not contribute significantly to the margin, so one can merely compare linear solutions and solutions with remote plasticity to learn something about margins in real plant piping. Additionally, further simplification can be introduced by ignoring time-phasing of moment response, crack orientation and crack location issues by comparing the maximum magnitudes of bending moments (square root of the sum of the squares) for the full duration of the seismic event at many possible critical locations. In a real margin analysis it would be necessary to consider the real crack orientation at a specific location, but for the purposes of this study, these issues can be ignored.

Margin is a function of the level of applied loading. The general sense is that margin should be 1.0 at very low levels of excitation and grow as the excitation gets larger. It is conceivable that margin may not increase monotonically at all locations due to the interaction among various pieces of the piping. In order to explore the evolution of margin with changing seismic excitation, the basic seismic load can be linearly scaled. At a scale factor of 0.25, the 2-percent in 50-year Boston excitation is still 50-percent larger than the Beaver Valley SSE in terms of peak g's. Furthermore, it is clear that the margin will also be a function of the phasing of the peaks of the seismic excitation and the direction of the excitation. In the present case, the phasing and direction have been arbitrarily fixed by choice of the specific seismic signature.

In summary, the demonstration margins for the PWR plant analyses were calculated on the following basis:

- $\text{Margin} = \dfrac{M_{elastic}}{M_{nonlinear}}$
- $M = Max\left(\sqrt{M_y^2 + M_z^2}\right)_{t=0}^{t=18}$, i.e. maximum of the square root of the sum of the squares of the bending moments for the full duration of the seismic loading.

- The margin calculation is performed at every piping run end and every straight pipe to elbow junction.
- Margin is calculated as a function of increasing, scaled amplitude seismic excitation.

C.4.2.4 PWR Model Analysis Results

Figures C.44 to C.47 show the locations where margins were calculated according to the procedures defined in Section C.4.2.3. Figures C.48 to C.52 show calculated margins as a function of load. The figures show the results for all of the locations in each line, with the mean value shown as a block and the length of the line going from the highest to lowest margin at a particular excitation level. The calculated margins are a function of the specific location in a line, the direction of the applied excitation, and the exact character of the forcing function itself. Because only one excitation direction with one forcing function was actually analyzed, the data have been presented as bar charts to illustrate the potential margins that might be achieved: Different directions of excitation and/or different forcing functions may yield different results. For the hot leg, cross-over leg, and cold leg, results for all three loops are included in the respective figures.

Looking at the hot leg margins, Figure C.48, it is clear that: a) For the vast majority of locations, the average margin is at or near 1.0, b) Margin does not necessarily grow monotonically with increasing forcing function amplitude, and c) At excitation levels around typical SSE levels (0.1 < scale factor < 0.5), some locations can have high margins.

The comments regarding the cross-over legs (Figure C.49) are consistent with the preceding hot leg comments with the exception that there is a more pronounced increase of margin with increasing amplitude excitation. Observations about the margins for the cold leg (Figure C.50) are identical to the hot leg.

The margins for the surge line (Figure C.51) are unique among all of the margins in that they are all generally much higher than the others and, in the range of typical SSE peak g accelerations (0.1 < scale factor < 0.5), the margins can be very high. The extreme margin for the surge line occurs at the beginning of the last elbow leading to the pressurizer.

For the one safety injection system line (Figure C.52) analyzed (there are many more in the plant), the location at the hot leg exhibits the largest margins. For the vast majority of the other locations in the SIS line, the margin hovers in the range of 1.1 to 1.5.

As indicated at the beginning of this section, the results presented here are only a demonstration of potential margins that might exist: A different seismic loading from a different direction may show more or less margin.

C.4.2.5 Conclusions From the PWR Plant Piping Analyses

The PWR plant analyses demonstrated that margin can exist in actual plant piping. Within the limitations of the finite element model, assumed loading, and necessary simplifying assumptions, the vast majority of locations exhibited margins around 1.1. Some locations, however, exhibited margins greater than 10. The results shown here are indeed consistent with the results from the IPIRG pipe system analyses, but are, perhaps, not quite as dramatic. The results do, however, reinforce the notion that if there is a location in plant piping where a flaw evaluation or LBB assessment shows inadequate margin, one can have some reasonable assurance that if a nonlinear analysis is conducted, some increased margin will be found.

C.4.3 Task Summary

The Actual Margins task has demonstrated, at least on a limited scale, that conducting nonlinear dynamic finite element analyses can, in all likelihood, lead to enhanced margins. Using the latest techniques for nonlinear analysis, such as a good model for crack unloading and taking advantage of tools within finite element programs to help define crack orientation, as long as the basic program's plasticity calculations are sound, margin can be found, if it exists. Admittedly, the analyses are far more difficult than linear analyses: The analyst needs stress-strain data at temperature for the remote plasticity calculations and a J-R curve plus stress-strain data in order to consider the effect of cracks. Furthermore, the analyses, since they are

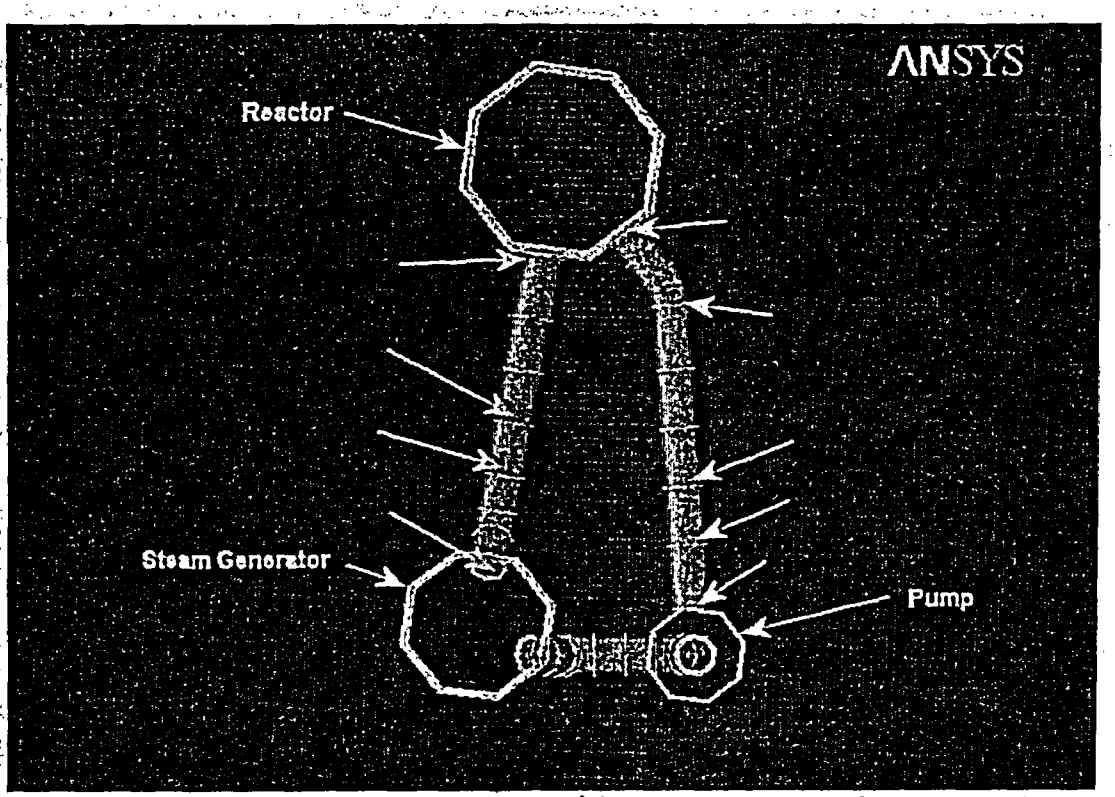

Figure C.44 PWR primary piping margin evaluation locations, 1 of 2

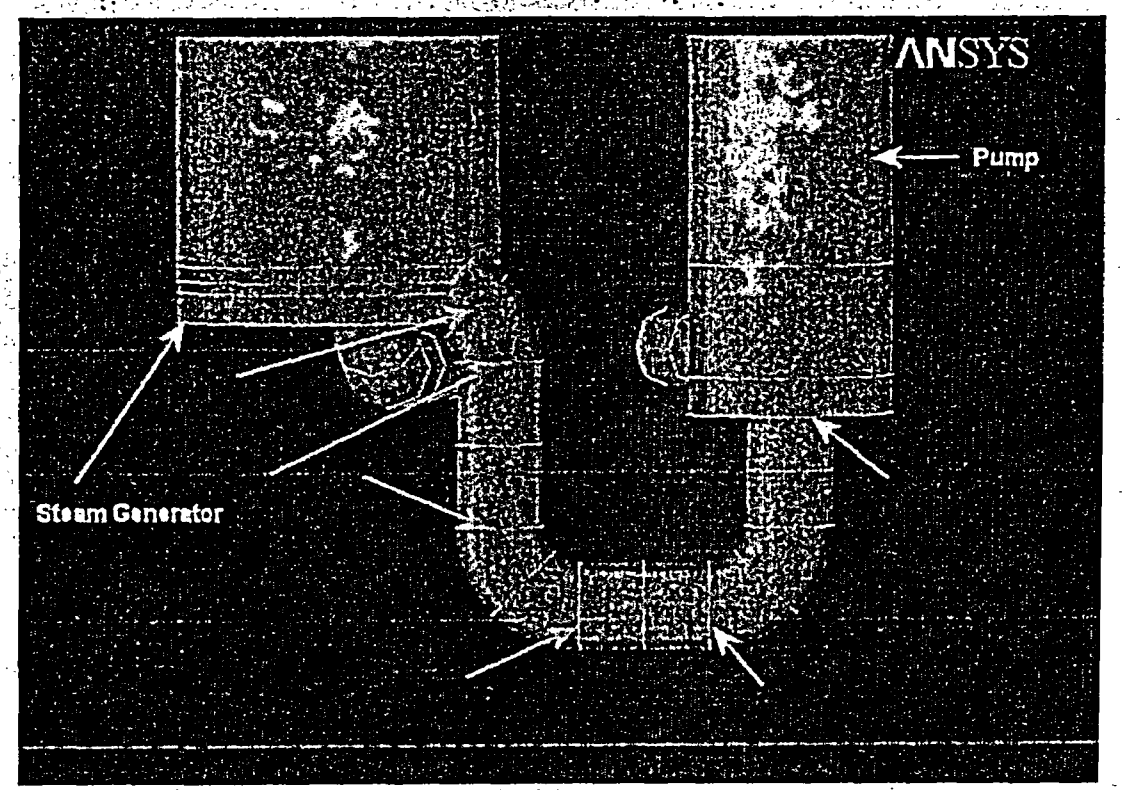

Figure C.45 PWR primary piping margin evaluation locations, 2 of 2

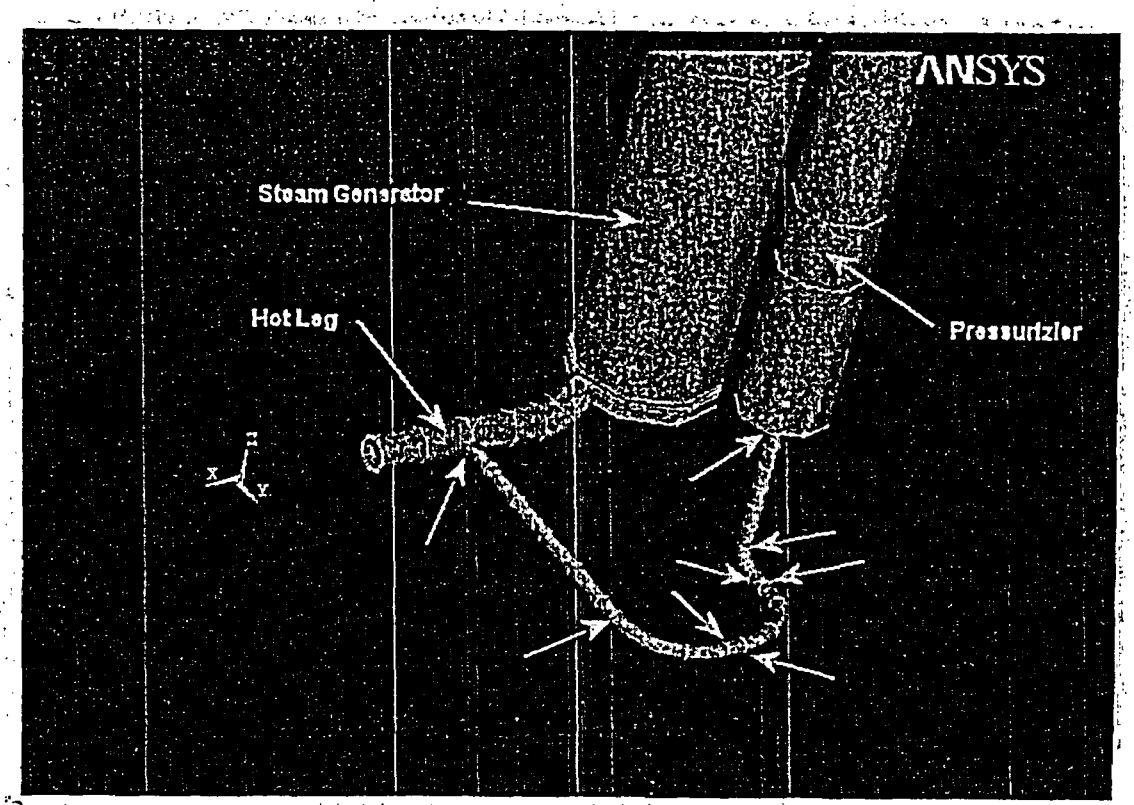

Figure C.46 PWR surge line margin evaluation locations

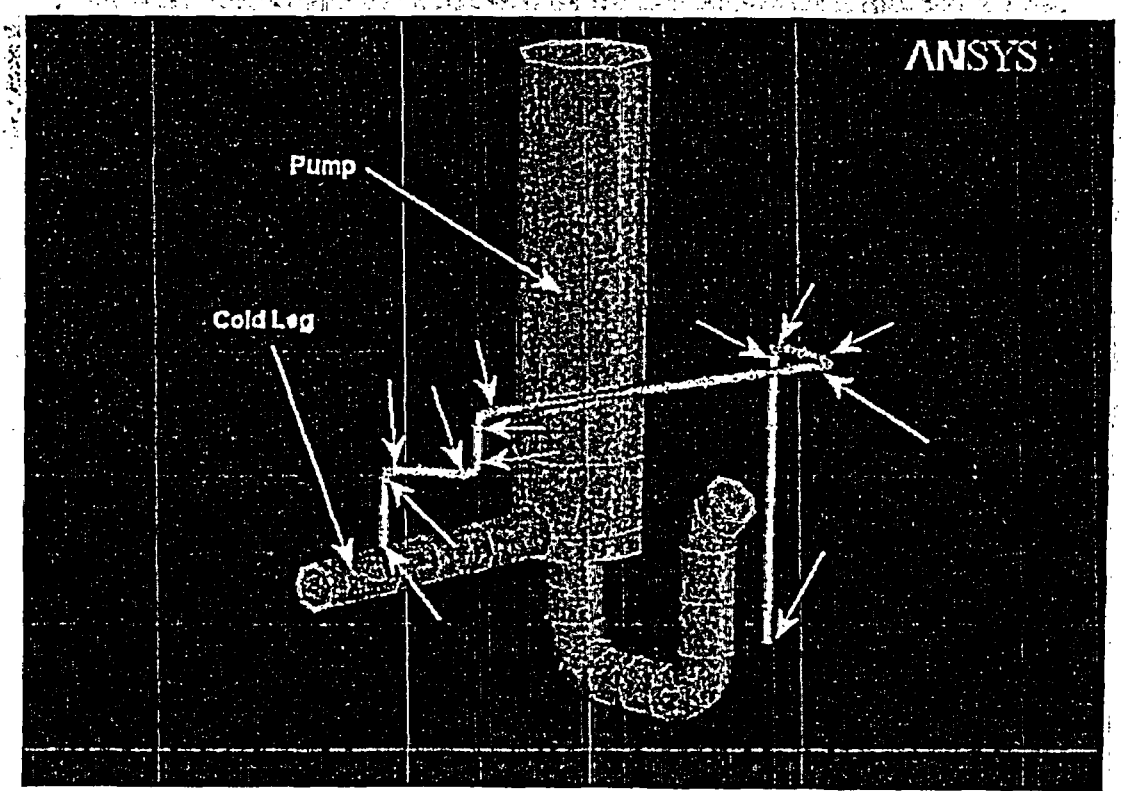

Figure C.47 Safety injection system line margin evaluation locations

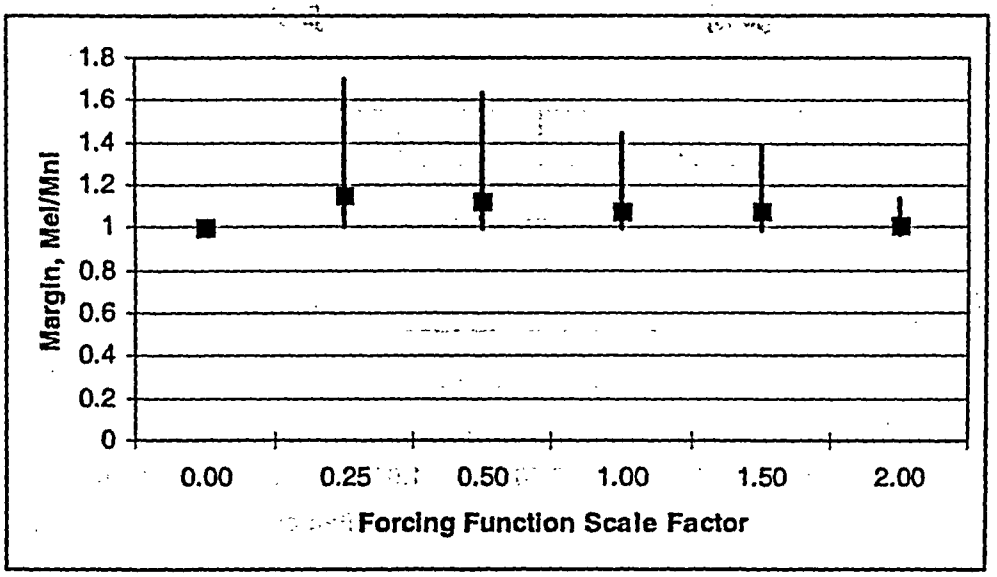

Figure C.48 Margins from the PWR hot leg locations

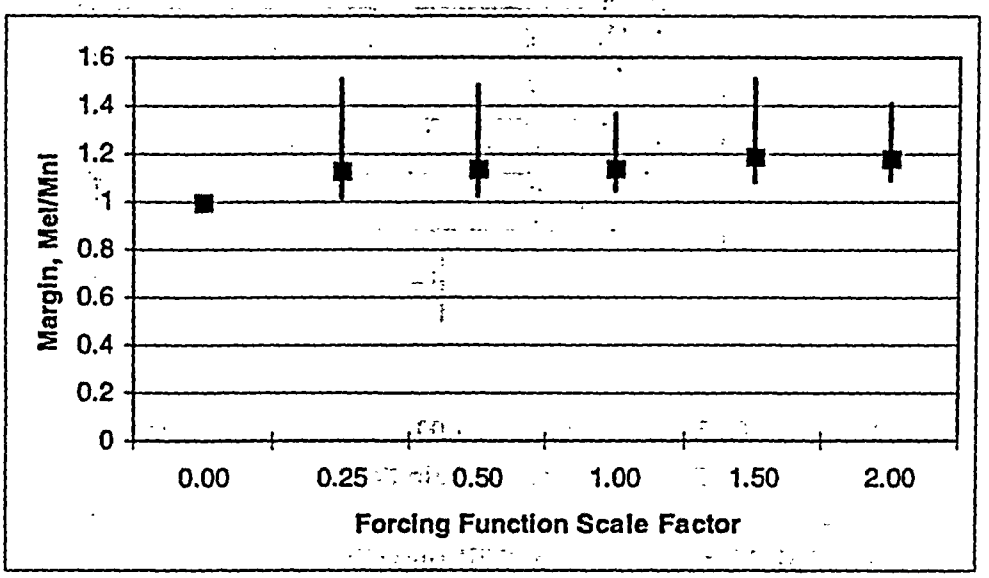

Figure C.49 Margins from the PWR cross-over leg locations

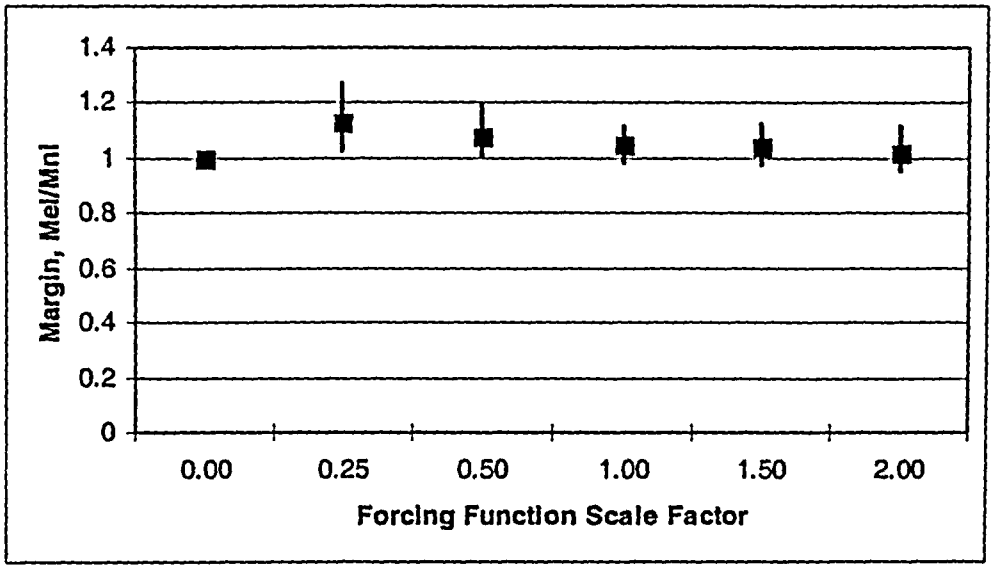

Figure C.50 Margins from the PWR cold leg locations

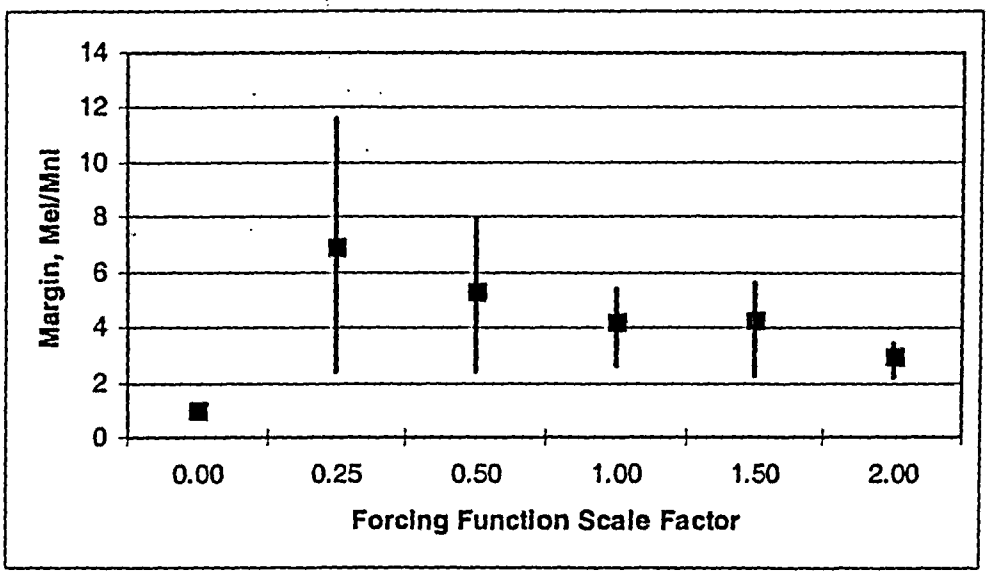

Figure C.51 Margins from the PWR surge line locations

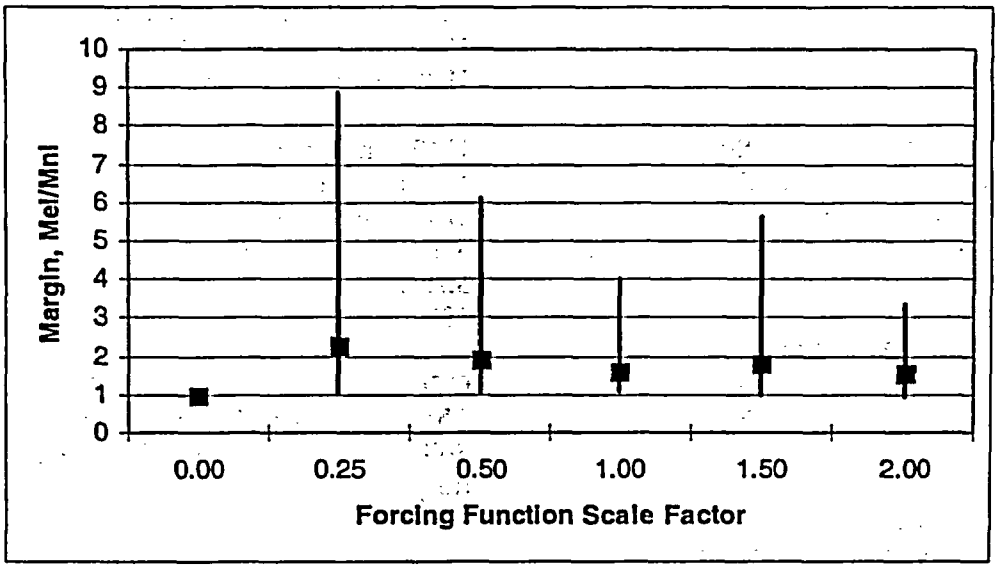

Figure C.52 Margins from the PWR safety injection system line locations

nonlinear and must be conducted in the time domain, they are significantly more expensive than the traditional linear analyses, because of the time stepping requirement, convergence issues, and inability to use superposition.

The IPIRG pipe system results from this task provide a tantalizing view of the potential to realize margin in plant piping. From a practical perspective, it is probably fortunate that the Actual Margins task was not conducted experimentally—very little could have been learned from one or two IPIRG pipe system experiments.

It must be recognized that, within the constraints of what was done in this task, it is not possible to categorically state that margin always exists in all plant piping. Only one seismic signature was applied from a single direction, only a normal operating condition was considered, flaws were not introduced into the piping, and the finite element model may have shortcomings. What can be stated, however, is: 1) That well-developed tools exist to conduct analyses that can determine if margin really exists, and 2) There is a distinct possibility that significant margin can be found, if the effort to conduct the required analyses can be justified.

C.5 References

C.1 Scott, P., Olson, R., and Wilkowski, G., "The IPIRG-1 Pipe System Fracture Tests: Analytical Results," PVP Vol 280, pp 153-163, June 1994.

C.2 Olson, R., Wolterman, R., and Wilkowski, G., "Margins from Dynamic FEM Analysis of Cracked Pipe Under Seismic Loading for the DOE New Production Reactor," PVP Vol 280, pp 119-134, June 1994.

C.3 Poole, A., Battiste, R., and Clinard, J., "Pipe Break Testing of Primary Loop Piping Similar to Department of Energy's New Production Reactor-Heavy Water Reactor," Oak Ridge National Laboratory, ORNL/NPR-92/64.

C.4 Scott, P. and others, "IPIRG-2 Task1 – Pipe System Experiments with Circumferential Cracks in Straight-Pipe Locations," NUREG/CR-6389, February 1997.

C.5 Olson, R., Wolterman, R., and Wilkowski, and G., Kot, C., "Validation of Analysis Methods for Assessing Flawed Piping Subjected to Dynamic Loading," NUREG/CR-6234, August 1994.

C.6 Hutchinson, J.W., "Plastic Buckling," *Advances in Applied Mechanics* (C.Yin, ed.) Academic Press, New York, 1974, pp. 67-144.

C.7 Scott, P., and others, "Crack Stability in a Representative Piping System Under Combined Inertial and Seismic/Dynamic Displacement-Controlled Stresses – Subtask 1.3 Final Report," NUREG/CR-6233 Vol. 3, June 1997.

C.8 Scott, P., Olson, R., and Marschall, C., "Data Record Book 1.2.8.3 for IPIRG Experiment 1.3-3," Report to US NRC, August 1990.

C.9 Rudland, D.L, Brust, F.W., and Wilkowski, G.M., "Fracture Toughness Evaluations of TP304 Stainless Steel Pipes," NUREG/CR-6446, January 1997.

C.10 Wilkowski, G. M., and others, "Short Cracks in Piping and Piping Welds" Seventh Program Report, March 1993 – December 1994, NUREG/CR-4599, Vol. 4, No., 1, April 1995.

C.11 Krishnaswamy, P., and others, "Fracture Behavior of Short Circumferentially Surface-Cracked Pipe," NUREG/CR-6298, November 1995.

C.12 Paul, D.D., and others, "Evaluation and Refinement of Leak-Rate Estimation Models," NUREG/CR-5128, Rev. 1, June 1994.

C.13 http://www.nucleartourist.com

C.14 http://www.nrc.gov (Note: much of the plant-specific content has been removed from the NRC's web site in light of the events of September 11, 2001)

C.15 Nero, A. V., "A Guidebook to Nuclear Reactors," University of California Press, Berkely CA, 1979.

C.16 Beaver Valley FSAR

C.17 http://www.sassi2000.com

C.18 Richart, F.E, Woods, R.D, and Hall, J.R., *Vibration of Soils and Foundations*, Prentice-Hall, Englewood Cliffs NJ, 1970.

C.19 American Society of Civil Engineers, *Seismic Analysis of Safety-Related Nuclear Structures and Commentary on Standard for Seismic Analysis of Safety Related Nuclear Structures*, ASCE 4-86, ASCE, New York, 1987.

C.20 Luco, J.E., and others, "Engineering Characterization of Ground Motion – Task II: Soil Structure Interaction Effects on Structural Response," NUREG/CR-3805 Vol. 4, August 1986.

C.21 Kennedy, R.P., "Engineering Characterization of Ground Motion – Task II: Effects of Ground Motion Characteristic on Structural Response Considering Localized Structural Nonlinearities and Soil-Structure Interaction Effects," NUREG/CR-3805 Vol. 1, March 1985.

C.22 Shao, L.C., "Summary of Frequencies for Reactor and Auxiliary Buildings," USNRC Private Communication, March 1975.

C.23 http://nisee.berkeley.edu/data/strong_motion/sacsteel/ground_motions.html

C.24 http://nisee.berkeley.edu/data/strong_motion/sac steel/motions/bo2in50yr.html

APPENDIX D

ANALYTICAL EXPRESSIONS INCORPORATING RESTRAINT OF PRESSURE-INDUCED BENDING IN CRACK-OPENING DISPLACEMENT CALCULATIONS

D. 1 Introduction

Among the factors that are important to leak-before-break (LBB) of nuclear piping systems is an effect called restraint of pressure-induced bending on crack-opening displacement (Ref. D.1). As shown in Figure D.1, the existence of a through-wall circumferential crack will result in a bending moment at the crack region for a pipe loaded axially from pressure, due to the eccentricity from the neutral axis in the cracked plane versus the center of the uncracked pipe. This pressure-induced bending (PIB) causes an unrestrained pipe to rotate, thereby resulting in an increase in crack-opening displacement.

In a real piping system, the ends of the pipe can be restrained from free rotation, reducing the degree of pressure-induced bending. Examples of the pipe restraints include nozzles, elbows, pipe hangers, and other pipe-system boundary conditions. The degree of the restraint also depends on the geometry of the pipe system. In general, the restraint of end rotation is a function of:

- the magnitude of the load (elastic or plastic effects),
- the length of the crack,
- the pipe geometry, i.e., R/t ratio, and
- the boundary conditions of the pipe on either side of the crack location.

The restraining effect on PIB in general results in an increase in the load-carrying capacity of the cracked pipe, but a decrease in the crack-opening displacement when compared with that of the same cracked pipe free from the restraints (Ref. D.2). This is illustrated in Figure D.2.

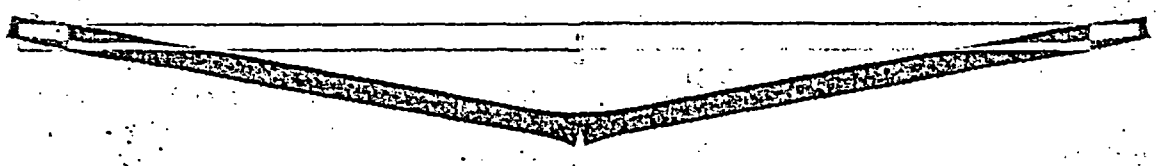

Figure D.1 Rotation of unrestraint pipe due to pressure induced bending. The rotation of the pipe is magnified by factor of 2.

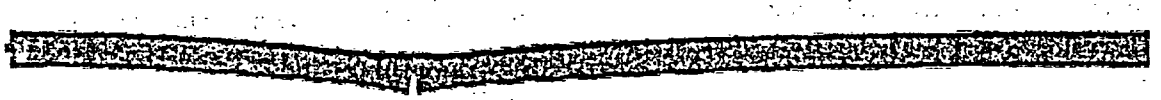

Figure D.2 Reduction of COD in pressure-induced-bending of a restrained pipe. An asymmetric pipe restraint condition is shown. Displacement magnified by a factor of 5.

The beneficial load-carrying capacity increase has a corresponding decrease in the cracking-opening area for leak detection that is detrimental to LBB. The trade-offs between the two effects appear to be case-dependent, and are influenced by the pipe diameter and crack length (Ref. D.3).

The common analysis practice for LBB is to determine the center crack-opening displacement (COD) by using the solution for an end-capped vessel. The so-called end-capped vessel model, although relatively simple to analyze, allows the ends of the vessel to freely rotate. Furthermore, it ignores the restraint to the ovalization at the crack plane imposed by the restraining end of the piping system. Therefore, the end-capped vessel model may over-estimate the COD more than if the pipe is not allowed to rotate in the real world piping systems.

In this program, a set of analytically based expressions has been developed. These expressions can be used to correct the end-capped COD solutions to account for the effect of piping restraint on PIB. The expressions are given in terms of the normalizing factor r_{COD}, defined as:

$$r_{COD} = \frac{COD_{res}}{COD_{unres}} \qquad (D.1)$$

where COD_{res} is the COD value of a crack in a restrained piping system, and COD_{unres} is the COD value in the corresponding unrestrained pipe. r_{COD} is also called the normalized COD. Solutions for COD_{unres} for various pipe and crack geometries are available in many publications in open literature. They can also be obtained rather easily using the end-capped vessel models. Once the COD_{unres} is known, the COD of a crack in a restrained pipe can be determined with the aid of the normalizing factor r_{COD} derived in this work:

$$COD_{res} = r_{COD} \cdot COD_{unres} \qquad (D.2)$$

The analytical expressions obtained in this work were based the results of the round-robin finite element (FE) calculations of COD values that were conducted earlier in this BINP program (Ref. D.4). As such, the expressions of the normalizing factor are limited, and should be used within the range in which the expressions were derived.

D. 2 Problem Statement

Due to the bending and the rotation of a cracked pipe, the crack-opening displacement is not uniform through the wall of the pipe – the crack-opening displacement at the inner surface of the pipe can be different from that at the outer surface. In this program, the term COD is specifically referred to as the *center crack opening displacement at the mid-thickness* of a through-wall circumferential crack in a straight pipe.

The cracked-pipe geometry investigated in this program is illustrated in Figure D.3. The basic geometric variables include the pipe outside diameter (OD), pipe mean radius to thickness ratio (R_m/t), half crack length (θ), and the restraint length – the distance between the restraint plane and the crack plane (L_{R1}, L_{R2}). The restraint is called symmetric if the restraint lengths from both ends are equal ($L_{R1}=L_{R2}=L_R$); otherwise, it is called asymmetric restraint. These variables are also given in Figure D.3.

The basic assumptions made in both the round-robin FE analyses and the derivation of the analytical expressions are:

- The deformation is linear elastic. The elastic modulus is 200 GPa (29,000 ksi), and the Poisson's ratio is 0.3.
- The displacement of the pipe is small – both the strain and the rotation of a cracked pipe from PIB are small. As such, the geometric nonlinearity effects due to large rotation and large strain are ignored. Also ignored is the change of loading directions associated with the deformation process.
- At the crack plane, the pipe is allowed to move vertically and horizontally (rotation in the crack plane and ovalization are not restricted), but it was pinned of any axial displacement in the ligament.
- For the restrained pipe, both ends of the pipe are restrained from rotation and ovalization, and only the axial displacement is allowed at the pipe end. This represents the most severe restraint conditions in a piping system.
- For the reference unrestrained pipe, the end-capped vessel model is assumed – the ends of the pipe are allowed to move freely. Theoretically, the unrestrained pipe should be infinitely long. The results from the round-robin FE calculations show that, if the pipe length is greater than 20 times of the pipe diameter ($L_R > 20$ OD), the pipe ends will then have negligible effect on the deformation in the vicinity of the cracked plane and the resultant COD value.
- An axial force is applied at the pipe end, passing through the central axis of the pipe. The applied load values are arbitrarily chosen because; (1) the deformation is

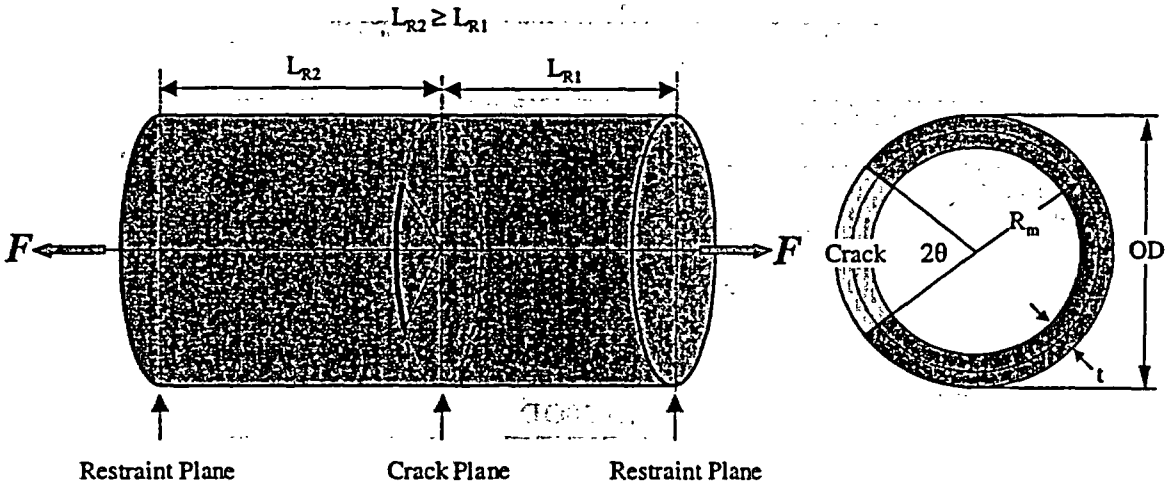

Figure D.3 Cracked-pipe geometry

linear-elastic and confined to the small displacement condition, and (2) the COD results are normalized with respect to the unrestrained COD.

- There is no pressure on the crack faces, and no internal pressure is present.

Figure D.4 depicts the boundary and loading conditions used in this investigation for the symmetrically restrained cases (L_1=L_2).

D.2.1 Round-Robin FE COD Analyses

The BINP round-robin FE COD analysis matrix included a total of 144 cases covering a wide range of pipe geometries and restraint conditions (Ref. D.4). Table D.1 and Table D.2 summarize the analysis matrix of the round-robin FE calculations. Details of the round-robin analysis can be found in Reference D.4.. The results from the round-robin analysis were used to validate the analytical expressions developed in this work.

D.3 Development of Analytical Expressions

The development of the analytical expressions for restraint of pressure induced bending was based on the recent work by Miura (Ref. D.5). Miura's expression was expanded to cover a wider range of R/t ratios for a symmetrically restrained pipe system. New expressions were developed for the asymmetric restraint conditions.

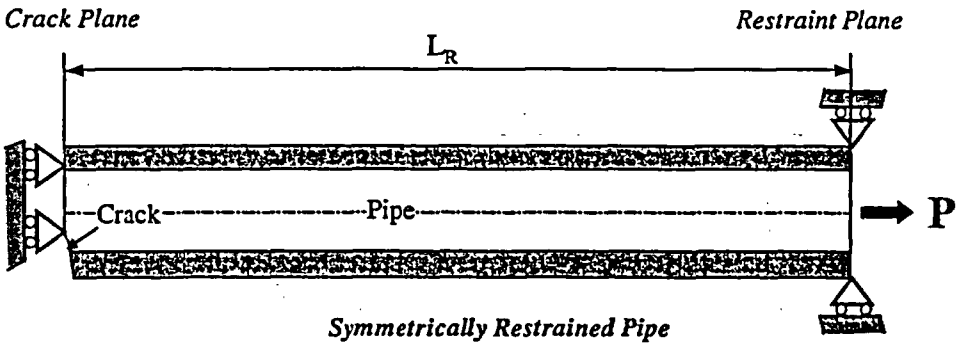

Symmetrically Restrained Pipe

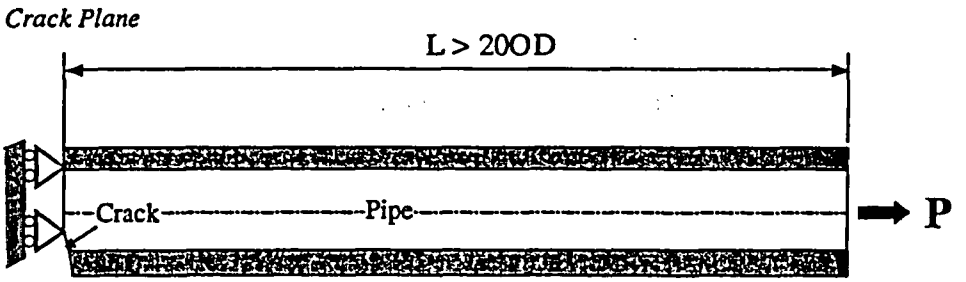

Unrestrained Pipe

Figure D.4 Loading and boundary conditions of a symmetrically restrained pipe

Table D.1 Analysis matrix for symmetric restraint cases in round-robin FE calculations

	OD (mm)	R_m/t	Axial Force (kN)	Half Crack Length			Restraint Length (L/OD)			
Case 1a	711.2	10	50,000	π/8	π/4	π/2	1	5	10	20
Case 1b	323.85	10	5,000	π/8	π/4	π/2	1	5	10	20
Case 1c	114.3	10	500	π/8	π/4	π/2	1	5	10	20
Case 2a	711.2	5	50,000	π/8	π/4	π/2	1	5	10	20
Case 2b	711.2	20	50,000	π/8	π/4	π/2	1	5	10	20
Case 2c	711.2	40	50,000	π/8	π/4	π/2	1	5	10	20

Table D.2 Analysis matrix for asymmetric restraint cases in round-robin FE calculations

	OD (mm)	Rm/t	Axial Force (kN)	Half Crack Length			L_{R_2}/OD			L_{R_1}/OD
							5	10	20	
Case 3a	711.2	10	50,000	π/8	π/4	π/2	X	X	X	1
	711.2	10	50,000	π/8	π/4	π/2		X	X	5
	711.2	10	50,000	π/8	π/4	π/2			X	10
Case 3b	323.85	10	5,000	π/8	π/4	π/2	X	X	X	1
	323.85	10	5,000	π/8	π/4	π/2		X	X	5
	323.85	10	5,000	π/8	π/4	π/2			X	10
Case 3c	114.3	10	500	π/8	π/4	π/2	X	X	X	1
	114.3	10	500	π/8	π/4	π/2		X	X	5
	114.3	10	500	π/8	π/4	π/2			X	10

D.3.1 Symmetrically Restrained Pipe

Miura's approach is schematically illustrated in Figure D.5. Miura treated the deflection of a cracked pipe due to pressure-induced bending as an elastic beam problem. The existence of the crack is represented by a beam section of reduced thickness in the vicinity of the cracked plane. The end-restraint of the pipe makes the deflection of the beam statistically indeterminate. He then makes the analogy that the COD and pipe rotations are linearly related, hence the ratios of the restrained to the unrestrained rotation is the same as the ratio for the restrained to unrestrained COD. Such an approach has also been used for developing J-estimation schemes in the past.

For symmetric restraint, Miura derived the following equation for the normalizing factor (normalized COD), r_{COD}:

$$r_{COD} = \frac{L_R/D_m}{L_R/D_m + \frac{I_b(\theta)}{4}} \qquad (D.3)$$

where D_m is the mean diameter of the pipe, L_R the restraint length, and θ the half-crack angle. $I_b(\theta, R_m/t)$ is an integral of the compliance term, $F_b(\theta, R_m/t)$, in the stress intensity factor definition, K_I:

$$I_b(\theta, R_m/t) = 4\int \theta\, F_b^2(\theta, R_m/t)\, d\theta$$

$$K_I = \sigma_b \sqrt{\pi R_m \theta}\, F_b(\theta, R_m/t) \qquad (D.4)$$

According to Equation D.3, r_{COD} is related to the normalized geometric parameters:

- normalized restraint length L_R/D_m,
- normalized pipe thickness R_m/t, and
- normalized half crack length θ/π.

Such a parametric relationship simplifies the application of the analytical expressions – it is unnecessary to distinguish the results from pipes with different diameters or restraint lengths, provided that the normalized parameters are the same. Indeed, the results from the round-robin FE calculations, as illustrated in Figure D.6, support the parametric relationship.

Miura used the following equations to evaluate the function $I_b(\theta, R_m/t)$:

$$I_b(\theta, R_m/t) = 2\theta^2\left[1 + 8\left(\frac{\theta}{\pi}\right)^{1.5} I_{b1} + \left(\frac{\theta}{\pi}\right)^3 (I_{b2} + I_{b3})\right]$$

$$I_{b1} = \frac{A_b}{7} + \frac{B_b}{9}\left(\frac{\theta}{\pi}\right) + \frac{C_b}{11}\left(\frac{\theta}{\pi}\right)^2 \qquad (D.5)$$

$$I_{b2} = \frac{A_b^2}{2.5} + \frac{A_b B_b}{1.5}\left(\frac{\theta}{\pi}\right) + \frac{2A_bC_b + B_b^2}{3.5}\left(\frac{\theta}{\pi}\right)^2$$

$$I_{b3} = \frac{B_bC_b}{2}\left(\frac{\theta}{\pi}\right)^3 + \frac{C_b^2}{4.5}\left(\frac{\theta}{\pi}\right)^4$$

where the coefficients A_b, B_b, and C_b are taken from Klecker et al.'s curve-fitting of Sander's solution for the stress intensity factor (Ref. D.6). These original coefficient are given in Equation D.6.

In this study, it was found that the coefficients used by Miura, as given in Equation D.6, are only valid for R_m/t ratios up to 16. Thus, these coefficients were revised to cover a wider range of R_m/t ratios up to 40, again through curve-fitting the Sander's solution. The revised coefficients are given in Equation D.7.

The differences in $I_b(\theta, R_m/t)$ are compared in Figure D.7. Clearly the discrepancies are significant for R_m/t values above 20.

Figures D.8 though Figure D.11 provide comparisons of the r_{COD} from the analytical expressions and the FE calculations for all the symmetric restraint cases in the round-robin analysis matrix. The analytical solutions are shown as solid lines, whereas the FE results are shown as various points in these figures. Clearly, the analytical expression by Miura (Equation D.3), combined with the revised coefficients (Equation D.7), is adequate for all the cases investigated in the present study. For comparison, Figure D.12 shows the analytical solution using the original coefficients by Miura for $R_m/t = 40$. The use of the original coefficients severely underestimates the values of r_{COD}, especially for the cases where the crack is long.

$$\begin{bmatrix} A_b \\ B_b \\ C_b \end{bmatrix} = \begin{bmatrix} -3.26543 & 1.52784 & -0.072698 & 0.0016011 \\ 11.36322 & -3.91412 & 0.18619 & -0.004099 \\ -3.18609 & 3.84763 & -0.18304 & 0.00403 \end{bmatrix} \begin{bmatrix} 1 \\ R_m/t \\ (R_m/t)^2 \\ (R_m/t)^3 \end{bmatrix} \qquad \text{for } R_m/t < 16 \quad (D.6)$$

$$\begin{bmatrix} A_b \\ B_b \\ C_b \end{bmatrix} = \begin{bmatrix} -2.6925 & 1.3148 & -0.049146 & 0.00080685 \\ 9.7042 & -3.3423 & 0.12768 & -0.0021944 \\ -1.9277 & 3.3798 & -0.13131 & 0.0022859 \end{bmatrix} \begin{bmatrix} 1 \\ R_m/t \\ (R_m/t)^2 \\ (R_m/t)^3 \end{bmatrix} \qquad \text{for } R_m/t < 40 \quad (D.7)$$

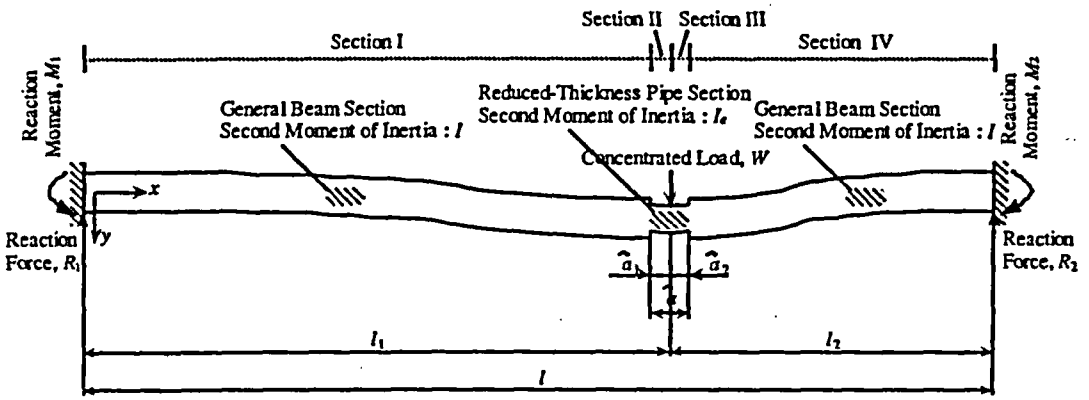

Figure D.5 Beam model representing deformation of cracked pipe under restraint (Ref. D.5)

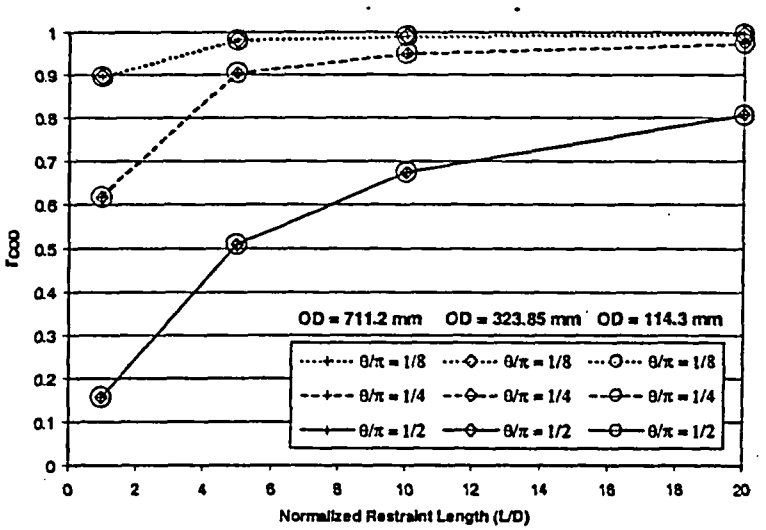

Figure D.6 Normalized COD for different pipe diameters (Ref. D.4)

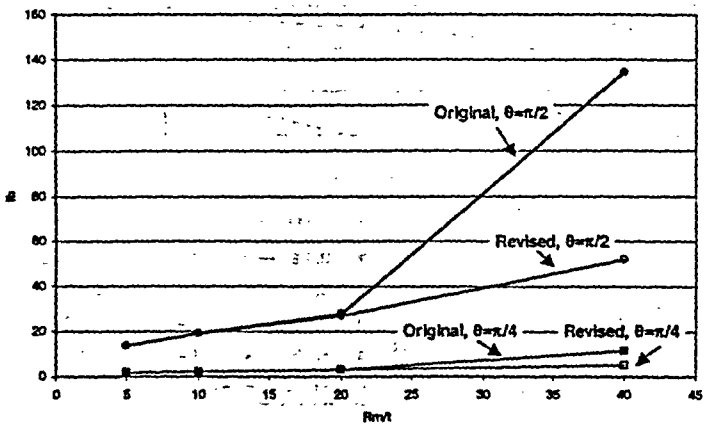

Figure D.7 Comparison of the $I_b(\theta)$ values for different curve-fitting coefficients

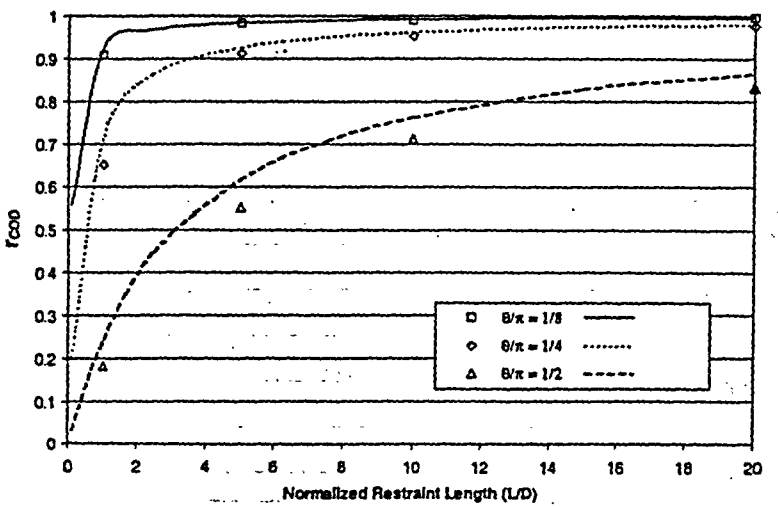

Figure D.8 Comparison of the normalizing factor between the analytical expression and the FE calculations. Symmetric restraint, $R_m/t=5$

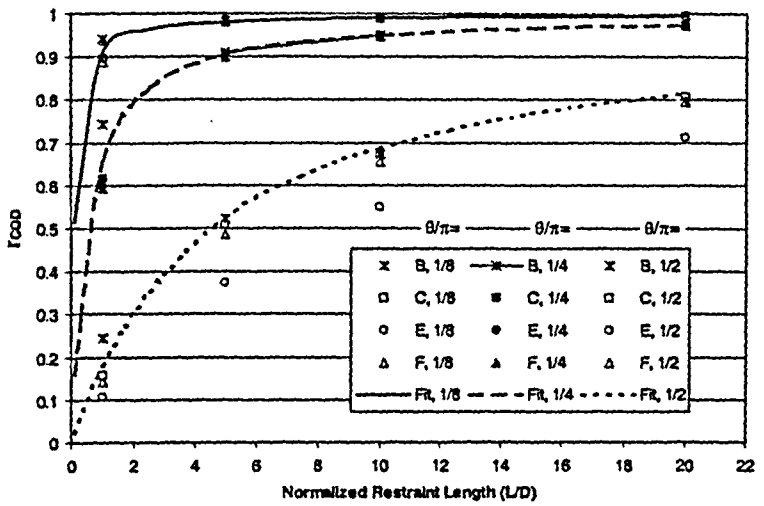

Figure D.9 Comparison of the normalizing factor between the analytical expression and the FE calculations. The FE results from different round-robin participants are indicated by different letters. Symmetric restraint, $R_m/t=10$

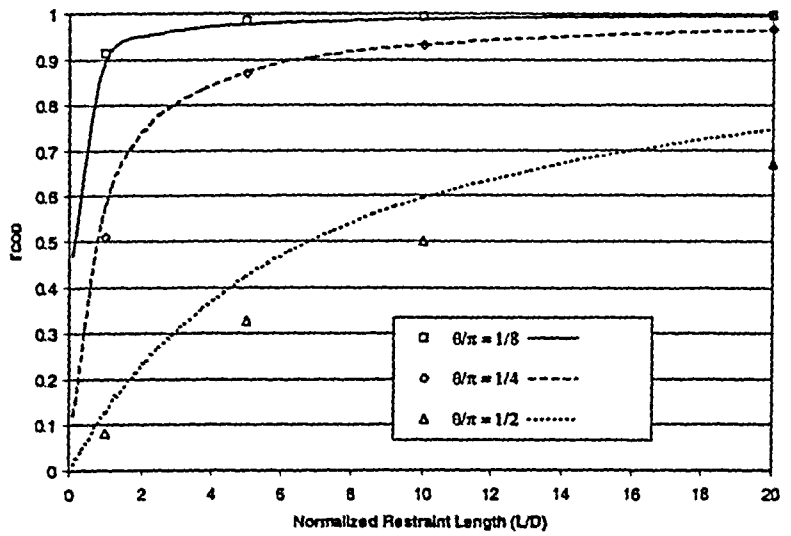

Figure D.10 Comparison of the normalizing factor between the analytical expression and the FE calculations. Symmetric restraint, $R_m/t=20$

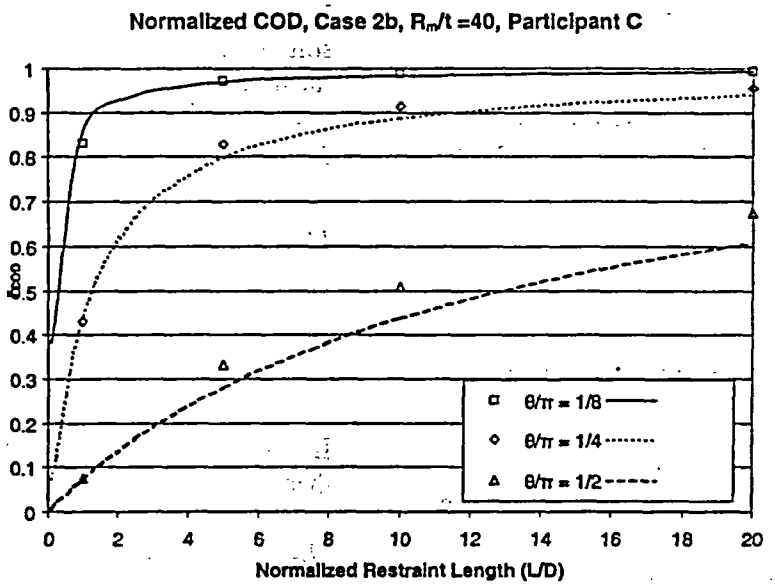

Figure D.11 Comparison of the normalizing factor between analytical expression and the FE calculations. Symmetric restraint, $R_m/t=40$

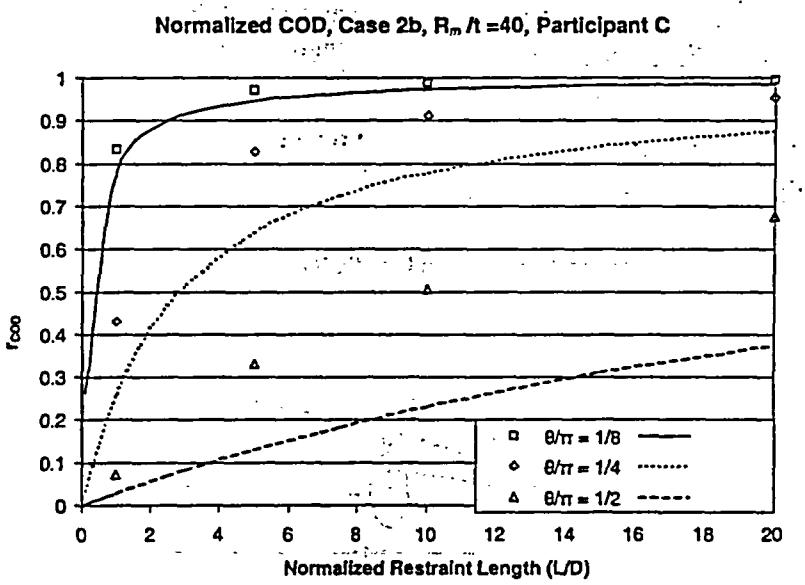

Figure D.12 Comparison of the normalizing factor between the analytical expression and the FE calculations. Symmetric restraint, $R_m/t=40$. NUREG/CR-4572 curve-fitting of coefficients of A_b, B_b, and C_b

D.3.2 Asymmetrically Restrained Pipe

Using the same beam approach for the symmetric restraint case, Miura derived the following solution for the asymmetrical restraint case:

$$r_{COD} = \frac{[L_R/D_m]_{eq}}{[L_R/D_m]_{eq} + \frac{I_b(\theta)}{4}} \qquad (D.8)$$

where $[L_R/D_m]_{eq}$ is the so-called equivalent normalized restraint length:

$$[L_R/D_m]_{eq} = 2\frac{[L_{R1}/D_m][L_{R2}/D_m]}{[L_{R1}/D_m]+[L_{R2}/D_m]} \quad or$$
$$\frac{1}{[L_R/D_m]_{eq}} = \frac{1}{2}\left(\frac{1}{[L_{R1}/D_m]} + \frac{1}{[L_{R2}/D_m]}\right) \qquad (D.9)$$

As shown in Equation D.9, the equivalent normalized restraint length is the harmonic average of the normalized restraint lengths L_{R1} and L_{R2}.

Comparisons with the round-robin FE results reveals that the Miura's solution tends to underestimate the restraint effect if the restraint length is short, and overestimate if the restraint length is long. The discrepancy is especially noticeable if the crack is long and the asymmetry of the restraint length is large, as shown in Figure D.13.

It appears that the inadequacy of Miura's solution for the asymmetric cases is related to the harmonic property of the equivalent normalized restraint length. To illustrate this point, rearranging Equation D.9 yields:

$$[L_R/D_m]_{eq} = 2\frac{[L_{R1}/D_m][L_{R2}/D_m]}{[L_{R1}/D_m]+[L_{R2}/D_m]} = 2\frac{L_{R1}/D_m}{1+L_{R1}/L_{R2}} \qquad (D.10)$$

If L_{R2} is the longer restraint length of the two, then

$$L_{R1}/L_{R2} < 1 \quad and \quad [L_R/D_m]_{eq} < 2L_{R1}/D_m \qquad (D.11)$$

This means that, regardless the length of the longer restraint L_{R2}, the harmonic equivalent normalized restraint length cannot be greater than twice of the shorter restraint length. The variation of the harmonic equivalent restraint length as function of the L_{R2}/L_{R1} is shown in Figure D.14.

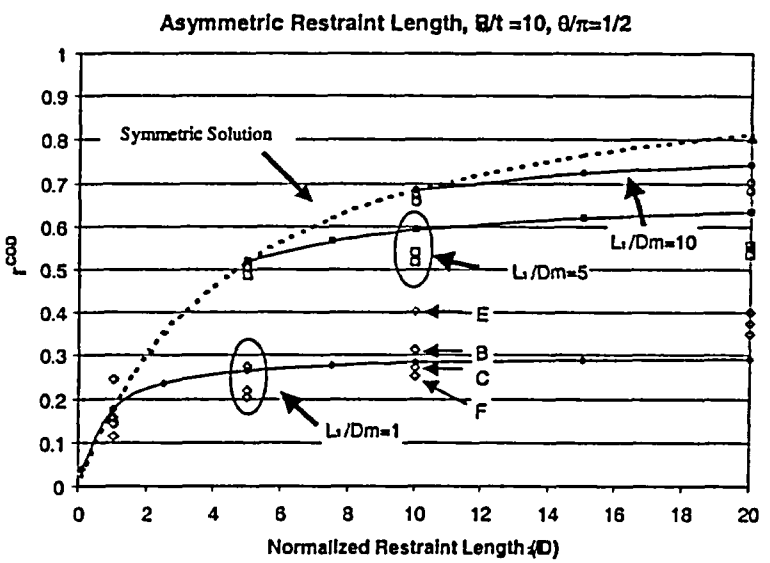

Figure D.13 Comparison of Miura's analytical solution with FE results for asymmetric restraint cases. Letters indicate the FE results from different round-robin participants. $R_m/t=10$, $\theta=\pi/2$

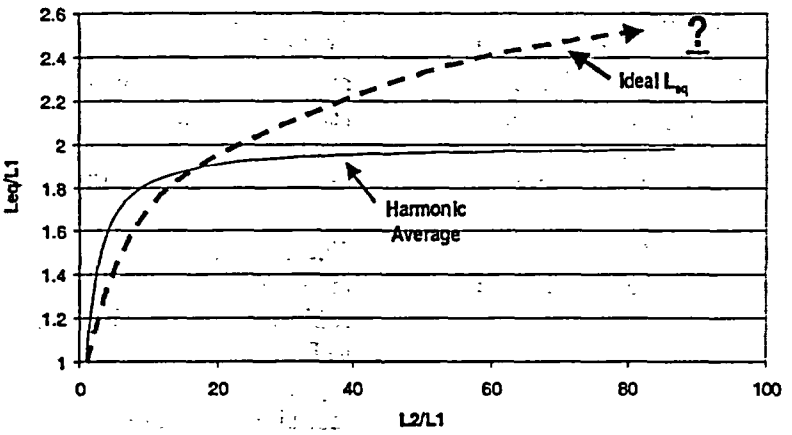

Figure D.14 Equivalent normalized restraint length as function of the ratio of L_{R2}/L_{R1}

Now consider a special case in which a pipe is restrained only at one end, at a distance of one D_m from the crack plane (i.e., $L_{R1}/D_m = 1$ and $L_{R2} \rightarrow \infty$). Equation D.10 becomes:

$$[L_R / D_m]_{eq} = \frac{2[L_{R2} / D_m]}{1+[L_{R2} / D_m]} = \frac{2}{1+\frac{1}{[L_{R2} / D_m]}} = 2 \qquad (D.12)$$

Hence, the harmonic equivalent normalized restraint length can only reach 2 even if the pipe is restrained only at one end. Further assuming $R_m/t=10$ and $\theta=\pi/2$, the resultant r_{COD} is 0.286, as shown in Figure D.13.

The same case was also analyzed using FE approach. The model is shown in Figure D.15. The restraint boundary condition was applied at $L_{R1}/D_m = 1$ from the crack plane at the left end of the pipe. The length of the pipe on the right side of the crack was set at $20D_m$, but the end was left unrestrained to allow free rotation and ovalization (end-capped condition). This effectively represents an infinitely long restraint length at the right side of the crack ($L_{R2}/D_m \rightarrow \infty$).

The r_{COD} from the FE model is 0.93, more than three times higher than the value obtained with the harmonic equivalent restraint length. Clearly, the harmonic expression of the equivalent restraint length penalizes the contribution of the longer pipe restraint length, and thus is inadequate if the restraint length of the longer pipe is relatively long.

More importantly, the FE analysis suggests that the restraint effect is nearly negligible ($r_{COD} \rightarrow 1$) in a one-side restrained pipe. This means that

$$L_{eq} \rightarrow \infty \quad if\ L_{R1} \neq 0\ and\ L_{R2} \rightarrow \infty \qquad (D.13)$$

Therefore, an improved definition of L_{eq} is required to improve the accuracy of the analytical expression of r_{COD} for the asymmetric restraint conditions. However, derivation of a theoretically sound closed-form analytic L_{eq} definition was found to be difficult.

A different approach was then adopted in this work – a correction function was used to relate the solution for asymmetrically restrained pipe to symmetrically restrained pipe. The correction function is proposed to take the following form:

$$r_{COD,asym} = (r_{COD,sym})_{L_{R1}} + \left[1-(r_{COD,sym})_{L_{R1}}\right] \cdot \min\left(\frac{\ln(L_{R2}/L_{R1})}{\ln(L_{ref}/L_{R1})}, 1\right) \qquad for\ L_{R1} < L_{R2} \qquad (D.14)$$

where $r_{COD,\,asym}$ is the normalizing factor for the asymmetrically restrained pipe. $(r_{COD,\,sym})_{LR1}$ is for the corresponding symmetrically restrained pipe, evaluated using Equation D.3 with the shorter restraint length L_{R1}. L_{ref} is a reference restraint length, representing the restraint length above when the restraint effect is negligible.

The correction function is expected to take the shape as illustrated in Figure D.16, and has the following properties:

$$r_{COD,asym} = r_{COD,sym} \quad if \; L_{R2} = L_{R1}$$
$$and$$
$$r_{COD} \to 1 \quad if \; L_{R2} \to L_{ref} \qquad (D.15)$$

L_{ref} is the only unknown variable of the correction function. L_{ref} is expected to be a function of R/t ratio and half crack length. Its values can be determined through curve-fitting of the FE calculation results. In this work, curve-fitting the round-robin FE calculations results in the second-order polynomial equation for L_{ref}, given in Equation D.16. The equation is plotted in Figure D.17.

The correction function for the asymmetrically restrained pipe is validated using the round-robin FE results. They are shown in Figrue D.18 to Figure D.20. Miura's solutions for the asymmetric case with the harmonic equivalent restraint length are also shown in the figures for comparison. The correction function clearly improves the accuracy of the analytical expressions of the normalizing factor.

$$\ln(L_{ref}/L_{R1}) = 38.52713\left(\frac{\theta}{\pi}\right)^2 - 5.658775\left(\frac{\theta}{\pi}\right) + 4.710531 \quad for \quad R_m/t = 10 \text{ and } \frac{1}{8} < \frac{\theta}{\pi} < \frac{1}{2} \qquad (D.16)$$

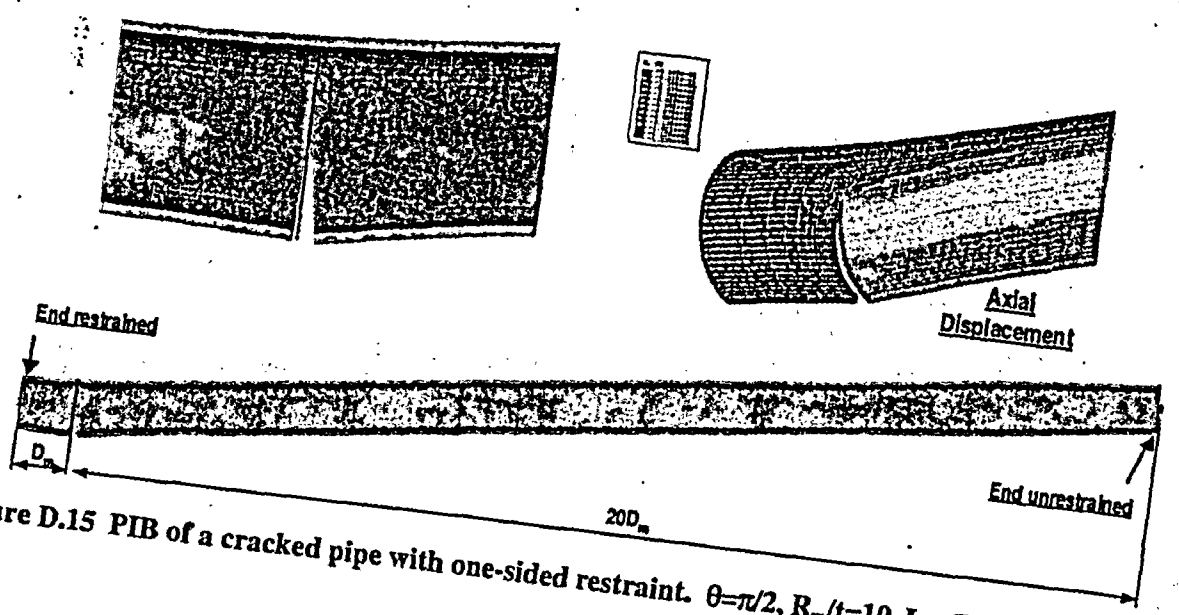

Figure D.15 PIB of a cracked pipe with one-sided restraint. $\theta=\pi/2$, $R_m/t=10$, $L_{R1}/D_m=1$, $L_{R2}/D_m\to\infty$

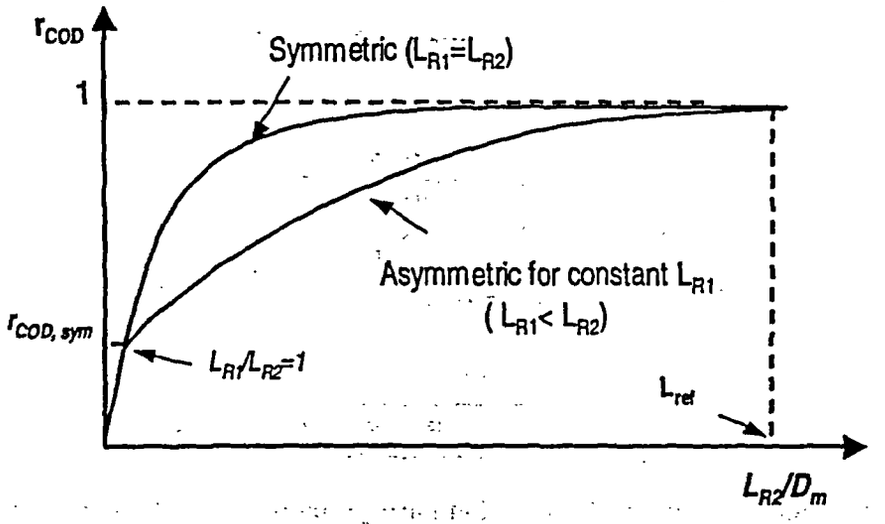

Figure D.16 General form of the correction function

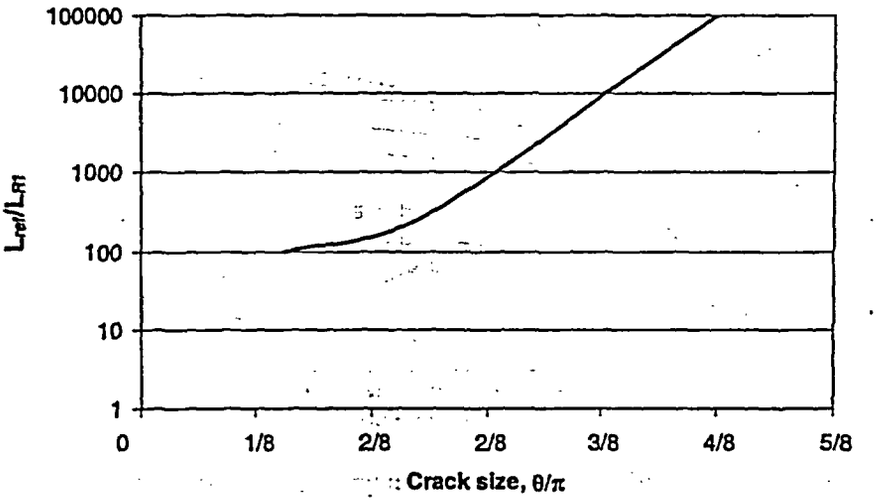

Figure D.17 Reference restraint length as function of crack size (R_m/t=10)

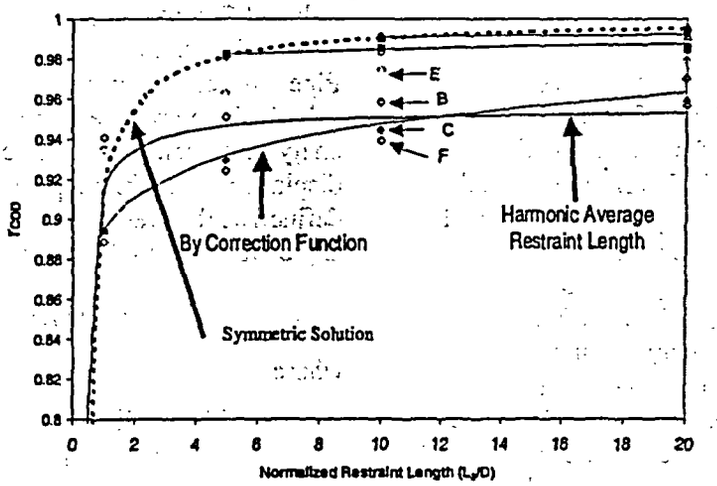

Figure D.18 Verification of analytical expression for asymmetric restraint cases (R_m/t=10, θ=π/8)

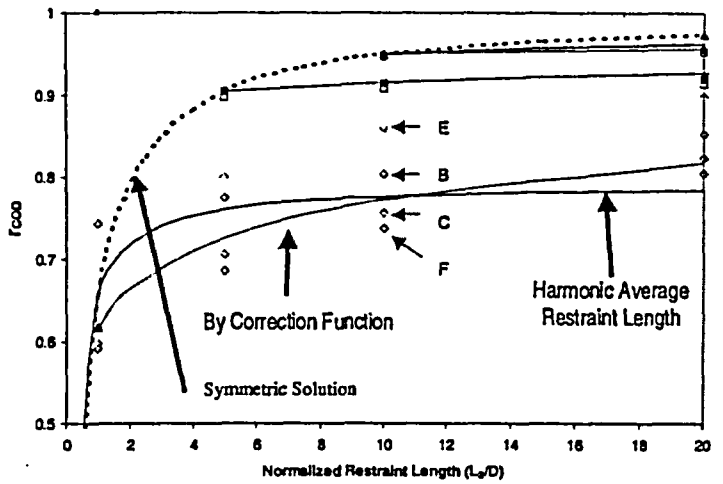

Figure D.19 Verification of analytical expression for asymmetric restraint cases ($R_m/t=10$, $\theta=\pi/4$)

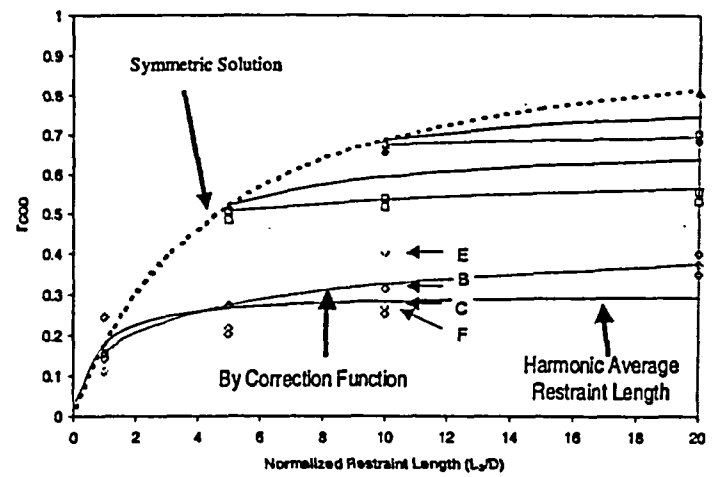

Figure D.20 Verification of analytical expression for asymmetric restraint cases ($R_m/t=10$, $\theta=\pi/2$)

D.4 Pipe Stiffness

In the previous sections of this appendix, the expression for the normalizing factor r_{COD} related the crack-opening displacement (COD) of restrained pipes to the COD for unrestrained pipes. The variable r_{COD} is expressed in terms of the restraint length to mean diameter ratio, L_R/D_m. Although conceptually easy to understand, the restraint length is a difficult parameter to determine directly. Restraint can occur in many forms, from pipe bends and curves to hinges and supports, all of which affect the restraint length in an unpredictable manner. Therefore, in order for the equations for the reduced COD to be practical, it is necessary to express L_R/D_m in terms of an alternate variable. Pipe stiffness is a parameter that is readily calculable in practice using a finite element analysis model. For the crack opening displacement problem, pipe stiffness k can be defined as the "relative moment for a unit kink angle" (see Figure D.21), or

$$k = M/\theta, \qquad (D.17)$$

where

M = applied moment, and
θ = the bending angle.

By deriving expressions relating the pipe stiffness to the normalized restraint length L_R/D_m, it is possible to utilize the r_{COD} equations in practical situations.

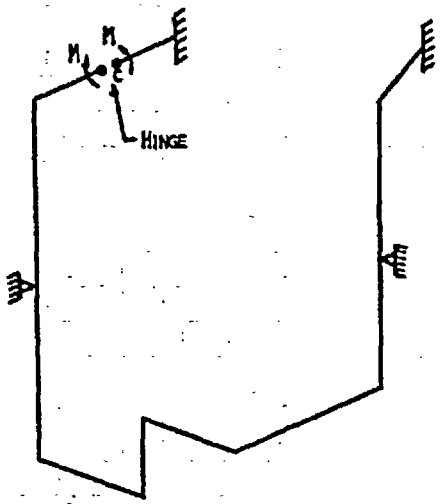

Figure D.21 Moment about a hinge; bends and various supports affect the restraint lengths of the pipe about the hinge

D.4.1 Case Matrix

The following work is based on a matrix of cases very similar to the ones presented in the previous sections. For the symmetric analysis, the cases consisted of the matrix of Table D.1, as well as the matrix of Table D.3 (below). Note that the additional cases in Table D.3 were not a part of the Round-Robin FE analyses or used to derive the r_{COD} equations. Rather, they were additional cases used in the derivation of the equations in the following sections, and allowed for a much more comprehensive analysis of the concept of pipe stiffness.

The r_{COD} equations for asymmetric restraint cover a much narrower range of data. Specifically, the expression for the reference restraint length (Eq. D.16) is valid only when $R_m/t = 10$ and $1/8 < \theta/\pi < ½$. The case matrix of Table D.2 adequately covers this limited range, and therefore only the matrix of Table D.2 is used to develop the L_R/D_m versus k relationship for the case of asymmetric restraint.

D.4.2 The ANSYS Model

In order to determine the pipe stiffness associated with various restraint lengths, a beam-type finite element model of a pipe was created with the ANSYS finite element program. The model elements were the same as the "pipe" elements that would be used in a plant piping stress analysis. The pipe was restrained at either end, and a hinge was created about which a moment could be applied (see Figure D.22).

In order to use the hinge model shown in Figure D.22, one has to settle on precisely how the analysis is to be performed. The hinge concept is quite simple, but there are subtle details that need to be defined. It was determined that the most rational way to proceed is to consider a separate "left" and "right" stiffness corresponding to L_1 and L_2 by finding the stiffness for the respective side assuming that the rotation for the opposite side is fixed at zero. This was, by no means, the only way to perform the stiffness analysis, but it had the desirable effect of more or less uncoupling the "left" and "right" rotations.

Following this idea, the steps for calculating the hinge stiffnesses for a pipe are as follows:

1. Put a hinge at the point of interest with the axis of rotation in the correct 3D orientation. Typically, this is most easily done using local coordinates at the point of interest.
2. Fix the rotation of the "left" side of the hinge at zero in the local coordinate system.
3. Apply a unit moment to the "right" side of the hinge and recover the rotation. The moment M and the recovered rotation θ_2 must both be in the local coordinate system.
4. Repeat steps 2 to 4 replacing "left" with "right" and vice versa in order to determine θ_1.

Table D.3 Additional Symmetric Cases used in Pipe Stiffness Analysis

	OD (mm)	R_m/t	Half Crack Length (radians)			Restraint Length (normalized to the *outer diameter*) L/OD			
Case 4.a	526.13	15	$\pi/8$	$\pi/4$	$\pi/2$	1	5	10	20
Case 4.b	465.23	15	$\pi/8$	$\pi/4$	$\pi/2$	1	5	10	20
Case 4.c	75.00	15	$\pi/8$	$\pi/4$	$\pi/2$	1	5	10	20
Case 5.a	465.23	5	$\pi/8$	$\pi/4$	$\pi/2$	1	5	10	20
Case 5.b	465.23	20	$\pi/8$	$\pi/4$	$\pi/2$	1	5	10	20
Case 5.c	465.23	40	$\pi/8$	$\pi/4$	$\pi/2$	1	5	10	20
Case 6.a	200.00	10	$\pi/8$	$\pi/4$	$\pi/2$	1	5	10	20
Case 6.b	500.00	10	$\pi/8$	$\pi/4$	$\pi/2$	1	5	10	20
Case 6.c	600.00	10	$\pi/8$	$\pi/4$	$\pi/2$	1	5	10	20
Case 7.a	200.00	15	$\pi/8$	$\pi/4$	$\pi/2$	1	5	10	20
Case 7.b	500.00	15	$\pi/8$	$\pi/4$	$\pi/2$	1	5	10	20
Case 7.c	600.00	15	$\pi/8$	$\pi/4$	$\pi/2$	1	5	10	20
Case 8.a	711.20	10	$\pi/8$	$\pi/4$	$\pi/2$	1	5	10	20
Case 8.b	711.20	15	$\pi/8$	$\pi/4$	$\pi/2$	1	5	10	20
Case 8.c	711.20	25	$\pi/8$	$\pi/4$	$\pi/2$	1	5	10	20
Case 9.a	465.23	10	$\pi/8$	$\pi/4$	$\pi/2$	1	5	10	20
Case 9.b	465.23	15	$\pi/8$	$\pi/4$	$\pi/2$	1	5	10	20
Case 9.c	465.23	25	$\pi/8$	$\pi/4$	$\pi/2$	1	5	10	20

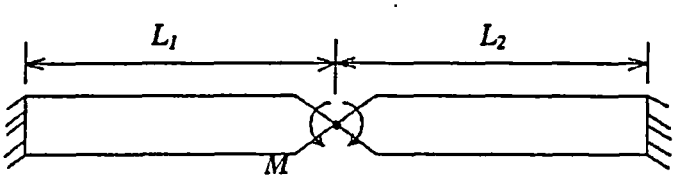

Figure D.22 Schematic of ANSYS pipe model used to determine stiffness values given various restraint lengths

5. For a case of symmetric restraint, divide the moment M by the difference of the rotations $|\theta_1| - |\theta_2|$ in order to determine $k = |M/(|\theta_1| - |\theta_2|)|$. For cases of asymmetric restraint, determine separate stiffness values for the two sides of the hinge as follows: $k_1 = |M/\theta_1|$ and $k_2 = |M/\theta_2|$.

The procedure outlined above can be applied as easily to a 3D pipe system with a crack in any orientation as it can be to the simple 2D model shown in Figure D.22.

D.4.3 Pipe Stiffness in Cases of Symmetric Restraint

After running the ANSYS model to determine the stiffnesses for the cases in Tables D.1 and D.3, plots of the restraint length in terms of pipe stiffness were generated for each case. From the plot of Case 1.a (see Figure D.23), it is evident that L_R/D_m and k are related by a power law function. Each case produced a similar plot, with a different constant in front of the power function. It was speculated that this constant was in some way related to the second moment of area of the pipe, I. Plotting the I of a pipe

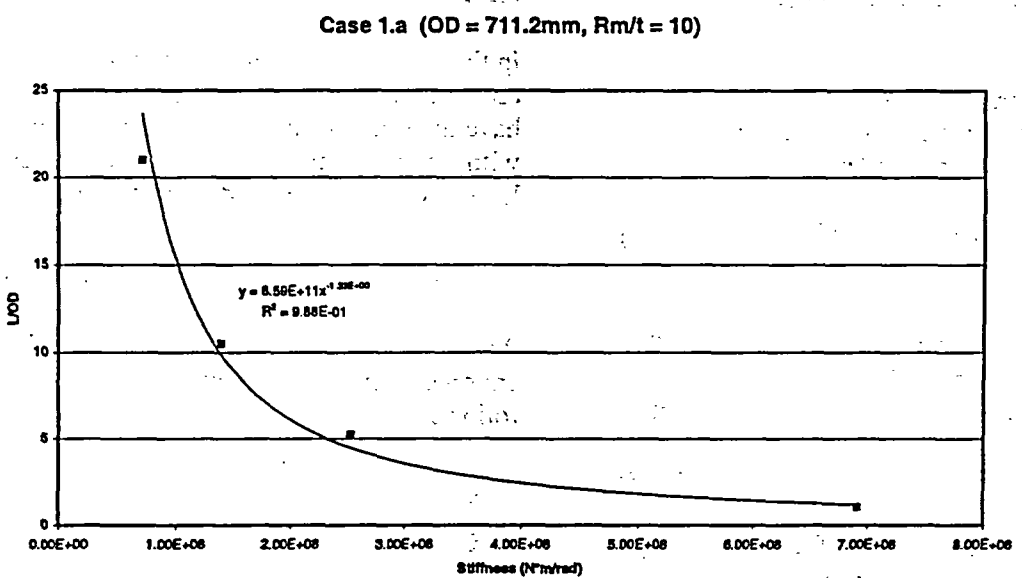

Figure D.23 Plot of restraint length in terms of stiffness for symmetric Case 1; k and L_R/D_m are related by a power function multiplied by a constant

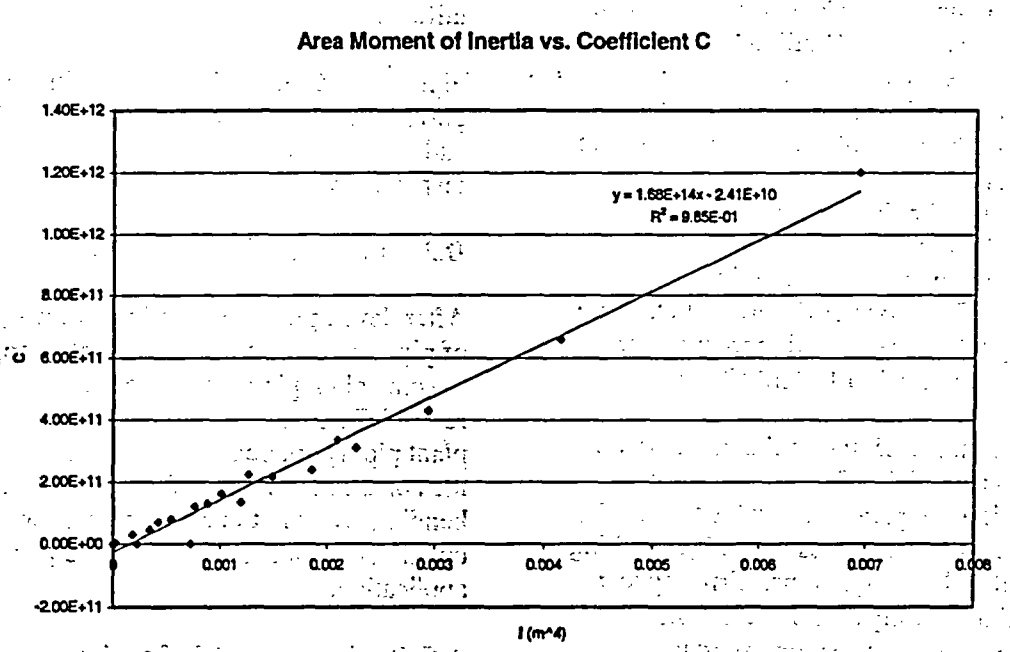

Figure D.24 Plot of constant C in terms of second moment of area I for all symmetric cases (The second moment of area is linearly related to the constant C)

against the required constant, it was clear that the constant is related linearly to I (see Figure D.24).

For cases of symmetric restraint, the following equation was developed relating pipe stiffness and the normalized restraint length,

$$L_R / D_m = Ck^{-1.33}, \qquad (D.18)$$

where L_R/D_m is the normalized restraint length and k is the pipe stiffness in N·m/rad. C is a constant obtained from the following equation

$$C = (1.68 \cdot 10^{14})I - 2.41 \cdot 10^{10} \qquad (D.19)$$

where I is the second moment of area of the pipe cross section (m^4), equivalent to

$$I = \frac{\pi}{64}(D_o^4 - D_i^4). \qquad (D.20)$$

The beam-type finite element analyses shows that the behavior of pipes with an I less than 10^{-4} m^4 does not fit the form of Equations D.18 and D.19 when subjected to a bending moment, and therefore must be related in a different manner to the restraint length. For instance, Cases 1.c and 4.c, where the outer diameters are 0.1143 m (4.5 inches) and 0.075 m (3.0 inches), respectively, and the thicknesses are both less that 10 mm (0.4 inches), show significant deviation from the expected behavior. Consequently, Equations D.18 through D.20 are accurate only when the second moment of area is greater than or equal to 10^{-4} m^4 (240 $inch^4$).

The plot in Figure D.25 shows the comparison between the normalizing factor r_{COD} when calculated using the parametric values of L_R/D_m and the stiffness-based values of L_R/D_m resulting from use of the above equations. Error appears to increase significantly as the second moment of area of the pipe cross-section approaches the range limit of 10^{-4} m^4 (240 $inch^4$).

D.4.4 Pipe Stiffness in Cases of Asymmetric Restraint

In the case of asymmetric restraint, the equations relating the pipe stiffness to the restraint length have the same form as in symmetric restraint with a slightly different scale. The two restraint lengths can be calculated using the equations

$$L_{R1} / D_m = C_1 k_1^{-1.11} \text{ and } L_{R2} / D_m = C_2 k_2^{-1.12}. \qquad (D.21)$$

Again, C_1 and C_2 are constants, and are dependent on the pipe's second moment of area as follows:

$$C_1 = (3.19 \cdot 10^{12})I + 2.07 \cdot 10^{8}$$
$$C_2 = (1.04 \cdot 10^{13})I + 6.92 \cdot 10^{8} \qquad (D.22)$$

In this case, k_1 and k_2 represent the stiffness of the pipe corresponding to the rotation of L_1 and L_2, respectively. As in the symmetric cases, the differences between parametric and stiffness-based L_R/D_m values when $I < 10^{-4}$ m^4 (240 $inch^4$) are significant, and the equations should not be utilized in this range.

Figures D.26 and D.27 (below) illustrate the power relationship between L_{R1}/D_m and L_{R2}/D_m and k, and the comparison between r_{COD} values, respectively.

D.5 Application of Equations

After developing the equations for r_{COD} in terms of pipe stiffness, it was important to apply them to some plant piping cases to see what effect the revised COD values have on leak rates for actual plant piping applications. This gives the user an idea of the importance of the pressure-induced bending effect in the calculation of crack-opening displacement values for a plant LBB application.

A finite element model of a 3-loop Westinghouse-style PWR nuclear power plant was developed, and hinges were placed at eighteen critical locations per the procedure given in Section D.4.2. Figures D.28 through D.31 show the 18 locations, all of which were at

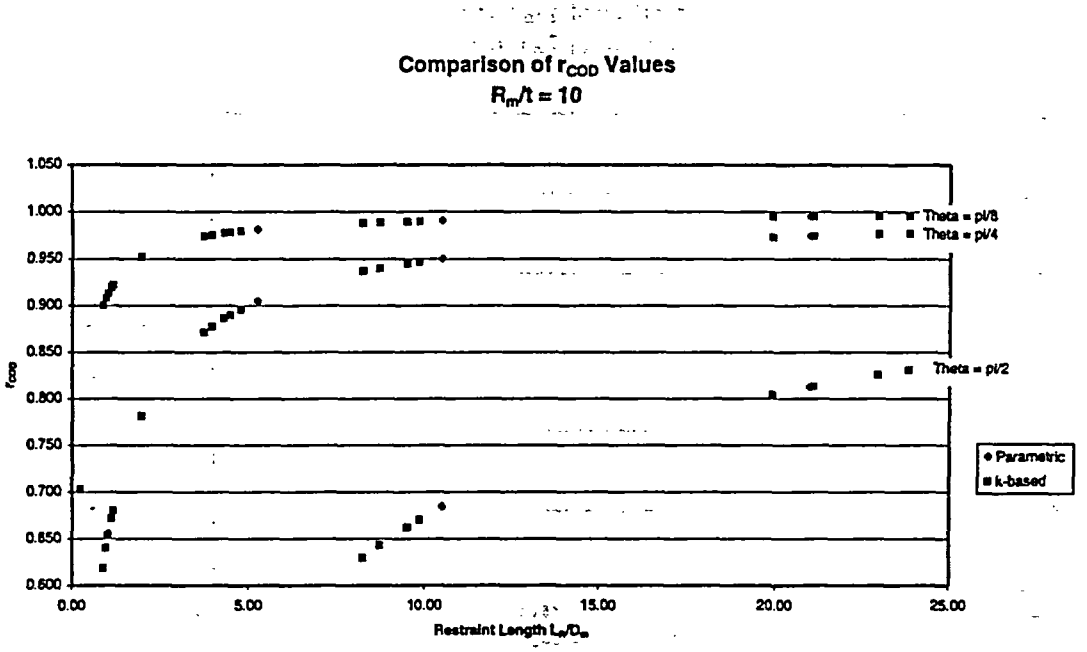

Figure D.25 Comparison of normalizing factors for parametric and stiffness-based L_R/D_m values in cases of symmetric restraint

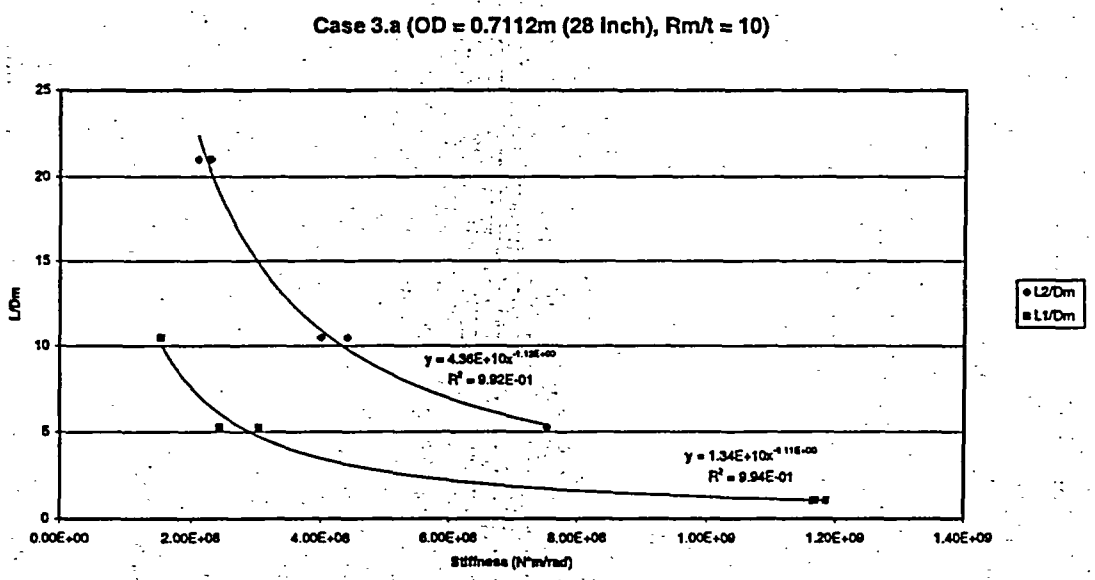

Figure D.26 Plot of restraint length in terms of stiffness for asymmetric Case 1.a

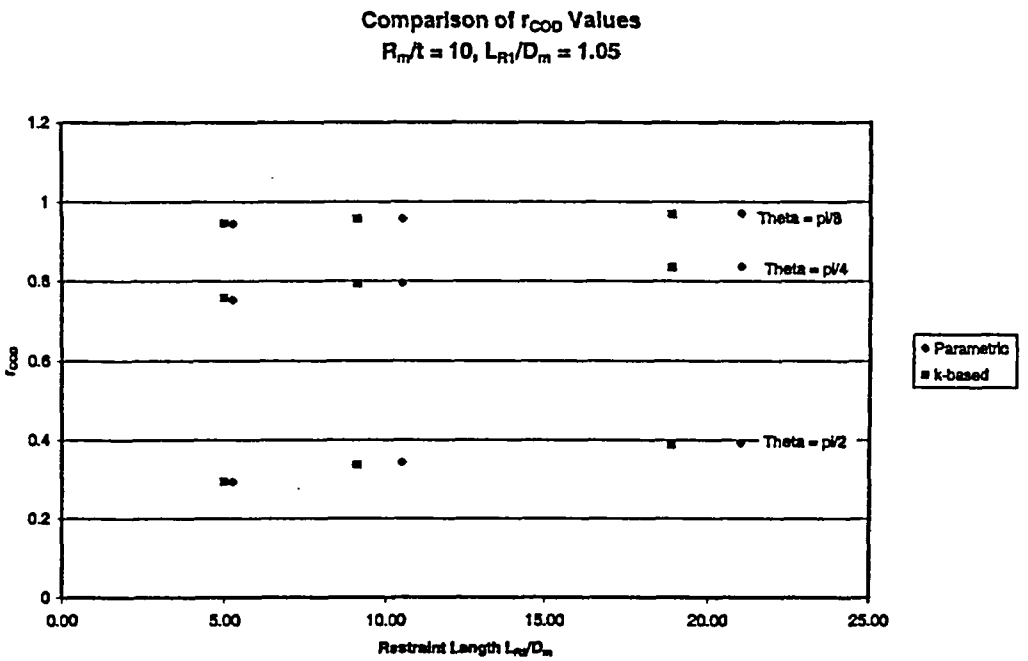

Figure D.27 Comparison of normalizing factor between parametric and stiffness-based values of L_R/D_m for asymmetric restraint

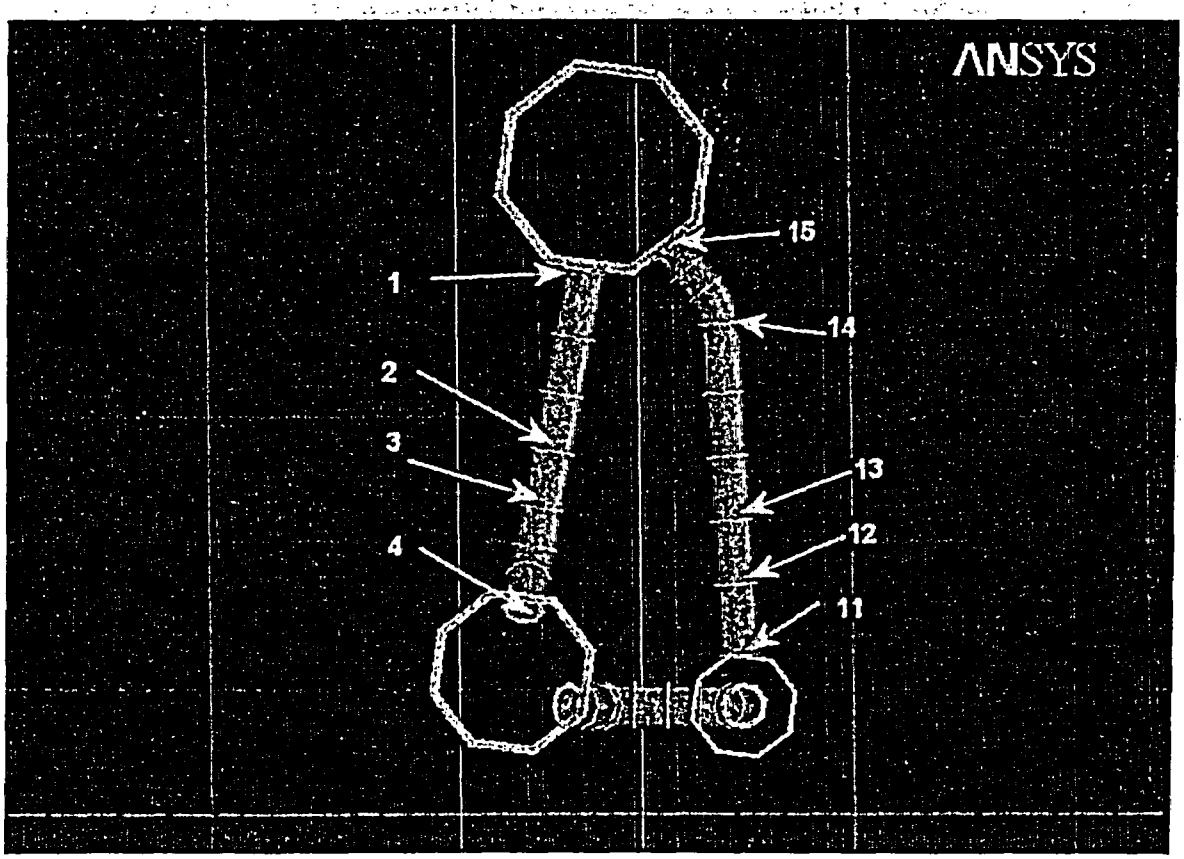

Figure D.28 Critical flaw locations in the hot and cold legs

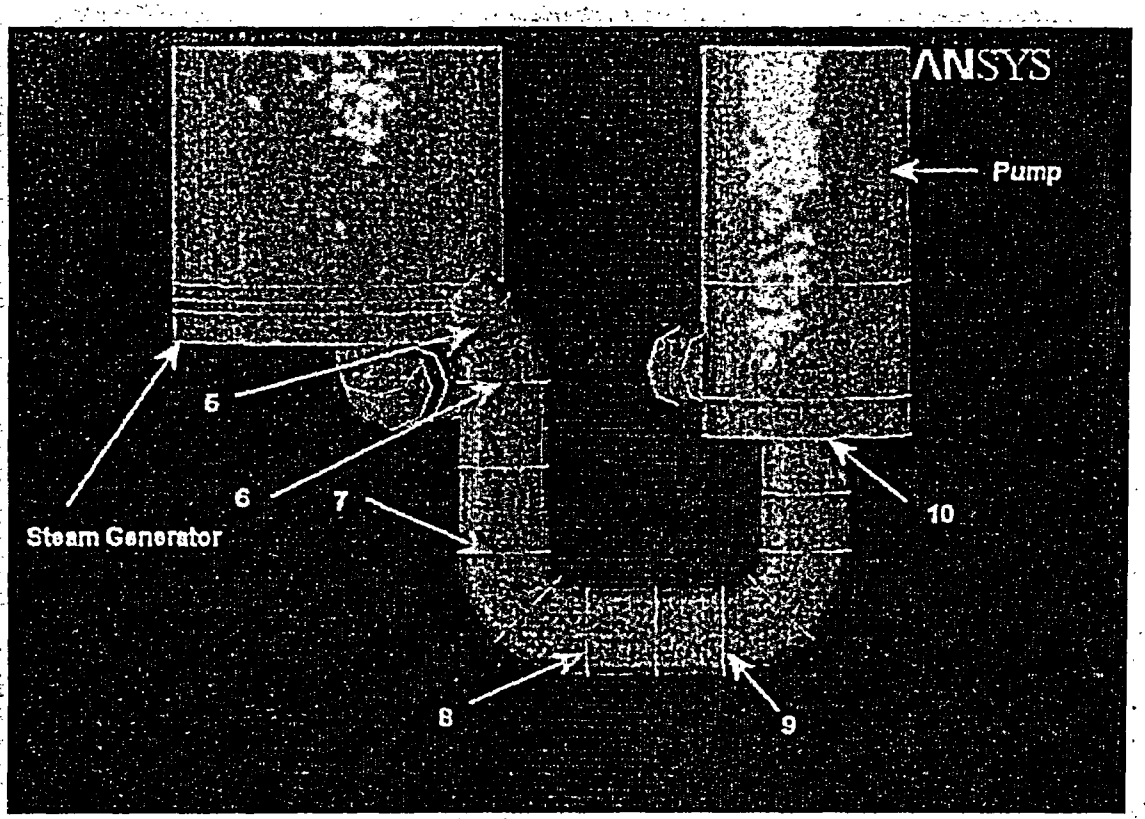

Figure D.29 Critical flaw locations in the crossover leg

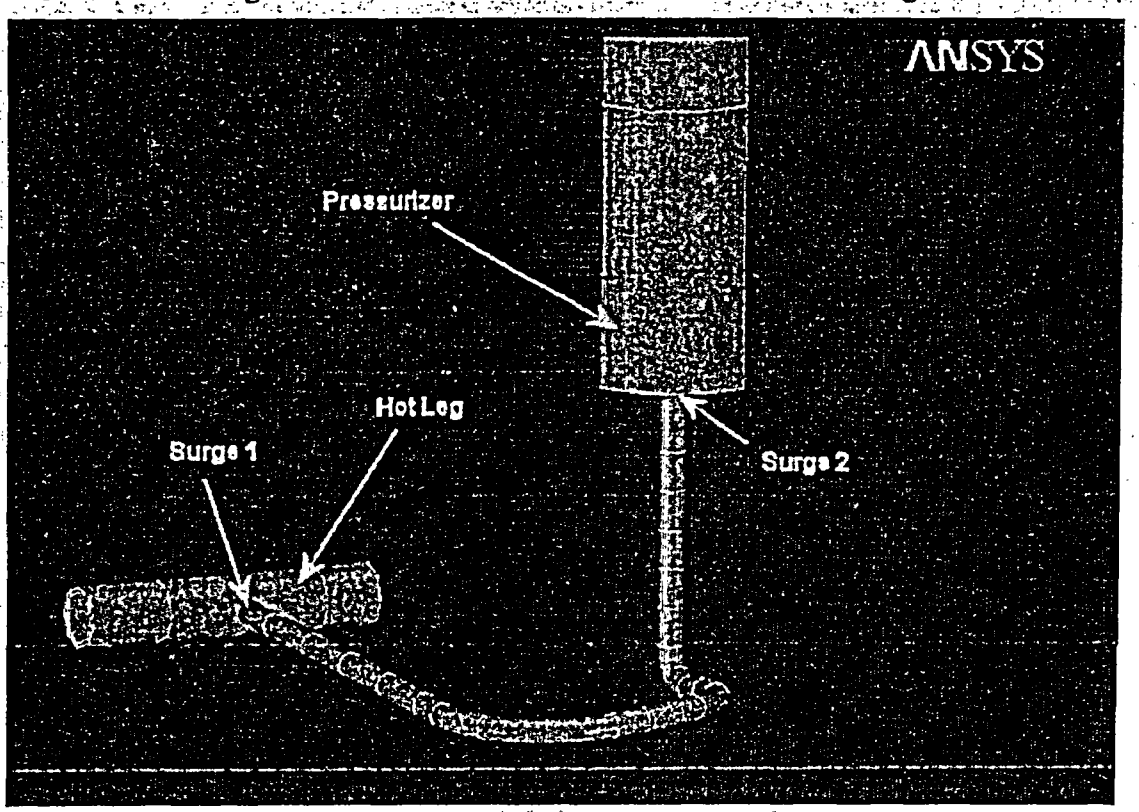

Figure D.30 Critical flaw locations in the surge line

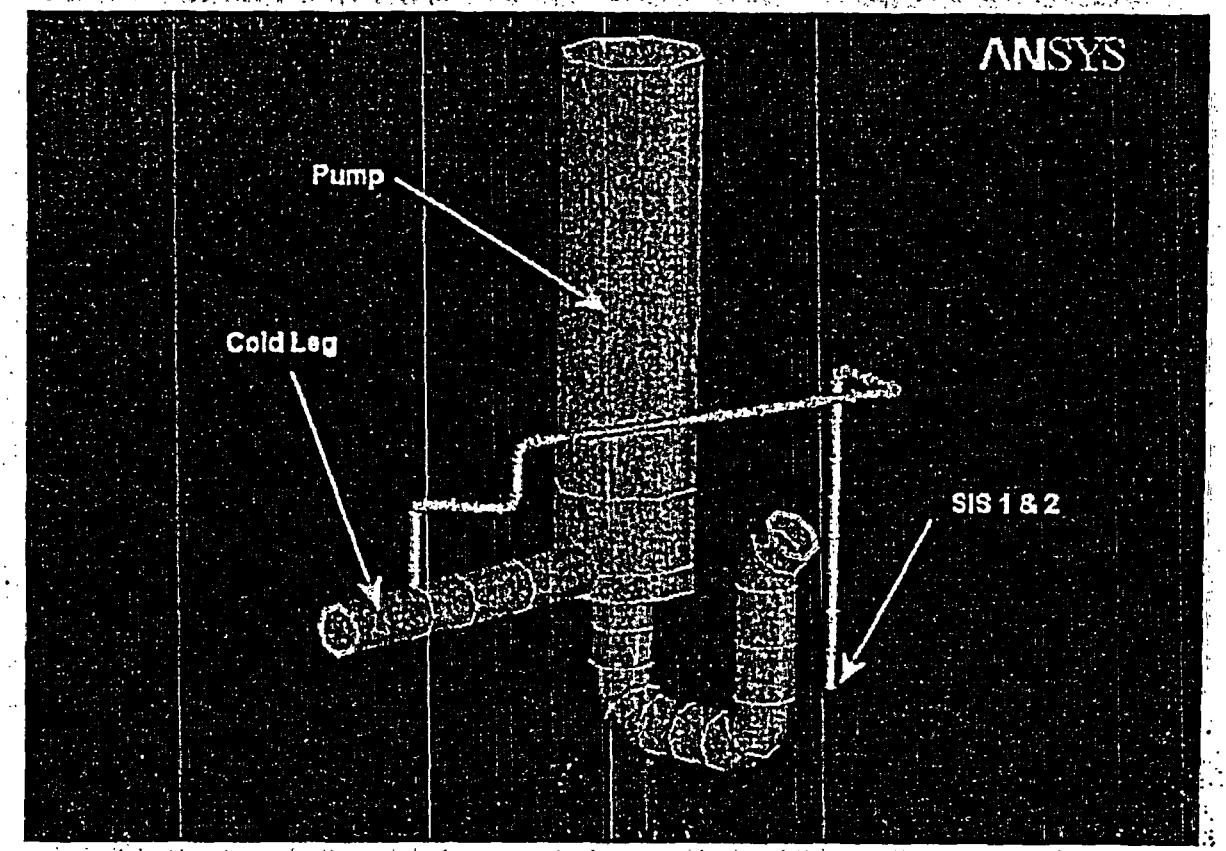

Figure D.31 Critical flaw locations in the safety injection system

Table D.4 Dimensional and loading conditions for 18 critical locations considered in sample plant piping system test cases

Case Data

	Location	R_i (in)	t_{wall} (in)	OD (in)	M_b (in*lb)	F_x	Temp (°F)	Pressure (psi)
Primary System	1	14.6	2.37	33.94	12591000	1504000	610	2235
	2	14.6	2.37	33.94	4491000	1504000	610	2235
	3	14.6	2.37	33.94	12435000	1505000	610	2235
	4	15.6	3.15	37.5	15098000	1633000	610	2235
	5	15.6	3.15	37.5	13805000	1597000	542	2200
	6	15.6	2.52	36.24	12632000	1564000	542	2200
	7	15.6	2.52	36.24	13047000	1557000	542	2200
	8	15.6	2.52	36.24	6425000	1684000	542	2200
	9	15.6	2.52	36.24	1086000	1684000	542	2200
	10	15.6	3.18	37.56	5639000	1844000	542	2200
	11	13.85	2.25	32.2	1689000	1388000	542	2300
	12	13.85	2.25	32.2	2398000	1389000	542	2300
	13	13.85	2.25	32.2	2339000	1389000	542	2300
	14	13.85	2.25	32.2	2418000	1386000	542	2300
	15	13.85	2.36	32.42	2742000	1342000	542	2300
Surge Line	1	5.754	1.246	14	1545839	221161	653	2327
	2	5.754	1.246	14	1766184	234511	617	2327
SIS	1	2.5945	0.718	6.625	136539	-1083	105	2327

high stress points or at field welds. Table D.4 provides the pertinent dimensional and loading conditions for these particular locations.

Because the angular position of the postulated leaking flaw was not known, the rotation was calculated at 15-degree intervals around the pipe circumference at each location. The largest rotation was assumed to correspond with the orientation of the flaw, and this rotation was used in subsequent calculations. After calculating the pipe stiffness, Equations D.18 and D.21 were used to determine the restraint lengths, and Equations D.3 and D.14 were used to calculate the values of r_{COD}. Note, Equations D.3 and D.18 are for the symmetric restraint case and Equations D.14 and D.21 are for the asymmetric restraint cases. While each of the cases were asymmetric, the equations for the asymmetric case were developed for a specific R/t ratio (R/t = 10). The R/t ratio for each of these cases was close to 5, typical of PWR piping. Thus, the symmetric case, which is was developed for a wider range of R/t ratios, was considered as well. Further note that preliminary analyses to date suggest that the effect of using the R/t solutions for the asymmetric case developed to date for pipes with R/t ratios less than 10 (typical of PWR piping) would result in a longer crack length for a given leak rate detection limit capability in an LBB analysis, i.e., a conservative assessment of crack length. Thus, the use of the asymmetric solution for these sample applications should provide an upper-bound illustration of the impact of this effect. However, if a more generalized asymmetric solution is desired, then a curve fit equation through multiple finite element analyses is needed for different R/t ratio cases.

Once the normalizing factors were obtained, it was necessary to calculate the COD of the unrestrained pipe. The SQUIRT program was utilized in this endeavor. The crack morphology parameters for an IGSCC crack were assumed. Once calculated, COD_{unres} was multiplied by r_{COD} to determine COD_{res}. On first glance, (see Table D.5), the values appear to be so close together that any difference would be insignificant, i.e., less than 10 percent.

Table D.5 Comparison between restrained and unrestrained COD values

Pipe System		SQUIRT Calcs.		Normalized Restraint Lengths			Symm. Rest. COD	% diff. respect to unrest. COD	Asymm. Rest. COD	% diff. respect to unrest. COD
(Leak Rate)	Location	Unrest. COD	Crack Length	Symmetric	Asymmetric					
				L/D_m	L_1/D_m	L_2/D_m				
		(in)	inch				inch		(in)	inch
Primary	1	0.0217	13.33	4.1	0.1	17.9	0.0212	2.5%	0.0217	0.0%
(5 gpm)	2	0.0178	16.3	11.2	5.8	23.8	0.0175	1.5%	0.0175	2.0%
	3	0.0216	13.38	11.6	6.4	22.9	0.0214	0.9%	0.0214	1.2%
	4	0.0203	16.48	15.3	0.3	58.1	0.0201	0.9%	0.0203	0.0%
	5	0.0147	14.31	11.4	0.8	42.9	0.0146	0.9%	0.0145	1.6%
	6	0.0154	12.22	16.8	6.5	40.2	0.0154	0.5%	0.0153	0.7%
	7	0.0156	12.13	29.0	6.9	73.4	0.0156	0.3%	0.0155	0.5%
	8	0.0136	13.97	20.9	10.0	42.0	0.0135	0.5%	0.0135	0.7%
	9	0.0088	21.8	18.3	9.9	34.8	0.0087	1.6%	0.0086	2.2%
	10	0.0126	16.75	38.5	1.0	125.3	0.0126	0.4%	0.0126	0.0%
	11	0.0112	15.85	4.8	1.0	16.5	0.0107	3.7%	0.0104	6.6%
	12	0.0124	14.17	7.1	3.6	16.2	0.0121	1.9%	0.0121	2.5%
	13	0.0123	14.31	9.1	5.6	16.8	0.0121	1.5%	0.0121	1.9%
	14	0.0125	14.17	9.9	6.1	17.8	0.0123	1.4%	0.0123	1.7%
	15	0.0126	14.34	5.6	0.1	22.7	0.0123	2.4%	0.0126	0.0%
Surge	1	0.0257	10.09	22.6	3.0	60.9	0.0252	1.9%	0.0241	6.1%
(5 gpm)	2	0.0233	9	7.9	0.1	29.0	0.0223	4.0%	0.0231	0.7%
Surge	1	0.0447	11.79	22.6	3.0	60.9	0.0435	2.8%	0.0405	9.5%
(10 gpm)	2	0.0392	10.85	7.9	0.1	29.0	0.0367	6.3%	0.0357	8.8%

After studying the cases listed above, it is natural to wonder when, if ever, the normalizing factor would have a significant effect on the COD. From the previous plots, it can be seen that as the crack angle increases, the difference between the unrestrained and restrained COD values increases. Referring back to Figures D.25 and D.27, it is clear that r_{COD} values for a half-crack angle of $\pi/2$ are much smaller than those for a half-crack angle of $\pi/8$. Thus, one condition that must be satisfied in order for the effect of restraint of pressure induced bending to be significant is the crack angle (2θ) must be relatively large. For leak-before-break analyses, this is most likely for smaller diameter pipe. However, as alluded to earlier, the L/D analysis developed as part of this program is presently limited to pipes with moments of inertia greater than 10^{-4} m^4 (240 inch^4). It can be readily shown that the pipe diameter must be at least 10-inch, regardless of pipe schedule, for this condition to be satisfied[1]. While the pipe schedule for 10-inch diameter pipe must be at least schedule 80.[2] For 10-inch diameter Schedule 160 pipe, the leakage crack size from a SQUIRT4 analysis, assuming a relatively low operating stress[3] of $0.4S_m$ ($P_m + P_b$) is only about 40 percent of the pipe circumference for a (1.0 gpm) leakage detection system and assuming crack morphology parameters for an IGSCC crack[4]. If the normal operating loads are higher, or the leakage

[1] The moment of inertia for a 8-inch diameter schedule 160 pipe is 7×10^{-5} m^4 (166 inch^4).
[2] The moment of inertia for a 10-inch diameter schedule 80 pipe is 10^{-4} m^4 (245 inch^4).
[3] The lower the operating stress, the longer the leakage crack size from an LBB perspective.
[4] The relatively coarse leakage detection limit (1.0 gpm versus 0.5 gpm) and relatively rough crack surface of an IGSCC crack versus a fatigue crack both tend to result in longer leakage flaw sizes.

detection system is better (0.5 versus 1.0 gpm), or if the crack surface is not so torturous (fatigue versus IGSCC), then the leakage crack size will be even shorter.

The other condition, besides large crack angle, that must be satisfied in order for the effect of restraint of pressure induced bending to be significant is that the L/D parameter must be small, see Figure D.16. This is more likely to occur for the stiffer (i.e., larger diameter) pipe. Thus, the two conditions that must both be satisfied for this effect to be significant are to an extent mutually exclusive, such that for most practical applications, one can probably ignore this effect. The only potentially significant applications where one may want to consider this effect is very small diameter pipe, less than 6- or 8-inch diameter. However, as noted previously, for these small diameter piping systems, the L/D analysis proposed herein that is based on rotational stiffness is not valid, or cases where one is considering a postulated crack at a location where the piping system attaches directly to a vessel, e.g., where the surge line connects to the pressurizer. However, that case was analyzed as one of the 18 locations already considered (Surge 2) and the effect on the COD was shown to be minimal.

D.6 Conclusion

The center crack-opening displacement at the mid-thickness of a through-wall circumferential crack in a straight pipe under end-restraint condition can be evaluated using the crack-opening displacement of the corresponding unrestrained pipe and the normalizing factor derived in this program.

$$COD_{res} = r_{COD} \cdot COD_{unres} \qquad (D.23)$$

Analytical expressions for the normalizing factor, r_{COD}, have been derived. It was found that Miura's solution of Equation D.4, combined with the revised $I_b(\theta, R_m/t)$ function of Equation D.7, can be used to evaluate r_{COD} for a symmetrically restrained pipe. A correction function (Equation D.14) has been proposed to relate the r_{COD} for an asymmetrically restrained pipe to that of the corresponding symmetrically restrained pipe. The validity of these analytical expressions has been examined using the COD results from the Round-Robin FE analyses conducted previously in the BINP program, see Appendix I.

In order to apply these equations in a practical manner, it was necessary to express the restraint length (L/D) in terms of another variable which was more easily calculable. Equations were developed relating the restraint length to the pipe stiffness. The results from these equations match closely with the previous L_R/D_m parametric equations, thus validating their accuracy. The expressions for the normalizing factor and the restraint length in terms of pipe stiffness are semi-empirical in nature, and should be used within the range which the expressions were derived.

In terms of practical application, it appears that effect of restraint of pressure-induced bending is negligible in PWR primary piping. Unless the tolerable leak rate is so large that the normal operating crack approaches 180 degrees, the effect of restraint of pressure induced bending on COD is not a factor.

D.7 References

D.1 Ghadiali, N., Rahman, S., Choi, Y. H. and Wilkowski, G., "Deterministic and Probabilistic Evaluations for Uncertainty in Pipe Fracture Parameters in Leak-Before-Break and In-Service Flaw Evaluations," U.S. Nuclear Regulatory Commission, NUREG/CR-6443, 1996.

D.2 Rahman, S., Ghadiali, N., Paul, D., and Wilkowski, G., "Probabilistic Pipe Fracture Evaluations for Leak-Rate Detection Applications," NUREG/CR-6004, April 1995.

D.3 Rahman, S., Brust, F., Ghadiali, N., Choi, Y. H., Krishnaswamy, P., Moberg, F., Brickstad, B., and Wilkowski, G., "Refinement and Evaluation of Crack-Opening-Area Analyses Circumferential Through-Wall Cracks in Pipes for Circumferential Through-Wall Cracks in Pipes," U.S. Nuclear Regulatory Commission, NUREG/CR-6300, 1995.

D.4 Wilkowski, G., Feng, Z., Miura, N, Choi, J.B., Ghadiali, N., Choi, Y.H., Santos, C., Brust, F. and Scott, P., "Round-Robin Finite Element Analysis of Crack-Opening Displacements in Axially Loaded Piping Systems for Leak-Before-Break Applications – Effect of Pipe System Restraint on Pressure-Induced Bending," BINP Program Report.

D.5 Miura, N. "Evaluation of Crack Opening Behaviors for Cracked Pipes – Effect of Restraint on Crack Opening," *Proc. ASME PVP Conf.* PVP-Vol. 423, 2001, pp. 135-143.

D.6 Klecker, R., Brust, F.W. and Wilkowski, G., "NRC Leak-Before-Break (LBB.NRC) Analysis Method for Circumferentially Through-Wall-Cracked Pipes under Axial Plus Bending Loads," NUREG/CR-4572, 1986.

APPENDIX E

DEVELOPMENT OF FLAW EVALUATION CRITERIA FOR CLASS 2, 3, AND BALANCE OF PLANT PIPING

The existing flaw evaluation criteria embodied in Section XI of the ASME Boiler and Pressure Vessel Code are for Class 1 high energy piping systems. Currently, no such criteria exist for Class 2, 3, and Balance of Plant (BOP) piping, even though some of these systems are being inspected more frequently due to increased inspection requirements in the ASME Code. It is also important to note that some of these Class 2 and Class 3 piping systems are more important relative to plant risk from a core damage perspective than some Class 1 piping systems. As such, criteria to evaluate flaws found during these inspections are needed.

The main technical differences between Class 1 piping and Class 2, 3, and BOP piping are that (1) the Class 2, 3, and BOP piping may operate at lower operating pressures, and thus may be fabricated from thinner pipe with higher R/t ratios, and (2) they may also operate at lower temperatures than Class 1 piping.

E.1 Effect of Pipe R/t Ratio on Pipe Fracture

As mentioned above, Class 2, 3, and BOP piping systems typically operate at lower pressures and thus are fabricated from thinner pipe, i.e., pipe with higher R/t ratios. The higher R/t ratios can influence the pipe fracture behavior under LEFM, EPFM, and limit-load conditions. As part of this effort, the effect of R/t ratio on all three potential failure modes was to be investigated.

E.1.1 Effect of Pipe R/t Ratio on the Elastic F-Functions (LEFM)

The crack driving force under linear-elastic fracture mechanics (LEFM) conditions is typically expressed in terms of the stress intensity factor K. The expression for K is:

$$K = F\sigma\sqrt{\pi a} \qquad \text{(E.1)}$$

where,

K = stress intensity factor,

F = Elastic F-function,

σ = remote applied stress, and

a = crack size.

Currently, for Class 1 piping, Section XI limits the applicability of the F-functions they report to pipes with R/t ratios of less than 15. While this limitation is acceptable for Class 1 piping, it is too restrictive for Class 2, 3, and BOP piping which typically are fabricated from pipes with much larger R/t ratios. In order to address this limitation, researchers working for The Materials Property Council (MPC) in this country (Ref. E.1) and researchers at CEA in France (Ref. E.2) have developed an extensive database of numerical solutions for F using the finite element method for a variety of pipe and flaw geometries (flaw depth (a/t) and flaw length [c/a or θ/π]), pipe R/t ratios, and crack location and loading conditions (i.e., internal flaw loaded in tension, internal flaw loaded in bending, external flaw loaded in tension, and external flaw loaded in bending). The flaws in each case were oriented in the circumferential direction. As part of this effort in the BINP program, these tabulated numerical results were curve fit to a series of mathematical expressions, with the goal of including these mathematical expressions into a code type document.

For the case of an internal surface crack loaded in tension, the equation for F (FT) at the deepest point along the crack was found to be:

$$F\left(\frac{R}{t},\frac{a}{t},\frac{\theta}{\pi}\right)=\left[S_3\left(\frac{a}{t}\right)^3+S_2\left(\frac{a}{t}\right)^2+S_1\left(\frac{a}{t}\right)\ln\frac{R}{t}+S_2\right]\left[\ln\frac{R}{t}+\ln\frac{\theta}{\pi}-\ln\frac{a}{t}+\ln\pi\right]+S_4 \qquad \text{(E.2)}$$

For the case of an internal surface crack loaded in bending, the F function (FB) at the deepest point along the crack was:

$$F\left(\frac{R}{t},\frac{a}{t},\frac{\theta}{\pi}\right)=S_1\ln\frac{R}{t}+\left[\left(S_3\left(\frac{a}{t}\right)^3+S_1\left(\frac{a}{t}\right)+S_2\left(\frac{a}{t}\right)^2\right)\ln\frac{R}{t}+S_2\right]\left[\ln\frac{R}{t}+\ln\frac{\theta}{\pi}-\ln\frac{a}{t}+\ln\pi\right]+S_4 \qquad \text{(E.3)}$$

For the case of an external surface crack loaded in tension, the F function (FT) at the deepest point along the crack was:

$$F\left(\frac{R}{t},\frac{a}{t},\frac{\theta}{\pi}\right)=\left[S_3\left(\frac{a}{t}\right)^2+\left(S_1\ln\frac{R}{t}+S_2\right)\left(\frac{a}{t}\right)+S_2\right]\left[\ln\frac{R}{t}+\ln\frac{\theta}{\pi}-\ln\frac{a}{t}+\ln\pi\right]+S_4 \qquad \text{(E.4)}$$

Finally, for the case of an external surface crack loaded in bending, the F function (FB) at the deepest point along the crack is:

$$F\left(\frac{R}{t},\frac{a}{t},\frac{\theta}{\pi}\right)=\left[S_3\left(\frac{a}{t}\right)^3+S_2\left(\frac{a}{t}\right)^2+S_1\left(\frac{a}{t}\right)\ln\frac{R}{t}+S_2\right]\left(\ln\frac{R}{t}+\ln\frac{\theta}{\pi}-\ln\frac{a}{t}+\ln\pi\right)+S_4 \qquad \text{(E.5)}$$

The above expressions are valid for:

$$5\le\frac{R}{t}\le 100,$$

$$0<\frac{a}{t}\le 0.8,$$

$$0\le\frac{c}{a}\le 16$$

where, the crack length expression (c/a) can be expressed in terms of (θ/π) using the relationship:

$$\left(\frac{\theta}{\pi}\right)=\left(\pi\frac{R}{t}\right)^{-1}\left(\frac{a}{t}\right)\left(\frac{c}{a}\right) \qquad \text{(E.6)}$$

As part of this effort, the curve fitting coefficients S1, S2, S3, and S4 were developed for each flaw location and each loading condition. Coefficients were developed for a best-fit through the data as well as developing a set of coefficients that would result in a 15 percent conservative assessment with respect to the tabular data from the finite element analyses. Table E.1 provides both the best-fit and 15 percent conservative values for these curve fitting coefficients.

Figures E.1 through E.3 illustrate how the best fit curve fitting equations compare with the numerical results developed at CEA (Ref. E.2). Each of these figures is for the case of an internal circumferential surface crack loaded in bending. Figure E.1 compares the best-fit curve fit F-function expression with the CEA tabulated data as a function of the R/t ratio for various crack lengths (c/a values) for a constant flaw depth of a/t = 0.4. Figure E.2 compares the best-fit expressions with the tabulated data as a function of crack length (c/a) for various R/t ratios for a constant flaw depth of a/t = 0.4. Figure E.3 compares the best-fit expressions with the tabulated data as a function of crack depth (a/t) for various crack lengths (c/a values) for a constant R/t value of 20. In each case, one can see that the agreement between the best-fit expressions and the tabulated data from the finite element

Table E.1 Best-fit curve fitting coefficients and 15 percent conservative curve fitting coefficients for various crack locations and loading conditions

	Best-fit coefficients	15 percent conservative coefficients
Internal Flaw Loaded in Tension (F^T)		
S_1	0.0919	0.1057
S_2	0.1517	0.1744
S_3	0.4057	0.4665
S_4	0.7066	0.8125
Internal Flaw Loaded in Bending (F^B)		
S_1	0.0328	0.0377
S_2	0.1645	0.1891
S_3	0.0292	0.0336
S_4	0.5529	0.6358
External Flaw Loaded in Tension (F^T)		
S_1	0.0286	0.0329
S_2	0.1529	0.1759
S_3	0.8527	0.9806
S_4	0.6847	0.7874
External Flaw Loaded in Bending (F^B)		
S_1	0.0864	0.0993
S_2	0.1781	0.2048
S_3	0.6988	0.8036
S_4	0.6670	0.7670

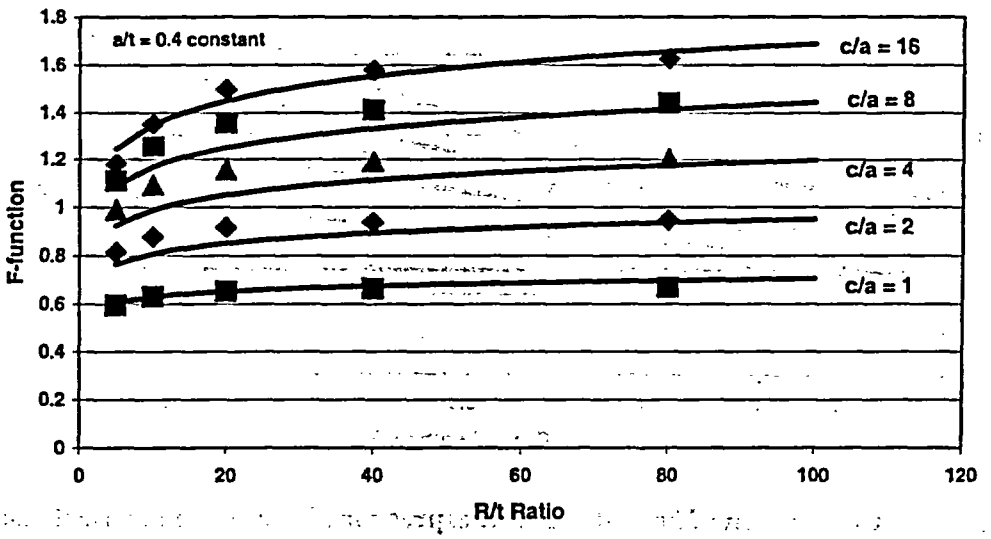

Figure E.1 Comparison of best-fit curve-fit expressions for F with numerical results from finite element analyses as a function of R/t ratio for various crack lengths for a constant crack depth of a/t = 0.4

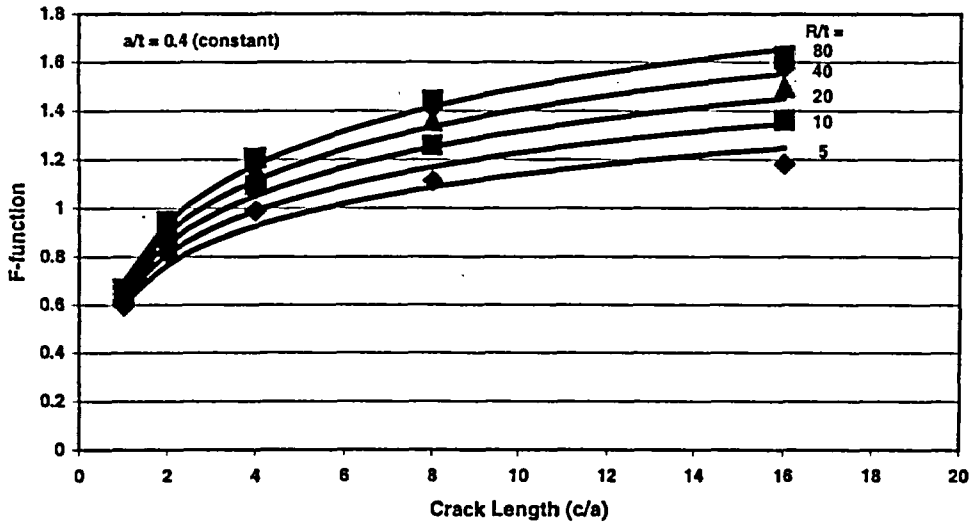

Figure E.2 Comparison of best-fit curve-fit expressions for F with numerical results from finite element analyses as a function of crack length for various R/t ratios for a constant crack depth of a/t = 0.4

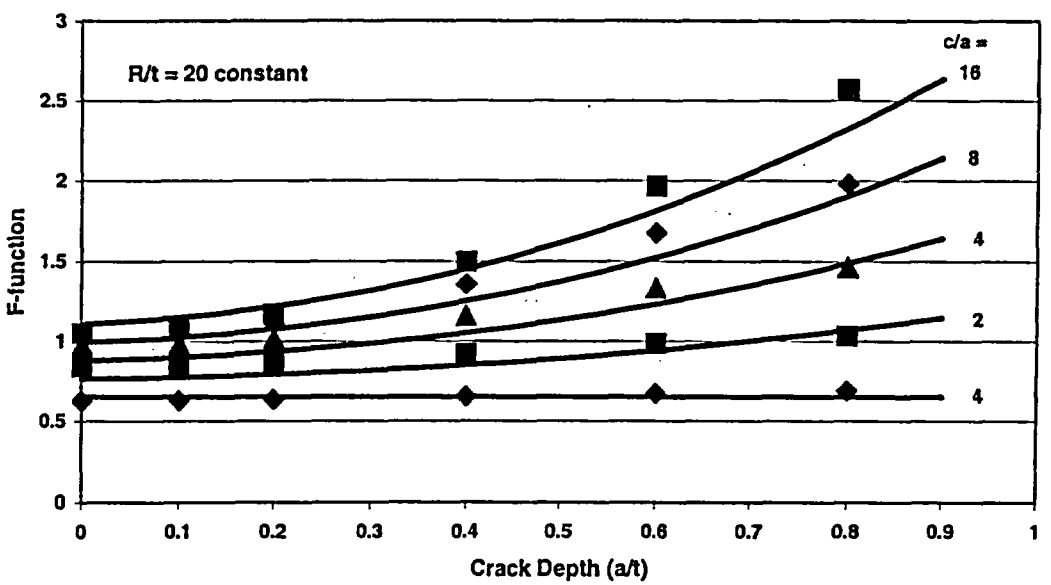

Figure E.3 Comparison of best-fit curve-fit expressions for F with numerical results from finite element analyses as a function of crack depth for various crack lengths for a constant R/t ratio of 20

analyses is quite good. Similar agreement was seen for the other flaw location and loading condition combinations, e.g., external flaws subjected to tension loading.

Of note from Figures E.1 through E.3 is the fact that the F-functions do not appear to be that sensitive to R/t ratio, especially once the R/t ratio gets larger than about 20. For the same size flaw, one can see from Figure E.1 that the difference in F between the value of R/t = 20 and R/t = 100 is at most 15 to 20 percent.

One limitation associated with this analysis, is that both the MPC data (Ref. E.1) and the CEA data (Ref. E.2) are limited in that they do not consider the case of very long cracks. The limit on c/a values for the MPC data set is 32 and the limit on c/a values for the CEA data set is 16. If one considers a crack in a pipe with an R/t ratio of 40 that is one-fourth of the pipe circumference in length and one-half of the pipe wall thickness in depth, it can be seen through simple mathematical manipulation that the c/a value is 20π, which is about twice the limit of the MPC data set and four times the limit of the CEA data set. The good news however, is that the F-function values are starting to level off to a near constant value for these longer crack lengths, see Figure E.2. Consequently, it may be possible to simply extrapolate the value for the F-functions at these higher c/a values.

The results of these efforts have been presented to the ASME Section XI Pipe Flaw Evaluation Working Group for consideration for possible incorporation into a future edition of the ASME Code.

E.1.2 Effect of R/t Ratio on Elastic-Plastic Fracture Mechanics (EPFM) Analyses

E.1.2.1 Existing *J*-Estimation Schemes - The *J*-estimation schemes for surface-flawed pipes have elastic and plastic contributions. The elastic solutions are known since there are tabular elastic *F*-functions for global bending and axial tension available in the literature. Furthermore, these tabulated values have been curve fit to simple mathematical expressions as discussed above.

The elastic-plastic contributions to *J* are more difficult to establish. During past NRC programs on piping, several circumferential surface-cracked-pipe *J*-estimation schemes were developed for Class 1 piping where the *R/t* ratios were less than 15. These estimation schemes are available in the NRCPIPES computer code, Ref. E.3. The surface-cracked pipe *J*-estimation scheme options in NRCPIPES are designated by the following procedures:

- SC.TNP1 and SC.TNP2,
- SC.TKP1 and SC.TKP2, and
- SC.ENG1 and SC.ENG2.

The differences in these solutions are briefly noted below.

- SC.TNP1 is the original SC.TNP solution by Ahmad in NUREG/CR-4872, Ref.E.4. This analysis used the 360-degree GE/EPRI surface-crack *h*-functions with a ***thin***-shell assumption in estimating the circumferential finite length surface flaw *h*-functions for pipes in bending.
- SC.TNP2 is a modification by Rahman in NUREG/CR-6298, Ref. E.5. This was a modification to the Ahmad solution where the distance from the crack plane to the point where the stress matched that of the unflawed pipe was modified. This length has been calibrated against numerous finite element (FE) analyses. The original assumption in the Ahmad SC.TNP solution (SC.TNP1) was that this distance was equal to the pipe thickness. Rahman found that this distance (L_W) was equal to the pipe thickness (t) times a function of the material strain-hardening exponent (n), i.e., $L_W = (n\text{-}1)*t$. This analysis was limited to pipes with $R/t \equiv 7.5$.
- SC.TKP1 is the original SC.TKP solution by Ahmad in NUREG/CR-4872,

Ref. E.4. This analysis used the 360-degree GE/EPRI surface-crack h-functions with a ***thick***-shell assumption in creating the circumferential finite length surface flaw h-functions for pipes in bending.

- SC.TKP2 is a modification by Rahman in NUREG/CR-6298, Ref. E.5. This was a modification to the Ahmad solution where the distance from the crack plane to the point where the stress matched that of the unflawed pipe was modified. This length has been calibrated against numerous finite element analyses. The original assumption in the Ahmad SC.TKP solution (SC.TKP1) was that this distance was equal to the pipe thickness. Rahman found that this distance (L_W) was equal to the pipe thickness (t) times a function of the material strain-hardening exponent, i.e., $L_W = [(n+1)/(2n+1)]t$. Again, only pipes with $R/t \equiv 7.5$ were used to develop this equation.

- SC.ENG1 is an estimation scheme developed by Rahman for circumferential surface flaws that parallels the circumferential through-wall-cracked pipe estimation scheme of Brust in NUREG/CR-4853 and NUREG/CR-6235, Refs. E.6 and E.7, respecttively. The Brust circumferential through-wall-cracked pipe estimation scheme was called LBB.ENG. Rahman's SC.ENG1 analysis used the ***original*** Net-Section-Collapse limit-load equations in calculating a parameter, $H(a/t)$, which was equal to the thickness of the unflawed pipe divided by an equivalent thickness needed to reach limit-load conditions.

- SC.ENG2 is an estimation scheme developed by Rahman for circumferential surface flaws that also parallels the through-wall-cracked pipe estimation scheme of Brust, Refs. E.6 and E.7. Rahman's SC.ENG2 analysis used the ***Kurihara modification of the original*** Net-Section-Collapse limit-load equations in calculating a parameter, $H(a/t)$, which was equal to the thickness of the unflawed pipe, divided by an equivalent thickness needed to reach limit-load conditions. The Kurihara solution modified the original Net-Section Collapse equations empirically so they would be more accurate for short, deep flaws, Ref. E.8.

Work done by Mohan and others for validation of the ASME FAD curve approach in Code Case N494-2, Ref. E.9, showed that several investigators obtained the same J versus moment values using 3D calculations and line-spring analyses. The results also showed that the Code-Case N494-2 was restricted to a maximum R/t of 15 to avoid under predicting the crack-driving force, see Figure E.4.

E.1.2.2 Objective of the Higher R/t Analysis - This task involved the development of analyses to evaluate circumferential surface flaws in nuclear pipe with radius-to-thickness (R/t) ratios greater than 15. This effort used the finite element method to assess the crack-driving force for higher R/t pipe. The results were then compared with existing estimation schemes available in the NRCPIPES computer code. The objective was to determine if a correction could be applied to one of the schemes available in NRCPIPES to obtain a more accurate estimation of the J versus moment behavior for higher values of R/t, rather than to develop a new J-estimation procedure that required a separate option to be programmed into NRCPIPES. This was a less costly option to stay within budgeting restrictions.

E.1.2.3 Approach - The first part of this task was to generate J versus bending moment curves for pipes with internal circumferential surface flaws with or without internal pressure. The surface flaws were centered in the plane of the bending on the tension side of the pipes. The J values were taken at the mid-length of the surface cracks, i.e., the location with maximum nominal tension stress. The bending moment was generated by application of a rotational

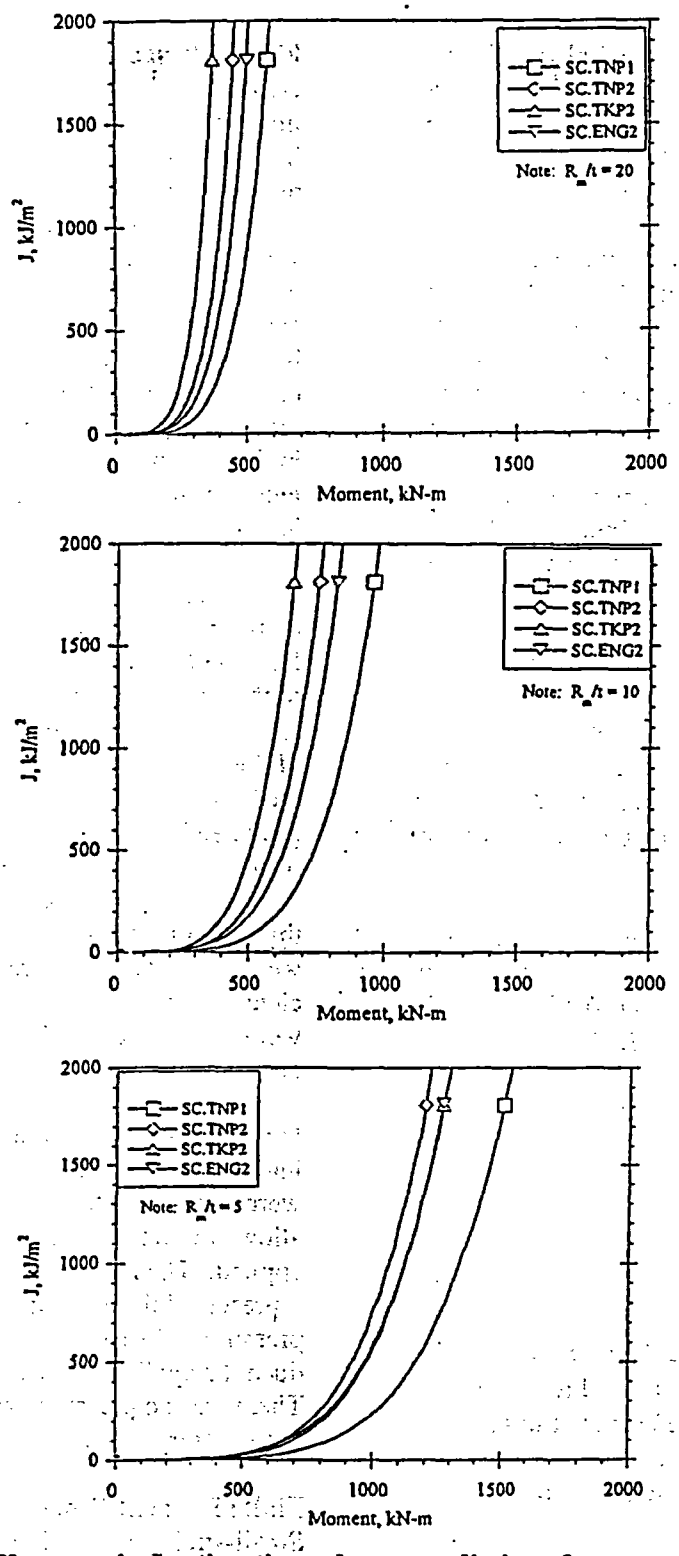

Figure E.4 Differences in J-estimation scheme predictions for same diameter pipe with crack dimensions of $\theta/\pi = 0.5$, $a/t = 0.5$ and $n = 5$

displacement to a cross-sectional plane of the pipe far from the crack plane. The location was a sufficient distance away from the crack plane to minimize the effects of the loading method on the behavior of the crack.

The pipe geometry used in the analyses consisted of a fixed mean radius (R_m) of 184.7 mm (7.27 inches). The pipe wall thickness (t) was calculated from the R_m/t ratio. For calculations involving the R_m/t ratio, the value of the radius used in this investigation was always the mean radius. R_m/t ratios of 5, 20, 40, and 60 were considered in the analyses. The results for R_m/t of 5 were considered the baseline, since the NRCPIPES estimation schemes were expected to yield similar results at this ratio.

The internal circumferential surface crack geometry was defined by the crack depth-to-thickness ratio (a/t) and the crack length-to-circumference ratio (θ/π). Crack depth ratios (a/t) of 0.25, 0.50, and 0.75 were used in the analyses. Likewise, crack length ratios (θ/π) of 0.25 and 0.50 were used.

The material properties for the analyses were typical of nuclear piping steels. The modulus of elasticity (E) was 182.72 GPa (26,500 ksi) and the Poisson's ratio (v) was 0.3. The stress-strain relation was assumed to obey the generic Ramberg-Osgood power-law hardening equation,

$$\frac{\varepsilon}{\varepsilon_0} = \frac{\sigma}{\sigma_0} + \alpha\left(\frac{\sigma}{\sigma_0}\right)^n, \qquad \text{(E.7)}$$

where σ_0 and $\epsilon_0 = \sigma_0/E$ are the reference yield stress and strain, respectively, and α is a dimensionless parameter. The reference stress (σ_0) was 150 MPa (21.8 ksi). From these data, the reference strain (ϵ_0) was calculated to be 820μm/m.

Four sets of problems and the associated geometry, material properties, and loading conditions are summarized in Table E.2. The analyses were conducted using the ABAQUS® general-purpose finite element code (Version 6.2-1).

Finite Element Geometric Models – The finite element models were constructed using shell and line-spring elements. A typical model is shown in Figures E.5 and E.6. Only one quarter of the pipe was modeled due to the symmetry conditions. The shell and line-spring elements were type S8R5 and LS3S per ABAQUS® notation, respectively. There were ten equally spaced line-spring elements covering the one-half length crack front in the model. Fourteen (14) shell elements were geometrically spaced around the circumference, with smaller elements in the region adjacent to the crack. The axial length of the quarter model was $10D_m$ where D_m is the mean diameter of the pipe.

Applied Loading - Bending loads were imposed on the pipe section by applying a rotation at the far end of the pipe along a plane perpendicular to the axis of the pipe. In the shell and line-spring element models, the nodes on the far end of the pipe were tied to a reference node through the "*KINEMATIC COUPLING" command provided in ABAQUS®. The rotational degree of freedom applied to the reference node was then transferred to the end of the pipe through this coupling constraint. The end of the pipe where the rotations were applied was sufficiently far from the crack plane so that there were no extraneous effects at the crack surface due to the loading.

In the cases with internal pressure loading, the internal pressure and the associated axial load were applied first. The ends of the pipe were allowed to freely rotate when the pressure was applied. The magnitude of the axial load represented the end cap load from the internal pressure. The rotational displacement to produce the applied moment was applied afterward. There was no pressure applied to the crack face in the cases with internal pressure loading.

Finite Element Procedure Formulation - Small-strain formulation was used for all of the analyses. The Ramberg-Osgood stress-strain relation of Equation E.7 conforms to the "*DEFORMATION PLASTICITY" definition of ABAQUS®; however, the "*DEFORMATION PLASTICITY" definition does not work with the line-spring element.

Table E.2 Analysis matrix and dimensional and material parameters

Rm/t	5, 20, 40, 60			Rm	184.725	mm	E	182.72	GPa	Ramberg-Osgood			
θ/π	0.25, 0.50			Dm	369.45	mm	σo	150.00	MPa	$\frac{\varepsilon}{\varepsilon_o} = \frac{\sigma}{\sigma_o} + \alpha\left(\frac{\sigma}{\sigma_o}\right)^n$			
a/t	0.25, 0.50, 0.75			t	(variable)	mm	εo	0.000821	σo/E				
P(i)	0, P(i) s.t. σ(h)=1.0*Sm			Rm=(Do-t)/2	(variable)	mm	v	0.30					
σ - ε	n=5 (n=3, 7, 10)			L >= 10*Dm	3694.5	mm	Sm (MPa)	122.5					
	α=1												
					Thickness	Crack	Crack			Internal	Axial		Limit
Rm/t	a/t	θ/π	Internal	Do	t	Depth, a	Length, s	a/s	Ri=Rm-t/2	Pressure	Load	I	Moment
			Pressure	(mm)	(mm)	(mm)	(mm)		(mm)	(MPa)	(N)	(m^4)	(MN-m)
5	0.25	0.25	0	406.40	36.945	9.236	145.1	0.064				7.3893E-04	1.3718
			Sm						166.25	24.020	1,042,851		1.2852
		0.50	0			9.236	290.2	0.032					1.1718
			Sm										1.1718
	0.50	0.25	0	406.40	36.945	18.473	145.1	0.127					1.0935
			Sm						166.25	24.020	1,042,851		1.0935
		0.50	0			18.473	290.2	0.064					1.0189
			Sm										0.8281
	0.75	0.25	0	406.40	36.945	27.709	145.1	0.191					0.8887
			Sm						166.25	24.020	1,042,851		0.8887
		0.50	0			27.709	290.2	0.095					0.4380
			Sm										0.4380
20	0.25	0.25	0	378.69	9.236	2.309	145.1	0.016				1.8302E-04	0.3146
			Sm						180.11	6.095	310,542		0.3146
		0.50	0			2.309	290.2	0.008					0.2846
			Sm										0.2845
	0.50	0.25	0	378.69	9.236	4.618	145.1	0.032					0.2649
			Sm						180.11	6.095	310,542		0.2649
		0.50	0			4.618	290.2	0.016					0.1955
			Sm										0.1955
	0.75	0.25	0	378.69	9.236	6.927	145.1	0.048					0.2122
			Sm						180.11	6.095	310,542		0.2122
		0.50	0			6.927	290.2	0.024					0.0954
			Sm										0.0954

Table E.2 Analysis matrix and dimensional and material parameters (continued)

Rm/t	a/t	θ/π	Internal Pressure	Do (mm)	Thickness t (mm)	Crack Depth, a (mm)	Crack Length, s (mm)	a/s	Ri=Rm-t/2 (mm)	Internal Pressure (MPa)	Axial Load (N)	I (m^4)	Limit Moment (MN-m)
40	0.25	0.25	0	374.07	4.618	1.155	145.1	0.008				9.1466E-05	0.1253
			Sm						182.42	3.055	159,675		0.1566
		0.50	0			1.155	290.2	0.004					0.1414
			Sm										0.1414
	0.50	0.25	0	374.07	4.618	2.309	145.1	0.016					0.1317
			Sm						182.42	3.055	159,675		0.1317
		0.50	0			2.309	290.2	0.008					0.0967
			Sm										0.0967
	0.75	0.25	0	374.07	4.618	3.464	145.1	0.024					0.1051
			Sm						182.42	3.055	159,675		0.1051
		0.50	0			3.464	290.2	0.012					0.0464
			Sm										0.0464
60	0.25	0.25	0	372.53	3.079	0.7697	145.1	0.005				6.0972E-05	0.0950
			Sm						183.19	2.038	107,440		0.1043
		0.50	0			0.7697	290.2	0.003					0.0942
			Sm										0.0942
	0.50	0.25	0	372.53	3.079	1.539	145.1	0.011					0.0876
			Sm						183.19	2.038	107,440		0.0876
		0.50	0			1.539	290.2	0.005					0.0643
			Sm										0.0643
	0.75	0.25	0	372.53	3.079	2.309	145.1	0.016					0.0699
			Sm						183.19	2.038	107,440		0.0699
		0.50	0			2.309	290.2	0.008					0.0307
			Sm										0.0307

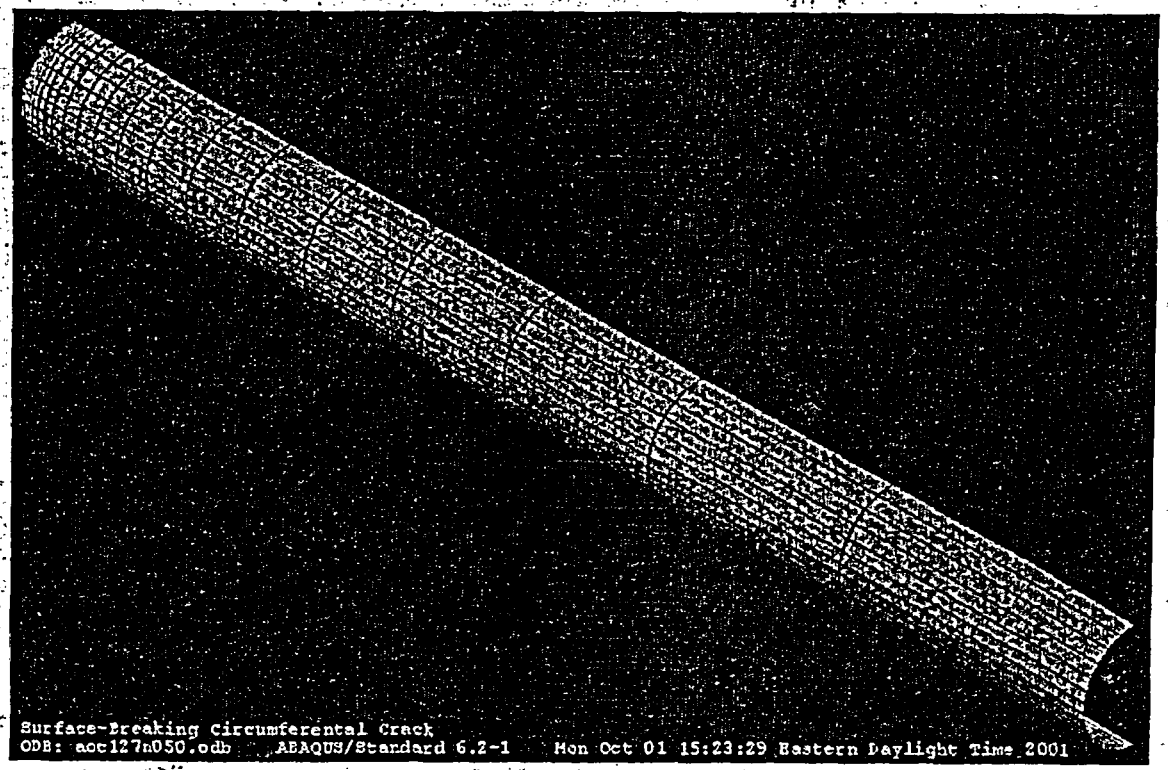

Figure E.5 A typical model using shell and line-spring elements

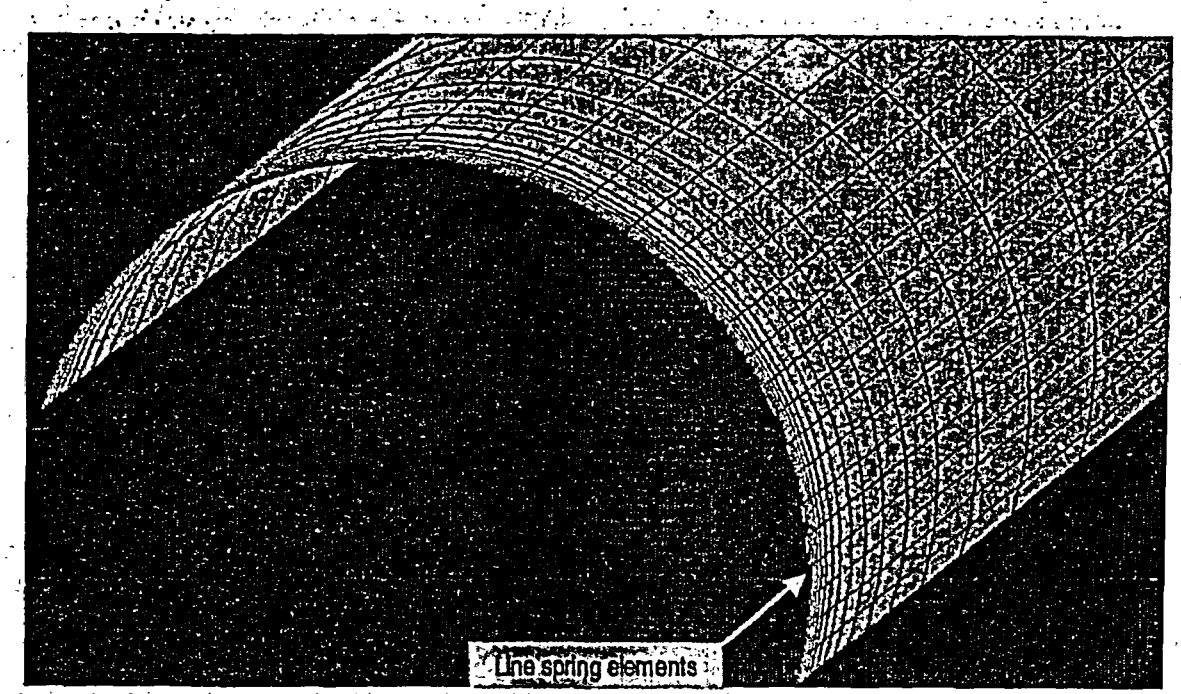

Figure E.6 Focused view of the shell and line-spring model, looking at the cross-sectional plane containing the line-spring elements

Therefore, the material properties were defined by the "*ELASTIC" and "*PLASTIC" commands in ABAQUS®. The first line of the "*PLASTIC" command defines the plastic flow stress at zero plastic strain. In the case of the Ramberg-Osgood stress-strain relation, the nonlinearity starts at zero stress. Strictly speaking, the first line in the "*PLASTIC" command would have zero plastic flow stress at zero plastic strain; however, ABAQUS® does not allow zero plastic flow stress at zero plastic strain. Consequently, a small finite plastic flow stress corresponding to zero plastic strain must be specified. The examination of the analysis results revealed that the magnitude of this finite plastic flow stress at zero plastic strain does not affect the J versus moment relation, provided the initial flow stress was less than one-third of the reference yield stress, σ_0.

E.1.2.4 Analysis Results – The results from the analyses are presented next.

Confirmation of the Analysis Procedure - To ensure the quality of the results, it was necessary to verify that the stress and strain state at the cracked plane was not affected by the boundary conditions applied at the far end of the model. The deformed shell and line-spring model, shown in Figure E.7, demonstrates that the cross-section at the far end of the pipe remains circular. Figure E.8 shows that the axial stress has the expected circumferential variation. This variation is independent of axial position for much of the model, except in the region close to the crack plane. As expected, the axial stress redistributes near the crack plane due to the reduced load-carrying capability along the length of the surface crack. The deformation and stress contours of Figures E.7 and E.8 confirm that the stress and strain states in the crack plane are free of end effects.

J versus moment Curves from Finite Element Analyses - One of the objectives of this task was to provide J versus moment curves so the *J*-estimation schemes from NRCPIPES can be investigated at higher R_m/t ratios. This section compares the J versus moment relationships generated from the finite element analyses. The results are plotted in the following figures based on R_m/t ratios and internal pressure. Figure E.9 shows the results of J versus moment for $R_m/t = 5$. As expected, the results in Figure E.9 show an increase in the crack driving force as the crack size, both length and depth, increases. The plots show a slight difference with change in crack length and a more significant increase in the driving force with increase in crack depth. Likewise, the crack-driving force increases with the application of internal pressure for the same crack size.

The results for $R_m/t = 20$ are shown in Figure E.10. These data show similar trends to the $R_m/t = 5$ results; however, the crack-driving force is significantly greater at the higher R_m/t for the same crack geometry. Likewise, these results show only a slight difference for the two crack lengths, but a significant difference as the crack depth changes.

These trends are also evident in the results for $R_m/t = 40$ and $R_m/t = 60$, as shown in Figures E.11 and E.12, respectively.

Following completion of the finite element analyses for all the cases in Table E.2, the J versus moment data was curve fit using a polynomial regression. The regression was then used to normalize the *J* results from the NRCPIPES output (J_{est}) with respect to the J value from the finite element analysis (J_{fe}). The ratio of J_{est}/J_{fe} provides an indication of the accuracy in the estimation scheme.

***J* Estimation Results from NRCPIPES** - The NRCPIPES program was used to investigate the various *J*-estimation schemes available for predicting J versus moment behavior for internal circumferential surface cracks. The six estimation schemes previously discussed (SC.TNP1, SC.TNP2, SC.TKP1, SC.TKP2, SC.ENG1, SC.ENG2) were used to generate J versus moment curves for the cases of $R_m/t = 5$, 20, and 40 and $a/t = 0.5$, $\theta/\pi = 0.25$, and $P_i = 0$. These corresponded to cases from the BINP Round Robin 2 problem set, see Appendix I. The results suggested that the SC.TNP2 estimation scheme produced the best approximation of the J versus moment behavior for the higher values

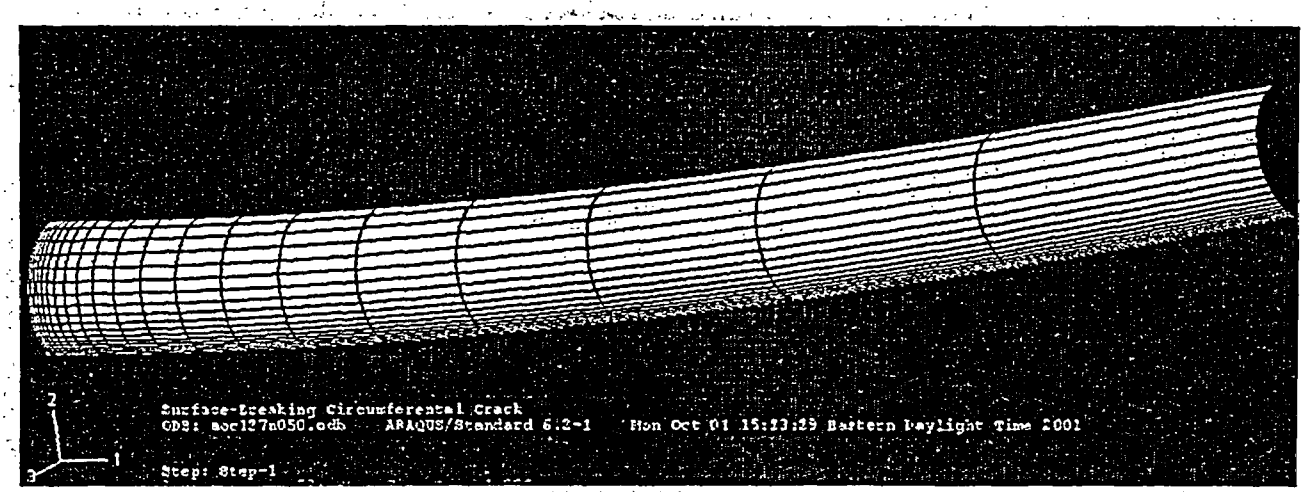

Figure E.7 A deformed shell and line-spring model

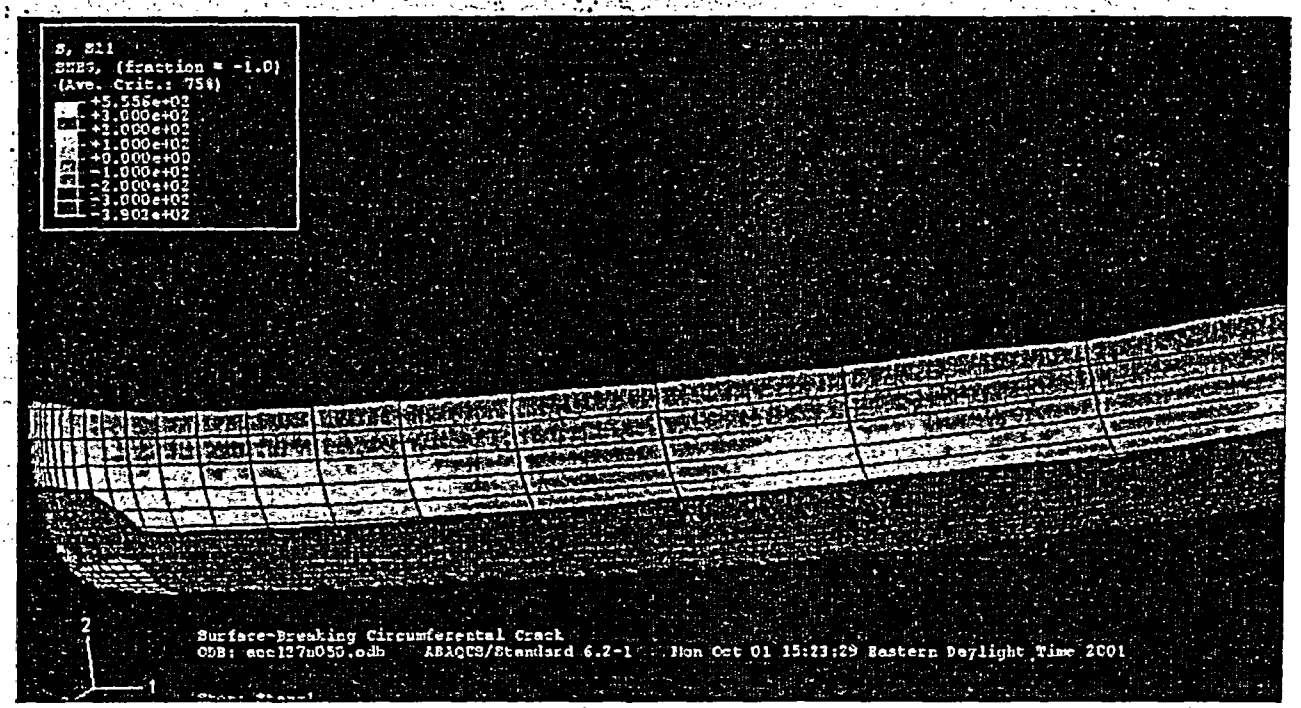

Figure E.8 Axial stress contours of a deformed shell and line-spring model

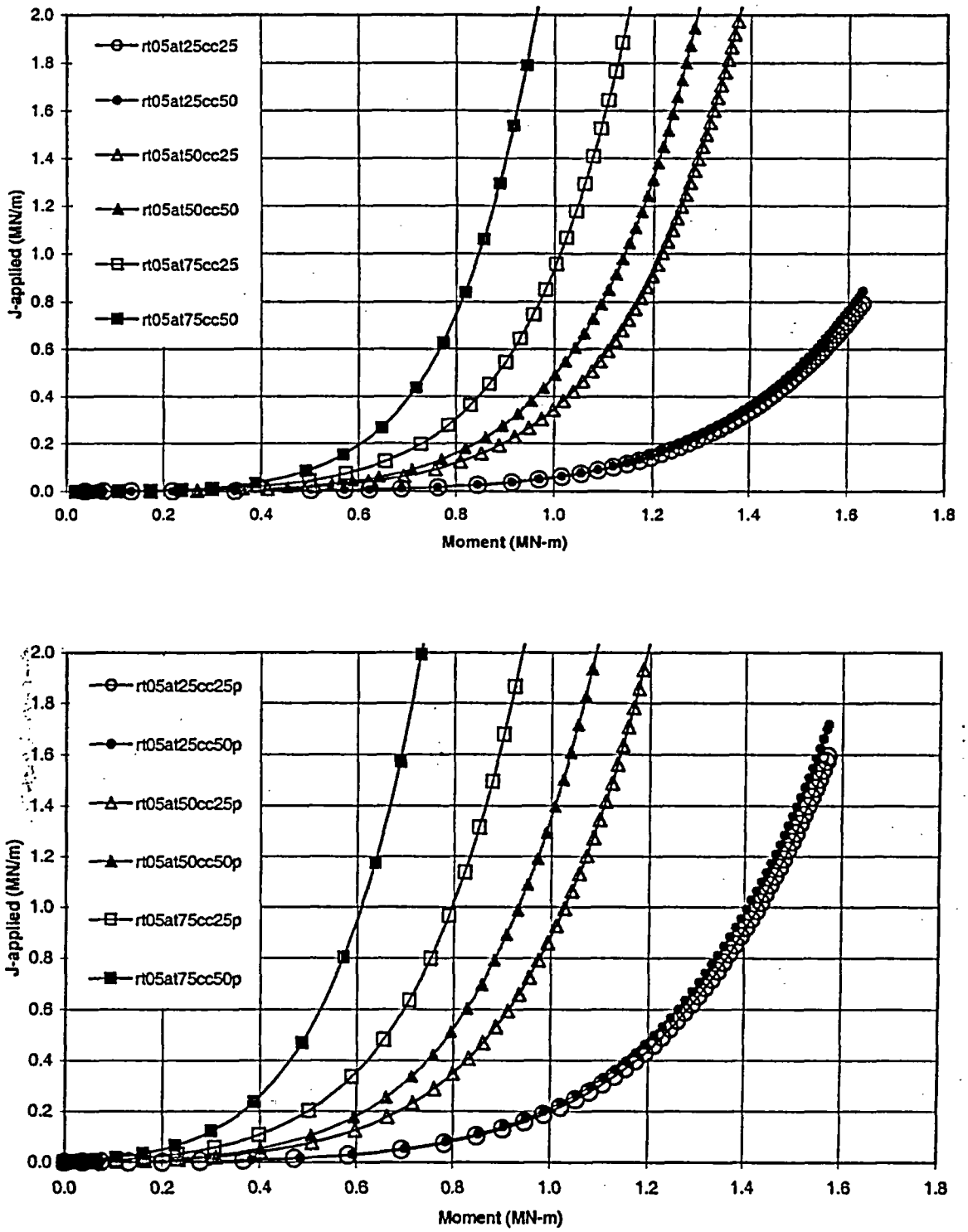

Figure E.9 J versus moment from finite element analyses for Rm/t = 5 and all a/t and θ/π values investigated. (Top) no internal pressure (Bottom) internal pressure (Notation: rt05→ Rm/t = 5, at 25→ a/t = 0.25, cc25→θ/π = 0.25, p→pressure)

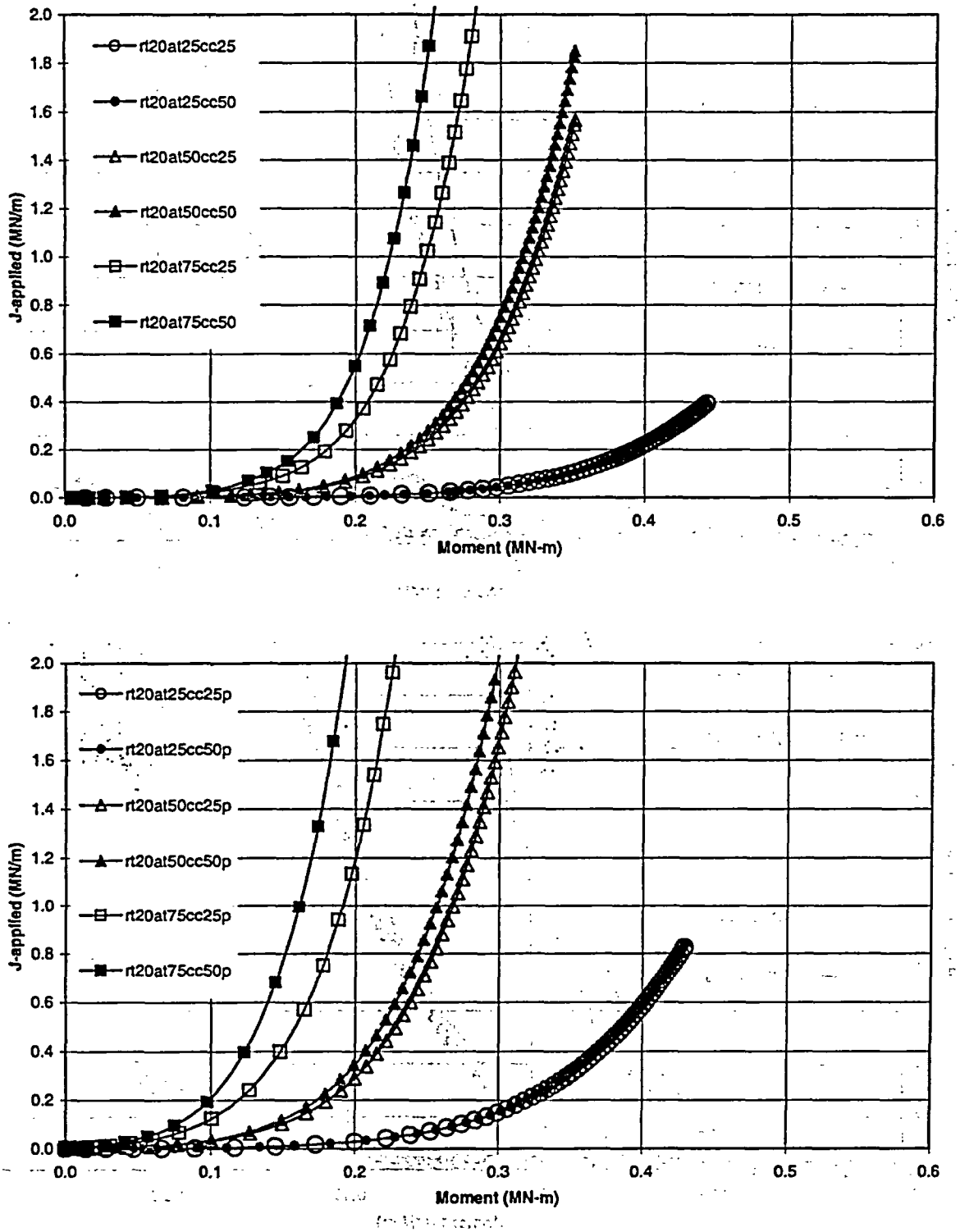

Figure E.10 J versus moment from finite element analyses for Rm/t = 20 and all a/t and θ/π values investigated. (Top) no internal pressure (Bottom) internal pressure (Notation: rt20→ Rm/t = 20, at25→ a/t = 0.25, cc25→θ/π = 0.25, p→pressure)

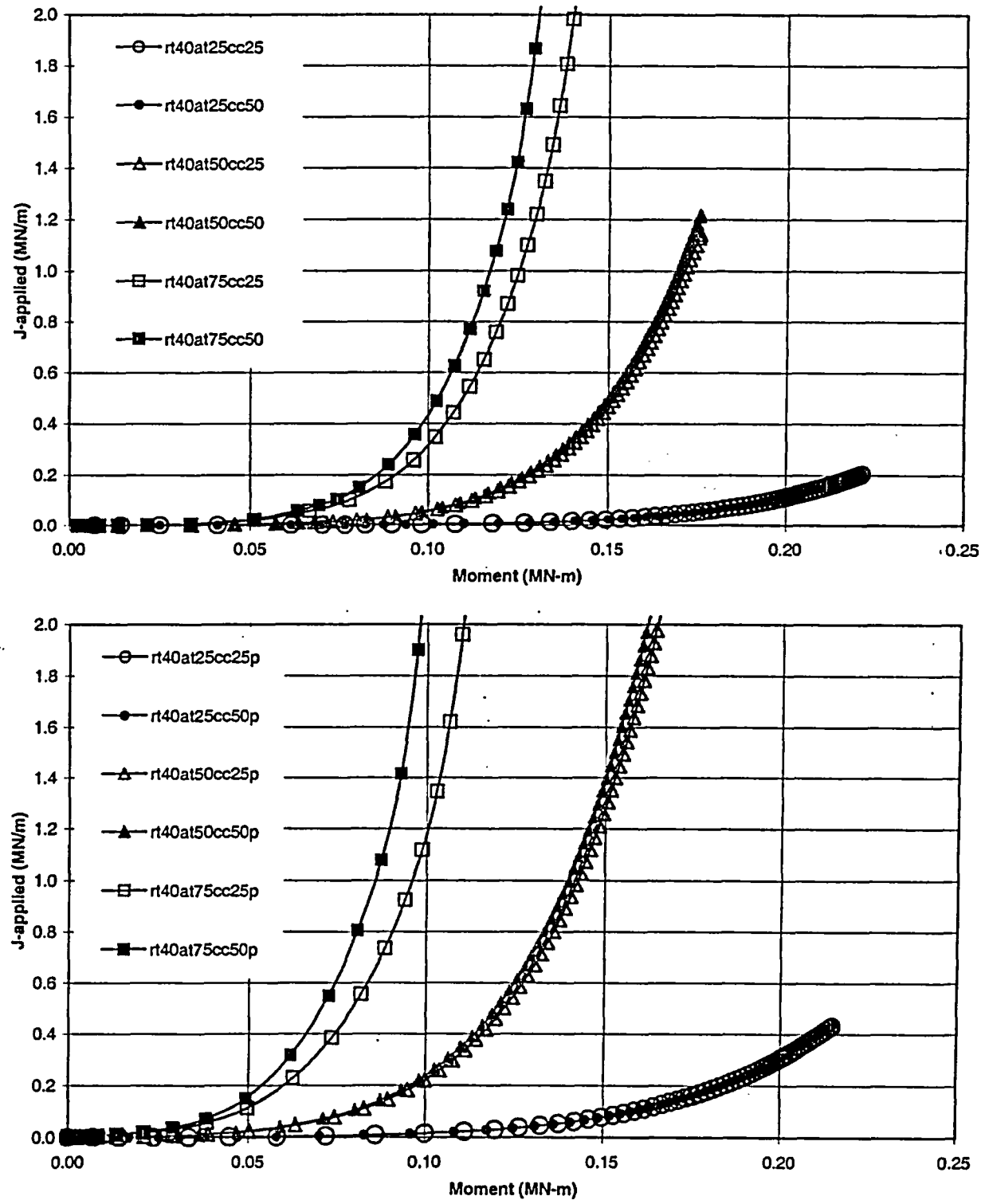

Figure E.11 J versus moment from finite element analyses for Rm/t = 40 and all a/t and θ/π values investigated. (Top) no internal pressure (Bottom) internal pressure (Notation: rt40→ Rm/t = 40, at25→ a/t = 0.25, cc25→θ/π = 0.25, p→pressure)

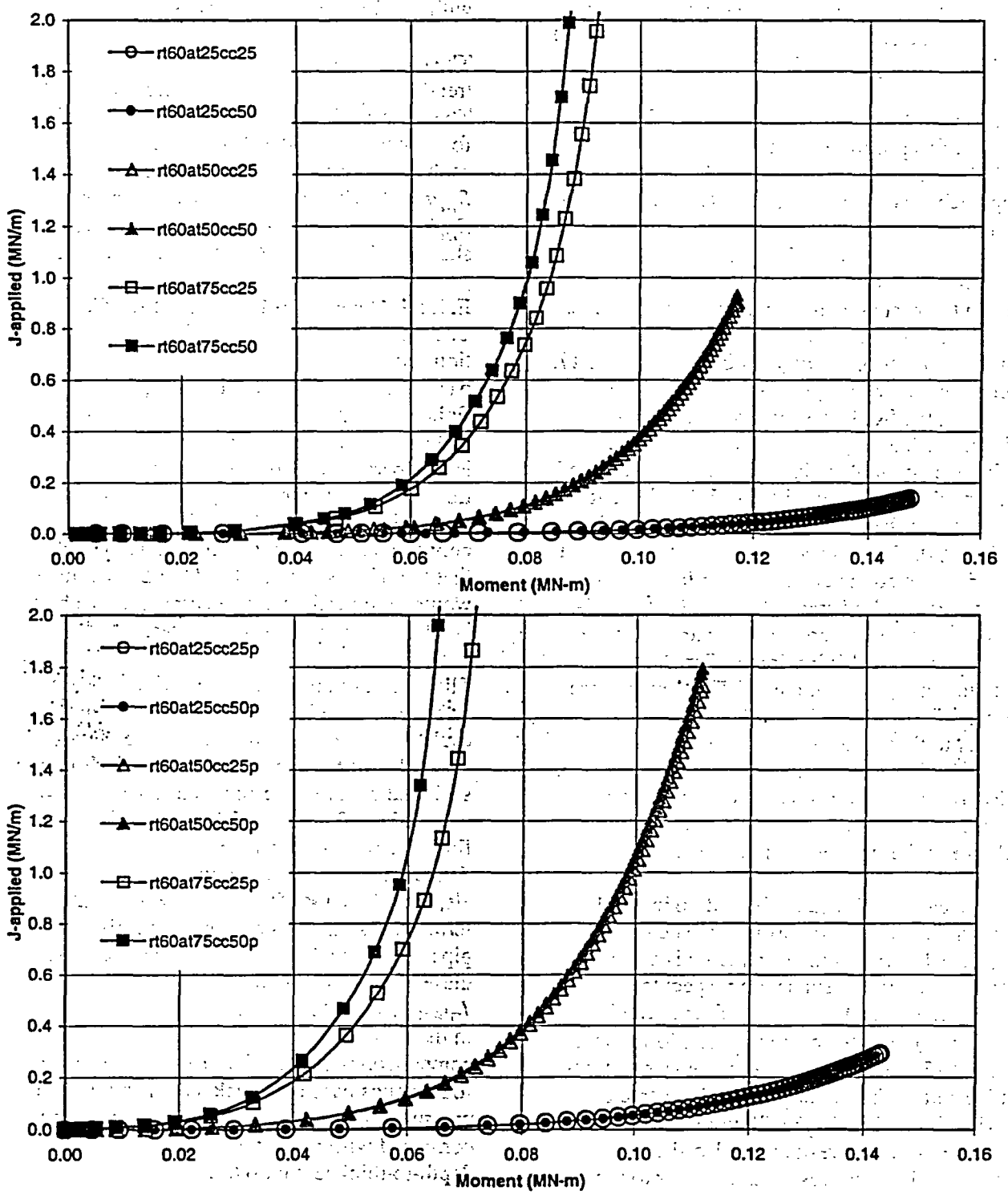

Figure E.12 J versus moment from finite element analyses for Rm/t = 60 and all a/t and θ/π values investigated. (Top) no internal pressure (Bottom) internal pressure (Notation: rt60→ Rm/t =60, at25→ a/t = 0.25, cc25→θ/π = 0.25, p→pressure)

of R_m/t. However, the SC.TNP2 method over predicted J at lower R_m/t values (R/t = 5) and under predicted J at higher R_m/t values (R/t = 20 and 40), see Figure E.13.

For each of the cases shown in Table E.2, the NRCPIPES program was run using the SC.TNP1 J-estimation scheme (L_w = t). The approach was to run SC.TNP1 (Lw = t) to establish the relationship between the SC.TNP1 estimation scheme and the FEA results. Then the Lw parameter was varied as a function of t to obtain the best agreement with the FEA results. The results are presented in four groups based on the R_m/t ratio, see Figures E.14 through E.17. For the cases with $R_m/t = 5$ and no internal pressure, the SC.TNP1 results are shown in Figure E.14, along with the FEA results for reference (symbols only). The method provided reasonable agreement with the finite element analyses for the larger size cracks ($\theta/\pi = 0.50$ and $a/t \geq 0.50$); however, the estimation method under predicted the crack-driving force. For the cases with shallow cracks ($a/t = 0.25$) the estimation scheme was conservative and over predicted the crack-driving force. For $R_m/t = 5$ with internal pressure, the SC.TNP1 results are also shown in Figure E.14. These results are similar to those without pressure, except the crack-driving force is higher for each crack size. Also, the estimation scheme for the shallow cracks ($a/t = 0.25$) is no longer conservative relative to the finite element results.

For the cases with $R_m/t = 20$ and no internal pressure, the SC.TNP1 results are shown in Figure E.15. All estimation methods provided non-conservative results with respect to the finite element analyses for the deeper cracks ($a/t \geq 0.50$). For the cases with shallow cracks ($a/t = 0.25$), the estimation scheme was conservative and slightly over predicted the crack-driving force. For $R_m/t = 20$ with internal pressure, the SC.TNP1 results are also shown in Figure E.15. These results are similar to those without pressure, except the crack-driving force is also higher for each crack size. In addition, the estimation scheme for the short, shallow crack ($\theta/\pi = 0.25$ and $a/t = 0.25$) is no longer conservative relative to the finite element results. However, the long, shallow crack ($\theta/\pi =$ 0.50 and $a/t = 0.25$) showed excellent agreement with the finite element analysis.

The cases with $R_m/t = 40$ and $R_m/t = 60$ showed trends very similar to those where $R_m/t = 20$. The primary difference is that the crack-driving force increases as the R_m/t ratio increases, for each crack size. The J versus moment curves for $R_m/t = 40$ with and without internal pressure and $R_m/t = 60$ with and without internal pressure are shown in Figures E.16 and E.17, respectively.

E.1.2.5 Correction Factor L_w for SC.TNP - The SC.TNP (SC.TNP1 and SC.TNP2) estimation scheme allows the use of a correction parameter (L_w) to obtain better agreement with finite element analyses for particular geometry and material inputs. It has been shown that the length parameter provides a reasonable correction when related to the pipe thickness for a material with a strain-hardening exponent between 3 and 10 (Ref. E.10). It was decided that the SC.TNP method and the L_w parameter would be investigated as a correction mechanism for higher R_m/t pipe analyses.

The matrix of analyses was previously shown in Table E.2. The NRCPIPES code was run for each of these cases using values of L_w = C1*t. The value of the coefficient C1 was determined such that J from the estimation scheme (J_{est}) was within 10 percent of the J value from the finite element analysis (J_{fe}) for the range of J values representative of nuclear piping materials, (i.e., 88 < J < 350 kJ/m2 [500 < J < 2000 in-lb/in2] for stainless steel welds or carbon steel pipe or welds where EPFM is expected). At these J levels, the total J was dominated by $J_{plastic}$, so that inaccuracies in the $J_{elastic}$ term in the NRCPIPES code are insignificant. For comparison purposes, the cases were placed in four groups based on crack length and internal pressure. Within these groups, the results are compared with respect to R_m/t ratio and crack depth-to-thickness ratio (a/t).

The coefficient C1 is plotted as a function of R_m/t and a/t in Figure E.18 for the cases where the crack length, θ/π, was 0.25 and there was no internal pressure on the pipe. The values of C1

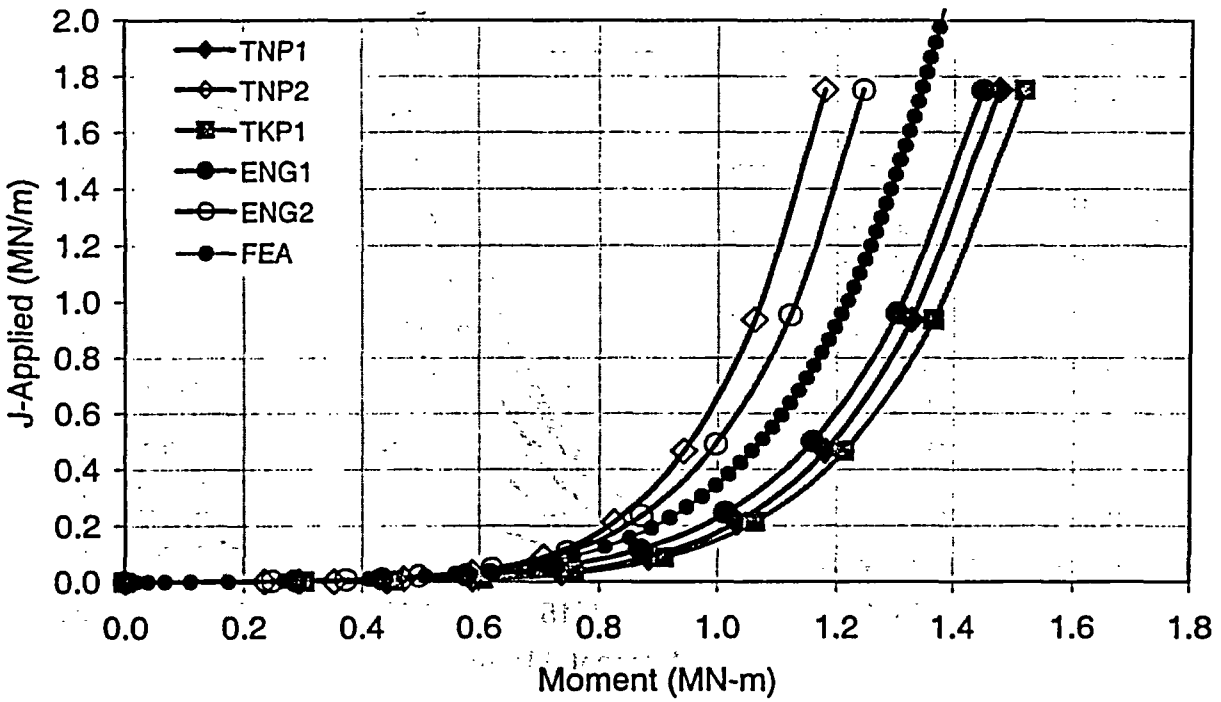

Figure E.13a J versus moment from FEA and NRCPIPES J-estimation schemes for $R_m/t = 5$, $a/t = 0.5$ and $\theta/\pi = 0.25$

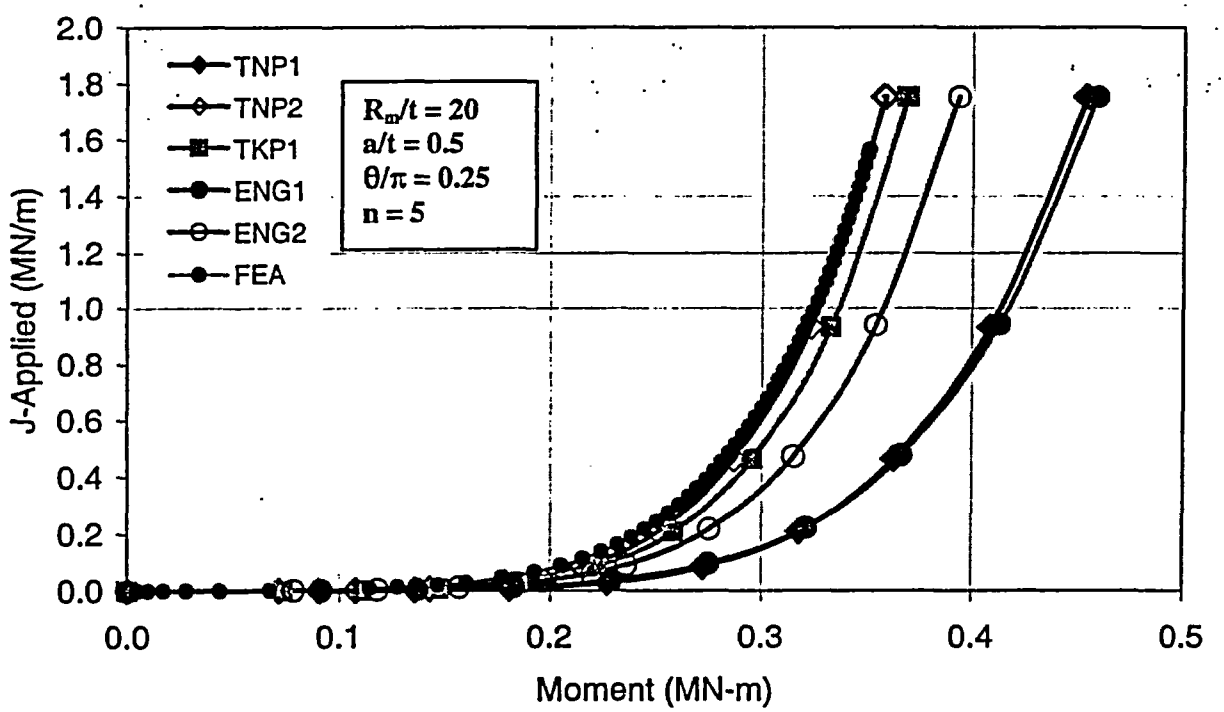

Figure E.13b J versus moment from FEA and NRCPIPES J-estimation schemes for Rm/t = 20, a/t = 0.5, and $\theta/\pi = 0.25$

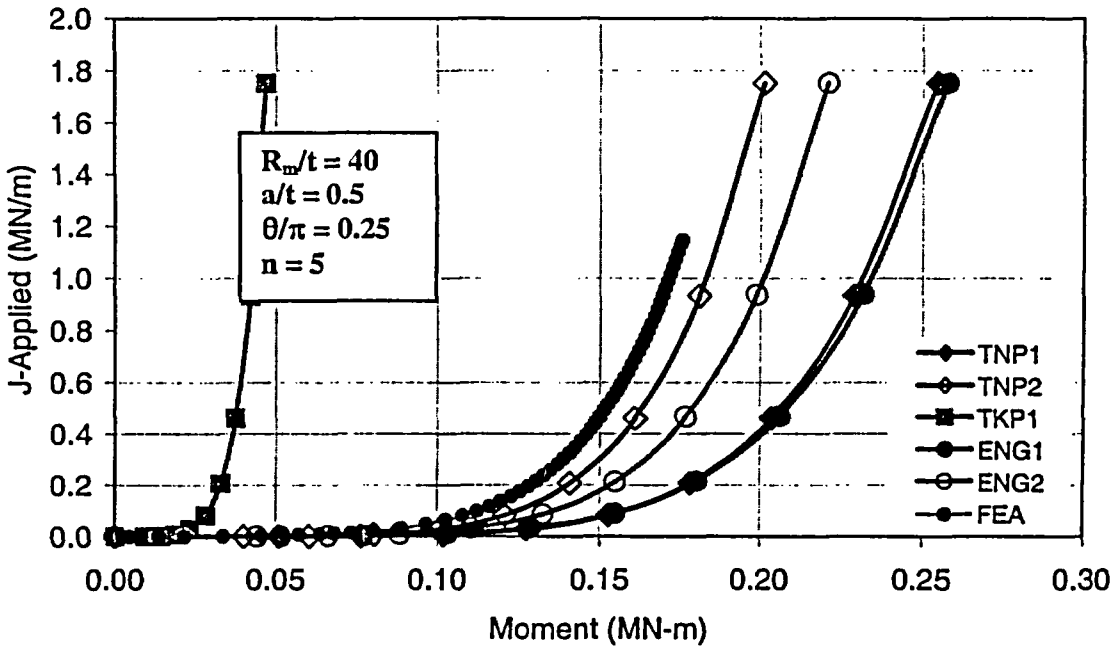

Figure E.13c J versus moment from FEA and NRCPIPES J-estimation schemes for $R_m/t = 40$, $a/t = 0.5$ and $\theta/\pi = 0.25$

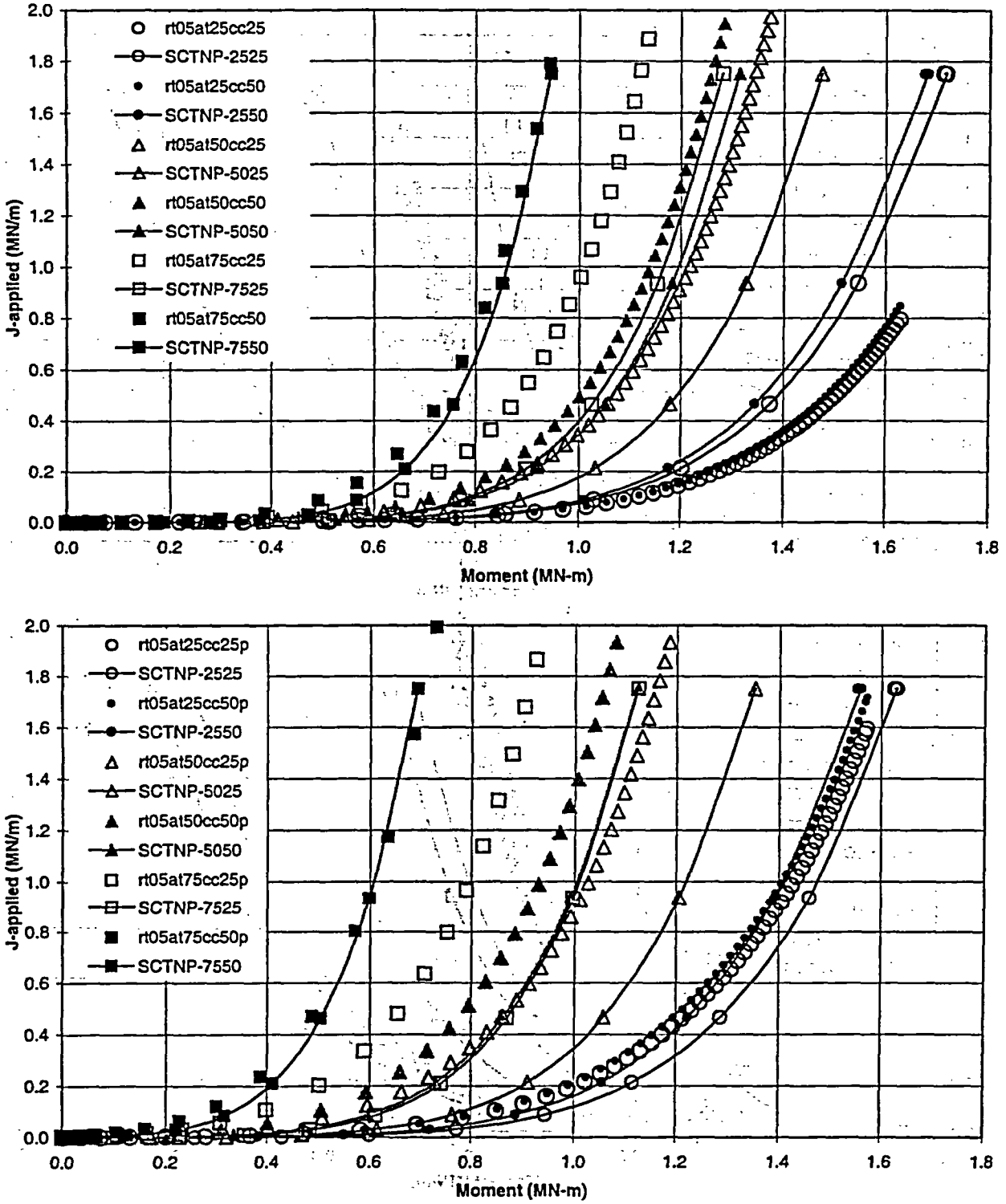

Figure E.14 J versus moment from FEA (symbol) and the SC.TNP1 analysis in NRCPIPES (symbol and line) for Rm/t = 5 and all a/t and θ/π values investigated. (Top) no internal pressure (Bottom) internal pressure (Notation as previously described)

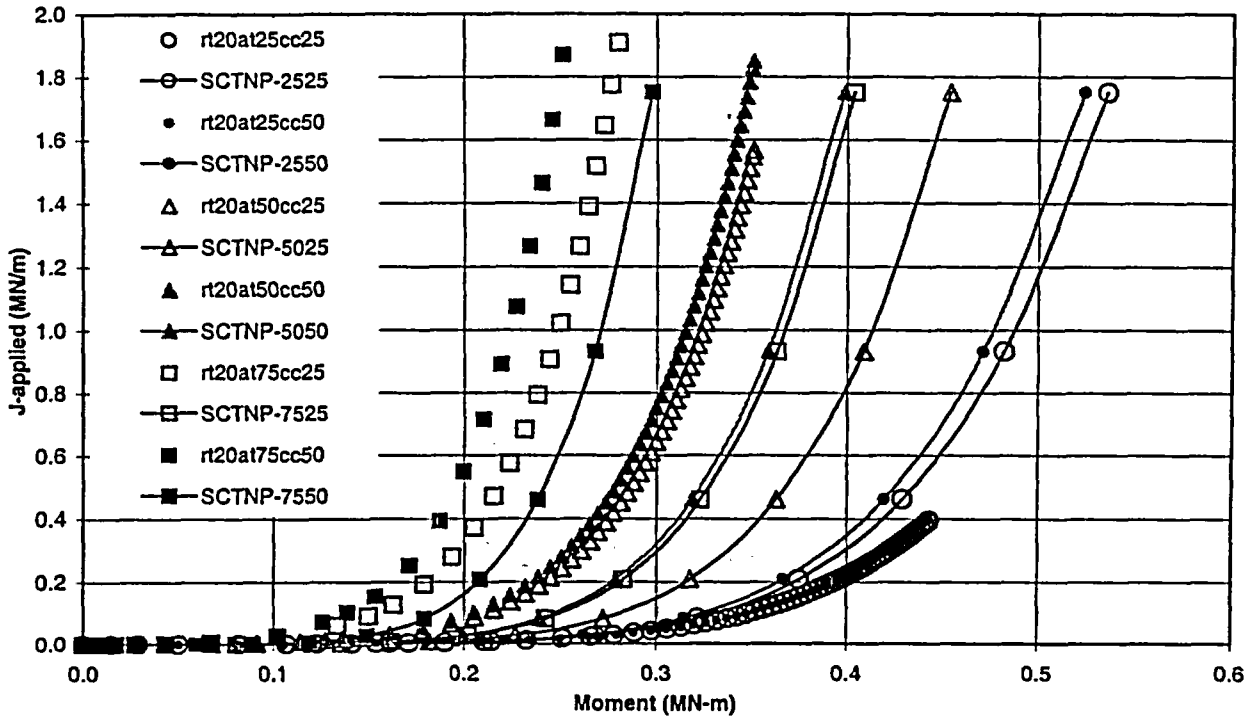

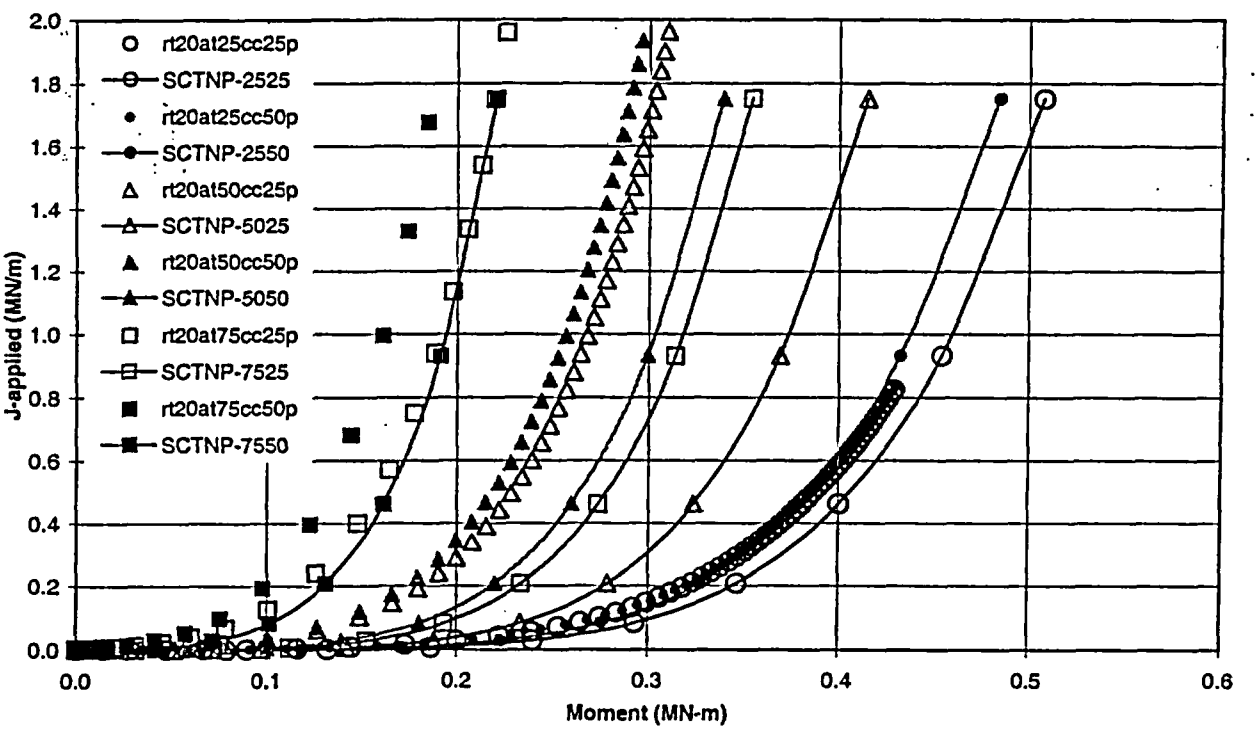

Figure E.15 J versus moment from FEA (symbol) and the SC.TNP1 analysis in NRCPIPES (symbol and line) for Rm/t = 20 and all a/t and θ/π values investigated. (Top) no internal pressure (Bottom) internal pressure (Notation as previously described)

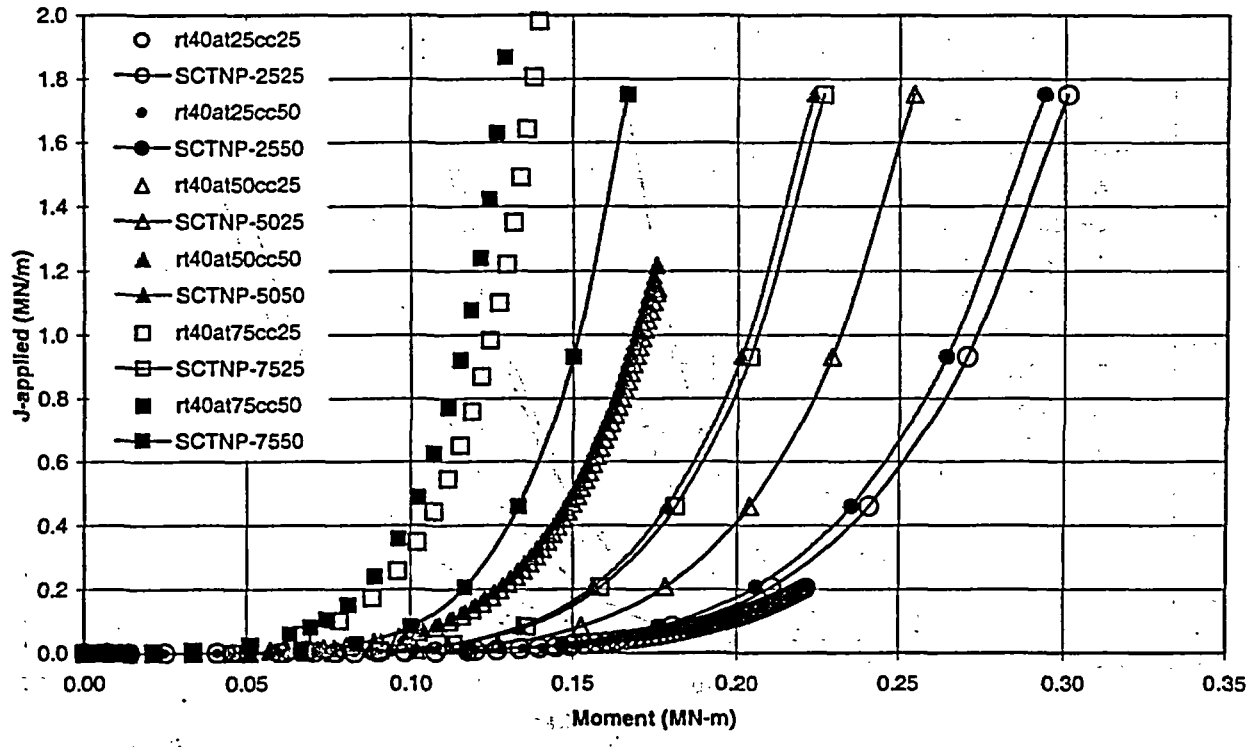

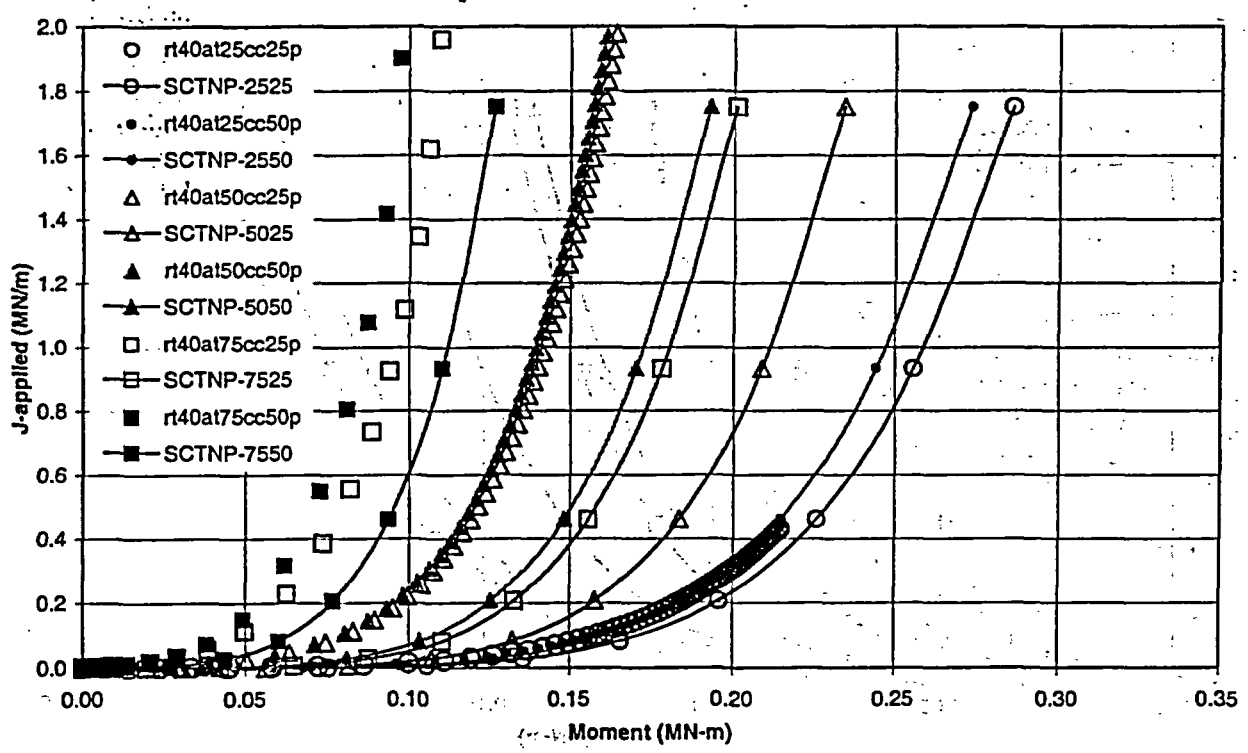

Figure E.16 J versus moment from FEA (symbol) and the SC.TNP1 analysis in NRCPIPES (symbol and line) for Rm/t = 40 and all a/t and θ/π values investigated. (Top) no internal pressure (Bottom) internal pressure (Notation as previously described)

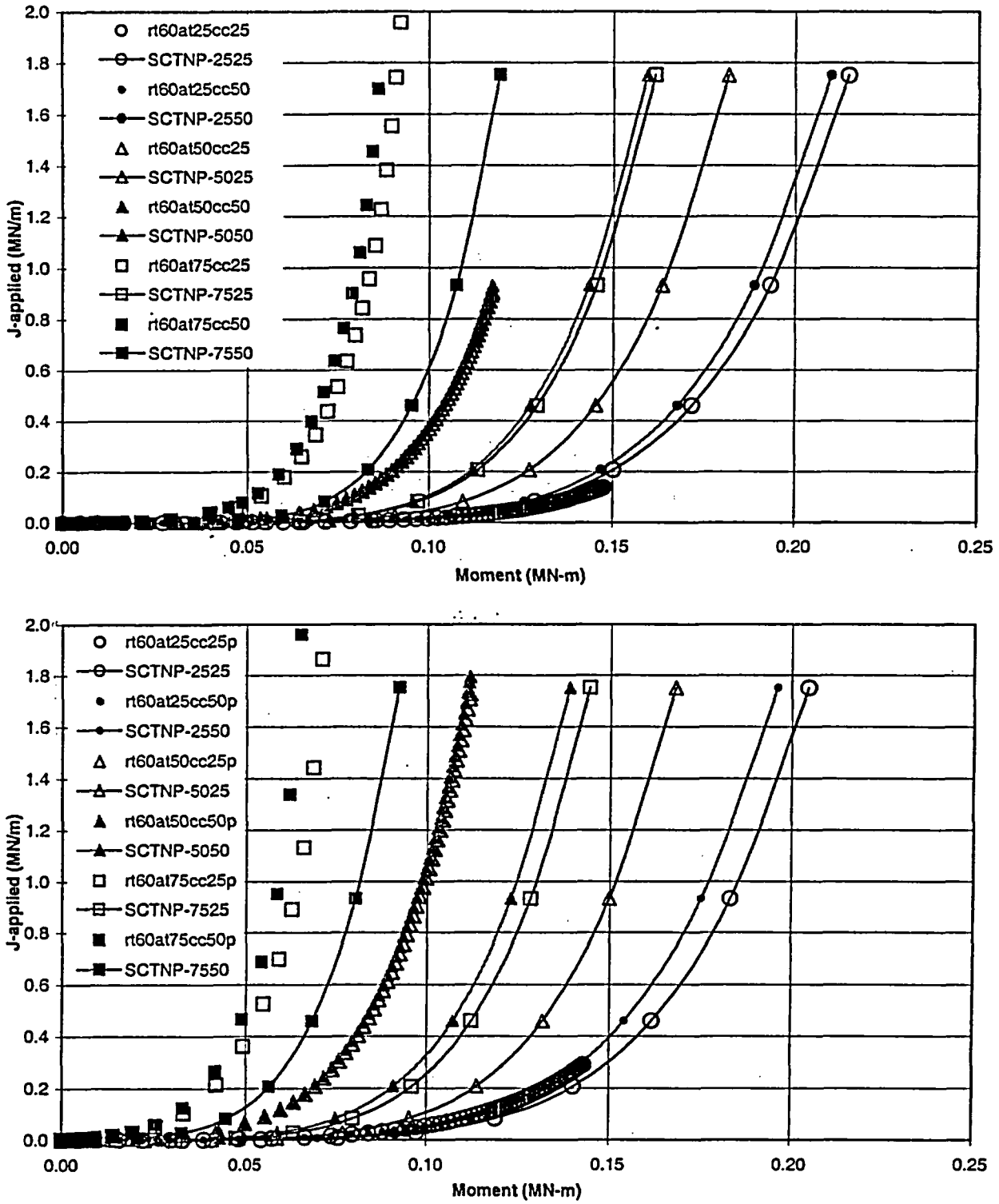

Figure E.17 J versus moment from FEA (symbol) and the SC.TNP1 analysis in NRCPIPES (symbol and line) for Rm/t = 60 and all a/t and θ/π values investigated. (Top) no internal pressure (Bottom) internal pressure (Notation as previously described)

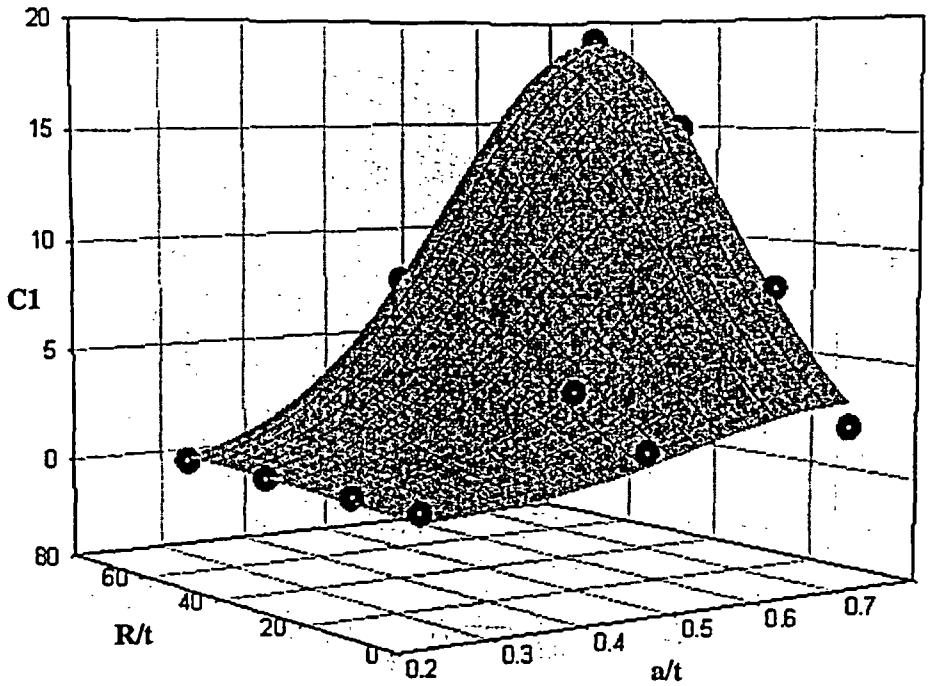

Figure E.18 Length correction coefficient (C1) as a function of Rm/t and a/t for θ/π = 0.25 and no internal pressure

as a function of R_m/t and a/t are shown as circular data points. A Gaussian regression was performed on these points to yield the surface plot shown in Figure E.18. This figure shows that the correction coefficient C1 increases slightly as the crack becomes deeper for the $R_m/t = 5$ case and remains relatively constant at the shallow crack depth $a/t = 0.25$ for the range of R_m/t values analyzed. However, the coefficient increases significantly as both R_m/t and a/t increase.

Figure E.19 shows the plot of C1 as a function of R_m/t and a/t for the cases where the crack length, θ/π, was 0.50 and there was no internal pressure on the pipe. This plot shows that the correction coefficient C1 increases and then decreases as the crack becomes deeper for $R_m/t = 5$ and remains relatively constant at the shallow crack depth $a/t = 0.25$. Again, the coefficient increases as both R_m/t and a/t increase; however, the corresponding increase in the value of C1 is much less for the longer crack length, compared to the results in Figure E.18. The shape of the regression surface suggests that the value of C1, as a function of R_m/t, reaches a maximum at $a/t < 0.75$, as the rate-of-change of C1 decreases at greater crack depths. This trend was not evident in the plot of Figure E.18 for the shorter crack length.

Figure E.20 shows the plot of C1 as a function of Rm/t and a/t for the cases where the crack length, θ/π, was 0.25 and internal pressure was applied to the pipe. The trends are similar to the previous surface plots, with the coefficient C1 increasing as both R_m/t and a/t increase. Also, the value of C1 is relatively constant for the shallow crack ($a/t = 0.25$) at all values of R_m/t and for $R_m/t = 5$ at each crack depth. Likewise, the shape of the regression surface suggests that the value of C1, as a function of R_m/t, reaches a maximum at $a/t < 0.75$, where the rate-of-change of C1 decreases with increasing crack depth.

The last group of results is shown in Figure E.21 for a crack length, θ/π, of 0.50 and internal pressure applied to the pipe. Again, the value of C1 increases as both R_m/t and a/t increase. This plot also suggests a maximum value of C1 occurs at crack depths less than $a/t = 0.75$.

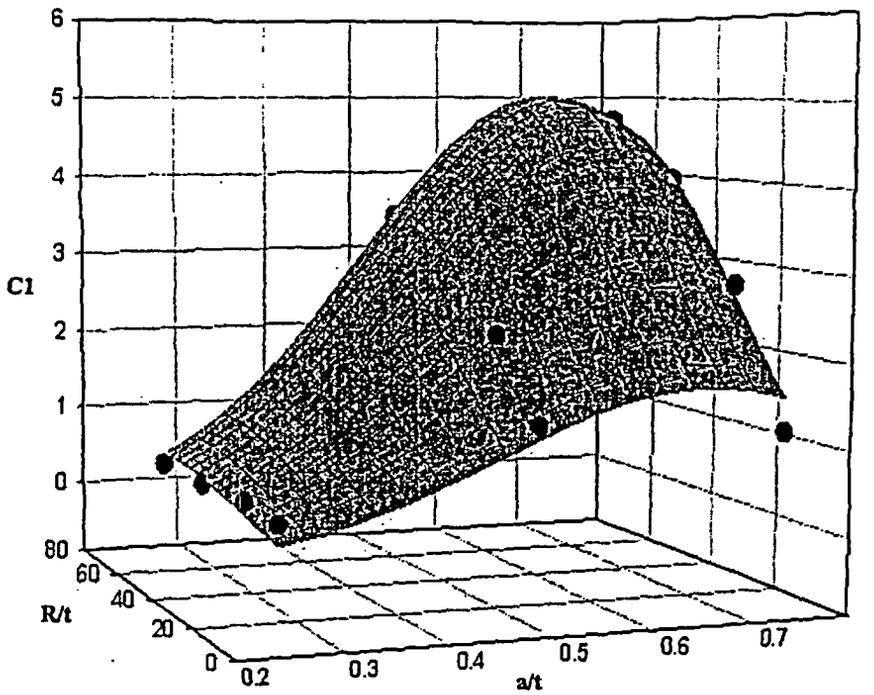

Figure E.19 Length correction coefficient (C1) as a function of Rm/t and a/t for $\theta/\pi = 0.50$ and no internal pressure

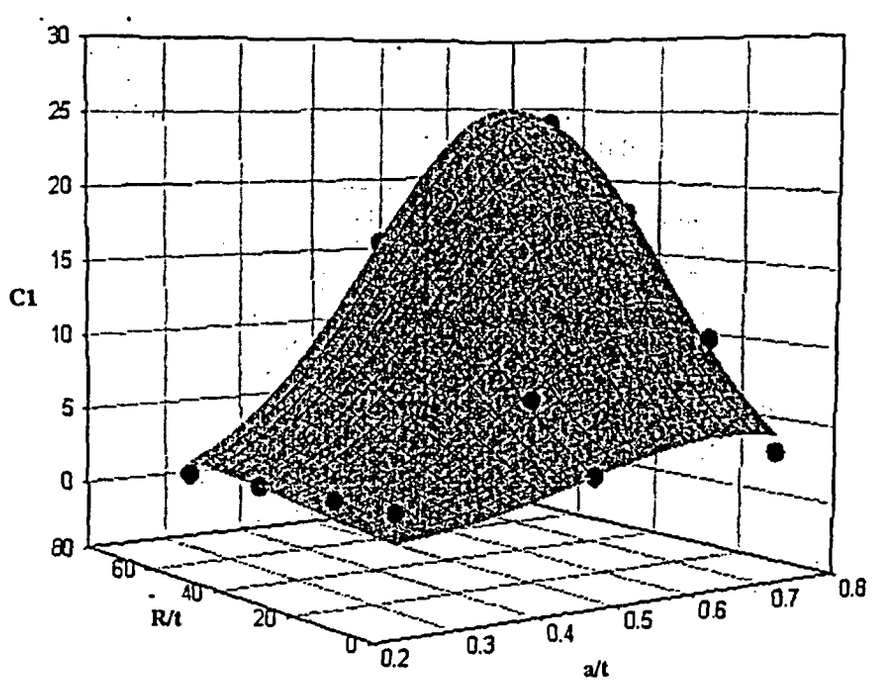

Figure E.20 Length correction coefficient (C1) as a function of Rm/t and a/t for $\theta/\pi = 0.25$ with internal pressure applied to produce a longitudinal stress equivalent to Sm/2

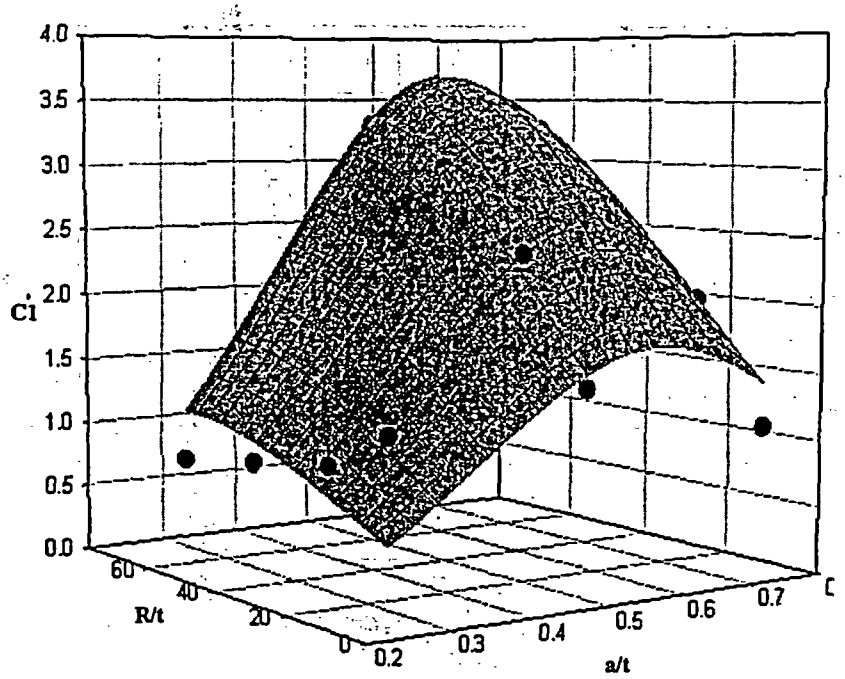

Figure E.21 Length correction coefficient (C1) as a function of Rm/t and a/t for $\theta/\pi = 0.50$ with internal pressure applied to produce a longitudinal stress equivalent to Sm/2

J Versus Moment as a Function of n - In addition to the previous results, a brief analysis was conducted on the influence of the material strain-hardening exponent on the J versus moment relationship for one pipe geometry. The analysis was conducted using the pipe model with $R_m/t = 5$ and a flaw geometry of $a/t = 0.5$ and $\theta/\pi = 0.50$. There was no internal pressure applied to the pipe. Figure E.22 shows the J versus moment results from both the finite element analyses, the lines with symbols, and the SC.TNP2 analysis in the NRCPIPES code where the Lw term for the SC.TNP2 analysis has been multiplied by a value of C1 that results in an acceptable match (within 10 percent) with the FEA results, lines only. The results indicate a linear increase in the value of the coefficient C1 as a function of increasing strain-hardening exponent between n = 3 and n = 10, see Figure E.23.

E.1.2.6 Discussion - The J versus moment relations from the finite element analyses shown in Figures E.9 thorugh E.12 are typical of those for circumferentially surface-cracked pipe. As expected, the crack-driving force increased as the crack size, length and depth, increased for a given pipe geometry. In addition, the crack-driving force was greater for the pipe and crack geometries that were subjected to internal pressure. As the radius-to-thickness ratio (R_m/t) increased, the crack-driving force also increased, as expected.

The initial analyses of the various *J*-estimation schemes available in NRCPIPES showed that the SC.TNP2 and SC.ENG2 estimation schemes produced conservative results compared with the finite element analysis for $R_m/t = 5$, i.e., the analysis overpredicted the FEA J values. The other schemes produced non-conservative estimations, see Figure E.13a. However, for the higher R_m/t pipe, all of the estimation schemes in NRCPIPES produced non-conservative results for the model with a crack depth of $a/t = 0.5$ and a crack length of $\theta/\pi = 0.25$. (The one exception is that the SC.TKP analyses were very conservative for the R/t = 40 case. This estimation scheme (SC.TKP) is known to have significant problems outside the range for which the influence functions GN were developed, $5 \leq R/t \leq 20$, Ref. E.5). These analyses were

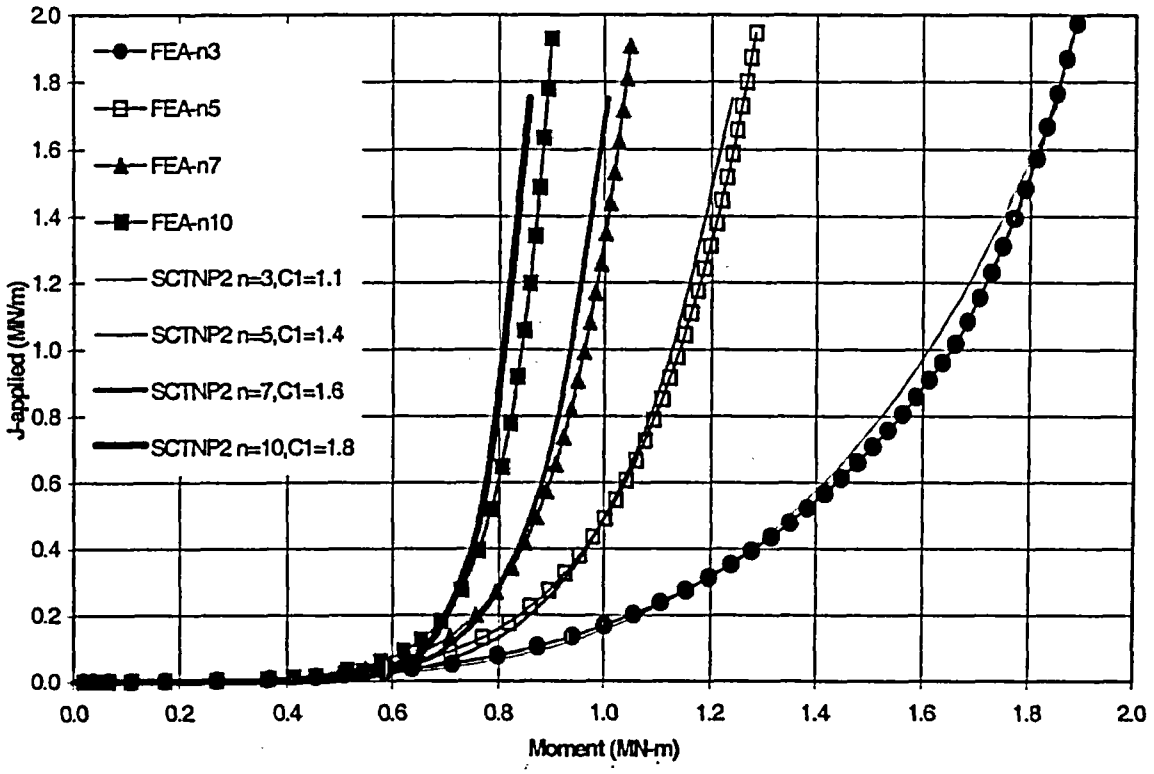

Figure E.22 J versus moment as a function on strain-hardening exponent (n)

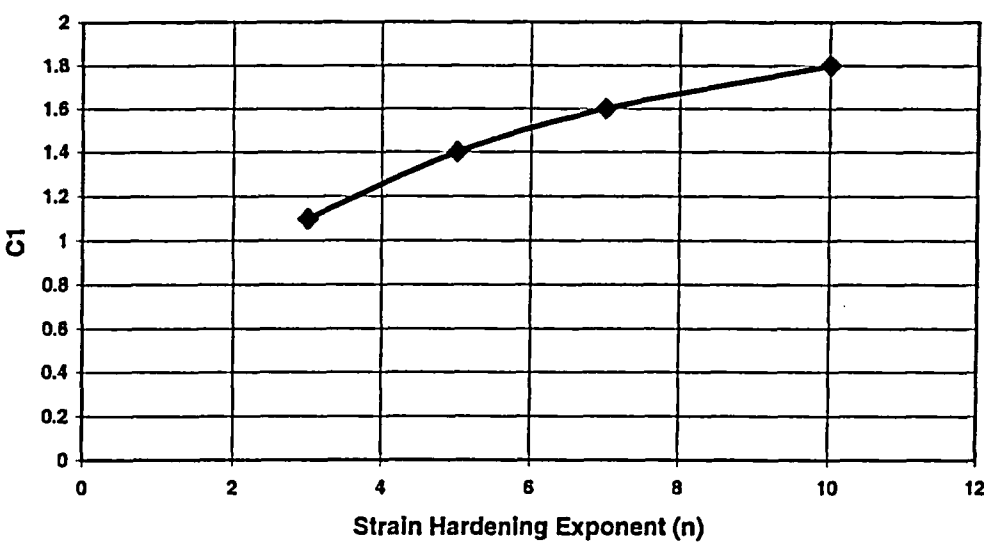

Figure E.23 C1 versus strain hardening exponent (n) relationship

conducted for a material with a strain-hardening exponent of 5.

Consequently, the L_W parameter within the SC.TNP method was used to calculate a correction factor for estimating the J versus moment response of higher R_m/t pipe. The L_W input parameter to SC.TNP was calculated as a function of the pipe thickness, t, as $L_W = C1*t$. For the various pipe and crack geometries, the values of C1 plotted as a function of R_m/t and a/t generated the surface plots shown in Figures E.18 through E.21. A Gaussian regression analysis of the surface produced a relationship of the form shown in Equation E.8.

$$C1 = \alpha_1 * \exp\left[-0.5*\left[\left(\frac{\frac{a}{t}-x_O}{b}\right)^2+\left(\frac{\frac{R_m}{t}-y_O}{c}\right)^2\right]\right] \qquad \text{(E.8)}$$

The results of the regression analyses for the four surfaces shown in Figures E.18 through E.21 are summarized in Table E.3. Note, the coefficients prescribed for Equation E.8 in Table E.3 were developed for the case where the strain hardening exponent (n) was 5. Hence, Equation E.8 using these coefficients is only valid for this case, n=5. Budgetary constraints precluded the development of these coefficients for other values of the strain hardening exponent. However, for most nuclear grade pipe materials, whether they be carbon or stainless steel, the value of n will be close to five such that this limitation was not deemed to be that great.

Within the bounds of the pipe and crack geometry parameters investigated, the coefficient C1 is used to calculate the NRCPIPES reference length input parameter L_W as $L_W = C1*t$, where t is the thickness of the pipe. The use of this parameter in the SC.TNP estimation scheme has been shown to produce a J versus moment response within ±10 percent of the results from the finite element analysis using the line-spring and shell element model previously described.

Figures E.24 through E.27 show comparisons of the J versus moment results from the revised SC.TNP analysis (Lw = C1*t; closed diamonds in the figures) with FEA results (open diamonds) from Figures E.9 through E.12 for the case of a/t = 0.5, $\theta/\pi = 0.25$, no internal pipe pressure, and R/t = 5, 20, 40, and 60, respectively. The same material property data as prescribed in Table E.2 that were used in the development of the FEA results for Figures E.9 through E.12 were used for these SC.TNP analyses. It can been seen from these figures that the revised SC.TNP analysis using the revised reference length parameter (Lw = C1*t) does an excellent job of matching the FEA results for the same test cases for all values of R/t ratio. In fact, the agreement between the SC.TNP results and the FEA results is near perfect at the higher R/t ratios (R/t = 40 and 60). As a check for other cases, a second analysis was conducted for the case of the longer but shallower crack ($\theta/\pi = 0.5$ and a/t = 0.25), R/t = 40, and an internal pipe pressure of 3.055 MPa (equivalent to 0.5 S_m). The results of that comparison between the revised SC.TNP analysis and the FEA analysis are shown in Figure E.28. As can be seen from that figure,the agreement is still quite good for this other case.

Table E.3 Surface regression coefficients

Coefficient	$\theta/\pi = 0.25$ $P_i = 0$	$\theta/\pi = 0.50$ $P_i = 0$	$\theta/\pi = 0.25$ $P_i = f(S_m)$	$\theta/\pi = 0.50$ $P_i = f(S_m)$
a_1	18.8942	5.02094	25.1609	3.69173
b	0.193618	0.199894	0.198097	0.231661
c	29.009	36.4407	31.7623	46.5544
x_O	0.752846	0.665584	0.68709	0.60135
y_O	59.2929	58.0279	63.3041	61.7603
R^2	0.9934	0.9841	0.9885	0.9018

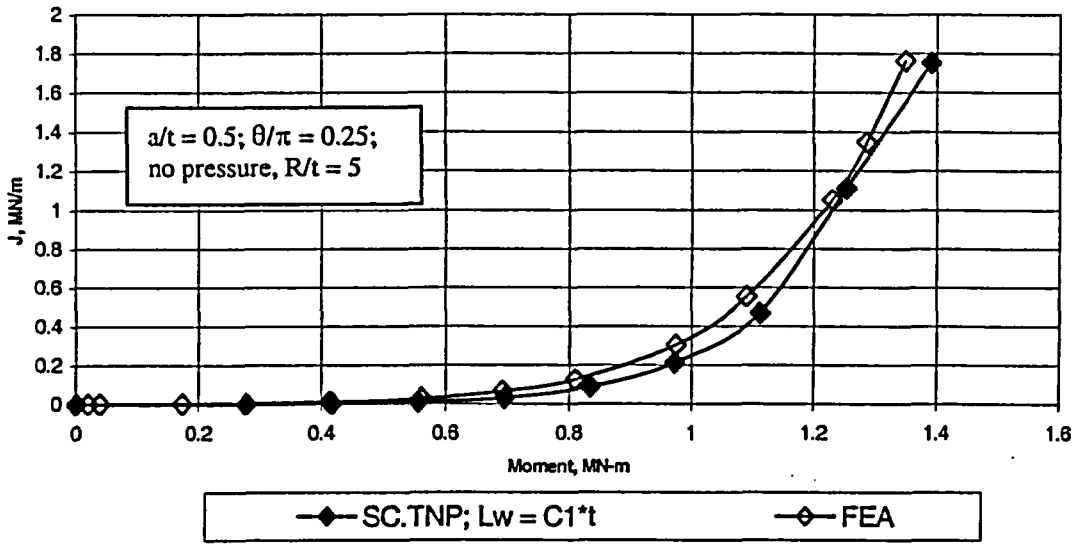

Figure E.24 Comparison of J versus moment response between the revised SC.TNP analysis (Lw = C1*t) and FEA analysis for the case of a/t = 0.5, θ/π = 0.25, no pressure, and R/t = 5

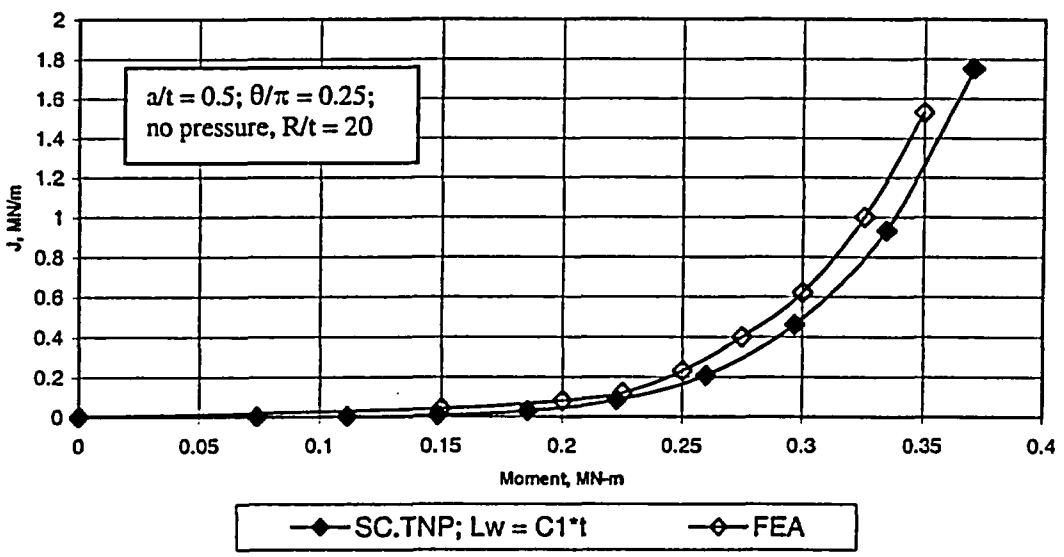

Figure E.25 Comparison of J versus moment response between the revised SC.TNP analysis (Lw = C1*t) and FEA analysis for the case of a/t = 0.5, θ/π = 0.25, no pressure, and R/t = 20

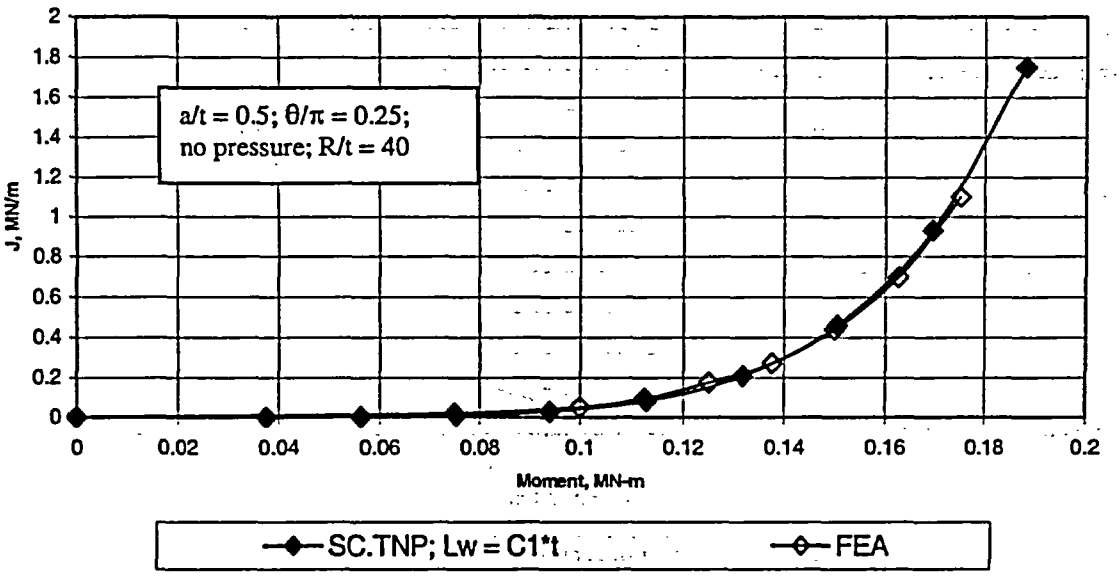

Figure E.26 Comparison of J versus moment response between the revised SC.TNP analysis (Lw = C1*t) and FEA analysis for the case of a/t = 0.5, θ/π = 0.25, no pressure, and R/t = 40

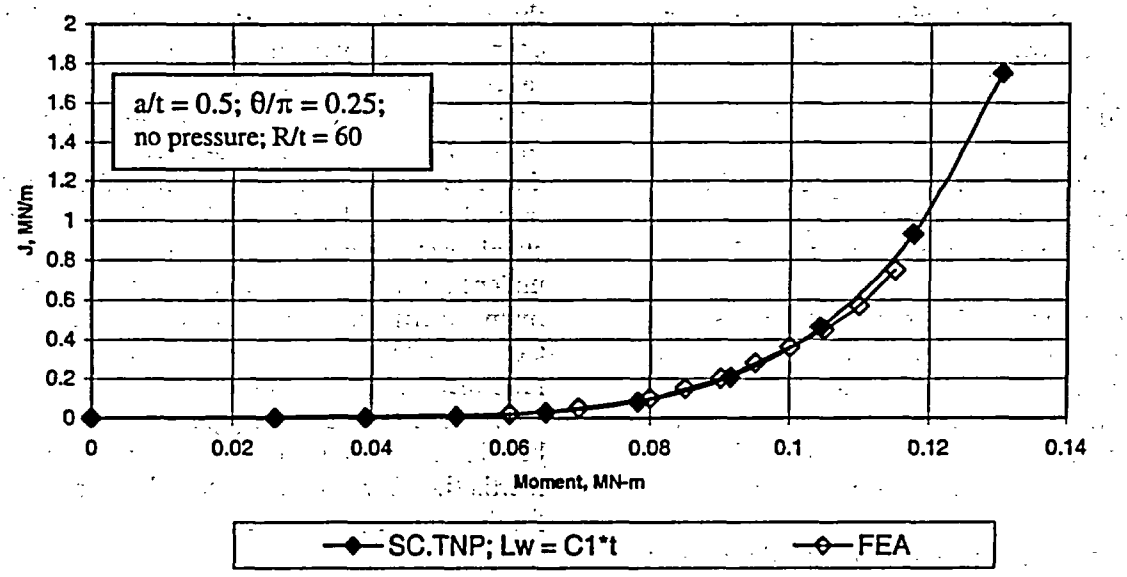

Figure E.27 Comparison of J versus moment response between the revised SC.TNP analysis (Lw = C1*t) and FEA analysis for the case of a/t = 0.5, θ/π = 0.25, no pressure, and R/t = 60

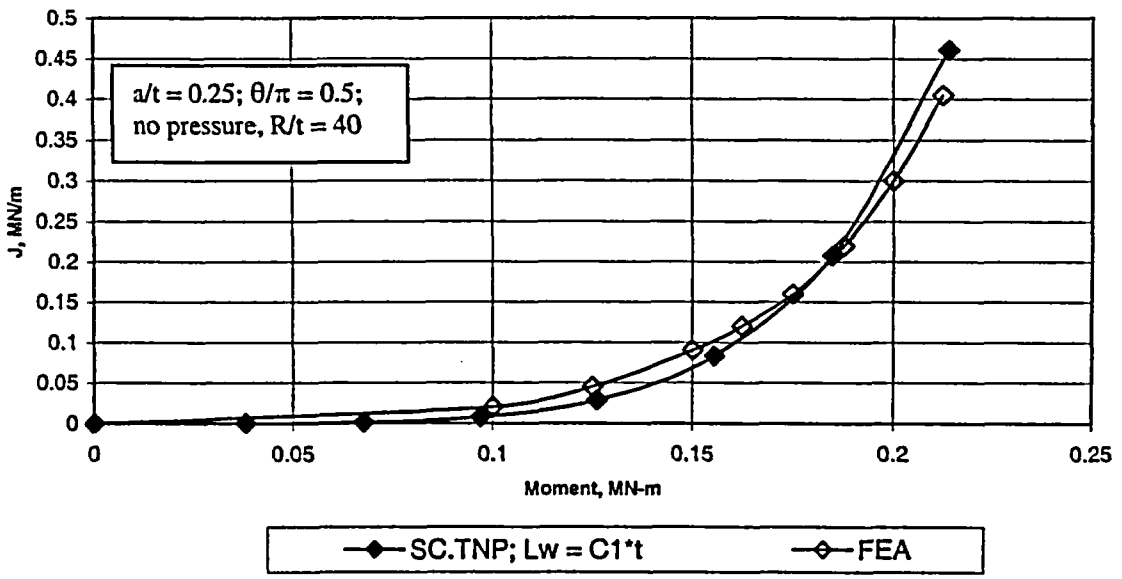

Figure E.28 Comparison of J versus moment response between the revised SC.TNP analysis (Lw = C1*t) and FEA analysis for the case of a/t = 0.25, θ/π = 0.50, pressure = 3.055 MPa, and R/t = 40

Consequently, Equation E.8 could be used in a spreadsheet analysis, where that value could be used in the existing SC.TNP analysis in the NRCPIPES code (Version 3.0). It should be noted that this would produce a more accurate solution for the crack-driving force. The material resistance, however, will be underestimated when using a typical L-C orientated specimen. This would be due to anisotropy and constraint issues, which are not addressed in this report. The anisotropy and constraint aspects could cause the actual surface-cracked pipe fracture resistance to increase by a factor of 3 to 5.

Finally, it should also be noted that there is evidence from the large strain analysis of Miura (see the results for the Second Round Robin in Appendix I), that for cases where $R_m/t = 40$ or greater there may be localized buckling that was not captured by the small-strain analyses required to be used with line-spring elements. The localized buckling gives lower failure loads; hence, this estimation procedure may overestimate the maximum loads in those cases. The precise limits on this estimation procedure have not been explored in this work.

E.1.3 Effect of R/t Ratio on Limit-Load Analyses

As part of the Degraded Piping (Ref. E.10) and Short Cracks (Ref. E.7) programs it was found that the pipe R/t ratio had an effect on the load-carrying capacity of surface cracked pipe that failed under limit-load conditions, see Figure E.29. As can be seen in this figure, for relatively small diameter (6- to 16-inch diameter) pipe experiments with surface cracks in the base metal of relatively high toughness stainless steel pipes which should have failed under limit-load conditions, the ratio of maximum experimental stress to the Net-Section-Collapse (Ref. E.11) decreased as the pipe R/t ratio increased. This was attributed to ovalization effects as the pipes ovalized during bending such that the effective moment of inertia (i.e., bending resistance) decreased more for the thinner pipes tested.

The experimental data available from References E.10 and E.7 are limited to R/t ratios less than 20. For Class 2, 3, and Balance of Plant piping, the R/t ratios may be significantly

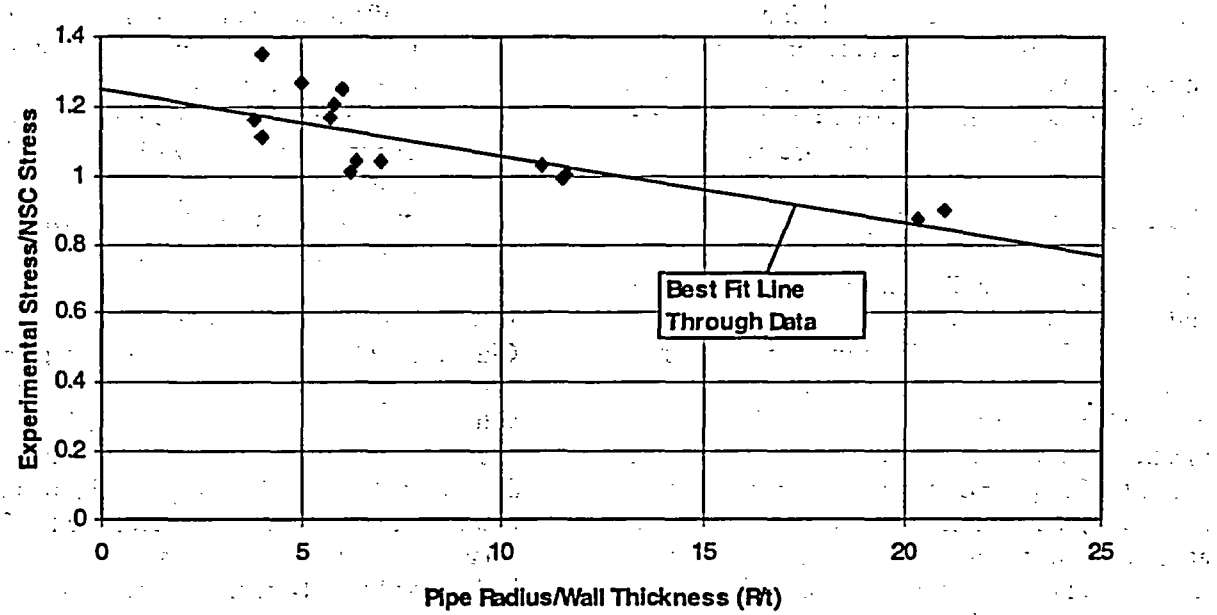

Figure E.29 Plot of the ratio of the experimental stress to the predicted stress as a function of pipe R/t ratio for pipes expected to fail under limit-load conditions

greater than 20. As such one of the original objectives of this overall effort was to develop additional experimental data for the case where the R/t ratio approached 40 to 50. However, during the course of this program it was decided to eliminate the proposed effort from the work scope due to the limited resources available. The cost to conduct the single experiment proposed was deemed to be prohibitive in light of the available funding available.

E.2 Effect of Lower Operating Temperatures for Class 2, 3, and BOP Piping on the Transition Temperature Behavior of Ferritic Pipes

The ASME Section XI pipe flaw evaluation criteria only apply to Class 1 piping. There is a desire in the industry to expand the Code procedures to Class 2, Class 3, and balance-of-plant (BOP) piping. Most of this piping is ferritic material. Oftentimes these pipes operate at lower temperatures. The current Appendix H ferritic pipe flaw evaluation procedures in Section XI of the ASME Boiler and Pressure Vessel Code currently requires that for pipe operating below 93°C (200°F), the use of a linear elastic fracture toughness value of $J_{Ic} = 45$ in-lb/in^2 ($K_{Ic} = 35.5$ ksi$\sqrt{\text{in}}$) be used, Ref. E.12. This toughness is equivalent to lower-shelf brittle fracture toughness behavior. Hence, a key question to be addressed is to determine if ferritic pipe with a surface crack actually exhibits brittle fracture initiation behavior at lower operating temperatures. If upper-shelf behavior for the start of ductile tearing can be demonstrated for all commonly used nuclear ferritic piping steels, then the flaw assessment rules can be simplified, and there will be larger flaw size tolerances. This work could lead to a simplified method to assess if upper-shelf flaw assessment rules can be extended to Class 2/3/BOP piping at lower operating temperatures.

The objective of this effort was to develop an initial procedure to assess the lowest temperature that ductile fracture initiation behavior might be expected for a surface crack in ferritic nuclear grade pipe. This involves a methodology to account for constraint effects on the ductile fracture initiation temperature and relating that back to Charpy impact data for typical ferritic pipe materials. This draft procedure could

then be the basis for future validation tests. If found to be reasonable, then this procedure could be used in the ASME pipe flaw evaluation procedures as a screening criterion to determine if LEFM or EPFM fracture will occur.

E.2.1 General Methodology

There are two main differences between Class 1 and Class 2/3/BOP piping. As previously discussed, Class 2/3/BOP piping has a higher ratio of pipe diameter-to-thickness than Class 1 pipe. Therefore, new F-functions and elastic-plastic fracture mechanics (EPFM) solutions are needed. (See prior discussions earlier in this appendix.) Also, Class 2/3/BOP piping operates at lower temperatures. Past results, primarily from the oil and gas industries, show that the constraint effects of surface cracks in ferritic pipe under global bending or pressure loading may result in a significantly lower brittle-to-ductile transition temperature than for a through-wall crack in the pipe or from standard C(T) or Charpy tests results.

There are three optional approaches that can be taken to determine the lowest temperature where ductile fracture occurs. These are;

- Option 1- Use a specimen that closely simulates the constraint conditions and anisotropy that exists for the surface crack in a pipe. As will be shown later, it is believed a fixed-grip single-edge-notched tension (SENT) test with the crack growing in the radial direction, i.e., L-R orientation for a circumferential surface crack and C-R direction for an axial surface crack, has the same constraint conditions as a surface-cracked pipe. Although there are some test data to support this approach, validating pipe tests should be conducted.

- Option 2 - Use standard C(T) specimen test data with a correction for constraint effects on transition temperature and upper-shelf toughness, or

- Option 3 - Use Charpy energy or shear area percent curves with temperature shifts to account for dynamic loading, thickness effects, and constraint effects to estimate the lowest temperature where ductile fracture initiation will still occur. If only a few Charpy test data points exist, then a procedure for estimating the entire Charpy transition curve needs to be used.

In many cases, the available data for Class 2/3/BOP piping will at best consist of Charpy impact energy and percent shear area values at a specified temperature such as 0°C (32°F), 10°C (50°F), or room temperature. Seldom is there a full Charpy transition curve, so that a procedure is needed to estimate the full Charpy curve from a few data points. Option 3 is the mostly likely method to be used.

Another approach based on the use of Option 3 procedure is to assess from a database of Charpy energy versus temperature curves what is the reasonable bound Charpy energy/shear area percent curves for a class of ferritic pipe steels. The lowest temperature for ductile fracture initiation for that class of steels can then be estimated. (This temperature will shift with the thickness of the pipe.) If that lower-bound temperature were less than the lowest temperature that the plant could operate at, then one would anticipate that that class of steels would always initiate in a ductile manner. This might provide a simple screening criterion to determine if LEFM or EPFM fracture is anticipated, and would be very useful for ASME or other Code applications.

The Option 3 procedure was the focus of this effort. The details of this procedure involve the following steps. Much of this methodology comes from older gas pipeline work and, as such, may be new terms that are not familiar to engineers dealing with nuclear piping. Table E.4 also gives a summary of the new terms and definitions to be used throughout this report.

1. Use Charpy V-notch impact specimen data to determine the transition temperature corresponding to an 85 percent shear area (Tc).

Table E.4 Definition and equivalence of different transition temperature fracture parameters

Fracture Parameter	Definition	Equivalent to	Related to
Fracture initiation transition temperature ($FITT_{(SC)}$) of surface-cracked pipe under quasi-static loading.	Lowest temperature for ductile fracture initiation of a surface-cracked pipe (axial or circumferential flaw) under quasi-static loading.	Believed to be equivalent to transition temperature of fixed-grip SENT specimen (L-R orientation for circumferential crack and C-R orientation for axial crack) under quasi-static loading	Figure E.40a shows surface crack to through-wall crack FITT differences.
Fracture initiation transition temperature ($FITT_{(TWC)}$) of a through-wall-cracked (TWC) pipe under quasi-static loading.	Lowest temperature for ductile fracture initiation of a TWC in a pipe (axial or circumferential flaw) under quasi-static loading.	Transition temperature of bend-bar or C(T) specimen. (L-C orientation for circumferential TWC and C-L orientation for axial TWC)	From full-scale ferritic pipe test data, $FITT_{(TWC)}$ is 33 to 50°C lower than FPTT.
Fracture propagation transition temperature (FPTT) of through-wall-cracked pipe	Lowest temperature where a dynamically propagating through-wall crack is ductile.	Experimentally shown to be equal to 85% shear area transition temperature of full-thickness DWTT specimen.	Related to Charpy 85% transition temperature as a function of the pipe thickness (validated for lower yield strength line-pipe steels and nuclear grade ferritic pipe).
Charpy V-notch impact transition temperature (T_c)	85% transition temperature of standard Charpy specimen.	Can also examine energy versus temperature curve if shear area percent not rated. (Not valid to use energy transition temperature for materials that have energy changes on upper shelf).	Can be determined by knowing the temperature and shear area percent of a few specimens. Correlations for other thickness Charpy specimens exist.

2. Relate the Charpy transition temperature (Tc) to the full-thickness transition temperature for dynamic fracture. This corresponds to a term called the fracture propagation transition temperature (FPTT). For gas pipelines steels, this is commonly determined from the drop-weight tear test (DWTT), Ref. E.13, where the temperature corresponding to 85 percent shear area in the DWTT is equal to the FPTT. There are correlations between the Charpy and the DWTT 85 percent shear area transition temperatures.

3. Relate the FPTT to the fracture initiation transition temperature (FITT) for a through-wall crack (TWC) in the pipe. The difference between the FITT and FPTT comes from fracture behavior of ferritic steels being sensitive to strain rate.

4. Relate the FITT for a through-wall crack to the FITT for a surface crack (SC). Constraint effects shift the fracture initiation transition temperature as a function of surface-crack depth.

5. The resulting FITT for a surface crack in a pipe corresponds to the lowest temperature where ductile fracture behavior will occur under quasi-static loading and can be calculated by knowing the upper-shelf toughness.

The technical background for these steps in the Option 3 procedure is given below. Following that, each step of the methodology is described along with an example calculation. An example of the estimated lowest operating temperature for ductile fracture initiation that is expected for A106B pipe is given.

E.2.2 Technical Background

The methodology developed for the Option 3 approach uses some terms not frequently used in the nuclear industry, but are familiar in the oil and gas industry, hence this background is described in detail. The Option 3 approach starts off by using the Charpy impact specimen data for the pipe material as the initial input. Through a series of adjustments to account for loading rate, thickness, and constraint effects; the approximate fracture initiation transition temperature (FITT) is determined for a piping material with a surface crack. The FITT is the lowest temperature where ductile fracture is expected to occur, so that the failure stress of the flawed pipe remains relatively constant at higher temperatures (not accounting for strength or upper-shelf toughness changes with increasing temperature). The methodology is the same for an axial or circumferential surface crack.

First of all, the general approach is to relate the dynamic transition temperature for crack behavior from Charpy impact tests to the minimum temperature for quasi-static ductile fracture initiation for a surface-cracked pipe. The minimum temperature where a through-wall crack might propagate as a ductile fracture was termed the fracture propagation transition temperature (FPTT) in the oil and gas industry back in the 1950's. It was highly desired not to have long-running brittle fractures in gas pipelines, of which there were some early cases of brittle fractures of 5 to 15 kilometers in length. Full-scale tests showed that the standard thickness Charpy test was not sufficient to determine the FPTT. Consequently, a full-thickness impact test called the drop-weight tear test, DWTT, (Ref. E.13) was developed. Note that the DWTT is not the same as the drop-weight test (Ref. E.14) used in reactor pressure vessel surveillance work. A drop-weight-tear test (DWTT) specimen is shown in Figure E.30 along with a Charpy specimen in the C-L orientation (through-wall axial crack growth direction). Figure E.31 shows the comparison of shear area percent values from 99 full-scale pipe burst tests and 37 DWTT, Ref. E.15. The gas pipeline industry typically stipulates that when the DWTT specimens had 85-percent shear area or more, then in the full-scale test the material was fully ductile (100% shear area) for a dynamic propagating crack. This 85-percent shear area transition temperature (85% SATT) is therefore equal to the FPTT, or the minimum temperature where an unstable growing crack will be ductile.

In the case that DWTT data does not exist, empirical equations between the Charpy test and the DWTT test can be used. It is assumed here that for ferritic nuclear piping steels there are no DWTT data, so that these correlations need to be used. From past testing results, it has been determined that the FPTT will vary to the square root of the thickness of the material, Ref. E.16. This is shown in Figure E.32 and Figure E.33 for gas linepipe steels having similar strength, chemistry, and fabrication histories to nuclear ferritic pipes.

The next step is to account for the strain-rate effect on the transition temperature shift between a propagating through-wall crack (FPTT) and the initiation of a through-wall crack (fracture initiation transition temperature or FITT(TWC)). Experimental data from ferritic linepipe steels with comparable strengths to nuclear ferritic pipe steels show that there is a shift in the dynamic to quasi-static transition temperature of about 33°C to 50°C (60°F to 90°F), see results in Figure E.34 and Figure E.35 from Kiefner (Ref. E.17). These figures show the results from full-scale axial through-wall-cracked pipe burst tests (keeping the flaw size constant), and DWTT test results. To put them on a common plot, the upper-shelf burst pressure for the pipe tests was normalized to 100 percent, and when the DWTT specimen had 100 percent shear area that was 100 percent ductile failure. The FITT(TWC) occurs when the pipe failure pressure just started to drop from the upper-shelf value. The shift in temperature between the FITT(TWC) and FPTT then is due to the strain-rate effects. (Again note that the FPTT coincides with the 85 percent shear-area transition temperature of the DWTT specimen.)

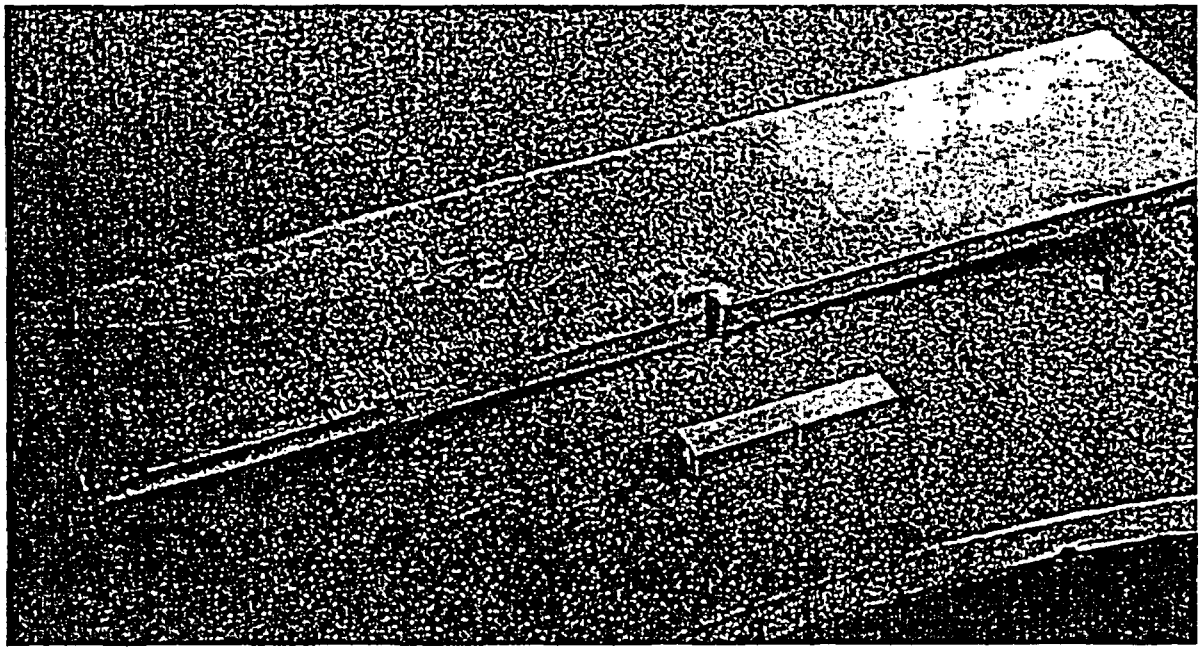

Figure E.30 Photo showing a Charpy and full-thickness DWTT specimens on a pipe

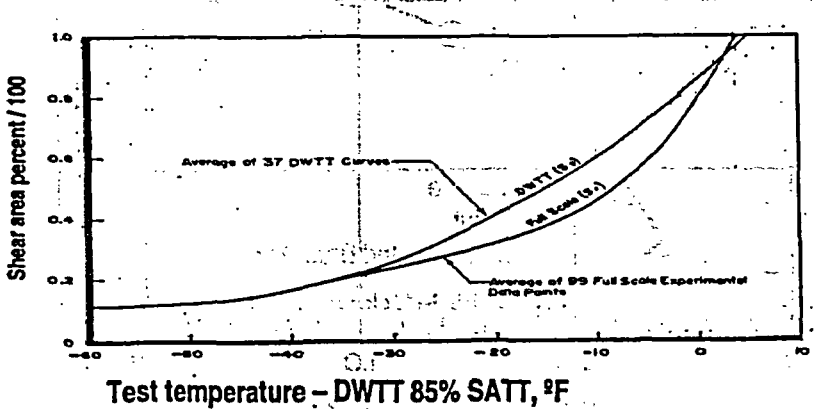

Figure E.31 Comparison of fracture appearances (percentage of shear area on the fracture) from full-scale dynamic crack propagation results to impact results from the DWTT

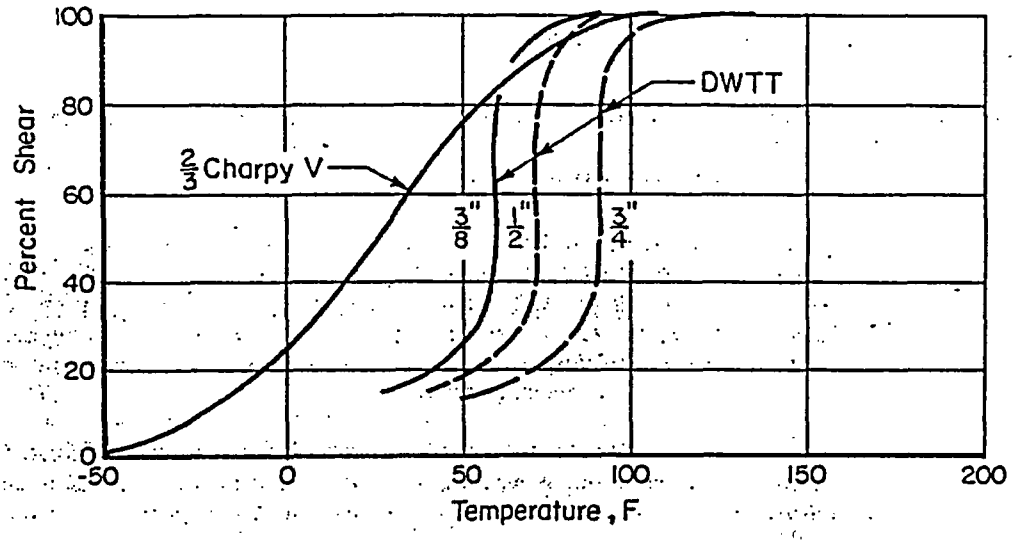

Figure E.32 Results showing the transition curve differences between a 2/3-thickness Charpy specimen and DWTT specimens of different thicknesses from the same material

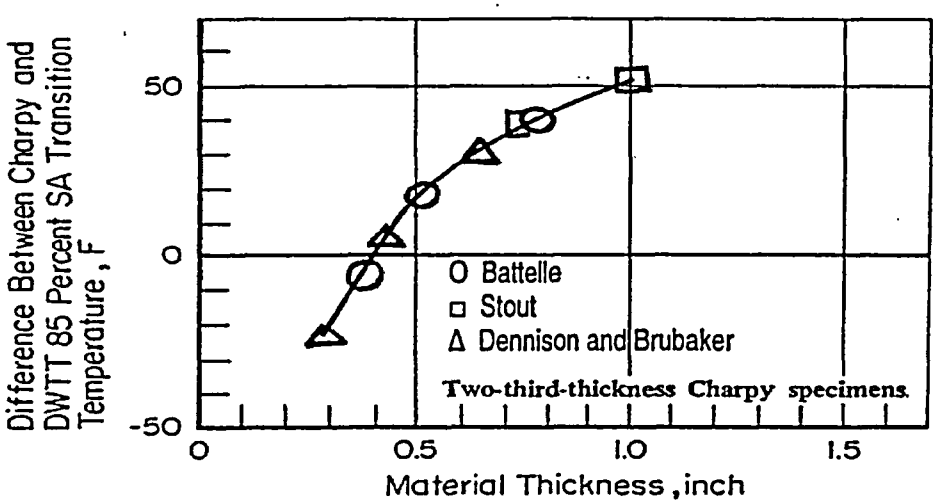

Figure E.33 Experimental results from several investigators showing the effect of thickness on the difference between the Charpy and DWTT 85% SATT, Ref. E.16

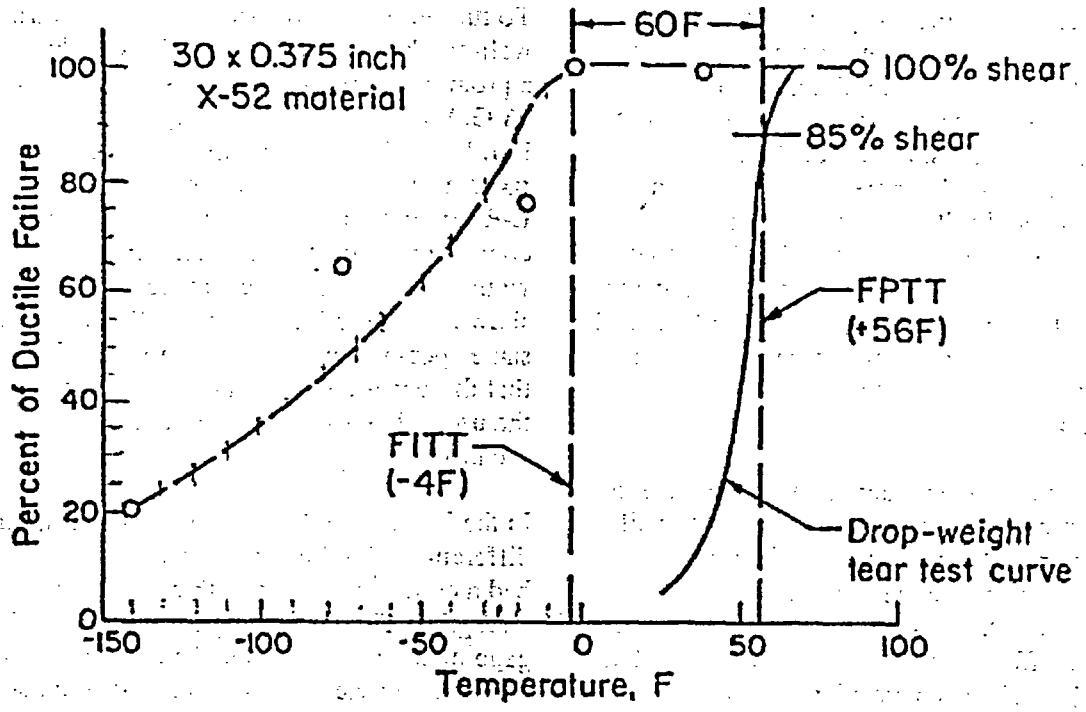

Figure E.34 Axial through-wall-cracked pipe and DWTT data showing the temperature shift from the FITT to the FPTT for linepipe steel – Case 1, Ref. E.17

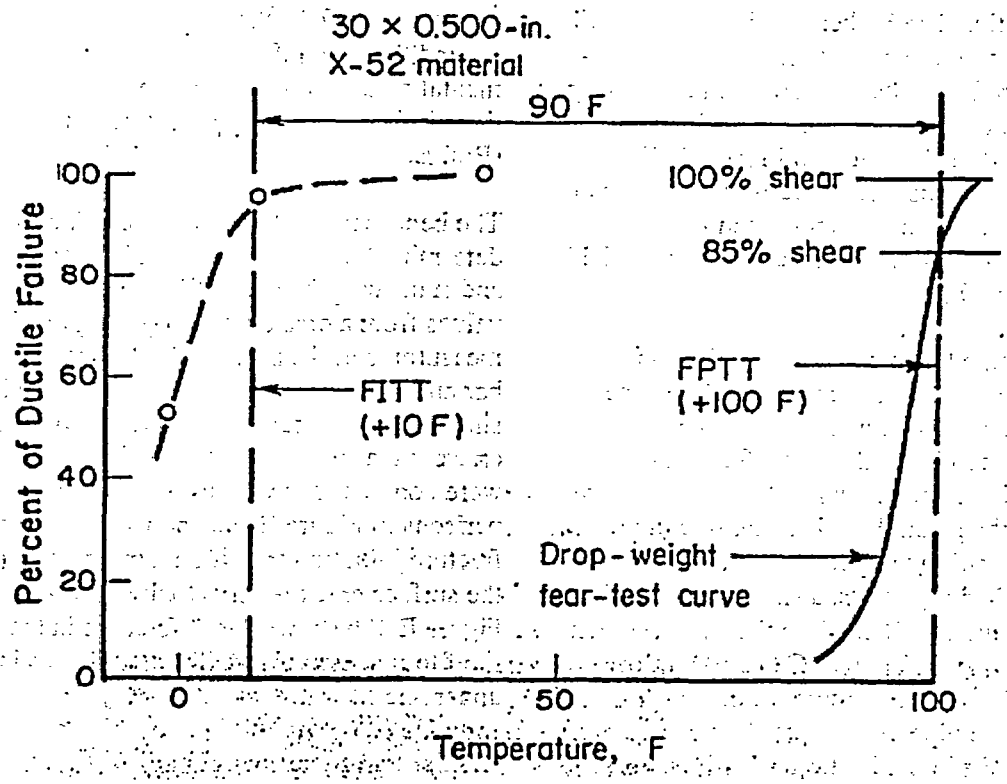

Figure E.35 Axial through-wall-cracked pipe and DWTT data showing the temperature shift from the $FITT_{(TWC)}$ to the FPTT for linepipe steel – Case 2, Ref. E.17

In the event that actual quasi-static fracture toughness data is available for the material of interest, the $FITT_{(TWC)}$ can directly be determined from C(T) or bend-bar specimen tests at various temperatures. Figure E.36 shows the comparison of bend-bar specimen transition temperature and full-scale axial through-wall-cracked pipe test results, Ref. E.18. Note that for the through-wall crack, the bend-bar gave the same FITT as the pipe tests. Since bend-bar and C(T) specimens have similar constraint conditions, either should give the FITT for a through-wall-cracked pipe.

The next step is to account for the difference in the transition temperature from a through-wall initiating crack to the initiation of a surface crack, i.e., determine the surface-cracked-pipe FITT ($FITT_{(SC)}$). This difference occurs due to constraint effects at the crack tip. The bend-bar and C(T) specimens have a large degree of bending which increases the triaxial stresses at the crack tip. On the other hand, the surface crack has mainly membrane loading in the ligament giving lower triaxial stresses and constraint at the crack tip. The higher triaxial stresses will trigger cleavage failure earlier. This can somewhat be seen from data by Kiefner in comparing the FPTT from the DWTT to the surface-cracked pipe FITT results. In Figure E.37, Kiefner showed this difference was greater than 75°C (136°F), which was more than for the through-wall-cracked pipe results in Figure E.34 and Figure E.35.

Additional pipe test data are available from Sugie (Ref. E.19) or base metal Grade B pipe with surface cracks having an a/t of 0.5 with a machined V-notch. In this case, Sugie had CTOD bend-bar specimen results that normally would give the through-wall-crack fracture initiation transition temperature. From these surface-cracked pipe tests, a shift in the FITT from the through-wall crack to the surface crack was observed to be from 40°C (72°F) to more than 95°C (171°F), see Figure E.38. Hence, these full-scale pipe test results showed a significant shift in the brittle-to-ductile transition temperature for fracture initiation between a through-wall crack and a surface crack.

To further explore the surface-crack to through-wall-crack FITT differences, Wilkowski conducted a program for the American Gas Association's (A.G.A.) Welding Supervisory Committee, Ref. E.20. In this program, it was postulated that a fixed-grip SEN(T) specimen with the crack in the L-R orientation would simulate anisotropic and constraint effects that a surface crack in a pipe would experience. A schematic of this specimen is shown in Figure E.39. Later in Reference E.21, this same specimen was further optimized for testing so that there was a straight fatigue crack produced with the use of blunt side grooves and a scalloped notch, see photo in Figure E.39.

In the initial A.G.A. work by Wilkowski, three different ferritic linepipe materials were tested that had a combination of two thickness and two strengths. The initial program used a double-clip gage method to determine the CTOD values, along with d-c electric potential data to determine the point of crack initiation. In addition to the L-R SEN(T) specimens meant to simulate surface-crack constraint conditions, t by 2t COD bend-bar specimens in the L-C orientation were also tested. This orientation is for a through-wall crack growing around the circumference, and based on past experimental results should represent the constraint condition similar to a through-wall crack in the pipe (Ref. E.18).

The bend-bar CTOD values at crack initiation were determined using the d-c electric potential method and standard procedures to calculate the CTOD values from a crack-mouth-opening displacement measurement. Hence, the difference in the bend-bar and SEN(T) specimens were expected to be similar to the differences between a through-wall crack and a surface crack in a pipe. Since tests were conducted at various temperatures, the comparisons in Figure E.40a show the differences in the fracture initiation transition temperatures (FITT) of the surface crack relative to the through-wall crack. Figure E.40b shows the differences in the upper-shelf toughness values. The differences in the upper-shelf toughness values may be due to a combination of constraint and anisotropy of the ferritic steel used, whereas the transition temperature effects are not affected by anisotropy. This assumption that the transition temperature is

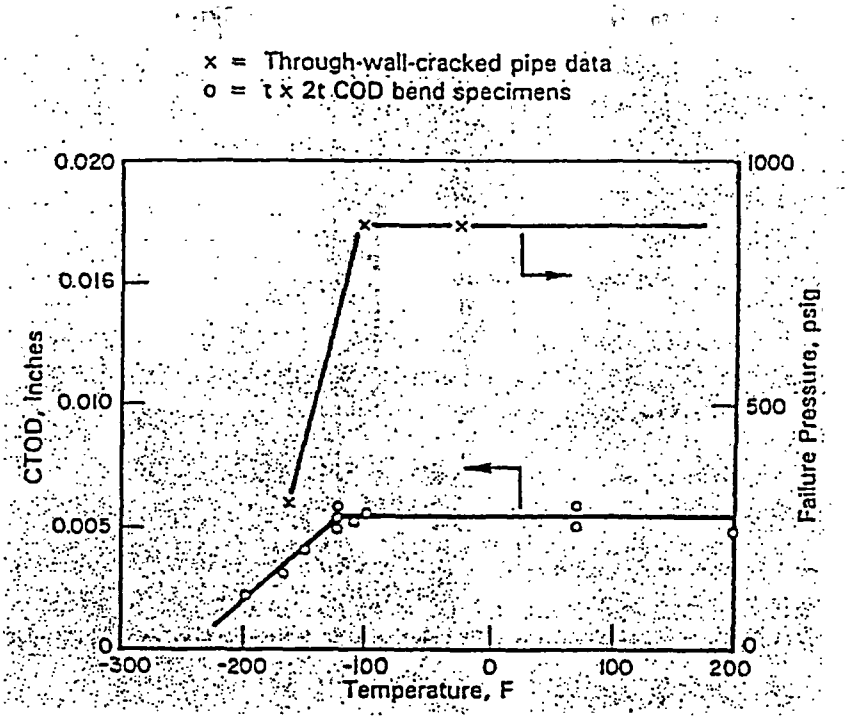

Figure E.36 Comparison of t x 2t CTOD transition temperature with axial through-wall-cracked 48-inch (1,219-mm) diameter pipe fracture data, Ref. E.18

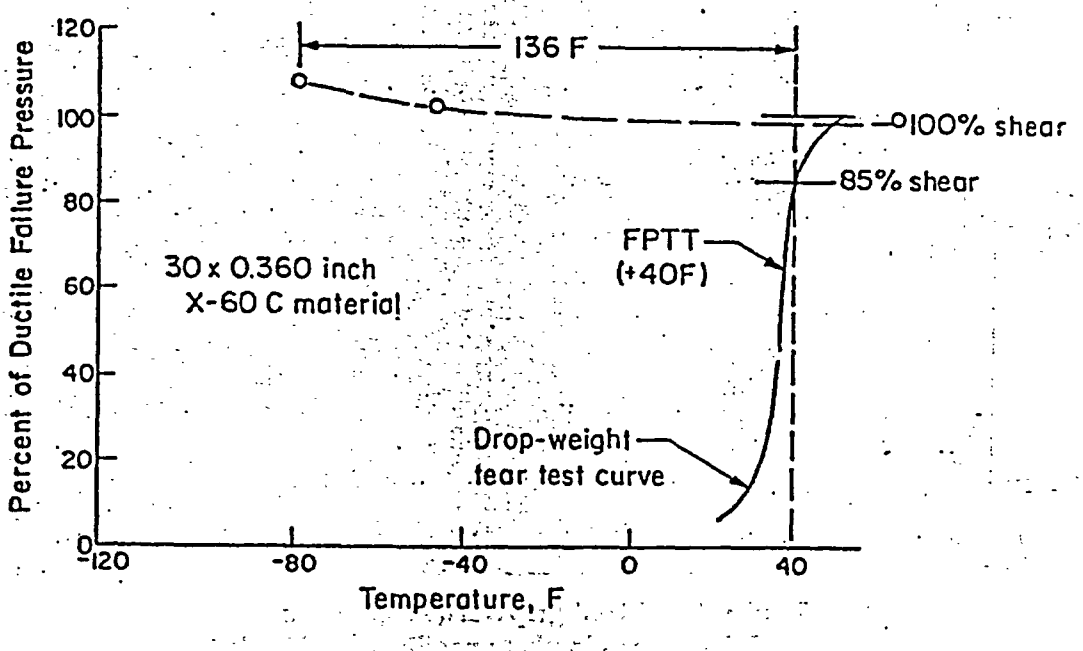

Figure E.37 Results from Kiefner showing surface-flawed pipe results relative to FPTT from DWTT data, Ref. E.17

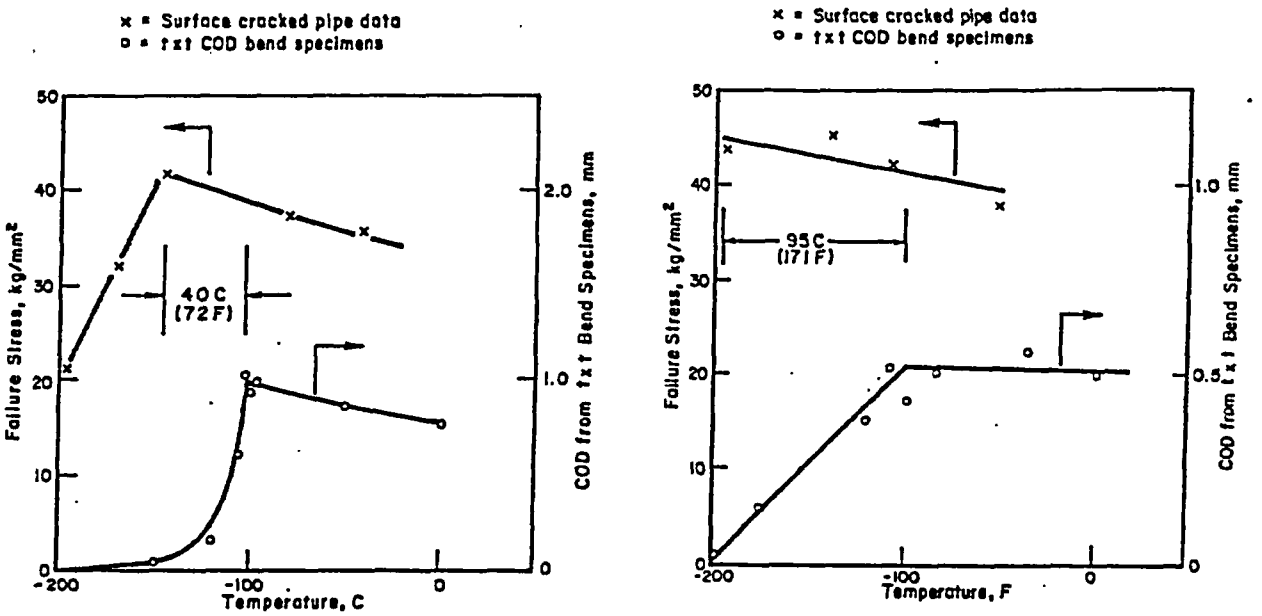

Figure E.38 Results from Sugie showing surface-flawed pipe results relative to bend-bar FITT, Ref. E.19

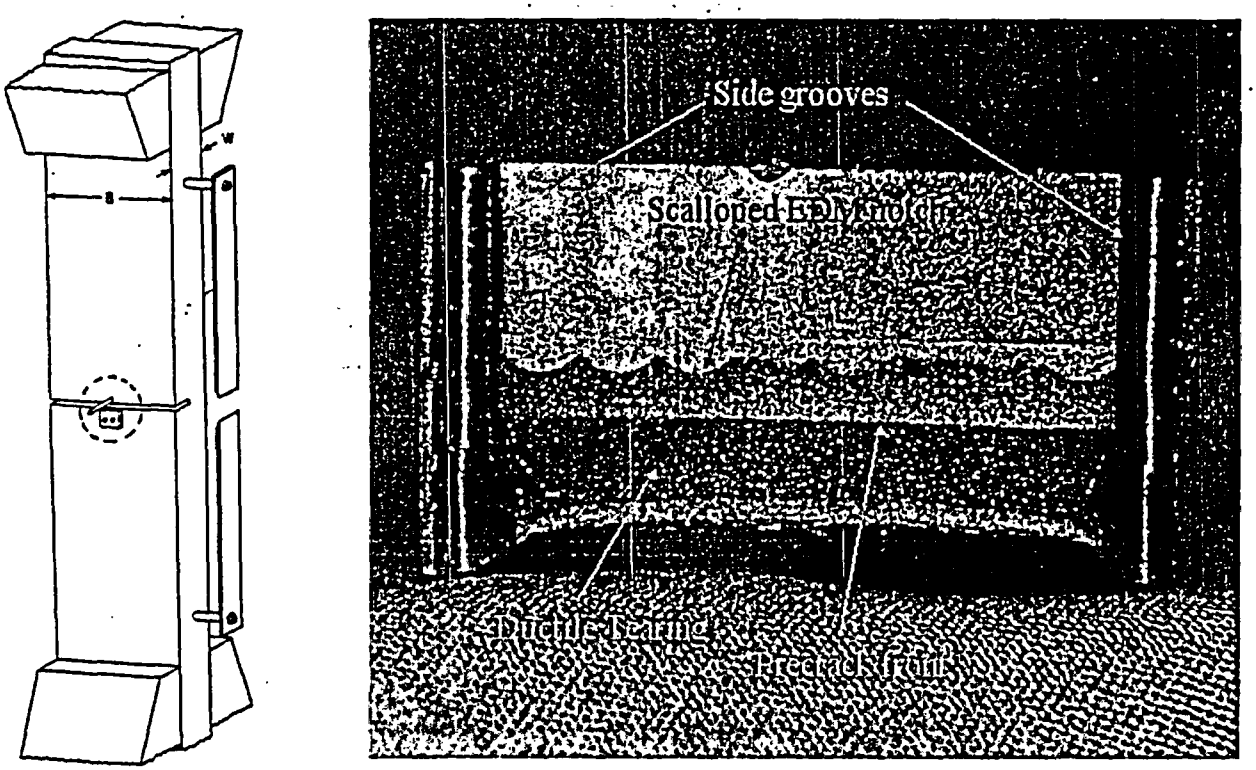

Figure E.39 Fixed-grip SEN(T) specimen (Side-grooves in photo not illustrated in sketch)

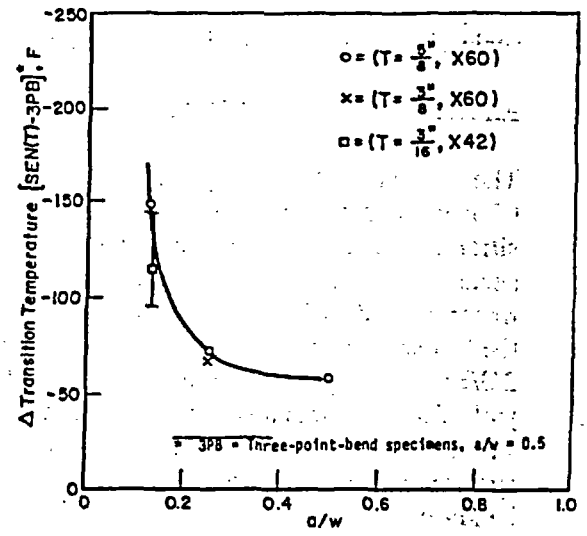

(a) Transition temperature shifts

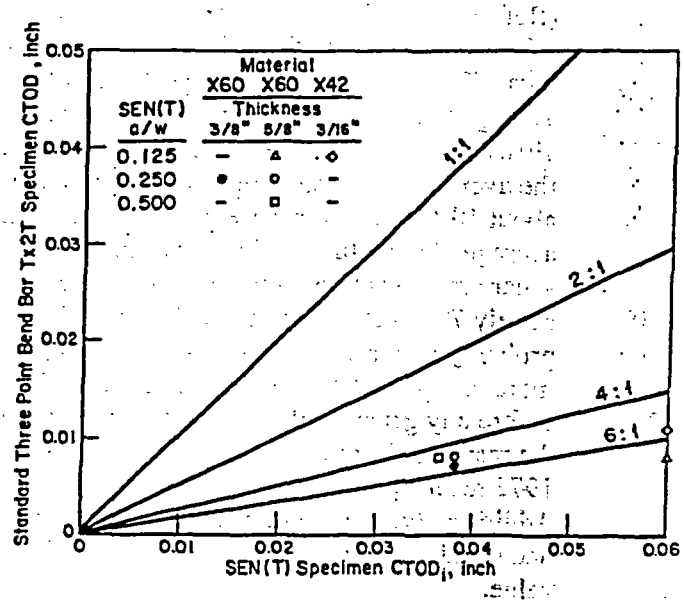

(b) Upper shelf CTOD values

Figure E.40 Results from Ref. E.20 in comparing transition temperatures of bend-bar specimens and fixed-grip SEN(T) specimen

not significantly affected by the anisotropy is illustrated in Figure E.41 (obtained from WRC Bulletin 175, Ref. E.22). This figure shows Charpy specimens in different orientation had different absorbed energies, but the brittle-to-ductile transition temperatures were about the same.

Figure E.40a therefore is expected to provide an initial estimate of the trends of the difference in the FITT for a surface crack versus the through-wall crack. Also knowing that:

1. the FITT to FPTT transition temperature is estimated to be 33 to 50°C based on the results in Figure E.34 and Figure E.35

2. the full-scale FPTT can be determined from the DWTT which is related to the Charpy transition temperature through the experimental data trends in Figure E.33,

then the transition temperature for a surface-cracked pipe by any combination of test data and empirical correlations can be determined. Obviously using a test specimen like the SEN(T) specimen in the L-R orientation should give the most accurate result, whereas the Charpy data is the most readily available data, and requires the use of several empirical relationships that are valid for this class of ferritic steels. Note that if only a few Charpy shear area versus temperature values are known, then a statistical temperature relationship such as that shown in Figure E.42 could be used to determine the Charpy 85 percent shear area transition temperature (TC). Also, if the Charpy specimens have a thickness less than the standard size (10 mm), then Figure E.43 can be helpful in determining the difference between the Charpy and DWTT 85 percent shear area transition temperatures.

The following section shows how the above data and trend curves can be used to assess the lowest temperature where ductile fracture is anticipated in A106 Grade B pipe with either a through-wall crack or a surface crack when only Charpy data are available. Of particular interest is to examine the trend curves from a statistical evaluation of Charpy data for A106 B pipe to see if some preliminary guidelines can be established. Afterwards, this relationship is compared to results from a number of other full-scale pipe tests available in the literature.

E.2.2.1 Charpy Input Data

The analysis methodology begins by using the Charpy impact energy data to determine the transition temperature corresponding to an 85 percent shear area. Depending upon the source of the test material used to develop the Charpy energy data, the test specimens may vary in size. Typical Class 2/3/BOP piping, for example, may be too thin to yield full-thickness test specimens. Since the transition temperature is a function of thickness, the specimen size used to develop the input data must be known.

The shear area versus temperature data from full-thickness Charpy test specimens for both the C-L and L-C orientations from the PIFRAC database (Ref. E.23) is given in Figure E.44. The L-C data were not necessarily from the same pipes as the C-L data. If so then it would be expected that the average transition temperature curves should be virtually identical. Nevertheless, the difference of the average transition temperature curves is only about 10°C (18°F) for these two data sets. The average Charpy full-thickness specimen 85 percent shear area transition temperature (T_c) is approximately 70°C (158°F) for these data, which is probably representative of most A106B pipes, but a more complete database should be established before any general rules should be applied. (Note, the results in Figure E.44 appear to be close to the 1972 results presented in Figure E.41). Additionally, one might want to use a mean plus one standard deviation T_C value instead of a mean value.

E.2.2.2 Drop-Weight Tear Test Transition Temperature

The drop-weight tear test (DWTT) is representative of full-thickness impact behavior. If experimental data exist from DWTT of the pipe material, the analysis can begin at Step 2 using these data to estimate the 85 percent shear area transition temperature (T_d). Otherwise, the DWTT transition temperature (T_d) can be calculated using the curves

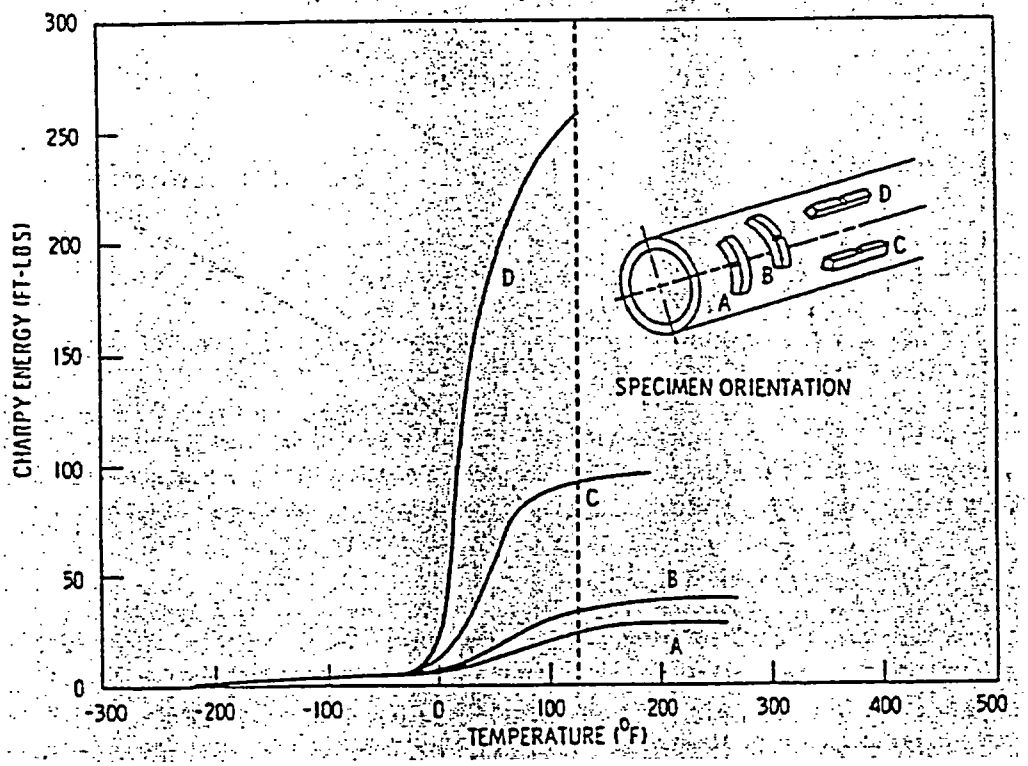

Figure E.41 Charpy energy curves for A106B – WRC Bulletin 175 (Ref. E.22) (Orientation D is for circumferential surface flaw Orientation A is for axial through-wall flaw – typically reported)

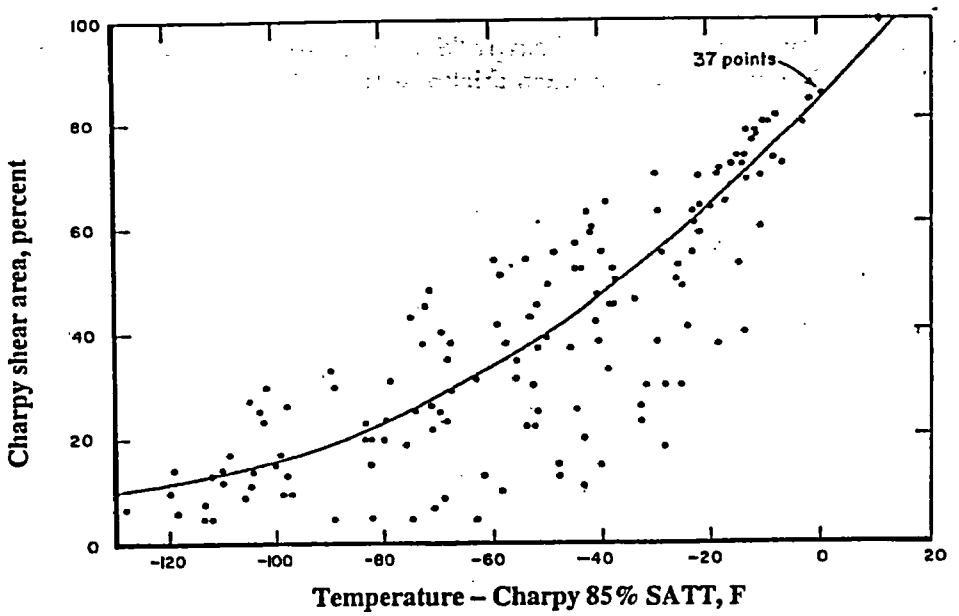

Figure E.42 Normalized fit of Charpy shear area transition curves from lower-strength linepipe steels (Ref. E.15)

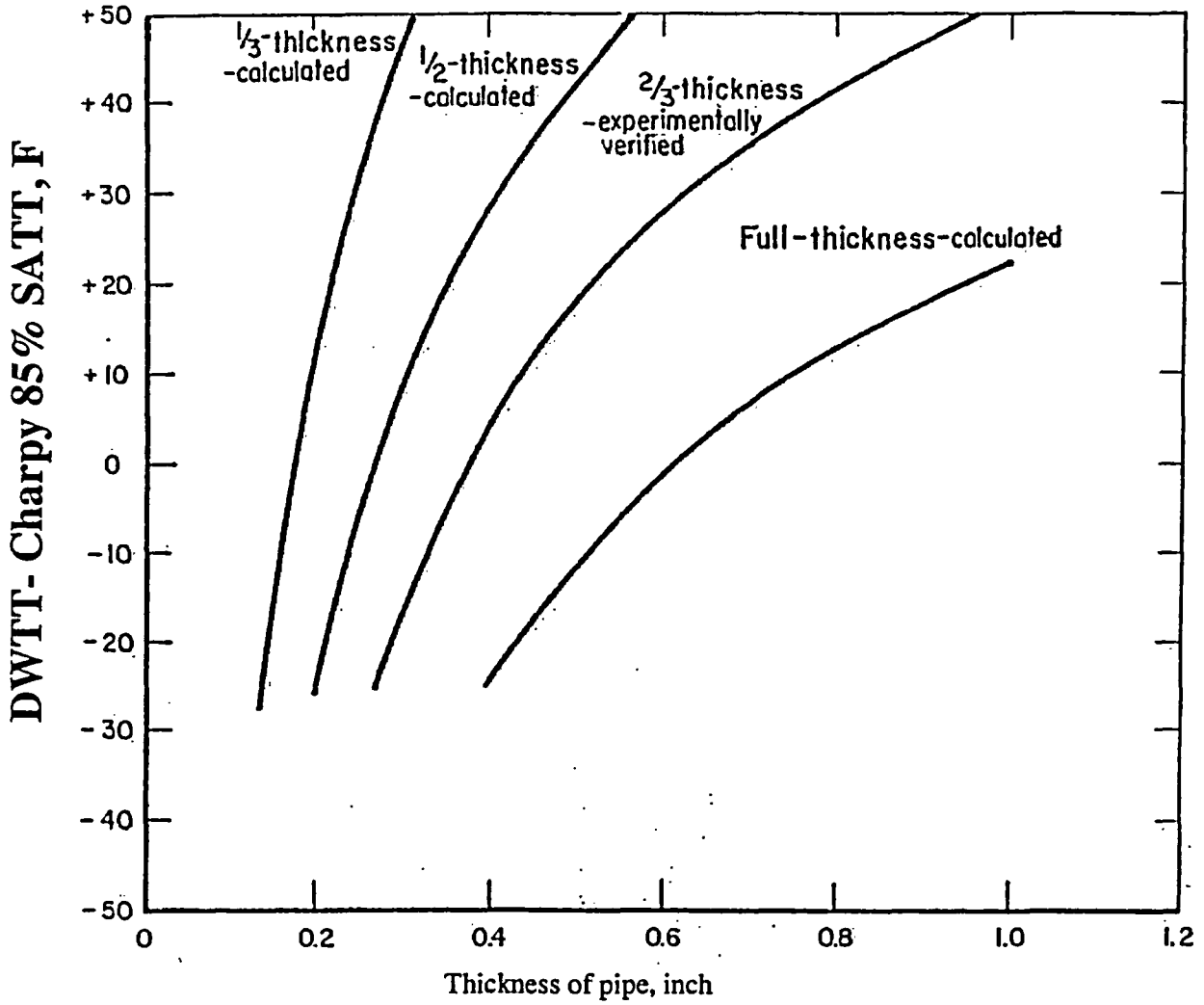

Figure E.43 Relationship between DWTT and Charpy 85% shear area transition temperatures (SATT) as function of Charpy specimen thickness (Ref. E.15)

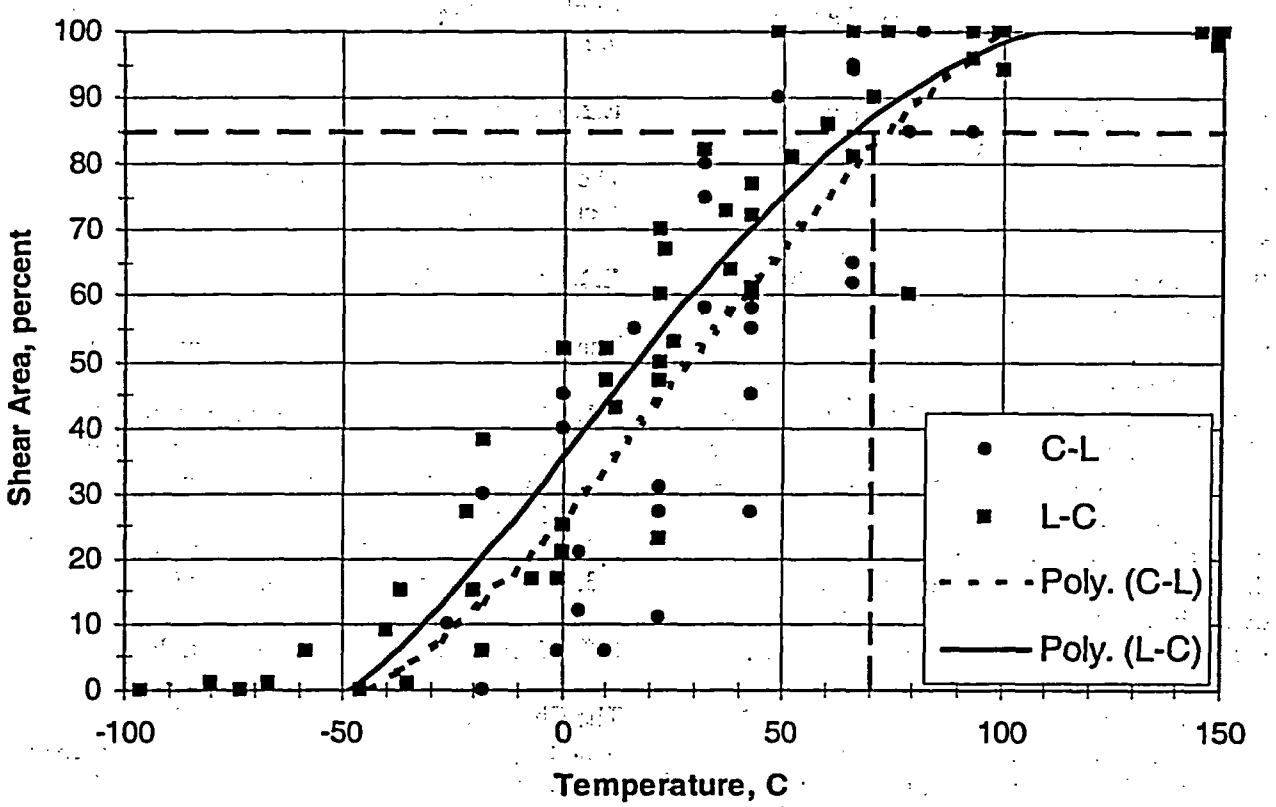

Figure E.44 Shear area versus temperature from full-thickness Charpy test data for A106B taken from PIFRAC database, Ref. E.23

in Figure E.43 which shows a transition temperature correction curve based on material thickness from DWTT results and Charpy specimen thickness which is based on experimental data for X52 and X60 linepipe steels. The lowest curve represents full-size Charpy behavior and was calculated based on the transition temperature being proportional to $1/\sqrt{t}$ and a function of the material yield strength. The thickness-temperature difference shift increases as the yield strength increases. While the curves in Figure E.43 are based on an average yield strength of 400 MPa (58 ksi), it is believed to be applicable for typical ferritic pipe in the Class 2/3/BOP applications.

The curves shown in Figure E.43 are used to estimate the shift in the transition temperature due to material thickness. For instance, a 12.7-mm (0.5-inch) thick pipe material will require an offset of approximately -10°C (-18°F) from the full-thickness Charpy derived transition temperature (T_c) to the DWTT transition temperature (T_d) at 85 percent shear area.

E.2.2.3 Fracture-Propagation Transition Temperature

The fracture-propagation transition temperature (FPTT) represents the temperature at which the mode of a dynamically propagating crack changes from shear to cleavage, Ref. E.16. The full-thickness transition temperature for pipeline material is typically determined by the drop-weight tear test (DWTT). As the thickness of the DWTT specimen increases, the transition temperature of the material also increases. This response is also observed in piping. Consequently, as was noted earlier, the DWTT has been shown to be a reasonable predictor of full-size pipe behavior, Ref. E.15. The shape of the curve from both DWTT and full-size pipe data is similar for shear area as a function of temperature. Therefore, the DWTT transition temperature (T_d), calculated either from Figure E.43 or directly from test data, is used to

predict the fracture propagation transition temperature (FPTT).

E.2.2.4 Fracture-Initiation Transition Temperature for Through-Wall-Cracked Pipe

The fracture-initiation transition temperature (FITT) represents the temperature at which the mode of fracture initiation changes from brittle to having enough ductile crack growth so that failure pressures are the same at higher temperatures, Ref. E.17. This FITT value will be different for a through-wall crack than a surface crack due to constraint effects. For a through-wall crack, it is expected that the FITT(TWC) will be lower than the FPTT (propagating through-wall crack) because propagation is a dynamic event involving high strain rates increasing the likelihood of cleavage fracture.

As previously noted, from a series of tests conducted on full-size pipe with axial through-wall flaws, it was shown that the fracture-initiation temperature was 33°C to 50°C (60°F to 90°F) below the FPTT determined from DWTT results, Ref. E.17. The variation in the FITT was attributed to differences in the flaw geometry and material properties.

In this methodology, the predicted upper-shelf FITT(TWC) for a pipe with a TWC is offset from the FPTT by approximately -33°C to -50°C (-60°F to -90°F).

E.2.2.5 Fracture-Initiation Transition Temperature for Surface-Cracked Pipe

Previously it was shown that surface-cracked pipe have a lower FITT than through-wall-cracked pipe. This is because of the constraint differences in the triaxial stresses at the crack tip that induce cleavage fracture. Therefore, the methodology applies an additional offset to the predicted transition temperature in the presence of a surface crack. The t x t 3-point bend-bar flaw orientation is representative of the behavior expected from through-wall-cracked pipe, even though the failure stresses are considerably lower. The change in transition temperature measured from 3-point bend-bar tests and single-edge-notch tension SEN(T) tests are shown in Figure E.40(a).

E.2.3 Example Problem

The methodology is demonstrated in the following sections by an example.

E.2.3.1 Input Data

The example is based on the following input data:

1. Charpy data for A106B pipe steel, L-C orientation, 10-mm thick specimen (full thickness). This data is shown in Figure E.44.
2. Surface crack depth-to-thickness, a/t = 0.25.
3. Pipe thickness, t = 15 mm (0.60 inch).

E.2.3.2 Application of the Methodology

The Charpy data shown in Figure E.44 was obtained from the PIFRAC database (Ref. E.23) for A106B pipe material. The figure contains data for test specimens that were 10-mm (0.394-inch) thick (full thickness) and machined in an L-C orientation. The data was curve fit and the transition temperature corresponding to 85 percent shear area was determined to be +70°C (+158°F). This represents the full-thickness Charpy transition temperature (T_c).

The transition temperature shift from the Charpy specimen to the full-size pipe transition temperature, represented by (T_d), is determined from Figure E.43 using the lower curve. The change in temperature (T_d-T_c) equals -5.5°C (-10°F). Thus $T_d = T_c$ + -5.5°C = +64.5°C (+148°F). This is the fracture propagation transition temperature (FPTT) for the full-thickness pipe material.

The next step is to determine the fracture initiation transition temperature (FITT) for a through-wall-cracked pipe. Based on the experimental data previously discussed (Figures E.34 and E.35), the change in temperature to obtain the FITT(TWC) is FPTT (or Td) –33°C to –50°C (–60°F to -90°F). Using the average, ΔT = -42°C (-75°F), the FITT(TWC) = T_d - 42°C = +22.5°C (+73°F).

The final step is to calculate the upper-shelf fracture initiation transition temperature (FITT) for a surface-cracked pipe with a flaw depth-to-thickness ratio of a/t = 0.25. The change in temperature to obtain the FITT(SC) is based on the curve in Figure E.40a. For a/t = 0.25, ΔT = -38.9°C (-70°F). Therefore, FITT(SC) = FITT(TWC) -38.9°C = -16.4°C (+2.5°F). Thus the predicted upper-shelf fracture initiation transition temperature for an A106B pipe with a wall thickness t = 15 mm (0.6 inch) and a/t = 0.25 equals –16.4°C (+2.5°F).

E.2.4 General Trends for A106B

This methodology was applied to predict the fracture initiation transition temperature for surface cracks (FITT(SC)) over a range of material thickness and crack depths using the A106B Charpy data shown in Figure E.44 in combination with Figure E.40a, Figure E.43, and the average shift of 42°C (75°F) from the FPTT to FITT for a through-wall crack. The results are shown in Figure E.45. Also shown in this plot are the propagation and initiation transition temperature curves for a through-wall crack. The data suggest that A106B pipe operating above 10°C (50°F) with a wall thickness less than 25 mm (1.0 inch) will exhibit ductile fracture initiation behavior so that the failure pressure for all surface-crack geometries of practical concern should be the same as that for warmer temperatures (not accounting for changes in strength properties with temperature). At 20°C (68°F), A106B pipe up to 50-mm (2-inch) is predicted to have ductile initiation for all surface-crack geometries.

E.2.5 Validation with Existing Data in Literature

There are a number of A106B and other ferritic nuclear grade pipe tests that have been conducted in the past that can be used to assess the validity of the general trend curve given in Figure E.45. These tests and their results are summarized in Table E.5. The results showed that the general trend in Figure E.45 is correct, however, the data for A106B pipe tests are not sufficient to accurately demark the predicted brittle-to-ductile transition temperatures, i.e., the tests were conducted much warmer than the minimum predicted temperature for ductile fracture.

In addition to the A106B tests, there have also been a limited number of tests on similar ferritic steels. Those test results and comparisons to the minimum predicted transition temperatures are given in Table E.6. In these cases, the actual Charpy 85 percent shear area transition temperature (or percent best estimate of that value) was used to determine the FITT for the flaw type (surface crack or through-wall crack) tested. Again, most of these results show that the analysis procedure is correct, however, the tests were generally conducted well above the minimum transition temperature so that there were no brittle fracture cases to bracket the FITT. Only in three cases were there tests that were close to the predicted FITT. These were the Kiefner X60 surface-cracked pipe tests, and the two sets of tests by Sugie on Grade B pipe. The Kiefner X60 lowest temperature test agrees with the predicted FITT(SC), but there was no brittle initiation data point to get the actual experimental FITT(SC). The Sugie tests had a lower FITT(SC) than predicted. This may be due to the experiments using a machined V-notch rather than a sharp fatigue crack, or scatter in the material behavior, where we used an average trend curve. Nevertheless, the results showed that the general procedure is at least conservative (assuming no great effect from the machine notch versus fatigue crack in the past pipe tests).

E.2.6 Limitations on the Methodology

The methodology developed to predict the fracture initiation transition temperature for a surface-cracked pipe is based on the use of empirical correlations between experimental data from standardized and non-standardized material properties tests and full-size pipe tests. Previous work has suggested that the shift in transition temperature is a function of material properties as well as pipe and crack geometry. As a result, the methodology relies on the extrapolation of standard test specimen data to predict full-scale pipe fracture behavior.

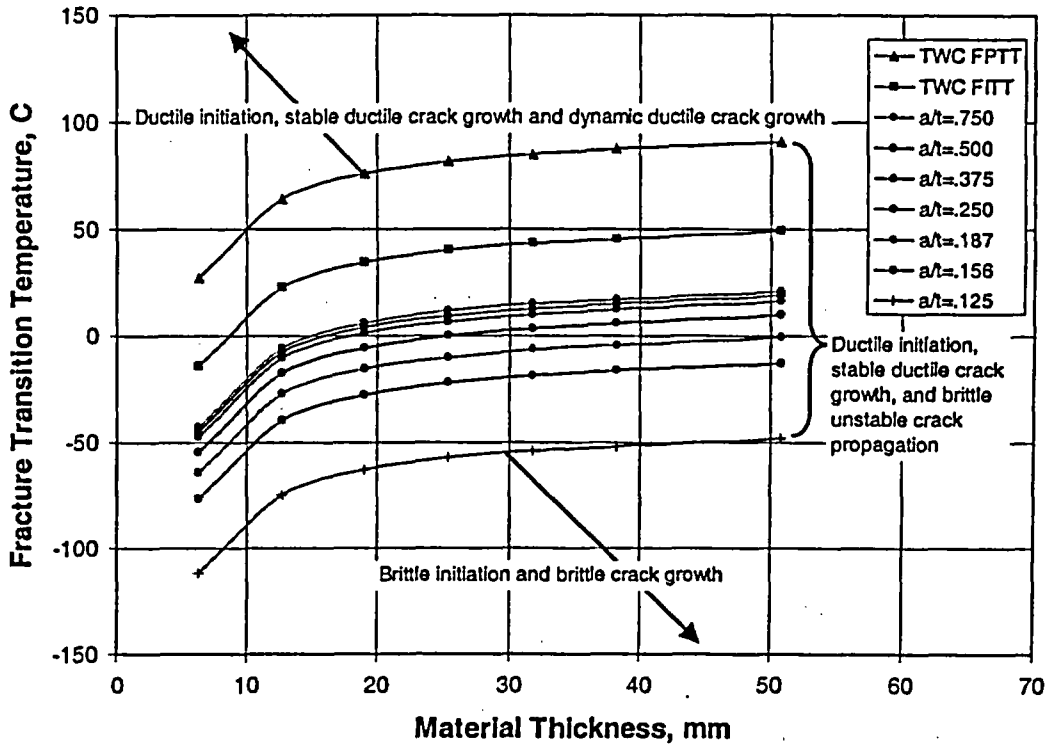

Figure E.45 Preliminary FITT relationship as a function of material thickness and crack depth (Based on upper-bound A106B data in PIFRAC database – L-C orientation)

Table E.5 Circumferentially cracked A106B pipe test results and comparison to minimum temperature for ductile fracture

Reference	Pipe thickness, mm (inch)	Flaw type	Test temperature, °C (°F)	Result	Predicted FITT, °C (°F)
CISE-a	5.5 (0.217)	TWC	20 (68)	Ductile initiation, brittle propagation	-17.9 (0)
CISE-b	10.9 (0.429)	TWC	20 (68)	Ductile	4.4 (40)
CISE-c	17.1(0.673)	TWC	20 (68)	Ductile	12.8 (55)
CISE-d	18.8 (0.740)	TWC	20 (68)	Ductile	15.5 (60)
GEAP	11.0 (0.432)	TWC	20 (68)	Ductile initiation, brittle propagation	4.4 (40)
DTRC	14.0 (0.55)	TWC	51.7 (125)	Ductile	7.2 (45)

Table E.6 Circumferentially cracked ferritic pipe test results and comparison to minimum temperature for ductile fracture

Ref.	Material	Full-size Charpy 85% SATT transition temperature °C (°F)	Thickness, mm (inch)	Flaw type	Test temperature °C (°F)	Result	Predicted FITT with adjustment for actual Charpy data °C (°F)
NUPEC-a	STS 42	<20 (<70)	9.14 (0.36)	TWC	20 (68)	Ductile	-35 (-31)
NUPEC-b	STS 42	<20 (<70)	8.79 (0.346)	SC a/t=0.5	20 (68)	Ductile	-65 (-85)
NUPEC-c	STS 42	<20 (<7)	19.00 (0.748)	SC a/t=0.5	20 (68)	Ductile	-45.5 (-50)
Kiefner[i]	API X60	20 (70)	9.14 (0.360)	SC a/t=0.5	-62 (-80)	Ductile	-65.6 (-86)
MPA	German ferritic pipe	0°C (32)[ii]	8.00 (0.315)	SC a/t=0.5	20 (68)	Ductile	-87.2 (-125)
JAERI-a	STS42	<20 (<70)[iii]	10.6 (0.429)	TWC	20 (68)	Ductile	-29.4 (-21)
JAERI-b	STS42	<20 (<70)[iv]	10.6 (0.419)	SC a/t=0.5	20 (68)	Ductile	-51.7 (-61)
DP^{3}II	API X65	-40 (-40)	15.9 (0.625)	TWC	-7 (20)	Ductile	-146 (-230)
Short Crack	A53-weld	-80 (-112)[iv]	6.02 (0.237)	SC a/t=0.6	20 (68)	Ductile	-181 (-293)
Sugie-HT	Grade B	-15 (5)[v]	9.5 (0.375)	SC a/t=0.5	-135 (-211)	SC FITT	-99 (-146)
Sugie-SR	Grade B	-20 (-4)[v]	9.5 (0.375)	SC a/t=0.5	-196 (-320)	Ductile	-104 (-155)

(i) Results in Figure E.37. Charpy calculated from DWTT. Transition temperature 27.8°C (50°F) lower than A106B for this steel.

(ii) ¾ thickness Charpy specimens – transition temperature 41.6°C (75°F) lower than A106B for this steel (accounting for Charpy specimen size). Unpublished data form Dr. Karl-Heinz Herter.

(iii) Using the NUPEC STS42 data.

(iv) ¼-thickness specimen in weld metal.

(v) Original data from 2/3-thickness Charpy tests. Correction to full-thickness specimen made. Accounted for actual material Charpy transition temperature for predicted surface-crack FITT.

The Charpy impact data, like that shown in Figure E.44, is based on a standardized test method; however, the thickness of the test specimens is dependent on the source material. As a result, sub-sized specimens are frequently required to characterize thin-walled pipe. The reasonable bounds on the Charpy 85 percent shear area transition temperature for typical nuclear ferritic pipe base metals and weld metals should be explored further before a general trend can be used for those grades of steel. Figure E.46 shows Charpy data from PIFRAC for A516 Grade 70 base metal and welds, and Figure E.47 shows Charpy data for A106B welds (also from PIFRAC). It is encouraging that the welds had a lower 85 percent transition temperature than the base metals, and the limiting case was the A106B base metal (Figure E.44).

The offset used to shift the transition temperature from propagation (FPTT) to initiation (FITT) for a through-wall crack was based on only two full-scale pipe experiments on X-52 material. The similitude between the FITT for the through-wall crack and bend-bar or C(T) specimens was also verified by only one set of pipe tests on line-pipe steel. These are steps in the analysis that could use further validation.

Likewise, the transition temperature shift from the TWC to the surface-crack pipe behavior as a function of crack depth was based on results from non-standard laboratory tests of X-42 and X-60 steel that are believed to be representative of the constraint in surface-cracked pipe. Further validation of this assumption is needed.

To validate the general Option 3 procedure, and several of the assumptions used, a series of specimen and surface-cracked pipe tests were conducted in this program and will be discussed next. These tests involved:

- Charpy tests (L-C orientation) at various temperatures on that same material,
- Modified DWTT specimens (L-C orientation) at various temperatures (full-thickness of pipe but with shorter ligaments due to pipe curvature – the dynamic tear test (DTT) was used instead of the DWTT – ASTM Standard E604),
- C(T) specimens (L-C orientation) at various temperatures,
- SEN(T) tests (L-R orientation) at various temperatures, and
- 6-inch diameter Schedule 120 A106 B pipe with circumferential surface cracks (fatigue sharpened) in the base metal at various temperatures.

This preliminary investigation of the general trend curve for determining the FITT for a surface crack from A106B Charpy data is encouraging since most the Class 2/3/BOP piping would be less than 25-mm (1.0-inch) thick and have a minimum operating temperature above 10°C (50°F). Furthermore, the A106B base metal appears to be a limiting case when compared to existing data for A516 Grade 70 base metal and weld metal data for these two pipe materials. Nevertheless, before these results are used, a larger database of ferritic nuclear pipe Charpy data and weld metal data are needed, as well as a statistical evaluation (rather than using average trend curves), and validation of all the steps in the procedure is needed. Preliminary validation tests were conducted in the BINP program as discussed next. Nevertheless, it is encouraging that the upper-shelf EPFM analyses in the ASME Appendix H can probably be used for most practical Class 2/3/BOP piping ferritic base metals.

E.2.7 Validation of Methodology

In order to validate this methodology for predicting the FITT of a surface-cracked pipe from the 85-percent shear area transition temperature from Charpy specimen tests, a series of Charpy, dynamic tear test (DTT), compact (tension), single-edge-notch [tension] (SEN(T)), and full-scale surface-cracked pipe experiments were conducted. The test specimens used in all of these tests came from two lengths of 6-inch nominal diameter, Schedule 120, A106 Grade B pipe that came from the same heat. The Battelle pipe identification numbers for these two lengths of pipe were DP2-F93 and F94.

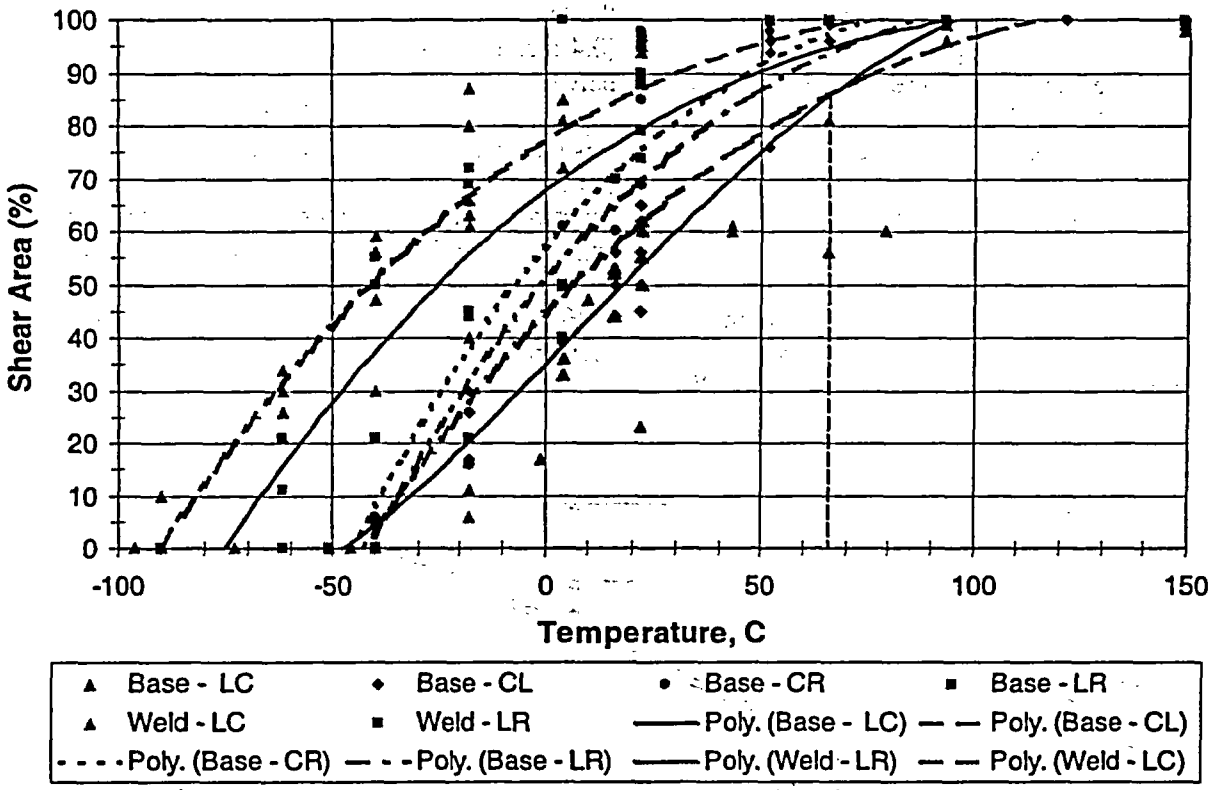

Figure E.46 Charpy data from PIFRAC for A516 Grade 70 pipe and welds

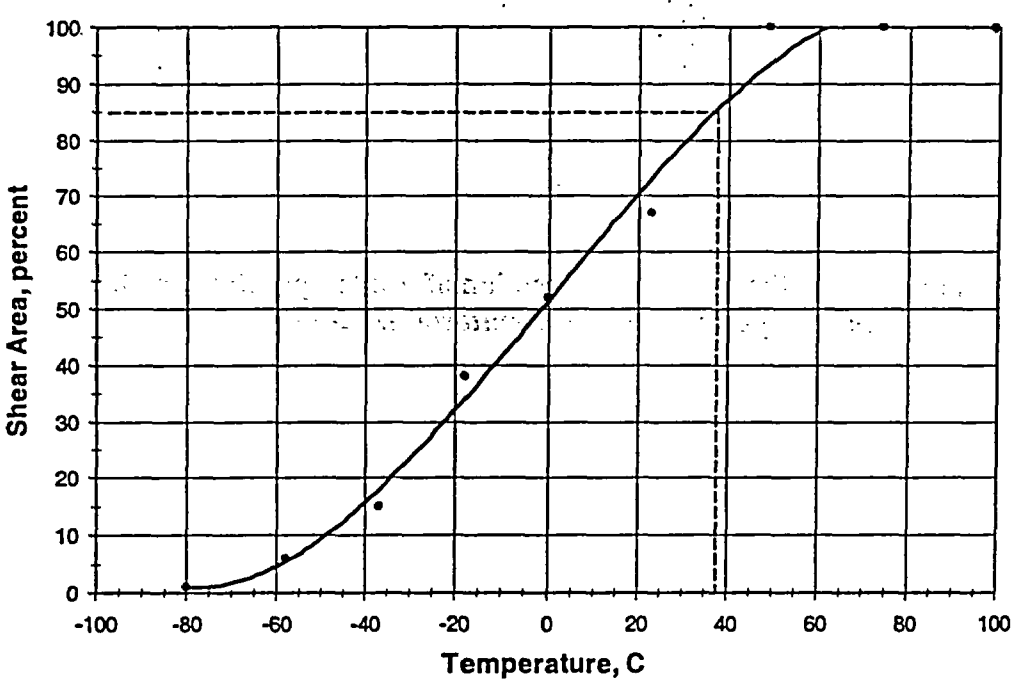

Figure E.47 Charpy data from PIFRAC for one A106B pipe weld

Figure E.48 is a plot of the shear area percent from a series of Charpy specimen tests as a function of the test temperature for both lengths of pipe, i.e., DP2-F93 and F94. From Figure E.48 one can see that the 85-percent shear area transition temperature for both lengths of pipe was approximately 58 C (136 F).

The next series of tests conducted were the dynamic tear tests (DTT). The test specimens for these tests were machined from the pipe without flattening. As such, the maximum wall thickness achievable was approximately 10 mm (0.4 inches). Based on Figure E.43, the FPTT 85-percent shear area transition temperature for this specimen geometry for this specimen thickness for this material should have been approximately 44 C (111 F). Figure E.49 is a plot of the shear area as a function of the test temperature for these DTT. As can be seen in Figure E.49, the actual measured 85-percent shear area transition temperature of 54 C (130 F) was approximately 10 C (19 F) warmer than anticipated.

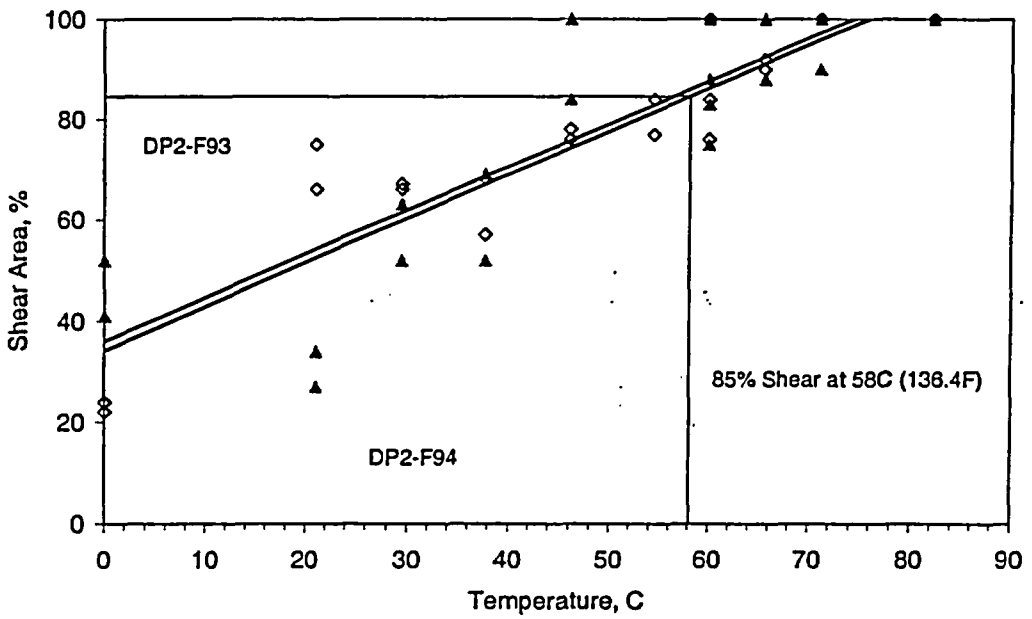

Figure E.48 Shear area as a function of test temperature for the Charpy specimen tests for material DP2-F93 and F94

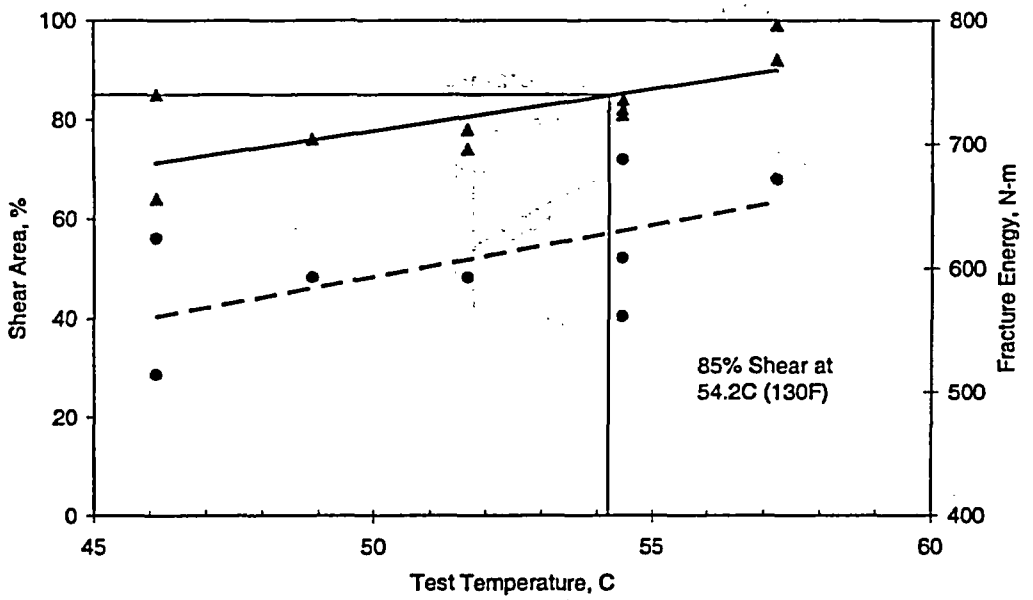

Figure E.49 Shear area as a function of test temperature for the DTT specimen tests for material DP2-F93 and F94

The next series of tests conducted were the compact (tension) specimen tests. It was anticipated that the transition temperature for these tests would provide an indication of the transition temperature for a through-wall cracked pipe. Based on Figures E.34 and E.35 it was anticipated that there would be a shift in the transition temperature of approximately 33 to 50 C (60 to 90 F) between the DTT specimen results and these compact (tension) specimen results. Based on the anticipated shift in transition temperature between the compact (tension) and the actual Charpy data, accounting for the anticipated shift between the DTT and the actual Charpy data, the transition temperature for these compact (tension) specimen tests was anticipated to be between 11 C (51 F) and -6 C (21 F). Figure E.50 is a plot of the load versus displacement records for eight compact (tension) specimen tests conducted as part of this effort. As can be seen from Figure E.50, even at a test temperature of -32 C (-26 F), there still was some evidence of ductile crack initiation for these compact (tension) specimen tests.

The last series of laboratory specimen tests was the SEN(T) specimen tests. Due to the similitude in the constraint conditions between the SEN(T) specimen geometry and the surface-cracked pipe geometry, it was thought that this specimen geometry would provide the most direct indication of the transition temperature

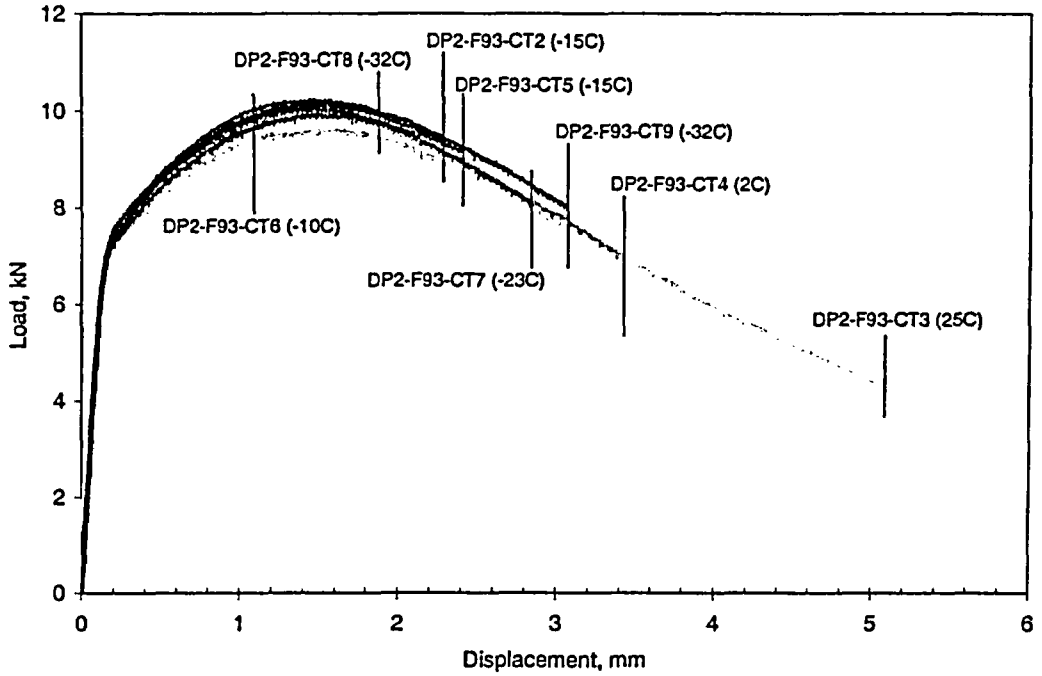

Figure E.50 Load versus displacement records for compact (tension) tests

for the actual surface-cracked pipe. For a surface crack which is 50 percent of the pipe wall thickness in depth, which is the crack depth used in both the SEN(T) and surface-cracked pipe tests, one would expect a 33 C (60 F) shift in transition temperature between the 3-point bend bar specimen geometry and the surface-cracked pipe geometry, see Figure E.40a. Since the 3-point bend bar specimen geometry is thought to provide similar constraint as a compact (tension) specimen and a through-wall-cracked pipe, one would expect a similar shift in transition temperature between those specimen geometries and a surface-cracked pipe. Thus, on the basis of the measured Charpy data alone and the analysis method developed as part of this effort, one might expect that the transition temperature for a surface-cracked pipe, or SEN(T) specimen, may be in the range of -23 C (-9 F) to -39 C (-39 F). Figure E.51 is a plot of the load versus actuator displacement data for these SEN(T) specimen tests. Each test appeared to initiate in a ductile manner followed by unstable brittle fracture. Figure E.52 is a plot of the ductile crack growth as a function of test temperature. As can be seen in Figure E.52, with the exception of one specimen, the data is fairly well grouped showing a general trend of decreasing ductile crack growth with decreasing test temperature. Based on the trends in Figure E.52 one might argue that one might reach the point of brittle fracture initiation for these SEN(T) specimens in the range of -50 to -60 C (-58 F to -76 F), which is approximately 25 C (45 F) colder than what one might have expected based on the measured Charpy specimen transition temperature and the methodology developed as part of this effort.

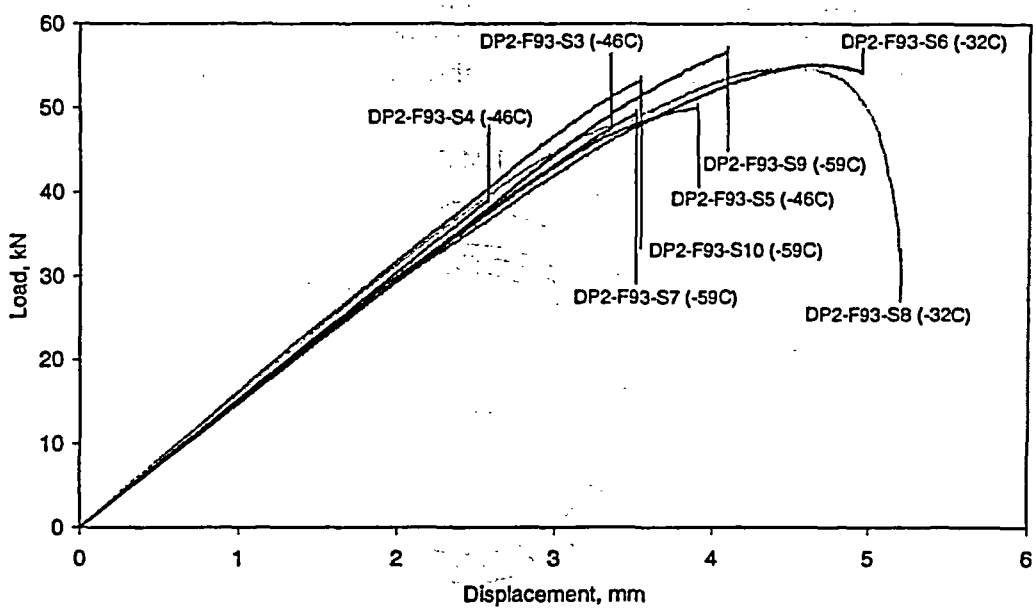

Figure E.51 Load versus actuator displacement data for the SEN(T) specimens

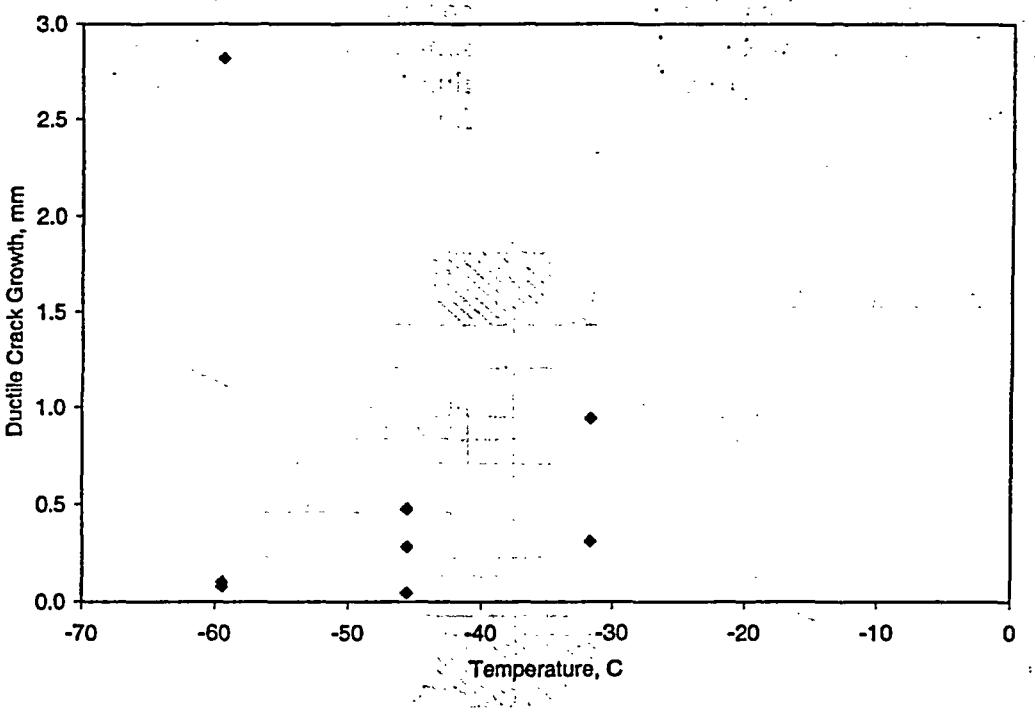

Figure E.52 Ductile crack growth as a function of temperature for the SEN(T) specimens

As a final measure of the validity of this methodology, three surface-cracked pipe experiments were conducted using this pipe material. In each case the crack was an external surface crack, approximately one-third around the pipe circumference in length and half way through the wall thickness in depth, see Figure E.53.

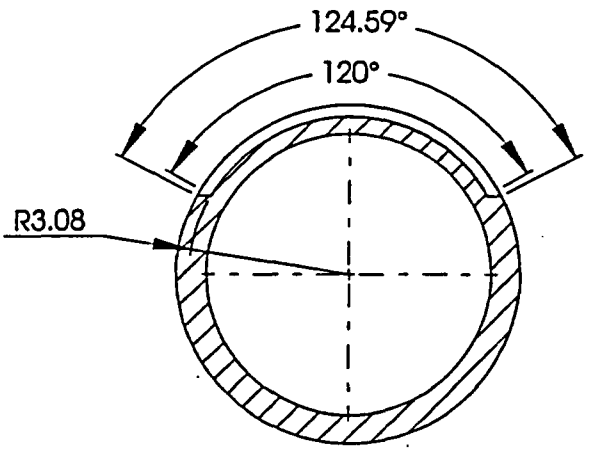

Figure E.53 Crack geometry for the surface-cracked pipe experiments

Figures E.54 and E.55 show schematics of the loading fixtures and cooling apparatus, respectively, for these three pipe experiments. The pipes were cooled by circulating Syltherm XLT, a Dow Chemicals Heat Transfer Fluid, through the pipe using a circulation pump. Copper tubes containing the fluid were coiled and submersed in a cooling bath of this same fluid with dry ice pellets added to cool the fluid.

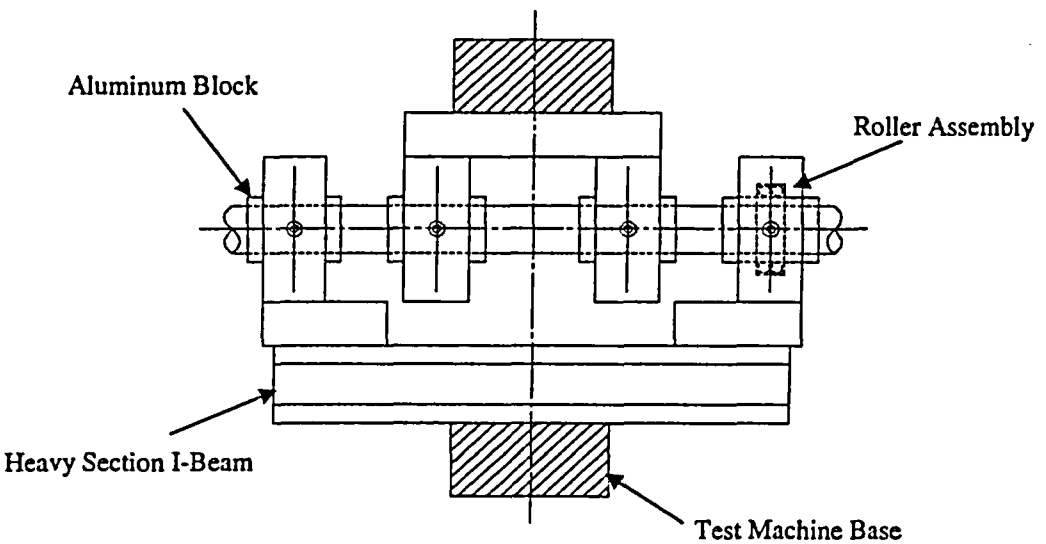

Figure E.54 Loading fixture used in the surface-cracked pipe experiments

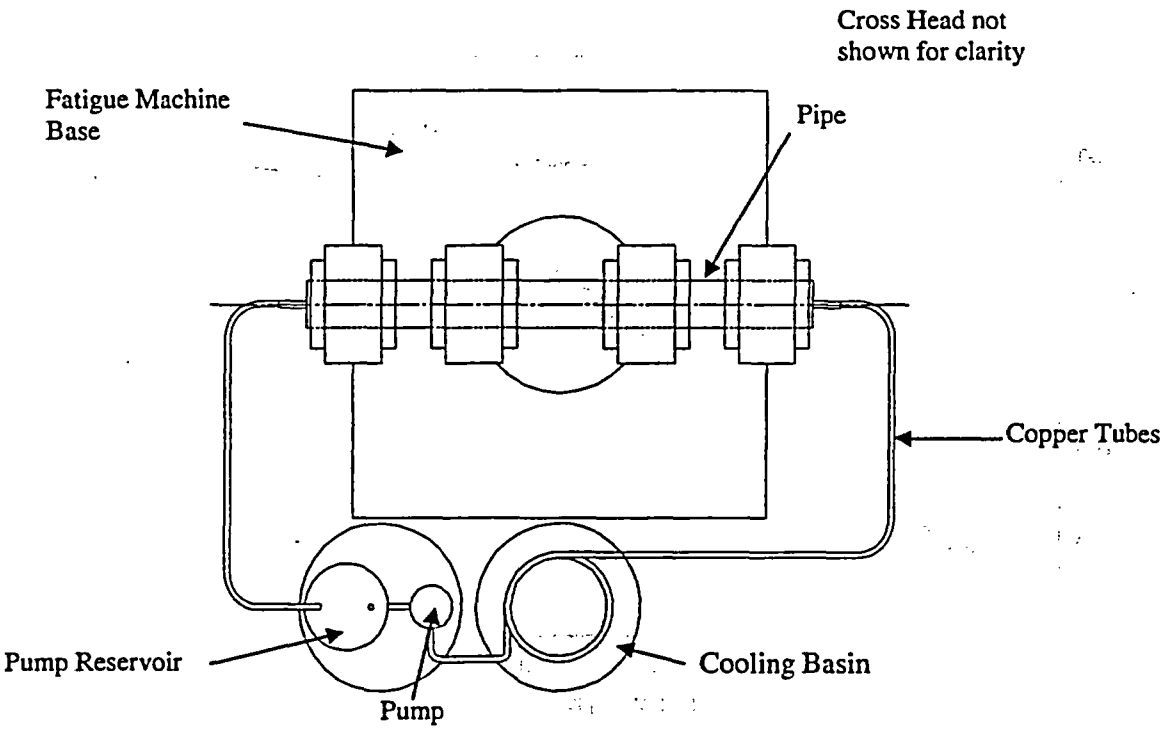

Figure E.55 Cooling apparatus used in the surface-cracked pipe experiments

Figure E.56 is plot of the load versus displacement records for the three surface-cracked pipe experiments. As can be seen, the test temperatures for these three experiments were -59 C (-75 F), -46 C (-50 F), and -32 C (-25 F). Both the load and displacement decreased as the test temperature decreased. The amount of ductile crack growth, prior to the final brittle fracture, was minimal for each of these experiments. In order to make an assessment of the transition temperature for these three surface-cracked pipe experiments, the maximum moment normalized by the calculated Net-Section-Collapse (NSC) moment was plotted against the test temperature, see Figure E.57. As can be seen in this figure the relationship between the ratio of M_{max}/M_{NSC} and the test temperature is very linear. The point on the graph where the straight line fit through the data reached a value where this ratio was equal to 1.0 was called the transition temperature. Based on this assessment, the transition temperature for these surface-cracked pipe experiments was -36 C (-33 F). This estimate of the actual surface-cracked pipe transition temperature is within the range of what one might expect the transition temperature to be based on the actual Charpy data and the analysis method developed as part of this effort, i.e., -23 C (-9 F) to -39 C (-39 F). Thus, even though some of the individual steps in the methodology (e.g., the shifts between the Charpy to the DTT transition temperatures and the DTT to the compact (tension) specimen transition temperatures) appeared to overpredict the transition temperature shift, the bottom line assessment of the transition temperature for a surface cracked pipe using only the measured Charpy 85-percent shear area transition temperature appears reasonable. In summary, Table E.7 provides a synopsis of the methodology and how the experimental data agreed with the anticipated transition temperatures for each specimen geometry.

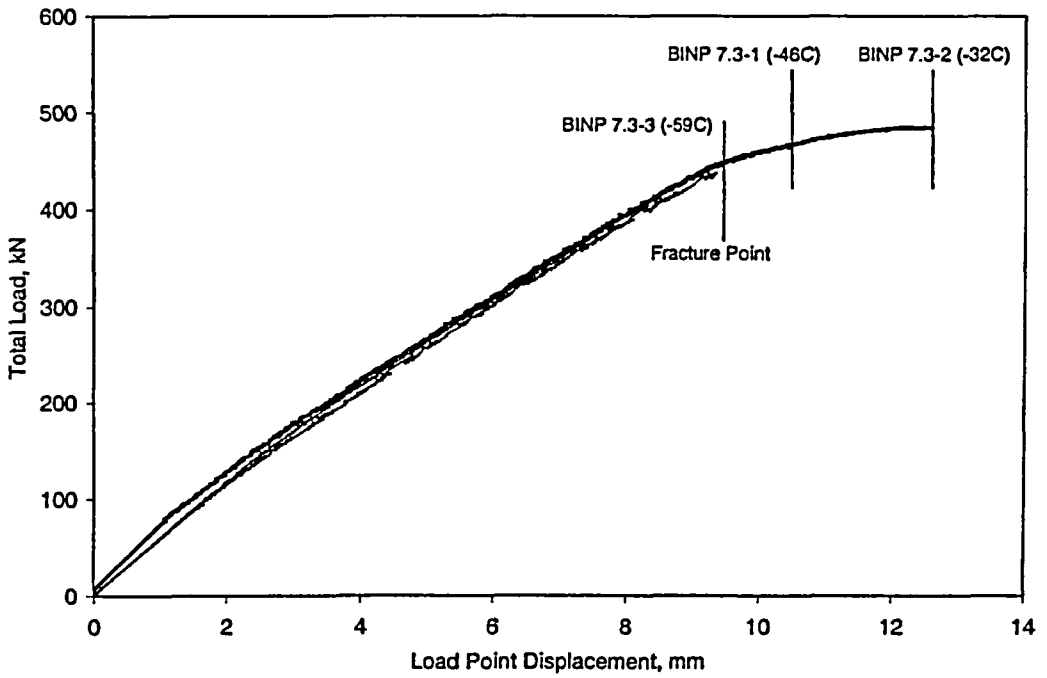

Figure E.56 Load versus displacement records for the three surface-cracked pipe experiments

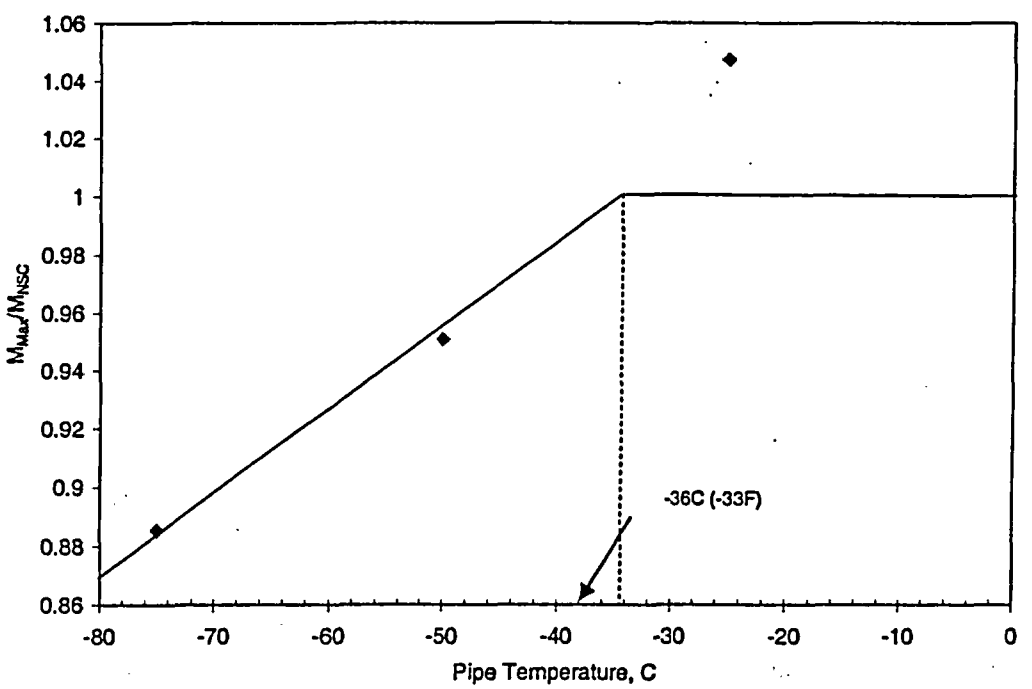

Figure E.57 Plot of the ratio of the maximum experiment moment normalized by the Net-Section-Collapse moment (M_{max}/M_{NSC}) as a function of the test temperatures for the three surface-cracked pipe experiments

Table E.7 Summary of the methodology and how the experimental data agreed with the anticipated transition temperatures for each specimen geometry

Specimen Geometry	Anticipated Transition Temperature, C (F)	Basis for Estimate of Transition Temperature	Actual Transition Temperature, C (F)
Charpy specimens			58 (136)
Dynamic Tear Tests	44 (111)	14 C (25 F) shift in transition temperature for 10 mm (0.4 inch) thick specimen	54 (130)
Compact (tension)	11 (51) to -6 (21)	33 to 50 C (60 to 90 F) shift in transition temperature between drop-weight-tear test results and 3-point bend specimen results	< -32 (-26)
SEN(T)	-23 to -39 (-9 to -39)	33 C (60 F) shift in transition temperature between 3-point bend specimen and 50% deep surface crack	-50 to -60 (-58 to -76)
Surface cracked pipe	-23 to -39 (-9 to -39)	33 C (60 F) shift in transition temperature between 3-point bend specimen and 50% deep surface crack	-36 (-33)

E.3 References

E.1 Anderson, T. L., "Stress Intensity Solutions for Surface Cracks and Buried Cracks in Cylinders, Spheres, and Flat Plates," prepared for The Materials Properties Council, Inc., March 2000.

E.2 Chapuliot, S., and Lacire, M. H., "Stress Intensity Factors for External Circumferential Cracks in Tubes Over a Wide Range of Radius Over Thickness Ratios," PVP Vol. 388, 1999.

E.3 *"NRCPIPES" Windows Version 3.0 – User's Guide*, April 30, 1996, Battelle document to 2nd IPIRG group, Contract NRC-04-91-063.

E.4 Scott, P. M., and Ahmad, J., "Experimental and Analytical Assessment of Circumferentially Surface-Cracked Pipes Under Bending," NUREG/CR-4872, April 1987.

E.5 Krishnaswamy, P., Scott, P., Mohan, R., Francini, S., Choi., Y. H., Brust, F., Kilinski, T., Ghadiali, N., Marschall, C., and Wilkowski, G., "Fracture Behavior of Circumferentially Short-Surface Cracked Pipe," NUREG/CR-6298, November 1995.

E.6 Brust, F. W., "Approximate Methods for Fracture Analyses of Through-Wall Cracked Pipes," NUREG/CR-4853, February 1987.

E.7 Brust, F., Scott, P., Rahman, S., Ghadiali, N., Kilinski, T., Francini, R., Marschall, C., Miura, N., Krishnaswamy, P., and Wilkowski, G., "Assessment of Short Through-Wall Circumferential Cracks in Pipes – Experiments and Analyses," NUREG/CR-6235, April 1995.

E.8 Kurihara, R., and others, "Estimation of the Ductile Unstable Fracture of Pipe with a Circumferential Surface Crack Subjected to Bending," *Nuclear Engineering and Design*, Vol. 106, pp. 265-273, 1988.

E.9 Mohan, R., Wilkowski, G., Bass, B., and Bloom, J., "Finite Element Analyses to Determine the R/t Limits for ASME Code Case N-494 FAD Curve Procedure," PVP Volume 350, pp. 77-88, July 1997.

E.10 Wilkowski, G. M., and others, "Degraded Piping Program – Phase II," Summary of Technical Results and Their Significance to Leak-Before-Break and In-Service Flaw Acceptance Criteria, March 1984 – January 1989, NUREG/CR-4082, Vol. 8, 1989.

E.11 Kanninen, M. F., and others, "Mechanical Fracture Predictions for Sensitized Stainless Steel Piping with Circumferential Cracks," EPRI Report NP-192, September 1976.

E.12 ASME Boiler and Pressure Vessel Code, Section XI, Rules for Inservice Inspection of Nuclear Power Plant Components, 1955 Edition, July 1995.

E.13 DWTT test procedures are given in both American Society of Testing and Materials (ASTM) Standard E436 and American Petroleum Institute (API) Recommended Practice 5L3.

E.14 DWT-NDT test procedures, ASTM E-208.

E.15 Maxey, W.A., Kiefner, J.F., and Eiber, R.J., "Brittle Fracture Arrest in Gas Pipelines", Report to Pipeline Research Committee of American Gas Association, July 1975.

E.16 Eiber, R.J., "Fracture Propagation", Symposium in Line Pipe Research, Pipeline Research Committee of American Gas Association, Section I, Dallas, Texas, November 1969.

E.17 Kiefner, J.F., "Fracture Initiation", Symposium in Line Pipe Research, Pipeline Research Committee of American Gas Association, Section G, Dallas, Texas, November 1969.

E.18 Podlasek, R. J., and others, "Predicting the Fracture Initiation Transition Temperature in High Toughness, Low Transition Temperature Line Pipe With the COD Test," ASME Journal of Engineering Materials and Technology, pp. 330-334, October 1974.

E.19 Sugie, E., Kudo, J., Kataoka, Y., Ohtani, T., "Influence of Thermal Stress Relieving on

Fracture Toughness of UOE Pipe", UTR-79019, Kawasaki Steel Corporation, Chiba, Japan, January 1979.

E.20 Wilkowski, G.M., Barnes, C.R., Scott, P.M., Ahmad, J., "Development of Analyses to Predict the Interaction of Fracture Toughness and Constraint Effects for Surface Cracked Pipe", Report to Welding Supervisory Committee of American Gas Association, April 1985.

E.21 Wilkowski, G. M., and others, "Degraded Piping Program - Phase II," Summary of Technical Results and Their Significance to Leak-Before-Break and In-Service Flaw Acceptance Criteria, March 1984 - January 1989, NUREG/CR-4082, Vol. 8, March 1989.

E.22 "PVRC Recommendations on Toughness Requirements for Ferritic Steels," WRC Bulletin 175, August 1972.

E.23 Ghadiali, N., and Wilkowski, G. M., "Fracture Mechanics Database for Nuclear Piping Materials (PIFRAC)," in Fatigue and Fracture - 1996 - Volume 2, PVP-Vol. 324, July 1996, pp 77-84. (Also on Pipe Fracture Encyclopedia CD-ROM set given to IPIRG-2 members.)

APPENDIX F

THE DEVELOPMENT OF A J-ESTIMATION SCHEME FOR CIRCUMFERENTIAL AND AXIAL THROUGH-WALL CRACKED ELBOWS

F.1 INTRODUCTION

Leak before break (LBB) considerations for pipe fittings such as tee joints and elbows have not been investigated in detail to date. Reference F.1 presented the development of a surface crack estimation scheme for elbows. These solutions were then used to investigate the possibility of using simple influence functions, based on ASME Section III stress indices, along with existing straight pipe solutions, to predict the fracture response of a surface-cracked elbow. The use of this small database of influence functions, combined with existing straight pipe J-estimation methods showed promise in predicting the fracture response of the surface-cracked elbows.

However, in order to perform LBB sensitivity studies on fittings, such as elbows, TWC solutions must be available. With the TWC elbow solutions available, one can investigate the feasibility of using influence functions and straight pipe TWC solutions to predict the LBB behavior of fittings. The main purpose of this effort is to provide a new J-estimation scheme for TWC elbows. Both circumferential and axial cracks are considered. In addition, crack-opening displacements can be estimated so that LBB considerations can be assessed.

F.2 BACKGROUND ON PIPING J-ESTIMATION SCHEMES

The nuclear industry has traditionally taken the lead in the development of J-estimation schemes to allow engineers to make estimates of the fracture behavior of nuclear piping components. These J-estimation schemes have permitted engineers to make simple fracture assessments of planar component geometries (Ref. F.2), through-wall-cracked (TWC) pipes (Ref. F.3), as well as surface-cracked (SC) pipe (Ref. F.4). This early work sometimes had inaccuracies implicit within the solutions, in part due to the fact that the finite element methods used at that time were not quite fully developed, nor as robust as today's' numerical tools.

Corrections and improvements to pipe fracture J-estimation schemes were made subsequent to this original work. References F.5 and F.6 represent the development of alternative J-estimation schemes for TWC pipe which are not based on the compilation of a series of numerical solutions; rather these solutions were developed from making certain geometric assumptions. References F.7 and F.8 are similar non-finite element based J-estimation schemes for surface cracked pipe. References F.9 and F.10 represent the improvements and corrections to the original numerical solutions using improved numerical finite element techniques (compared with the original solutions) and permitted pipes with "small" cracks to be more accurately modeled. In addition, some of these methods were specifically developed to account for cracks in welds (Refs. F.8 and F.11). References F.8 to F.12, and many references cited therein, summarize many of these methods, both numerical and engineering based, and compare predictions to full-scale experimental test data.

The J-estimation schemes discussed above were appropriate for cracked pipe. Fracture estimates for more complicated geometries, such as pipe fittings, had to be performed on a case-by-case basis using finite element analysis. These analyses are time consuming, often requiring significant resources, and the results are only appropriate for the specific geometry and material considered. As such, the development of more general J-estimation schemes for pipe fittings, such as elbows and Tee joints, has begun. A surface crack estimation scheme for axial and circumferential cracked elbows was developed in Reference F.1.

The purpose of this effort is to develop a J-estimation scheme for axial and circumferential through-wall cracks in elbows. Solutions are compiled for the pure pressure, combined pressure and bending, and pure bending cases. However, before presenting these solutions, it is first instructive to discuss some unique features associated with fracture of elbows, which are not necessarily intuitive based on experience with straight pipe. Many of these anomalies are associated with the way that elbows ovalize.

F.3 GENERAL OVERVIEW OF DEFORMATION AND FRACTURE RESPONSE OF ELBOWS

F.3.1 Geometry

The geometry of the cracked elbows considered here is illustrated in Figure F.1. We are interested in estimating J and crack opening displacement (COD) for both circumferential and axial 'flank' cracks. The ratio of $R_{el}/R_m = 3$ here represents a long radius elbow. The loading cases considered are pure pressure, pure bending, and combined pressure and bending. The pressure loading turns out to be very important consideration for elbows. Note that the outer length of the elbow [i.e. $(R_{el} + R_m/2) * \psi$] is greater than the inner length of the elbow [i.e. $(R_{el} - R_m/2) * \psi$]. From the free body diagram alone, this means that the integrated pressure along the outer length of the elbow is greater than that along the inside of the elbow, i.e., there is a net outward force that must be equilibrated by the end cap pressure T (see Figure F.1). This means that, due to pressure alone, the elbow wants to straighten out. Therefore, for the cases of pressure and combined pressure and bending, both the pressure and end cap tension must be applied. This is not the case for a straight pipe, where the pressure can be neglected when developing J-estimation schemes for circumferential cracks. It turns out that the effect of pressure also has an important effect on the ovalization of the elbow, which in turn, affects the J- and COD- solutions.

F.3.2 Solution Procedure

Figure F.2 shows a typical finite element mesh that was used for the analyses. Figure F.2(a) shows an example of a 90-degree circumferential crack in an elbow. A quarter model, with symmetry about the plane of the crack and a symmetry plane about the half crack length, θ, was used to simplify the analyses. As seen in Figure F.2, a long length of straight pipe, equal to L = 9 D (with D the diameter), was included in the model. At the end of the length of pipe, a series of very stiff beams were attached to the pipe, which met at a point node at the center of the pipe. The bending moment, M, was applied at this node. The length, 9D, was determined by performing a series of mesh sensitivity studies. This technique simplified the analysis procedure, the reduction of data, and assured that the elbow solutions were not distorted by end effects. Figure F.2(b) shows a typical mesh for a 15-degree axial crack. For the axial cracks, half symmetry models were used. For both circumferential and axial cracks, pressure along the entire inside pipe and elbow surfaces were included along with end cap pressure at the end of the long length of straight pipe.

The ABAQUS commercial finite element package was used for all analyses. The 20-node isoparametric brick element was used for all solutions. A deformation theory plasticity model was used, although, as will be seen later, flow theory was used for some of validation studies. Because the ABAQUS deformation solution procedure includes the elastic strains, each solution was monitored and considered complete (i.e., fully plastic) when the plastic strain at each integration point became greater than ten times the elastic strain. As an independent check on the adequacy of the fully plastic solution, the h-functions (see next section), were plotted as a function of load at each load step in the analysis. Typically, h reached a constant, converged value long before the analysis was automatically completed using the criteria discussed above. The compilations of h-functions were performed using one element through the thickness, as illustrated in Figure F.3. However, as seen in Figure F.3(b) several solutions were performed using a mesh with four elements through the thickness. The average J-integral, and COD, solutions for the four elements through the thickness mesh compared well with the results for the one element mesh. It is noted that there is a variation of J through the thickness, especially for the axial flank cracks, but the use of one, average value for J, is adequate for engineering estimation purposes. An extensive mesh sensitivity study was performed to ensure adequate solution convergence. The procedure was also validated by comparing results for known straight pipe solutions. Because of the use of parabolic elements, the values of J for the

one element through the thickness meshes (Figure F.3(a)) were calculated using:

$$J_{AVG} = J_I + 4J_M + J_O \quad \text{(F.1)}$$

where J_I is the value of J at the inner surface node at the crack, J_M is J at the mid side node, and J_O is J at the outside node.

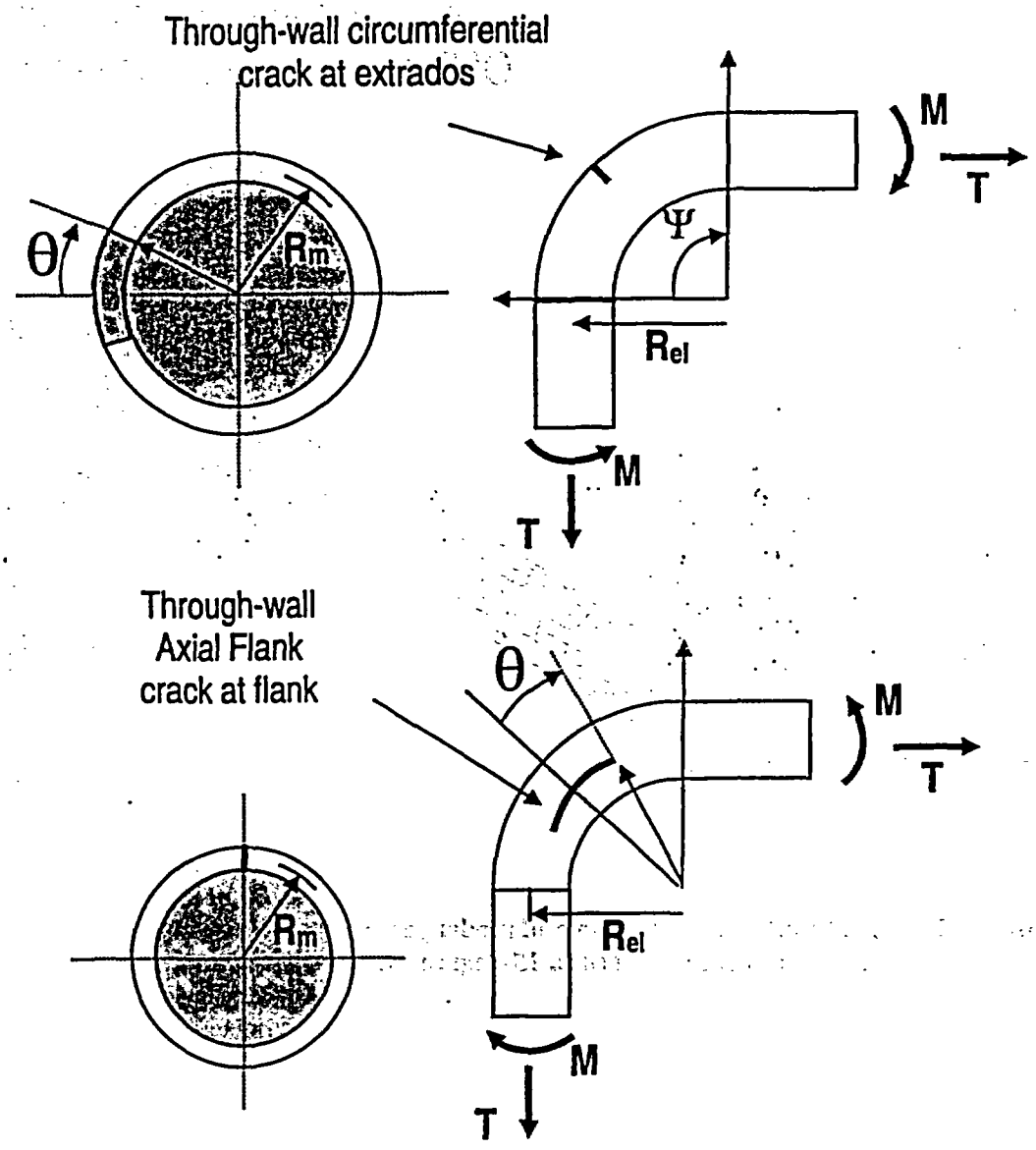

Figure F.1 Crack geometries considered for elbows

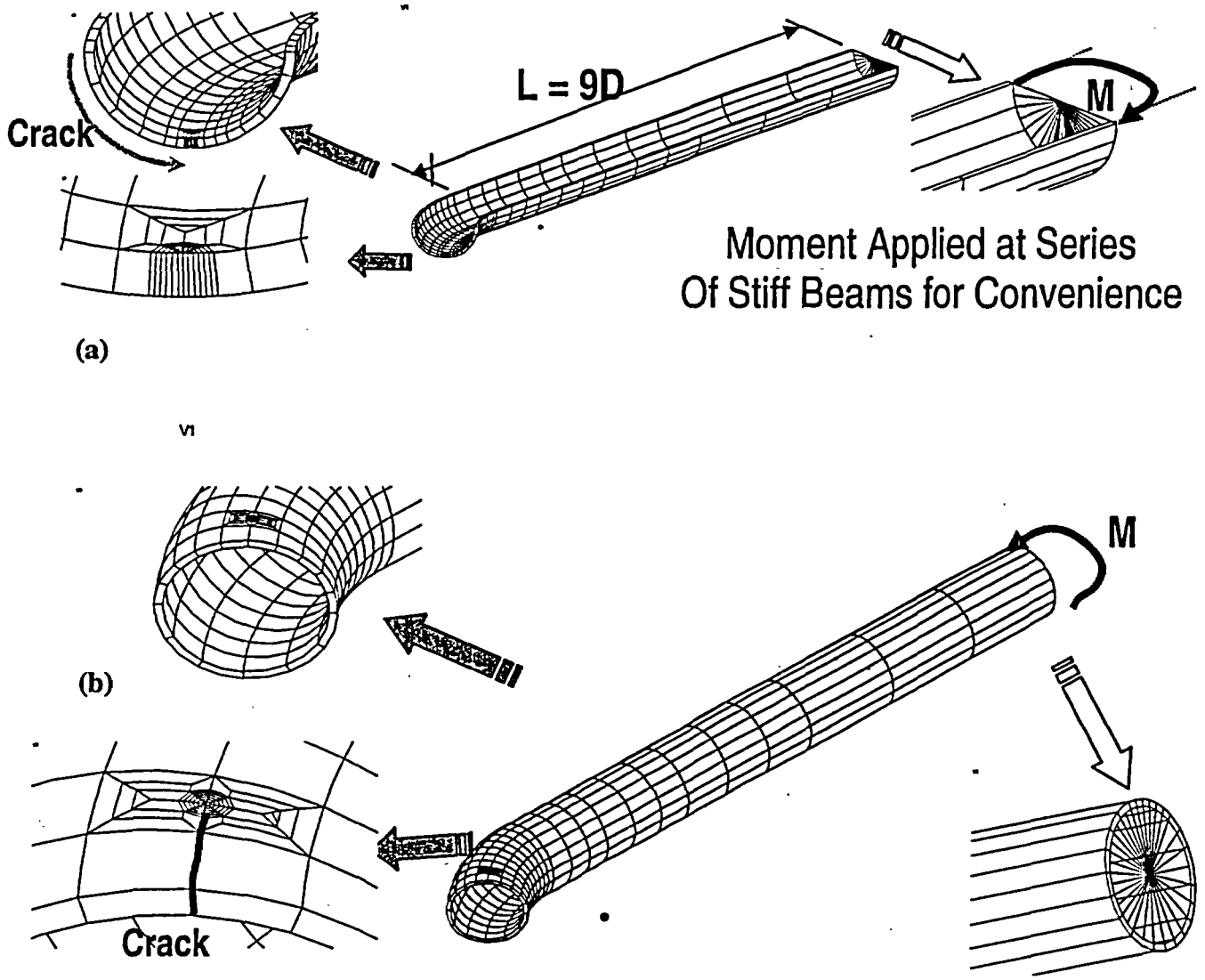

Figure F.2 Typical finite element mesh and model geometry for (a) a 90-degree circumferential crack and (b) a 15-degree axial flank crack

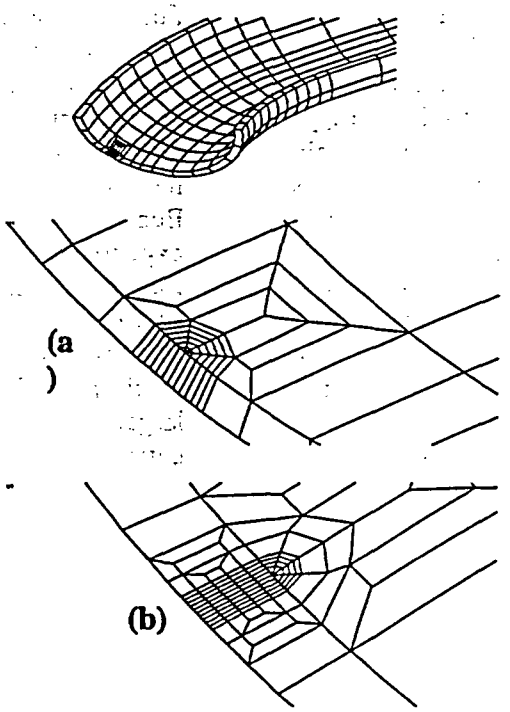

Figure F.3 Typical mesh (circumferential crack, 45-degree crack) (a) one element through thickness and (b) four elements through thickness

F.4 OVALIZATION EFFECTS ON ELBOW FRACTURE

F.4.1 Circumferential Cracks

The ovalizations induced in elbows that are subjected to bending loads turns out to have an important effect on the predicted J-integral, crack opening displacements, and fracture response. Consider the simple example of Figure F.4. In the upper plot (Figure F.4(a)), an illustration of a circumferentially cracked elbow subjected to a closing moment is shown. Intuitively, an elbow closing moment would be expected to open the crack, similar to what occurs in a straight length of pipe subjected to a crack opening moment. The illustration to the right in Figure F.4(a) shows a deformed plot caused by the applied moment. The shaded areas represent contour plots of the crack opening stress and the numbers represent normalized stress (normalized with yield stress). For this elastic case, the magnitude of the stresses is not important. Notice that the stresses are negative ahead of the crack. For the illustration in Figure F.4b, the moment was applied in the opposite direction, i.e., an elbow opening moment. For this case, a low level of tension exists ahead of the crack tip despite the fact that the moment is attempting to close the crack faces.

The reason for this somewhat surprising behavior lies in the way that the elbow ovalizes due to bending moment. As seen, the closing moment ovalizes the elbow cross section into the shape of an oblate spheroid while the elbow opening moment causes a prolate spheroid deformed shape. The case illustrated in Figure F.4 represents a radius to thickness ratio, $R / t = 20$. The same behavior occurs for $R / t = 5$, i.e. the stiffer case. In fact, for the un-cracked case, an elbow closing moment results in compressive stresses that develop up to an angle of between 20 and 25 degrees at the toe of the elbow, depending on the R / t ratio.

This response is further summarized in Figure F.5. The top illustration summarizes the response to an elbow closing moment. As illustrated, this results in an oblate spheroid type ovalization. As illustrated, one can think of this ovalization as being caused by 'pinching' forces applied along a plane at the center of the crack. This type of ovalization will induce a compressive contribution to the stress state in this region. Hence, there is a competition between the crack closing caused by ovalization, and the opening caused by the global bending load. It turns out that this competition is won by the ovalization component for crack sizes less than 20 to 25 degrees, depending on R / t ratio.

For an elbow opening (or straightening) moment, bottom illustration in Figure F.5, the opposite occurs. The prolate type ovalization component causes crack opening while the global moment closes the crack. This leads to a modest crack opening for smaller crack sizes. Because of this, **circumferential cracks are not expected to develop at the knee of the elbow.** Rather, they are expected to develop for crack size angles on the order of 45 to 90 degrees. The solutions tabulated below are complied for crack sizes of 45 and 90 degrees. For these larger crack sizes, the cracks are open along the entire length.

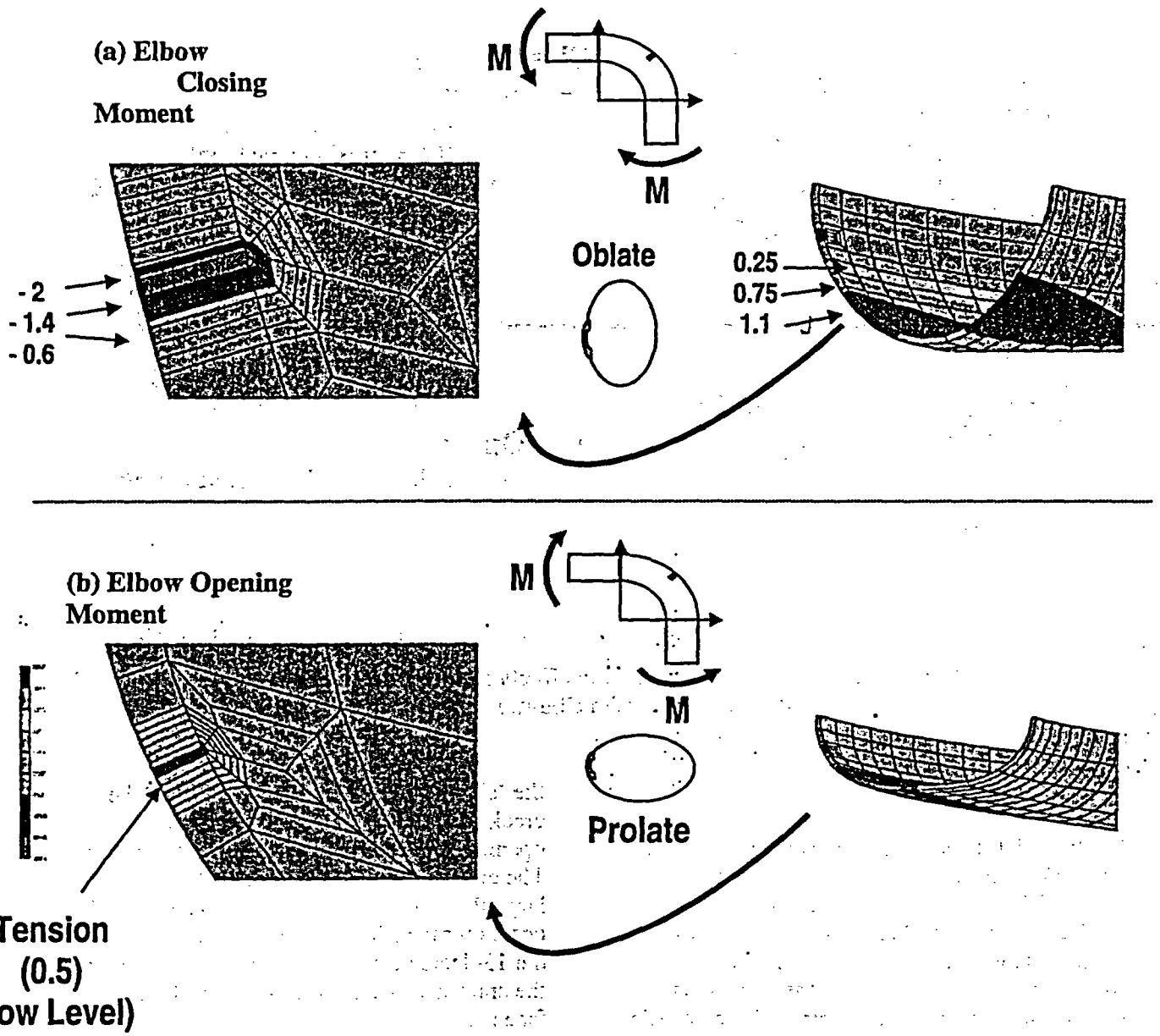

Figure F.4 Illustration of ovalization effects on stresses near the crack tip (Numbers represent crack opening stresses normalized with yield strength)

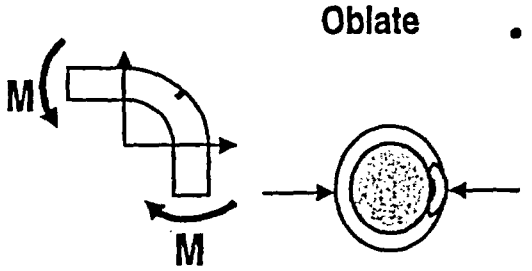

- **Closing Moment**
  - **Additional Compression at Crack**
    - **R/t = 20 (Full Closing)**
    - **R/t = 10 (OD Closing)**
    - **R/t = 5 (Opening - Reduced K or J)**

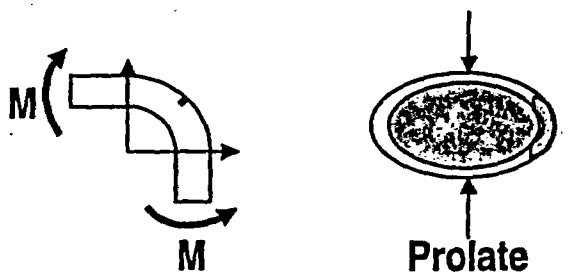

- **Opening Moment**
  - **Additional Tension at Crack**

Figure F.5 Summary of ovalization effects on crack opening response of circumferential cracks in elbows subjected to bending

F.4.2 Axial Cracks

For the axial flank cracks the ovalization effect on crack opening is even more important. Figure F.6 illustrates the response of an axial flank crack, with total crack size angle of 15-degrees, subjected to bending. An elbow straightening moment causes tensile opening stresses in the crack region (this is also an elastic case).

The shaded contours on these plots represent the opening stress, σ_x, and all stress contours in the crack region are tensile. This means that the crack should open. However, it is also seen that the 'oblate' spheroid ovalization causes the crack faces to rotate, with the inner crack opening greater than the outer diameter opening. The example illustrated in Figure F.6 is for the large R / t ratio case of 20. This same behavior occurs for the stiffer R / t = 5 case. In fact, for the 15-degree crack, the outer diameter region of the crack actually closes. Because of this crack face rotation, the crack opening functions were compiled for both the inner and outer surfaces. This 'pinching' of the crack opening along the outer surface should impede leaking, and hence LBB considerations. Hence, for LBB predictions one should account for crack face rotation in the leak rate models.

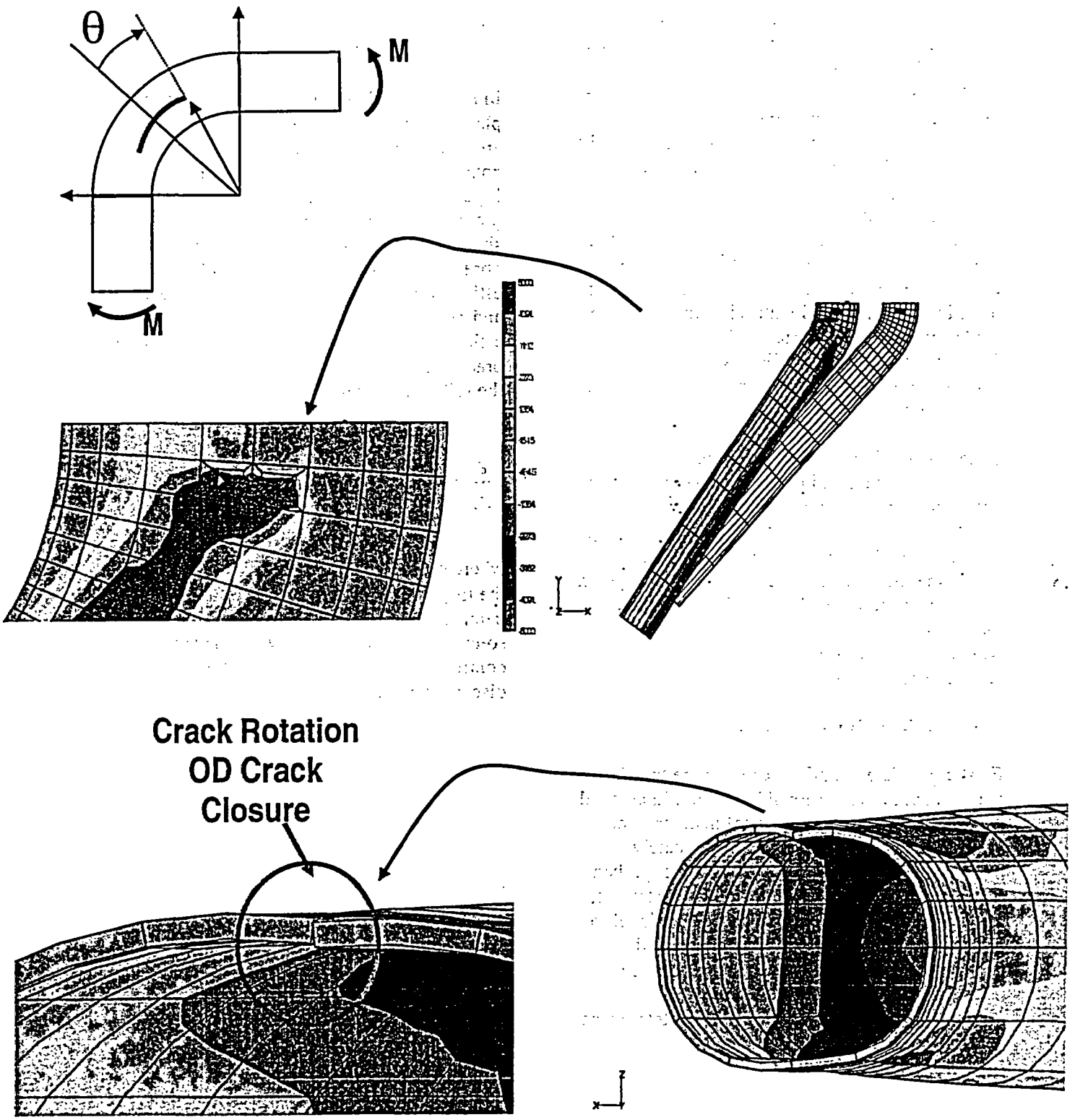

Figure F.6 Illustration of ovalization effects for 15-degree axial flank crack

Figure F.7 illustrates this effect further. Crack opening profile plots are illustrated for the outer diameter (OD), middle surface (MS), and along the inner diameter (ID) for an axial crack subjected to bending alone. In Figure F.7(a), which is for a 15-degree (total) crack angle (i.e. 2θ = 15-degrees – see Figure F.1), the OD predicts negative crack opening. Of course, the negative crack openings are physically impossible, but it means that the crack faces will be closed and contacting each other at the OD. This will impede fluid leakage and affect leak rate calculations. Figure F.7(b) shows similar results for a 30-degree total crack angle. While the closure is not as severe as for the smaller crack, some crack face contact will occur along the OD. The predicted values in Figure F.7 are made assuming an elliptic crack opening shape. It is seen that elliptic profile is still a good approximation for the opening even if the crack faces rotate.

In an actual elbow, which is subjected to combined tension and pressure, the competition between the pressure, which causes opening COD's at both the ID and OD, and the bending, which closes the crack at the OD, will ultimately determine the service opening profile. However, the ovalization induced from elbow bending must be considered in the COD predictions which are then used in leak rate calculations for LBB considerations.

F.5 ESTIMATION SCHEMES

Elastic-plastic estimation schemes are based on the concept of proportional loading. If a cracked body is loaded in a proportional manner, such that the constitutive response is adequately modeled via deformation theory plasticity, then Illyushin has shown that deformations, stresses, and energies (e.g. J-integral) are proportional to a load parameter, material parameters, and geometric quantities. This concept has been overviewed extensively in the fracture mechanics literature (see for instance References F.1 through F.6).

For a cracked structure that obeys an elastic/power law constitutive relation, the stress/strain response follows:

$$\varepsilon = \varepsilon^e + \varepsilon^p = \frac{\sigma}{E} + k(\sigma)^n \qquad \text{(F.2)}$$

In Equation F.2, ε^e and ε^p are the elastic and plastic strains, E is the elastic modulus, and k and n are fitted material constants. This constitutive law leads to a violation of Illyushin's theorem since an elastic term is present (only the second term in Equation F.2 should be present). However, it has been observed that developing elastic-plastic estimation schemes using the separate elastic and plastic components provides a reasonable estimate for engineering purposes. It is common practice to write the constitutive relationship in the following form:

$$\frac{\varepsilon}{\varepsilon_0} = \frac{\sigma}{\sigma_0} + \alpha\left(\frac{\sigma}{\sigma_0}\right)^n \qquad \text{(F.3)}$$

where σ_0 is a reference stress, $\varepsilon_0 = \sigma_0 / E$, n is the fitted material parameter, and α is a material parameter related to k. The approximate solutions are determined by adding the contributions from an elastic and plastic part, as discussed next.

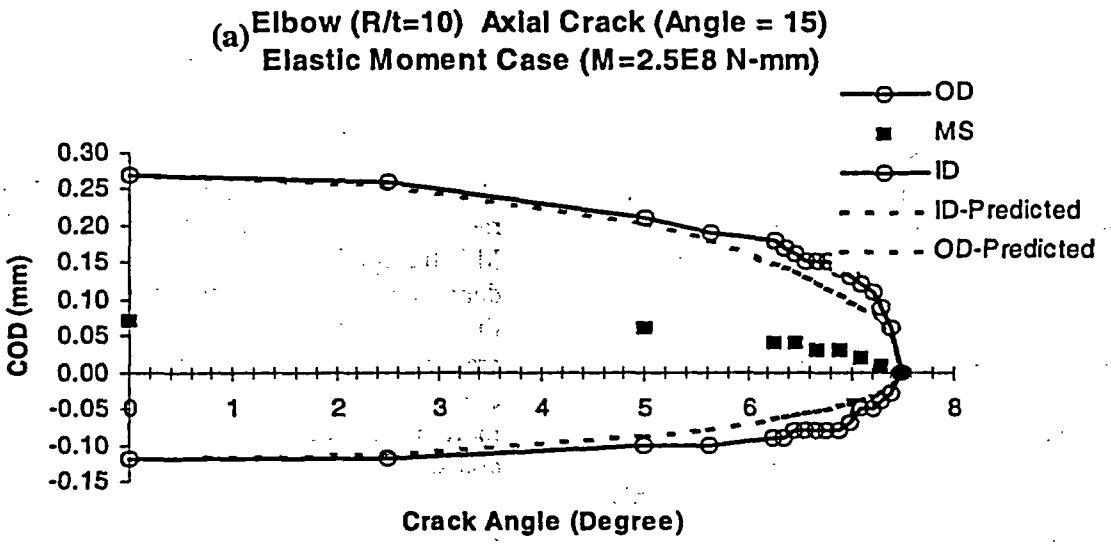

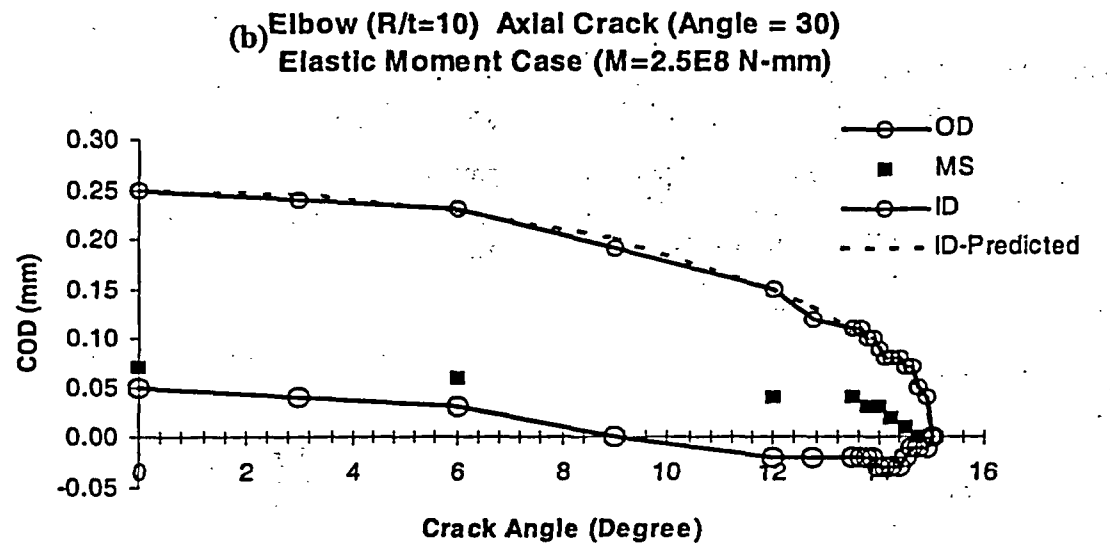

Figure F.7 Crack opening plots for axially cracked elbows – bending

F.5.1 Estimating J and Crack Opening Displacement (COD)

The estimation scheme for J is written as:

In Equation F.4, J represents the total estimated value for J, and J^e and J^p are the elastic and plastic components of J, respectively.

$$J = J^e + J^p \qquad \text{(F.4)}$$

The estimation scheme for crack opening displacement is written as:

$$\delta_T = \delta^e + \delta^p \qquad \text{(F.5)}$$

In Equation F.5, δ_T is the total crack opening displacement at the mouth (i.e. displacement at the center of the crack), while δ_e and δ_p are the elastic and plastic contributions to the total COD, respectively.

F.5.2 Elastic Component J-Integral

The elastic component of J is estimated by superimposing the component contributions from the pressure (designated 'T' for 'Tension') and bending (designated 'B' for 'Bending'). This can be written as:

$$J^e = J_T^e + J_B^e = \frac{\left[F_T \sigma_T \sqrt{\pi a}\right]^2}{E} + \frac{\left[F_B \sigma_B \sqrt{\pi a}\right]^2}{E} = \frac{K_T^2 + K_B^2}{E} \qquad \text{(F.6)}$$

In Equation F.6, 'a' is crack size and F_T and F_B have been compiled in Tables F.1 to F.4 for the through-wall cracked elbow cases. The F_T functions were compiled by performing elastic solutions for the pure pressure case (with end cap tension present), and F_B functions were compiled for pure bending. σ_T and σ_B are calculated as nominal stresses using:

For Circumferential Cracks

$$\sigma_T = \frac{p\left(\pi R_i^2\right)}{\pi\left(R_o^2 - R_i^2\right)} \qquad \text{(F.7)}$$

For Axial Cracks

$$\sigma_T \equiv \sigma_H = \frac{2p\left(\pi R_i^2\right)}{\pi\left(R_o^2 - R_i^2\right)} \qquad \text{(F.8)}$$

Bending

$$\sigma_B = \frac{M\left(R_m\right)}{\frac{\pi}{4}\left(R_o^4 - R_i^4\right)} \qquad \text{(F.9)}$$

Here, p is the internal elbow pressure, R_i is inner radius, R_o is outer radius, R_m is mean radius, and M is the applied bending moment. The denominator in the bending stress definition is the moment of inertia. Notice that for the axial cracks, σ_T is defined as twice that for the circumferential crack, or a nominal σ_H since it is more like a 'hoop' stress that opens the axial cracks.

F.5.3 Elastic Component COD

Likewise, the elastic component of COD is estimated by superimposing the pressure (tension) and bending components of COD.

$$\delta_e = \delta_e^T + \delta_e^B \qquad \text{(F.10)}$$

where δ_e^T is the elastic COD contribution from pressure alone and δ_e^B is the elastic COD contribution from bending alone, and are written as:

$$\delta_e^T = \frac{4\sigma_T a}{E} V_1(T) \qquad \text{(F.11)}$$

$$\delta_e^B = \frac{4\sigma_B a}{E} V_1(B) \qquad \text{(F.12)}$$

The same definitions of the stress for the pressure loading apply, i.e., Equation F.7 is the tensile stress for circumferential cracks and Equation F.8 is the hoop stress used for axial cracks.

The functions $V_1(T)$ and $V_1(B)$ are compiled in Tables F.1 and F.2 for the circumferential crack cases and Tables F.3 and F.4 for the axial cracks. Notice from Tables F.3 and F.4 that $V_1(T)$ and $V_1(B)$ are tabulated for both the inside

and outside surfaces. Hence, the user can estimate the COD angle that occurs through the elbow wall as discussed in Section F.4. Figure F.8 illustrates this effect. The rotation through the elbow wall remains nearly linear, even when five parabolic elements are used to model the wall thickness.

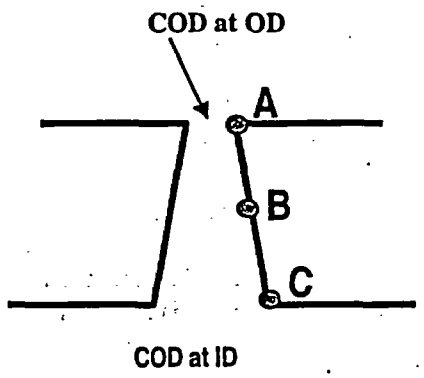

Figure F.8 Crack opening profile for axial cracks

F.5.4 Plastic Components of J

The plastic component of J is estimated as:

$$J^p = \alpha\sigma_0\varepsilon_0 a(1-\theta/\pi)h_1(P/P_0')^{n+1} \quad \text{(F.13)}$$

Everything has been previously defined in Equation F.13 except P_0', which is defined as:

$$P_0' = \frac{1}{2}\left[\frac{-\lambda P_0^2 R_m}{M_0} + \sqrt{\left\{\frac{\lambda P_0^2 R_m}{M_0}\right\}^2 + 4P_0^2}\right] \quad \text{(F.14)}$$

In Equation F.14, λ is the load ratio defined as:

$$\lambda = \frac{M}{PR_m} \quad \text{(F.15)}$$

P in Equations F.13 and F.15 is defined as:

$$P = \sigma_T \pi (R_o^2 - R_i^2) \quad \text{(F.16)}$$

It is emphasized that the h_1 functions from Equation F.13 have a strong dependence on load ratio, λ. Again as described above, σ_T is defined using Equation F.7 for circumferential cracks and using Equation F.8 for axial cracks. The two as yet undefined parameters in Equation F.14, M_o and P_o, are:

$$M_0 = 4\sigma_0 R_m^2 t[\cos(\theta/2) - 0.5\sin(\theta)] \quad \text{(F.17)}$$

For Circumferential Cracks

$$P_0 = 2\sigma_0 R_m t[\pi - \theta - 2\sin^{-1}(0.5\sin\theta)] \quad \text{(F.18a)}$$

For Axial Cracks

$$P_0 = \sigma_0 R_m t[\pi - \theta - 2\sin^{-1}(0.5\sin\theta)] \quad \text{(F.18b)}$$

Notice that, for the axial cracks the value of P_o (Equation F.18b) is one half that for circumferential cracks. This is because hoop stresses dominate the failure for axial cracks, and hence P_o should be smaller. Equation F.18a represents the standard limit load estimate for a circumferential crack in a pipe subjected to pressure. These definitions of P_o lead to reasonable values for the h-functions that are easily interpolated to provide very accurate estimates between the values tabulated in Tables F.1 to F.4.

The values of h_1 are tabulated in Tables F.1 and F.2 for circumferential cracks and Tables F.3 and F.4 for axial cracks. They have been tabulated for values of λ = [0, 0.5, 1.0, 2.0, 4.0, 8.0, and infinity]. The case $\lambda = 0$ corresponds to the pure pressure case without bending, while λ = infinity corresponds to the pure bending solution.

For typical nuclear piping LBB applications, the pipe experiences uniform or constant pressure the entire time while the moment is applied. As such, for a given crack size and material, the

only quantity that changes in the estimate for J in Equation F.13 is λ which continually increases as the moment increases, while P in Equation F.15 remains constant. The values of λ for which h_1 were tabulated are quite sufficient for practical nuclear applications. In fact, for practical purposes, a λ value of 18 should be used for interpolation when λ is between 8 and infinity. Most practical nuclear fracture assessments for pressurized elbows rarely find λ greater than about 6.

The compilations in Tables F.1 to F.4 represent 336 full nonlinear finite element solutions. These were compiled by proportionally applying the pressure and moment simultaneously. However, as will be seen in the validation section, solutions where pressure is applied first, followed by moment compare very well with the estimation scheme.

It is recommended that the plastic zone correction applied to the elastic solution be neglected. In general, as discussed in References F.1 to F.6, these type of J-estimation solutions have fundamental errors associated with them in the transition region between elastic and fully plastic solution ranges. However, we have found the plastic zone corrections to be unnecessary for most of the numerous validation cases that were performed (to be summarized later) here. However, the user can assure conservative solutions by including the form of the plastic zone correction procedure summarized on page 2-4 in Reference F.4. The user might want to use the plastic zone correction procedure for large 'n' values in cases where the elastic contribution to J is large (large crack size in high (R / t) elbow).

F.5.5 Plastic Components of COD

The plastic contribution to the crack opening displacement can be calculated using:

$$\delta^p = \alpha\varepsilon_0 a h_2 (P / P_0')^n \qquad \text{(F.19)}$$

The h_2-function is tabulated in Tables F.1 and F.2 for circumferential cracks and Tables F.3 and F.4 for axial cracks. The functions for the axial cracks are tabulated for both the ID and OD so the user can estimate the variation of COD through the elbow thickness. As discussed above, the usual assumption of an elliptic crack opening shape works well for elbows even when the opening varies through the thickness. P in Equation F.19 is defined in Equations F.7 and F.16 for circumferential cracked elbows, and Equations F.8 and F.16 for axial cracks. P_o is defined in Equation F.18a for circumferential cracks and Equation F.18b for axial cracks.

F.6 ESTIMATION SCHEME FOR PURE BENDING OF ELBOWS (λ = INFINITY)

For the λ = infinity case, a bending moment only was applied. For this case, one can design the estimation scheme based on an alternative approach. The total estimate for J still uses Equation F.4 and Equation F.6, for the elastic estimate remains the same. Likewise, the total estimate for COD (Equation F.5) remains the same with Equations F.10 to F.12 providing the estimate for the elastic values. However, the estimates for J^p (Equation F.13) and δ^p (Equation F.19) can be replaced by:

$$J^p = \alpha\sigma_0\varepsilon_0 a(1-\theta/\pi)h_1^M (M/M_0)^{n+1} \qquad \text{(F.20)}$$

$$\delta^p = \alpha\varepsilon_0 a h_2^M (M/M_0) \qquad \text{(F.21)}$$

The compilations for h_1^M and h_2^M are provided in Tables F.5 and F.6. These can be compared directly with similar compilations for straight pipe to observe the differences.

Alternatively, all of the h-functions could have been based on formulas (Equations F.20 and F.21). It is instructive to investigate the choice made here to use Equations F.13 and F.19 rather than Equations F.20 and F.21. It will be seen that, in theory, one will obtain the same prediction of the plastic components of J and COD using either normalizing parameters, the choice made here results in much more accurate interpolation within the tables for predictions made for cases not directly tabulated.

First of all, from Figure F.9 the nature of the convergence of the h_1^M functions can be observed. The dashed horizontal line represents the converged solution of $h_1^M = 1.3$. This is for R / t = 10. The curve with the filled circles represents the convergence of the h-function versus load for a pure bending case (no internal pressure). The analyses were all performed using ABAQUS and the constitutive law represented by Equation F.2. Typically, the solution is monitored until the plastic strains become greater than ten times the elastic strains at every Gauss point in the body that is monitored. It is seen that it converges to the correct value at an M/M_o value of about 5. Here, the monitoring procedure kept the analysis going until $M/M_o = 15$. This was clearly adequate. In fact, convergence was assured for every value listed in Tables F.1 to F.4 in this fashion.

Also shown in Figure F.9 is a curve designated with solid diamonds. This was a case where a pressure of 10 MPa (typical operating pressure) was applied first, and then the bending moment was applied until it converged to the pure bending solution. With the definition of lamda ($\lambda = M/(PR)$), since PR remains constant for this case (constant pressure), it is clearly seen that h_1^M depends on λ. As λ approaches infinity, the pure bending solution is obtained. This convergence to the pure bending solution occurs at large values of M/M_o approaching 35. The h-functions published in Reference F.1 were developed in this way – pressure applied and held while the moment was applied. As such, the h-functions really are those for the pure bending case. Unfortunately, the h-functions obtained in this way are non-conservative and one will typically under predict the value of J – sometimes significantly, depending on λ.

Figure F.10 compares the h-functions calculated using Equations F.13 and F.20. The value of h based on Equation F.20 is very large for smaller values of λ (for instance, $h_1 = 3450$ for $\lambda = 0.5$). It is seen that the h-values based on Equation F.13 have much more uniform values. It should be clear that the interpolation between values in the tables will be much more stable using the normalization based on Equation F.13 versus Equation F.20.

F.7 VALIDATION EXAMPLES

This next Section illustrates independent validation of the estimation schemes developed here. Before presenting the validation examples, it is useful to discuss the Ramberg-Osgood representation of material stress-strain data versus actual data. Figure F.11 illustrates a typical relationship. The bottom plot shows an example of idealized data that are to be fit with a Ramberg-Osgood equation. The 'flow-2' curve has an elastic slope and a yield stress of 200 MPa (29 ksi) in this case. The Ramberg-Osgood curve (Equation F.3) permits plastic strains to occur throughout the deformation. It is seen that, over the entire strain range, there is negligible difference between a Ramberg-Osgood and 'flow' representation (upper curve, Figure F.11). However, in the small strain regime, there are some small differences which manifest themselves as slight differences in predicted displacements, and J-Integral values. It will be seen that the representation in Figure F.11 results in a slightly conservative prediction of J-integral values in the following results. It is useful for the user of the estimation schemes to keep this in mind when making engineering predictions of fracture. How one fits a Ramberg-Osgood relation to actual test data can have an influence on predictions. See References F.5 and F.6 for more details.

In addition to the consistency checks on solution accuracy discussed above (see Figures F.9 and F.10), additional quality control was maintained by performing independent analyses. For each crack type and size, an independent analysis was performed for at least one set of material parameters and often for several sets. These validation analyses were performed as follows: pressure was applied first followed by bending. This violates the formal definition of a deformation theory solution. However, it is an excellent independent check on the accuracy of the solution procedure since, in actual nuclear piping, pressure is typically present, at constant

value, and then bending is applied. It will be seen that this results in slight differences between the flow theory solutions (which are strictly required for this set of loading conditions), and deformation theory solutions. For the examples which follow, the pressure applied was 5 MPa (0.75 ksi) for R/t = 20, 10 MPa (1.5 ksi) for R/t = 10, and 20 MPa (2.9 ksi) for the R/t = 5 cases. After the solution for pressure was complete, bending was applied. Solutions obtained in this manner are then directly compared to predictions using the estimation schemes developed here. The plastic-zone correction to the elastic solution are not included in the following.

F.7.1 Axial Cracks

Figures F.12 to F.14 illustrate the validation for some of the axial crack cases. It is clearly seen that the estimation scheme is quite accurate, even for the flow theory cases. Notice that the crack opening displacement (COD) begins at a non zero value which corresponds the pressure case before applying a moment. Note also that the outer diameter (OD) COD's are typically much smaller than the ID cases. In fact, crack closure (Figure F.13) occurs for some cases.

F.7.2 Circumferential Cracks

Figures F.15 to F.17 illustrate the validation for some of the circumferential crack cases. Again, the estimation scheme performs very well. It is seen that there are some small differences between the deformation and flow theory solutions. However, in general, the deformation theory solution is more conservative and the estimation scheme typically falls between the two solutions.

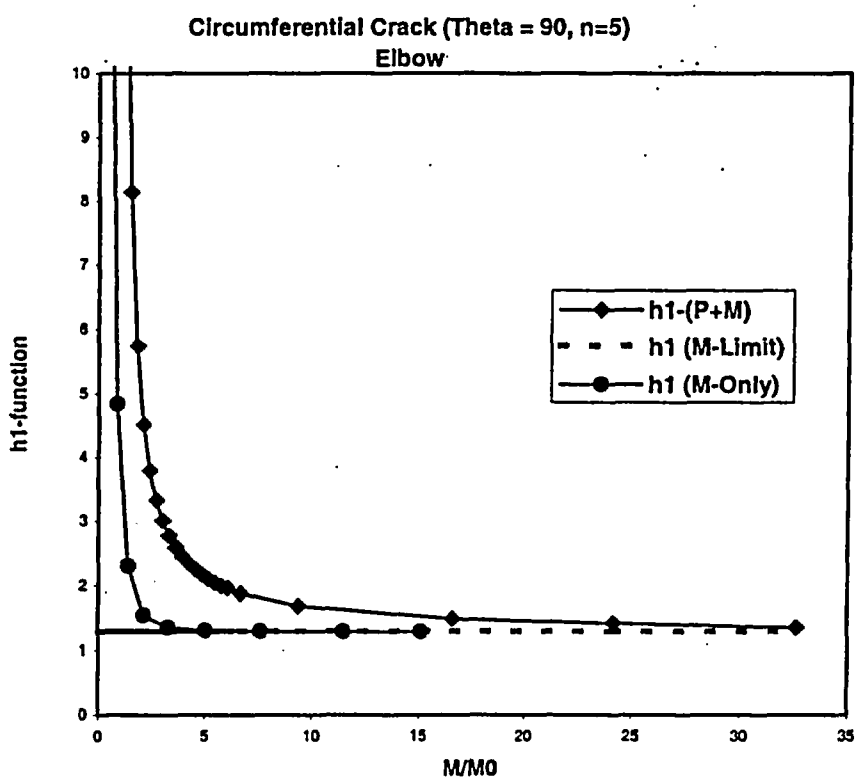

Figure F.9 Convergence of h-functions versus applied load

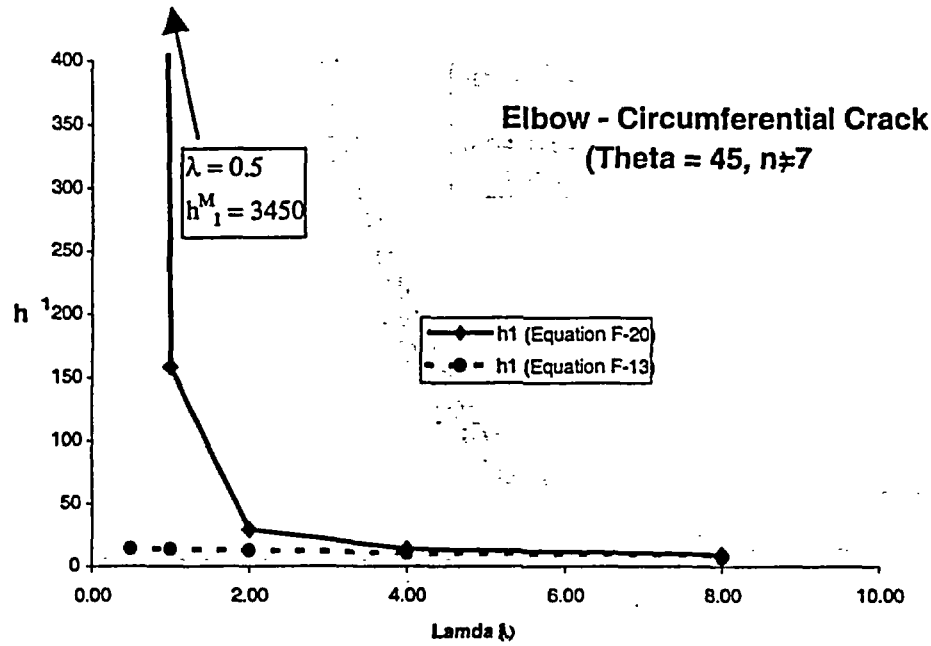

Figure F.10 Convergence of h-functions versus lamba

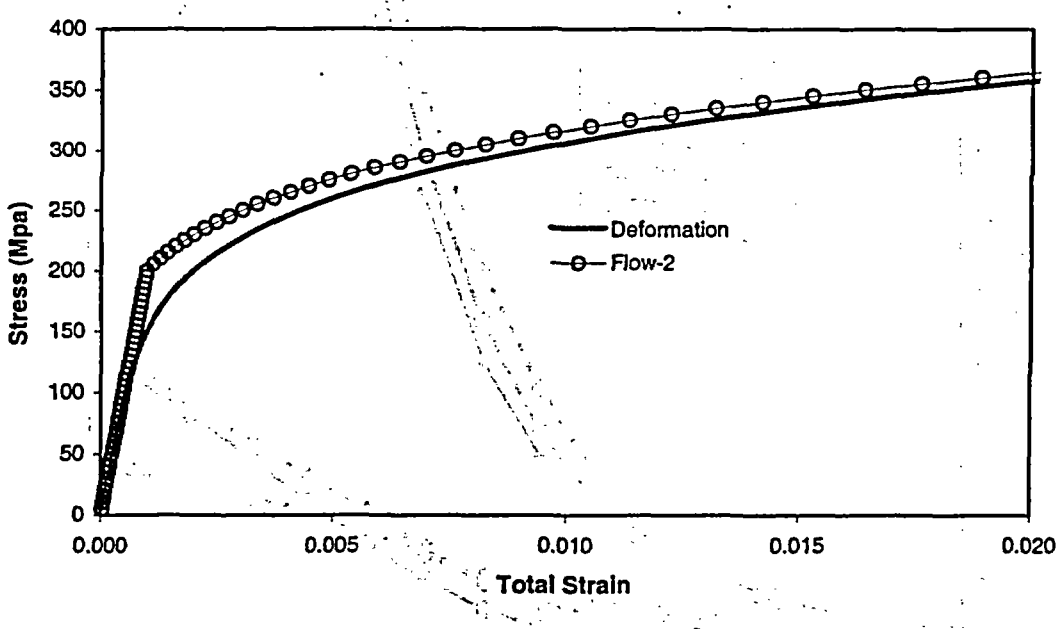

Figure F.11 Comparison between Ramberg-Osgood relationship and typical flow theory representation

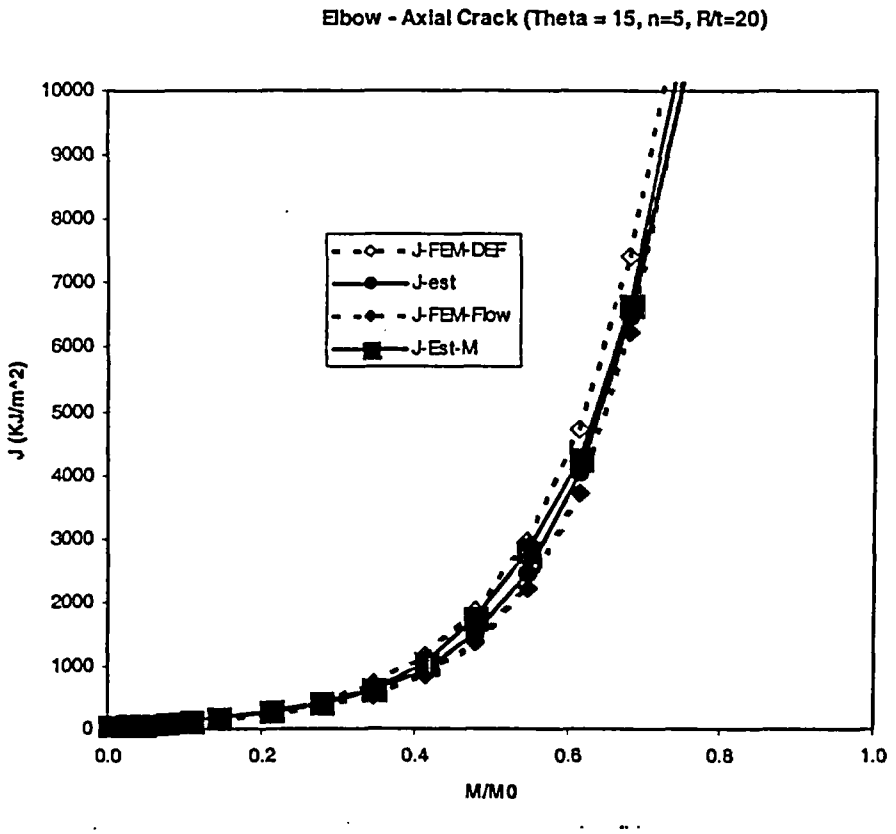

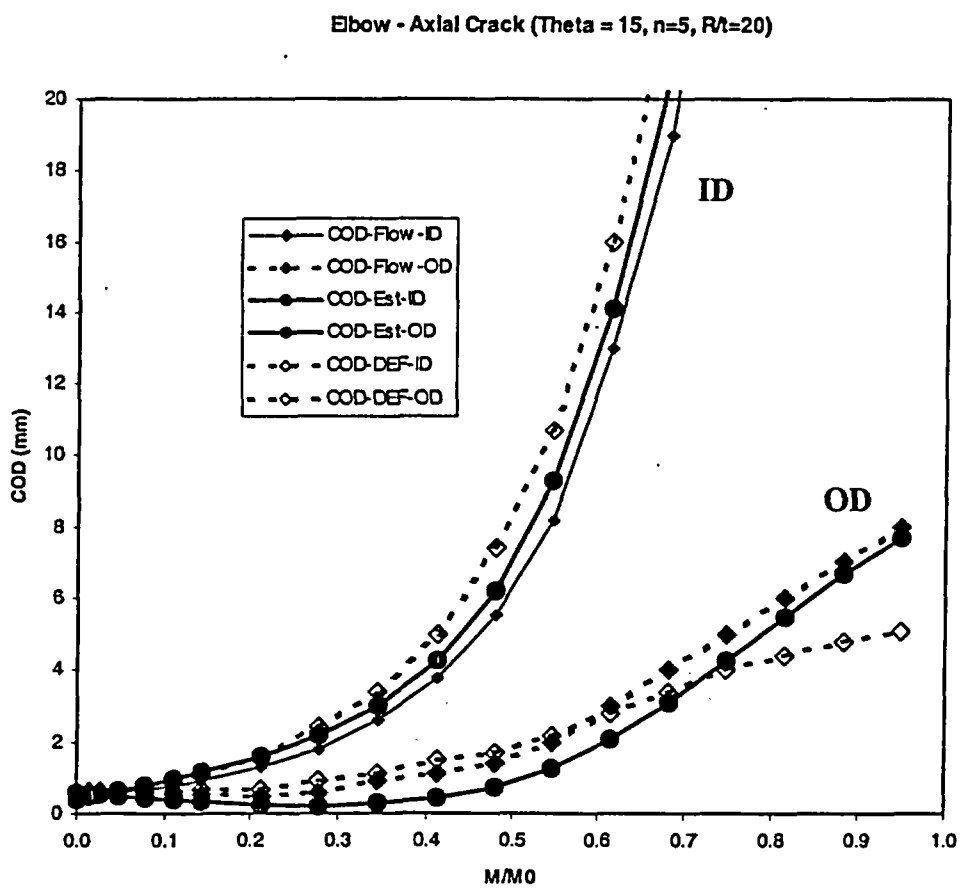

Figure F.12 Validation check (R/t = 20, axial crack 2θ = 15 degrees, n = 5)

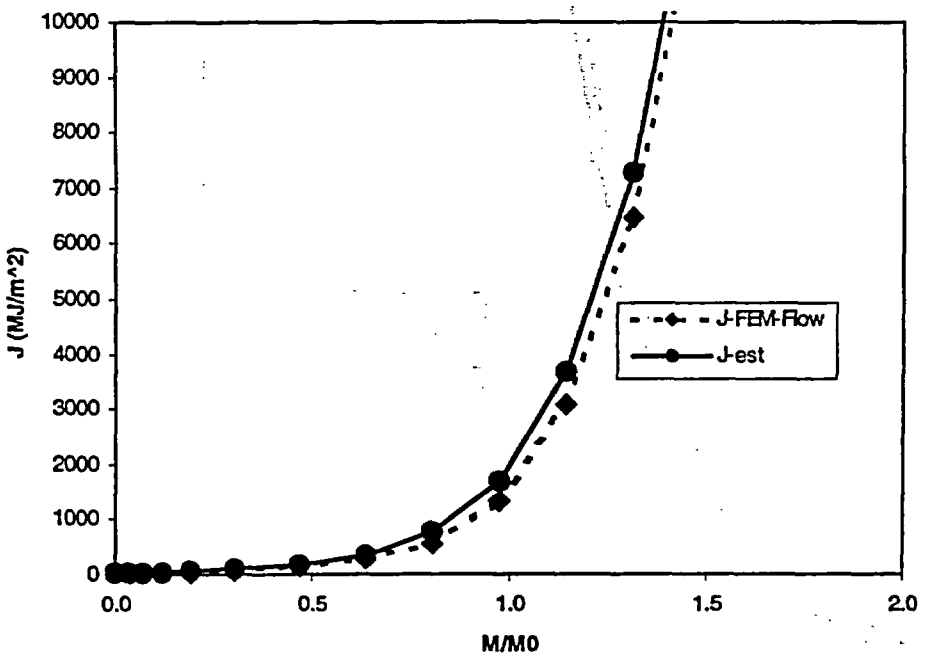

Elbow - Axial Crack (Theta = 15, n=5,R/t=5)

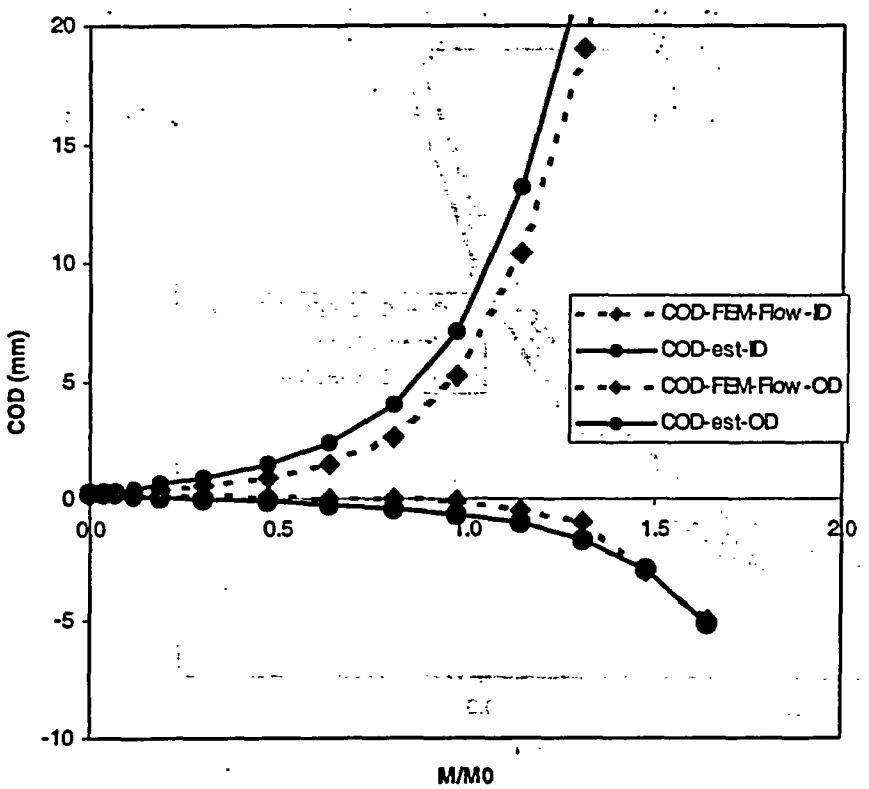

Figure F.13 Validation check (R/t = 5, axial crack, 2θ = 15 degrees, n = 5)

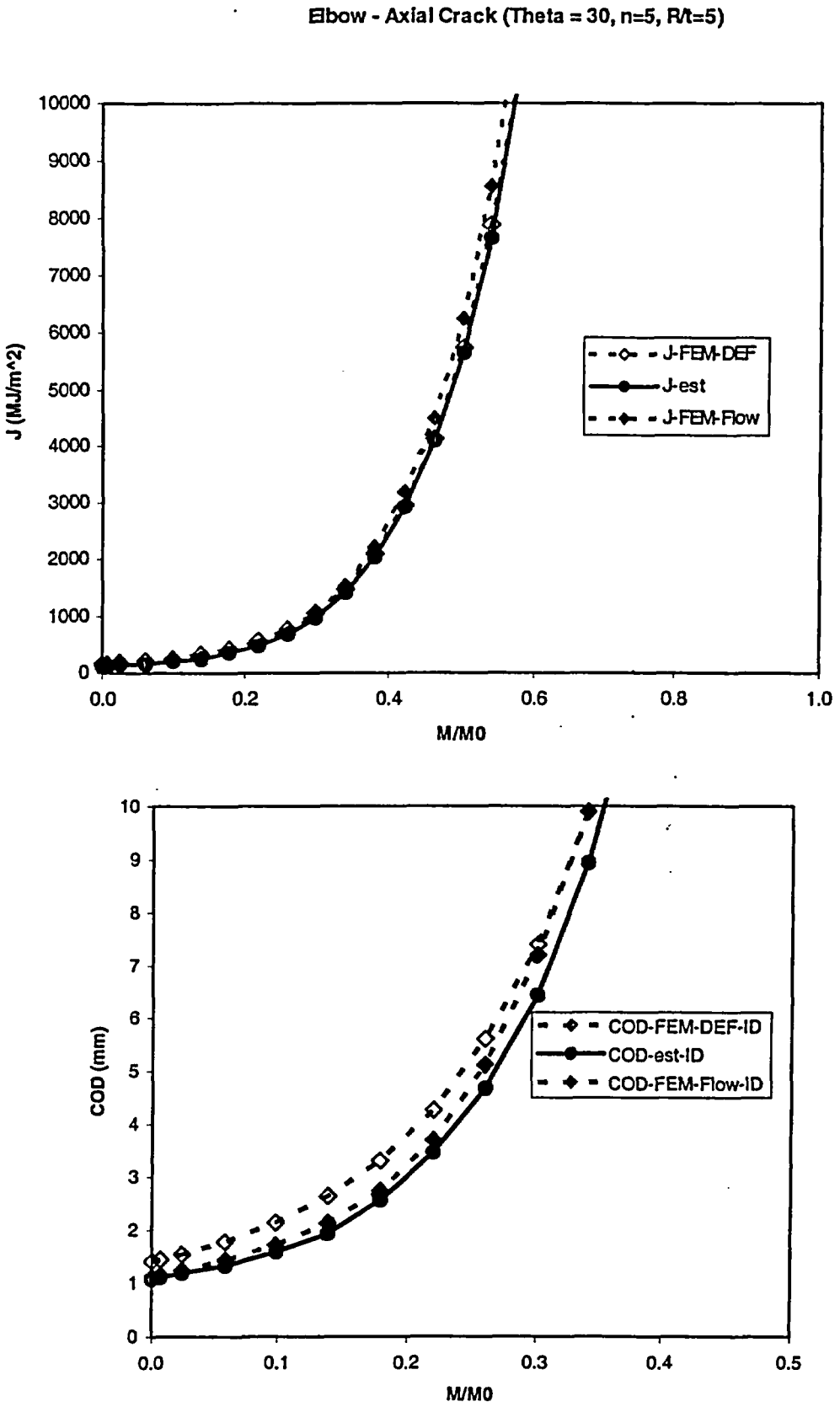

Figure F.14 Validation check (R/t = 5, axial crack, 2θ = 30 degrees, n = 5)

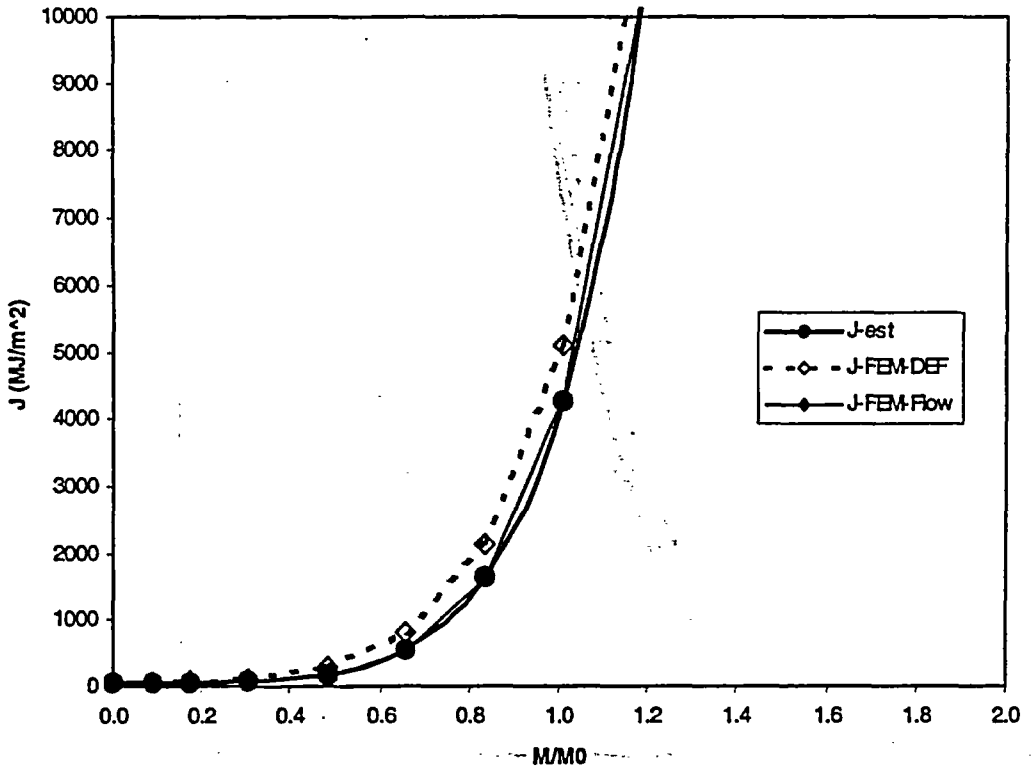

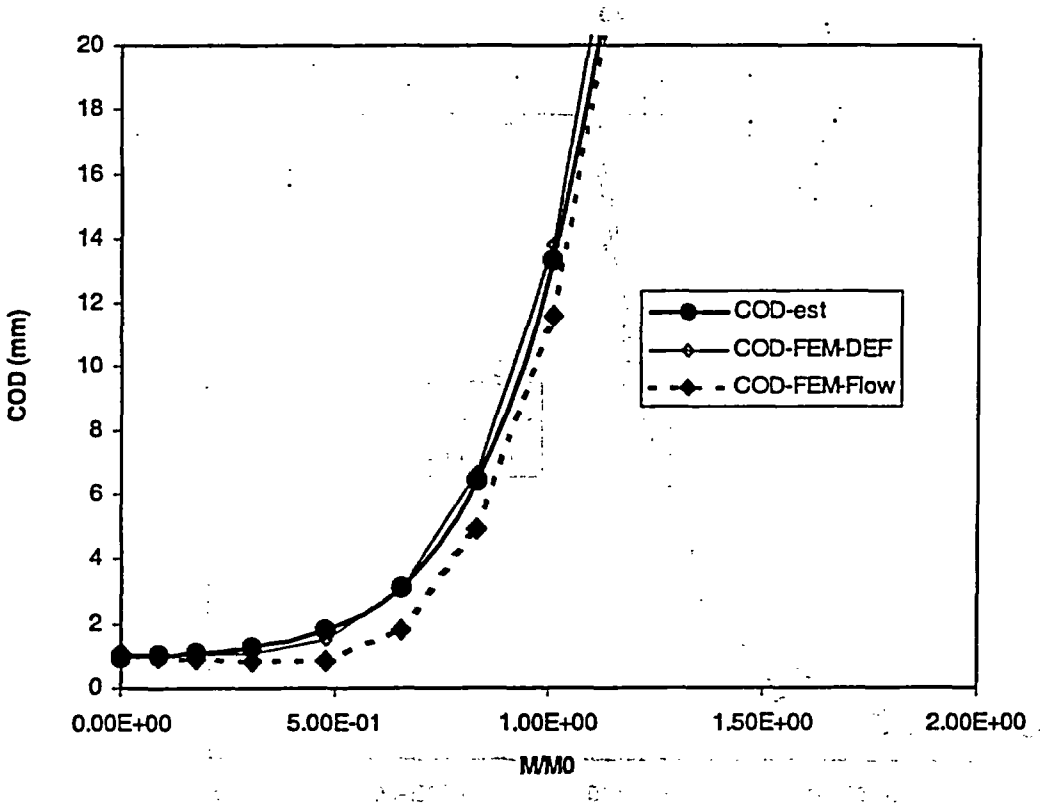

Figure F.15 Validation check (R/t = 5 circumferential crack, 2θ = 90degrees, n= 5)

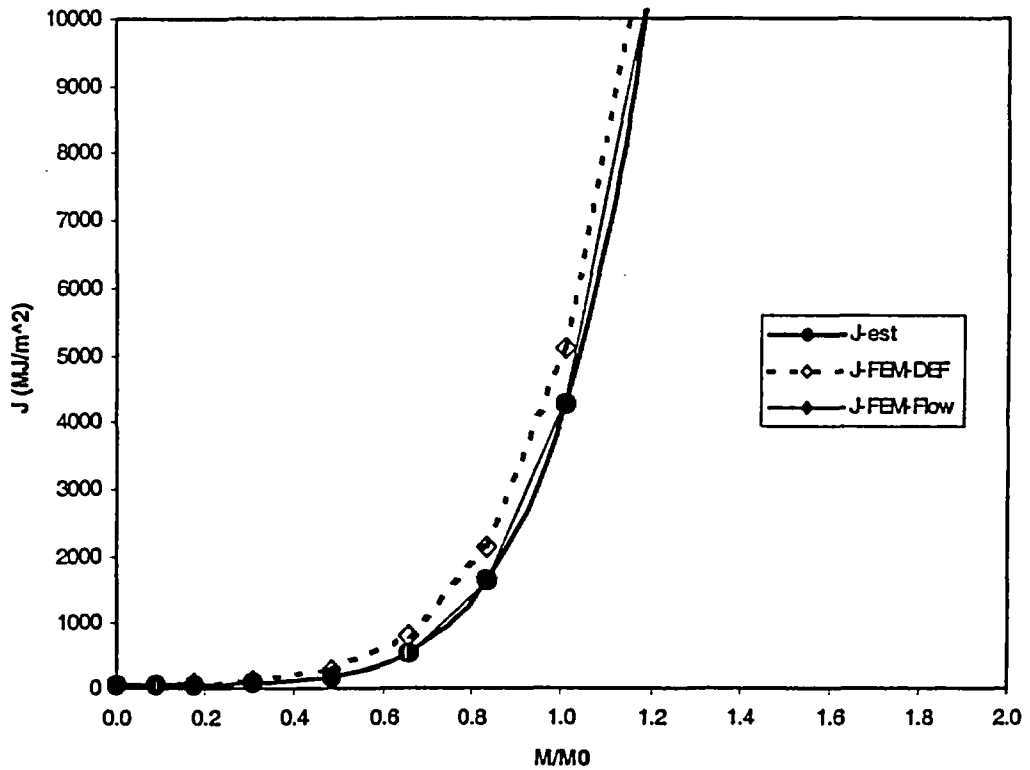

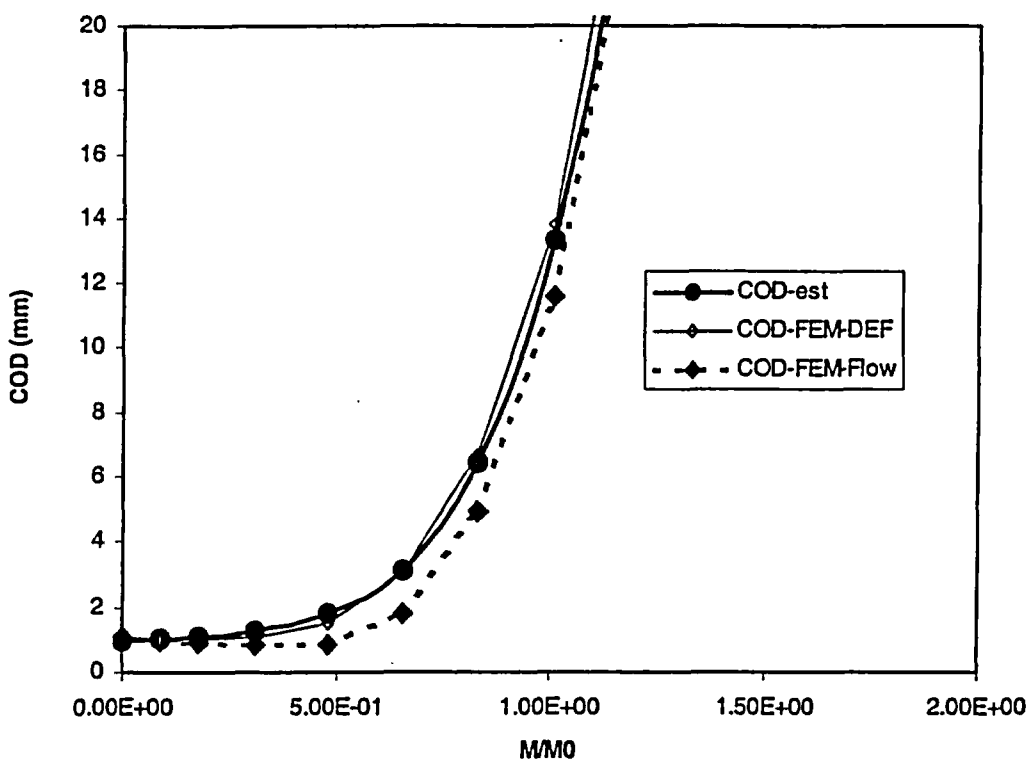

Figure F.16 Validation check (R/t = 20, circumferential crack, 2θ = 90 degrees, n = 5)

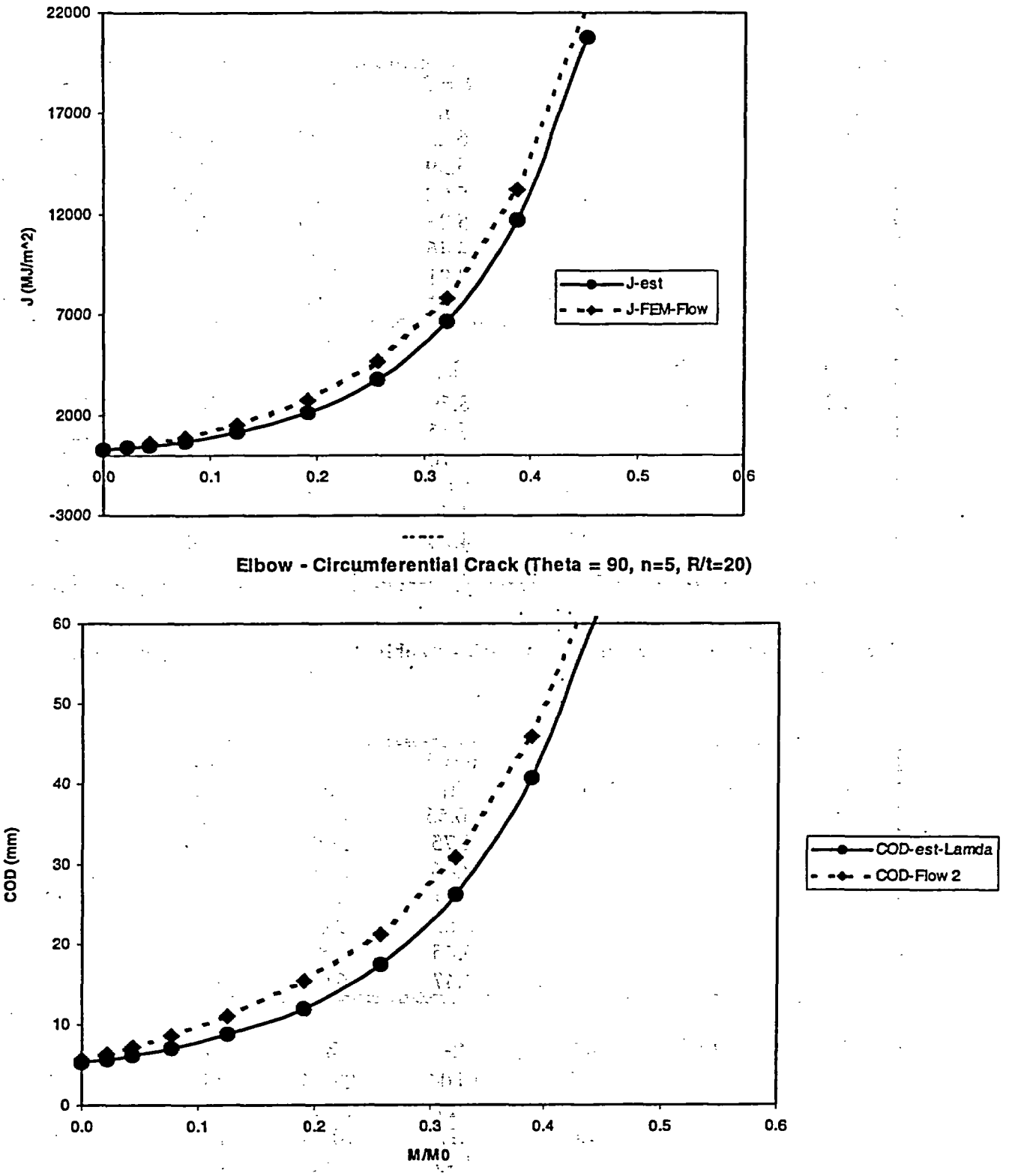

Figure F.17 Validation check (R/t = 20, circumferential crack, 2θ = 180 δεγρεεσ, ν = 5)

Table F.1 (a) Elbow with circumferential crack – combined pressure and bending compilation (R/t = 5, θ = 45°)

F-(T)	F-(B)	Lamda	n = 3 h_1	n = 5 h_1	n = 7 h_1	n = 10 h_1
1.69	1.22	0.0	6.23	10.67	17.47	34.68
		0.5	6.39	8.04	9.75	12.42
		1.0	5.92	6.55	6.92	7.34
		2.0	5.23	5.10	4.78	4.25
		4.0	4.46	4.05	3.47	2.58
		8.0	3.91	3.43	2.79	2.01
		inf (=18)	3.17	2.76	2.11	1.36
V-1 (T)	**V-1 (B)**	**Lamda**	h_2	h_2	h_2	h_2
2.04	1.19	0.0	8.59	14.87	24.65	49.31
		0.5	6.56	7.99	9.56	12.05
		1.0	5.70	6.17	6.45	6.78
		2.0	5.09	4.92	4.61	4.08
		4.0	4.59	4.17	3.57	2.67
		8.0	4.24	3.71	3.04	2.20
		inf (=18)	3.72	3.13	2.46	1.60

Table F.1(b) Elbow with circumferential crack – combined pressure and bending compilation (R/t = 10, θ = 45°)

F-(T)	F-(B)	Lamda	n = 3 h_1	n = 5 h_1	n = 7 h_1	n = 10 h_1
2.16	0.87	0.0	10.55	17.79	28.26	53.93
		0.5	8.75	11.96	14.42	18.32
		1.0	8.46	11.86	13.60	16.54
		2.0	7.91	10.47	12.80	15.27
		4.0	6.83	9.06	10.76	12.08
		8.0	5.85	7.82	8.99	10.76
		inf (=18)	4.47	6.06	6.89	7.87
V-1 (T)	**V-1 (B)**	**Lamda**	h_2	h_2	h_2	h_2
3.39	0.67	0.0	15.04	27.26	45.21	90.60
		0.5	9.17	12.29	14.89	19.01
		1.0	7.92	10.28	12.24	14.88
		2.0	7.45	9.61	11.60	13.82
		4.0	6.83	8.93	10.48	11.75
		8.0	6.18	8.21	9.37	11.09
		inf (=18)	5.07	6.89	8.06	8.86

Table F.1(c) Elbow with circumferential crack – combined pressure and bending compilation (R/t = 20, θ = 45°)

			n = 3	n = 5	n = 7	n = 10
F-(T)	F-(B)	Lamda	h_1	h_1	h_1	h_1
3.01	0.25	0.0	21.04	33.34	46.65	61.68
		0.5	15.57	27.30	41.30	72.98
		1.0	13.48	26.87	44.95	88.46
		2.0	11.14	26.02	49.25	113.49
		4.0	7.82	21.81	44.90	115.15
		8.0	5.66	17.59	38.84	96.94
		inf (=18)	3.22	11.07	25.92	66.57
V-1 (T)	V-1 (B)	Lamda	h_2	h_2	h_2	h_2
6.30	0.66	0.0	33.70	54.86	81.83	112.34
		0.5	19.23	34.59	54.73	100.90
		1.0	14.06	26.80	44.28	86.08
		2.0	11.75	25.37	45.85	102.22
		4.0	8.95	24.18	47.14	114.72
		8.0	6.43	21.00	45.08	108.47
		inf (=18)	2.99	14.08	33.69	86.77

Table F.2 (a) Elbow with circumferential crack – combined pressure and bending compilation (R/t = 5, θ = 90°)

			n = 3	n = 5	n = 7	n = 10
F-(T)	F-(B)	Lamda	h_1	h_1	h_1	h_1
4.04	2.52	0.0	1.33	0.82	0.53	0.31
		0.5	2.30	1.77	1.53	1.29
		1.0	2.67	2.26	2.05	1.99
		2.0	2.59	2.08	1.82	1.64
		4.0	2.12	1.56	1.20	.90
		8.0	1.75	1.14	0.79	0.50
		inf (=18)	1.26	0.69	0.41	0.20
V-1 (T)	V-1 (B)	Lamda	h_2	h_2	h_2	h_2
6.52	4.46	0.0	2.11	1.14	0.70	0.38
		0.5	2.92	2.08	1.72	1.42
		1.0	3.26	2.55	2.26	2.14
		2.0	3.21	2.43	2.07	1.83
		4.0	2.83	1.95	1.47	1.08
		8.0	2.49	1.53	1.04	0.65

Table F.2 (b) Elbow with circumferential crack – combined pressure and bending compilation (R/t = 10, θ = 90°)

			n = 3	n = 5	n = 7	n = 10
F-(T)	F-(B)	Lamda	h_1	h_1	h_1	h_1
4.16	3.24	0.0	1.99	1.00	0.62	0.36
		0.5	3.28	2.45	2.02	1.69
		1.0	4.04	3.23	2.88	2.68
		2.0	4.12	3.19	2.72	2.46
		4.0	3.53	2.46	1.88	1.38
		8.0	2.98	1.88	1.33	0.82
		inf (=18)	2.24	1.22	0.71	0.35
V-1 (T)	V-1 (B)	Lamda	h_2	h_2	h_2	h_2
9.66	5.93	0.0	2.99	1.51	0.86	0.47
		0.5	4.25	2.92	2.30	1.85
		1.0	4.91	3.72	3.19	2.58
		2.0	4.05	3.78	3.12	2.74
		4.0	4.59	3.15	2.34	1.67
		8.0	4.09	2.57	1.77	1.06
		inf (=18)	3.35	1.84	1.06	0.50

Table F.2 (c) Elbow with circumferential crack – combined pressure and bending compilation (R/t = 20, θ = 90°)

F-(T)	F-(B)	Lamda	n = 3 h_1	n = 5 h_1	n = 7 h_1	n = 10 h_1
5.00	4.56	0.0	2.87	1.75	1.13	0.62
		0.5	6.27	4.93	4.21	3.36
		1.0	8.43	7.34	6.69	6.31
		2.0	9.34	8.28	7.64	6.90
		4.0	8.60	7.13	5.99	4.57
		8.0	7.59	5.58	4.52	3.21
		inf (=18)	5.95	3.96	2.69	1.55
F- (T)	**F- (B)**	**Lamda**	**h_1**	**h_1**	**j_1**	**h_1**
17.08	7.94	0.0	5.83	3.26	1.95	0.99
		0.5	8.27	6.31	5.22	4.03
		1.0	9.94	8.69	7.85	7.26
		2.0	10.72	9.85	9.16	8.25
		4.0	10.09	8.95	7.69	5.93
		8.0	9.13	7.32	6.12	4.44
		inf (=18)	7.57	5.57	3.96	2.35

Table F.3 (a) Elbow with axial crack – combined pressure and bending compilation (R/t = 5, θ = 15°)

			n = 3	n = 5	n = 7	n = 10
F-(T)	F-(B)	Lamda	h_1	h_1	h_1	h_1
1.57	0.81	0.0	1.01	0.49	0.22	0.07
		0.5	0.73	0.28	0.10	0.02
		1.0	0.65	0.25	0.09	0.02
		2.0	0.59	0.24	0.09	0.02
		4.0	0.53	0.22	0.09	0.02
		8.0	0.46	0.19	0.07	0.02
		inf (=18)	0.33	0.12	0.04	0.01
Inner	Diameter					
V-1 (T)	V-1 (B)	Lamda	h_2	h_2	h_2	h_2
1.45	1.20	0.0	1.42	0.70	0.32	0.10
		0.5	1.49	0.59	0.21	0.04
		1.0	1.61	0.62	0.22	0.04
		2.0	1.76	0.73	0.27	0.06
		4.0	1.81	0.78	0.31	0.07
		8.0	1.68	0.72	0.29	0.07
		inf (=18)	1.30	0.51	0.19	0.04
Outer	Diameter					
V-1 (T)	V-1 (B)	Lamda	h_2	h_2	h_2	h_2
2.04	-0.45	0.0	2.40	1.22	0.58	0.18
		0.5	1.42	0.60	0.23	0.05
		1.0	0.96	0.41	0.16	0.03
		2.0	0.48	0.22	0.09	0.02
		4.0	0.09	0.06	0.03	0.01
		8.0	-0.15	-0.03	-0.01	-0.01
		inf (=18)	-0.37	-0.11	-0.04	-0.01

Table F.3 (b) Elbow with axial crack – combined pressure and bending compilation (R/t = 10, θ = 15°)

			n = 3	n = 5	n = 7	n = 10
F-(T)	F-(B)	Lamda	h_1	h_1	h_1	h_1
1.79	1.26	0.0	1.44	0.78	0.41	0.15
		0.5	1.16	0.49	0.19	0.04
		1.0	1.20	0.56	0.23	0.06
		2.0	1.39	0.77	0.39	0.14
		4.0	1.56	0.97	0.57	0.25
		8.0	1.57	0.92	0.58	0.27
		inf (=18)	1.25	0.73	0.39	0.17
Inner	Diameter					
V-1 (T)	V-1 (B)	Lamda	h_2	h_2	h_2	h_2
1.83	1.73	0.0	2.08	1.18	0.63	0.24
		0.5	2.28	0.99	0.39	0.08
		1.0	2.73	1.30	0.55	0.14
		2.0	3.53	2.06	1.08	0.40
		4.0	4.10	2.77	1.68	0.79
		8.0	4.15	2.76	1.81	0.89
		inf (=18)	3.39	2.23	1.28	0.59
Outer	Diameter					
V-1 (T)	V-1 (B)	Lamda	h_2	h_2	h_2	h_2
2.59	-0.77	0.0	3.50	2.05	1.13	0.43
		0.5	2.28	1.12	0.48	0.11
		1.0	1.73	0.96	0.45	0.13
		2.0	0.98	0.70	0.41	0.17
		4.0	0.11	0.22	0.18	0.10
		8.0	-0.59	-0.21	-0.09	-0.03
		inf (=18)	-1.25	-0.64	-0.32	-0.13

Table F.3 (c) Elbow with axial crack – combined pressure and bending compilation (R/t = 20, θ = 15°)

			n = 3	n = 5	n = 7	n = 10
F-(T)	F-(B)	Lamda	h_1	h_1	h_1	h_1
2.18	1.94	0.0	2.89	2.19	1.60	1.02
		0.5	2.46	1.37	0.67	0.22
		1.0	2.95	1.96	1.16	0.58
		2.0	4.21	3.59	2.87	2.04
		4.0	5.39	5.34	5.14	5.39
		8.0	5.60	5.82	6.44	6.91
		inf (=18)	4.71	4.81	4.54	4.59
Inner	Diameter					
V-1 (T)	V-1 (B)	Lamda	h_2	h_2	h_2	h_2
2.68	2.64	0.0	4.47	3.65	2.78	1.90
		0.5	4.70	2.75	1.40	0.48
		1.0	4.72	4.25	2.61	1.31
		2.0	8.76	8.16	6.85	5.04
		4.0	11.00	12.27	12.62	13.66
		8.0	11.10	13.35	15.64	17.76
		inf (=18)	9.13	10.76	11.17	12.03
Outer	Diameter					
V-1 (T)	V-1 (B)	Lamda	h_2	h_2	h_2	h_2
3.72	-1.04	0.0	7.08	3.91	4.65	3.15
		0.5	4.98	3.35	1.85	0.69
		1.0	4.33	3.57	2.40	1.30
		2.0	3.18	3.62	3.37	2.71
		4.0	1.11	3.00	2.58	3.10
		8.0	-0.95	-0.14	0.26	0.78
		inf (=18)	-3.14	-2.88	-2.62	-2.46

Table F.4 (a) Elbow with axial crack – combined pressure and bending compilation (R/t = 5, θ = 30°)

			n = 3	n = 5	n = 7	n = 10
F-(T)	F-(B)	Lamda	h_1	h_1	h_1	h_1
2.18	0.79	0.0	2.32	1.67	1.20	0.83
		0.5	1.45	0.72	0.35	0.13
		1.0	1.07	0.45	0.18	0.05
		2.0	0.79	0.32	0.12	0.03
		4.0	0.56	0.22	0.08	0.02
		8.0	0.40	0.15	0.05	0.01
		inf (=18)	0.22	0.07	0.02	0.00
Inner	Diameter					
V-1 (T)	V-1 (B)	Lamda	h_2	h_2	h_2	h_2
2.67	1.24	0.0	3.78	2.93	2.23	1.58
		0.5	2.80	1.49	0.76	0.29
		1.0	2.34	1.05	0.44	0.12
		2.0	2.34	1.05	0.44	0.12
		4.0	2.01	0.85	0.33	0.08
		8.0	1.68	0.69	0.26	0.06
		inf (=18)	0.96	0.33	0.11	0.02
Outer	Diameter					
V-1 (T)	V-1 (B)	Lamda	h_2	h_2	h_2	h_2
3.87	0.16	0.0	6.35	4.90	4.03	2.91
		0.5	4.05	2.33	1.25	0.49
		1.0	2.90	1.38	0.60	0.16
		2.0	1.95	0.89	0.35	0.08
		4.0	1.21	0.52	0.21	0.05
		8.0	0.73	0.31	0.12	0.03
		inf (=18)	0.25	0.10	0.04	0.01

Table F. 4 (b) Elbow with axial crack – combined pressure and bending compilation (R/t = 10, θ = 30°)

			n = 3	n = 5	n = 7	n = 10
F-(T)	F-(B)	Lamda	h_1	h_1	h_1	h_1
2.58	1.22	0.0	4.26	4.35	4.70	5.88
		0.5	2.64	1.73	1.22	0.80
		1.0	2.18	13.16	0.62	0.24
		2.0	1.95	1.11	0.59	0.22
		4.0	1.67	0.99	0.57	0.24
		8.0	1.37	0.80	0.19	0.20
		inf (=18)	0.88	0.47	0.24	0.09
Inner	Diameter					
V-1 (T)	V-1 (B)	Lamda	h_2	h_2	h_2	h_2
4.13	2.01	0.0	8.48	9.81	11.35	14.96
		0.5	5.99	4.48	3.41	2.40
		1.0	5.21	3.12	1.78	0.67
		2.0	4.93	3.03	1.68	0.62
		4.0	4.61	2.91	1.75	0.76
		8.0	4.05	2.54	1.52	0.69
		inf (=18)	2.91	1.68	0.90	0.34
Outer	Diameter					
V-1 (T)	V-1 (B)	Lamda	h_2	h_2	h_2	h_2
5.64	0.40	0.0	12.92	15.37	18.03	23.83
		0.5	8.21	6.59	5.20	3.16
		1.0	6.27	4.01	2.38	0.87
		2.0	4.81	3.12	1.77	0.70
		4.0	3.48	2.34	1.87	0.64
		8.0	2.39	1.64	1.02	0.48
		inf (=18)	1.00	0.67	0.38	0.15

Table F. 4 (c) Elbow with axial crack – combined pressure and bending compilation (R/t = 20, θ = 30°)

			n = 3	n = 5	n = 7	n = 10
F-(T)	F-(B)	Lamda	h_1	h_1	h_1	h_1
3.13	1.91	0.0	9.38	15.32	27.79	79.02
		0.5	5.87	5.53	6.71	9.57
		1.0	5.51	4.46	3.55	2.68
		2.0	5.96	5.13	4.35	3.43
		4.0	5.96	6.14	6.07	2.95
		8.0	5.33	5.61	5.89	5.68
		inf (=18)	3.64	3.47	3.23	3.03
Inner	Diameter					
V-1 (T)	V-1 (B)	Lamda	h_2	h_2	h_2	h_2
6.78	3.64	0.5	22.16	41.11	79.18	233.37
		1.0	15.12	17.82	22.37	16.14
		2.0	14.03	13.13	11.61	9.62
		4.0	14.72	14.20	12.74	10.53
		8.0	14.96	16.90	17.65	17.73
		inf (=18)	13.76	16.00	17.75	18.10
		inf (=18)	9.95	10.57	10.48	10.29
Outer	Diameter					
V-1 (T)	V-1 (B)	Lamda	h_2	h_2	h_2	h_2
8.71	1.36	0.0	28.07	57.82	111.73	329.87
		0.5	19.34	24.05	30.95	15.74
		1.0	16.16	15.95	14.60	12.49
		2.0	14.43	14.48	13.25	11.15
		4.0	12.42	14.78	15.70	16.00
		8.0	9.74	12.18	13.97	14.47
		inf (=18)	5.20	6.03	6.20	6.29

Table F.5 Elbow with circumferential crack – pure bending compilation ($\theta = 45, 90°$)□ for use with Equations E.19 and E.20
(a) R/t = 5, (b) R/t = 10, (c) R/t = 20

(a)

	n = 3	n = 5	n = 7	n = 10
θ	h_1	h_1	h_1	h_1
45.0	3.27	2.89	2.24	1.47
90.0	1.31	0.73	0.44	0.22
θ	h_2	h_2	h_2	h_2
45.0	3.81	3.25	2.60	1.72
90.0	2.05	1.08	0.64	0.32

(b)

	n = 3	n = 5	n = 7	n = 10
θ	h_1	h_1	h_1	h_1
45.0	4.61	6.34	7.32	8.55
90.0	2.32	1.29	0.77	0.38
θ	h_2	h_2	h_2	h_2
45.0	5.18	7.16	8.49	9.55
90.0	3.45	1.93	1.13	0.55

(c)

	n = 3	n = 5	n = 7	n = 10
θ	h_1	h_1	h_1	h_1
45.0	3.32	11.58	27.53	72.32
90.0	6.18	4.20	2.91	1.72
θ	h_2	h_2	h_2	h_2
45.0	3.06	14.62	35.51	93.56
90.0	7.79	5.84	4.24	2.58

Table F.6 Elbow with axial crack – pure bending compilation (θ = 15, 30°)□ for use with Equations E.19 and E.20
(a) R/t = 5, (b) R/t = 10, (c) R/t = 20

(a)

	n = 3	n = 5	n = 7	n = 10
θ	h_1	h_1	h_1	H_1
15.0	5.8	9.1	13.6	22.8
30.0	4.0	5.6	7.5	11.4
Inner Diameter				
θ	h_2	h_2	h_2	h_2
15.0	11.2	18.5	28.4	49.4
30.0	8.3	12.0	16.5	25.8
Inner Diameter				
θ	h_2	h_2	h_2	h_2
15.0	-3.2	-4.1	-5.6	-8.7
30.0	2.1	3.6	5.4	9.0

(b)

	n = 3	n = 5	n = 7	n = 10
θ	h_1	h_1	h_1	h_1
15.0	22.1	54.6	123.0	467.5
30.0	15.5	35.4	76.5	240.1
Inner Diameter				
θ	h_2	h_2	h_2	h_2
15.0	29.2	80.8	195.8	777.9
30.0	25.1	61.3	138.6	457.0
Inner Diameter				
θ	H_2	h_2	h_2	h_2
15.0	-10.8	-23.1	-49.5	-176.30
30.0	8.7	24.5	58.8	205.6

(c)

	n = 3	n = 5	n = 7	n = 10
θ	h_1	h_1	h_1	h_1
15.0	83.4	358.0	1422.8	12395.0
30.0	64.6	259.4	1017.9	8254.8
Inner Diameter				
θ	h_2	h_2	h_2	h_2
15.0	78.8	390.7	1705.8	15853.2
30.0	86.1	385.3	1609.4	13664.0
Inner Diameter				
θ	H_2	h_2	h_2	h_2
15.0	-27.1	-104.5	-400.8	-3240.7
30.0	45.0	219.7	951.6	8350.6

F.8 SIMPLIFIED ANALYSIS FOR THROUGH-WALL CRACKS IN ELBOWS

To establish a more complete Regulatory Guide for Leak-Before-Break, an evaluation procedure for through-wall cracks in elbows was desired. Finite element solutions for elbows with axial and circumferential cracks under combined pressure and bending have been developed as discussed above. This effort was somewhat similar to the work done for surface cracks in NUREG/CR-6444, "Fracture Behavior of Circumferentially Surface-Cracked Elbows" that was done for the IPIRG-2 program, Ref. F.14.

The recent through-wall-cracked elbow work developed a limited number of finite element solutions and a J-estimation scheme with h-function fits through these solutions. As with the case of the prior surface-cracked elbow work, it was desirable to see if a simplified solution could be developed from these results and be applicable over a wider range of through-wall cracks in elbows.

F.8.1 Finite Element Analyses

As discussed above, numerous 3-D finite element analyses were developed for the intent of developing a J-estimation scheme analyses. In developing these analyses, there were a limited number of analyses that could be conducted. The analyses conducted were for:

- Axial (flank) cracks with two crack lengths,
- Circumferential (extrados) cracks with two crack lengths,
- Elbows with two different cross-sectional radius-to-thickness (R/t) ratios,
- 90-degree, long-radius elbows,
- Materials with several different strain-hardening exponents, and
- Combined internal pressure and bending.

The initial finite element analyses were made with a constant pressure and varying the bending moment. For the estimation scheme developed, additional analyses were conducted where the pressure was varied in proportion to the bending moment. In the constant pressure cases, the pressure was fixed so that the hoop stress corresponded to the average design stress (S_m) of nuclear pipe materials. From NUREG/CR-6445, this S_m value was estimated to be 122.5 MPa (17.7 ksi), Ref. F.1.

For the purpose of evaluating an estimation procedure, the constant pressure elbow finite element results were used directly, rather than using the estimation procedure.

The cases chosen to evaluate were:

- The longest and shortest crack lengths,
- Both axial and circumferential crack orientations, and
- The largest and smallest cross-sectional R/t ratios.

Since most nuclear pipe materials have strain-hardening exponents of about 5, only that case was examined. Thus, the extreme eight cracked elbow cases were examined.

F.8.2 Simplified Procedures

In NUREG/CR-6444, a simplified procedure was developed for surface cracks in elbows, Ref. F.14. This involved comparing the elbow results to those for a circumferential surface crack in a pipe of the same dimensions and with the same material properties.

From that report, it was found that the ratio of the pipe to the elbow moments at the same J value was constant as the J value increased. This constant ratio between the elbow and pipe moment values for a particular case was found to be theoretically correct when comparing the general equations for fully plastic solutions for straight pipes and elbows as given below:

$$J^{pipe} = \alpha\sigma_0\varepsilon_0 b h_1^{pipe}(M^{pipe}/M_0^{pipe})^{n+1} \quad \text{(F.22a)}$$

$$J^{elbow} = \alpha\sigma_0\varepsilon_0 b[R_m/(\lambda_1 t)]h_1^{elbow}(M^{elbow}/M_0^{elbow})^{n+1} \quad \text{(F.22b)}$$

where,

$\alpha, \sigma_o, \varepsilon_o, n$ = Ramberg-Osgood parameters
h_1^{pipe}, h_1^{elbow} = FEM determined geometric parameters relating moment to J
M_o^{pipe}, M_o^{elbow} = reference moments at a stress of σ_o
b = t-a
t = thickness
λ_1 = an elbow parameter = $R_{el}t/R_m^2$
R_{el} = bend radius of the elbow
R_m = mean radius of pipe and elbow

Considering the case where $J^{pipe} = J^{elbow}$, for the same material, pipe size, and crack size gives

$$h_1^{pipe}(M^{pipe}/M_o^{pipe})^{n+1}|_J = h_1^{elbow} [R_m/(\lambda_1 t)](M^{elbow}/M_o^{elbow})^{n+1}|_J \quad \text{(F.23)}$$

Rearranging Equation F.23 gives

$$(M^{pipe}/M^{elbow})|_J = [(h_1^{elbow}/h_1^{pipe})^{1/(n+1)} [R_m/(\lambda_1 t)]^{1/(n+1)}(M_o^{pipe}/M_o^{elbow})]|_J \quad \text{(F.24)}$$

For a given material, pipe, and elbow geometry and similar crack size, the right-hand side of Equation F.24 is a constant and independent of the J value, and hence $(M^{pipe}/M^{elbow})|_J$ is a constant. The plastic part of J dominates the moment ratio for $J_{applied}$ values of generally greater than 100 kJ/m^2 (570 in-lb/in^2), which bounds the toughness range of typical nuclear piping materials, except perhaps some aged CF8M steels. It was then found that the constant value for the particular crack-size/pipe radius-to-thickness geometry/material case varied linearly with the elbow stress indices, B_2. This same simplified approach was examined for through-wall cracks in elbows as part of this effort.

F.8.2.1 Straight-Pipe Solutions - For the relative comparison of the moment versus J solutions of the straight pipe to the elbow cases, two different circumferential through-wall-cracked straight-pipe solutions were used. These were the LBB.ENG2 and original GE/EPRI methods in Version 3.0 of NRCPIPE.

The LBB.ENG2 method was used since it was the most accurate in predicting the maximum moment for through-wall-cracked straight-pipe experiments, Ref. F.9. However, the LBB.ENG2 analysis requires an additional parameter that was not used in the FE solutions, that is, the ultimate strength of the material. For this analysis procedure it was assumed that the yield to-ultimate strength ratio was 0.85.

The GE/EPRI solution does not need the ultimate strength of the material, so it was also used. However, it was experimentally found that the GE/EPRI analysis was the most conservative analysis in predicting the full-scale straight-pipe experiments, i.e., it overpredicted the crack-driving force, Ref. F.9.

All analyses were for 410-mm (16.14-inch) outside diameter pipe. Additionally, all analyses were conducted with non-growing cracks.

F.8.2.2 Comparison of Circumferential Extrados Through-Wall-Cracked Elbow and Straight-Pipe Solutions - To make this comparison, the J versus moment curves from both the straight pipe and elbow solutions were first compared. Figures F.18 and F.19 show the results for the circumferential crack case with an R/t of 20 and total crack lengths of 90 and 180 degrees. Note in Figure F.18 that there is also a curve for an elbow curve-fit equation. This was done since the pipe and elbow solutions did not have values at exactly the same J values. The elbow curve-fit equation (as shown in Figure F.18) was used to compare the moments of the elbow to the straight pipe at the same J values, i.e., for $(M^{pipe}/M^{elbow})|_J$.

Figure F.18 shows that the curve fit is a very close approximation of the FE data points. Also, there is a difference in the two straight-pipe solutions, with the GE/EPRI solution giving higher J-values as was expected.

In Figure F.19, it is interesting to note that the elbow and LBB.ENG2 straight-pipe analyses give similar results, whereas the GE/EPRI solution for the straight pipe gives much higher J values. After these analyses were completed, it was recalled that the 180-degree crack R/t=20 analysis in the GE/EPRI solution in NRCPIPE was found to be in error, so that in this case only the LBB.ENG2 analysis should be used.

The results for the R/t = 5 case are show in Figures F.20 and F.21.

The next step was to compare the ratio of the moments at the same J value. A graph of the J value versus the moment ratio is given for each case in Figures F.22 to F.25.

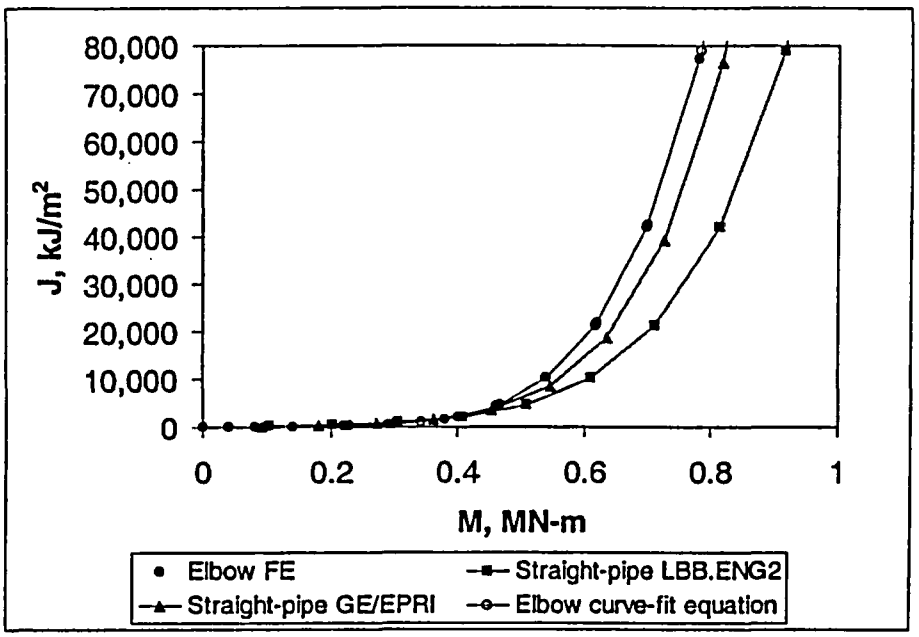

Figure F.18 Comparison of J versus moment curves for a circumferential through-wall crack in a straight pipe and centered on the extrados of an elbow with an R/t = 20 and 2θ=90 degrees

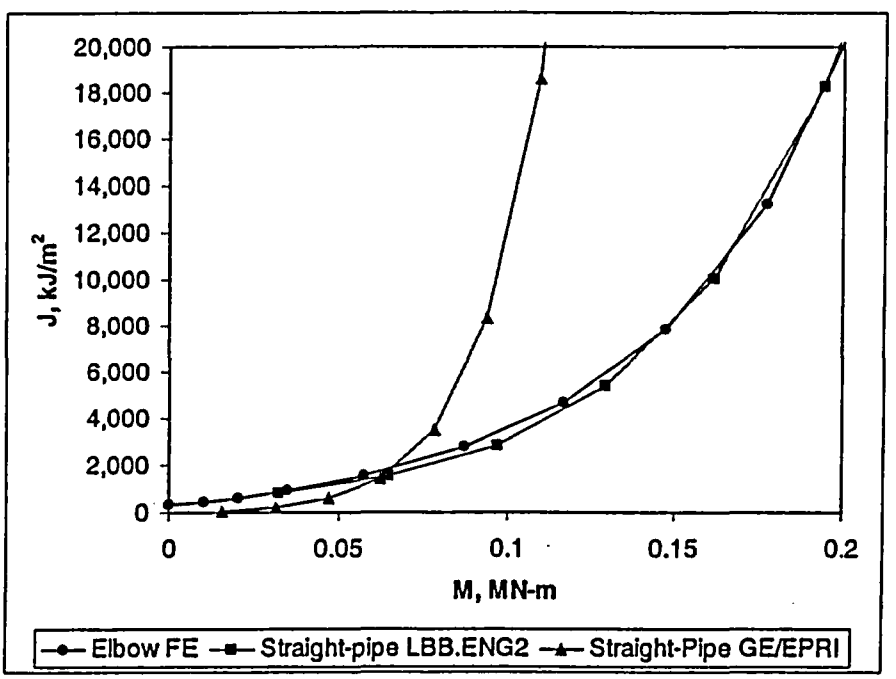

Figure F.19 Comparison of J versus moment curves for a circumferential through-wall crack in a straight pipe and centered on the extrados of an elbow with an R/t = 20 and 2θ=180 degrees

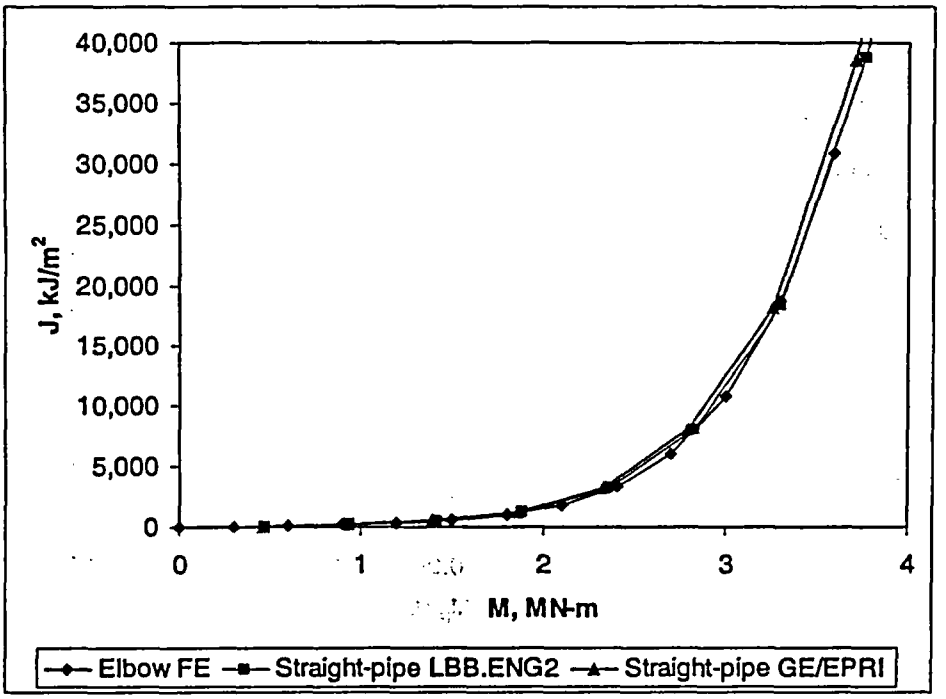

Figure F.20 Comparison of J versus moment curves for a circumferential through-wall crack in a straight pipe and centered on the extrados of an elbow with an R/t = 5 and 2θ=90 degrees

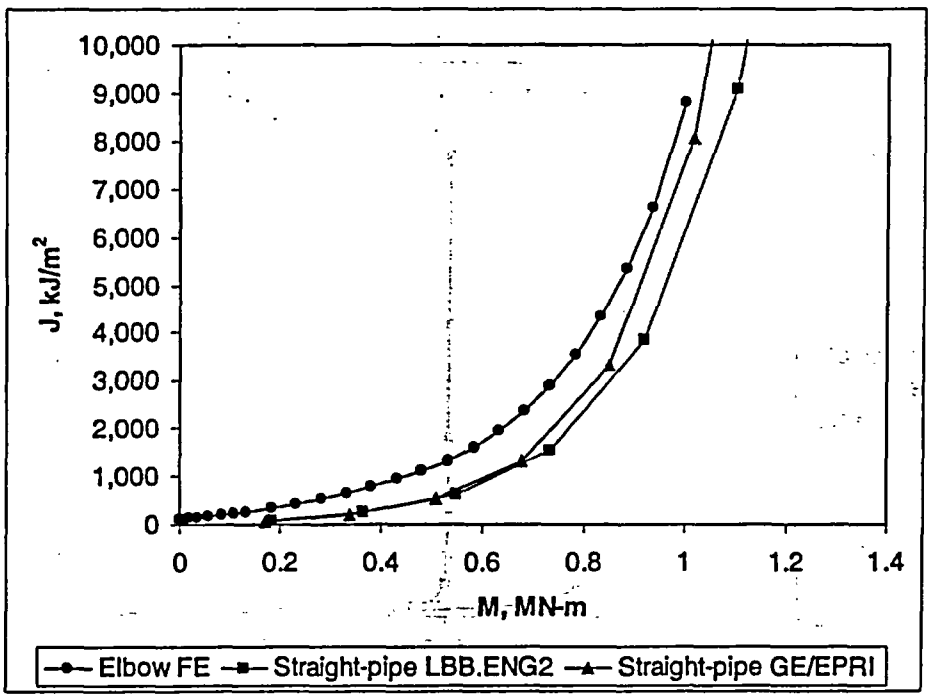

Figure F.21 Comparison of J versus moment curves for a circumferential through-wall crack in a straight pipe and centered on the extrados of an elbow with an R/t = 5 and 2θ=180 degrees

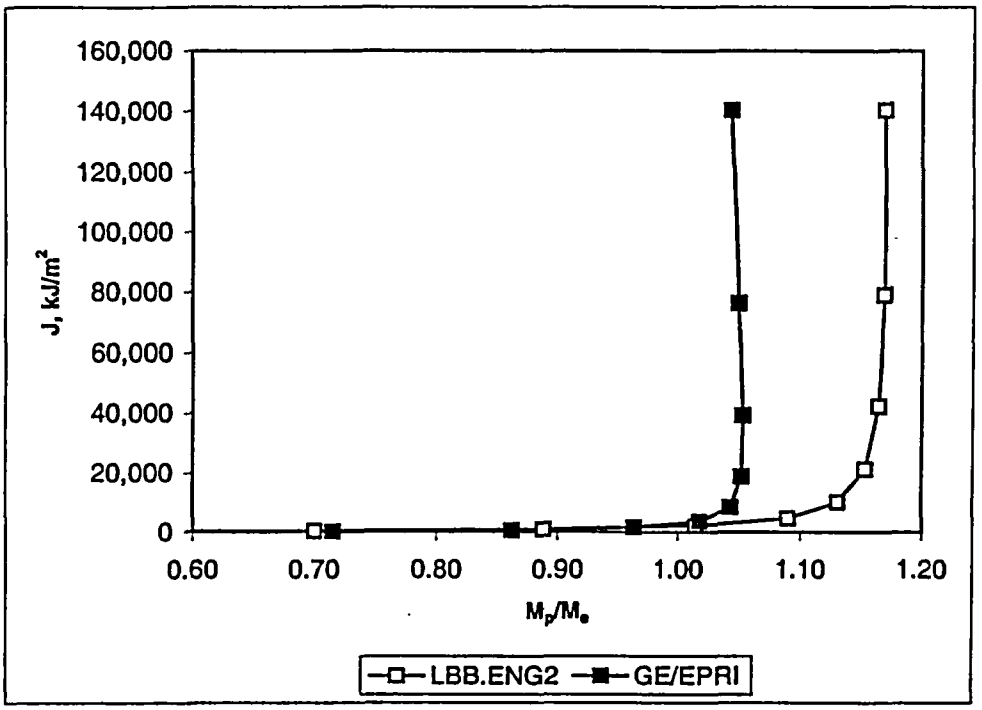

Figure F.22 Comparison of J versus moment ratios for a circumferential through-wall crack in a straight pipe and centered on the extrados of an elbow with an R/t = 20 and 2θ=90 degrees

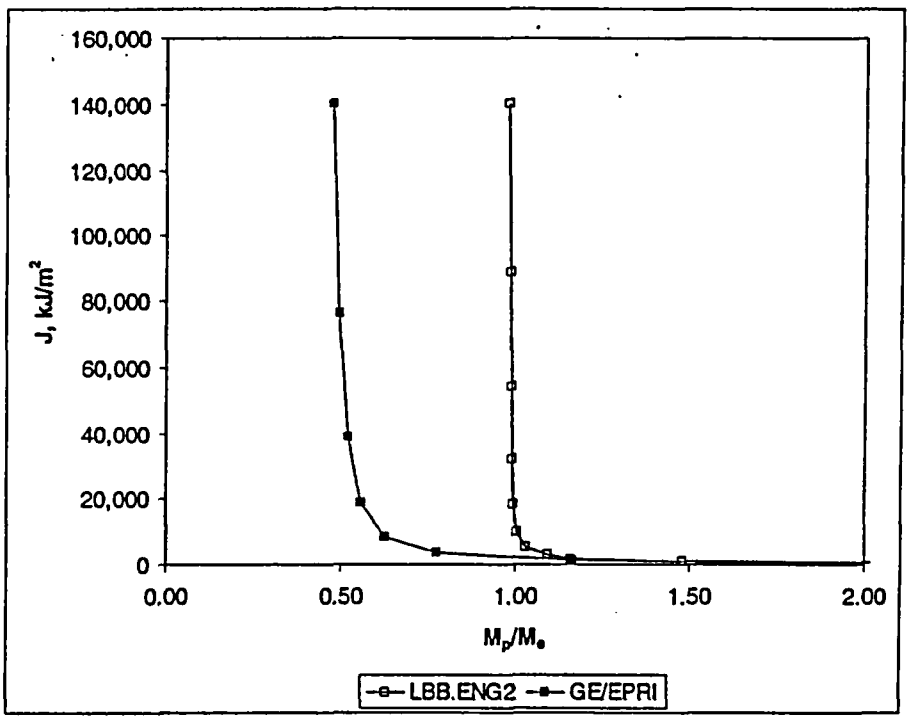

Figure F.23 Comparison of J versus moment ratios for a circumferential through-wall crack in a straight pipe and centered on the extrados of an elbow with an R/t = 20 and 2θ=180 degrees

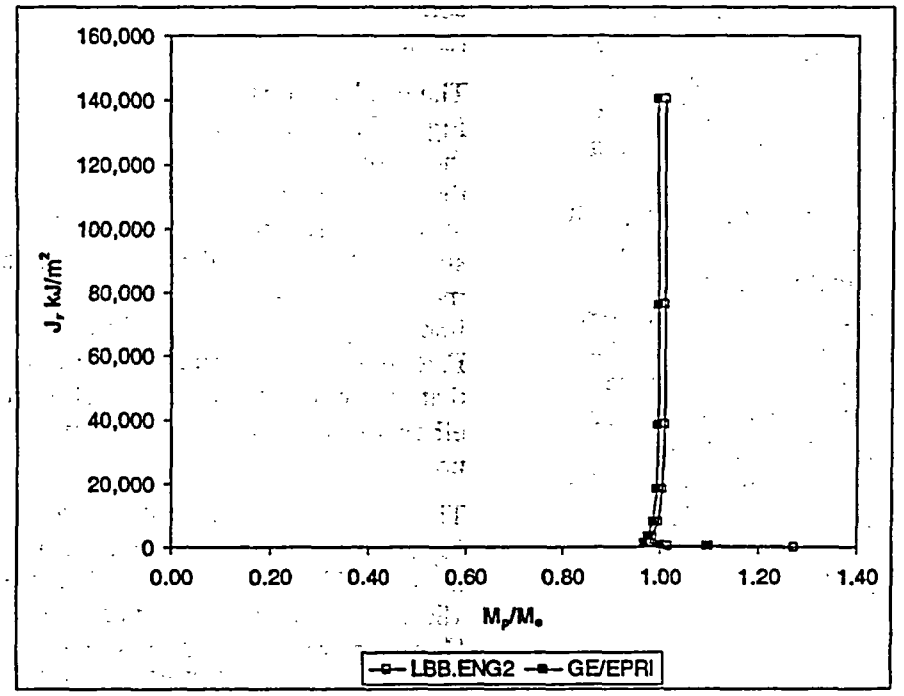

Figure F.24 Comparison of J versus moment ratios for a circumferential through-wall crack in a straight pipe and centered on the extrados of an elbow with an R/t = 5 and 2θ=90 degrees

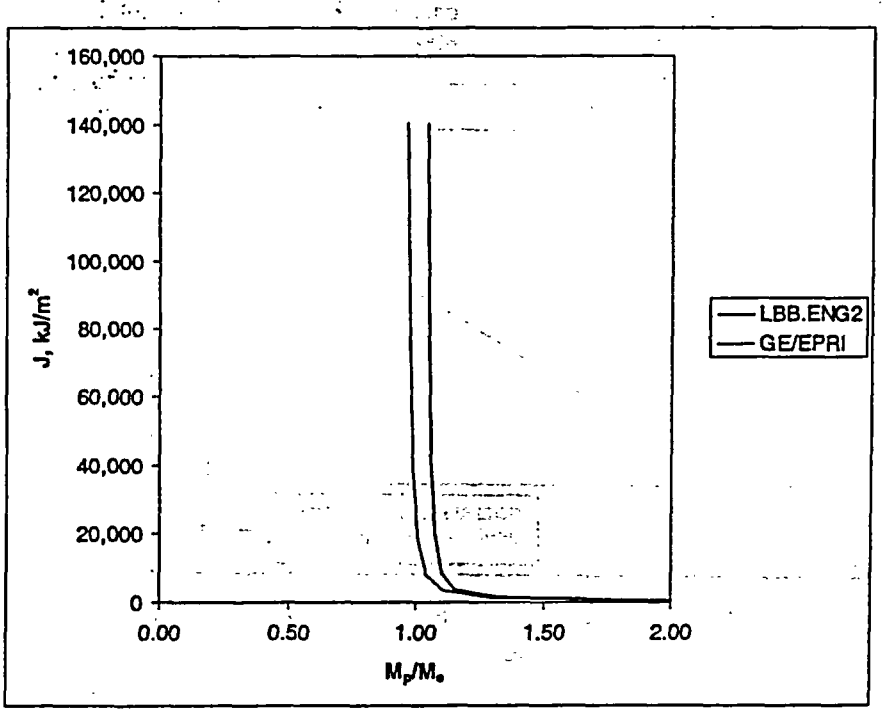

Figure F.25 Comparison of J versus moment ratios for a circumferential through-wall crack in a straight pipe and centered on the extrados of an elbow with an R/t = 5 and 2θ=180 degrees

The final step was to compare the constant moment ratio values from Figures F.22 to F.25 to the stress indices for the elbows. Since the elbow was under bending, the ASME B_2 index was used. The B_2 index is for primary bending stresses to avoid failure by collapse (using the design stress analysis definition of limit load). It should be noted that the elbow stress indices essentially gives a stress multiplier for the location in the piping product where the stresses are the highest. For the case of an elbow under bending, the stresses are the highest along the flank of the elbow normal to the axial direction. Equations F.25 and F.26 define the B_2 stress index from Section III, Article NB-3683.7 of the ASME Boiler and Pressure Vessel Code.

$$B_2 = 1.3h^{2/3}, B_2 \geq 1.0 \qquad \text{(F.25)}$$

Where,

$$h = tR_{el} / R_m^2 \qquad \text{(F.26)}$$

These equations assume the elbows have a perfectly circular cross section, which was a condition in the development of the FE elbow results.

The results of this comparison are shown in Figure F.26. If there is essentially no effect of the elbow curvature on the fracture behavior, then the moment ratios should be close to 1.0 for all B_2 values. On the other hand, if there was a strong effect of the elbow curvature, then the moment ratios should be close to the 45-degree line in Figure F.26. As can be seen in Figure F.26, the values are all close to 1.0 indicating that for a circumferential through-wall flaw in an elbow that the straight-pipe solution could be used.

There was one data point that gave an M_{pipe}/M_{elbow} value of about 0.5. This was when the GE/EPRI solution was used for the case of a 180-degree flaw in pipe with an R/t of 20. However, we know that the solution in this case is not correct in NRCPIPE so that this data point can be disregarded. Consequently, the circumferential through-wall-flaw straight-pipe solution could be used in the new LBB Regulatory Guide for the fracture analyses of the case of a circumferential through-wall flaw in an elbow.

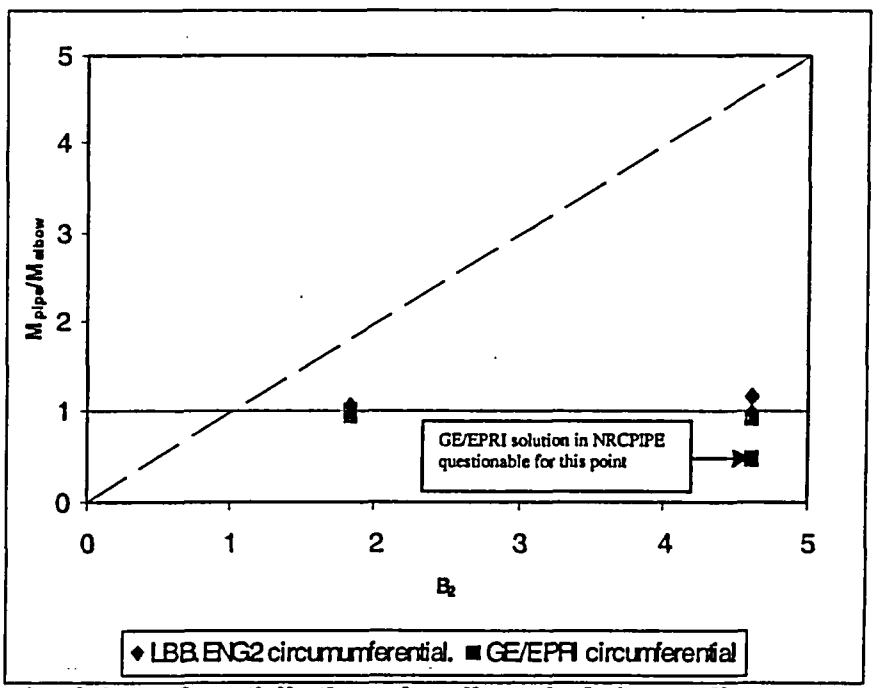

Figure F.26 Ratio of circumferentially through-wall-cracked pipe-to-elbow moments for constant applied J values versus the ASME B_2 index for the elbow

F.8.2.3 Comparison of Axial Flank Through-Wall-Cracked Elbow and Straight-Pipe Solutions - To make this comparison, the J versus moment curves from both the straight-pipe and elbow solutions were compared in a similar manner as was done for the elbow circumferential crack case. Figures F.27 and F.28 show the results for the axial flank crack case with an R/t of 20 and total crack lengths of 15 and 30 degrees. Figures F.29 and F.30 show the results for the axial flank crack case with an R/t of 5 and total crack lengths (2θ) of 15 and 30 degrees.

In Figures F.27 to F.30, it can be seen that the elbow solutions give higher J values than the straight pipe solutions for the same moment. The GE/EPRI solution always gives a higher crack-driving force than the LBB.ENG2 analysis for the two straight-pipe solutions. This is consistent with past experience. The crack lengths are much shorter in these analyses than what was used in the circumferential cracked elbow analysis, so that there was no problem with either straight-pipe solution in the NRCPIPE code.

The next step was to compare the ratio of the moments at the same J value. A graph of the moment ratio versus the J value is given for each case in Figures F.31 to F.34. Again note how the moment ratio reaches a constant value as the plastic solution of J dominates.

The final step was to compare the constant moment ratio values from Figures F.31 to F.34 to the B_2 stress indices for the elbows.

The results of this comparison are shown in Figure F.35. If there is essentially no effect of the elbow curvature on the fracture behavior, then the moment ratios should be close to 1.0 for all B_2 values. On the other hand, if there was a strong effect of the elbow curvature, then the moment ratios should be close to the 45-degree line in Figure F.35.

As can be seen in Figure F.35, the moment ratio values show that there is an effect of the elbow curvature on the crack-driving force for an axial through-wall crack on the flank of an elbow. A conservative option would be to divide the circumferential through-wall straight-pipe moment by the elbow B_2 value for an axial through-wall flaw on the flank of the elbow. Alternatively, a linear correction such as suggested by the lines in Figure F.35 could be used. Consequently, the moment from a circumferential through-wall-flaw straight-pipe solution (under pressure and bending) divided by the elbow B_2 stress index could be used in the new LBB Regulatory Guide for the fracture analyses for the axial flank through-wall flaw case in an elbow.

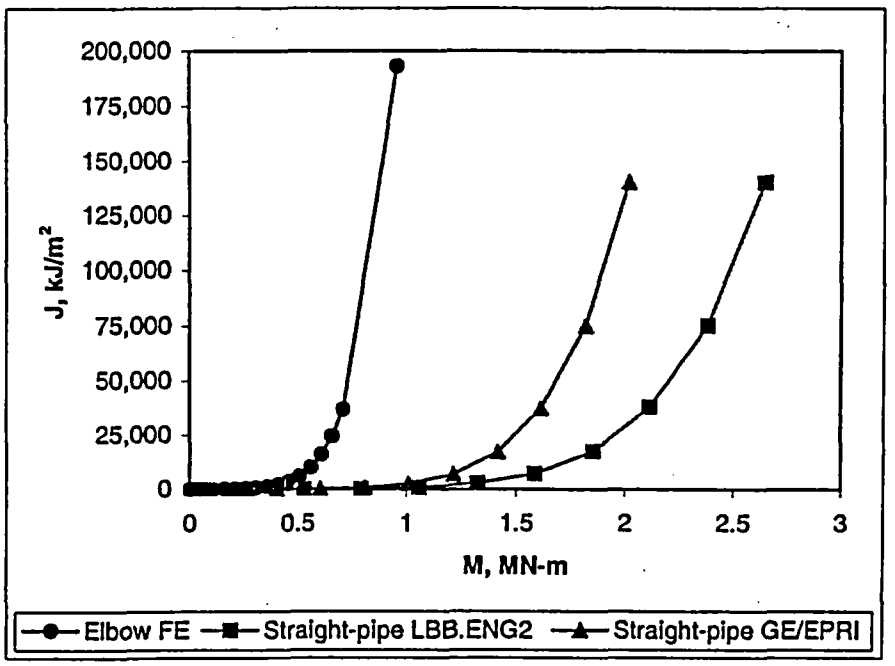

Figure F.27 Comparison of J versus moment curves for an axial through-wall crack in a straight pipe and an axial through-wall crack on the flank of an elbow with an R/t = 20 and 2θ=15 degrees

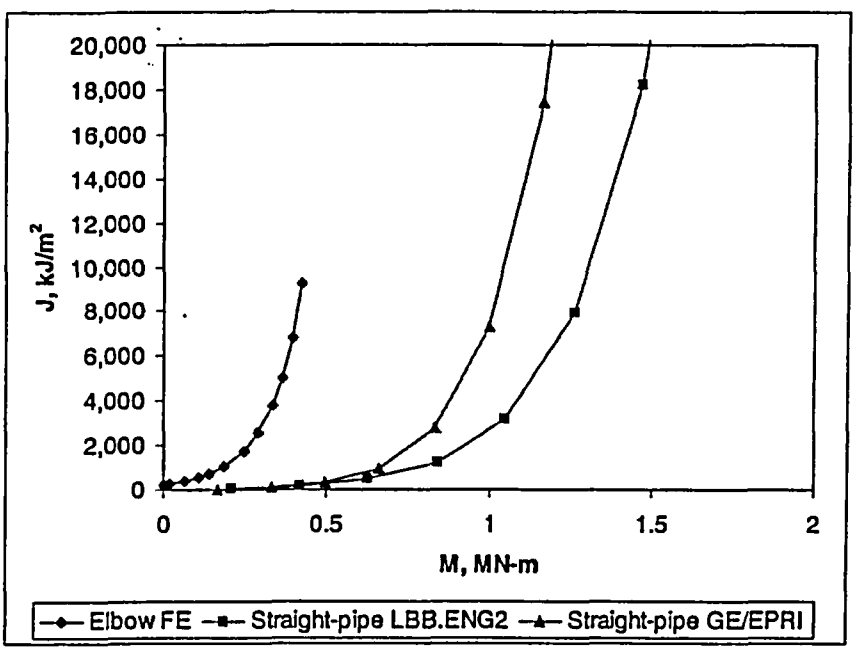

Figure F.28 Comparison of J versus moment curves for an axial through-wall crack in a straight pipe and an axial through-wall crack on the flank of an elbow with an R/t = 20 and 2θ=30 degrees

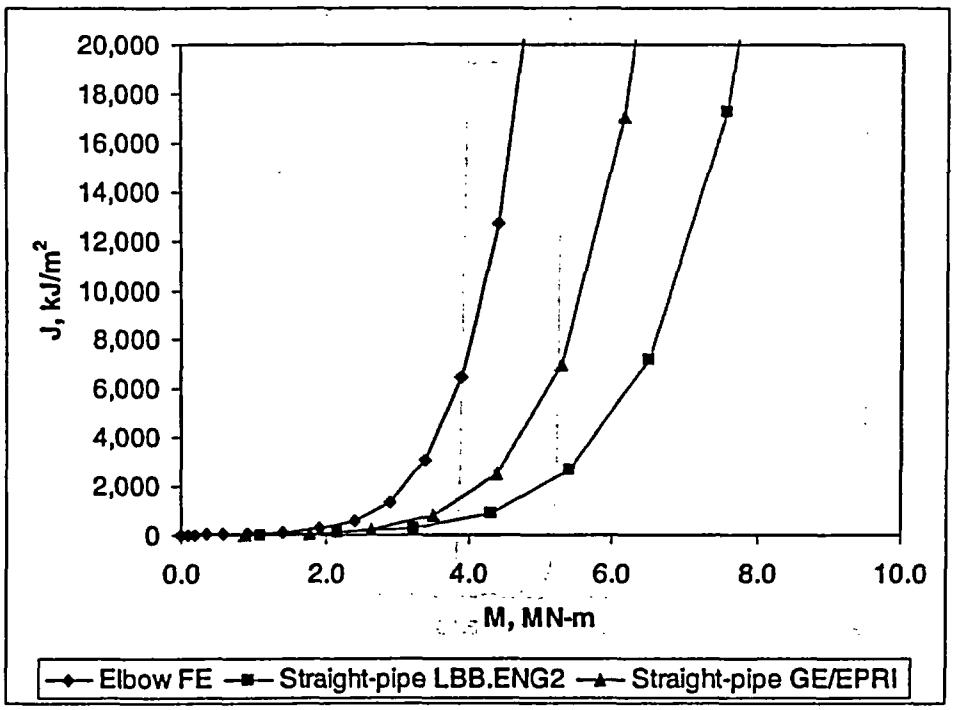

Figure F.29 Comparison of J versus moment curves for an axial through-wall crack in a straight pipe and an axial through-wall crack on the flank of an elbow with an R/t = 5 and 2θ=15 degrees

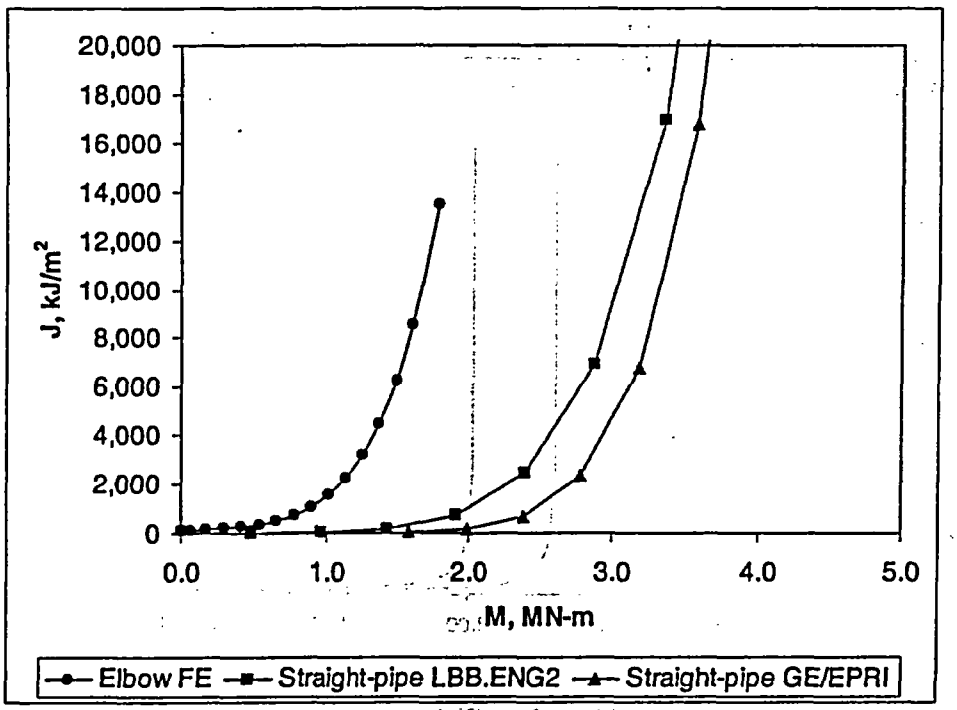

Figure F.30 Comparison of J versus moment curves for an axial through-wall crack in a straight pipe and an axial through-wall crack on the flank of an elbow with an R/t = 5 and 2θ=30 degrees

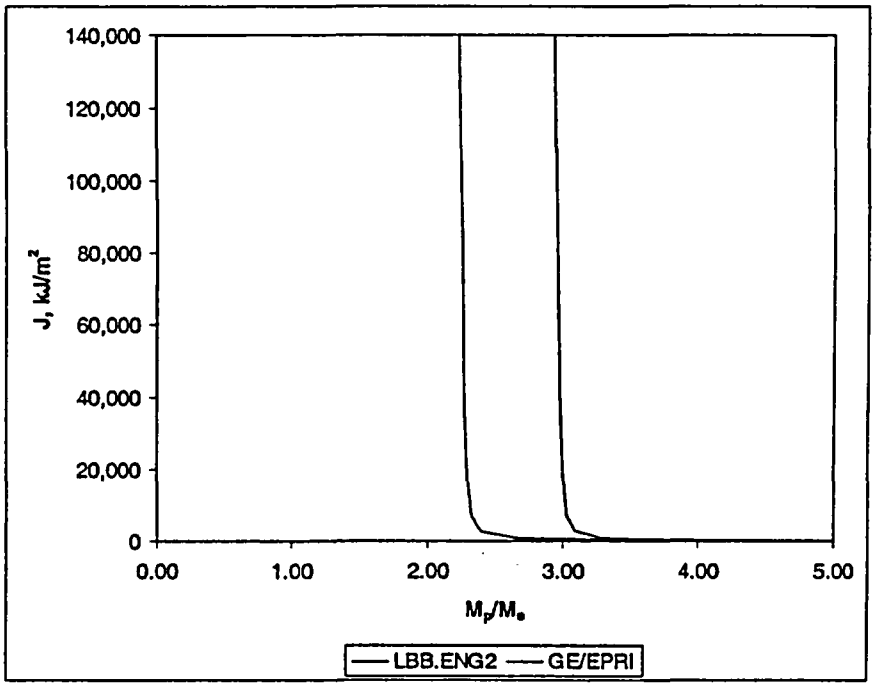

Figure F.31 Comparison of J versus moment ratios for an axial through-wall crack in a straight pipe and an axial through-wall crack on the flank of an elbow with an R/t = 20 and 2θ=15 degrees

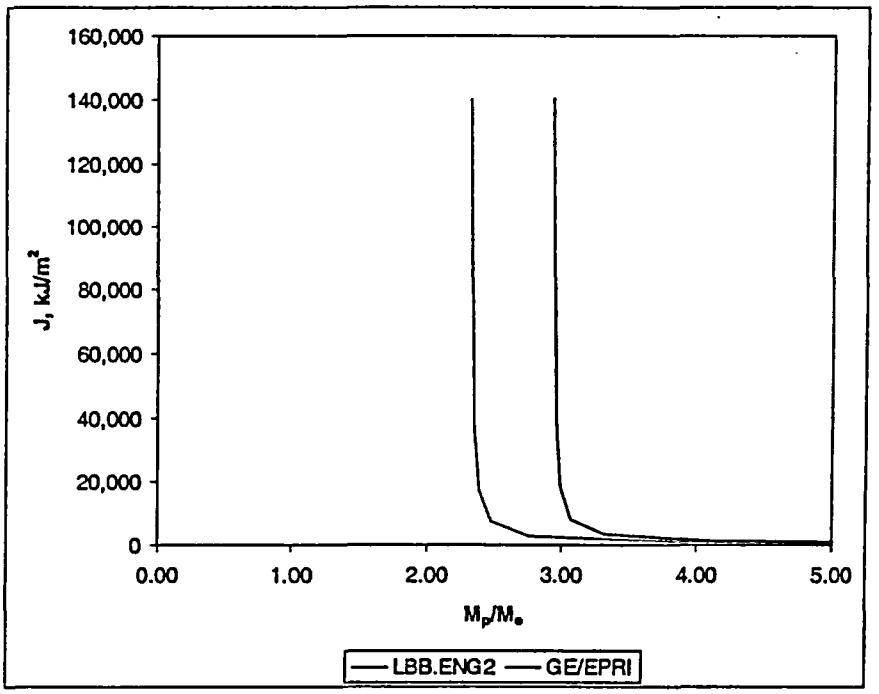

Figure F.32 Comparison of J versus moment ratios for an axial through-wall crack in a straight pipe and an axial through-wall crack on the flank of an elbow with an R/t = 20 and 2θ=30 degrees

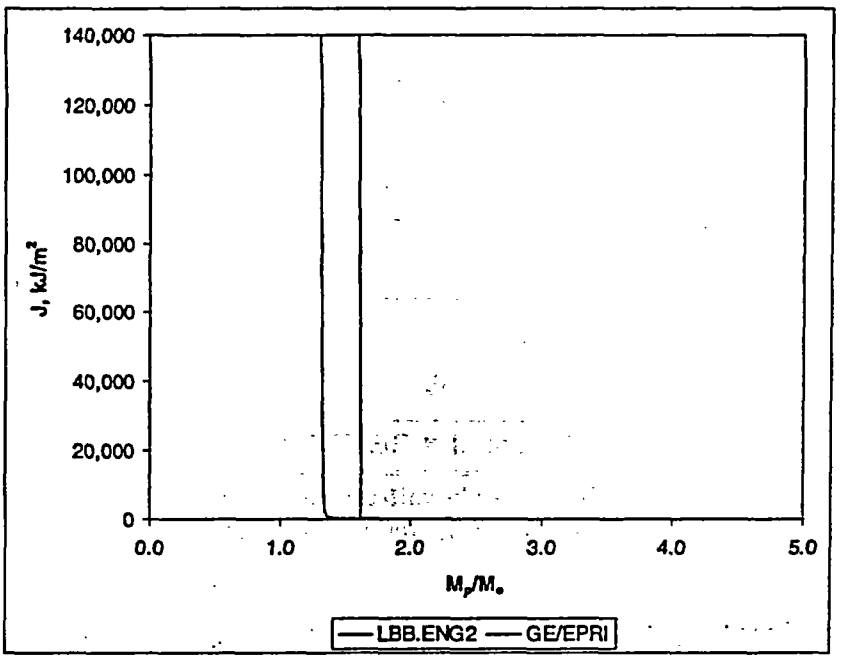

Figure F.33 Comparison of J versus moment ratios for an axial through-wall crack in a straight pipe and an axial through-wall crack on the flank of an elbow with an R/t = 5 and 2θ=15 degrees

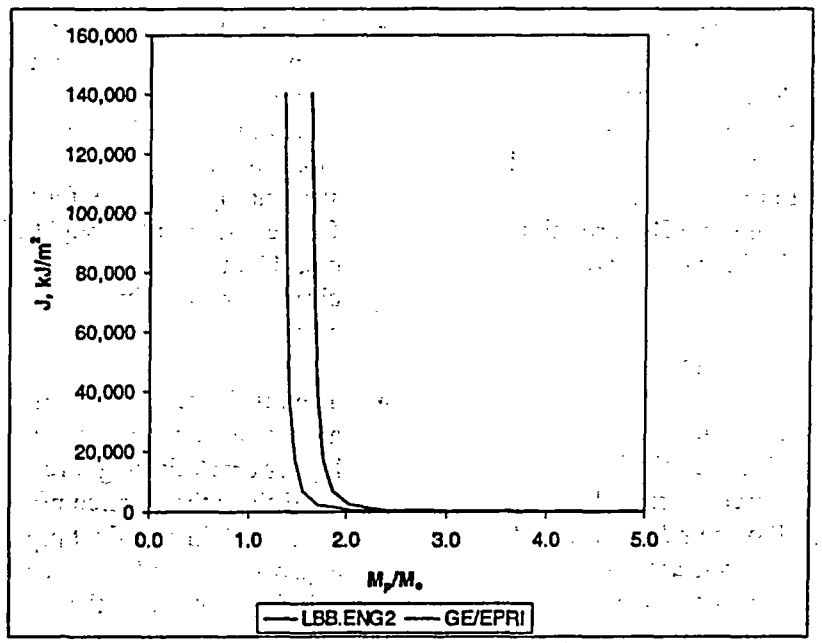

Figure F.34 Comparison of J versus moment ratios for an axial through-wall crack in a straight pipe and an axial through-wall crack on the flank of an elbow with an R/t = 5 and 2θ=30 degrees

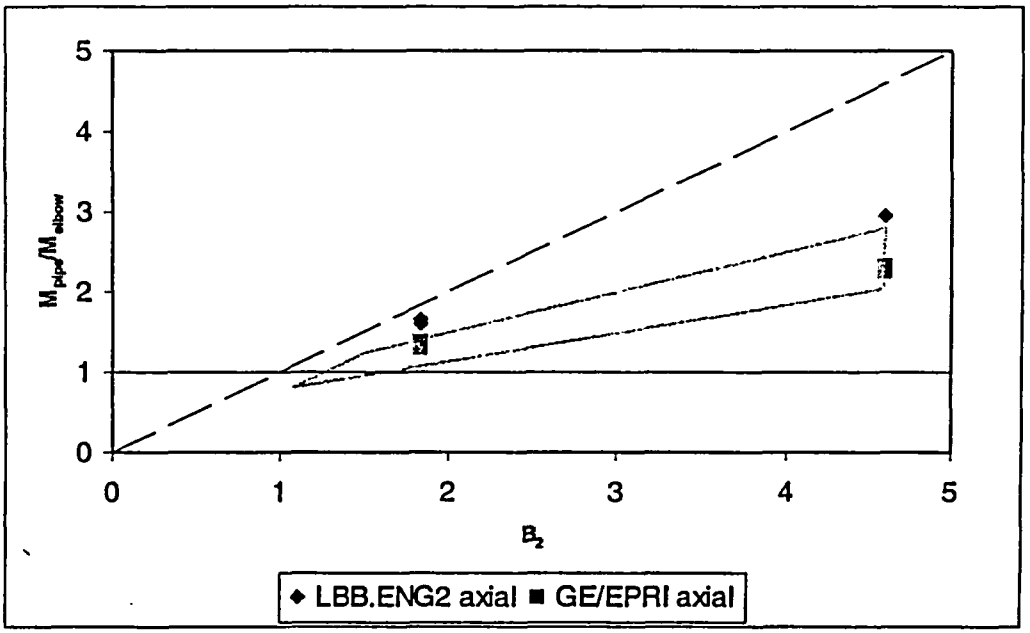

Figure F.35 Ratio of axially through-wall-cracked pipe-to-elbow moments for constant applied J values versus the ASME B_2 index for the elbow

F.8.2.4 Comments on Crack-Opening Displacement - The analyses conducted in Sections F.8.2.2 and F.8.2.3 for circumferential and axial through-wall cracks in elbows, respectively, were for determining the crack-driving force when plasticity occurs. This would be valid for the LBB fracture assessment under normal plus SSE loads. The crack-opening displacement, however, occurs under more elastic loading conditions. It was beyond the scope of this effort to make those comparisons, and using the same B_2 correction approach should be used with caution with the COD analysis.

F.8.3 Summary and Conclusions

The objective of this evaluation was to determine if a more simplified analysis could be established for axial and circumferential through-wall cracks in elbows under combined pressure and bending. This was assessed by using the elbow finite element analyses developed as part of this effort with a hoop stress loading of 1.0 S_m for typical nuclear piping steels. The approach undertaken was to compare the ratio of the moments for the same size crack in an elbow and straight-pipe at the same applied J values. This was similar to efforts done for circumferential surface flaws in elbows in the IPIRG-2 program. The following conclusions came from this analysis.

- The results of the analysis showed that a circumferential crack centered on the extrados of an elbow had the same crack-driving force under plastic conditions as a circumferential through-wall crack in a straight pipe. Hence, for the new LBB Reg. Guide, the simple straight-pipe solutions could be used for the fracture analysis of a circumferential through-wall crack in an elbow.

- The results of the analysis showed that an axial crack on the flank of an elbow had a higher crack-driving force under plastic conditions than a circumferential through-wall crack in a straight pipe. A conservative approach would be to use the straight-pipe solution, but divide the straight-pipe moment by the elbow B_2 index. This could readily be done in the new LBB Reg. Guide Level 1 or 2 analyses for the fracture analysis of an axial flank through-wall crack in an elbow.

- The COD evaluations were not conducted in this effort. Caution should be used in applying this same approach for the COD values since the COD should be for elastic loading where the constant moment ratio that occurs under plastic conditions does not exist.

F.9 References

F.1 Mohan, R., Brust, F. W., Ghadiali, N. D., and Wilkowski, G. M., "Development of a J–Estimation Scheme for Internal Circumferential and Axial Surface Cracks in Elbows", NUREG/CR 6445, June, 1996.

F.2 Kumar, V., German, M., and Shih, E., "An Engineering Approach for Elastic-Plastic Fracture Analysis ", EPRI Report No. NP-1931, July 1981.

F.3 Kumar, V., German, M., Wilkening, Andrews, W., deLorenzi, H., and Mowbray, D., "Advances in Elastic-Plastic Analysis " EPRI Final Report NP-3607, August 1984.

F.4 Kumar, V., and German, M. D., "Elastic-Plastic Fracture Analysis of Through-Wall and Surface Flaws in Cylinders", EPRI Final Report NP-5596, January, 1988.

F.5 P. Gilles and F. W. Brust, "Approximate Fracture Methods for Pipes, Part I, Theory", Nuclear Engineering and Design, Vol. 127, pp. 1-17, 1991.

F.6 P. Gilles, K. S. Chao, and F. W. Brust, "Approximate Fracture Methods for Pipes, Part II, Applications," Nuclear Engineering and Design , Vol. 127, pp. 19-31, 1991.

F.7 Scott, P. M., and Ahmad, J., "Experimental and Analytical Assessment of Bending Circumferentially Surface-Cracked Pipes Under Bending", NUREG/CR-4872, April 1987.

F.8 Rahman, S. and Brust, F. W., "Approximate Methods for Predicting J-integral of a Circumferentially Surface-Cracked Pipe Subject to Bending," International Journal of Fracture, Vol. 85, No. 2, October 1997, pp. 111-130.

F.9 Brust, F., Scott, P., Rahman, S., Ghadiali, N., Kilinski, T., Francini. R., Krishnaswamy, P., and Wilkowski, G., "Assessment of Short Through-Wall Cracks in Pipes - Experiments and Analyses," Topical Report, NUREG/CR-6235, U. S. Nuclear Regulatory Commission, Washington, DC, April 1995

F.10 Krishnaswamy, P., Scott, P., Choi, Y., Mohan, R., Rahman, S., Brust, F., and Wilkowski, G., "Fracture Behavior of Short Circumferentially Surface-Cracked Pipe," Topical Report, NUREG/CR-6298, U. S. Nuclear Regulatory Commission, Washington, DC, November 1995.

F.11 Rahman, S., and Brust, F. W., "Elastic-Plastic Fracture of Circumferential Through-Wall Cracked Pipe Welds Subject to Bending", ASME Journal of Pressure Vessel Technology, Vol. 114, pp 410-416, November, 1992.

F.12 Mohan, R., Krishna, A., Brust, F. W., and Wilkowski, G., " J-estimation Scheme for Internal Circumferential and Axial Surface Cracks in Pipe Elbows," ASME *J. of Pressure Vessel Technology*, Vol. 120, Nov. 1998.

F.13 Kilinski, T., and others, "Fracture Behavior of Circumferentially Surface-Cracked Elbows," NUREG/CR-6444, December 1996.

APPENDIX G

EVALUATION OF REACTOR PRESSURE VESSEL (RPV) NOZZLE TO HOT-LEG PIPING BIMETALLIC WELD JOINT INTEGRITY FOR THE V. C. SUMMER NUCLEAR POWER PLANT

G.1 SUMMARY

In October 2000 the V. C. Summer Plant was shut down for a normal refueling outage. During the normal inspection a leak was discovered in the vicinity of one of the reactor pressure vessel (RPV) outlet nozzle to hot-leg pipe bimetallic welds. Ultrasonic tests performed on the pipe from the inside surface revealed a single axial flaw near the top of the pipe. During destructive inspection of the crack zone, additional smaller axial flaws were identified, along with several small circumferential indications. The cracking was attributed to primary water stress corrosion cracking (PWSCC).

In order to be able to predict the growth rates for these PWSCC cracks, and therefore, predict the amount of time required before leakage occurs, a detailed analytical model of the V. C. Summer bimetallic pipe weld was performed. All of the fabrication processes involved in the construction and repair of the V. C. Summer hot leg bimetal weld were considered. This included hot leg buttering and welding of a pressure vessel nozzle to a stainless steel pipe using Inconel 82/182 filler material, material removal and repair, heat treatment, and service loads. PWSCC crack growth predictions were made for the cases of weld residual stresses only, and residual stresses with service loads. Predictions of axial cracks growth rates along with circumferential crack growth rates were made. Some of the key results from this series of analyses are summarized in the following paragraphs.

For reducing the effect of both axial and circumferential PWSCC after weld repairs, inside welding followed by outside welding is preferred. Both cases were considered in the analyses since the precise repair sequence in the V. C. Summer plant was not known. This illustrates the power of computational weld models and suggests that field weld repairs should be designed and driven by a corresponding weld analysis to reduce the propensity for SCC in piping.

In particular, hoop residual stresses (which lead to axial cracking) after complete fabrication are mostly tensile in the weld region. For the case of outside weld repair followed by inside welding, high tensile residual stresses are produced everywhere. For the inside weld followed by outside weld case, a small zone of compressive hoop residual stresses develop at the pipe inside surface at the weld. Moreover, hydro testing does not alter fabrication residual stresses very much.

Service load effects on PWSCC were also considered. Heating the hot leg pipe system up to operation temperature of 324°C (615°F) actually reduces axial fabrication stresses to mainly compressive values due to the expansion of the hot leg pipe and the rigid constraint provided by the vessel and steam generator. Hoop residual stresses are unaffected by heating up to operating temperatures. Since as fabricated axial residual stresses are low at operating temperature, circumferential stress corrosion cracking is not expected due solely to fabrication stresses. Service loads dominate circumferential PWSCC.

Axial crack growth is dominated by fabrication residual stresses, but the internal pressure does play an important role in PWSCC. Weld repairs can alter residual stresses in pipe fabrications. In general, stress reversal in sign occurs near the start/stop locations of the repair. This can possibly result in a PWSCC crack stopper or can slow down the crack growth rate as the crack approached these locations. A similar reversal in the sign of the stress occurs in a baseline weld near the torch start/stop locations or weld repairs.

The analysis results here show that axial cracking should be confined to the weld region. Starting from a crack 5 mm (0.2 inches) in depth, the crack should break through the pipe wall within two years. The crack nucleation time is something that should be studied in more detail in the future. Circumferential cracks should take about twice as long to become a through wall crack compared with axial cracks. Circumferential cracks will tend to grow longer than axial cracks. However, since service loads dominate circumferential cracks, they will slow their circumferential growth as they grow toward the bottom of the pipe. Here, by bottom of the pipe,

it is understood to be the compressive bending stress region of the pipe. The service loads consist of thermal expansion mismatch, tension caused by 'end cap' pressure, and bending. The bending stresses caused by a bending moment are compressive 180 degrees from tension zone. Part through circumferential cracks that initiate in the tension zone and grow beyond the bending neutral axis may slow down as they approach the compressive bending stress zone. However, for non-fixed bending axes, where the tension zone changes, this may not be significant.

Grinding of welds may lead to scratches, which in turn may lead to crack initiation sites. Grinding of welds should be performed carefully. It is of use to study the effect of grinding on both residual stresses (caused by grinding) and crack initiation sites. Numerical models of the grinding process can and should be developed and used to guide field grinding operations.

Finally, PWSCC growth would be best considered using a risk based probabilistic approach using TRACLIFE or similar code because of the inherent variability in many factors that lead to corrosion cracking.

G.2 INTRODUCTION

In October 2000 the V. C. Summer Plant was shut down for a normal refueling outage. During the normal inspection, significant boron deposits were discovered in the vicinity of an RPV outlet nozzle to pipe weld for the hot leg pipe (large pipe from the reactor pressure vessel to the steam generator). Leakage records showed a nearly constant value of 0.3 GPM unidentified leakage from all sources, well below the plant technical specification limit of 1.0 GPM (Ref. G.1).

The design geometry of the nozzle to pipe weld is shown in Figure G.1. Ultrasonic tests performed on the pipe from the inside surface revealed a single axial flaw near the top of the pipe [Ref G.1]. The flawed region was then removed, and a new spool piece was welded in place. The repair weld was made with Alloy 52, a material which is much more resistant to SCC (stress corrosion cracking) compared with Alloy 82/182.

The purpose of this study was to study the cracking behavior in bimetallic welds of the type used in the V. C. Summer plant. Tensile weld residual stresses, in addition to service loads, contribute to PWSCC (Primary Water SCC) crack growth. In order to be able to predict crack growth rates, and therefore, predict the amount of time required before leakage occurs for normal PWR conditions, a detailed analytical model of the V. C. Summer bimetallic pipe weld was performed.

The work plan outlined here was to help support the NRC's assessment of the cracking found in the 'A' RPV nozzle to hot-leg pipe bimetal weld in the Virgil C. Summer nuclear plant. The hot leg weld is a bimetallic weld joining a SA-508 (Class 2) reactor vessel nozzle with a Type 304N stainless steel pipe using an Inconel weld procedure (Figure G.1). Figure G.2 illustrates the geometry of this type of nuclear plant in simple format. The hot leg pipe carries reactor-heated water to the steam generator. It is then re-circulated by the pump back through the 'cold leg'. Both the hot and cold leg stainless steel pipes are joined to the reactor vessel nozzles via bimetallic welds. The cracking of concern occurs in the Inconel weld only.

The analysis work reported here was broken into three tasks. The first task was to model the residual stresses that develop from welding. This analysis included the effects of selected repair weld analyses. The second was to validate the model by performing measurements on a similar bimetallic welded pipe that was obtained during an earlier NRC program at Battelle (Ref. G.2). The final task involved evaluating stress intensity factors along with performing simple pressurized water stress corrosion cracking (PWSCC) analyses of the cracks. All work was performed as part of Task 8 of the BINP Program. Funding for this Task 8 activity was provided by the US NRC.

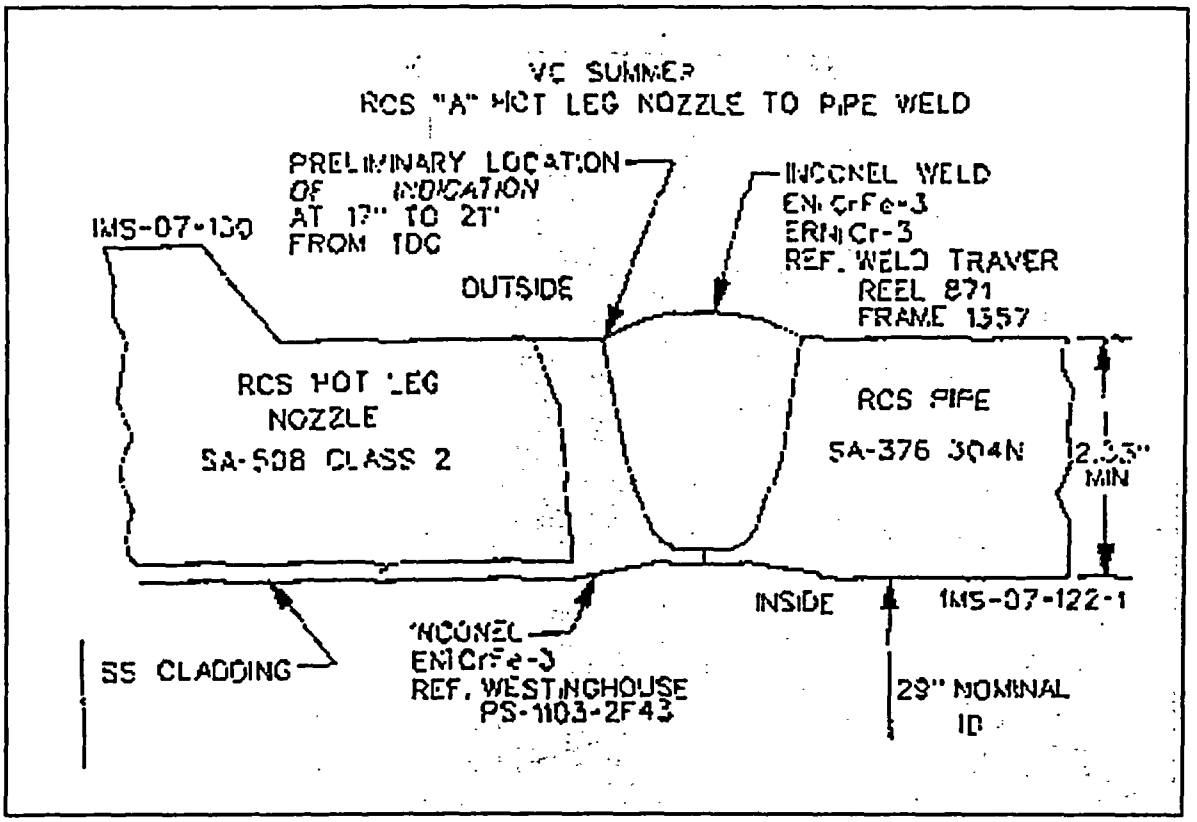

Figure G.1 Geometry of VC Summer hot leg/RPV nozzle bimetallic weld joint

G.3 GENERAL OVERVIEW OF ANALYSIS WORK PERFORMED

Three separate sets of weld analyses were performed. These included: (i) analysis of a cold leg bimetallic weld used in an experiment conducted by Battelle in an earlier NRC sponsored program [2], (ii) analysis of a typical design bimetallic weld in the V. C. Summer plant for V. C. Summer hot legs 'B' and 'C', and (iii) repair weld analyses of several typical repairs. The first analysis was planned for model validation purposes while (ii) was planned to predict the crack growth response within residual stress fields and operating loads for a typical hot leg plant weld. Analysis set (iii) quantified the important effect that weld repairs have on weld induced residual stresses and on the corresponding crack growth through the repair weld residual stress fields.

The analyses in sets (i) and (ii) were performed using both axis-symmetric analysis and full 3D analysis. The analysis set (iii) was performed using full 3D analysis. It is noted that 3D welding considerations can have an important effect on the residual stresses, especially in the region of the weld start/stop locations and for considering the effects of weld repairs. The axis-symmetric analyses of (i) and (ii) provided an initial 'general' overview of the residual stress fields in this bimetallic weld. However, as discussed below, full 3D effects will be included in the fracture assessment even for the axis-symmetric weld modeling case.

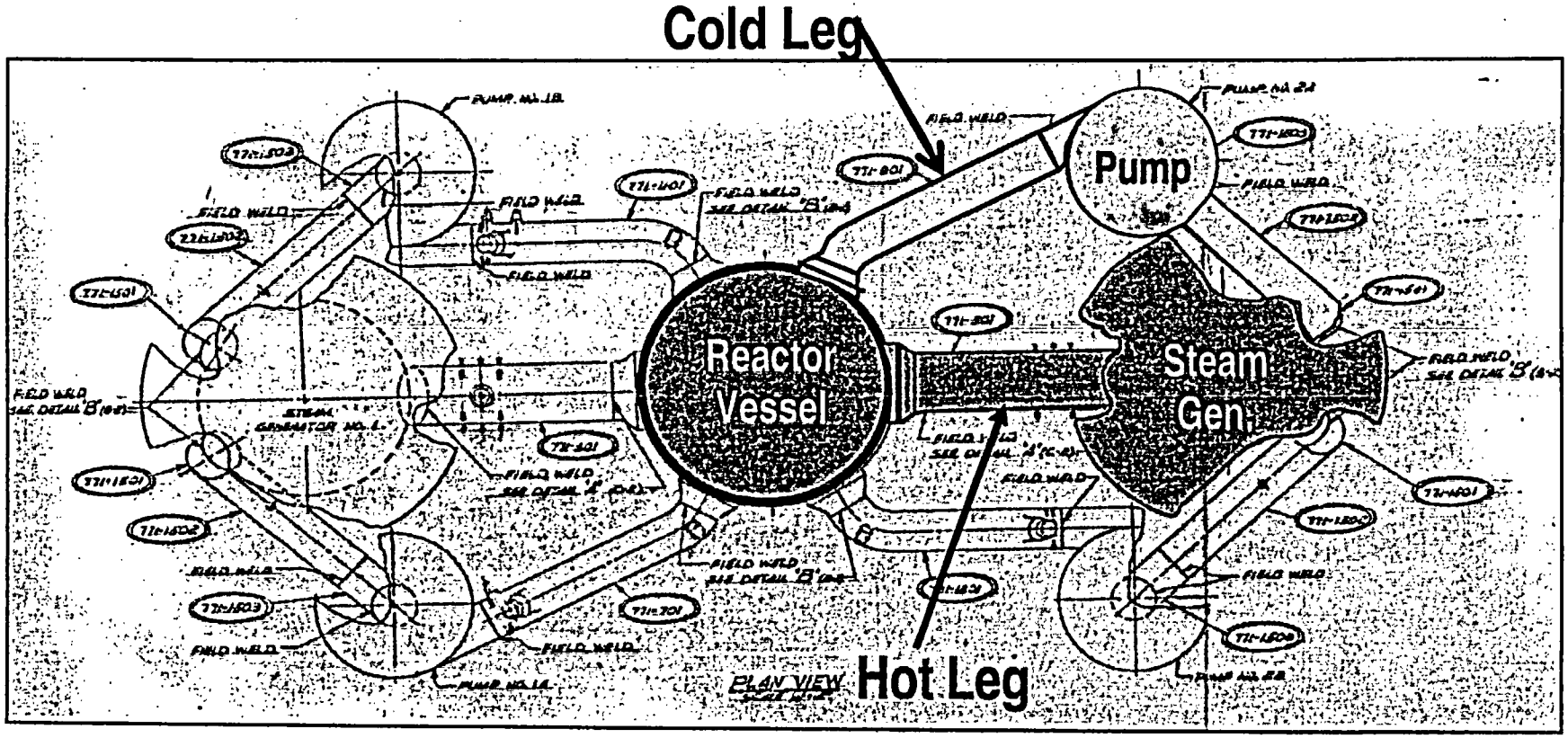

Figure G.2 Piping system geometry

G.3.1 Weld Residual Stress Analysis

The series of weld modeling analyses listed below were performed.

- **Axis-symmetric Cold Leg Analysis.** A weld analysis of a bimetallic weld from a cold leg that was tested as part of the NRC program 'Short Cracks in Piping and Piping Welds' program was performed first. The weld analyzed joined an A516 Grade 70 carbon steel pipe to a 316 SS safe end using an Inconel weld procedure (Figure G.3). The pipe diameter was 36-inch with a thickness of 3.4 inches. The materials and geometry of this case are similar to the hot and cold leg welds in the V. C. Summer plant. The purpose of this analysis was to validate the weld models for the bimetallic weld case. It should be noted that Battelle's weld models (VFT™ [3]) have extensive validation from other programs in industry, US Government, and overseas utilities. It will be seen, however, that the residual stress measurements from this effort are of questionable validity.

- **Axis-symmetric Hot Leg Analysis.** Weld analysis of the design hot leg bimetallic welds in the V. C. Summer plant were conducted. This analysis was quite complicated since the actual field welds sequence; including grinding and repair were considered. This analysis predicted the residual stresses for use in a fracture assessment in Task 3. Weld joint specifications and material properties available from the licensee were provided by the NRC so as to accurately model the residual stresses.

- **Three Dimensional Analysis of Hot Leg.** The analyses discussed above assumed axis-symmetric conditions for the analysis. It is known that full three dimensional weld residual stress states can vary significantly from an axis-symmetric solution near the regions of the weld torch start/stop positions. In general, compressive residual stresses often develop near the regions of the start/stop locations. As such, an axis-symmetric solution is normally considered conservative compared with a full three dimensional solution. With this in mind, the three dimensional analysis of the hot leg weld was performed to quantify the '3-D' effects on PWSCC in PWRs. Two separate repair lengths and two depths (a total of three repair analyses) were performed. These consisted of a long and short length repair with a shallow depth, and a short length repair with a deeper depth. The repair solution procedure consists of first modeling the original bimetallic weld. This is a computationally intense solution since there are so many passes involved. Next, the material removal in preparation for the repair was modeled. Finally, the repair passes were modeled. For all repair cases, the predicted residual stresses were used to predict SCC crack growth.

Finally, all analyses were performed using the VFT™'s weld analysis code (Ref. G.3), which was developed jointly by Battelle and Caterpillar. This code has an extensive database of validation for complex welded structures and is considered to be the best available weld analysis code.

G.3.2 Weld Residual Stress Measurements

This task involved determining the residual stresses from the Battelle bimetallic test case to further validate the models for bimetallic welds. Battelle still has sections of the original pipes that were taken from a canceled plant. A trepanning technique was used to obtain surface measurements of the residual stresses.

G.3.3 Fracture Mechanics and PWSCC Analysis

Stress intensity factors were determined by first mapping the results obtained from the weld analyses to a full three-dimensional finite element model. The stress intensity factors were determined from the residual stress fields using the finite element alternating method (FEAM) code developed by Battelle (Ref. G.4). In addition, service loads were applied over top the residual stresses to obtain the loads for PWSCC analysis as well. FEAM is an extremely

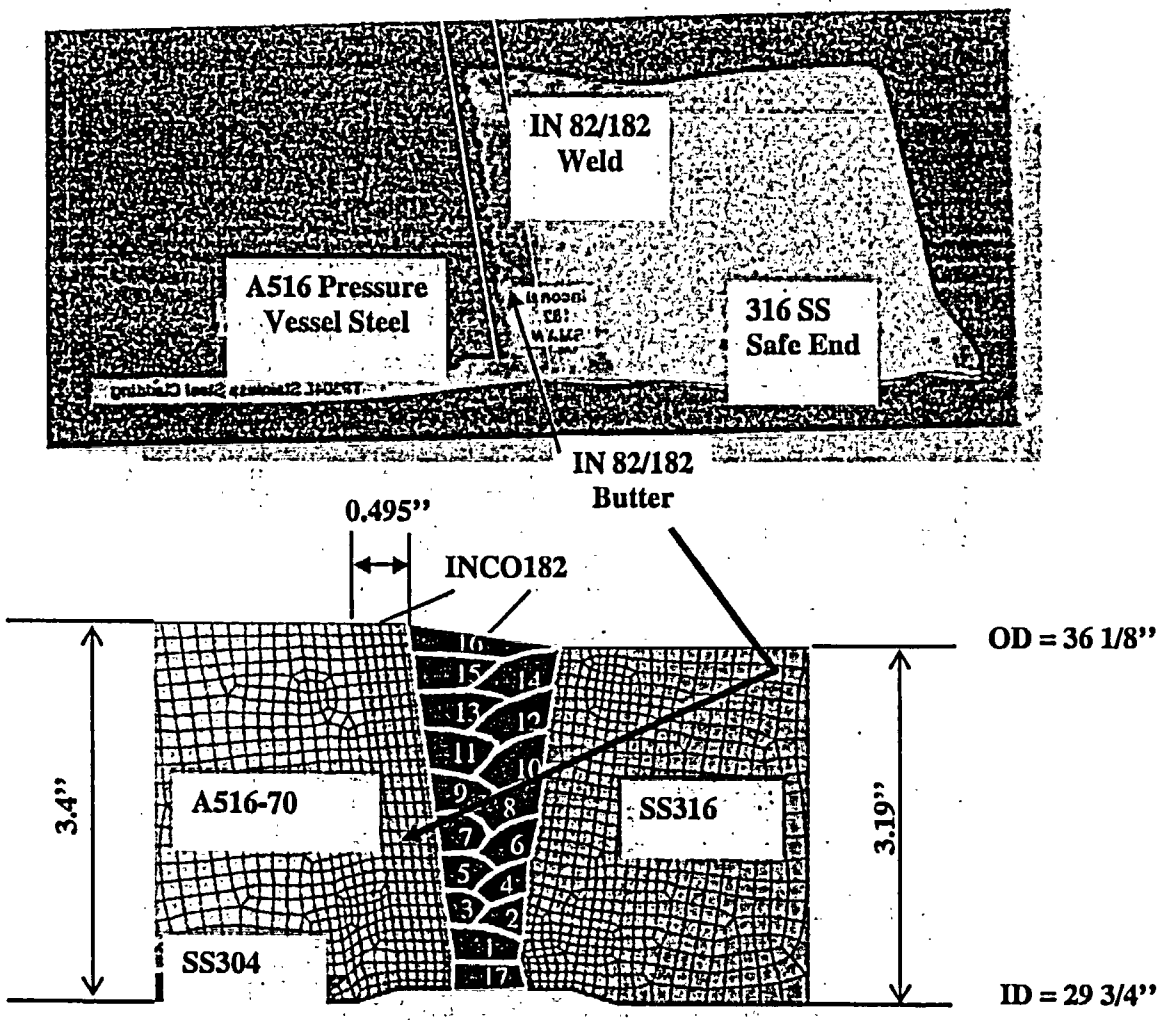

Figure G.3 Photo of cold leg weld cross section (top) and computational weld model of cold leg

efficient method for fracture analysis that was developed recently in the aerospace community and has FAA and Air Force acceptance. In addition, Battelle has been using FEAM for weld fracture analyses for Argonne National Laboratory (as part of another NRC program), as part of a DOE weld fracture analysis program for Savannah River, and for European utilities. It is accepted as accurate and has been extensively validated. The effect of weld residual stress redistribution during crack growth is accurately accounted for with FEAM. The efficiency of FEAM is because a special crack mesh is not needed – rather the mesh for the *uncracked* geometry is all that is required, and K solutions can be obtained for many crack sizes, shapes, and locations with this one mesh.

Both circumferential and axial crack solutions were obtained for both surface and through-wall cracks. From the recent documentation of the V. C. Summer cracking it is clear that both types of cracking have been observed. Flaw indications have been identified using ultrasonic testing (UT) and eddy current testing (ECT) in hot legs A, B, and C as reported in December 2000 and January 2001 licensee public meeting presentations. The stress intensity factor (K) was determined for about 20 cracks of various sizes and locations. It is emphasized that the full 3D analysis using ABAQUS is time consuming and costly compared with FEAM solutions.

Finally, PWSCC predictions were made using the K solution results. The analyses of PWSCC include the effect of residual stress redistribution caused by crack growth. The TRACLIFE code (Ref. G.5), originally developed for the FAA, was used to make the crack growth life predictions.

G.4 ANALYSIS TOOLS

From the discussion above, it is seen that three different analysis tools were used to perform these analyses. The analysis tools are:

1. VFT™ – Virtual Fabrication Technology and Weld Modeling Code.
2. FRAC@ALT - Finite Element Alternating Method (FEAM) Code.
3. TRACLIFE – Probabilistic and Deterministic Life Prediction Code.

G.5 RESULTS COLD LEG ANALYSIS

As discussed above, the first step in the analysis of the hot leg PWSCC issue was to obtain confidence in the computational weld model. As discussed in Reference G.3, the VFT code used for the weld modeling analyses has an extensive validation data base library for same material welding (stresses and displacements). However, little data exists for bimetallic welds. As part of the validation of the analysis procedures for bimetallic welds, it was decided to perform a weld analysis of a cold leg pipe that Battelle had stored from the US NRC Short Cracks in Piping and Piping Welds program (Ref. G.2). This stored pipe then had its residual stresses measured using the classic trepanning technique (Ref. G.6). The predicted residual stresses were then compared with the measured stresses. Unfortunately, the measured stresses appeared to be quite low compared with what was expected. This is discussed later in this section.

G.5.1 Cold Leg Computational Weld Model

Figure G.3 illustrates the axis-symmetric weld model in the lower figure and a photograph of the weld cross-section for the bimetallic weld that was tested in the upper figure. It is seen that this section had an A516 Grade 70 pipe welded to a Type 316 stainless steel safe end pipe with Inconel 82/182 filler metal. Sixteen passes were required to complete the weld. This is a large diameter, thick pipe.

The analysis sequence flow chart is shown in Figure G.4 and graphically illustrated in Figure G.5. The A516 pipe was first machined and a 304 stainless steel cladding was applied to the inner surface. The weld deposition of the 304 stainless steel cladding layer was not modeled here. However, the material properties of the cladding were considered, i.e., a thin layer of 304 stainless steel material properties was

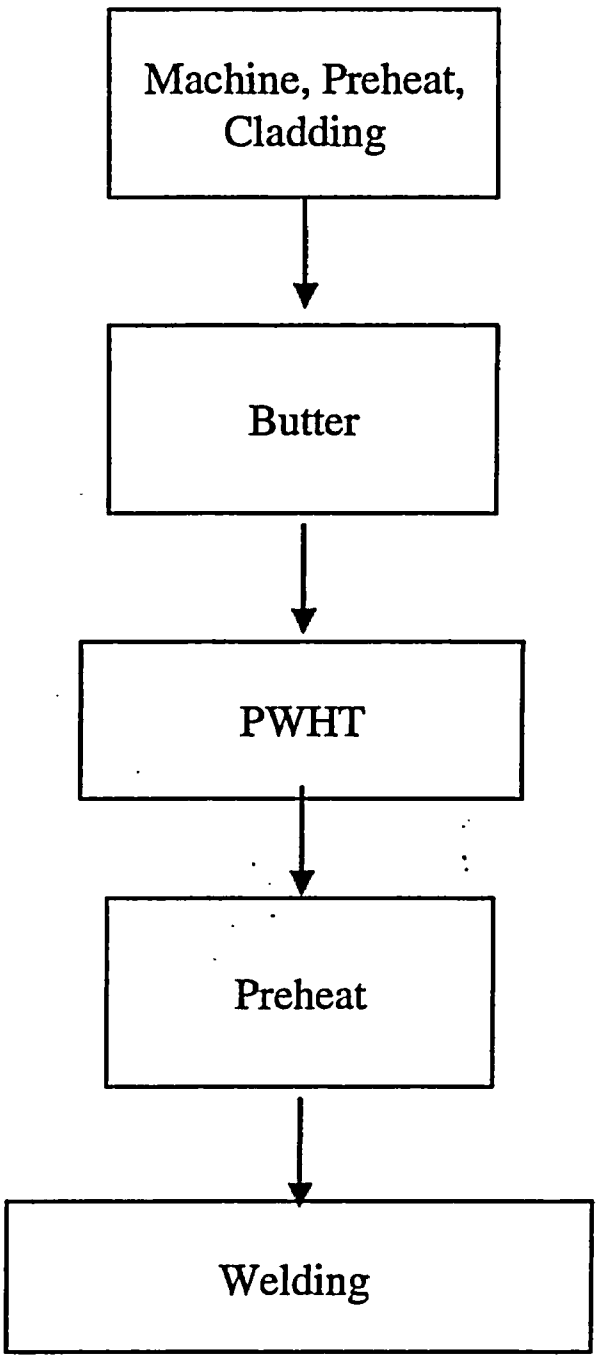

Figure G.4 Welding process analysis flow chart for cold leg

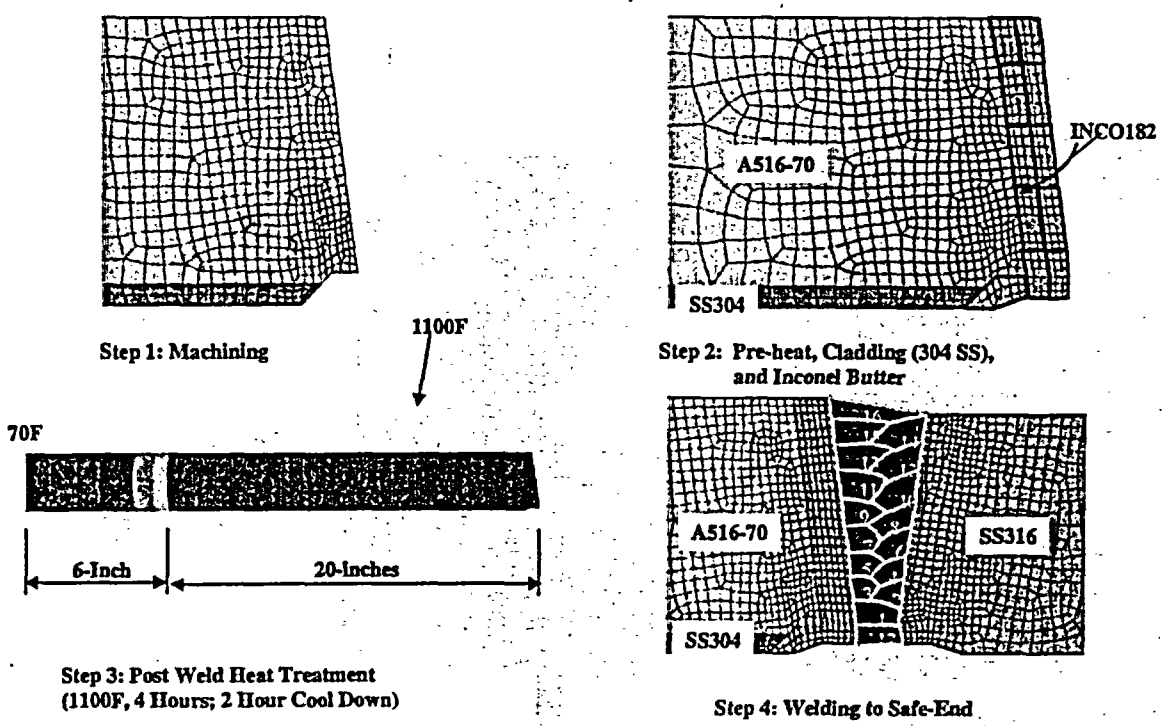

Figure G.5 Cold leg axis-symmetric cladding (buttering) and weld model

used at this region so that the material property mismatch is included in the Inconel weld modeling steps. The weld cladding deposition step was not included here because cracking in the buttering and Inconel weld metal was of main concern in this analysis. The residual stresses from the buttering, PWHT, and butt weld deposition will tend to dominate residual stresses in the region of interest (weld and butter zone). In effect, the local cladding residual stresses are 'annealed' or 'stress relieved' by the buttering and later weld processes, and were thought to be of second order importance. Of course, such residual stresses are indeed important at regions away from the butt weld.

An Inconel buttering layer was then applied to the A516 pipe in preparation for the weld. From Figure G.5 it is seen that the buttering was deposited in 11 passes. The A516 pipe was then subjected to a post weld heat treat of 1100°F for four hours. The post weld heat treat was modeled by permitting the stresses to relax via creep. The weld metal was then deposited to complete the bimetallic weld. Again from Figure G.5, 16 passes were required. The buttering and weld sequence and weld pass sizes were estimated from the weld paper work for the actual production weld, and from the photograph of the weld cross section.

Figure G.6 further illustrates the weld modeling process. It is also seen that the root pass was ground out after welding and re-deposited. It is not clear why this was done in the field, but the process of grinding and re-welding the root pass was included in the model.

In modeling the weld process, particularly for multi-pass welds, it is important to properly model the history annihilation (or local 'annealing') process. More details of this constitutive model can be found in References G.7 and G.8. It is important to note that without modeling this history annihilation process, unrealistic plastic strains develop in the model predictions that have a significant effect on the predicted residual stress state. Moreover, the solution times of the computational model are significantly increased. The constitutive law is a classical thermal elastic-plastic law with features which permit history annihilation, phase changes (not important here), large deformations, melting/re-melting, and accounts for 'not yet

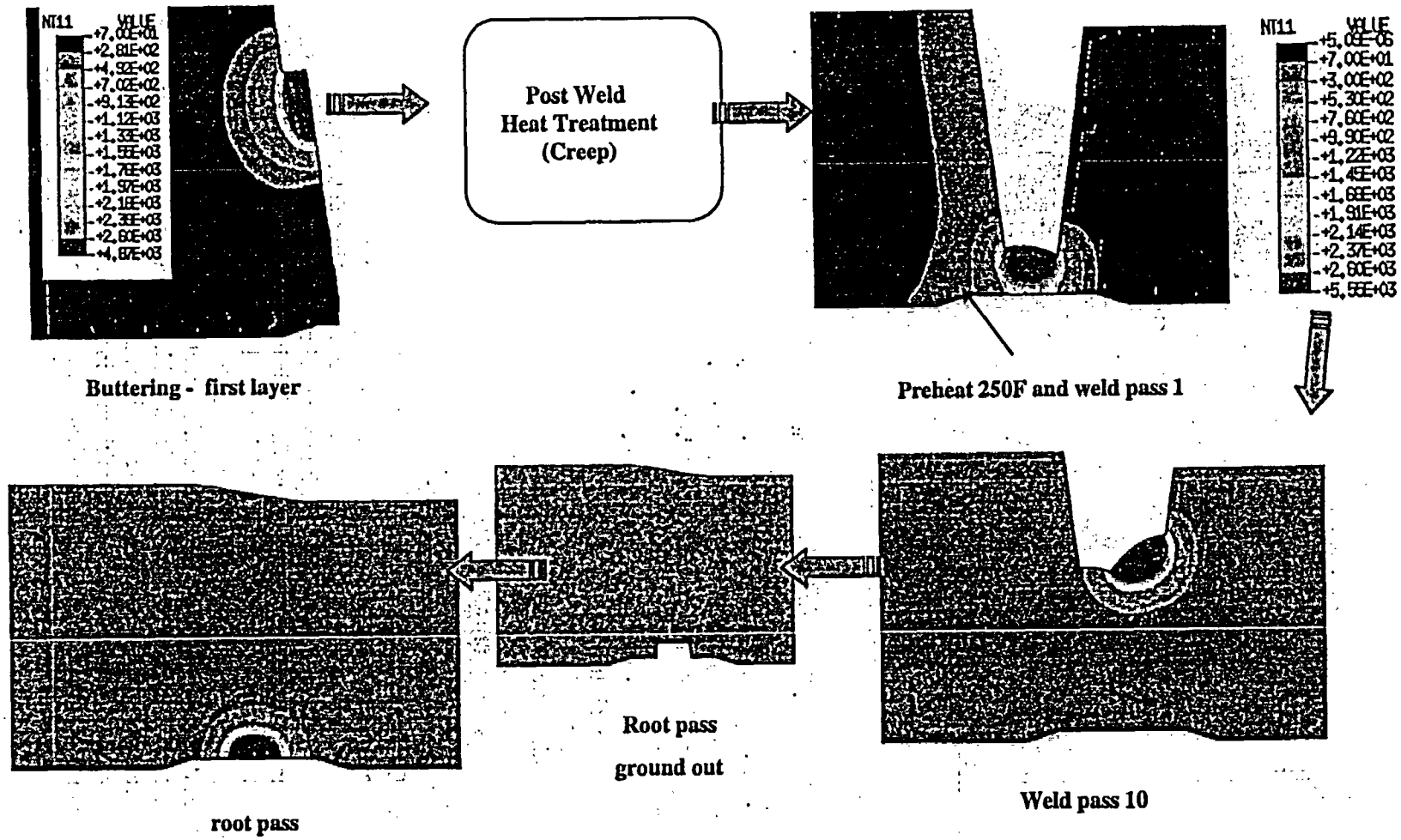

Figure G.6 Weld process simulation

deposited' weld metal in a computationally efficient manner using a concept called virtual element detection (Ref. G.8).

The material properties used for the thermal analysis for the Inconel 82/182 weld metal, the A516 Grade 70 pipe, and the 316 and 309 stainless steels are shown in Tables G.1 to G.5. Tables G.1 to G.5 also list elastic properties used in the constitutive modeling of the weld process. Figure G.7 illustrates the temperature dependent elastic plastic properties for the Inconel weld, A516 Grade 70 carbon steel pipe, and Type 316 stainless steel safe end used in the analyses. The tensile properties for Inconel 182 were obtained specifically for this program by Oak Ridge National Laboratory (ORNL). The elastic-plastic properties for the A516 Grade 70 pipe were obtained from the literature, and the stainless steel properties were obtained from prior work done at Battelle. It is important to note that the thermo-plastic properties used for a proper weld modeling analysis (for the weld material) should be stress relieved and annealed prior to testing since the weld modeling process itself models the work hardening process caused by the welding.

Finally, Table G.6 shows creep properties used to model stress relaxation during the post weld heat treatment. Note that at 1100F (the post weld heat treat temperature (PWHT)) the A516 Grade 70 steel experiences the most creep deformation. Moreover, note that the stainless steel (see Figure G.5) is not in the model yet for the PWHT.

G.5.2 Cold Leg Results After Butter and PWHT

Figure G.8 illustrates the axial residual stress state of the A516 pipe after buttering and PWHT is complete. (Note: all stresses in this report are in ksi units.) The analysis sequence begins in the upper left figure and proceeds clockwise. Note that by the time the PWHT is complete and cooling to room temperature occurs, the initial residual stress state has changed significantly. Likewise, the axis-symmetric hoop stresses through the PWHT process after buttering is shown in Figure G.9. It is clear the hoop stresses are relaxed via PWHT more so the than axial stresses. Moreover, including the effect of the PWHT in the analysis process is important.

The equivalent plastic strains after buttering and after PWHT are shown in Figure G.10. It is noted that when modeling the PWHT process via a creep constitutive model, plasticity is included (i.e., a combined creep-plasticity model was used). It is seen that the creep relaxation process is mainly due to creep, with additional plasticity having a second order effect. Figure G.11 shows the effective creep strains that accumulate after the PWHT. The top illustration in Figure G.11 is of a large portion of the pipe. Notice the accumulation of creep strains near the end of the PWHT region (see Figure G.5 also). Other researchers have observed this as well when modeling the heat treat process. Notice from the bottom illustration of Figure G.11 that the largest tensile creep strains occur near the outer diameter of the A516 pipe adjacent to the Inconel butter.

G.5.3 Cold Leg Results After Completed Weld

The axial residual stresses after completion of the weld are shown in Figure G.12. The outline of the buttering and weld are shown in this figure outlined in white. The stresses start as tensile near the inner radius, become compressive in the mid thickness region of the pipe, and return to tensile near the outer surface of the pipe. This behavior is quite typical for same material welds in thick pipe (Refs. G.6 and G.9). Axial residual stresses at the cold leg operating temperature of 291°C (556°F) are illustrated in Figure G.13. The main difference between the room temperature (Figure G.12) and operating residual stresses (Figure G.13) are magnitude.

The hoop residual stresses at room temperature and operating temperature are shown in Figures G.14 and G.15, respectively. Notice that hoop residual stresses remain tensile through out the entire pipe thickness in the region of the weld for both temperatures. Again, this is quite typical for same material (i.e., non bimetallic) welds in both thick and thin pipe (Refs. G.6 and G.9). Moreover, these higher hoop stresses and

Table G.1 Material properties for Inconel 182 weld material

T	C_p	λ	E	ν	σ_y	α
(°F)	(BTU/Lbm-F)	BTU/Sec-inch-F)	(ksi)		(ksi)	(10^{-6}/(°F)
70	0.095	0.00013	22674.70	0.3	38.50	6.50
200	0.110	0.000145	22023.96	0.3	36.18	6.73
400	0.120	0.000162	21022.83	0.3	33.55	7.09
600	0.125	0.000185	20021.70	0.3	30.00	7.44
800	0.130	0.000206	19051.70	0.3	28.26	7.62
1000	0.135	0.000226	18081.70	0.3	26.60	7.80
1200	0.140	0.000247	17987.40	0.3	26.20	8.10
1400	0.150	0.000273	17893.10	0.03	25.70	8.40
1600	0.160	0.000298	15621.95	0.3	19.03	8.70
1800	0.165	0.000324	13350.80	0.3	12.10	9.00
2000	0.170	0.000354	10000.00	0.3	3.70	9.20
2550	0.170	0.000354	200.00	0.3	0.40	9.20

T = Temperature
C_p = Specific heat
λ = Conductivity
E = Elastic Modulus
ν = Poisson's constant
σ_y = Yield stress
α = thermal expansion

Table G.2 Temperature dependent material properties for A516-70

C_p		λ		T	E	ν	σ_y	α
(°F)	(BTU/Lbm-F)	(°F)	BTU/Sec-inch-F)	(°F)	(ksi)		(ksi)	10^{-6}/(°F)
70	0.11	32	0.000694	72	31000.00	0.3	40.76	7.67
122	0.116	212	0.00067	300	29849.24	0.3	32.98	7.67
302	0.124	392	0.000647	550	28297.79	0.3	32.00	7.67
392	0.127	572	0.000617	700	26991.11	0.3	31.50	7.67
482	0.133	752	0.000571	932	25500.00	0.3	30.10	8.33
572	0.137	932	0.000527	1112	24300.00	0.3	23.70	8.33
662	0.143	1112	0.000476	1292	21000.00	0.3	15.90	8.61
842	0.158	1292	0.000425	1472	17000.00	0.3	8.00	8.61
1022	0.179	1472	0.000348	2732	203.00	0.3	0.44	8.89
1202	0.202	1832	0.000364					
1292	0.342	2192	0.000397					
1382	0.227							
1562	0.215							
1832	0.202							
2192	0.201							

T = Temperature
C_p = Specific heat
λ = Conductivity
E = Elastic Modulus
ν = Poisson's constant
σ_y = Yield stress
α = thermal expansion

Table G.3 Temperature dependent material properties for A508 Class 3

C_p		λ		T	E	ν	σ_y	α
(°F)	(BTU/Lbm-F)	(°F)	BTU/Sec-inch-F)	(°F)	(ksi)		(ksi)	10^{-6}/(°F)
70	0.11	32	0.000694	71.60	30784.93	0.3	54.52	7.67
122	0.116	212	0.00067	600.00	28807.05	0.3	43.78	7.67
302	0.124	392	0.000647	1000.00	25633.87	0.3	29.55	8.33
392	0.127	572	0.000617	1400.00	14540.00	0.3	9.78	8.61
482	0.133	752	0.000571	1800.00	10243.06	0.3	2.78	8.89
572	0.137	932	0.000527	2732.00	203.00	0.3	0.44	8.89
662	0.143	1112	0.000476					
842	0.158	1292	0.000425					
1022	0.179	1472	0.000348					
1202	0.202	1832	0.000364					
1292	0.342	2192	0.000397					
1382	0.227							
1562	0.215							
1832	0.202							
2192	0.201							

T = Temperature
C_p = Specific heat
λ = Conductivity
E = Elastic Modulus
ν = Poisson's constant
σ_y = Yield stress
α = thermal expansion

Table G.4 Temperature dependent material properties for Type 316 and Type 309

C_p		λ		T	E	ν	σ_y	α
(°F)	(BTU/Lbm-F)	(°F)	BTU/Sec-inch-F)	(°F)	(ksi)		(ksi)	10^{-6}/(°F)
74.2	0.1079	70	0.000173	75	28400.00	0.30	38.00	8.09
165.4	0.1132	200	0.000186	300	27500.00	0.30	30.00	8.77
191.1	0.1143	400	0.000207	550	25950.00	0.30	23.40	9.33
399.6	0.1229	623	0.000231	700	24900.00	0.30	23.00	9.57
602.6	0.1291	800	0.000248	900	23500.00	0.30	22.00	9.84
794.4	0.132	1011	0.000269	1100	22200.00	0.30	20.50	10.09
1020.5	0.136	1195	0.000288	1300	20820.00	0.30	20.00	10.21
1203.7	0.1398	1391	0.000308	1500	19100.00	0.30	17.00	10.43
1409.6	0.145	1583	0.000327	1652	16900.00	0.30	14.10	10.60
1595.5	0.1505	1783	0.000348	1832	14500.00	0.30	8.46	10.70
1784.2	0.1556	1996	0.000369	2012	14500.00	0.30	3.77	10.90
1995.8	0.1622			2732	203.04	0.30	0.44	11.20

T = Temperature
C_p = Specific heat
λ = Conductivity
E = Elastic Modulus
ν = Poisson's constant
σ_y = Yield stress
α = thermal expansion

Table G.5 Temperature dependent material properties for Type 304

C_p		λ		T	E	ν	σ_y	α
(°F)	(BTU/Lbm-F)	(°F)	BTU/Sec-inch-F)	(°F)	(ksi)		(ksi)	10^{-6}/(°F)
74.2	0.1079	70	0.000173	75	28400.00	0.30	36.90	8.09
165.4	0.1132	200	0.000186	300	27500.00	0.30	27.70	8.77
191.1	0.1143	400	0.000207	550	25950.00	0.30	23.25	9.33
399.6	0.1229	623	0.000231	700	24900.00	0.30	21.80	9.57
602.6	0.1291	800	0.000248	900	23500.00	0.30	19.90	9.84
794.4	0.132	1011	0.000269	1100	22200.00	0.30	18.10	10.09
1020.5	0.136	1195	0.000288	1300	20820.00	0.30	16.20	10.21
1203.7	0.1398	1391	0.000308	1500	19100.00	0.30	11.40	10.43
1409.6	0.145	1583	0.000327	1652	16900.00	0.30	10.10	10.60
1595.5	0.1505	1783	0.000348	1832	14500.00	0.30	8.46	10.70
1784.2	0.1556	1996	0.000369	2012	14500.00	0.30	3.77	10.90
1995.8	0.1622			2732	203.04	0.30	0.44	11.20

T = Temperature
C_p = Specific heat
λ = Conductivity
E = Elastic Modulus
ν = Poisson's constant
σ_y = Yield stress
α = thermal expansion

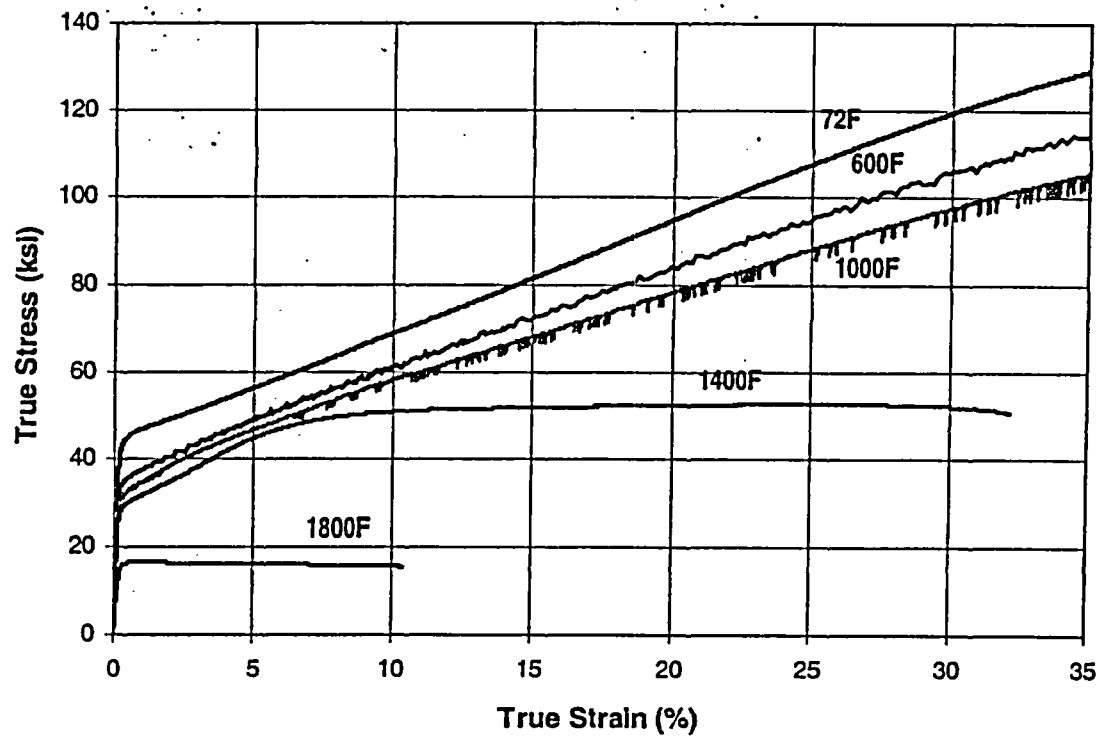

Figure G.7(a) Temperature dependent true stress-strain curves of Inconel 182 tested by ORNL

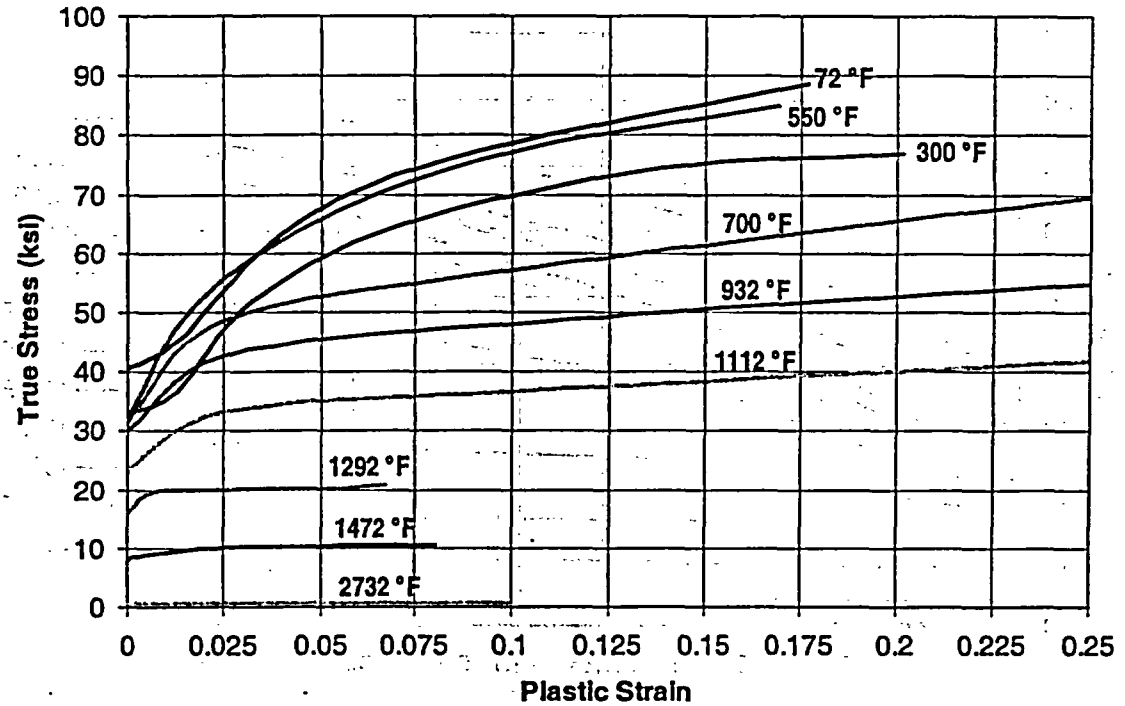

Figure G.7b Temperature dependent true stress-strain curves at A516 Grade 70

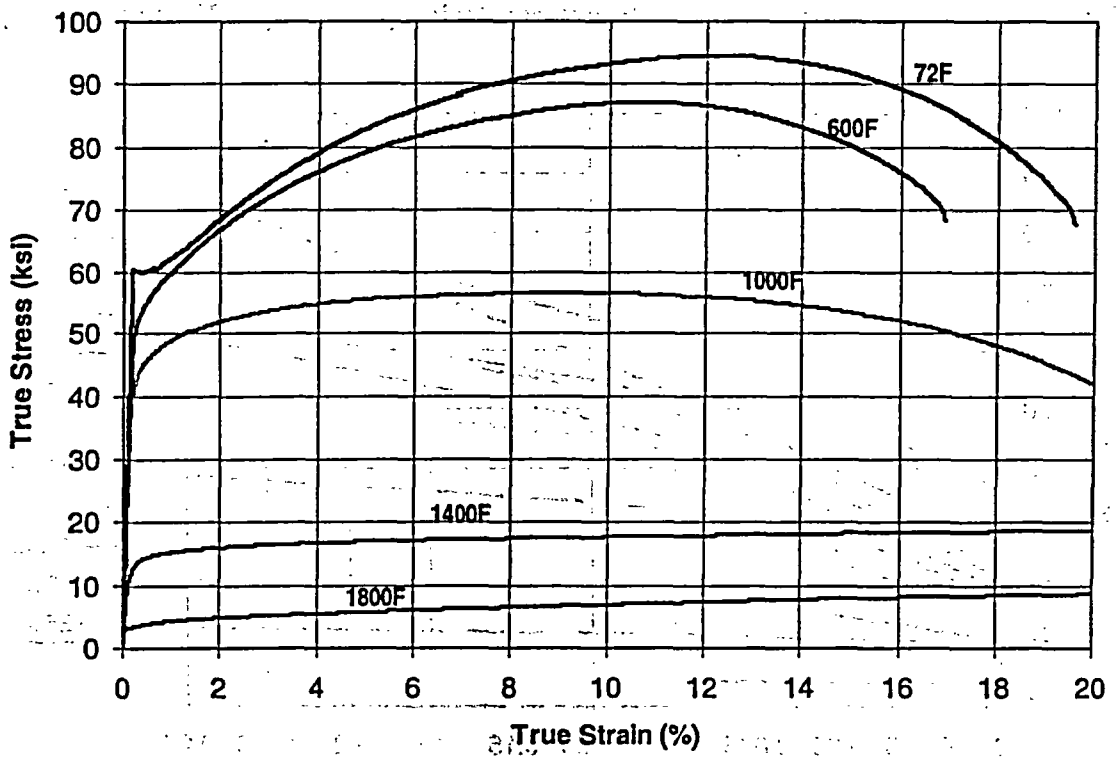

Figure G.7c Temperature dependent true stress-strain curves of A508 Class 3 tested by ORNL

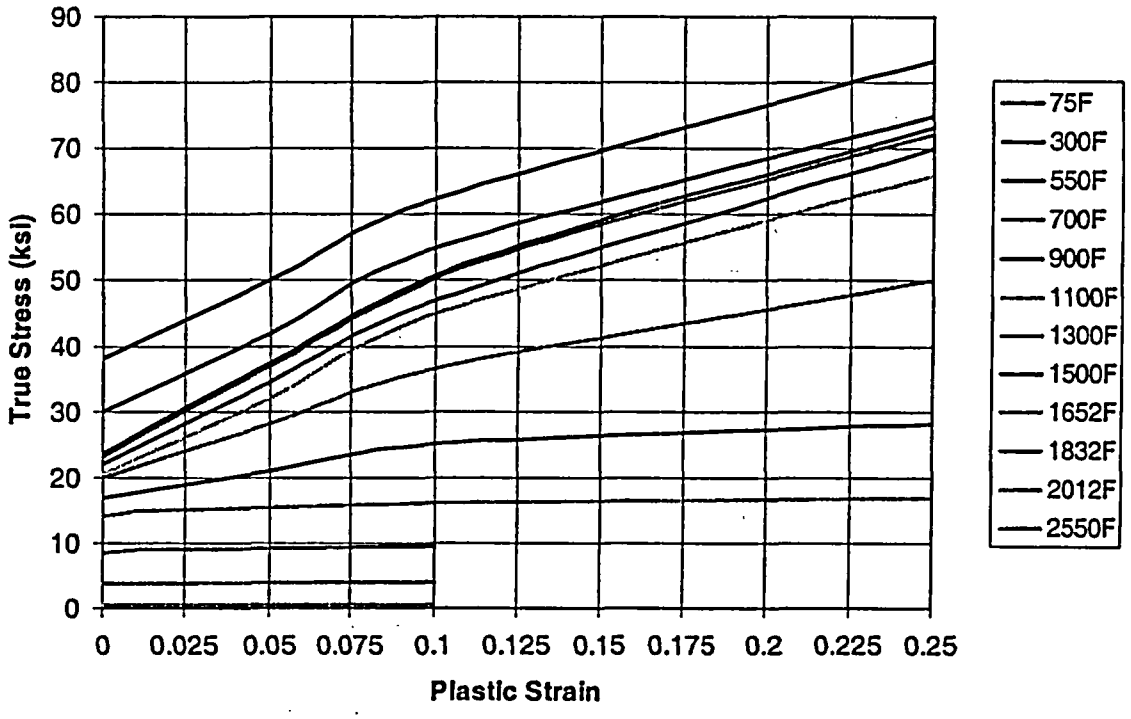

Figure G.7d Temperature dependent true stress-strain curves of Type 316 and Type 309

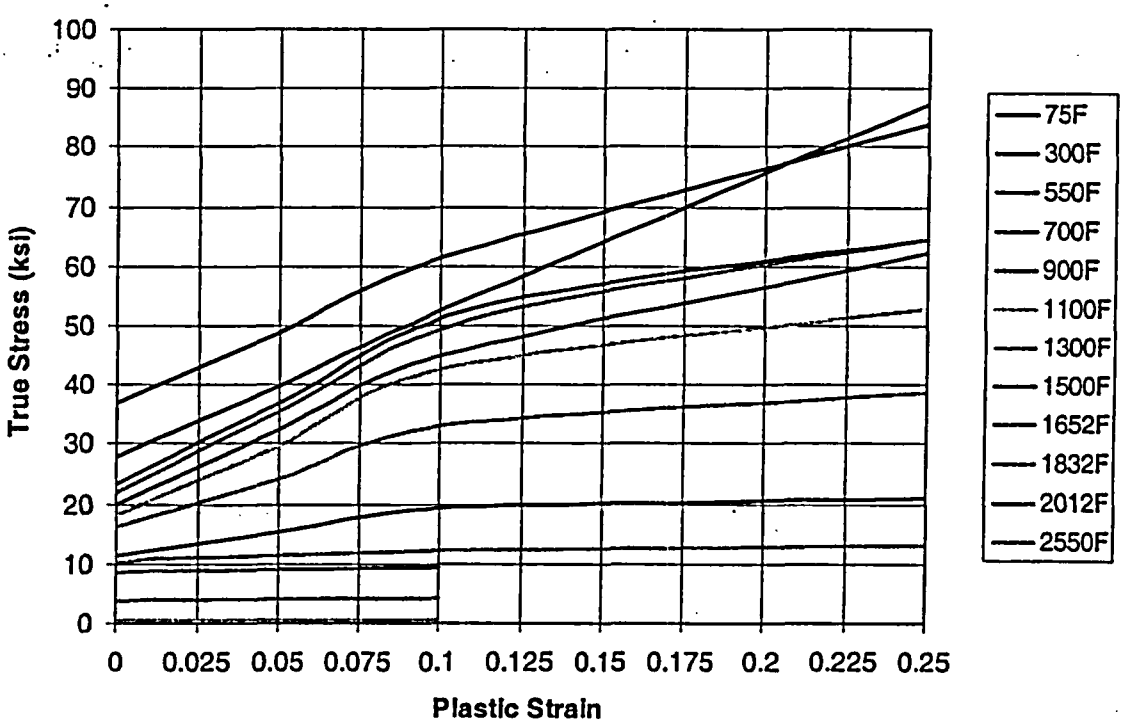

Figure G.7e Temperature dependent true stress-strain curves of Type 304

Table G.6 Temperature dependent creep constants for all the materials

$$\dot{\varepsilon}^{s} = A_s \sigma^{n_s}$$

A_s	n_s	T
MATERIAL: A508 Class 2		
1.0000E-26	4.0000	70
2.2910E-12	6.0451	1000
3.2670E-07	4.8865	1200
3.2670E-07	4.8865	2500
Material: A516-70		
1.0000E-26	4.0000	70
2.5060E-13	6.3261	900
1.9920E-09	4.4071	1000
6.9010E-08	4.5039	1100
6.9010E-08	4.5039	2500
MATERIAL: S309, S304, S316		
1.0000E-26	4.0000	70
9.2650E-25	9.7800	887
4.6900E-24	9.9700	932
1.6410E-21	9.0600	977
3.9710E-19	8.2000	1022
2.7540E-18	8.2000	1067
1.7060E-17	8.2000	1112
1.1700E-16	8.1800	1157
7.2180E-16	8.1600	1202
3.4110E-14	7.4200	1247
1.3300E-12	6.7200	1292
2.0930E-11	6.2500	1337
3.2310E-10	5.7700	1382
MATERIAL: INCO182		
1.0000E-26	4.0000	70
1.0000E-26	4.0000	990
2.1478E-16	6.1709	1000
4.6025E-15	6.6426	1100
4.6025E-15	6.6426	2500

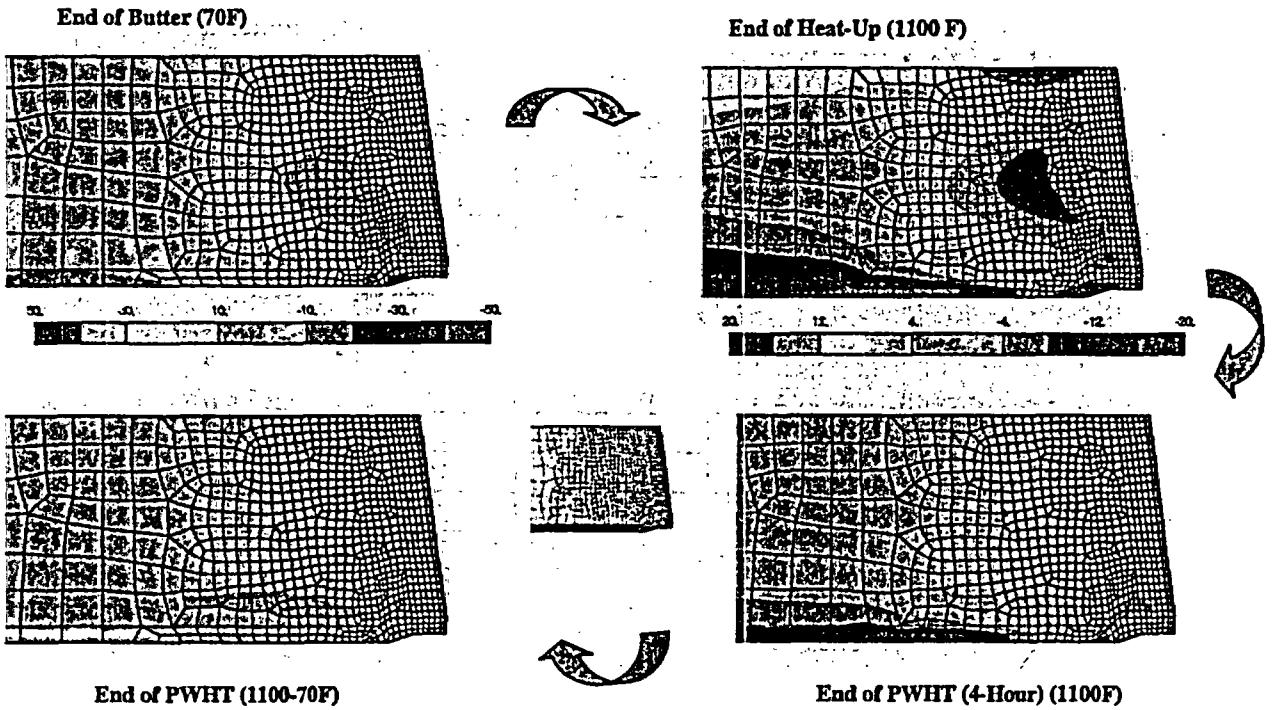

Figure G.8 Axial stresses during heat treat process

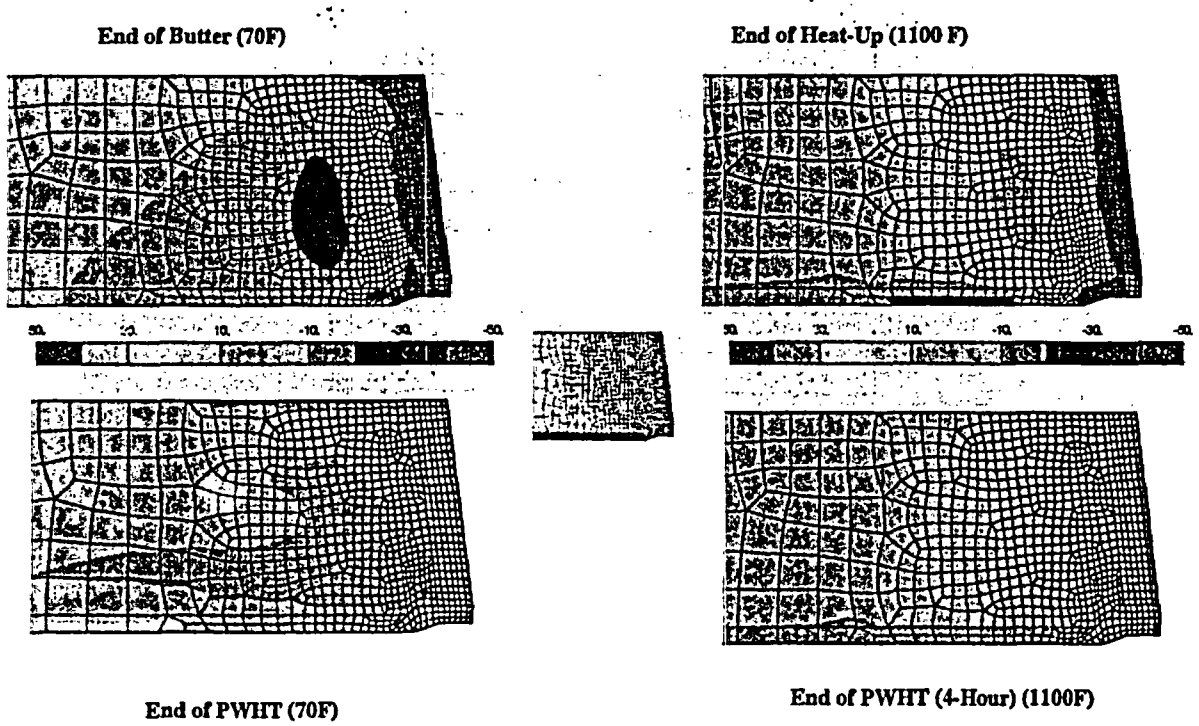

Figure G.9 Hoop stresses during heat treat process

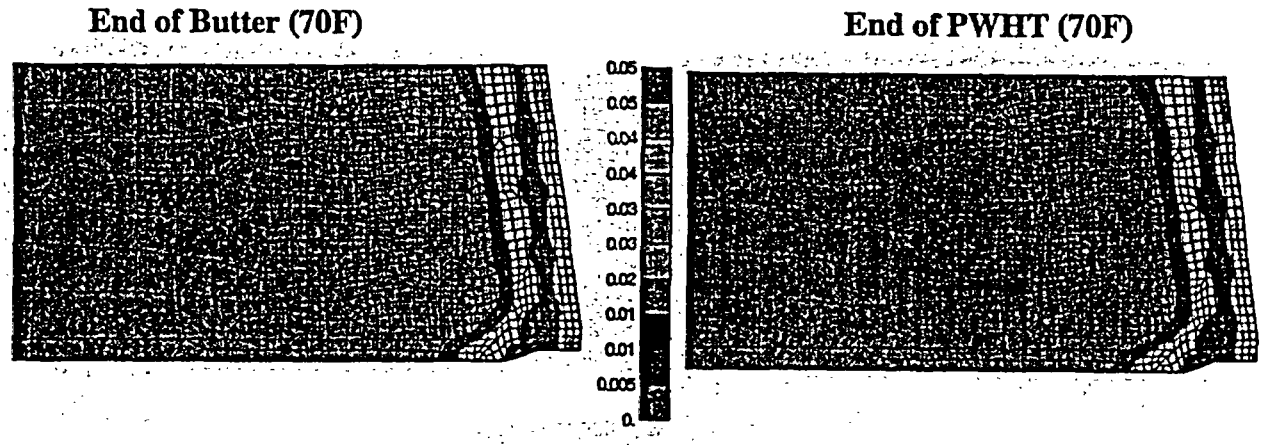

Figure G.10 Equivalent plastic strains

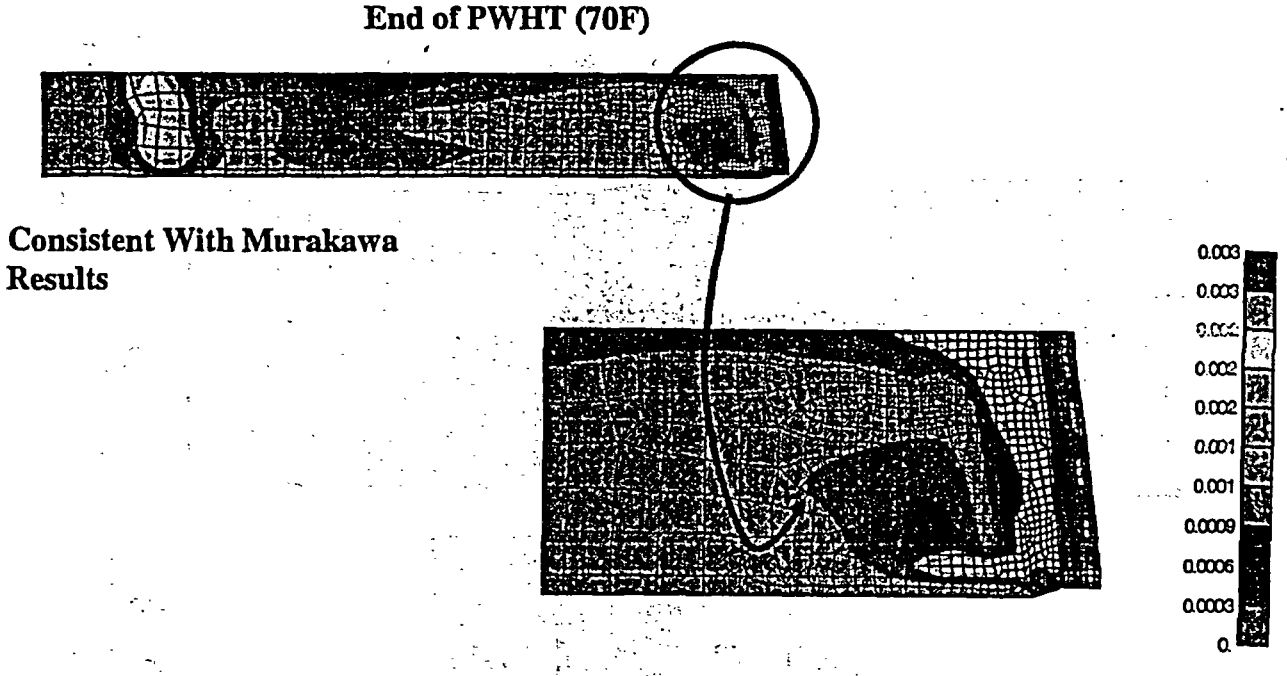

Figure G.11 Equivalent creep strains

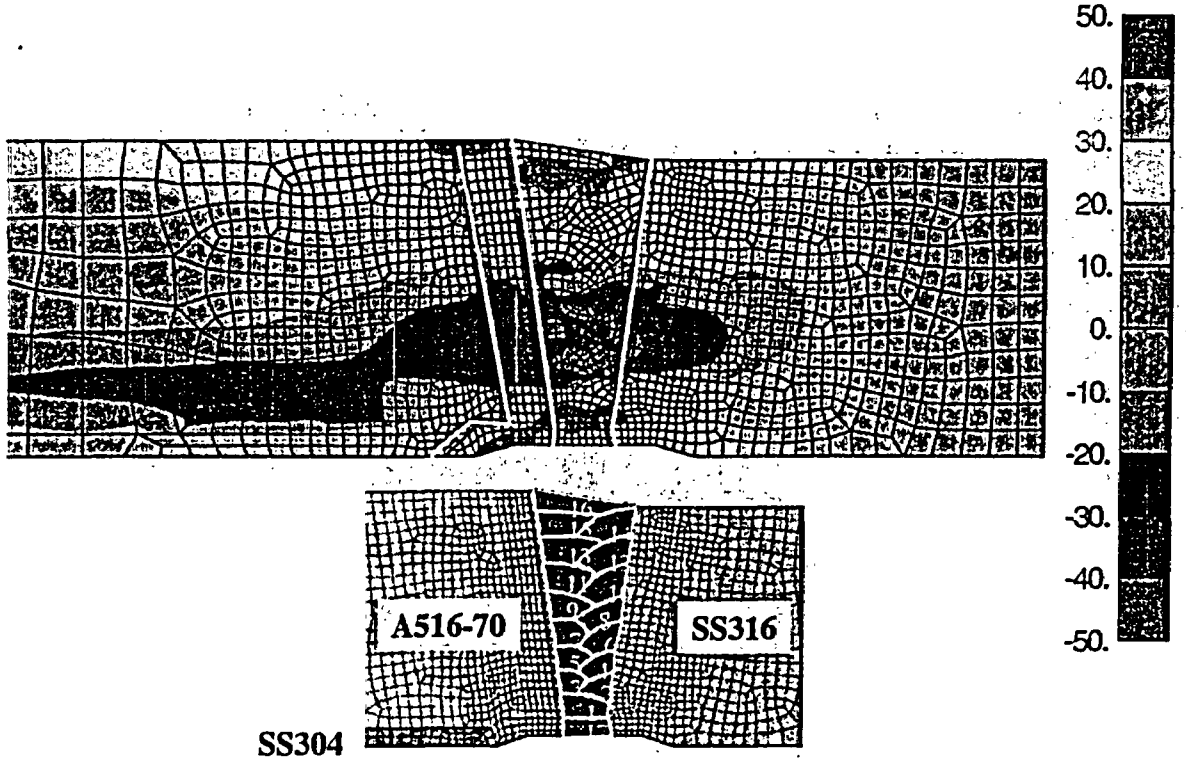

Figure G.12 Residual stresses final (axial) at room temperature 22C (70°F)

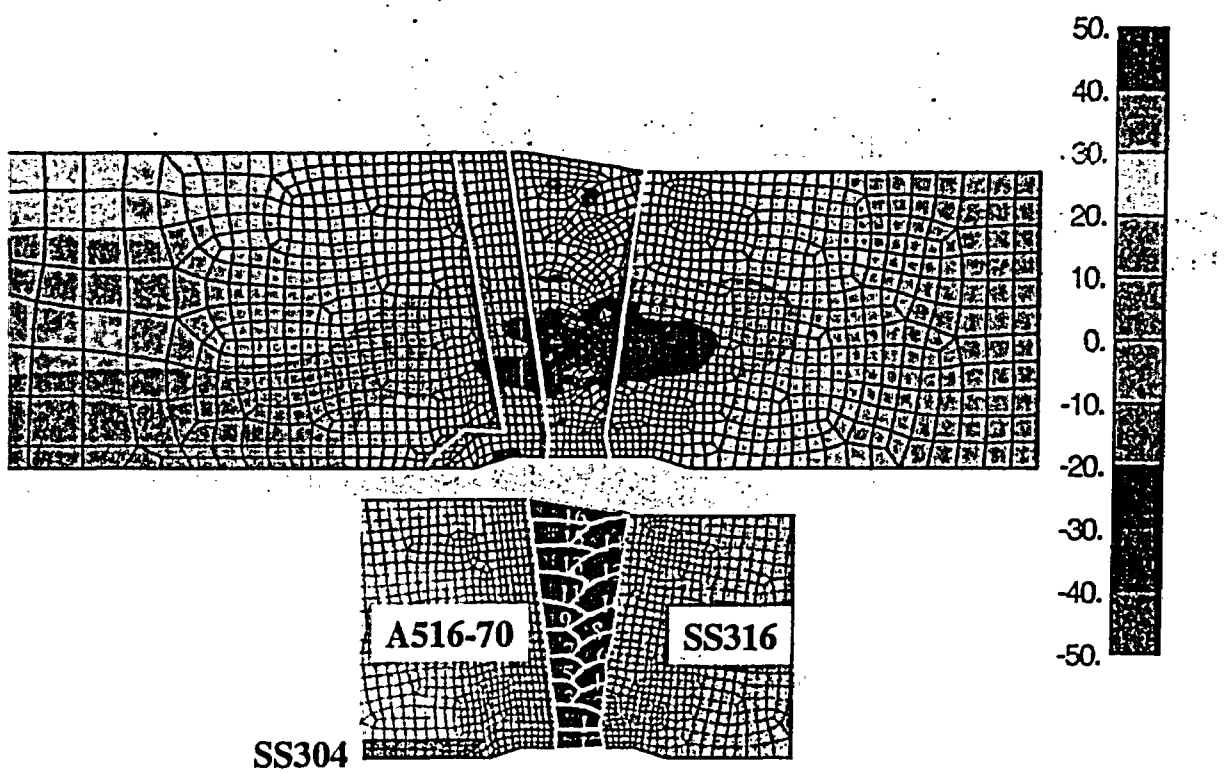

Figure G.13 Residual stresses final (axial) at operating temperature 291°C (556°F)

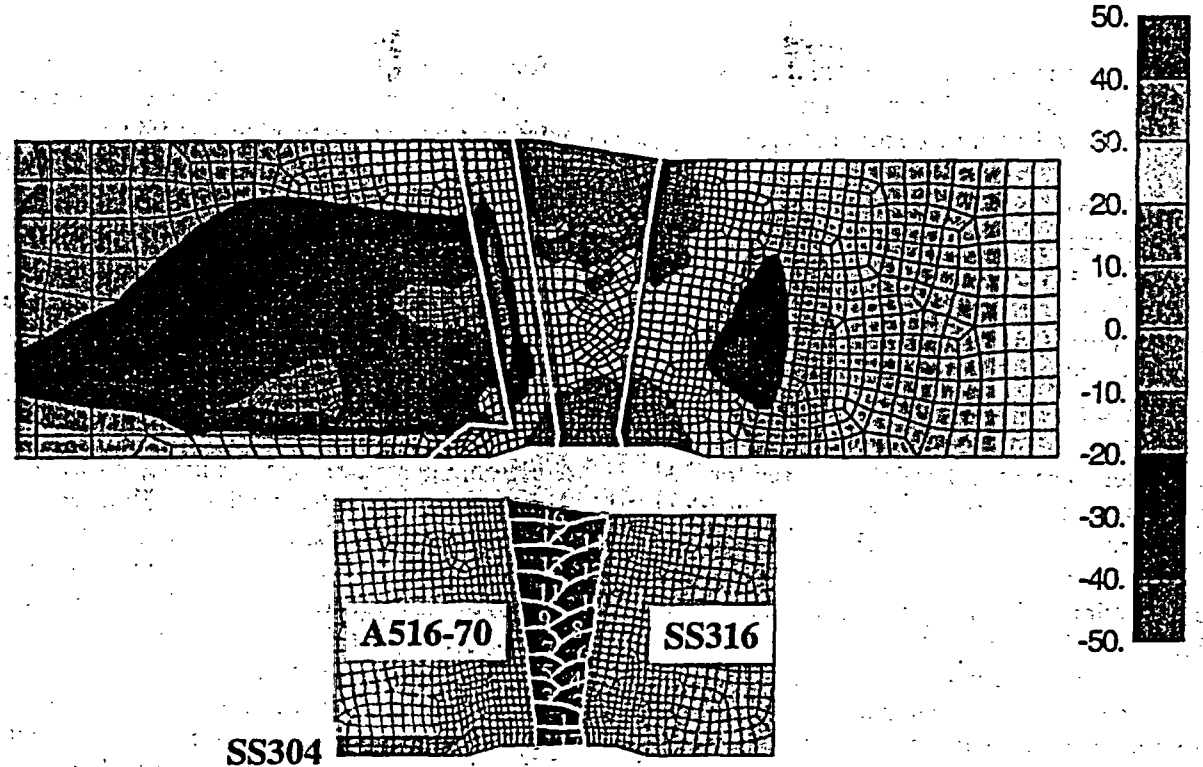

Figure G.14 Residual stresses final (hoop) at room temperature 22°C (70°F)

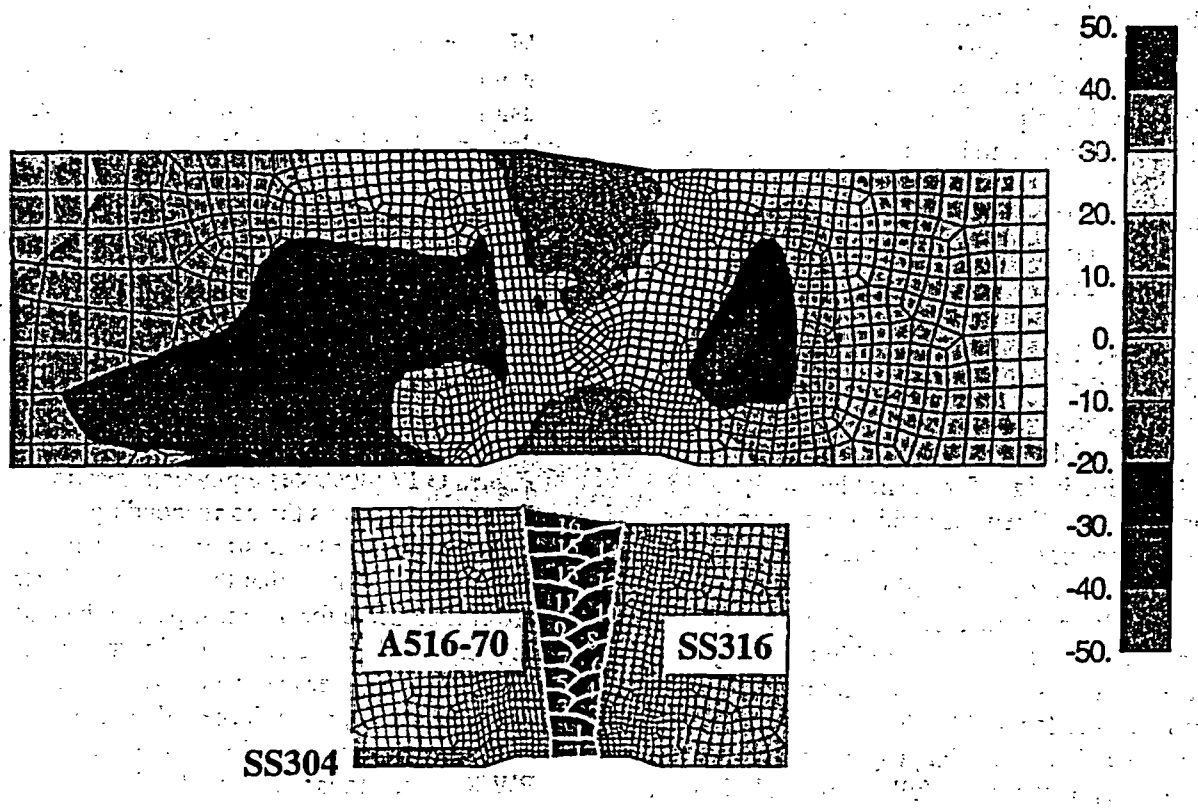

Figure G.15 Residual stresses final (hoop) at operating temperature 291°C (556°F)

through thickness stresses favor axial crack growth via stress corrosion cracking mechanisms if entirely driven by residual stresses.

Figures G.16 (a) and (b) show comparisons of axial weld residual stresses to measurements, while Figures G.16 (c) and (d) show the corresponding hoop stress comparisons. The measurements were made at Battelle at our West Jefferson, Ohio site, where the cold leg pipe has been stored since 1988. The 'chip removal' or trepanning technique of Reference G.6 (and many references sited therein) was used for the measurements. The trends for the axial residual stresses comparisons (Figure G.16 (a) and (b)) are similar, but the measurements are lower than the predictions. The hoop residual stresses (Figures G.16 (c) and (d)) measurements are quite low compared with predictions. Hoop residual stress measurements in bimetallic welds have not been reported in the literature as far as can be determined. However, from prior measurements and predictions of pipe (Refs. G.6 and G.9) for same material welded pipe and many reference sited therein), hoop residual stresses are nearly always tensile and approaching yield, especially in the regions of the weld for both thick and thin pipe. The measured stresses here (Figure G.16 (c) and (d)) are actually compressive in this region. This is considered unrealistic. Despite efforts to resolve this quandary, no errors in the measurement technique could be found.

Therefore, the main purpose of this analysis effort for the cold leg, to validate the VFT weld modeling procedure for bimetallic welds, was not successful. However, the results are useful and provide insight for the hot leg analysis discussed next. When the residual stress measurements were obtained, and the low values were measured, the weld modeling procedure was completely re-evaluated. The post weld heat treatment was then considered in the analysis process. The weld processes and procedures for both the cold leg and hot leg were carefully re-evaluated. The material properties used for the weld analysis were carefully evaluated. In fact, a separate test program was initiated at Oak Ridge National Laboratory (ORNL) to obtain better temperature dependent material properties for Inconel 182/82 weld metal and for A508 steel. It is important to recognize that the material properties of the weld material must be obtained on annealed weld samples because the weld modeling itself models the heating and cooling strain hardening explicitly. Hence, while the experimental residual stress measurements did not provide direct validation of the weld modeling, the insight that was obtained by considering all of the above processes was very important. Indeed, after all of these effects were considered, and re-analysis of the cold leg completed, the residual stresses predicted were lower than those originally predicted. However, they were still higher than the measurements. The fact that the hoop residual stresses measured at both the inside and outside surfaces are so low clearly indicates that the measurements were not accurate. Because the constraint in the weld direction (hoop direction) is high, as the weld bead cools, it shrinks and is constrained by the already cool material, producing high tensile residual stresses in all cases the present authors have seen in over twenty five years.

Measurement of residual stresses in bimetallic welds should be pursued in the future, perhaps using the new deep hole drilling procedures developed by Professor Smith of Bristol University (Ref. G.10). Regarding the trepanning method of measuring residual stresses, it has served very well in past studies at Battelle in the late 1970's and should be regarded as a viable method for measuring residual stresses. However, it requires a skilled and experienced technician to carefully remove the pyramid shaped chips from the pipe.

Figure G.17 illustrates equivalent plastic strains. Figure G.18 shows the corresponding axial, hoop, and shear plastic strains after welding. It is interesting to note that the axial plastic strains are compressive for the most part in the buttering region while the hoop plastic strains are tensile in the butter and weld. Moreover, from Figure G.18 (c), rather large values of shear strain develop in the region of the butter. While PWSCC growth is considered to be driven by tensile stress, or stress intensity factors, it may be useful to consider the role of tensile plastic strains in SCC growth in future studies.

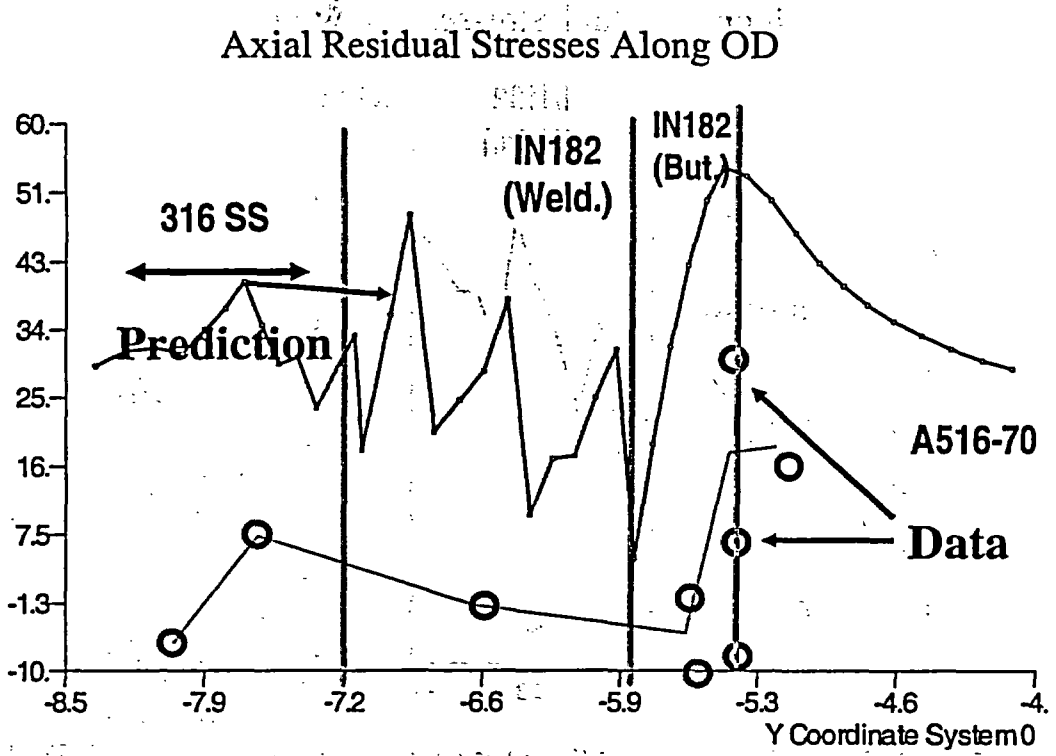

Figure G.16(a) Residual stresses final (axial) at operating temperature 291°C (556°F)

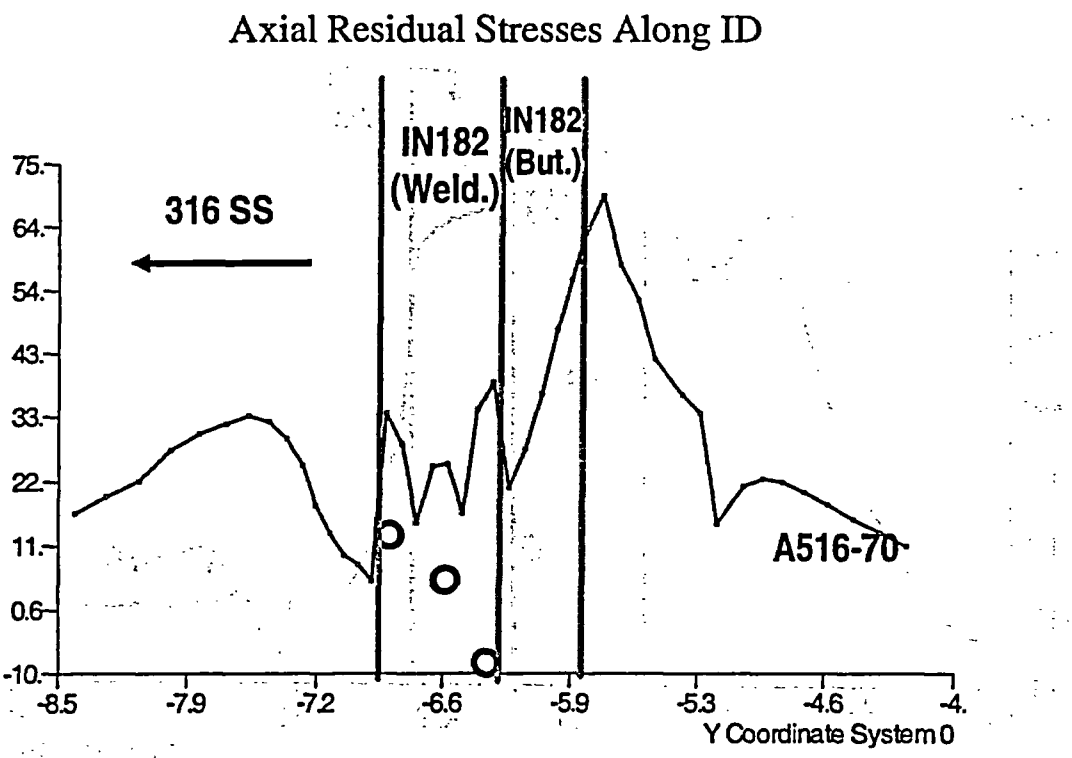

Figure G.16(b) Residual stresses final (axial) at operating temperature 291°C (556°F)

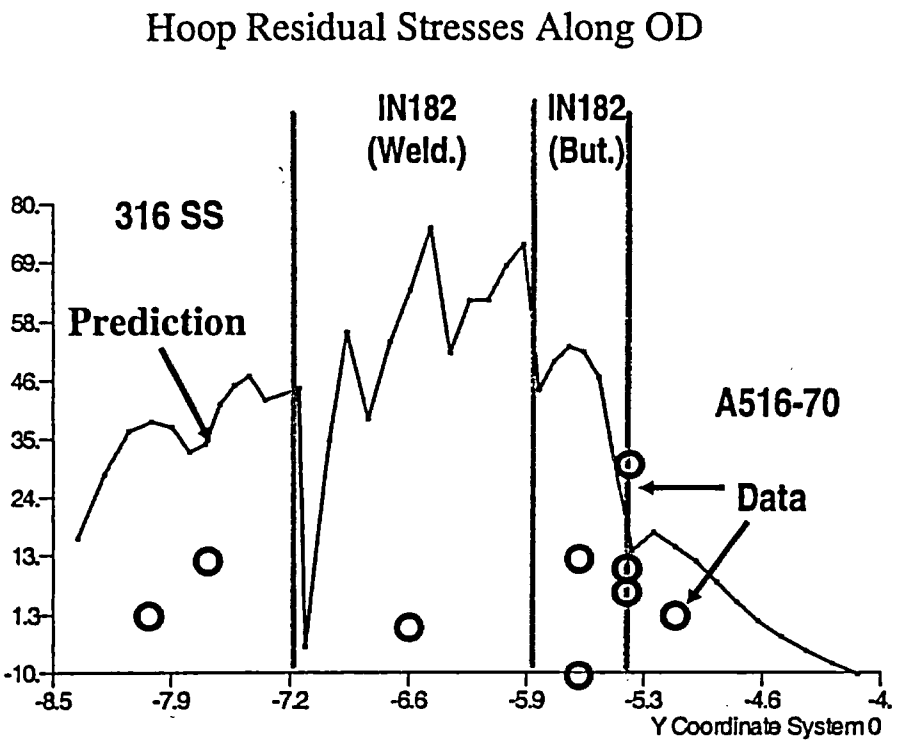

Figure G.16(c) Residual stresses final (hoop) at operating temperature 291°C (556°F)

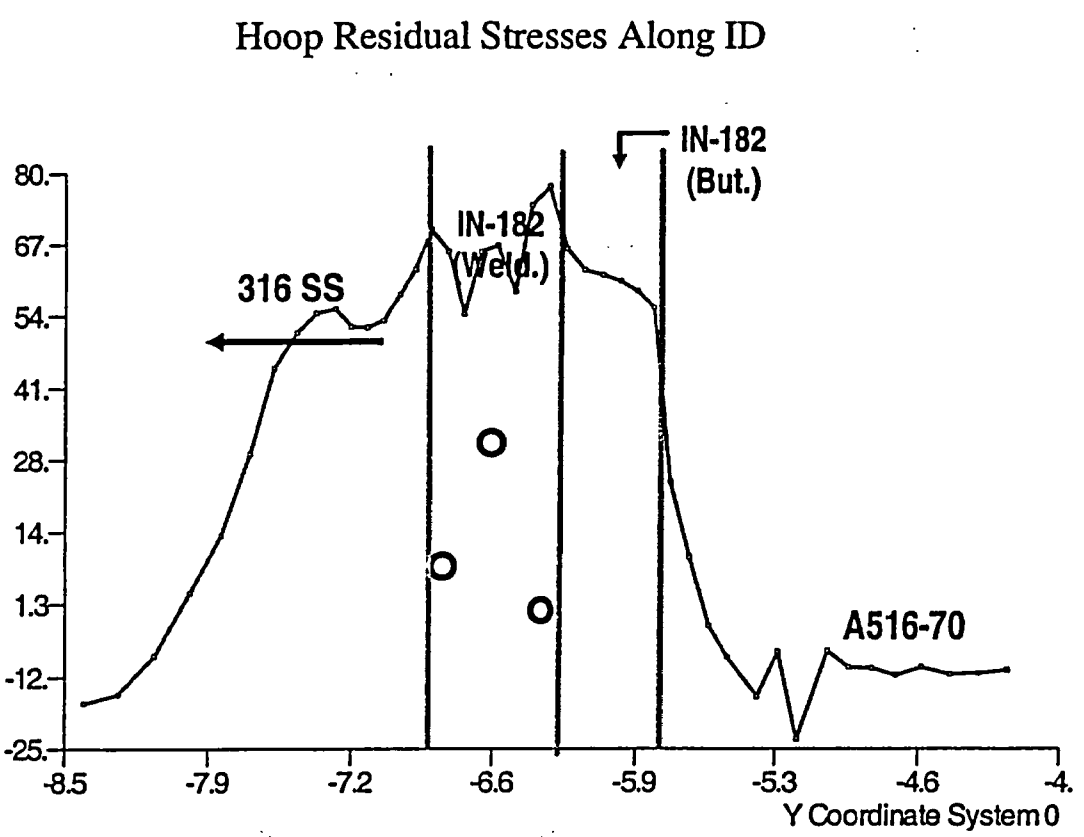

Figure G.16(d) Residual stresses final (hoop) at operating temperature291°C (556°F)

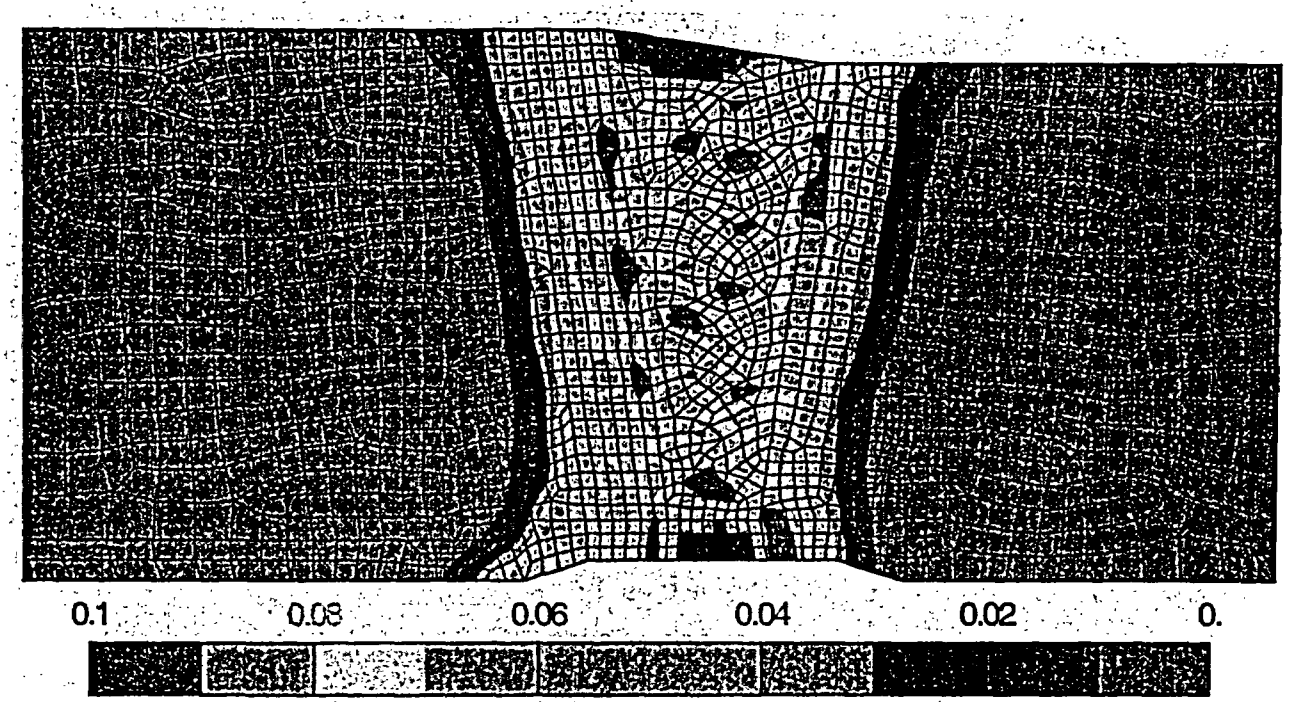

Figure G.17 Residual equivalent plastic strains in cold leg at room temperature

(a)

Axial

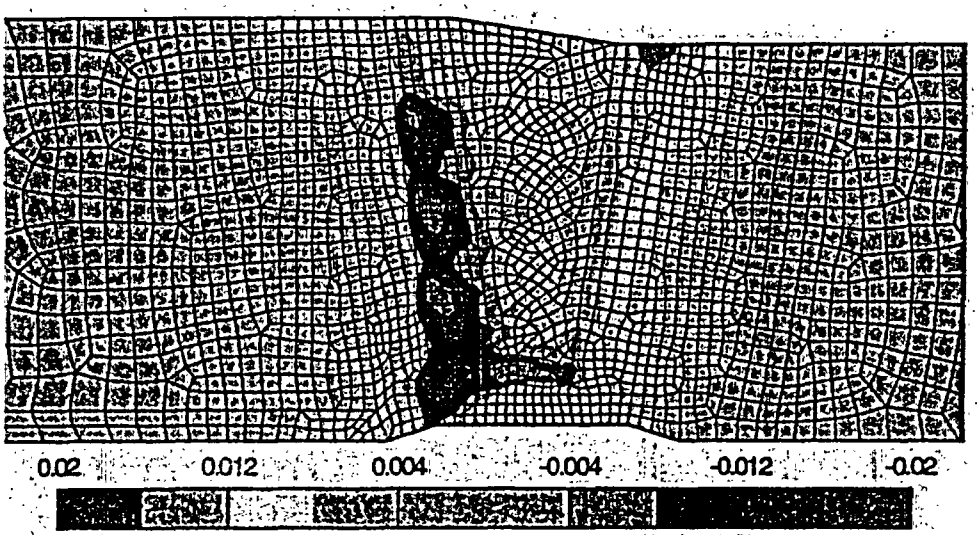

(b)

Hoop

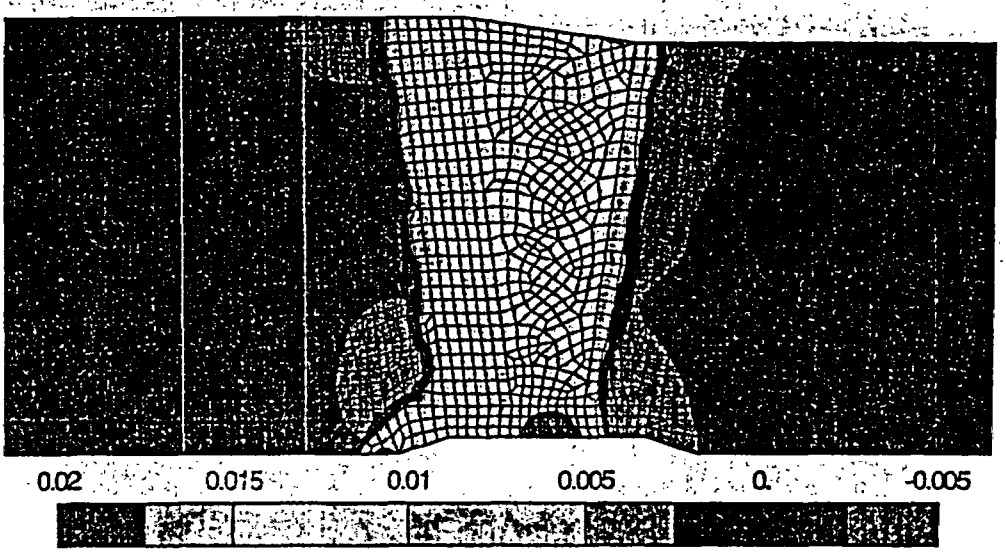

Figure G.18 Residual axial (a), hoop (b), and shear (c), plastic strains in cold leg at room temperature

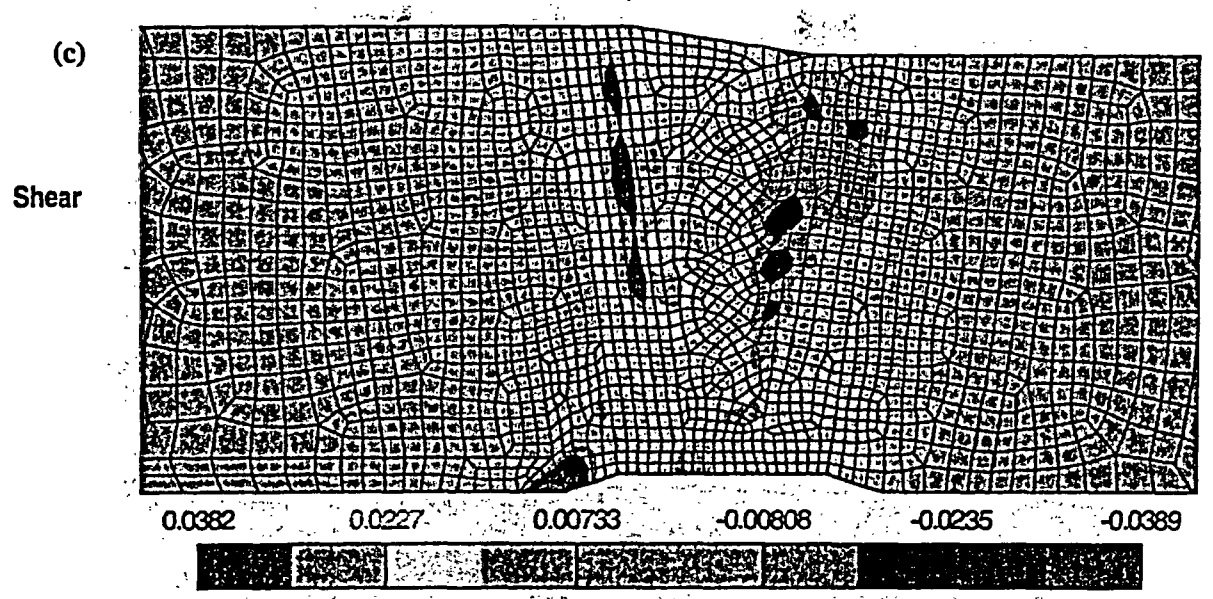

Figure G.18 Residual axial (a), hoop (b), and shear (c), plastic strains in cold leg at room temperature

G.6 RESULTS HOT LEG ANALYSIS

This section presents the axis-symmetric results for the hot leg analysis. The results of this analysis were used to calculate stress intensity factors so that PWSCC predictions could be made (Section G.7).

G.6.1 Hot Leg Computational Weld Model

The geometry of the hot leg bimetallic weld joint is illustrated in Figures G.19 and G.20. Note that the hot leg analysis for the V. C. Summer plant is similar to the cold leg analysis discussed in Section G.5 except that the geometry is different (smaller diameter and thickness), and the materials are different for the nozzle (compare with Figure G.3).

Please follow Figure G.21 for the description of the weld modeling process. The modeling sequence is quite complicated since the V. C. Summer hot leg in question had several repairs made to it. The sequence of the repairs was not entirely known, so two repair sequences were considered. Figure G.21 illustrates the welding sequence modeled. The nozzle was first pre-heated and a buttering layer deposited. The nozzle was then post weld heat treated (PWHT). As with the cold leg, the PWHT was modeled via creep analysis applied to the buttered weld residual stress state.

The buttered nozzle along with the stainless steel pipe was then pre-heated again and weld metal was deposited from the inside of the pipe to a depth of 18 mm (0.7 inch). After this amount of weld metal was deposited, the weld was rejected. In preparation for weld grind out (of the original 18 mm (0.7 inch) of weld metal), a weld bridge was deposited. The weld was then ground out from the pipe inside. There were then two weld sequences that were considered in the analysis since it was uncertain whether the weld repair was deposited from the bridge first on the outside of the pipe, followed by the inner weld or vice-versa. Both were modeled to examine the effect of the repair sequencing on the final residual stress state.

All of the processes listed in Figure G.21 were considered in the model. Figure G.22 further illustrates the modeling process pictorially. Figure G.22 (a) shows the original buttering model results. Figure G.22 (b) shows the PWHT modeling process. Figure G.22 (c) shows the completion of the weld prior to weld rejection, building of a weld bridge, and then

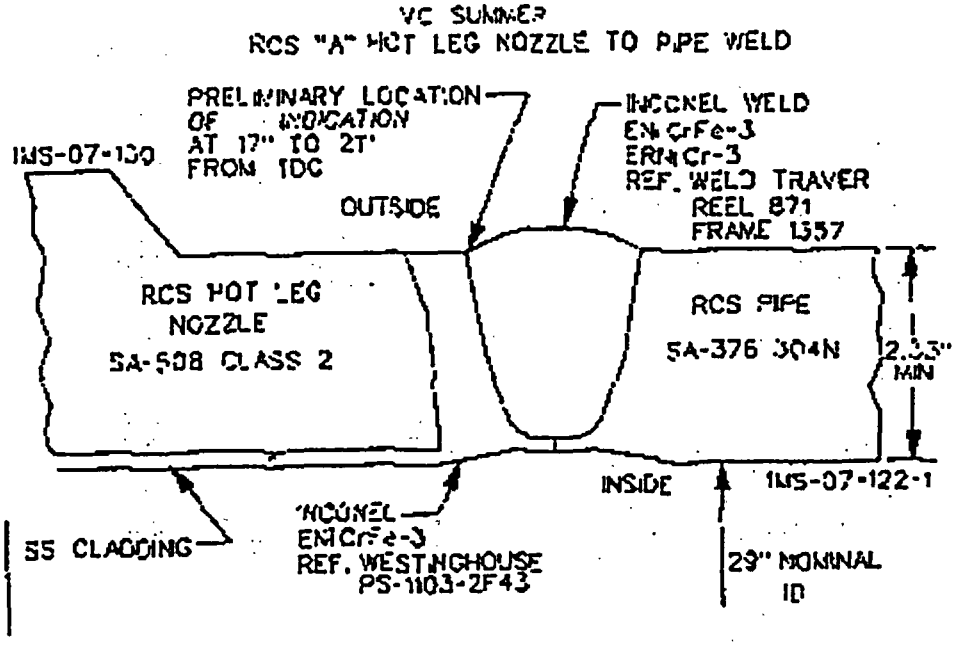

Figure G.19 Geometry of V.C. Summer bi-metallic weld joint

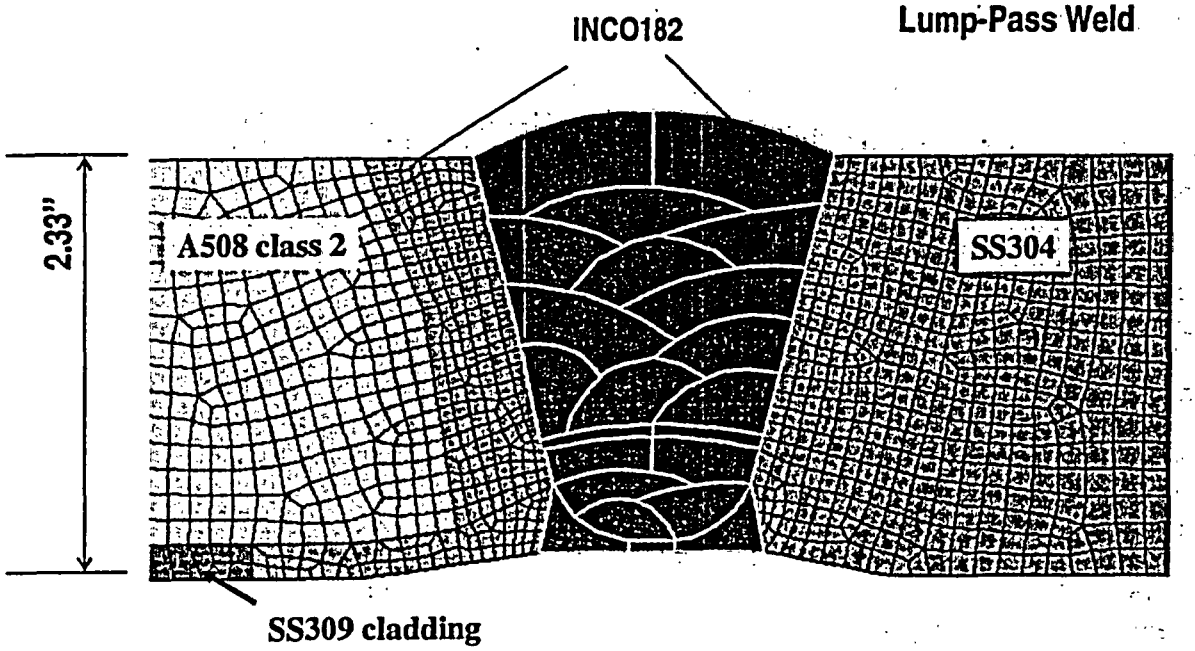

Figure G.20 Axis-symmetric model of V.C. Summer bimetallic weld joint

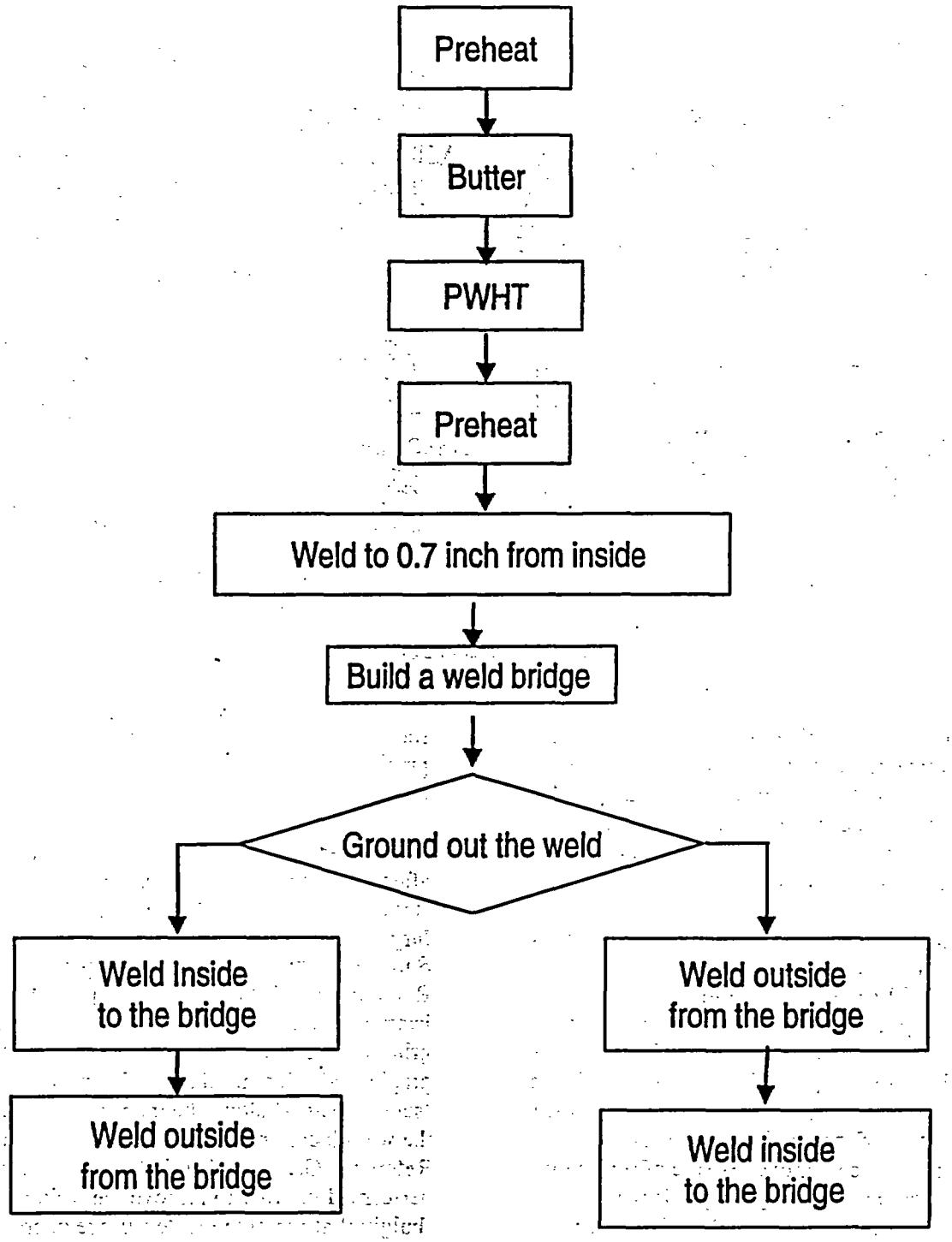

Figure G.21 Welding process simulated on hot leg

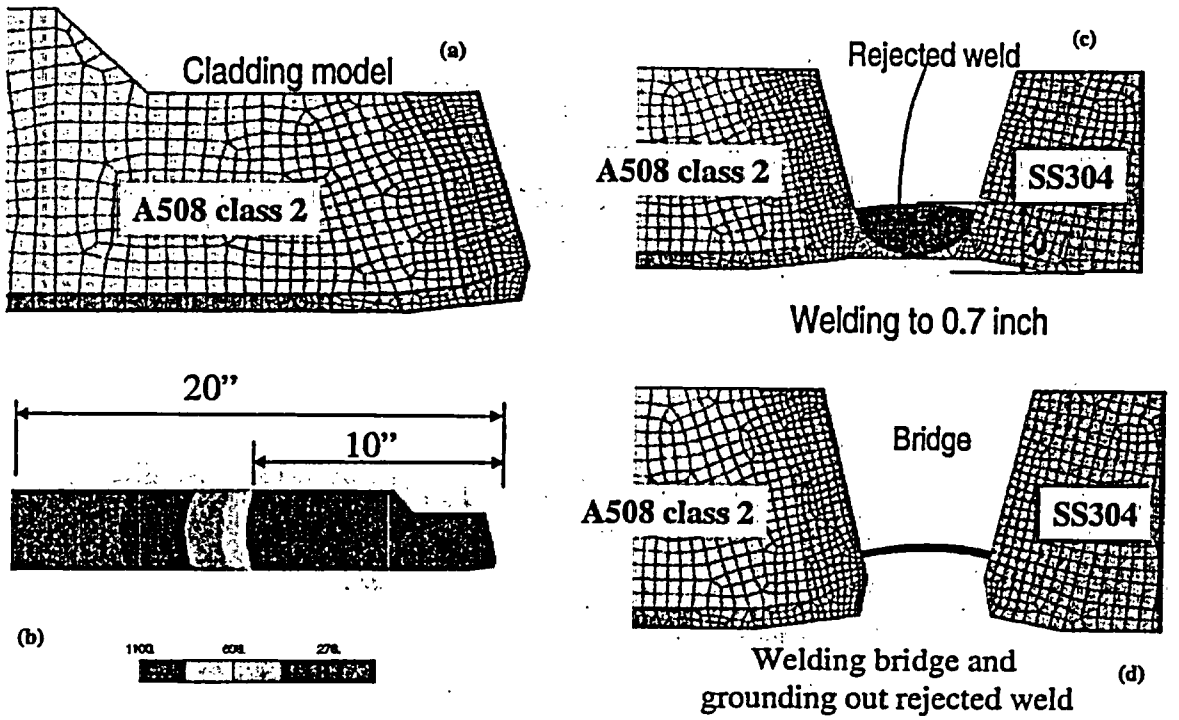

Figure G.22 Cladding (butter) and rejected weld model

grinding out the original weld so that only the bridge remains. Finally, the weld was either deposited from the inside surface first, then the outside surface, or vice-versa. Both were modeled since the precise repair weld deposition sequence was not known.

An important point regarding the analysis steps is in order at this point. Referring to Figures G.21 to G.23, grinding of weld material prior to deposition of the final weld passes was included in the modeling process. For instance, from Figures G.22 (c) to G.22 (d), material was ground out to make a bridge of weld metal prior to deposition of the weld repair layers. This grinding process simply consisted of removing material 'computationally'. By this we mean that the material was removed mathematically by eliminating the stiffness of these elements and therefore redistributing the residual stresses. The actual grinding process, whereby a rigid (or nearly rigid) sharp tool impacted the weld region and material was 'chipped away' was not considered. This is a complex modeling problem, but it can be done. However, the main effect of the grinding is to redistribute the residual stress state in the pipe as material is removed and the precise modeling of the chipping process is not necessary.

There is another source of grinding that occurs after the entire weld repair is completed. Reference G.12 provides summary of the metallurgical investigation of the cracking in the V. C. Summer plant. As discussed on page 9 of Reference G.12, 'The surface appeared highly irregular with evidence of significant surface grinding and machining distress marks'. Photographs and micrographs clearly show small 'scratch marks' along the inner pipe surface at the weld location (Figures 10 and 19 from Reference G.12). This grinding was presumably performed in order to remove the weld repair 'bulging' at the pipe inside surface in order to permit more uniform flow through the pipe. The grinding will redistribute residual stresses (as discussed above regarding the grinding before weld repair). However, because the material ground out is a small volume, it is not included in the analysis (i.e., the final geometry, already ground, is modeled).

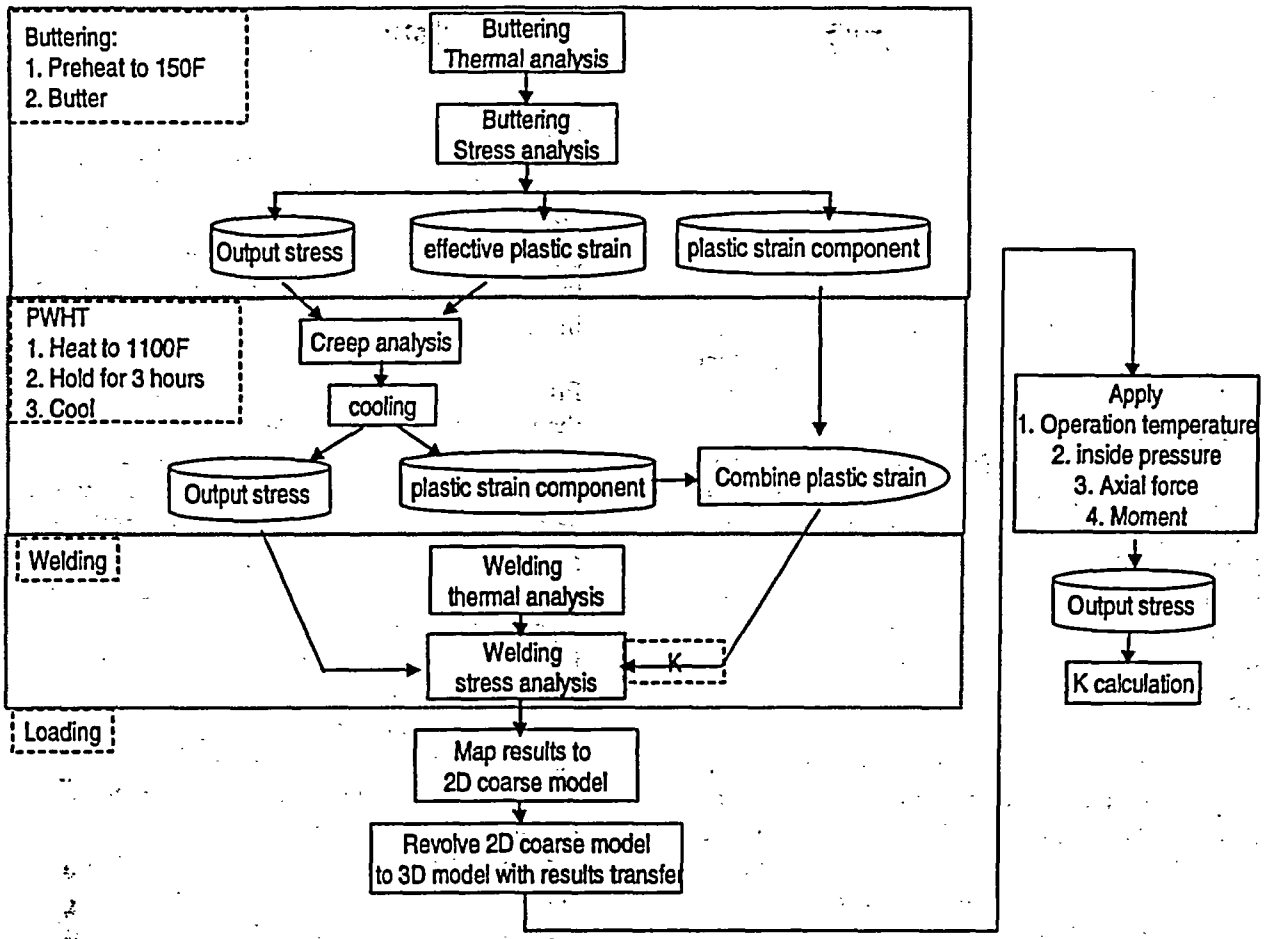

Figure G.23 Finite element analysis process flow

In essence, if additional material was added to the inside surface weld, and then removed, the final residual stress state should be very similar to that from ignoring it except for very localized grinding stresses. The very local residual stresses from the grinding process are ignored in this case. Typically, additional residual stresses from grinding are considered to be important for only a very short depth into the thickness of the pipe. Certainly, after the crack grows a very short distance into the pipe thickness, these local residual stresses are eliminated and the weld induced residual stresses dominate for most of the PWSCC growth life.

However, the geometric effects of the scratches are expected to be very important. These scratches should be considered as crack initiation sites for PWSCC, fatigue, or any possible cracking mode. Such grinding, which produces scratches, may serve as PWSCC initiation sites and should be avoided. It may be a useful exercise to include the actual modeling of grinding in such a model as an additional step in order to further prove this hypothesis. Moreover, since grinding is common practice, and is apparently not specifically considered by the code bodies, such a series of 'grinding' model studies may be of use in setting standards in future construction and aging repair.

G.6.2 Hot Leg Computational Weld Model – Buttering and PWHT Results

Figure G.23 illustrates the entire analysis procedure for the hot leg. As seen, after the weld modeling is completed, results were mapped to a coarser two-dimensional model. The coarser two-dimensional model was then revolved to a three-dimensional model in preparation of the three dimensional PWSCC crack growth analysis. Service loads were then applied and

crack growth analyses were performed for the case of residual stress only and for residual stress with service loading. The crack growth portions of these analyses are discussed in Section G.7.

The finite element model used for the analyses is shown in Figure G.24. Note that the entire long length of pipe from the nozzle to the steam generator is included. It was originally thought that the long length of pipe could have an effect on the predicted weld residual stresses. However, two analyses were performed here: one with a free end (in the Type 304 stainless steel length of pipe), and one with the length of pipe extending to the steam generator. It turns out that the weld residual stresses are not affected much by the length of the pipe. However, for the thermal loading (discussed next), it was important to include this length of pipe to accurately predict service axial stresses.

Figure G.25 shows sequence plots of axial and hoop residual stresses after buttering and after post weld heat treatment. It is clearly seen that residual stresses are strongly affected by the PWHT. The hoop stresses are relaxed quite significantly. Figure G.26 illustrates the equivalent plastic strains after buttering and after PWHT. After PWHT, plastic strains do increase somewhat more compared with the similar cold leg results (Figure G.10). Corresponding creep strains after PWHT are illustrated in Figure G.27. It is these creep strains that relax the weld induced residual stresses.

G.6.3 Hot Leg Computational Weld Model Results

Figure G.28 (a) and (b) shows axial and hoop stresses after depositing the first 18 mm (0.7 inch) of weld on the inside of the pipe and after depositing the bridge layer. The bridge layer was apparently deposited to keep the pipes together during grinding and re-deposition of new weld passes. It is interesting to note that, due to global bending, compressive axial stresses (Figure G.28 (a)) develop before removal of the material. Figure G.28 (c) and (d) show the maximum and minimum principle stresses after removal of the weld metal with only the bridge material remaining.

Figure G.29 shows axial and hoop residual stresses before repair (i.e., before grinding and re-deposition of weld metal) and after depositing the repair weld (inside weld repair case). Axial stresses actually reverse sign after the repair and the hoop stresses increase in magnitude after the inside repair.

Figure G.30 shows axial residual stresses after the repair is complete. Two cases are shown: one where the inside weld is deposited first following repair, followed by the outer passes, and vice-versa. As discussed above, both cases are considered since the complete repair sequence is not known. The outline of the buttering layer and the weld material is shown for convenience. *It is important to note that axial residual stresses are more tensile, and cover a larger area at the inner surface of the pipe for the outside deposition first followed by inside welding.* This suggests that circumferential PWSCC (caused by axial stresses) is more likely for the outside weld first case. These results, and the model itself, can be used to define optimum weld sequencing for both repairs and for original welding. Figure G.31 shows a similar comparison for hoop residual stresses for the two sequences. Again, the outside weld repair first case produces larger hoop residual stresses along the inner pipe surface compared with the inside weld first case. Axial cracking is expected to be more severe for this case as well. This will be further shown in Section G.7, which discusses PWSCC analyses.

Figures G.32 through G.35 provide comparisons of residual plastic strains caused by welding between the two sequences. In all cases except for shear strains (Figure G.35), residual plastic strains are larger in magnitude, and cover a larger area for the outside weld first case.

Figure G.36 shows the axial residual stress state after applying a hydro-test pressure at room temperature to the pipe over top the weld induced residual stresses. Hydro-test analysis assumes an end cap condition so axial stresses

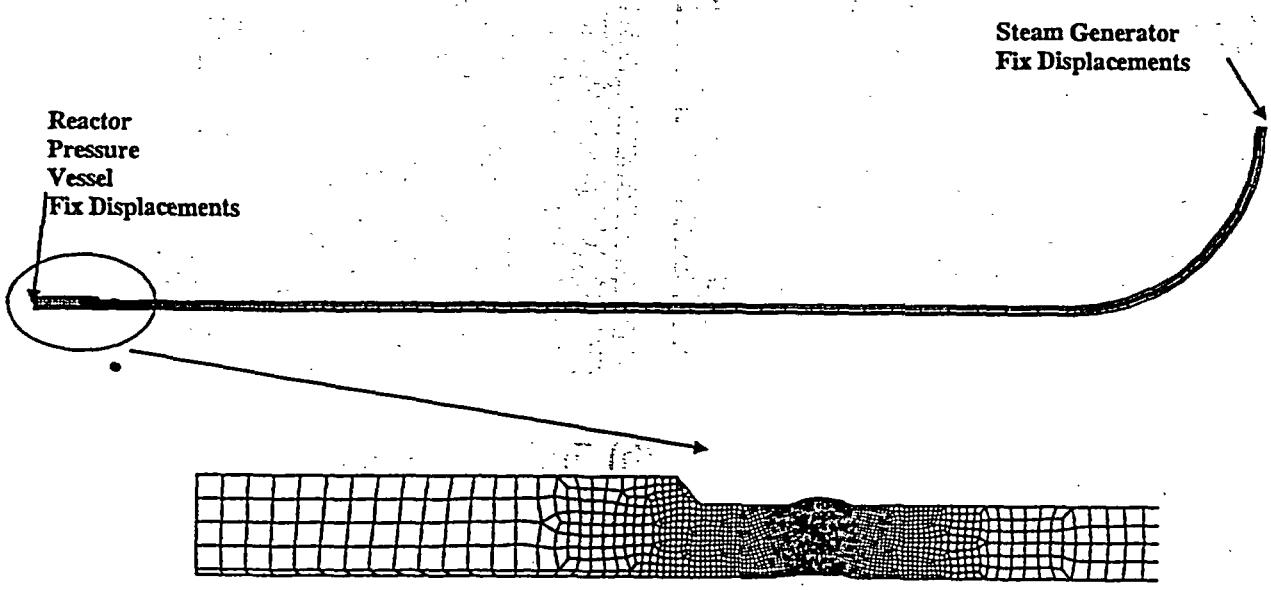

Figure G.24 Full finite element model

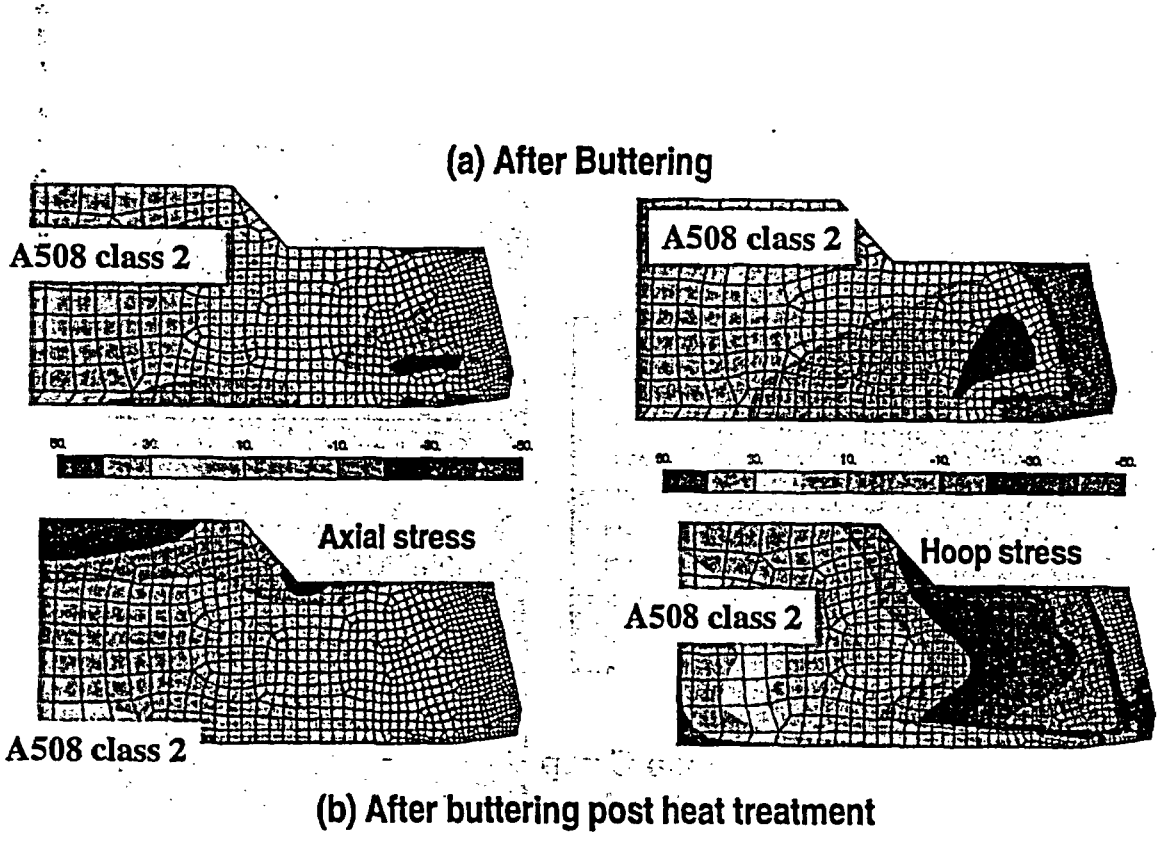

Figure G.25 Cladding simulation stresses (after cooling to room temperature)

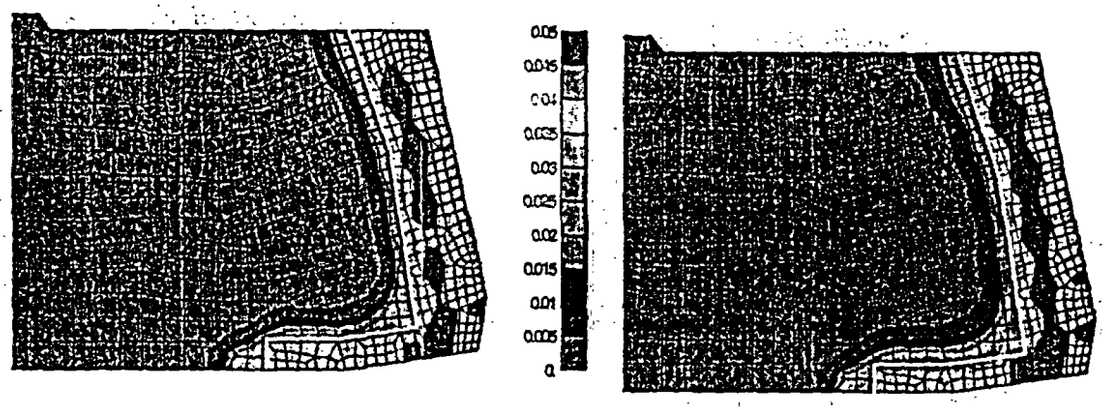

(a) End of Cladding

(b) End of Post cladding heat treatment

Figure G.26 Cladding simulation – effective plastic strains

Axial Creep Strain

Equivalent Creep Strain

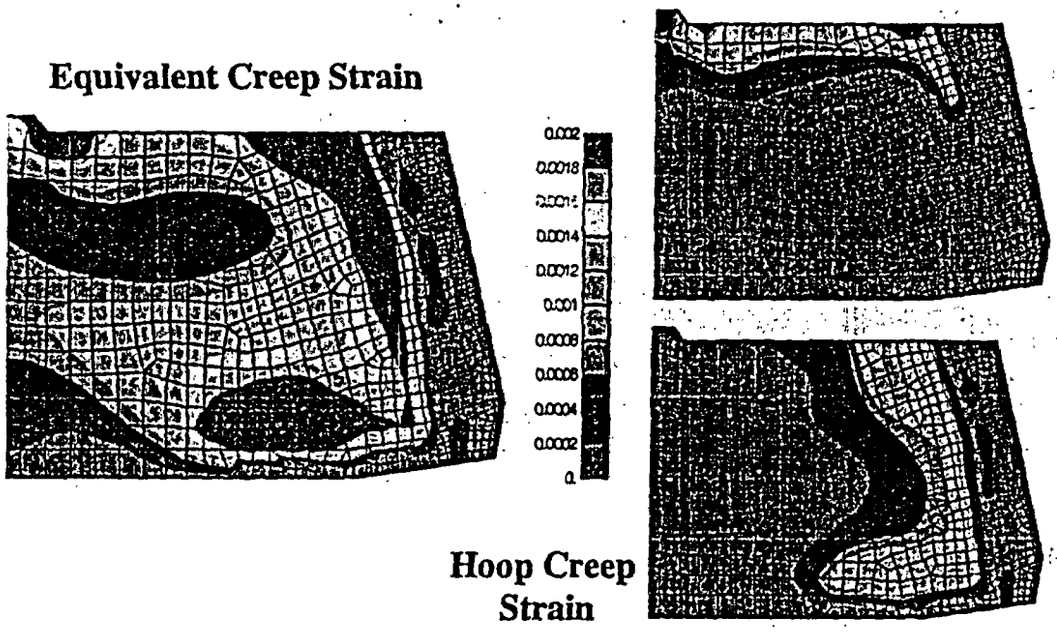

Hoop Creep Strain

Figure G.27 Post cladding heat treatment simulation – creep strains

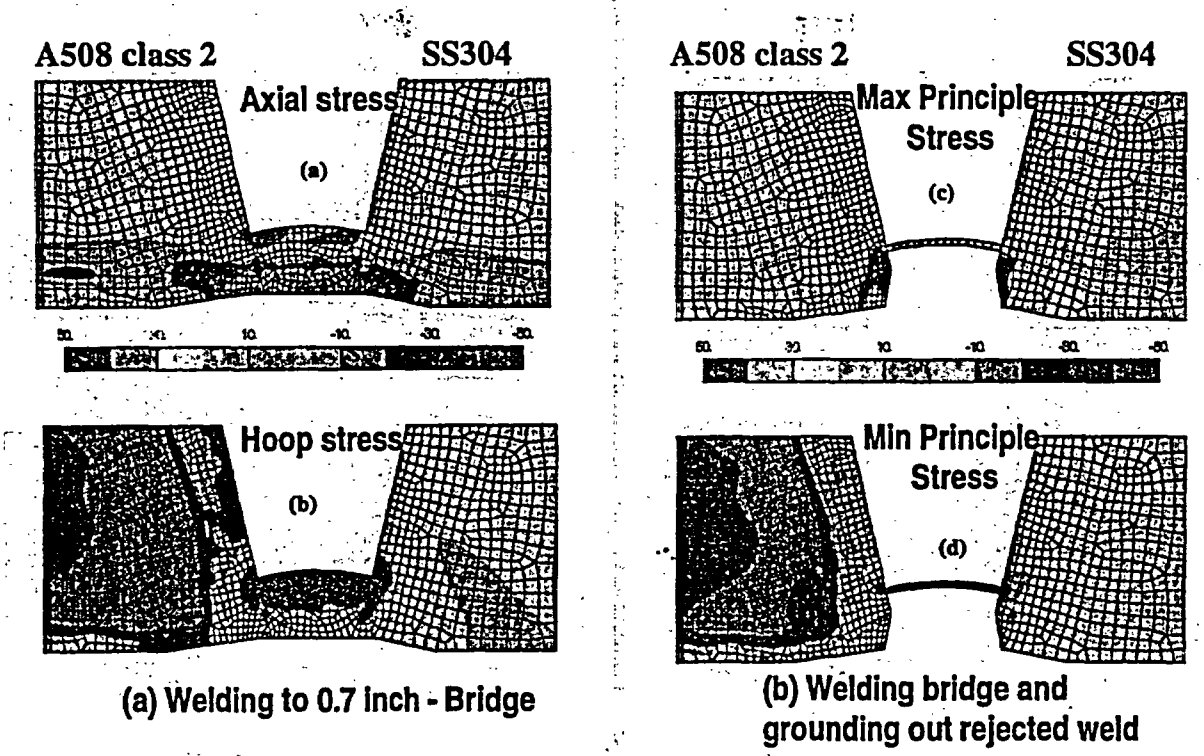

Figure G.28 Rejected weld and bridge simulation

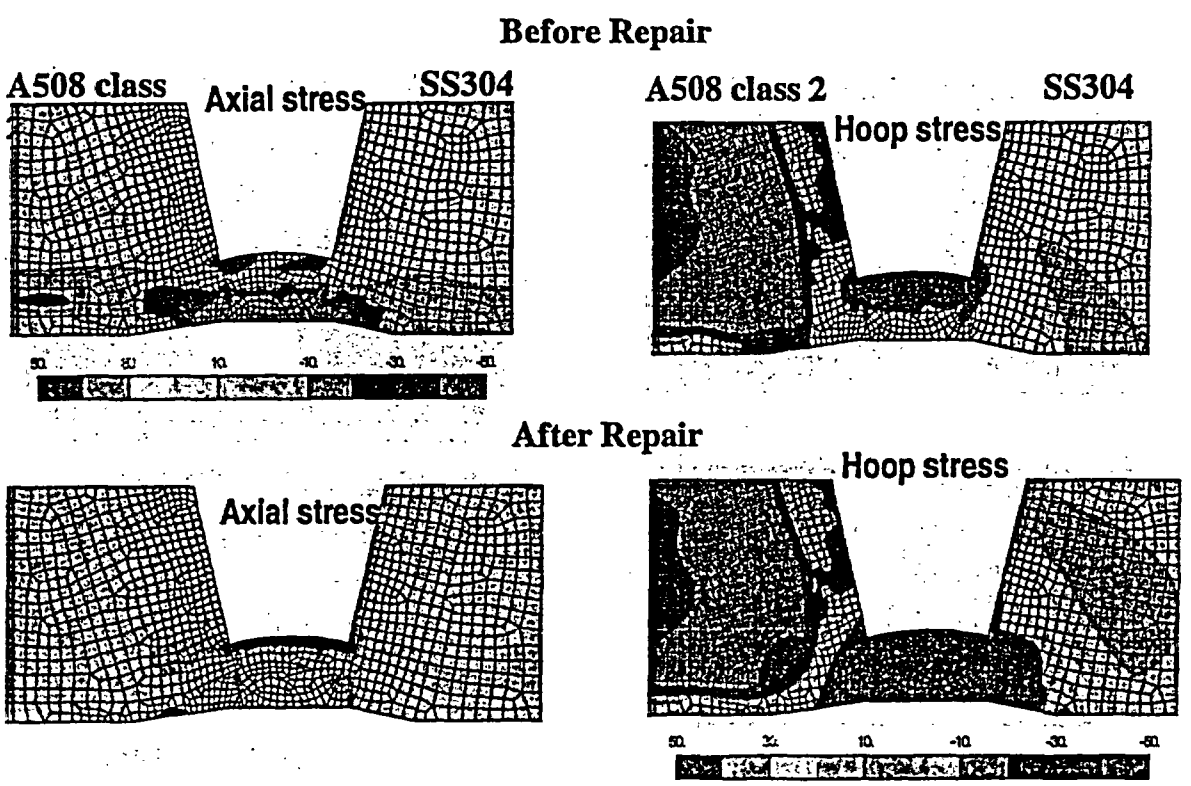

Figure G.29 Comparison of rejected weld and bridge simulation

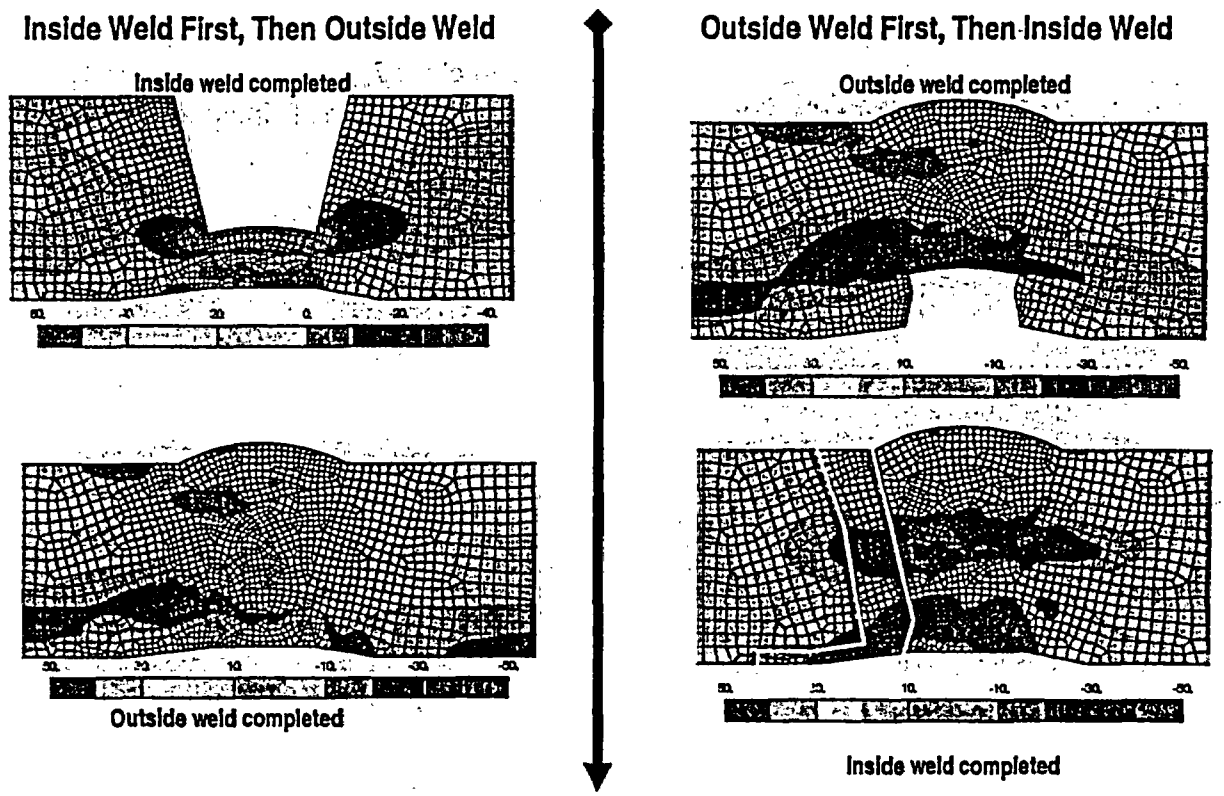

Figure G.30 Axial stress comparison between two sequences

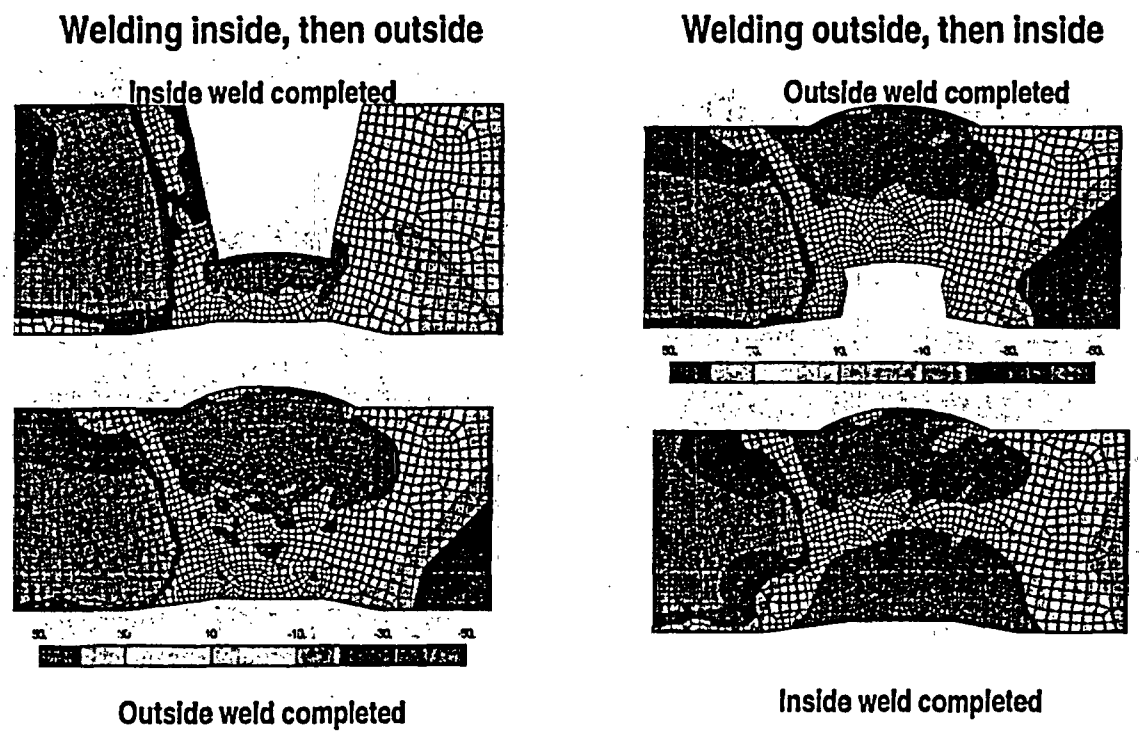

Figure G.31 Hoop stress comparison between two sequences

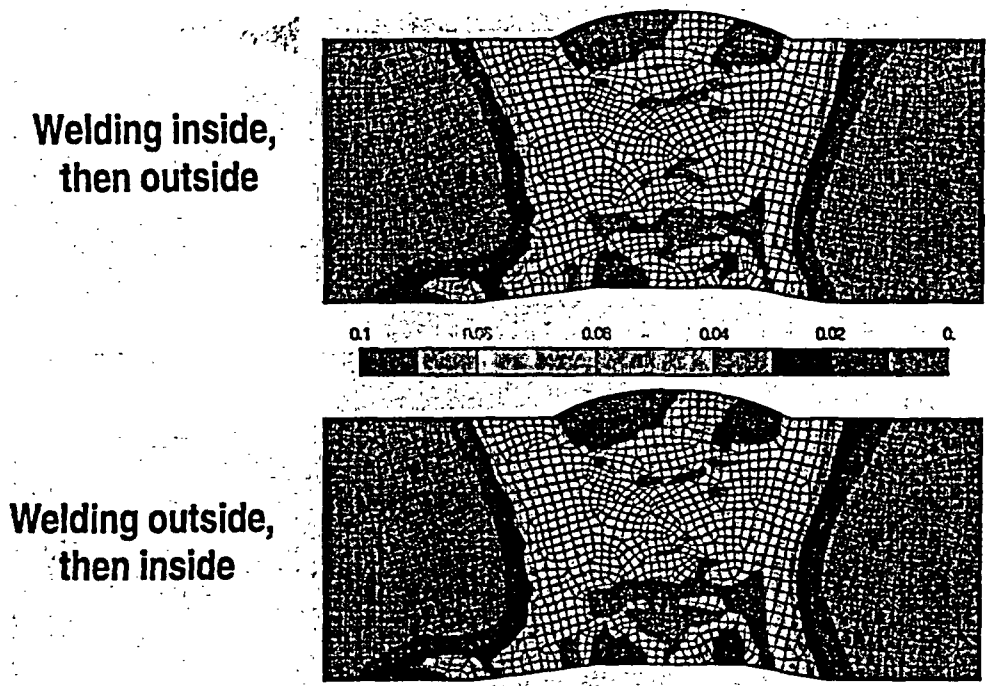

Figure G.32 Effective plastic strain comparison between two sequences

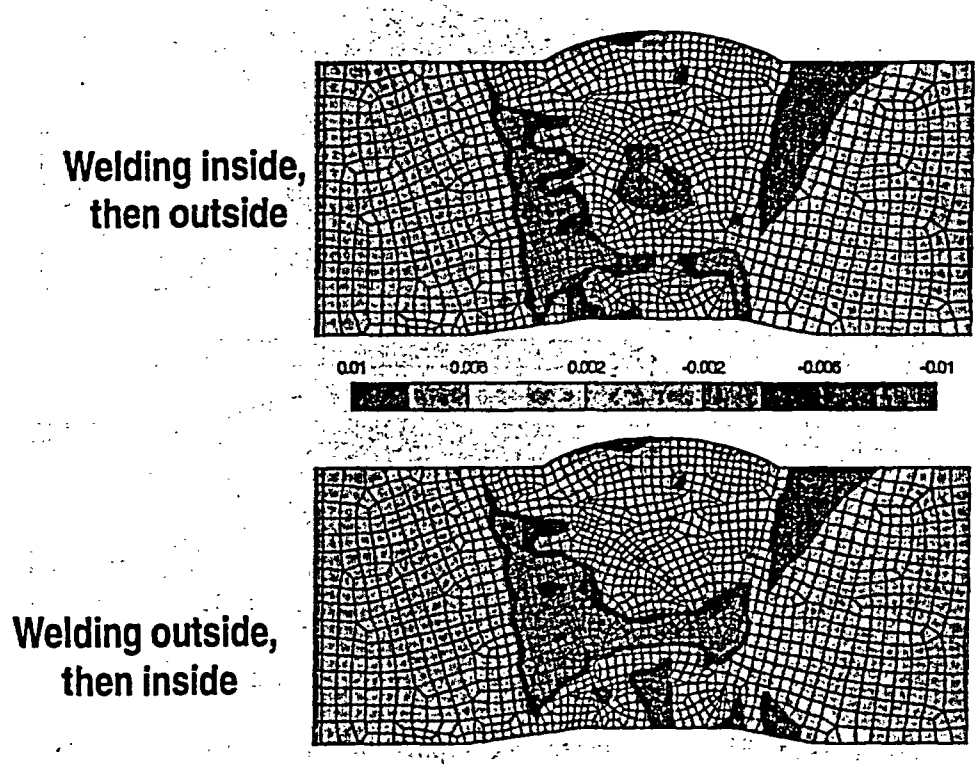

Figure G.33 Axial plastic strain comparison between two sequences

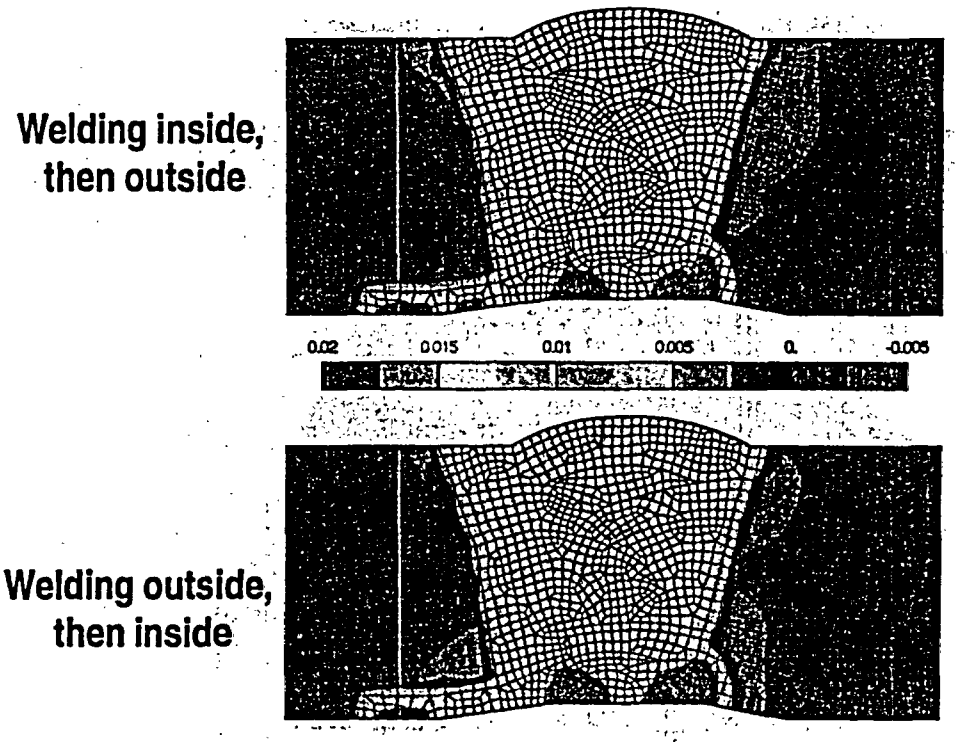

Figure G.34 Hoop plastic strain comparison between two sequences

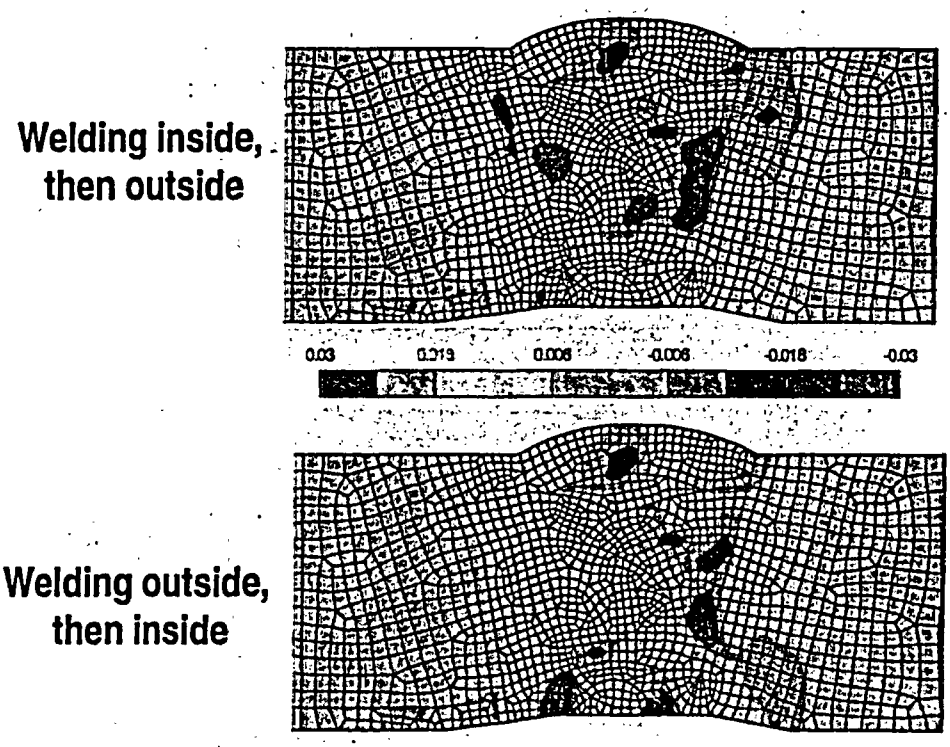

Figure G.35 Shear plastic strain comparison between two sequences

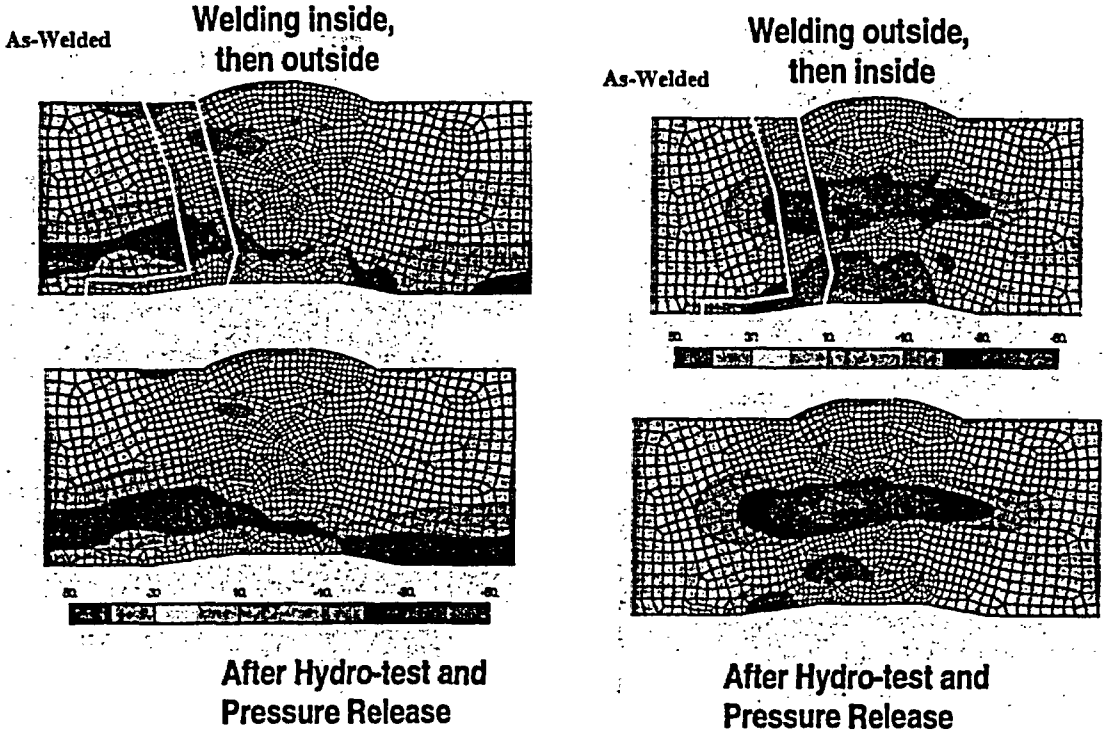

Figure G.36 Effect of hydro-test – axial stresses (pressure = 3.125 ksi, then unload)

are applied as well as pressure. The hydro-test pressure was 1.4 times the PWR operating pressure of 15.5 MPa (2.25 ksi). The hydro-test does reduce the axial residual stresses somewhat. Figure G.37 illustrates the effect of hydro testing on hoop residual stresses. It is seen that hoop residual stresses are not affected much by the hydro-test compared to the axial stresses.

As discussed in Section G.5 regarding the cold leg analysis, the residual stress measurements performed using the trepanning method were somewhat disappointing. During the metallurgical investigation into the PWSCC cracking reported in Reference G.12, residual stress measurements were made on sectioned pieces of the hot leg bimetallic pipe weld. Since the measurements were made on the pipe that was already cut up and sectioned, all component residual stresses are expected to be lower than in the intact pipe. However, from Table 2 of Reference G.12 the measured hoop residual stresses ranged from -59 to 161 MPa (–8.6 to 23.4 ksi) and the measured axial residual stresses ranged from 56 to 373 MPa (8.1 to 54.1 ksi). By comparing these numbers to the predicted residual stress plots in Figures G.36 and G.37 (after hydro-test and unloading), it is seen that the numbers are qualitatively similar. The hoop stresses measured from the cut pipe are expected to be most inaccurate since the weld bead (hoop) tension is relieved when the axial cuts are made to the pipe, and the hoop stress measurements are expected to be quite low. However, axial stresses are expected to be closer to the intact pipe. The ranges of measured axial stresses, when compared to Figure G.36, compare reasonably well and provide some validity to the predictive methodology used here.

G.6.4 Hot Leg Computational Weld Model Results – With Operational Loads

The next step before calculating stress intensity factors for the PWSCC analyses is to obtain operating stresses. For the PWSCC analysis, we consider crack growth for both residual stress only and residual stresses with operational loading. The operational loading consists of temperature, which is 324°C (615°F), followed by a bending moment and the pressure/tension load case.

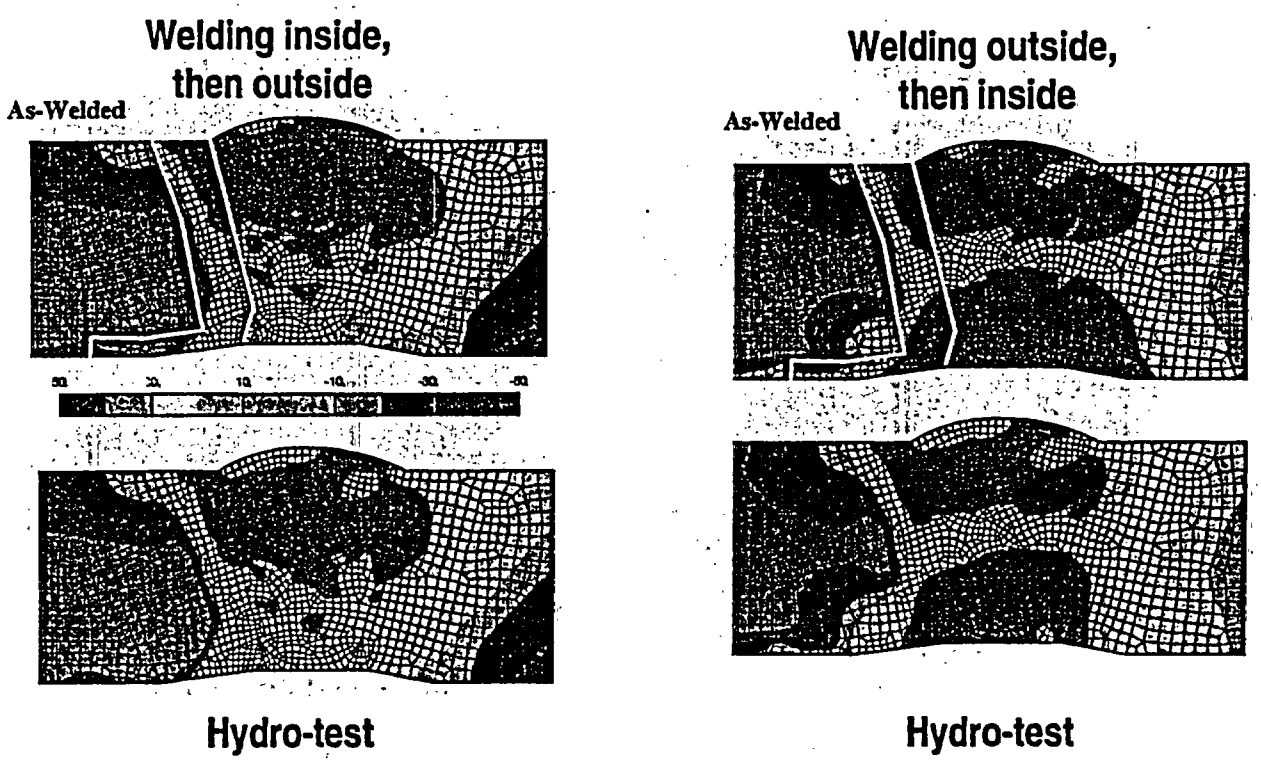

Figure G.37 Effect of hydro-test – hoop stresses (pressure = 3.125 ksi, then unload at room temperature)

The thermal loading was applied to the model of Figure G.24. It was assumed that the entire hot leg was heated (and expands) to 324°C (615°F). The vessel and steam generator were assumed to be massive, providing the fixity constraints illustrated in Figure G.24. Hence, the hot leg expands while the vessels provide constraint. Figure G.38 compares the axial residual stress states before and after heat up to 324°C (615°F). The axial stresses decrease due to the hot leg expansion and vessel constraint. Figure G.39 shows the corresponding hoop residual stresses at 324°C (615°F). The small reduction in hoop stress is mainly due to the heat up (and corresponding reduction in material properties at high temperature). The constraint has little effect on the hoop stresses.

The detailed fine mesh required for the weld analysis is not required for the service load (moment and bending) case analyses. A fine mesh is also not required for the subsequent fracture analyses to be discussed next. As discussed in connection with Figure G.23, the residual stresses are mapped from the fine weld (2D axis-symmetric) analysis model to a coarser (2D axis-symmetric) model. Figure G.40 (a) and (b) provide axial and hoop residual stresses as mapped from the fine to coarse model. Figure G.41 (a) and (b) provide the same mapping comparison for the outside first weld. It is seen that the mapping procedure is quite accurate.

Figure G.42 shows a similar mapping between the coarse two-dimensional mesh to a full three-dimensional mesh. Again, the comparison is quite good (compare to Figure G.41) illustrating that the mapping procedure is adequate. Figures G.43 and G.44 show similar comparisons between the 2D stresses and mapped 3D stresses. Finally, Figure G.45 shows the plastic strains mapping from the coarse 2D mesh to the 3D mesh. This is explicitly shown to illustrate that stresses and strains are mapped to the three dimensional model. As such, the service load cases (moment, tension, and pressure) include the effects of plasticity.

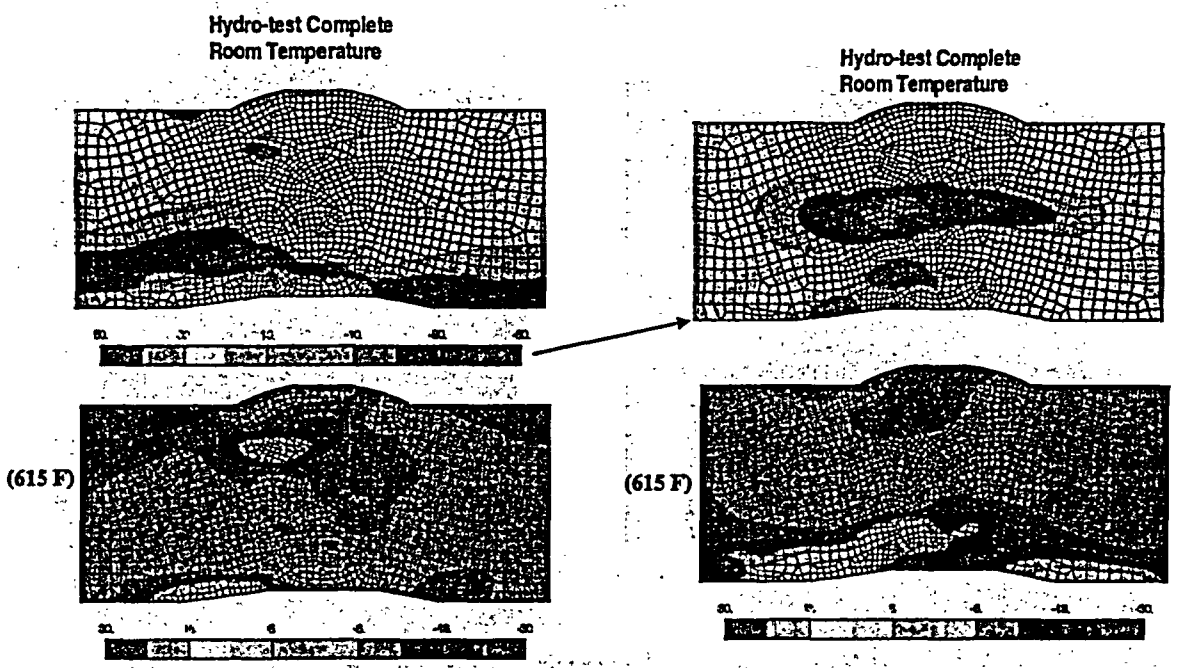

Figure G.38 Axial residual stresses at operating temperature (after all welding and hydro-test) Top: room temperature before heat up to 324°C (615°F); Bottom: after heat up; left is for welding inside then outside, right is for welding outside then inside

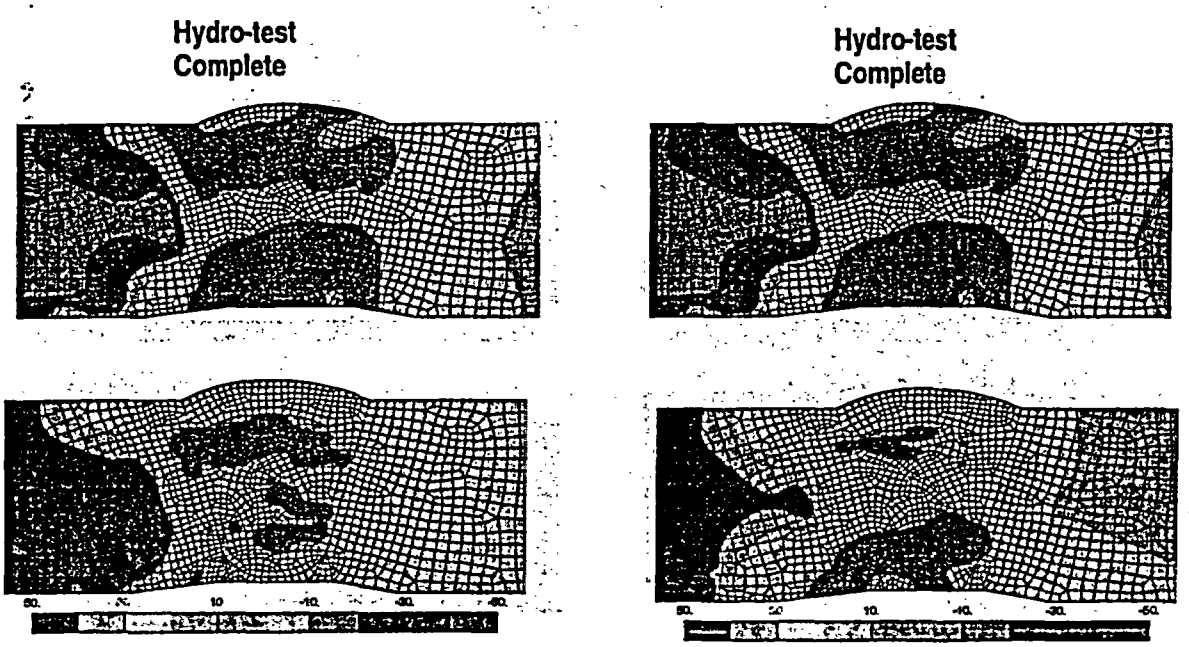

Figure G.39 Hoop residual stresses at operating temperature (after all welding and hydro-test) Top: room temperature before heat up to 324°C (615°F); Bottom: after heat up; left is for welding inside then outside; right is for welding outside then inside

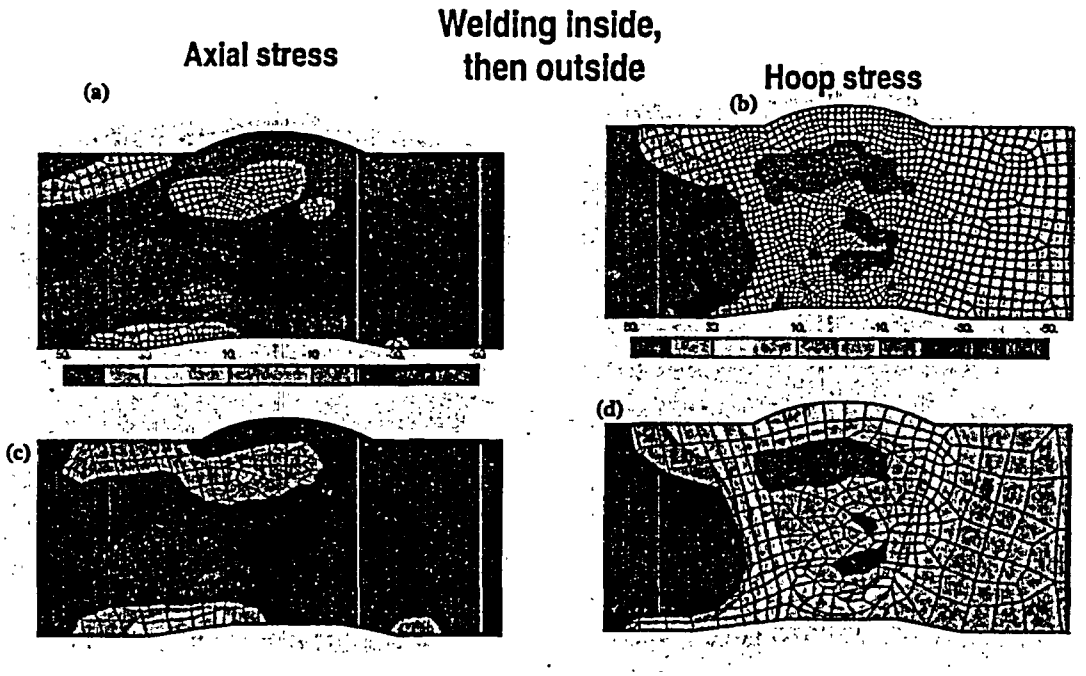

Figure G.40 Operation residual stresses (324°C (615°F) – no loading) for inside first weld (a) and (b). (c) and (d) mapped residual stresses at operating temperature from fine to coarse mesh. These stresses are then mapped to a three dimensional mesh (inside weld first, then outside weld)

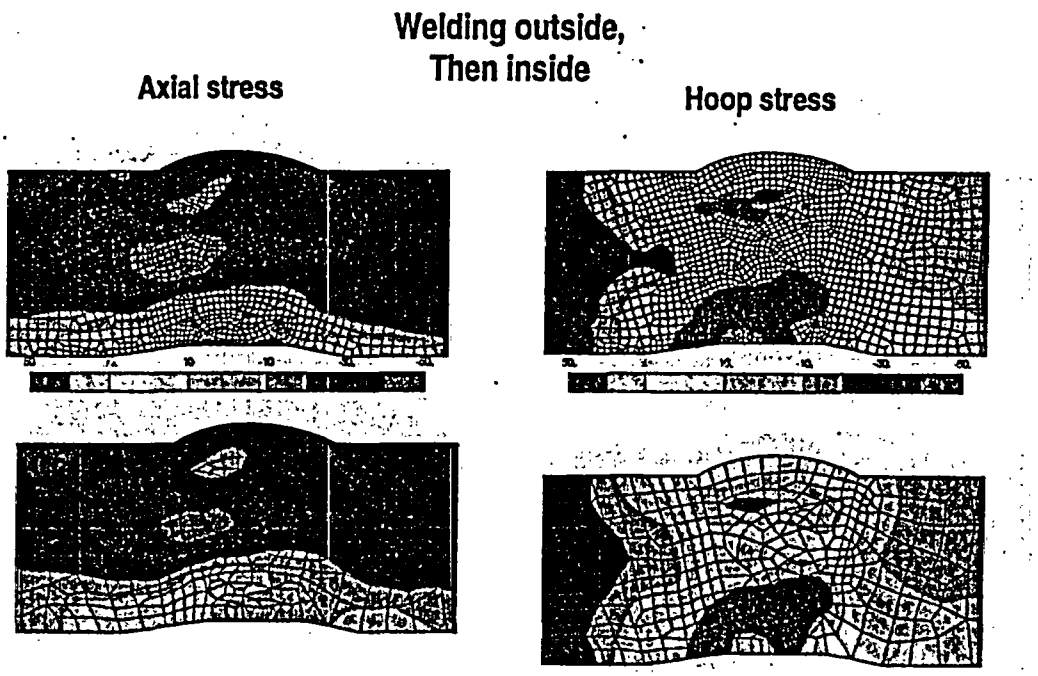

Figure G.41 Operation residual stresses (324°C (615°F) – no loading) for outside first weld (a) and (b). (c) and (d) mapped residual stresses at operating temperature from fine to coarse mesh. These stresses are then mapped to a three dimensional mesh (outside weld first, then inside weld)

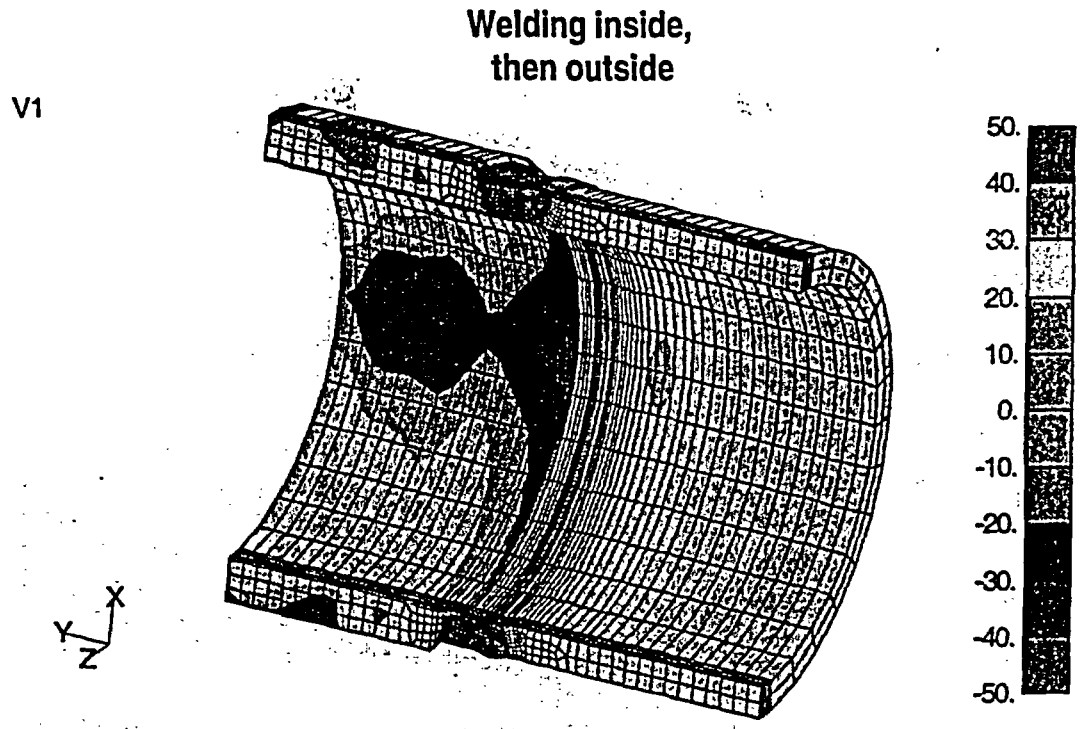

Figure G.42 Mapped hoop residual stresses at operating temperature from coarse axis-symmetric mesh to 3D mesh (inside weld first, then outside weld). (This 3D model is then used to obtain stress intensity factors via the finite element alternating method)

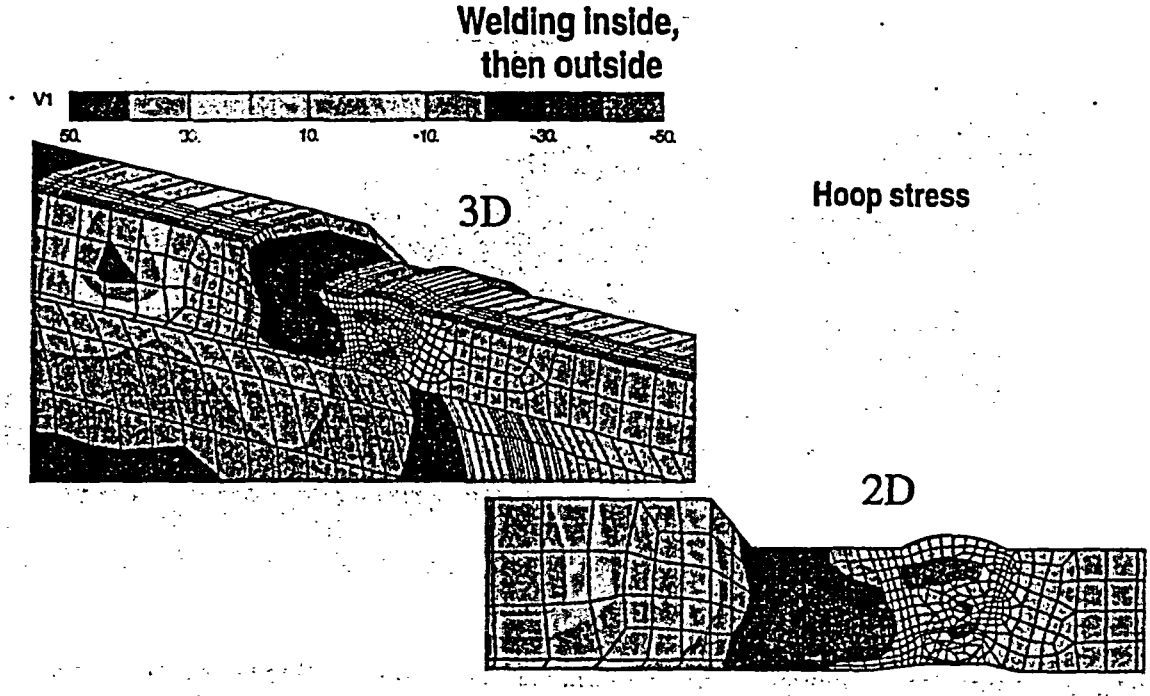

Figure G.43 Comparison of mapped hoop residual stresses at operating temperature from coarse axis-symmetric mesh to 3D mesh (inside weld first, then outside weld)

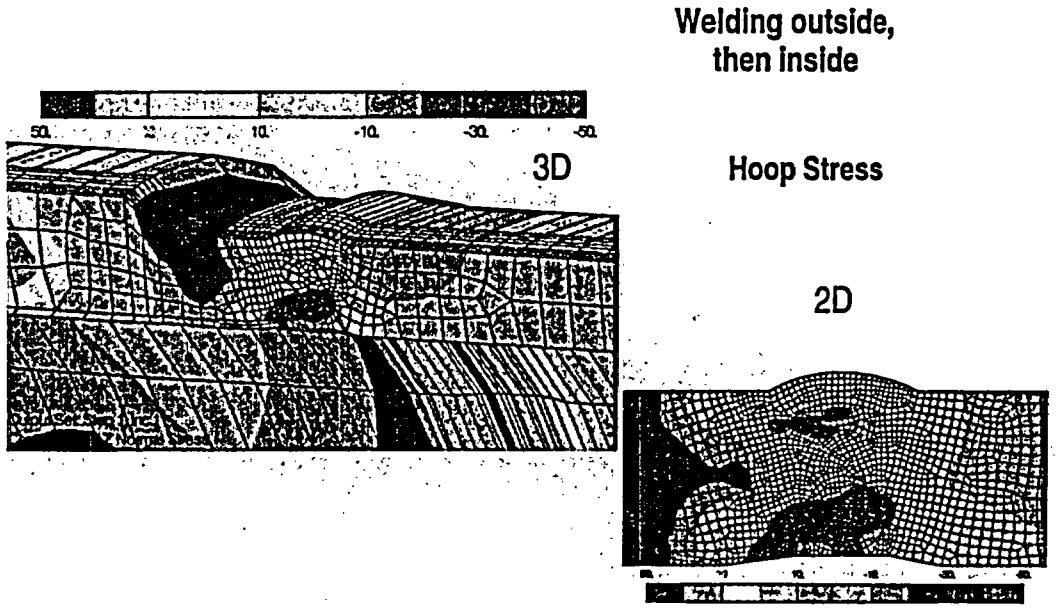

Figure G.44 Comparison of mapped hoop residual stresses at operating temperature from coarse axis-symmetric mesh to 3D mesh (outside weld first, then inside weld)

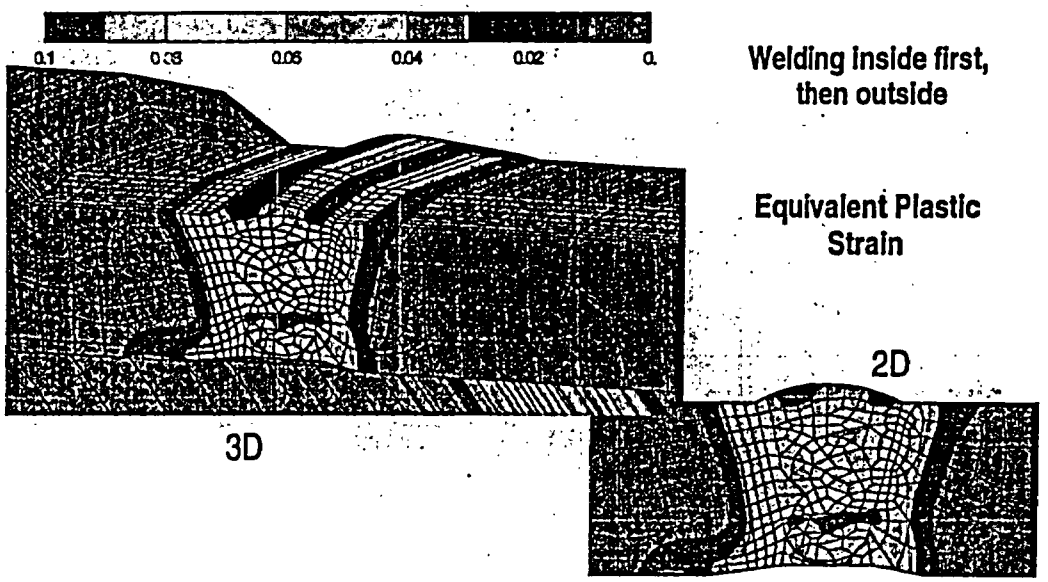

Figure G.45 Comparison of mapped equivalent plastic strains at operating temperature from coarse axis-symmetric mesh to 3D mesh (inside weld first, then outside weld)

G.7 PRIMARY WATER STRESS CORROSION CRACKING AND FRACTURE ASSESSMENT OF HOT LEG/RPV BIMETAL WELD

The finite element alternating method (FEAM) was used to obtain stress intensity factors to perform the PWSCC analyses. FEAM is very convenient for obtaining mixed mode stress intensity factors in complex structures. Stress intensity factors were obtained for numerous crack sizes and shapes for cases of:

- Inside weld first, then outside weld repairs
- Outside weld first, then inside weld repairs
- Residual stress only
- Residual stress plus normal operating loads
- Circumferential cracks
- Axial cracks

Typically it required about two minutes for a new solution on a high-end personal computer once the stiffness matrix was reduced once. Typical 3D meshes consisted of about 20,000 elements. In all, about sixty K solutions were obtained and used to model crack growth via SCC equations (discussed later). Although mode I stress intensity factors dominated, there were some cases where mode II was about 20 percent of the mode I value. However, mixed mode effects were not considered here.

The FEAM method properly accounts for stress redistribution as the cracks grow. As such, cracks that grow through a residual stress field that reach a compressive residual stress field (after stress re-distribution) can stop growing. Weight function methods often have problems accounting for stress redistributions properly.

The results of the stress corrosion cracking assessment are provided here. For the SCC analyses, crack growth was predicted for the case of residual stress alone (at operating temperature of 324°C [615°F]), and for normal operating loads. The normal operating loads were obtained from Reference G.11 and are included in Figure G.46. The residual stress states that serve as input to the FEAM analysis are illustrated in Figures G.47 to G.50 for both the inside weld first case (Figures G.47 and G.48) and outside weld first case (Figures G.49 and G.50). The top illustrations in Figures G.47 to G.50 consist of only the residual stress state at the operating temperature of 324°C (615°F). The bottom illustrations consist of residual stresses including operating loads. Plasticity (if any) was included in the analysis where loading was applied to the weld residual stress results.

Stress Intensity Factors. Figure G.51 provides a few of the stress intensity factor plots used for the PWSCC assessment. This case is for an axial elliptic crack positioned with aspect ratio as shown in Figure G.51. Both the 'residual stress only' and 'residual stress plus normal operating load' conditions were considered for all cases. In all K was calculated for cracks of many different sizes and shapes (a total of 60 cracks for both axial and circumferential locations).

The crack growth rate equation, taken from Reference G.13, is:

$$\frac{da}{dt} = 1.4\times10^{-11}(K_I - 9)^{1.16}(m/\sec) \qquad \text{(G.1)}$$

Here K_I has units of MPa $m^{1/2}$ and the range for the data is for K values between 20 and 45. The K values calculated in this study are both lower and higher than this range. Moreover, this equation represents the Scott model based on the application of a factor of 5. Hence, while this equation may need improvement for future analyses, it is used for the crack growth and life predictions shown in the following. Moreover, for this study, this was the only available data for the PWSCC crack growth analyses, i.e., no other PWSCC laws were used here.

G.7.1 The 3 Dimensional Growth of Axial Cracks Through the Hot Leg Weld

The growth of a 3 Dimensional (3D) crack through a thick pipe must account for both the residual stress field left from the welding process as well as the stress imposed from the applied loadings. Because the residual stresses can change from compressive to tensile (or vice

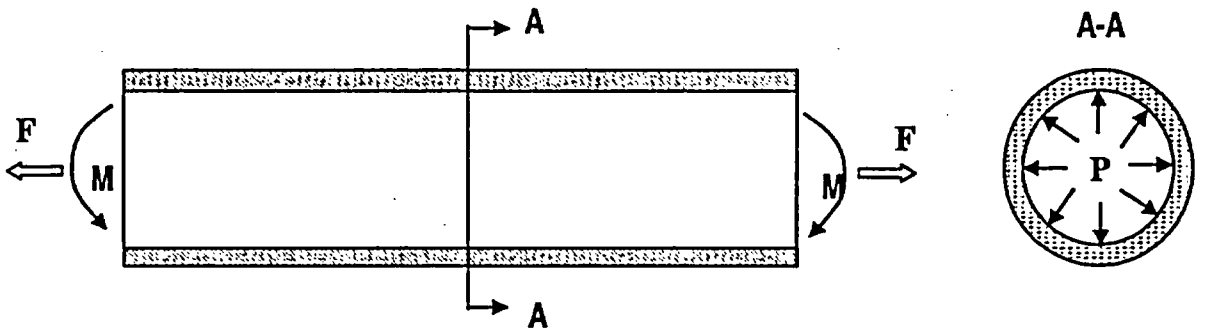

P-pressure: 2.25 (ksi)
F-force: 1476 kips (including the force due to the pressure)
M-bending moment: 22052 in-kips

Figure G.46 Normal operating loads applied on hot leg

Residual Stress Only:
615F

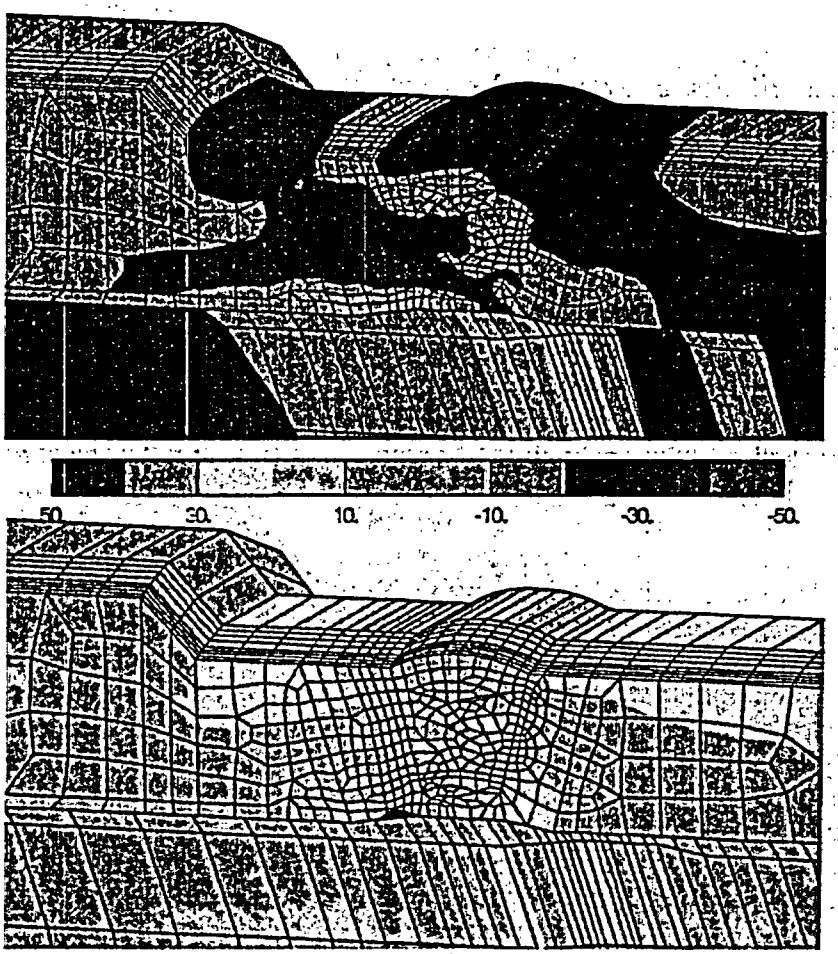

Residual Stress Plus:
615F
Normal Operating
Loads

Figure G.47Axial stresses – used for FEAM analyses: inside weld first then outside weld

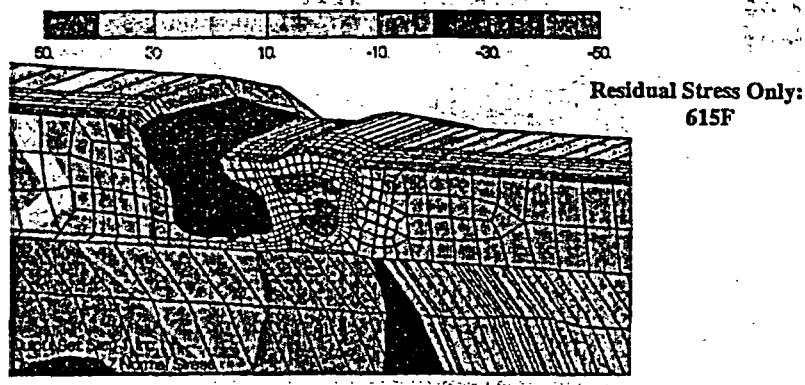

Residual Stress Only:
615F

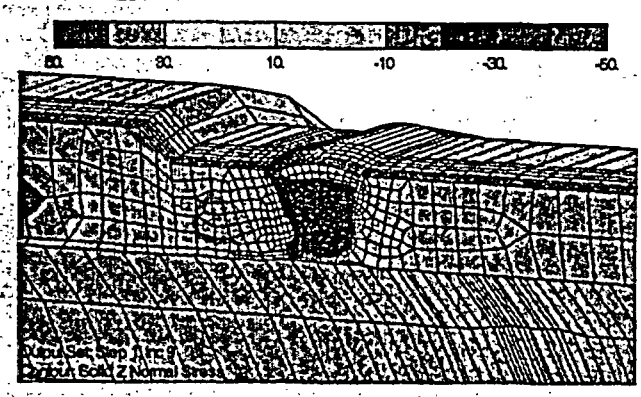

Residual Stress Plus:
615F
Normal Operating
Loads

Figure G.48 Hoop stresses – used for FEAM analyses: inside weld first then outside weld

Residual Stress Only:
615F

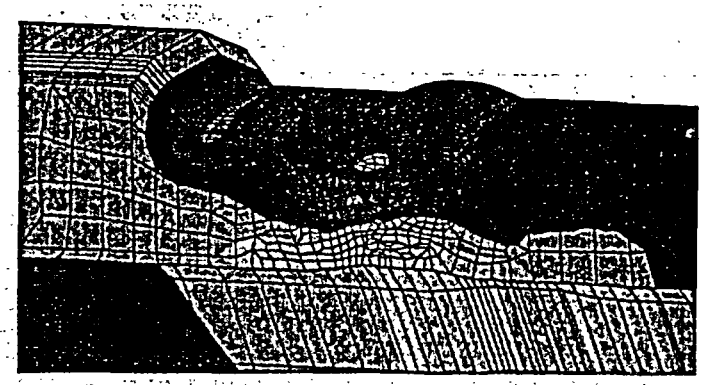

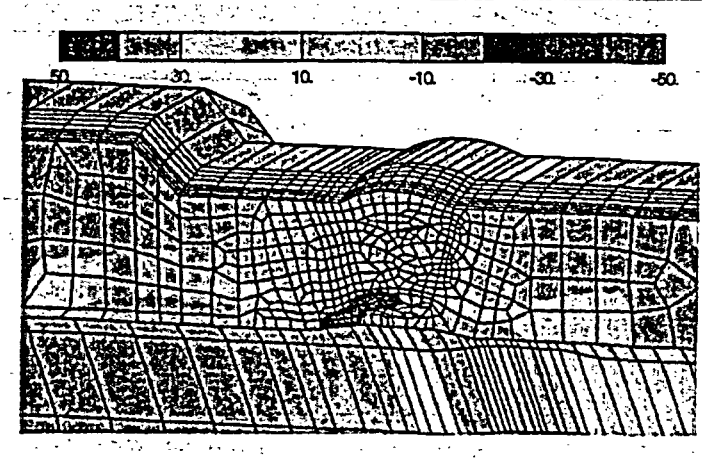

Residual Stress Plus:
615F
Normal Operating
Loads

Figure G.49 Axial stresses – used for FEAM analyses: outside weld first then inside weld

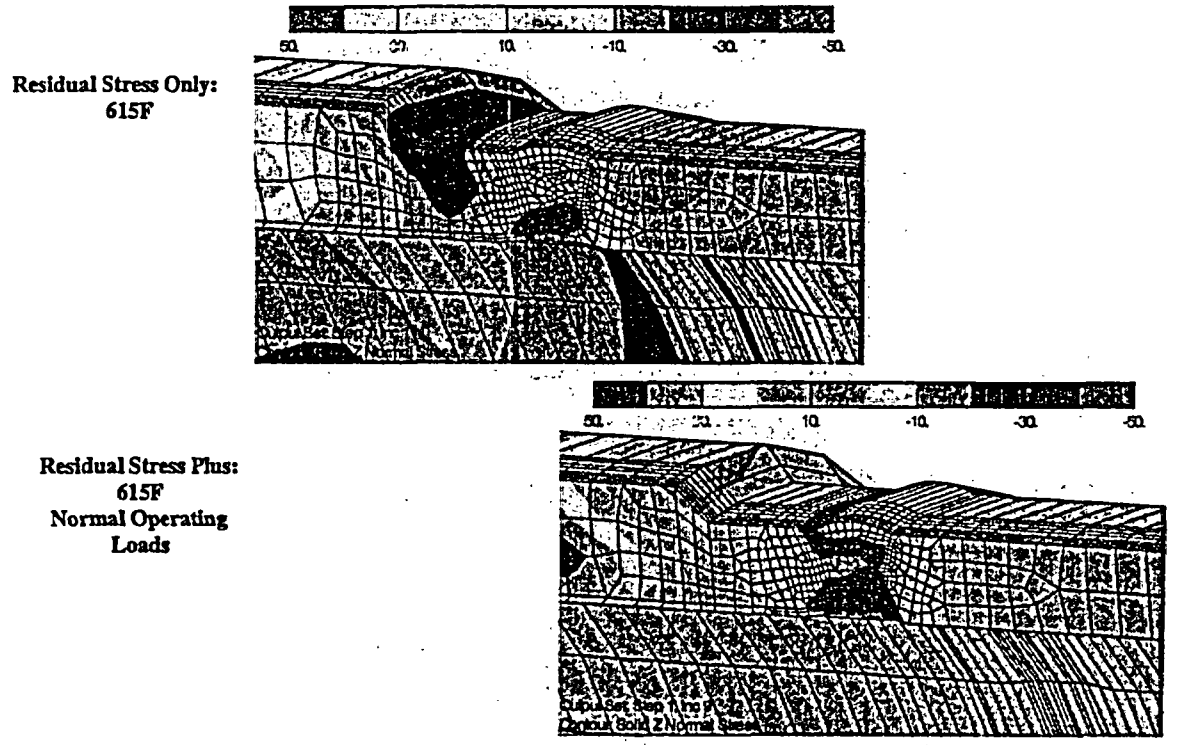

Figure G.50 Hoop stresses – used for FEAM analyses: outside weld first then inside weld

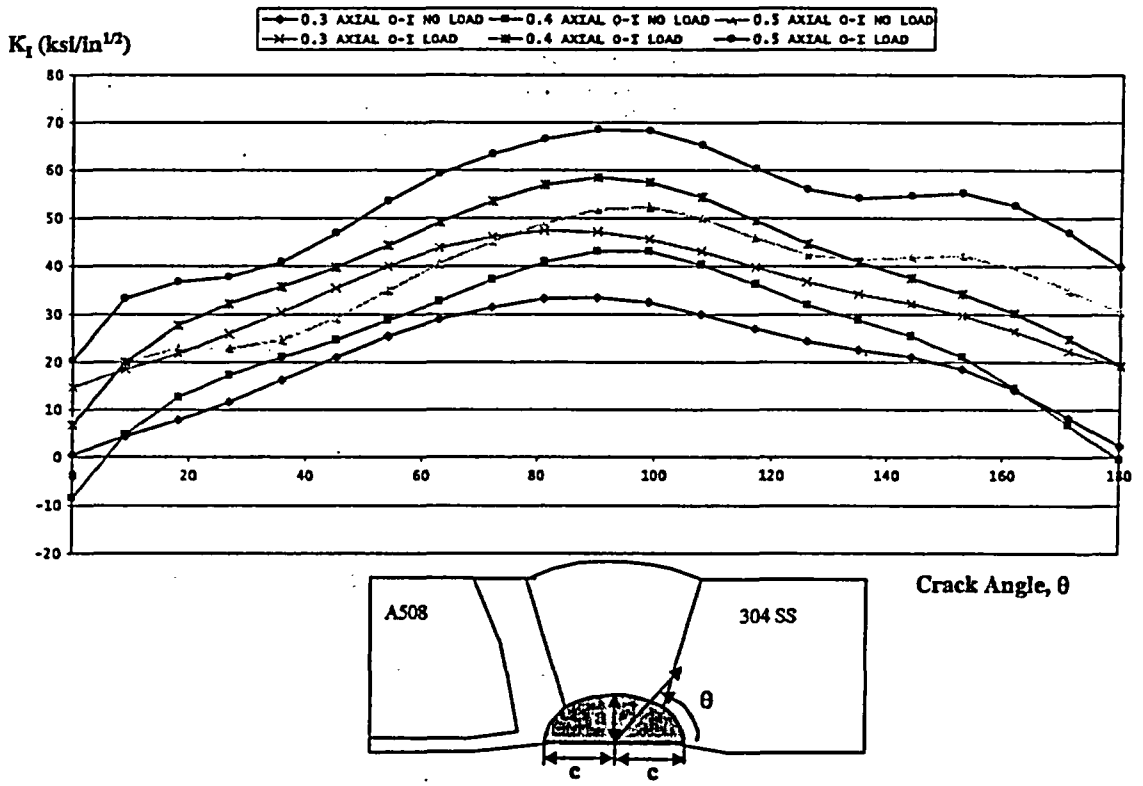

Figure G.51 Stress intensity factors; a = 0.3, 0.4, 0.5; c/a = 1.5. 'NO LOAD' = 'Residual Stress Only', 'LOAD' = 'Residual Stress Plus Normal Operating Load'

versa) depending on the welding process, it is important to model the welding process as well as the pipe geometry and multi-axial loading.

For these analyses, two weld processes were studied. In the first, the weld was assumed to start from the inner diameter and proceed to the outer surface. This is denoted Inside-Out or I-O. The second was the reverse process, denoted Outside-In or O-I, where the weld was completed from the outside and then the inside weld was deposited. All results presented in Figures G.52 through G.55 use this designation in the description above the illustration. Using the results of the finite element analysis we can impose a residual stress field on the calculated results. Both I-O and O-I were considered since it is not known how the actual hot leg in the V. C. Summer plant was repair welded (see the discussion related to Figure G.22).

Once the residual stress field has been calculated, the applied loading is modeled, the FRACALT code is used to determine the stress intensity factors, K, for a pre-defined set of crack sizes and orientations. These values of K are then normalized by $a^{1/2}$, where 'a' is the crack depth. A table of these normalized K values was then sent to the probabilistic mechanics code TRACLIFE and the surface crack changes during PWSCC growth calculated using the above equation. For the purpose of this analysis, it was assumed that the value of K along the crack drove the growth and shape. TRACLIFE was selected for the analysis because it has already built into the program the necessary 3D calculation tools. In addition, it is possible to examine the impact of uncertainty on these calculations at a later time.

The first case examined was the Inside-Out weld process. Because the residual stress field can lead to crack growth, **given that a crack exists**, two sets of calculations were performed. In the first, only the residual stresses were included. The second set of calculations added the applied loading. Note that the applied loading included the history of the entire weld process, and plasticity was included in the analysis.

It is critical to remember that the calculations were started with an assumed crack depth of 5 mm (0.20 inches). The question of initiation times and subsequent growth to the point at which the crack is 5 mm (0.20 inches) deep is completely ignored in these analyses. What was found was that there were relatively short growth times until the crack grows through the thickness. However, in addition to the two sources of uncertainty already mentioned, there are some serious reservations about the stress-corrosion cracking growth model. The discussion sections will overview alternative ways to estimate the PWSCC crack growth law and the corresponding constants based on observed field crack growth data. However, it is what was available, so it was used.

Figure G.52 (a-c) provides the results of these calculations. The axial cracks were introduced into the center of the weld. As discussed previously, there are numerous crack initiation sites provided by the grinding process of which any could begin to grow. In reality, the grinding scratch near the region of highest residual stress is expected to be the preferred dominant crack initiation site. Identification of the different plots is made as follows. In the legend above the plots, the curves are labeled as '3.0 Residual I-O' for instance (Figure G.52 (a)). This represents the crack shape after 3.0 months of PWSCC with residual stresses only and welding from the inside first followed by completing the outside welds. The label '3.0 Load I-O' indicates the 3 month PWSCC crack shape for the case where the operating loads are applied overtop the residual stress field (nonlinear analysis) for the I-O weld case.

The first thing of note is that the growth of the crack in the residual stress field without any applied loading is lower than when the load is applied. The plot shows the normalized (by the pipe thickness) crack depth. At the end of two years, with only the residual stresses, the crack is about 20 percent through the thickness. When the operating load is applied, the crack is 95 percent through the thickness after one year. At about 14 months the crack becomes a through wall crack (TWC).

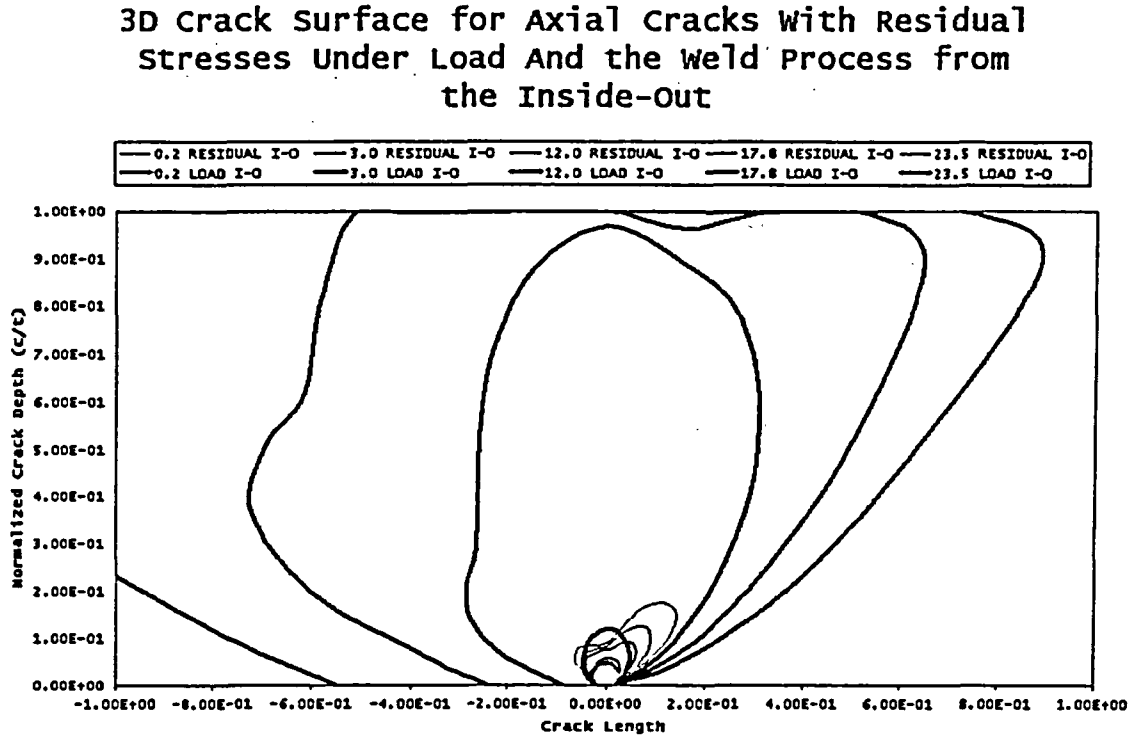

Figure G.52(a) Axial crack growth for the inside-out weld process

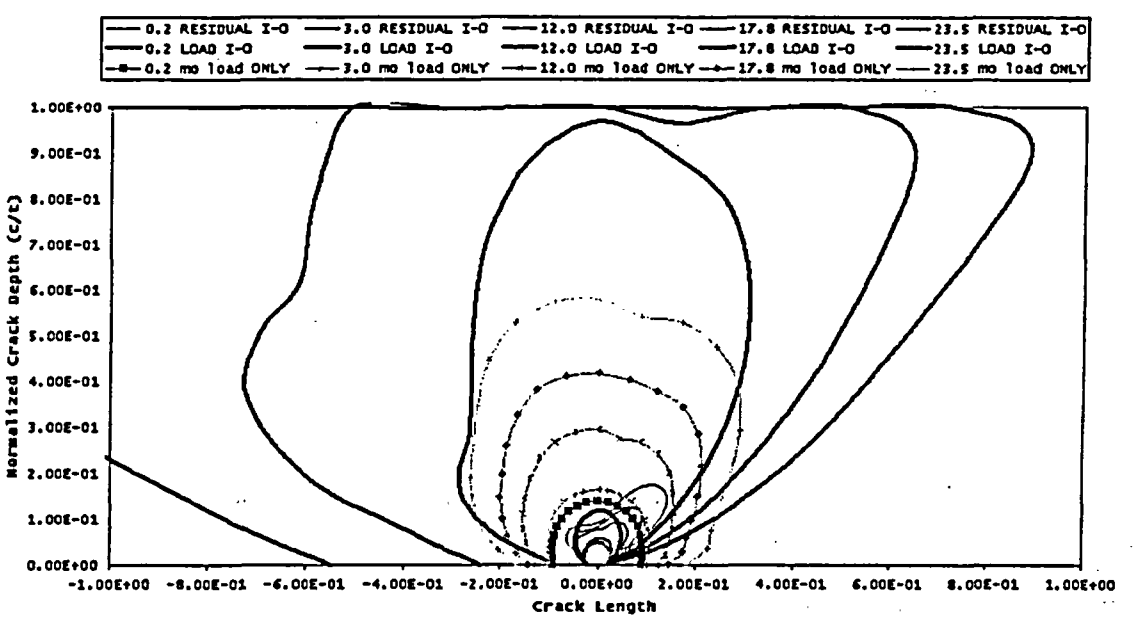

Figure G.52b Approximation for the impact of the residual stress field on the crack size and shape

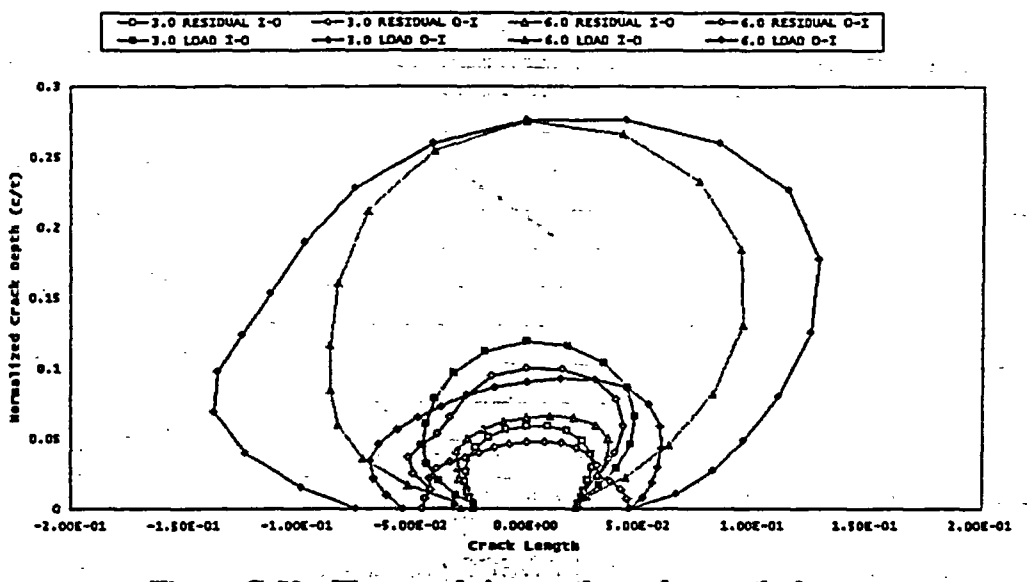

Figure G.52c Three and six month crack growth shapes

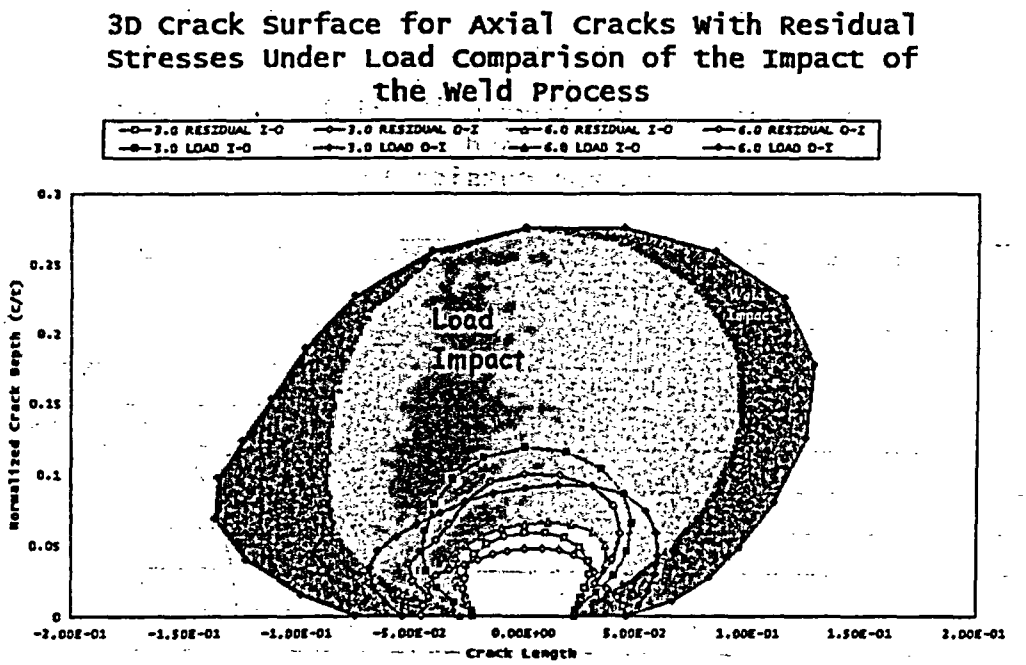

Figure G.53 Approximation for the impact of the residual stress field on the crack size and shape. The 'red' shape represents the crack shape for the case of loading and residual stresses (for the I-O case) and the 'white' shape is the crack shape for the residual stress only case after 6 months of PWSCC growth. The 'red' curve (I-O case) can be compared to the 'gray' (O-I case) curve for a comparison of the weld sequence effect

3D Crack Surface for Circumferential Cracks With Residual Stresses Under Load And the Weld Process from the Inside-Out

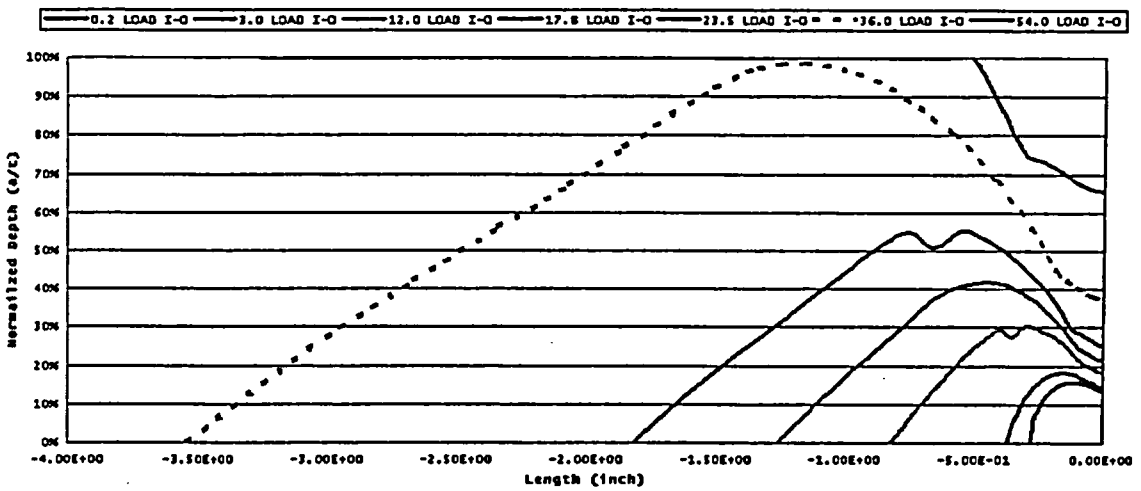

Figure G.54(a) Circumferential PWSCC growth – inside weld first case

3D Crack Surface for Circumferential Cracks With Residual Stresses Under Load And the Weld Process from the Outside-In

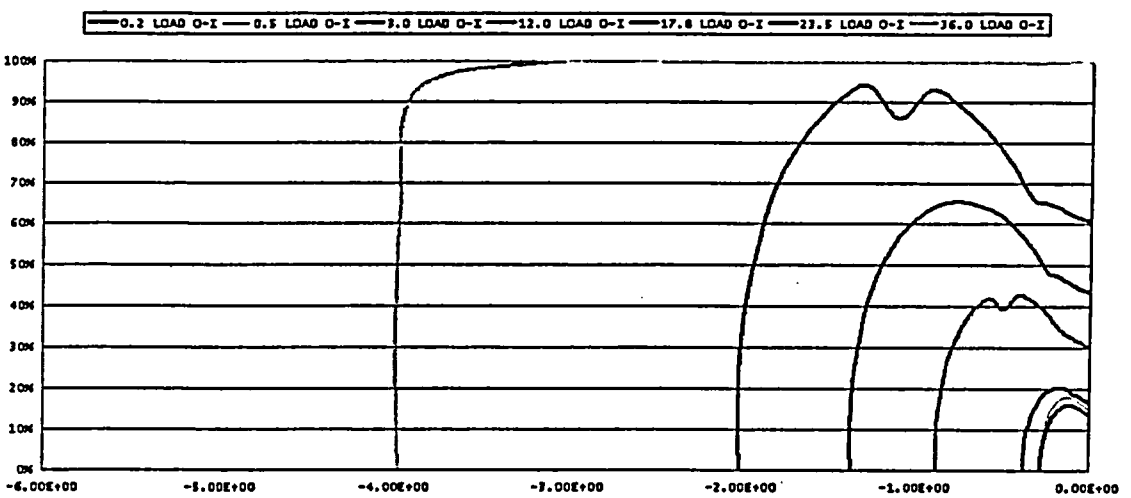

Figure G.54b Circumferential PWSCC growth – outside weld first case

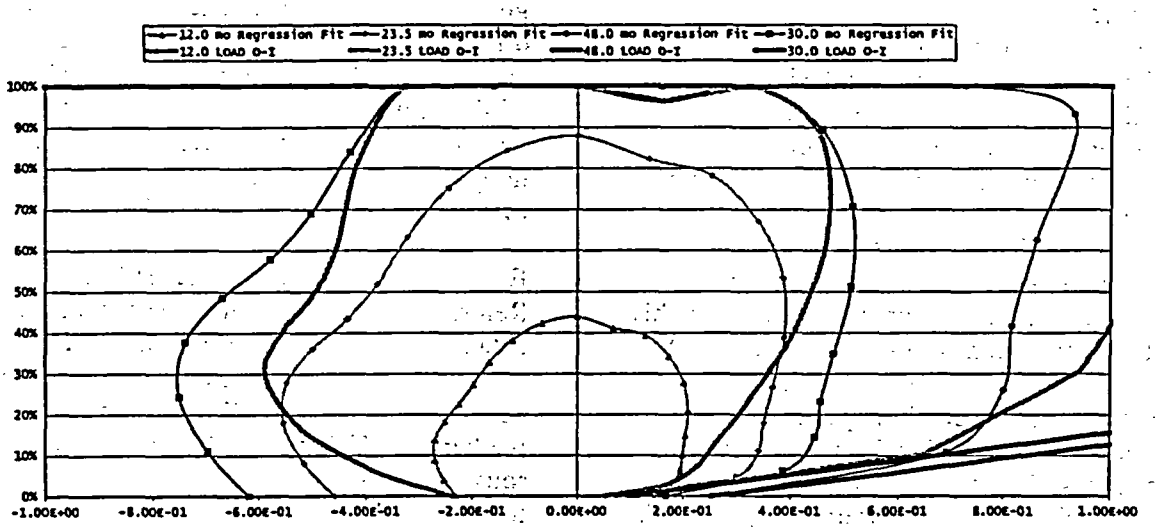

Figure G.55(a) The impact of using a conservative PWSCC law on crack growth – axial crack

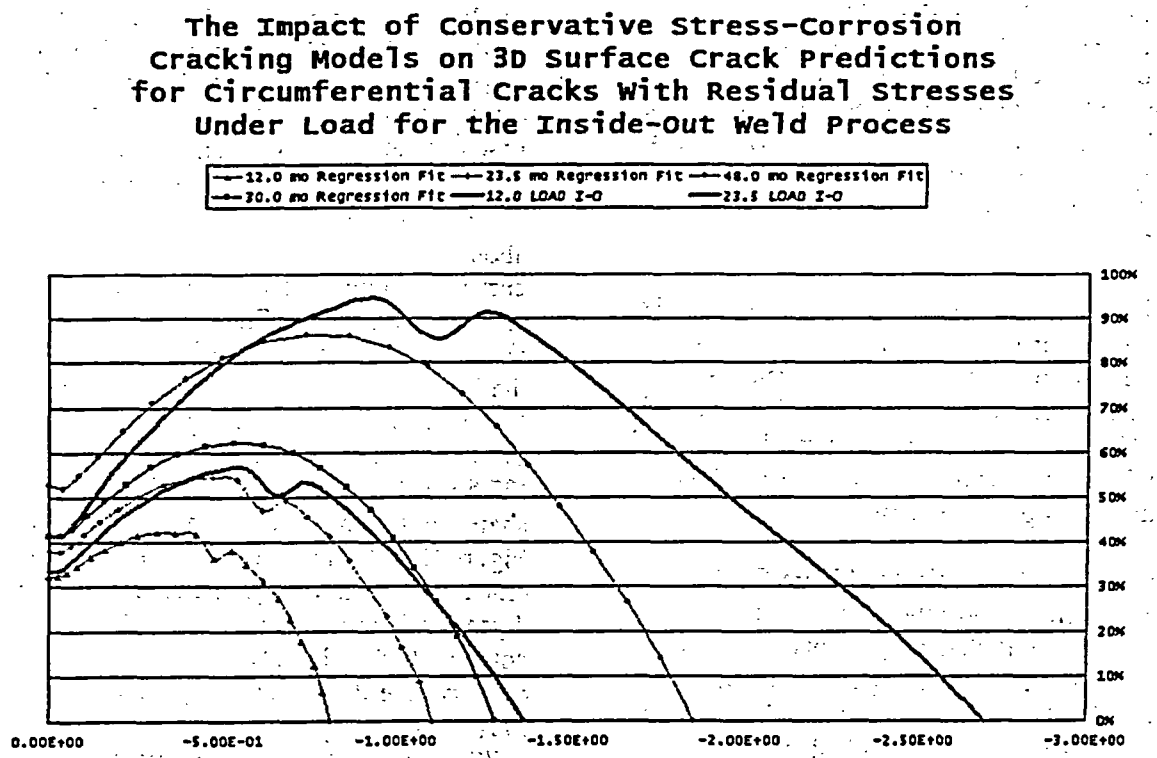

Figure G.55b The impact of using a conservative PWSCC law on crack growth – circumferential crack

The small growth due solely to the residual stresses may seem like these residual stresses have little impact on PWSCC. However, if we perform an approximate analysis and assume that superposition applies in determining the stress intensity factors to use in the PWSCC equation, then we can estimate the impact of the residual stress field. For this we subtracted the stress intensity factors for the residual stress fields only from the residual stress fields with the operating loads applied. (Recall that the loads were applied on top of the residual stress fields and all history, including plastic strains were accounted for.) Figure G.52 (b) shows this calculation for a number of different times. As an example, after 12 months, the 'dark blue' curve represents the crack shape for the I-O weld for the case of residual stress and applied service loads. It is seen that the crack is approximately 95 percent through the pipe wall. The pink curve labeled '12 mo load only' represents the crack shape for a load only case after 12 months of PWSCC, i.e., no residual stresses are included. This crack is about 32 percent through the pipe wall. The small light blue curve represents the crack shape for residual stress only after 12 months. This crack is only about 12 percent through the pipe wall. Hence, because the crack growth law is a nonlinear function of stress intensity factor, and additional plasticity occurs as the service loads are applied over top the weld residual stresses, the effect of the residual stresses on PWSCC is significant.

Finally, Figure G.52 (c) shows the three and six month crack growth shapes for both the inside first weld followed by the outside weld (I-O) and the outside weld first, then inside weld (O-I) case. One can also compare the crack shape and depth for the residual stress only case and the residual stress plus load cases.

In Figure G.53 is identical to Figure G.52 (c) except shading is introduced to point out these effects. The 'red' shape represents the crack shape for the case of loading and residual stresses (for the I-O case) and the 'white' shape is the crack shape for the residual stress only case after 6 months of PWSCC growth. The 'red' curve (I-O case) can be compared to the 'gray' (O-I case) curve for a comparison of the weld sequence effect.

Figure G.54 shows the circumferential crack growth shape after three and six months for the different cases. The O-I case tends to grow cracks wider than the corresponding I-O case while for the I-O case, the cracks grow somewhat deeper. This is expected by comparing the hoop residual stresses between the two analysis cases (Figures G.43, G.44, G.48 and G.50).

Equation (G.1), which was taken from Reference G.13, was a fit to the available test data (Figure 4-2 in Reference G.13). The fit of the data was conservative and tends to represent an upper bound to the PWSCC crack growth predictions. If that same data is taken and a least squares regression fit to the data provided, the following is obtained:

$$\frac{da}{dt} = 2.16\times10^{-11}(K_I - 9)^{0.8}(m/\text{sec}) \qquad \text{(G.2)}$$

Comparing Equations G.1 and G.2, one notices that the constant is larger and the exponent is smaller in Equation G.2. A comparison of the predicted PWSCC crack growth using the less conservative regression fit (Equation G.2) to the original law is shown in Figure G.55.
Figure G.55 (a) illustrates that an axial crack will break through the pipe wall sometime after 2 years using the regression fit compared to about 1 year using the conservative PWSCC rate curve. In Figure G.55 (a) and G.55 (b), the label '12.0 mo Regression Fit' represents the crack shape after 12 months of PWSCC growth using the Equation G.2 regression fit while '12.0 Load O-I' is the crack shape using Equation G.1. Similar notation is used for other times, i.e., '23.5 Load O-I' represents the PWSCC crack shape after 23.5 months using Equation G.1, etc. Figure G.55 (b) indicates that the circumferential crack will break through the pipe wall after 4 years using the regression PWSCC rate curve compared with about two years using the conservative PWSCC rate equation. This illustrates the importance of using a correct PWSCC law and the need for more PWSCC data. Moreover, from Figure 4-2 in

Reference G.13, it is clear that significant scatter exists in the PWSCC test data. Because of this scatter, a risk based probabilistic assessment of PWSCC is in order.

G.7.2 The 3 Dimensional Growth of Circumferential Cracks Through the Hot Leg/RPV Nozzle Bimetal Weld

Axial crack growth in the hot leg/RPV nozzle bimetal weld is mainly driven by the hoop stresses, although stress redistribution during PWSCC crack growth through the pipe wall thickness is influenced slightly by other stress components. Figures G.48 and G.50 show the contour plots of hoop stresses (i) after welding and heating to 324°C (615°F) and (ii) service loads applied to the (i) case.

Circumferential crack growth is mainly driven by the axial stresses. Referring to Figure G.38, note that the tensile axial stresses at room temperature are nearly all reversed to compression in the weld region as the pipe system is heated to 324°C (615°F). The end conditions of the hot leg (reactor vessel and stream generator) are assumed fixed for the thermal analysis. As such, when the hot leg is heated up, it is constrained from expansion at the ends. The residual stresses reduce to compression as seen in Figure G.38. In contrast, the axial expansion of the hot leg has minimal effect on hoop stresses.

Referring to Figures G.38, G.47 and G.49, compressive axial stresses exist in the pipe near the weld region for the case of no load except in a small region on the inside surface near the buttering region. Hence, circumferential crack growth *due solely to residual stresses (at 324°C (615°F) operating temperature)* is not expected except for possible small growth at the inside surface near the butter region. The bottom illustrations in Figures G.47 and G.49 represent axial stresses with the loads (pressure, tension, and bending – see Figure G.46) applied. The loads were applied to the initial conditions of residual stress state at 324°C (615°F). Very little additional plasticity occurred during application of the loads because the axial residual stress state is compressive before application of the load. For the hoop load case, because the initial hoop residual stresses are high before application of the load, plasticity during application of the pressure does occur. From Figures G.47 and G.49, it is clear that the applied loads would be the main contributor to circumferential crack growth in contrast to axial crack growth where the hoop residual stresses dominate crack growth.

The circumferential crack growth profiles for the I-O and O-I cases are shown in Figures G.54a and G.54b. The initial flaw size for this case is 5 mm (0.2 inch) also. Because the 3D model has a symmetry plane at the center of the elliptic cracks, only the crack shape from 0 to 90-degrees is shown. It is seen that crack growth favors a location at an angle away from the deepest point of the crack. This is somewhat typical for circumferential cracks in homogeneous materials (Ref. G.14). It takes approximately 3 years for the crack to break through the pipe wall. The axial cracks grow about twice as fast.

The crack growth law shown in the above equation was obtained from (Ref. G.13) and was necessarily conservative. If a regression fit is made of the PWSCC test data for Alloy 182 at 324°C (615°F) (Figure 4-2 of Reference G.13), different growth response is obtained. Figure G.55a and G.55b compare axial and circumferential crack growth for different PWSCC growth laws. It is clearly seen that crack growth predictions depend strongly on the accuracy of the SCC data fit. The SCC predictions would be best interpreted using a probabilistic approach using TRACLIFE.

G.8 THREE DIMENSIONAL WELD EFFECTS

As discussed in References G.1, G.11, and G.13, the bimetallic hot leg weld that experienced field cracking had a number of repairs done to it. Because repair welds are inherently three dimensional in nature, some limited analyses were performed in order to obtain a qualitative assessment of three-dimensional effects on the bimetallic weld and weld repair process.

Figure G.56 illustrates the model that was considered. The butter layer, PWHT, and hydro-test were not considered, and the boundary conditions at the vessel and steam generator were not considered (i.e., the length of pipe shown in Figure G.56 was modeled). All of the weld passes shown in Figure G.20 were not considered. Rather, passes were lumped together to form 7 passes as shown in Figure G.56. All of the conditions in Figure G.23 could well have been considered, but were neglected due to time constraints. In the future, it may be useful to perform complete 3D analyses of this pipe.

Figure G.57 illustrates the repair cases considered: two different lengths and two different depths. All four analyses considered the baseline weld first followed by grinding and deposition of the repair weld passes. The definitions of the original weld and repair weld geometry convention are shown in Figure G.58. The X = 0 location represented the start/stop positions of the baseline weld. The repair welds modeled ranged from A to B (Length L_2) and A to C (Length L_1) with the angular definitions shown in Figure G.58. Figure G.59 shows the analysis on the long (L_1) and deep (d_2) weld repair in progress.

Axial residual stresses for the baseline three-dimensional weld are shown in Figure G.60. The section is at the center of the weld and includes the A508 nozzle. Notice that the axial stresses near the start location are different from a location far away from the start location where near steady state conditions exist. In essence, the axial stresses reverse sign compared with locations away from the start/stop location. This can actually help in slowing down circumferential SCC growth as the crack grows into this location. Figure G.61 shows a similar axial stress plot for the baseline weld for a longitudinal cut section. Figure G.62 shows a similar plot of the Z-component stresses (see coordinate axis in Figure G.62). It is also seen that compressive stresses develop near the start/stop location that can slow down longitudinal crack growth. However, this reduction in residual stress state must be balanced by the fact that start/stop locations are often regions where weld defects can occur. Note that the Z-component stresses represent hoop stresses on the cut planes.

Figure G.63 compares weld residual stresses between the axis-symmetric and three-dimensional analyses at room temperature. Of course, the three-dimensional solution did not include the butter step, the PWHT after buttering, and the passes were deposited in only seven passes. Despite these differences, the comparison of hoop stresses at a location far from the start/stop location is not entirely dissimilar. In general, the three dimensional solution predicts more compression in the weld at the inside surface compared with the axis-symmetric solution.

Figure G.64 shows weld residual stresses after repair weld case 1 is complete. This is the case of the long, shallow weld repair (see definitions in Figure G.58). Axial residual stresses reverse sign near the start and stop locations of the repair while stresses within the middle of the repair do not change much from the baseline steady state locations. Figure G.65 shows a similar plot of axial stresses for a segment that consists of an angular cut of the weld repair. The effect of the repair on residual stresses is evident. Figures G.66 and G.67 show similar results for the repair case for the short, shallow weld repair. Figure G.67 is a plot of mean stress, which is a measure of constraint caused by welding and repair. It is seen that the weld repair does induce significant constraint near the beginning and end points of the repair. Constraint can influence fracture response, and possibly SCC rates, but were not considered here since little work has been performed to date that investigates the effect of constraint on SCC rates.

Figures G.68 and G.69 show axial and mean stress for the short, deep weld repair. Comparing Figures G.66 and G.67 to Figures G.68 and G.69 shows that the compressive stress that develops near the beginning and end of the weld repairs is deeper for the deeper repair. This actually suggests that weld repairs may help slow down SCC growth and act as crack stoppers. Figure G.70 provides a plot of

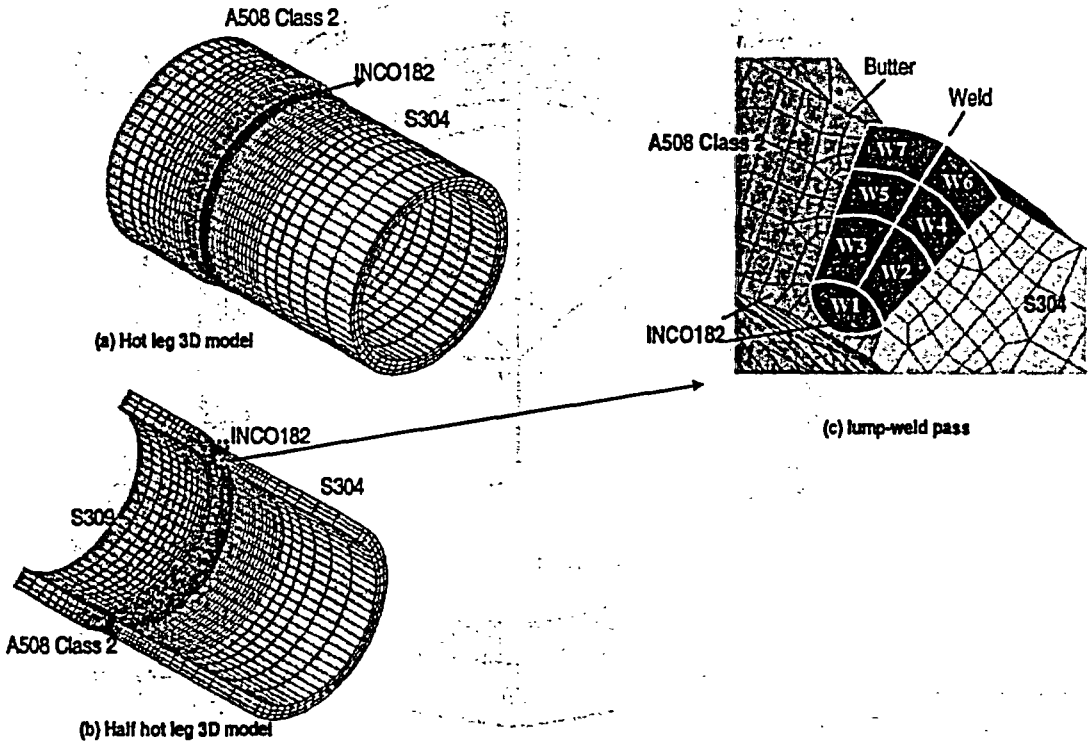

Figure G.56 Hot leg 3D analysis geometry

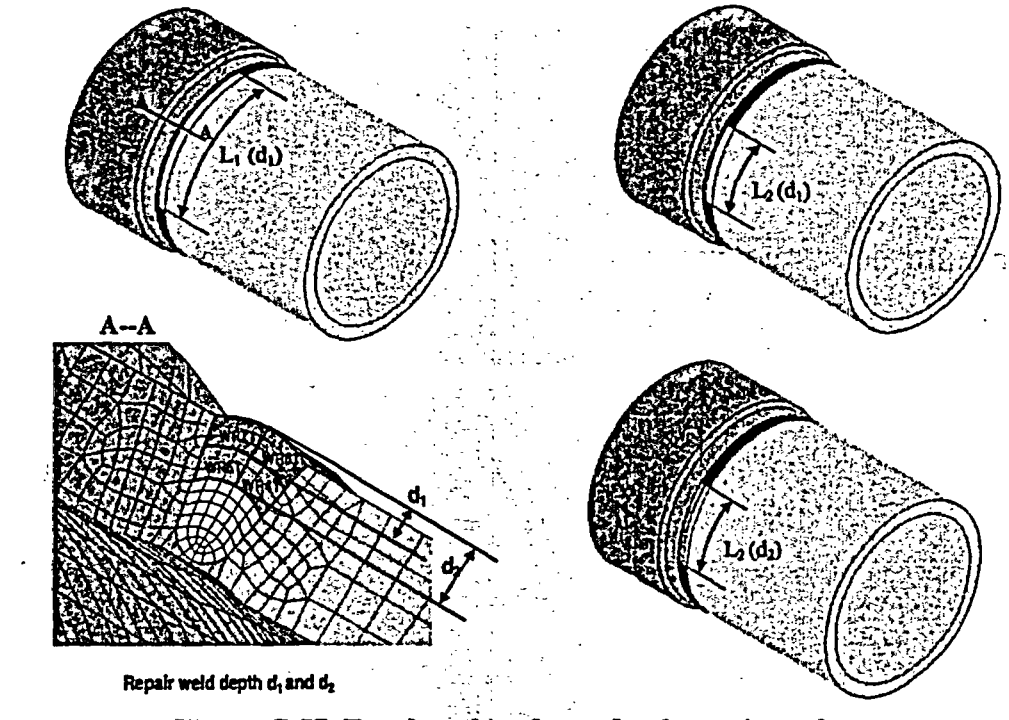

Figure G.57 Two-length and two-depth repair analyses

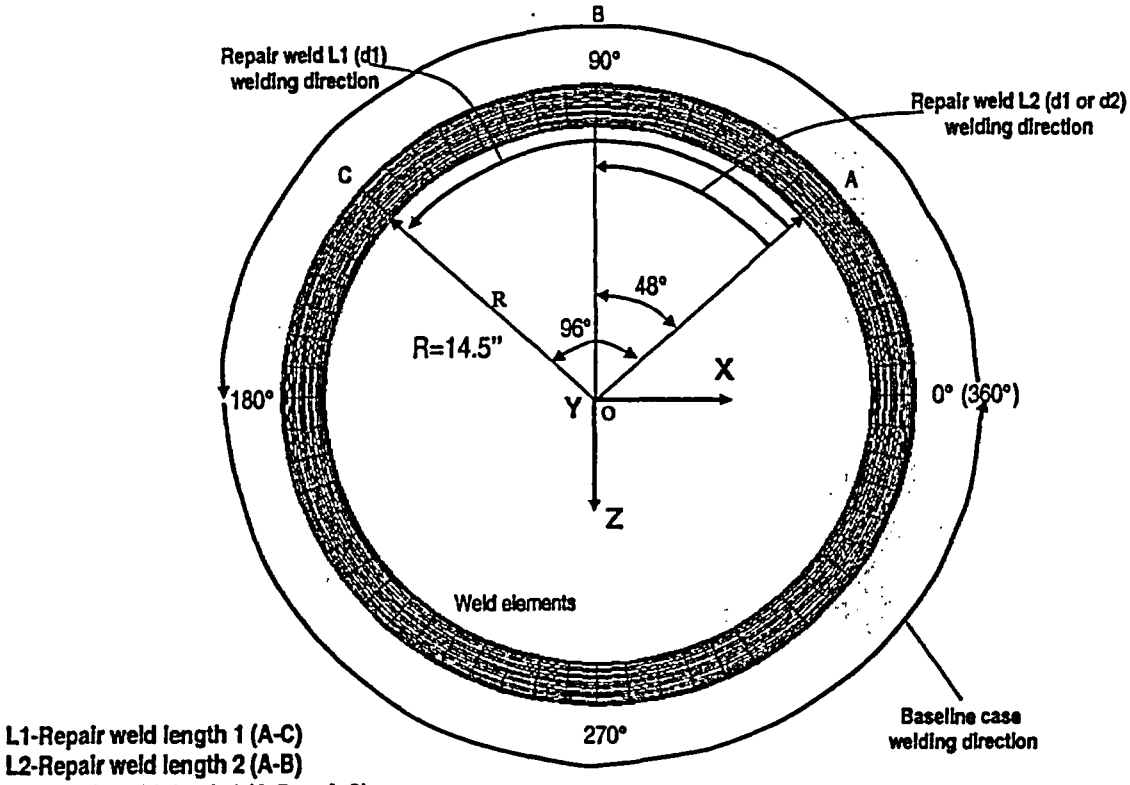

Figure G.58 Weld directions

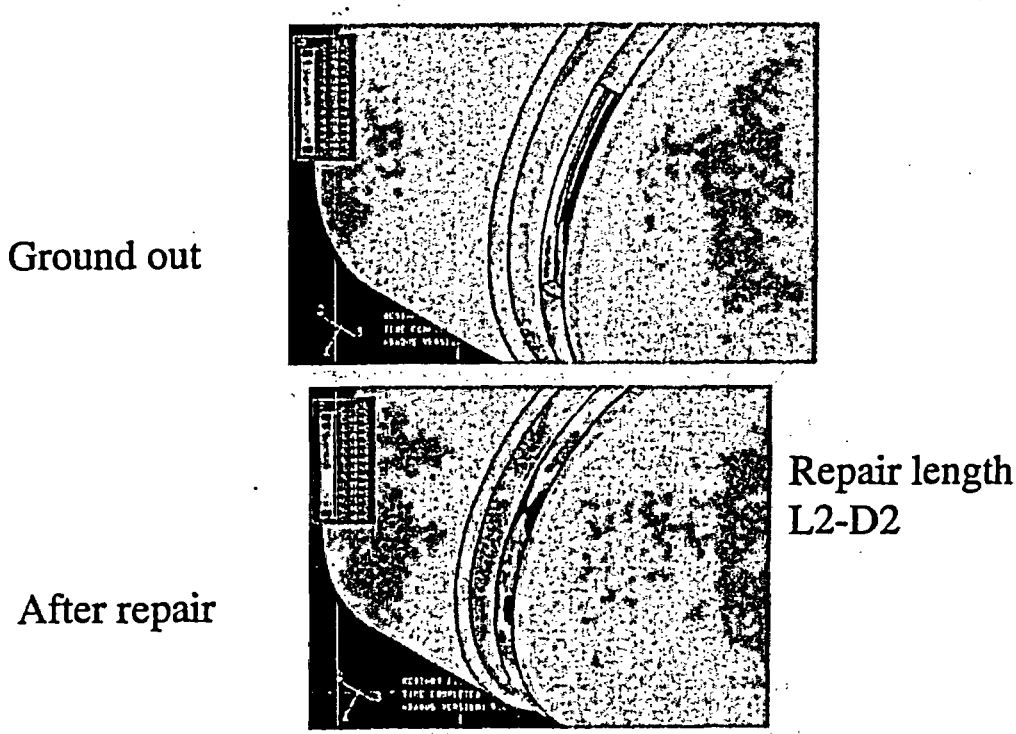

Figure G.59 An example of the grinding and weld repair model during analysis

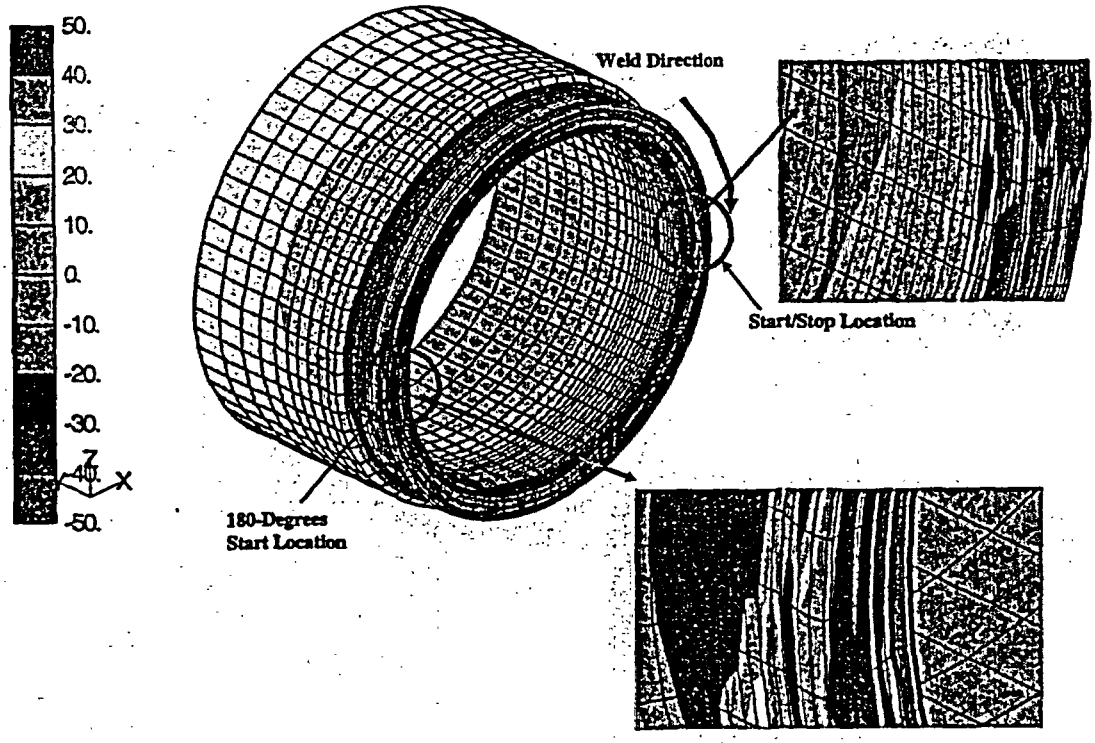

Figure G.60 Baseline weld – axial stresses

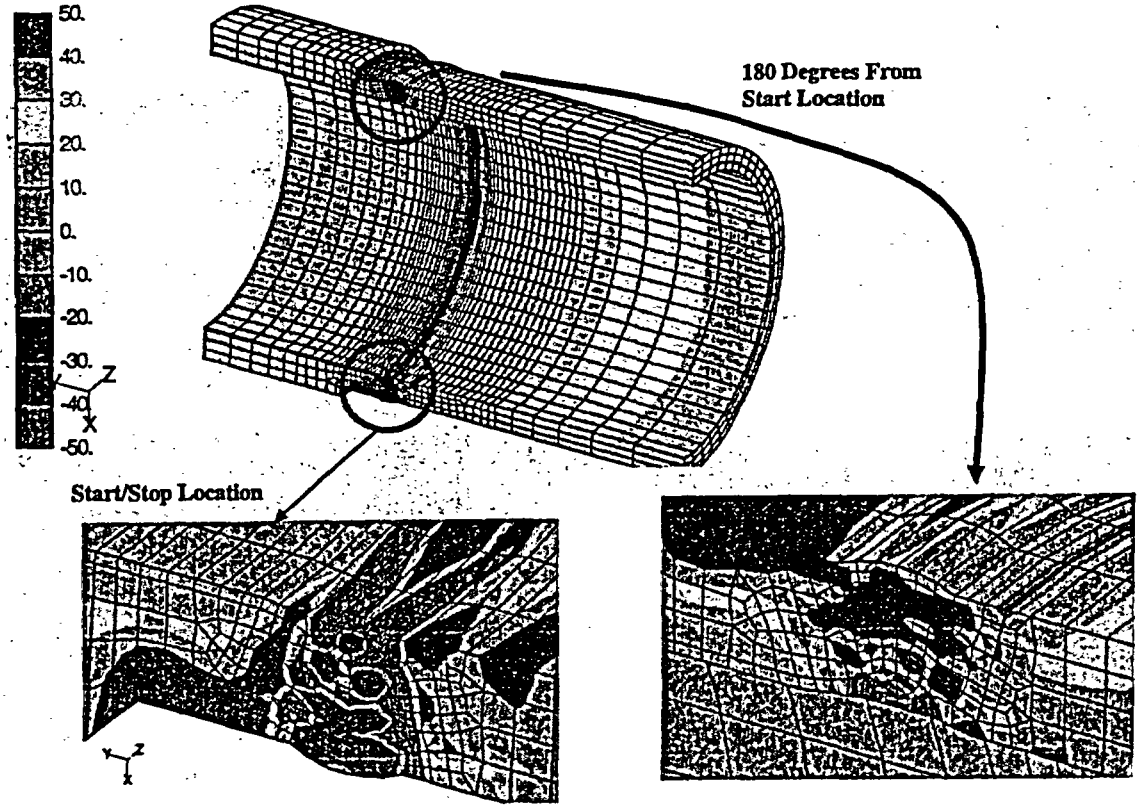

Figure G.61 Baseline weld – axial stresses

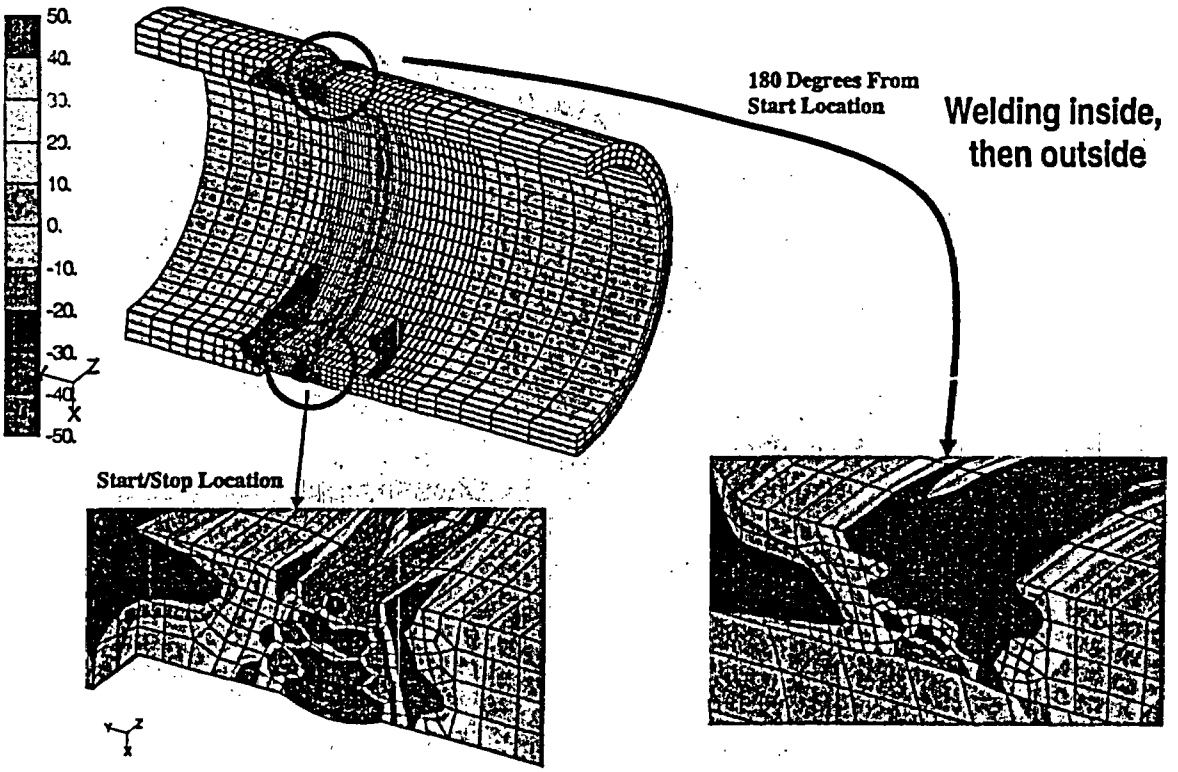

Figure G.62 Baseline weld – Z-component stresses (these represent hoop stresses on the cut planes)

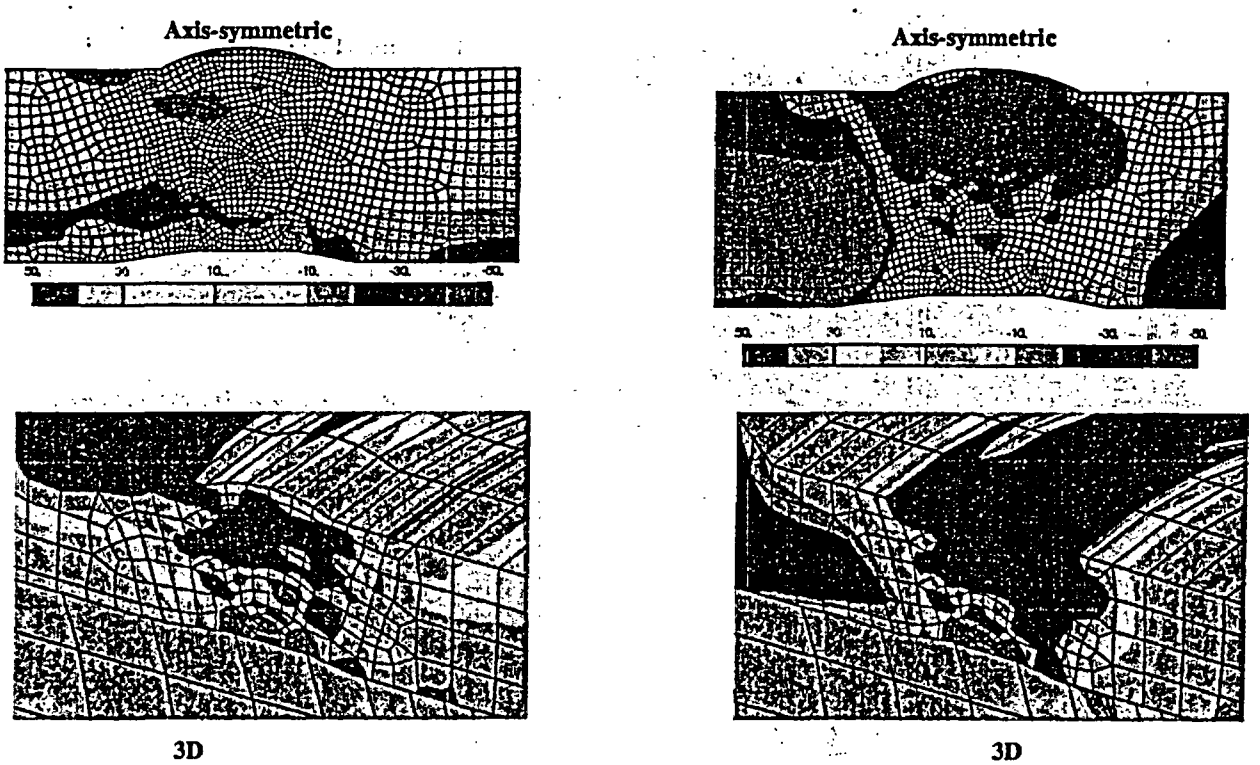

Figure G.63 Comparison of axial and hoop stresses between the axis-symmetric and 3D solutions

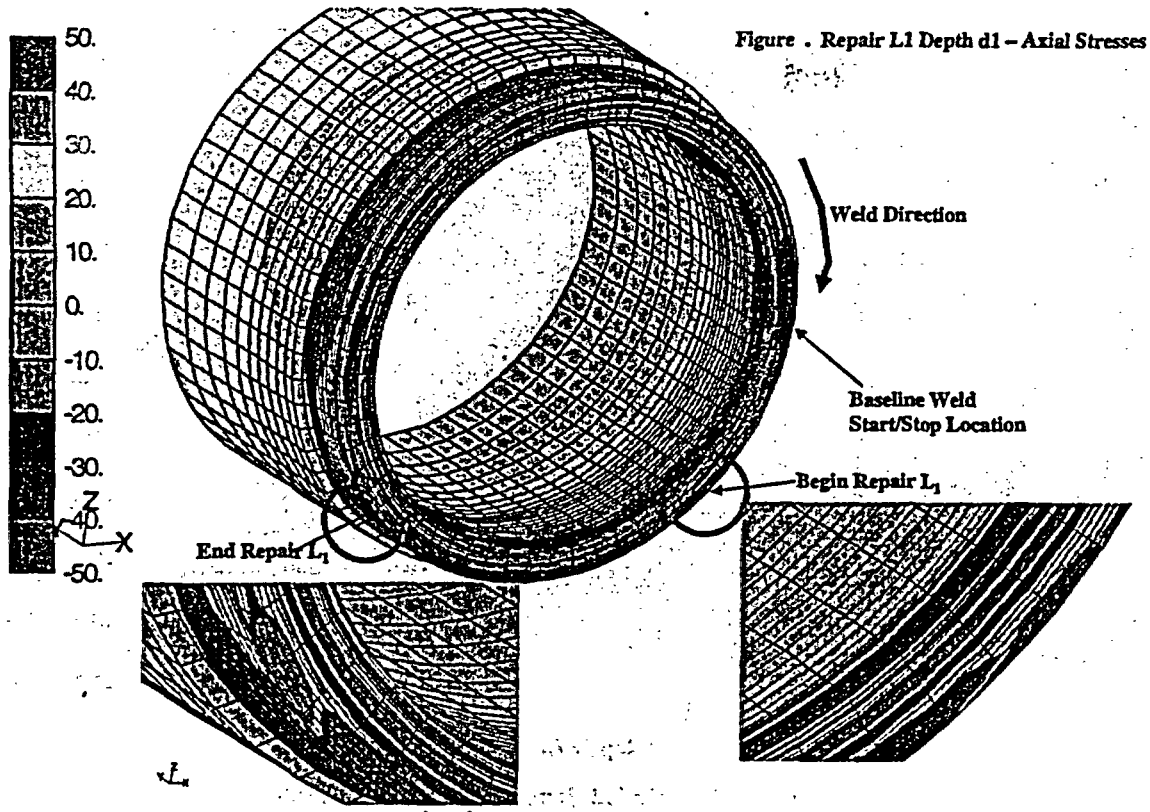

Figure G.64 Comparison of axial stresses for repair case number 1

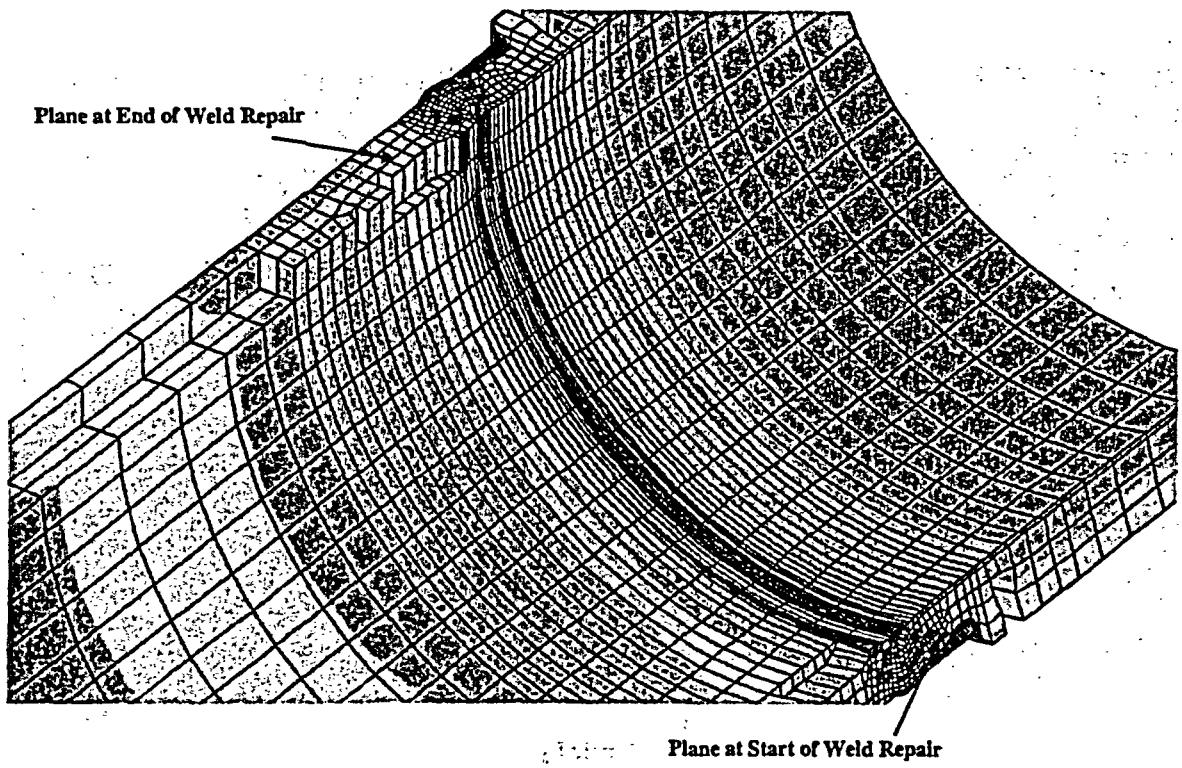

Figure G.65 Comparison of axial stresses for repair case number 1

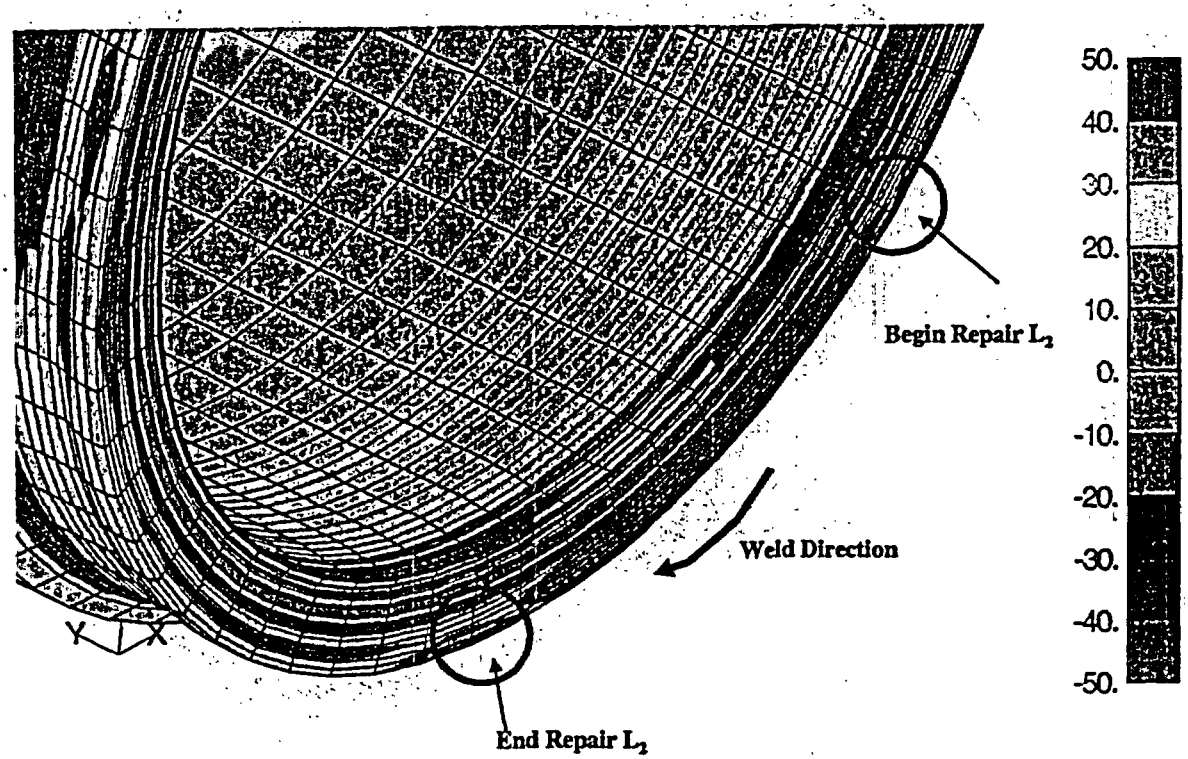

Figure G.66 Repair L2 depth d1 – axial stresses

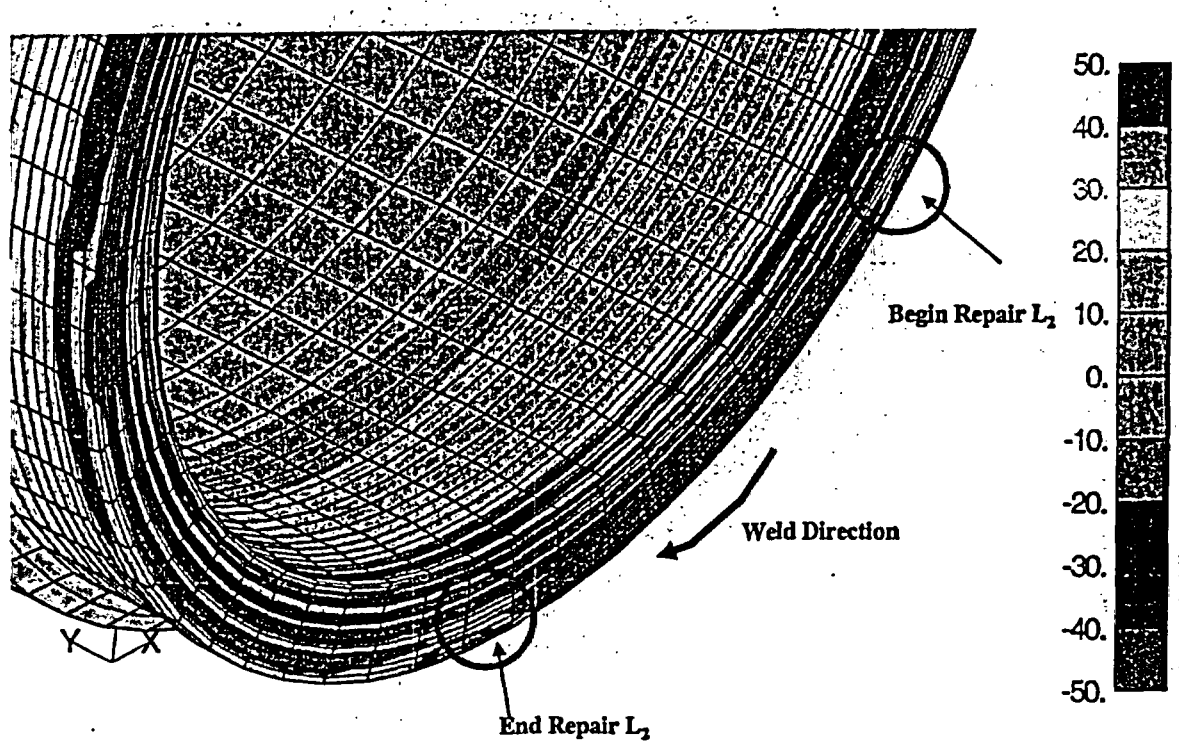

Figure G.67 Repair L2 depth d1 – mean stress ($\sigma_{kk}/3$)

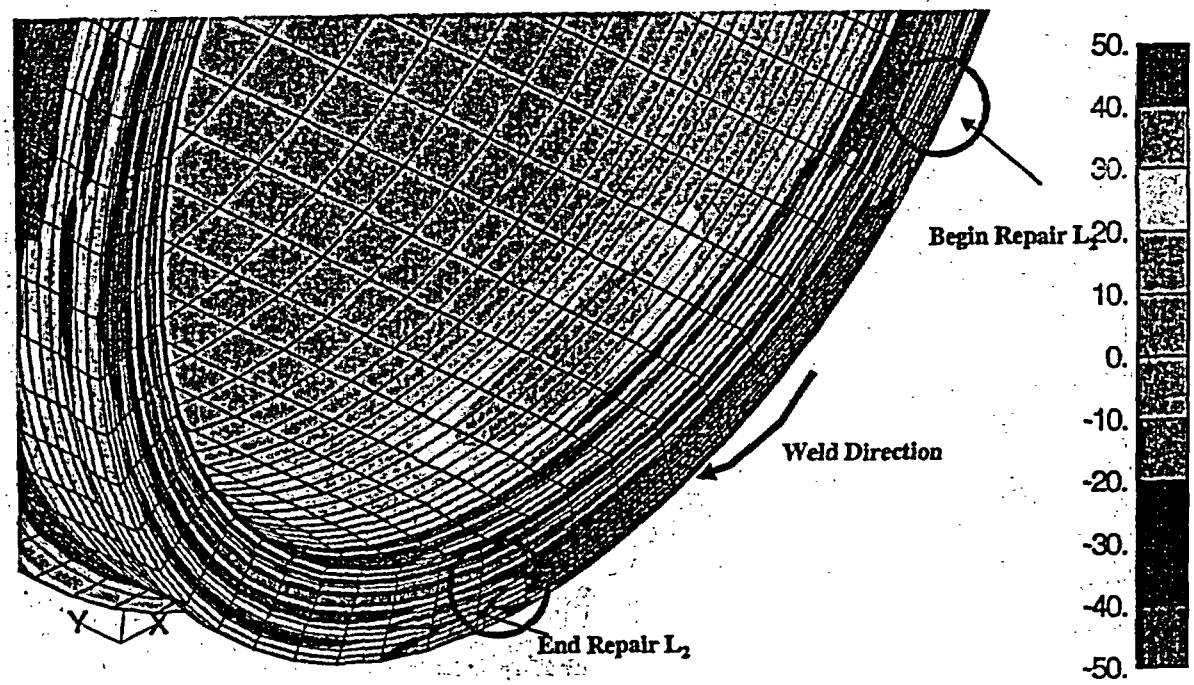

Figure G.68 Repair L2 depth d1 – axial stresses

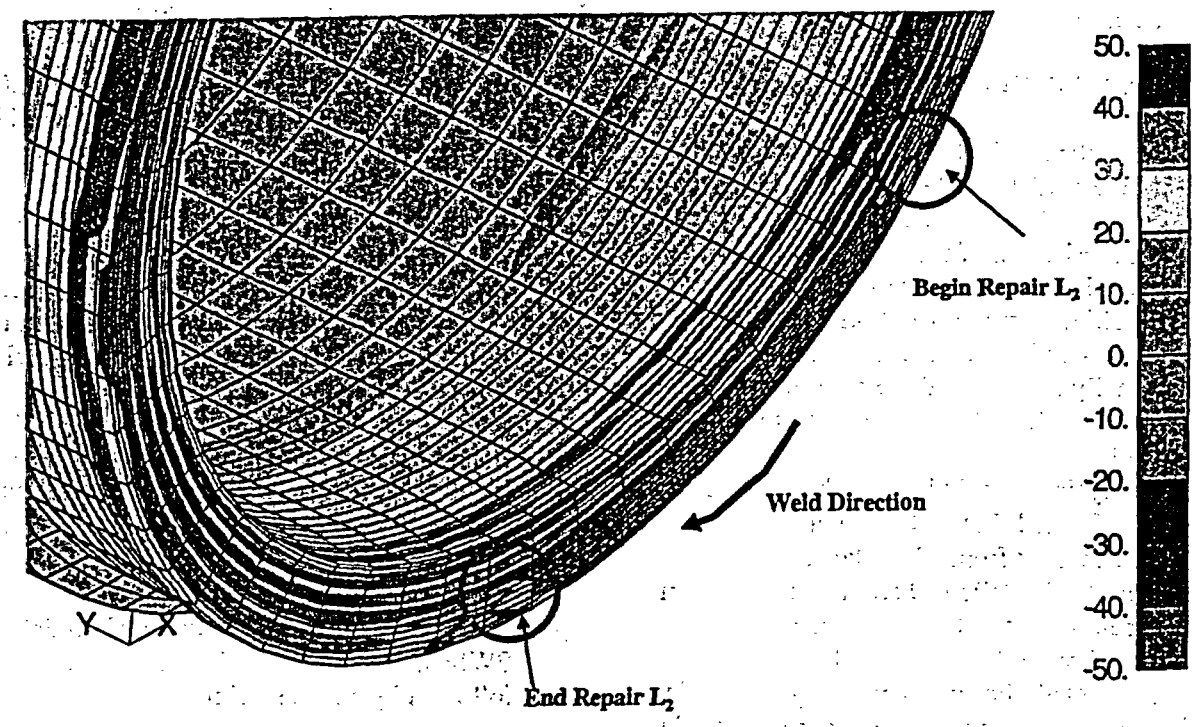

Figure G.69 Repair L2 depth D2 – mean stress ($\sigma_{kk}/3$)

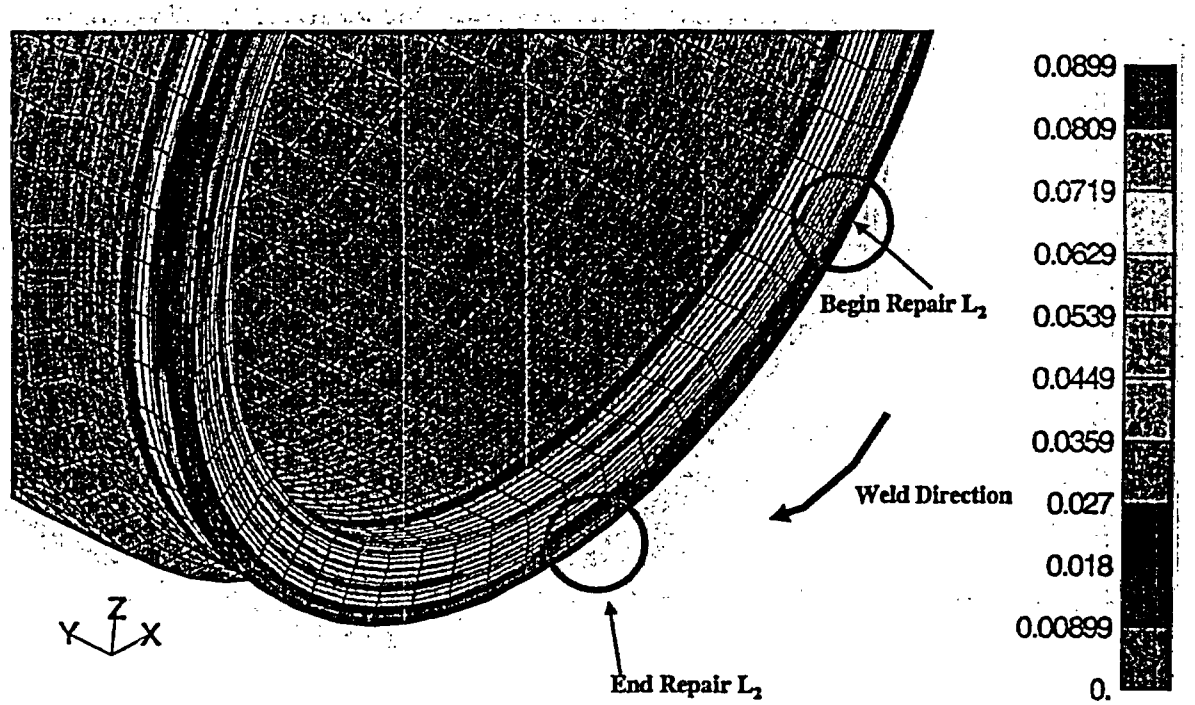

Figure G.70 Repair L2 depth d2 – equivalent plastic strain

equivalent plastic strain for the short, deep repair. It is clear that plastic strains increase along the entire length of the repair.

G.9 DISCUSSION AND CONCLUSIONS

Analyses of the residual stresses and PWSCC for the hot leg/RPV nozzle bimetal weld of the V. C. Summer plant were performed. The entire history of fabrication of the weld was included in the analysis, including Inconel buttering, PWHT, weld deposition, weld grind-out and repair, hydro-testing, service temperature heat-up, and finally service loads. Some of the conclusions are described in the bullets below.

- An analysis of a cold leg pipe bimetal weld was performed first and residual stresses were measured from a bimetallic weld section that Battelle had secured earlier from a canceled plant. The measurements appeared rather low compared with what was expected. For instance, hoop stresses in the weld were compressive at both the inside and outside surfaces of the pipe. This does not appear reasonable based on experience. As such, additional measurements of bimetallic pipe welds should be made using a different measurement technique.

- To obtain a reasonable description of fabrication induced residual stresses, all of the fabrication steps should be considered in the analyses.

- The as fabricated axial weld residual stresses alternate sign as one proceeds from the inside to the outside surface of the pipe near the weld region. Tension to compression to tension back to compression axial residual stresses develop in the as fabricated pipe weld. The tensile stresses were highest at the inside surface for the case of the outside weld repair deposited first and finishing with the inside weld compared with the opposite case.

- For reducing the effect of circumferential PWSCC after weld repairs, inside welding followed by outside welding is preferred.

- Final hoop residual stresses after complete fabrication are mostly tensile in the weld region. For the case of outside welding

followed by inside welding after the bridge repair, high tensile residual stresses are produced everywhere. For the inside weld followed by outside weld case, a small zone of compressive hoop residual stresses develop at the pipe ID in the weld.

- Hydro testing does not alter fabrication residual stresses very much.

- Heating the hot leg pipe system up to operating temperature of 324°C (615°F) reduces axial fabrication stresses to mainly compressive values due to the rigid constraint provided by the vessel and steam generator. Hoop residual stresses are unaffected by heating up to operating temperatures.

- Since as fabricated axial residual stresses are low at operating temperature, circumferential stress corrosion cracking is not expected due solely to fabrication stresses. Service loads dominate circumferential SCC.

- Axial crack growth is dominated by fabrication residual stresses.

- Weld repairs can alter residual stresses in pipe fabrications. In general, stress reversal in sign occurs near the start/stop locations of the repair. This can possibly result in a SCC crack stopper or slow down the crack growth. A similar reversal in the sign of the stress occurs in a baseline weld near the torch start/stop locations.

- Based on the PWSCC crack growth law from Reference G.13 and the analysis results here, axial cracking should be confined to the weld region. Starting from a crack 5 mm (0.2 inches) in depth, the crack should break through the pipe wall within two years. The crack nucleation time is something that should be studied in more detail.

- Circumferential cracks should take about twice as long to become a through wall crack compared with axial cracks. Circumferential cracks will tend to grow longer than axial cracks. However, since service loads dominate circumferential cracks, they will slow their circumferential growth as they grow toward the bottom of the pipe. Here, by bottom of the pipe, it is understood to be the compressive bending stress region of the pipe. The service loads consist of thermal expansion mismatch, tension caused by 'end cap' pressure, and bending. The bending stresses caused by a bending moment are compressive 180 degrees from tension zone. Part through circumferential cracks that initiate in the tension zone and grow beyond the bending neutral axis may slow down as they approach the compressive bending stress zone. However, for non-fixed bending axes, where the tension zone changes, this may not be significant.

- PWSCC growth would be best considered using a risk based probabilistic approach using TRACLIFE.

- Weld repairs alter pipe residual stress fields near the start/stop regions of the repairs. This may help slow down a growing stress corrosion crack.

- Grinding of welds may lead to scratches, which in turn may lead to crack initiation sites. Grinding of welds should be performed carefully. It is of use to study the effect of grinding on both residual stresses (caused by grinding) and crack initiation sites. Numerical models of the grinding process can be developed.

G.10 REFERENCES

G.1 McIlre, A. R., "PWR Materials Reliability Project Interim Alloy 600 Safety Assessments for US PWR Plants (MRP-44) – Part 1: Alloy 82/182 Pipe Butt Welds", EPRI Report, TP-1—1491, April, 2001.

G.2 Scott, P. M., et al., "Fracture Evaluations of Fusion Line Cracks in Nuclear Pipe Bimetallic Welds", NUREG/CR-6297, January, 1995.

G.3 VFT™ (Virtual Fabrication Technology Software), Version 1.3, Developed Jointly by Battelle and Caterpillar (Caterpillar owned),

exclusively distributed by Battelle Columbus Ohio, and The Welding Institute (TWI) (via separate contract with Battelle), Cambridge, England.

G.4 FRAC@ALT© (FRacture Analysis Code via ALTernating method), Version 2.0, January, 1999, Battelle Memorial Institute.

G.5 TRACLIFE™, Probabilistic Life Prediction Code, R. E. Kurth, Battelle, 2001.

G.6 Brust, F. W., Stonesifer, R., Effects of Weld Parameters on Residual Stresses in BWR Piping Systems EPRI NP-1743, Project 1174-1, 1981.

G.7 Brust, F.W., Dong, P., and Zhang, J., 1997, "A Constitutive Model for Welding Process Simulation Using Finite Element Methods," Advances in Computational Engineering Science, Atluri, S.N., and Yagawa, G., eds., pp. 51-56.

G.8 F. W. Brust and M. F. Kanninen, "Analysis of Residual Stresses in Girth Welded Type 304-Stainless Pipes", ASME Journal of Materials in Energy Systems, Vol. 3, No. 3, 1981.

G.9 Dong, P., and Brust, F. W. "Welding Residual Stresses and Effects on Fracture in Pressure Vessel and Piping Components: A Millennium Review and Beyond", Transactions of ASME, Journal Of Pressure Vessel Technology, Volume 122, No. 3, August 2000, pp. 329-339.

G.10 Thomas, A., Ehrlich, R., Kingston, E., and Smith, D. J., "Measurement of Residual Stresses in Steel Nozzle Intersections Containing Repair Welds", in ASME PVP Volume PVP 434, Computational Weld Mechanics, Constraint, and Weld Fracture, Edited by F. W. Brust, August, 2002.

G.11 Schmertz, J. C., Swamy, S. A., and Lee, Y. S., "Technical Justification For Eliminating Large Primare Loop Pipe Rupture As the Structural Design Basis for the Virgil C. Summer Nuclear Power Plant", Westinghouse Report, WCAP-13206, April, 1992.

G.12 Rao, G. V., et al., "Metallurgical Investigation of Cracking in the Reactor Vessel Alpha Loop Hot Leg Nozzle to Pipe at the V. C. Summer Nuclear Generating Station", WCAP-15616, Westinghouse Electric Company, January 2001.

G.13 Westinghouse Electric Co., "Integrity Evaluation for Future Operation Virgil C. Summer Nuclear Plant: Reactor Vessel Nozzle to Pipe Weld Regions", WCAP-15615, December 2000.

G.14 F. W. Brust, P. Dong, J. Zhang, "Influence of Residual Stresses and Weld Repairs on Pipe Fracture", Approximate Methods in the Design and Analysis of Pressure Vessels and Piping Components, W. J. Bees, Ed., PVP-Vol. 347, pp. 173-191, 1997.

G.15 J. Zhang, P. Dong, F. W. Brust, W. J. Shack, M. Mayfield, M. McNeil, "Modeling of Weld Residual Stresses in Core Shroud Structures", International Journal for Nuclear Engineering and Design, Volume 195, pp. 171-187, 2000.

G.16 Brust, F. W., and Dong, P., "Welding Residual Stresses and Effects on Fracture in Pressure Vessel and Piping Components: A Millennium Review and Beyond", Transactions of ASME, Journal Of Pressure Vessel Technology, Volume 122, No. 3, August 2000, pp. 329-339.

APPENDIX H

THE EFFECT OF WELD INDUCED RESIDUAL STRESSES ON PIPE CRACK OPENING AREAS AND IMPLICATIONS ON LEAK-BEFORE-BREAK CONSIDERATIONS

As part of Task 9 of the BINP program the effect of weld residual stresses on the predicted crack-opening displacements (COD) used in Leak-Before-Break (LBB) analyses was investigated. The key findings from that effort are:

- Weld residual stresses tend to hold circumferential cracks closed
- Traditional crack opening displacement equations over-predict crack opening displacements in areas with weld residual stresses
- Over-prediction of crack opening causes under-prediction of the postulated crack length for a prescribed leak rate
- Correction factors for traditional equations have been developed to model this effect for tension, bending, and combined loading

The details supporting these findings are documented in this appendix.

The USNRC is anticipating updating their leak-before-break (LBB) procedures. One of the technical areas of concern in the existing procedures is the prediction of the crack-opening-displacements (COD) needed for estimating the postulated leakage crack size for a prescribed leakage detection capability. If cracks develop in the welded area of a pipe, as is often the case, residual stresses in the weld may cause the crack to be forced closed. Earlier studies have shown that pipe welding produces high residual stresses with a sharp stress gradient ranging from tension to compression through the thickness of the welded area of the pipe[1]. The current guidelines are inadequate to predict crack size based on leak rates for cracks in welded areas of pipes.

The current guidelines rely on the calculation of the crack-opening-displacement as related to pipe loading. Values from the current guidelines are used to predict a crack's cross sectional area and, in turn, to determine the severity of an existing crack by monitoring in-service leakage rates. The equations currently in use are applicable to service loaded pipe material only. Residual stresses caused by cold work, welding, etc. are neglected.

This study uses two and three dimensional finite element models and weld residual stress calculation software developed at Battelle to develop correction factors to be used with the traditional crack-opening displacement equations. The correction factors will compensate for the effects of welding induced residual stresses on cracks in pipe welds.

This study concentrates on type 316 stainless steel material properties, but the COD corrections should be equally applicable to all stainless steels, and also can be used for ferritic steels by a simple ratio correction of the room temperature yield strengths. However, this contention still needs to be verified. A test matrix of pipe radius, thickness, and crack size was used to develop the equation correction factors. Pipe wall thicknesses (t) of 7.5 mm (0.295 in.), 15 mm (0.590 in.), 22.5 mm (0.886 in.), and 30 mm (1.181 in.) were studied in pipes with mean radius to thickness ratios of 5, 10, and 20. Cracks with half-lengths in radians of $\pi / 16$, $\pi / 8$, $\pi / 4$, and $\pi / 2$ were introduced in these virtual pipes. The matrix of results was used to produce correction factors for crack opening displacement equations applicable to a broad range of pipe sizes.

H.1 NOMENCLATURE

A - Weld pass cross section area (in^2)
a - Half the cracks length in linear units $a = R\theta$
b - Half the pipe's mean circumference $b = \pi R$
C_1 - Non-dimensional function of a / b, R / t, and t used to modify the slope of the GE/EPRI equation to predict crack opening displacements in weld created residual stress fields
E - Modulus of elasticity
I - Weld current (amps)
I_D - Non-dimensional function of a / b, R / t, and t used to calculate intercept

[1] For very thick pipe, the residual stress state tends to be tension-compression-tension through the thickness.

of the linear equation describing crack opening displacement on the inside diameter of the pipe

I_{OD} - Non-dimensional function of a / b, R / t, and t used to calculate intercept of the linear equation describing crack opening displacement on the outside diameter of the pipe

M - Applied Moment

P - Applied load

q' - Weld power input per volume [(BTU/sec)/in^3]

R - Mean radius of the pipe in question

t - Pipe wall thickness

V - Weld voltage (volts)

V_1 - Non-dimensional function of a / b and R / t used in GE/EPRI equation to predict crack opening displacements

δ - Total crack opening displacement at the center of a crack's length

δ_{ID} - Crack centerline displacement on the pipe inner diameter

δ_{OD} - Crack centerline displacement on the pipe outer diameter

η - Weld energy transfer efficiency

σ_T^∞ - Applied nominal stress in tension = P / 2πRt

σ_B^∞ - Applied nominal outer diameter stress in bending on bending axis = MR_{OD} / I

$\sigma^\infty_{Critical}$ - Stress loading below which a crack in a weld residual stress field will remain closed

Δt - Δz / v (sec)

v - Weld pass speed (in / sec)

Δz - Unit Depth (1 in)

θ - Half the cracks length in radians

H.2 INTRODUCTION

The USNRC is anticipating updating their leak-before-break (LBB) procedures with the publication of a new Regulatory Guide and possibly a finalized version of the Standard Review Plan (SRP) section for LBB. The reason that the NRC is updating these procedures now is that most of the key research topics related to the subject of LBB technology have been addressed in past research programs or are being addressed in ongoing research programs, such as the Battelle Integrity of Nuclear Piping (BINP) program. One of those topics is the issue of the effect of weld residual stresses on the crack-opening-displacement predictions used to estimate the size of the postulated leakage crack for a LBB analysis. Past studies have shown that weld residual stresses can cause the crack faces of a leaking through-wall crack to rotate causing the flow through the crack to be somewhat restricted. One of the tasks of the BINP program was to quantitatively assess this effect and to develop a means of accounting for this effect in the analysis.

The purpose of this work was to develop correction factors, which account for the effects of weld residual stresses, for the currently used crack-opening-displacement (COD) estimation equations. One such equation is Equation H.1 which is the linear elastic crack opening displacement prediction equation developed by Kumar and German (Ref. H.1) which is known as the GE/EPRI equation for COD.

$$\delta = \frac{4\sigma^\infty a}{E} \cdot V_1\left(\frac{a}{b}, \frac{R}{t}\right) \qquad \text{(H.1)}$$

In this equation, δ is the total crack opening displacement, and V_1 is a dimensionless function that is tabulated for both tension stress and bending stress. This equation is valid for service loading only, i.e., it does not account for the effects of residual stresses.

It will be shown that residual stresses due to welding tend to set up an axial stress field that is in tension on the inner diameter of the pipe in the weld heat affected zone and in compression on the outer diameter of the welded area. This is true for all the pipe sizes examined except those with 30 mm (1.181 in.) thickness. The compression stresses on the outer diameter of the pipe tend to hold an existing through wall crack closed under zero load conditions, and the tension residual stresses on the inner diameter tend to hold the crack surfaces apart.

The GE/EPRI equation predicts that a crack will open in a linear fashion starting at zero load. This is not the behavior, however, that would be expected from a crack in the weld area of a pipe.

Because the crack would be forced closed by the residual stresses under zero load conditions, one would expect that a certain critical load, greater than zero, would be required to start opening the crack. Also, because the crack face on the inner diameter of the pipe can be expected to be open under zero load, the intercept of the equation describing crack opening displacement would not be expected to be zero.

A matrix of analyses have been performed using ABAQUS finite element software in conjunction with a welding simulation subroutine developed at Battelle (Ref. H.2). Table H.1 and Table H.2 show the pipe geometries, wall thicknesses, mean radius to thickness ratios, and crack sizes that were evaluated.

Table H.1 Pipe geometries studied

Wall Thickness mm (in)	R_{mean} / thickness Ratio		
7.5 (0.295)	5	10	20
15 (0.590)	5	10	20
22.5 (0.886)	5	10	20
30 (1.181)	5	10	20

Table H.2 Crack sizes studied

Crack Half Length (θ), Radians	Crack Half Length (θ), Degrees
$\pi / 16$	11.5
$\pi / 8$	22.5
$\pi / 4$	45
$\pi / 2$	90

Two dimensional axi-symmetric models were constructed to determine the residual stresses due to welding. These stresses were then mapped into a three dimensional model in which the various crack sizes described in Table H.2 were introduced. The three dimensional models were used to determine the effect of tension and bending loads on the crack opening displacement. Welding related factors such as current, voltage, efficiency, speed, weld pass cross section, and geometric factors shown in Table H.1 were all considered.

The data extracted from the analysis results allowed the creation of correction factors for the GE/EPRI equation, which account for the critical load necessary to start opening the crack ($\sigma^{\infty}_{Critical}$) and the non-zero intercepts found for crack opening displacements under zero load. Cracks in a zone of weld residual stresses will open asymmetrically, and therefore it is necessary to use both a crack opening displacement value for the outer diameter and inner diameter crack faces to properly describe the crack profile. Equation H.2 shows the format of the weld residual stress correction to the GE/EPRI equation.

$$
\begin{cases}
\text{IF:} & \sigma^{**} < \sigma^{**}_{Critical}\left(\frac{a}{b},\frac{R}{t},t\right) \\
\text{THEN:} & \delta = 0 \\
\\
\text{IF:} & \sigma^{**} \geq \sigma^{**}_{Critical}\left(\frac{a}{b},\frac{R}{t},t\right) \\
\\
\text{THEN:} & \delta_{OD} = \frac{4\sigma^{**}a}{E}\cdot V_1\left(\frac{a}{b},\frac{R}{t}\right)\cdot C_1\left(\frac{a}{b},\frac{R}{t},t\right) + a\cdot I_{OD}\left(\frac{a}{b},\frac{R}{t},t\right) \\
\\
 & \delta_{ID} = \frac{4\sigma^{**}a}{E}\cdot V_1\left(\frac{a}{b},\frac{R}{t}\right)\cdot C_1\left(\frac{a}{b},\frac{R}{t},t\right) + a\cdot I_{ID}\left(\frac{a}{b},\frac{R}{t},t\right)
\end{cases}
\qquad \text{(H.2)}
$$

Where C_1 is a tabulated slope correction factor and I_{OD} and I_{ID} are used to modify the outer and inner diameter displacement equation intercepts.

H.3 MODEL DEVELOPMENT

The welding residual stresses were calculated using a half symmetry, axi-symmetric model. The finite element model was subjected to a thermal analysis, which simulated the weld process functions of laying down the molten bead of weld rod, introducing heat energy into the weld bead and cooling the weld to an inter-pass temperature. The thermal analysis calculated the temperatures throughout the finite element model through the welding process. A subsequent stress analysis was performed which used the previously defined temperatures to calculate the elastic-plastic residual strains in the welded pipe segment due to the thermal effects of welding. A Battelle developed subroutine, which represents a constitutive law specific to the many peculiarities of the weld process, is interfaced with ABAQUS during the weld analysis. Figure H.1 shows a typical weld model. Standard weld groove and weld pass geometries commonly used for stainless steel welding were adapted from Figures C-2, and C-3 of the report by Barber, et. al, (Ref. H.3). In the same report it was shown that precise weld groove geometry has a second order effect on the weld induced residual stress state.

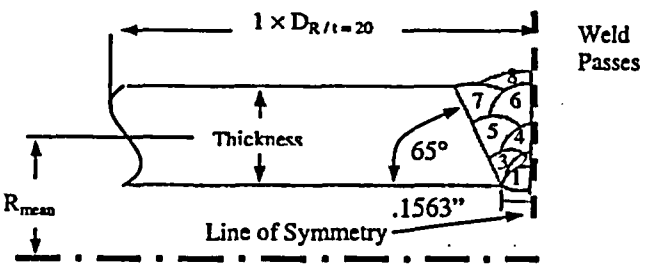

Figure H.1 Typical axi-symmetric weld model construction

A relationship between weld heat energy and pipe thickness was developed from test data. Actual weld parameters of voltage and current were measured for multiple weld passes on several pipe thicknesses and were documented in Table C-3 of Reference H.2. A linear curve fit of this data was constructed to create an equation describing heat energy input per linear inch of weld pass as a function of pipe thickness. Equation H.3 shows the linear equation describing heat input per weld bead length in (J/in) vs. pipe thickness in inches. This equation, and an additional efficiency multiplication factor of 75%, was used to create the heat energy input table used for the specific pipe thicknesses examined in this analysis. These values are shown in Table H.3. These weld parameters are quite typical of those used in nuclear piping for austenitic steels.

$$\frac{Energy}{Length}\left(\frac{J}{in.}\right) = 15{,}393\left(\frac{J}{in^2}\right)\cdot t(in.) + 13{,}265\left(\frac{J}{in.}\right) \qquad \text{(H.3)}$$

Table H.3 Energy inputs used in the current analysis

Pipe Thickness mm, (in)	Energy / in KJ / mm , (KJ / in)
7.5, (0.295)	0.526, (13.354)
15.0, (0.590)	0.660, (16.760)
22.5, (0.886)	0.794, (20.177)
30.0, (1.181)	1.01, (23.583)

A more detailed description of the weld analysis energy input follows. The analysis steps, per pass, for the axisymmetric model included a thermal analysis and then a stress analysis using the results from the previous thermal analysis. The steps were as follows:

- Deposition of weld pass for t = 0.01 sec at molten temperature.
- Heating of weld pass calculated as:

$$\frac{(I\cdot V\cdot\eta)}{v} := A\cdot\Delta z\cdot q'\cdot\Delta t$$

$$q' := \left[\frac{(I\cdot V\cdot\eta)}{(A\cdot\Delta z\cdot\Delta t\cdot v)}\right]\cdot(\text{conversion factor}) \qquad \text{(H.4)}$$

$$\Delta t := \frac{\Delta z}{v}$$

I = Weld Current (Amps)
V = Weld Voltage (Volts)
η = Efficiency (.75)
v = Speed (in / sec)
A = Weld pass cross section area (in^2)
Δz = Unit Depth (1 in)
Δt = Δz / v (sec)
q' = Power Input per volume [(BTU/sec)/in^3]

Conversion Factor = 0.0009472 [(BTU/sec)] = 1 Watt

- Cooling of the weld pass for t ≈ 300 sec. Allowing the weld pass to cool to below 300 °F before applying the next pass.

The stress portion of the two dimensional axisymmetric analysis used the results from the temperature analysis and developed the residual stresses over the same time steps as were used in the thermal analysis and used the custom subroutine to assign the proper welding strains, including the effects of melting and annealing of the weld and parent material.

The heat energy input values used in the analyses are described using the pipe geometry with a pipe thickness of 0.590 inches and a radius to thickness ratio of 10 as an example. The power input per unit volume of each axisymmetric weld pass was calculated as shown in the Equation H.4.

These measured inputs were extrapolated to the thicknesses that were evaluated in this effort. The tabulated energy values do not contain an efficiency factor. Assuming that the welds were all made at the same weld pass speed (0.117 in / sec) [3 mm / sec], and with the same voltage setting (25 volts), the average current was derived. The weld parameters used in this study are tabulated below in Table H.3a.

Table H.3a Energy inputs used in the current analysis

Pipe Thickness (in) [mm]	Energy / in (KJ / in) [KJ / mm]	I (amp)	V (volt)	E / in * .75 Efficiency (KJ / in) [KJ / mm]
0.295 [7.5]	17.806 [0.701]	83	25	13.354 [0.525]
0.590 [15.0]	22.347 [0.880]	105	25	16.760 [0.660]
0.886 [22.5]	26.903 [1.06]	126	25	20.177 [0.794]
1.181 [30.0]	31.444 [1.24]	147	25	23.583 [0.828]

For example, the following values were used for the 0.590 inch thick pipe:

I = 105 Amps
V = 25 Volts
η = .75
v = 0.117 in / sec
A = Weld pass cross section area (in^2)
Δz = 1 in
Δt = 8.547 sec
q' = Power Input per volume [(BTU/sec)/in^3]

Conversion Factor = 0.0009472 [(BTU/sec)] = 1 Watt

$$\Delta t := \frac{\Delta z}{v}$$

$$q' = 1.865 / A$$

Values for power per volume based on the 0.590 inch thick geometry and the weld pass cross sectional areas are tabulated below.

H.4 TENSION LOAD RESULTS

For the remainder of this paper the model associated with the pipe thickness of 15 mm and a mean radius to thickness ratio of 10 will be used as an example. Figure H.2 shows the progression of the weld build-up using the energy values from Table H.4. The contours on the model indicate the temperature of the two dimensional axisymmetric model during each weld pass.

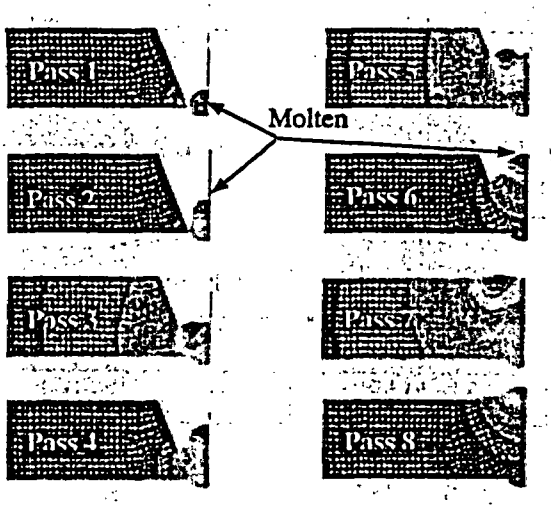

Figure H.2 The thermal analysis showing weld build-up

Table H.4 Weld pass power input per unit volume for 0.590 inch thick pipe

Weld Pass	A (in^2)	q' [(BTU/sec)/in^3]
1	0.0238	78
2	0.0159	117
3	0.0186	100
4	0.0226	83
5	0.0305	61
6	0.0298	62
7	0.0462	40
8	0.0154	121

The results from the thermal analyses were used as input for the stress analyses. Figure H.3 shows an axial stress contour plot and the corresponding graph shows the axial stress on the outer and inner diameter of the pipe. Figure H.4 shows the hoop stress contour plot and the corresponding graph. (Similar plots of axial and hoop stress for the other weld geometrics (pipe thickness and R/t ratio) analyzed are shown in the attachment at the end of this Appendix.)

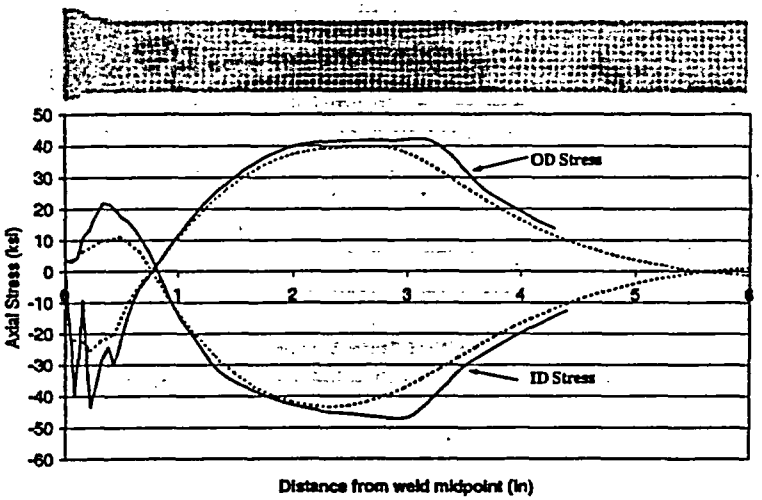

Figure H.3 2-D Weld residual stress – axial stress

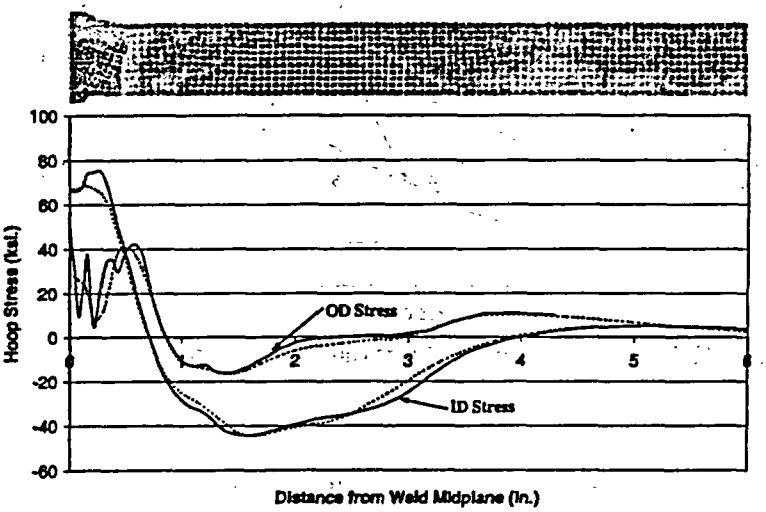

Figure H.4 2-D Weld residual stress – hoop stress

Figures H.5 and H.6 show measured axial and hoop weld residual stresses for a type 304 stainless steel pipe. The data was taken from Table D-5 of Reference H.4. The pipe was 0.84 inches thick with an R / t ratio of 19. The measured data is scattered due to the fact that the pipe was not annealed to remove manufacturing stresses before it was welded. These values are compared to the finite element predictions for a 0.886 inch thick pipe with a R / t ratio of 20 with type 316 stainless steel properties. The graphs show that the predictions are of similar values and magnitudes despite the scatter in the measured data. Likewise, an extensive database of validation examples for the VFT™ software exists for both small specimen welds and complicated structures.

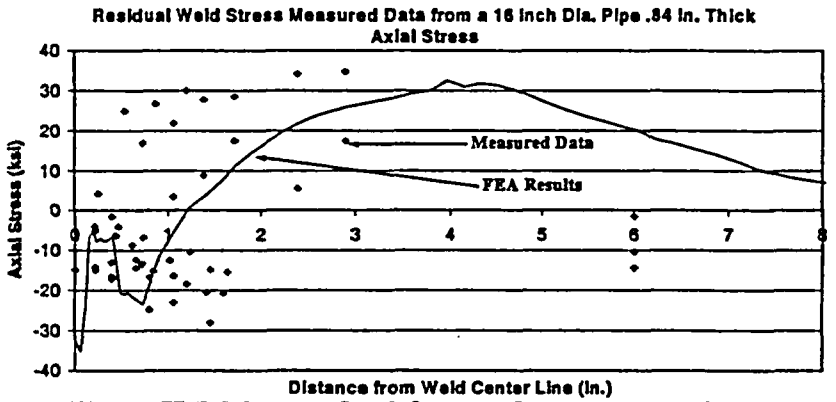

Figure H.5 Measured axial stress data versus analysis

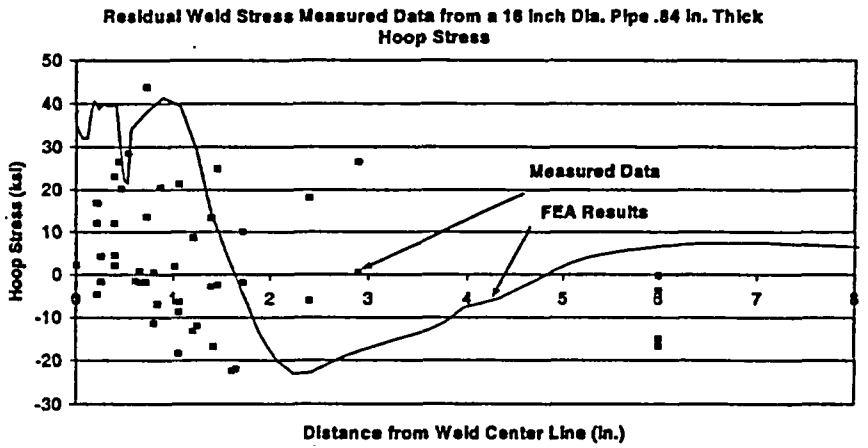

Figure H.6 Measured hoop stress data versus analysis

The two dimensional residual stress results were then mapped from the fine meshed model to a coarser meshed model and then rotated into a quarter symmetry, three dimensional model as shown in Figure H.7. The stress results shown in Figures H.3 and H.4 as solid lines represent the results from the finely meshed 2-D models. The data plotted with dotted lines represent the stresses in the coarse two dimensional model which were transferred to the quarter symmetry, three dimensional model.

The 3-D models were used to evaluate the crack behavior due to residual stresses and externally applied loads. Cracks were introduced into the weld centerline by releasing the symmetric boundary conditions on the finite element nodes which represent the crack surface. Figure H.8 shows the crack surface areas for $\theta = \pi/16$, $\pi/8$, $\pi/14$, and $\pi/2$ length cracks in the quarter symmetry, three dimensional model.

The models were analyzed with and without a rigid surface boundary condition at the weld centerline. In the cases without the rigid surface boundary condition, called free boundary, the portion of the crack face in compression moved in the direction closing the crack ("negative" crack closing displacement). This displacement was used along with the GE/EPRI equation to predict the critical load necessary to overcome the crack closure and to just start to open the crack. Figure H.9 shows a view of a typical crack at the crack mid-length for the rigid surface boundary condition. The top view shows the crack under zero load. The weld residual tension stress in the pipe has opened the crack on the inner diameter, and the residual

compression stresses have forced the crack closed on its outer diameter. In the bottom view, the pipe has been put under the specific "critical load" for this case that will just start to open the crack.

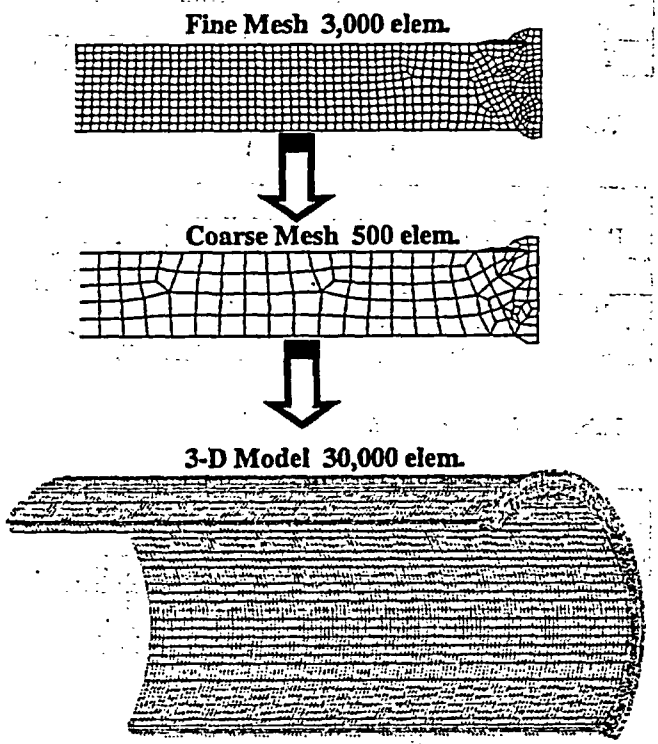

Figure H.7 Model development - fine mesh - coarse mesh - 3-D mesh

Critical crack opening loads were calculated for all 48 cases examined. Analyses were conducted in which 0 ×, 1 ×, 2 × and 3 × this critical load were applied to the pipe model with free crack boundary conditions for all 48 cases.

A sample of cases was conducted with the rigid, symmetric weld centerline boundary condition as shown in Figure H.9. It was found that the behavior of the crack faces under load was exactly the same with the rigid and free boundary conditions once the cracks were fully opened.

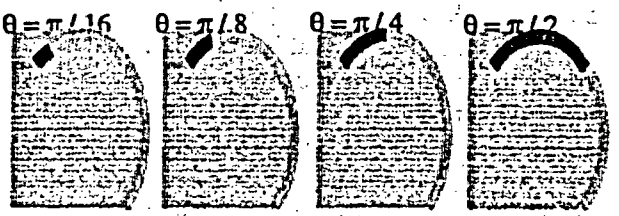

Figure H.8 Crack sizes

Figure H.9 shows the importance of reporting both the inner diameter and outer diameter crack opening displacement values. Examples run with the SQUIRT leak rate prediction software (Ref. H.5) show that cracks with non-parallel faces leak at different rates than those with parallel faces. Therefore, it is important to report both the outer diameter and inner diameter crack opening displacements in the case of cracks affected by a weld residual stress field. The SQUIRT program allows the user to input an OD COD and an ID COD for asymmetric cracks. The load versus displacement data extracted from the analysis results was used to develop linear equations that can be used to predict crack centerline displacements.

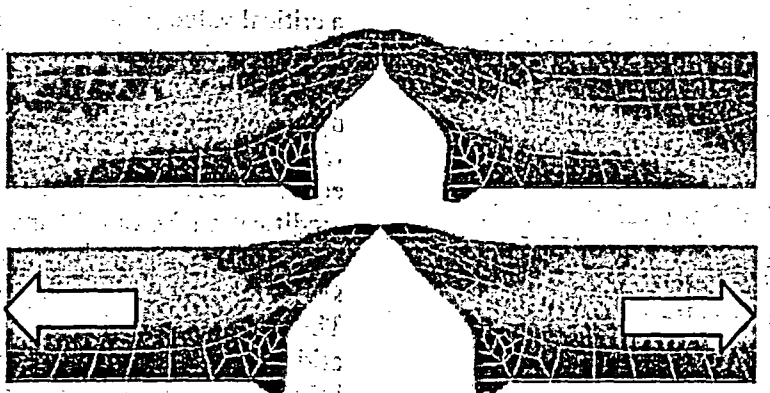

Figure H.9 3-D crack mid-surface closed under zero load (top) and ready to open under critical tension loading (bottom)

Figure H.10 shows crack half-displacements for the outer diameter crack edge in the example case (thickness = 15 mm, R / t = 10, $\theta = \pi/4$) under various loading conditions. The figure shows a crack with $\theta = \pi / 8$ loaded with multiples of the critical load. The crack has begun to open in the crack center, but is not completely open along its length under the critical load. The crack quickly becomes fully open and takes on a roughly elliptical shape, once 1.5 times the critical load is applied. An elliptical crack shape is usually assumed in leak rate calculations as a way to calculate crack opening area using only two parameters: crack opening displacement and crack length. The inner diameter crack opening profile (not shown) starts out open and elliptically shaped under zero loading.

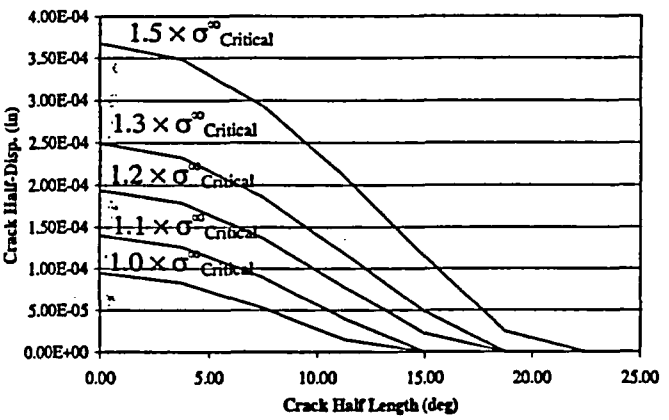

Figure H.10 Crack OD opening profile under tension load, $\theta = \pi / 8$

Equation H.1 is valid for describing crack opening displacements in pipe materials with no residual stress. The crack opening displacements found with the weld residual stress models were used to develop corrections for Equation H.1 to make it better match the crack behavior in a weld induced residual stress field. Tables H.5 and H.6 show the values for V_1 used in Equation H.1 for tension (Table H.5) and bending (Table H.6) from Reference H.1. Table H.7 provides updated values of V_1 for bending developed with more sophisticated finite element models from Reference H.6.

Table H.5 V_1 values for tension from Table 2-1 of Reference H.1

	θ/π			
R / t	1 / 16	1 / 8	1 / 4	1 / 2
5	1.05	1.202	1.827	6.367
10	1.082	1.319	2.243	8.324
20	1.144	1.530	2.922	11.089

Table H.6 V_1 values for bending from Table 2-5 of Reference H.1

	θ/π			
R / t	1 / 16	1 / 8	1 / 4	1 / 2
5	1.052	1.194	1.732	4.958
10	1.081	1.304	2.116	6.510
20	1.141	1.510	2.753	8.727

Table H.7 V_1 values for bending from Tables 4.3 and 4.8 of Reference H.6

	θ/π			
R / t	1 / 16	1 / 8	1 / 4	1 / 2
5	1.234	1.388	2.008	5.331
10	1.206	1.480	2.379	7.165
20	1.111	1.482	3.079	11.585

Equation H.1 is a linear function with an intercept of zero displacement at zero load. It has been shown earlier that cracks in weld areas are initially forced closed on the OD surface due to axial compressive residual stresses. It has also been shown that it is important to report the crack opening displacement for both the crack outer diameter and inner diameter. These facts force a modification of Equation H.1 in order to predict the behavior of cracks in welds. If the externally applied stress on the pipe is less than a critical value ($\sigma^{\infty}_{Critical}$), then the crack remains closed. If the applied stress is greater than this value, then the ID and OD crack opening displacements are greater than zero and different from each other. To modify the GE/EPRI equation to represent both of these facts, a slope modification factor (C_1) and two intercept values (I_{OD} and I_{ID}) must be introduced. Figure H.11 shows the equation modification graphically. The modified equation shows a step at the critical load. The crack is assumed to be closed below this load. Above the critical load, both

the ID and OD crack center displacements are represented. The values for $\sigma^{\infty}_{Critical}$, C_1, I_{OD}, and I_{ID} have been tabulated and are shown below in Tables H.8 through H.11 for tension loading. The cells that are shaded gray in Table H.8 indicate stresses above those that would be caused by the standard pressurized water reactor (PWR) operating pressure of 2,250 psi. This means that cracks of these sizes would remain closed at standard operating pressure, if no additional external load were applied to the pipe system.

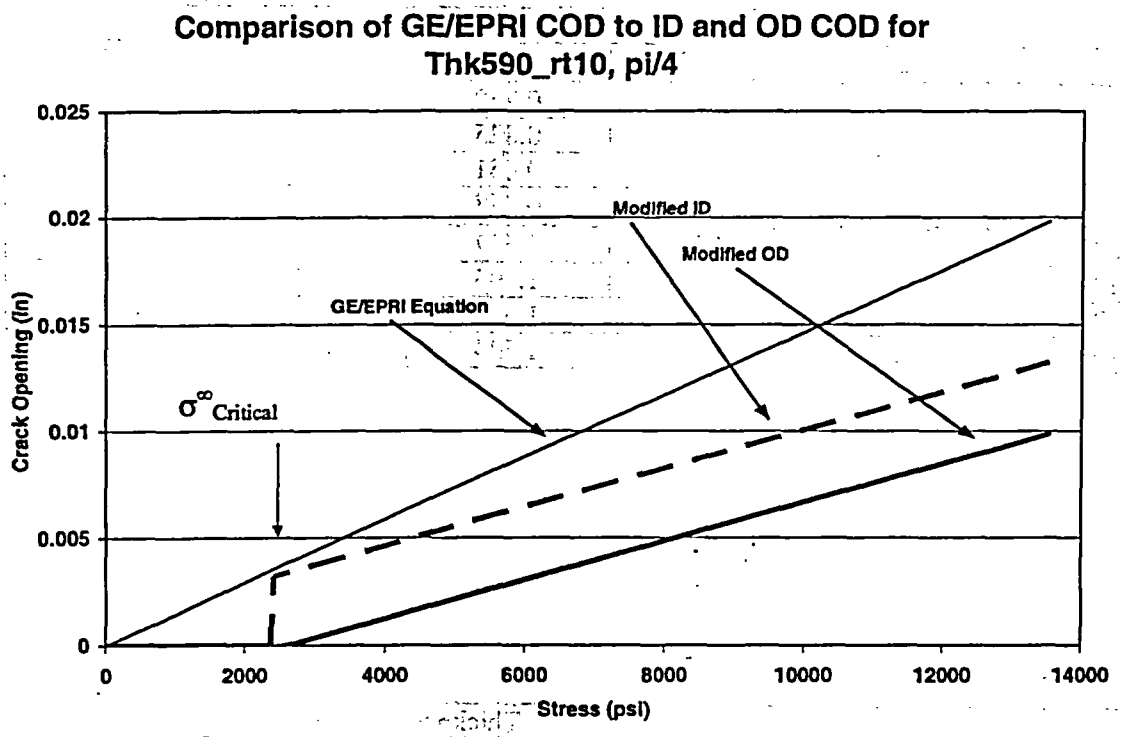

Figure H.11 GE/EPRI tension equation modification

Table H. 8 $\sigma^{\infty}_{Critical}$ values for tension loads kPa, (psi)
[Highlighted values are greater than PWR operating pressure]

R / t	θ/Π	Thickness mm, (in) 7.5, (0.295)	15, (0.59)	22.5, (0.886)	30, (1.181)
5	1/16	132952, (19283)	105008, (15230)	44030, (6386)	31475, (4565)
5	1/8	134573, (19518)	48477, (7031)	25001, (3626)	20609, (2989)
5	1/4	83717, (12142)	28738, (4168)	14748, (2139)	10839, (1572)
5	1/2	21167, (3070)	9611, (1394)	3978, (577)	0
10	1/16	84696, (12284)	35653, (5171)	21953, (3184)	13010, (1887)
10	1/8	52525, (7618)	24676, (3579)	13369, (1939)	9446, (1370)
10	1/4	33433, (4849)	16679, (2419)	8646, (1254)	5061, (734)
10	1/2	11280, (1636)	4502, (653)	2420, (351)	0
20	1/16	28669, (4158)	6543, (949)	9349, (1356)	5295, (768)
20	1/8	21746, (3154)	3820, (554)	5785, (839)	427, (62)
20	1/4	16051, (2328)	2082, (302)	3503, (508)	2179, (316)
20	1/2	4826, (700)	655, (95)	1000, (145)	0

Table H.9 C_1 values for tension (C_T)

		Thickness, mm (inch)			
		7.5 (0.295)	15 (0.59)	22.5 (0.886)	30 (1.181)
R/t	θ/π	I_{OD}			
5	1/16	0.869	1.007	0.789	0.813
5	1/8	0.906	0.959	0.861	0.899
5	1/4	0.731	0.744	0.722	0.726
5	1/2	0.852	0.862	0.827	0.868
10	1/16	0.883	0.769	0.806	0.817
10	1/8	0.918	0.825	0.803	0.847
10	1/4	0.650	0.651	0.617	0.661
10	1/2	0.762	0.758	0.709	0.767
20	1/16	0.786	1.517	0.769	0.801
20	1/8	0.766	1.795	0.720	0.765
20	1/4	0.572	1.526	0.515	0.587
20	1/2	0.806	1.524	0.638	0.810

Table H.10 I_{OD} values

		Thickness, mm (inch)			
		7.5 (0.295)	15 (0.59)	22.5 (0.886)	30 (1.181)
R/t	θ/π	I_{OD}			
5	1/16	-0.00256	-0.00240	-0.00074	0.00038
5	1/8	-0.00288	-0.00119	-0.00053	0.00049
5	1/4	-0.00271	-0.00086	-0.00040	0.00050
5	1/2	-0.00295	-0.00112	-0.00042	0.00055
10	1/16	-0.00172	-0.00060	-0.00037	0.00019
10	1/8	-0.00132	-0.00055	-0.00028	0.00026
10	1/4	-0.00103	-0.00051	-0.00024	0.00027
10	1/2	-0.00147	-0.00058	-0.00028	0.00033
20	1/16	-0.00051	-0.00022	-0.00016	0.00009
20	1/8	-0.00051	-0.00021	-0.00012	0.00012
20	1/4	-0.00055	-0.00019	-0.00010	0.00014
20	1/2	-0.00086	-0.00024	-0.00013	0.00021

Table H.11 I_{ID} values

		Thickness, mm (inch)			
		7.5 (0.295)	15 (0.59)	22.5 (0.886)	30 (1.186)
R/t	θ/π	I_{ID}			
5	1/16	0.00214	0.00016	0.00028	-0.00050
5	1/8	0.00207	0.00082	0.00039	-0.00038
5	1/4	0.00139	0.00073	0.00027	-0.00025
5	1/2	-0.00012	-0.00001	0.00001	0.00004
10	1/16	0.00071	0.00019	0.00020	-0.00022
10	1/8	0.00082	0.00029	0.00026	-0.00019
10	1/4	0.00076	0.00022	0.00018	-0.00013
10	1/2	-0.00014	-0.00004	0.00001	0.00002
20	1/16	0.00033	0.00004	0.00007	-0.00009
20	1/8	0.00038	0.00008	0.00009	-0.00009
20	1/4	0.00028	0.00007	0.00007	-0.00007
20	1/2	-0.00017	-0.00003	-0.00001	0.00004

H.5 TENSION LOAD EXAMPLE

An example will help illustrate the use of Equation H.2 and the significant difference in crack opening displacement from the results found with Equation H.1. The pipe size that has been used for illustration purposes throughout the paper will be used again here. The pipe is 15 mm (0.59 in.) thick and has a mean radius to thickness ratio of 10. The internal pressure is standard operating pressure for a PWR of 15.5 MPa (2,250 psi.). Crack half-length is $\theta = \pi / 4$. The pipe is made from type 316 stainless steel with a Modulus of Elasticity of: E = 206,840 MPa (30×10^6 psi).

The first step is to check to see if the loads on the pipe exceed $\sigma^{\infty}_{Critical}$. The calculated nominal stress on the pipe produced from only the internal pressure is 70 MPa (10.15 ksi). Looking at Table H.8, one finds that the critical stress for this instance is 16.7 MPa (2,419 psi.). The applied pressure is well above this limit, so the crack will be open.

The second step is to calculate the coefficient for Equation H.2. The crack half length (a) is equal to $R\theta$ = 118 mm (4.634 in.). The coefficient of the equation $4a\sigma^{\infty} / E$ = 0.159 mm (0.0063 in.).

The third step is to look up the tabulated values for the equation variables in Tables H.9 through H.11.

$V_1(^1/_4, 10) = 2.243$ [from Table H.5]
$C_T(^1/_4, 10, .59) = 0.651$ [from Table H.9]
$I_{OD}(^1/_4, 10, 15\text{ mm}) = -0.00051$ [from Table H.10]
$I_{ID}(^1/_4, 10, 15\text{ mm}) = 0.00022$ [from Table H.11]

Substituting these values into Equation H.2, the outer diameter and inner diameter crack opening displacements are calculated as follows:

δ_{OD} = 0.159 mm (2.243)(0.651) + 118 mm (-0.00051) = 0.1722 mm (0.0068 in.)
δ_{ID} = 0.159 mm (2.243)(0.651) + 118 mm (0.00022) = 0.258 mm (0.0102 in.)

These values can be verified graphically by looking for the OD and ID COD values in Figure H.11. For a nominal stress of 70 MPa (10,153 psi.), the values of the outer and inner diameter crack displacements can be read directly from the chart. The value predicted by the GE/EPRI equation, without a correction for residual stresses, can also be read directly from the chart, or calculated as 0.357 mm (0.0141 in.). There is a disagreement of 38 percent on

the inner diameter displacement and 107 percent on the outer diameter crack opening displacement.

When these weld residual stress corrected COD values were used in the SQUIRT leak-rate code analysis of the example test case, the predicted leak rate for the half crack length of 118 mm (4.634 inches) was 33 lpm (8.74 gpm). When the uncorrected values from the GE/EPRI equations were used for this same test case, the predicted leak rate was 66 lpm (17.5 gpm), a factor of two greater. What this implies is that the predicted size of the postulated leaking through-wall crack for an LBB analysis is going to be much shorter if one does not account for the effect of the weld residual stresses on the COD values. If the crack size is proportional to the leak rate, then in this example case, the leakage crack, accounting for residual stresses, may be twice as long as the leakage crack, when one does not account for residual stresses, assuming the same prescribed leakage detection capability. Thus, not accounting for residual stresses may have eroded the margin on crack size of 2.0, typically assumed in a LBB analysis, to 1.0.

H.6 MODEL CHECKS

Two model checks, or sensitivity studies were performed to make sure that the results produced from the specific models used in this study would be applicable over a range of conditions. The two checks that were performed were a mesh density study in which the number of elements used in one of the 3-D models was increased by a factor of 2.8 and the resulting crack opening displacement values at no load were compared to those of the standard model. The second study examined the effect on weld residual stresses of altering the heat input in the weld. This was checked by varying the heat input ± 25 percent and examining the effect on axial and hoop stresses in one of the finely meshed 2-D models.

H.6.1 Mesh Density Study

A mesh density study was done to show that the number of elements that were used in the standard models was sufficient. This was done, in part, by comparing the results from the stress results from the coarse and finely meshed 2-D models as shown in Figures H.3 and H.4. Remember, the solid lines represent the stress results from the finely meshed model and the dotted lines represent the stress from the coarsely meshed model. Figure H.7 shows that the mesh density reduction in going from the finely meshed 2-D model to the coarsely meshed 2-D model was a factor of 6. These results were considered to match well enough to proceed with using them for the 3-D models in which cracks were introduced. But, a 3-D comparison was never made of the effect on crack opening displacement.

The ABAQUS routine, "Symmetric Model Generate," was used to revolve the 2-D models into 3-D models while mapping stresses as well. It was used on all of the test cases. The easiest method to create a finely meshed 3-D model was to revolve one of the finely meshed 2-D models directly into a 3-D model. For the example case of 0.59 inches thick with a radius to thickness ratio of 10 this would not work. This is why the coarser models were originally created with the stresses mapped to them. The original fine meshed models had to be made more coarsely meshed before revolving because of a limitation in the number of elements that can be revolved. The 2-D fine mesh model with the least number of elements (1,233 elements) was the model with a thickness of 0.886 inches. Its coarse mesh model had 439 elements. Revolving the fine mesh model into a 3-D model would produce a finely meshed 3-D model with 2.8 times the number of elements as the original version. This worked, and the crack opening displacements were compared.

Figure H.12 shows the half-crack opening displacement comparison for the coarsely and finely meshed model of the pipe 0.886 inches thick with a radius to thickness ratio of 10. The figure shows that there is a good comparison between the results of the two models. The ID values are shown on the upper part of the graph and the OD values are shown on the lower part of the graph. The graph shows the crack face displacement at the centerline when there is no

rigid boundary condition at the crack center. The OD of this crack moves in a direction that would create an interference fit (negative displacement) and the ID values show the crack opening. The graph also shows these crack profiles for the four crack sizes studied ($\pi/16$, $\pi/8$, $\pi/4$, $\pi/2$). In all cases, the finely meshed model produced resulting crack displacements outboard of those produced by the coarser model. The outer diameter results were more closed than the closed outer diameter of the coarsely meshed model, and the inner diameter results were more open than the open crack displacements of the more coarsely meshed model.

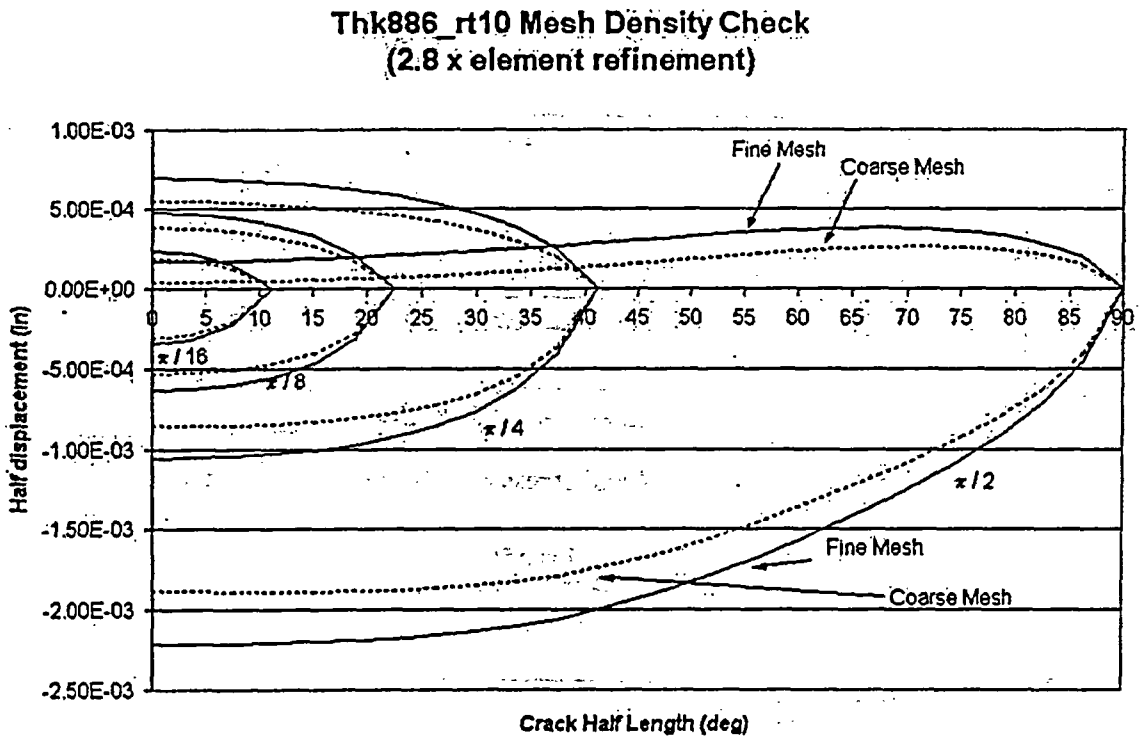

Figure H.12 Mesh density study results

The more coarsely meshed model is always conservative because it predicts that the cracks will be slightly more closed on the OD than the more finely meshed model. The conclusion of this study was that the results for the models used in developing the correction factors would be conservative and acceptable.

H.6.2 Heat Input Study

A heat input check was done for similar reasons. The check was done to find the effect of heat input on the stresses obtained in the weld model. The standard example case of a 0.59 inch thick pipe with radius to thickness ratio of 10 was used in this study. Only the stresses produced in the finely meshed 2-D model were examined. The heat input values used were varied by ± 25 percent from those used in the nominal case and the models were rerun.

The resulting axial and hoop stress profiles are shown in the following two figures (Figures H.13 and H.14). The figures show that the resulting change in stresses due to the change in heat input over the ± 25 percent range is almost insignificant.

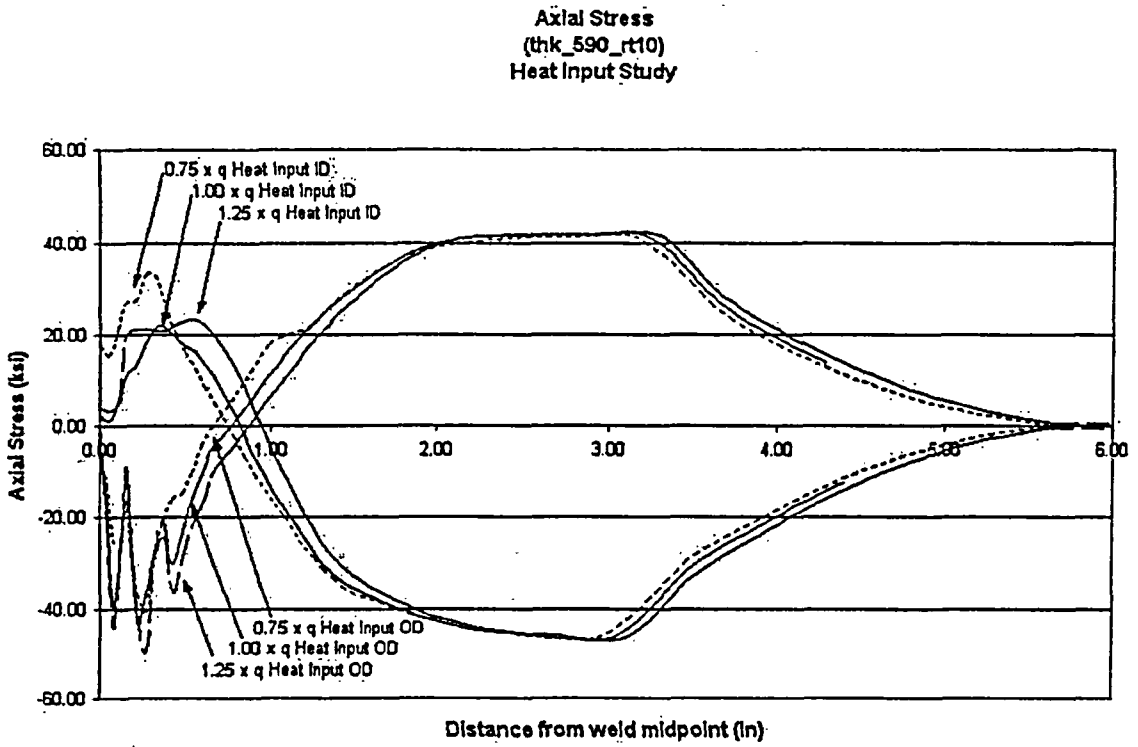

Figure H.13 Axial stress results from heat input study

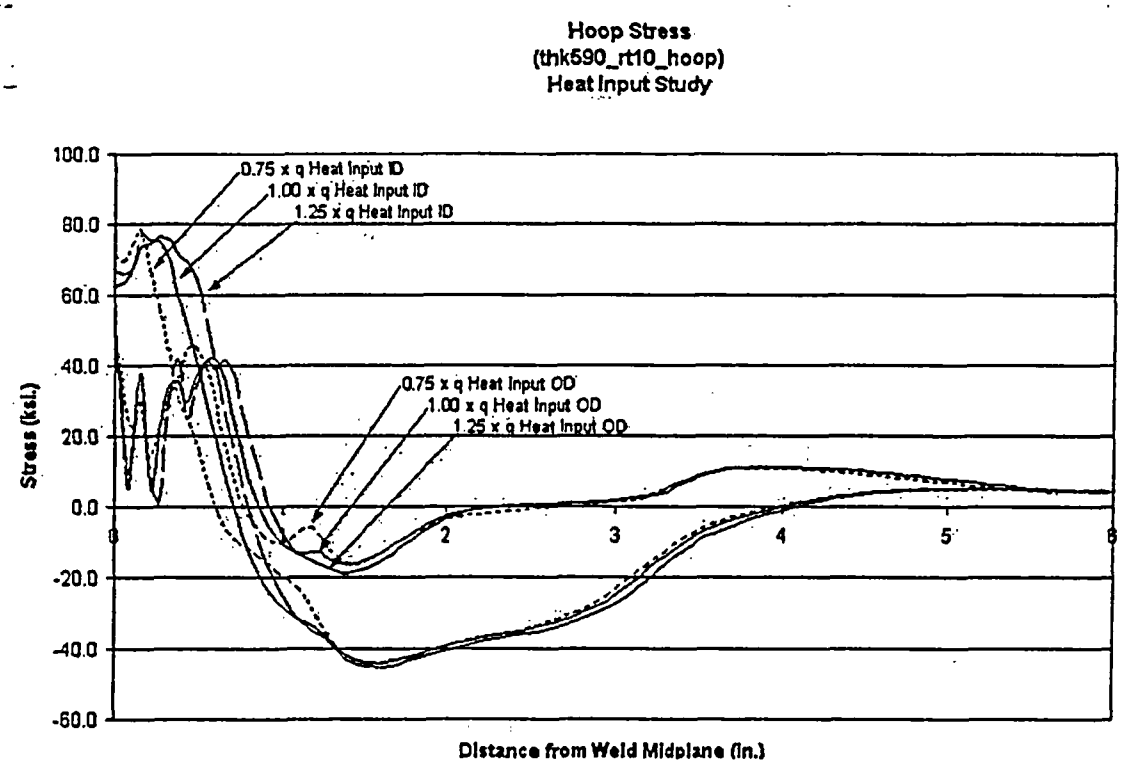

Figure H.14 Hoop stress results from heat input study

H.7 MOMENT LOAD AND COMBINED LOAD RESULTS

A similar logic was used to determine the correction factors necessary to compensate for the effects of welding residual stresses on the crack opening displacements under moment loading. It was assumed that another correction factor could be created and used in an equation of similar form to that of Equation H.2. It was also assumed that the equations for crack opening displacement due to tension and bending could be superimposed to form an equation to be used in the more common situation of combined loading.

The original GE / EPRI equation for combined loading is shown as Equation H.5 where the subscripts "T" and "B" indicate tension and bending, respectively. The proposed form of the equation corrected to include the effects of weld residual stress is shown in Equation H.6. A separate correction factor is used to modify the original "V" factors for both tension and bending loads. The intercept factors, I_{OD} and I_{ID}, are assumed to remain the same for both tension load and bending loads because they are a function of the no-load state of the welded pipe segment. The correction factors were calculated from the results of the analyses that will be described here, and the assumptions were validated.

$$\delta = \frac{4a}{E} \cdot \left[\sigma_T \cdot V_T\left(\frac{a}{b}, \frac{R}{t}\right) + \sigma_B \cdot V_B\left(\frac{a}{b}, \frac{R}{t}\right) \right] \tag{H.5}$$

$$\delta_{OD} = \frac{4a}{E} \cdot \left[\sigma_T \cdot V_T\left(\frac{a}{b}, \frac{R}{t}\right) \cdot C_T\left(\frac{a}{b}, \frac{R}{t}, t\right) + \sigma_B \cdot V_B\left(\frac{a}{b}, \frac{R}{t}\right) \cdot C_B\left(\frac{a}{b}, \frac{R}{t}, t\right) \right] + a \cdot I_{OD}\left(\frac{a}{b}, \frac{R}{t}, t\right) \tag{H.6a}$$

$$\delta_{ID} = \frac{4a}{E} \cdot \left[\sigma_T \cdot V_T\left(\frac{a}{b}, \frac{R}{t}\right) \cdot C_T\left(\frac{a}{b}, \frac{R}{t}, t\right) + \sigma_B \cdot V_B\left(\frac{a}{b}, \frac{R}{t}\right) \cdot C_B\left(\frac{a}{b}, \frac{R}{t}, t\right) \right] + a \cdot I_{ID}\left(\frac{a}{b}, \frac{R}{t}, t\right) \tag{H.6b}$$

The same 3-D pipe segment models, with welding residual stresses, as were used in the tensions analyses were reused for the bending analyses. The loads were applied differently. In the cases with tension loading, the pipe surface opposite the weld was put under a uniform tension load. In the moment analysis, a moment load was applied to a reference node at the center of the loaded end of the pipe, and this load was coupled to the nodes on the load face with the ABAQUS feature "KINEMATIC COUPLING." The reference node was restricted with boundary conditions in all directions except rotation in the direction of the applied moment. The moment load necessary to produce the critical axial stress on the outer surface of the pipe segment was calculated for each pipe geometry.

As in the tension loading studies, 1×, 2× and 3× this calculated critical load were applied to each of the pipe geometries and crack sizes. Crack displacement values were extracted for the inner and outer diameters for each of the cases. Linear equations were developed for the crack opening behavior for the inner and outer diameter crack centerlines using the displacements found with 2× and 3× the critical load.

Slope and intercept values were determined to describe the crack opening behavior. As in the tension equations, the slope values, which were slightly different for the outer diameter and inner diameter, were averaged to make one correction factor which was applicable to both locations.

The intercept values calculated from this data were determined to be close enough to the values found in the tension case to use the values determined from the tension analysis to apply for both tension and moment loading. Figure H.15 shows the equation modification graphically. The modified equation shows a step at the critical load. The crack is assumed to be closed below this load. Above the critical load, both the ID and OD crack center displacements are represented. The values for C_B and $\sigma_B{}^{\infty}{}_{Critical}$ have been tabulated and are shown in Tables H.12 and H.13, respectively.

This graph can be compared to the one shown in Figure H.11 for the tension case. The GE / EPRI equation line was constructed using the improved V_1 values from Table H.7 (Ref. H.6), and the correction factors created were based on these values as well. The graph shows a similar situation as is shown for the tension case. The GE / EPRI equation over predicts the crack opening displacement in this case where the weld residual stresses hold the crack closed until some critical stress level is reached.

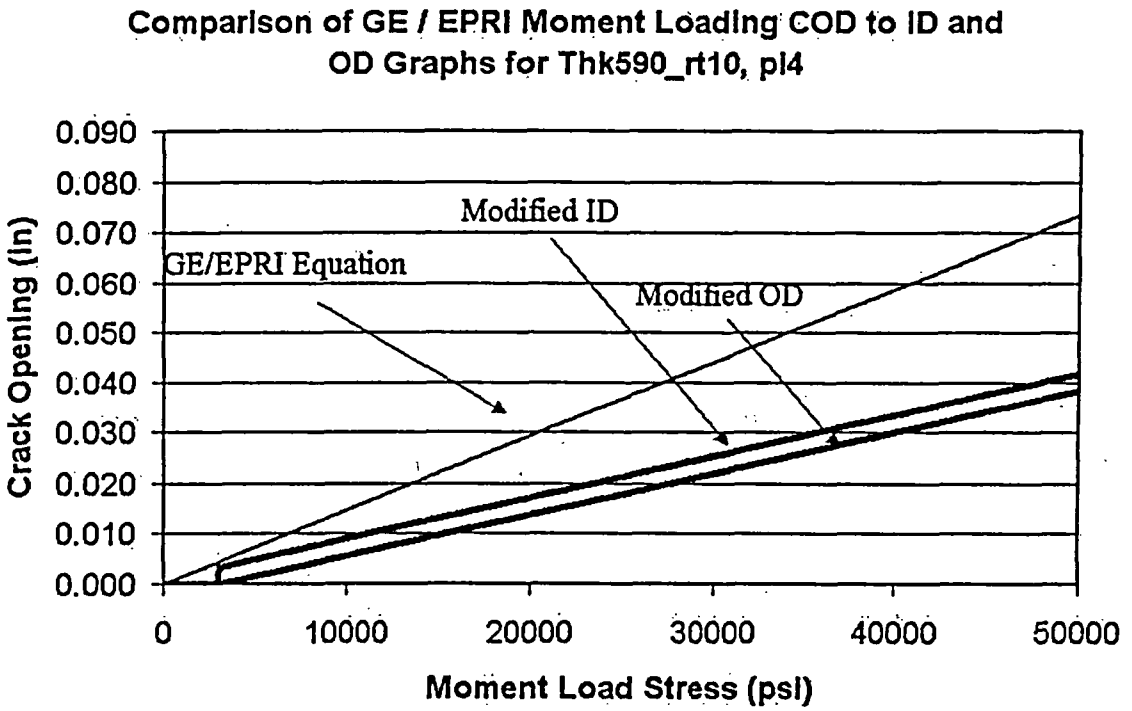

Figure H.15 GE/EPRI bending equation modification

The modification factors for bending are shown in Table H.12. They are to be used with the original slope factors for bending from Table H.7, and can be combined with the tension loading equation as shown in Equation H.6.

Table H.12 C_1 values for moment loading (C_B)

		Thickness, mm (inch)			
		7.5 (0.295)	15 (0.59)	22.5 (0.886)	30 (1.181)
R/t	θ/π	I_{OD}			
5	1/16	0.397	0.711	0.586	0.608
5	1/8	0.874	0.672	0.662	0.676
5	1/4	0.480	0.574	0.549	0.573
5	1/2	0.369	0.446	0.410	0.441
10	1/16	0.699	0.706	0.651	0.695
10	1/8	0.641	0.703	0.660	0.686
10	1/4	0.501	0.541	0.489	0.520
10	1/2	0.258	0.276	0.253	0.266
20	1/16	0.763	0.758	0.749	0.776
20	1/8	0.677	0.700	0.661	0.698
20	1/4	0.376	0.384	0.355	0.382
20	1/2	0.105	0.106	0.101	0.105

The critical bending stresses necessary to open the pipe cracks are shown in Table H.13. These values are based on the stress on the outer diameter of the pipe with the center of the crack aligned with the maximum tension stress in bending. These values apply to pure moment loading only. If the combined loading equation is used as shown in Equation H.6, then the critical load is calculated for the unique tension and bending load combination simply by finding the stress value at which both the inner diameter and outer diameter crack centers are open. The following combined tension and bending load example will help make the use of the correction factors clearer.

Table H.13 $\sigma_B^{\infty}{}_{Critical}$ values for moment loading kPa, (psi)

		Thickness mm, (in.)			
R / t	θ/π	7.5, (0.295)	15, (0.59)	22.5, (0.886)	30, (1.181)
5	1/16	231369, (33557)	127554, (18500)	44471, (6450)	36267, (5260)
5	1/8	190986, (27700)	54883, (7960)	29165, (4230)	23787, (3450)
5	1/4	77222, (11200)	57847, (8390)	19926, (2890)	14617, (2120)
5	1/2	41300, (5990)	26752, (3880)	8619, (1250)	2572, (373)
10	1/16	96300, (13967)	37584, (5451)	23029, (3340)	13927, (2020)
10	1/8	51649, (7491)	25483, (3696)	14203, (2060)	9929, (1440)
10	1/4	54338, (7881)	20291, (2943)	10342, (1500)	6419, (931)
10	1/2	31771, (4608)	10818, (1569)	5357, (777)	2434, (353)
20	1/16	31716, (4600)	12893, (1870)	9446, (1370)	5716, (829)
20	1/8	23994, (3480)	9653, (1400)	6005, (871)	4854, (704)
20	1/4	22684, (3290)	7584, (1100)	4461, (647)	3634, (527)
20	1/2	17582, (2550)	5509, (799)	3123, (453)	2827, (410)

H.8 COMBINED TENSION AND MOMENT LOAD EXAMPLE

An example will help illustrate the use of Equation H.6 and the significant difference in crack opening displacement from the results found with Equation H.5. This example will look at a case in which real world loads will be used. The loading in this case is from the design values used for the Unit # 2 surge line in the Beaver Valley plant. The pipe is 31.6 mm (1.246 in.) thick and has a mean radius to thickness ratio of 5.11. The internal pressure is near standard operating pressure for a PWR of 14.9 MPa (2,160 psi.). The bending load is 187.67 kN-m (1,661,000 in-lb). All four crack half-lengths will be examined ($\theta = \pi / 16, \pi / 8, \pi / 4, \pi / 2$). The pipe is made from type 316 stainless steel with a Modulus of Elasticity of: E = 206,840 MPa (30×10^6 psi.).

The first step is to calculate the coefficients for Equation H.6. The crack half length (a) is equal to $R\theta$ and has been calculated to be equal to the following values for the four crack sizes [$\pi / 16$: a = 29.4mm (1.16 in.), $\pi / 8$: a = 56.6 mm (2.32 in.), $\pi / 4$: a = 117.9 mm (4.64 in.), $\pi / 2$: a = 235.5 mm (9.27 in.)].

The loads applied to the pipe segment must be converted into terms of tension and bending stress to be used in the equations. The tension load can be converted into terms of stress by dividing it by the cross sectional area of the pipe. The cross section of the finite element pipe model with the 1.181 inch thickness and radius to thickness ratio of 5 was used as a check because this model was used, with these loads applied. The tension stress calculated to be 31,026 kPa (4,500 psi). The bending stress must be calculated using the equation $\sigma_B^\infty = MR_{OD} / I$, and came out to be 96,451 kPa (13,989 psi).

The second step is to look up the tabulated values for the equation variables in Tables H.5, H.7, and H.9 through H.12. This process can be best illustrated with a table showing the different factors and calculations for each of the four crack sizes, see Table H.14. V_T is found in Table H.5, and V_B is found in Table H.7. C_T is found in Table H.9, and C_B is found in Table H.12. The intercept coefficients I_{OD} and I_{ID} are found in Tables H.10 and H.11, respectively. The example values of thickness and R / t are considered close enough to the tabulated values to use those values without modification. If they were further away from the tabulated values, interpolation could be used.

Table H.14 Combined loading example factors

θ (rad)	a (in)	4a/E (in^3/ lb)	V_T	C_T	V_B	C_B	I_{OD}	I_{ID}
$\pi / 16$	1.1594	1.546E-07	1.05	0.813	1.234	0.608	0.00038	-0.0005
$\pi / 8$	2.3189	3.092E-07	1.202	0.894	1.388	0.676	0.00049	-0.00038
$\pi / 4$	4.6378	6.184E-07	1.827	0.726	2.008	0.573	0.0005	-0.00025
$\pi / 2$	9.2756	1.237E-06	6.367	0.868	5.331	0.441	0.00055	0.00004

Table H.15 Calculated results for modified equation and GE / EPRI

θ (rad)	Calculated Results δ_{OD}	Calculated Results δ_{ID}	GE / EPRI Results GE δ	Ratio of COD with residual stresses to COD without residual stresses (inside diameter)
π / 16	0.00266	0.00164	0.003399	0.48
π / 8	0.00667	0.00468	0.007676	0.61
π / 4	0.01596	0.01247	0.022454	0.56
π / 2	0.07657	0.071839	0.127665	0.56
Average				0.55

Table H.15 shows a comparison of the resulting crack opening displacement predictions using the modified equations which include the effects of weld residual stresses, and the GE / EPRI equation. The results are better visualized in Figure H.16 which shows a bar graph of crack opening displacement for the various crack sizes and a single loading case. The important fact to note is that the crack size is governed by the smallest crack opening displacement. For this example, the smallest displacement can be found on the pipe inner diameter. The crack opening displacement for the inner diameter averages only 55 percent of the crack opening prediction of the GE / EPRI equation which does not include the effect of weld residual stresses.

Running an elastic-plastic finite element model including this combined loading scheme made a check of the predicted results. The results predicted by the equations very closely matched the displacements predicted by the finite element model for all but the crack size of π / 2, which was under predicted by both the modified equations and the GE / EPRI equation. It should be remembered that the predictive equations were developed using the displacements found at 2 times and 3 times the load necessary to start to open the crack. The predictive models are designed to work in the linear region of material behavior, and break down with loads or displacements that are too great. The equations can only be expected to be accurate in the range of loads that are in, or slightly beyond, the range of zero to three times the critical opening load. The bending load for the π / 2 crack is actually 34 times the critical load and gives a poor match while the smaller crack sizes which range from 17 times to 27 times the critical bending load make a good prediction. One thing is clear, that welding induced residual stresses reduce crack opening displacements in the linear displacement range, and that the predictions used for pipes with no residual stresses over-predict the crack opening displacements for these cases.

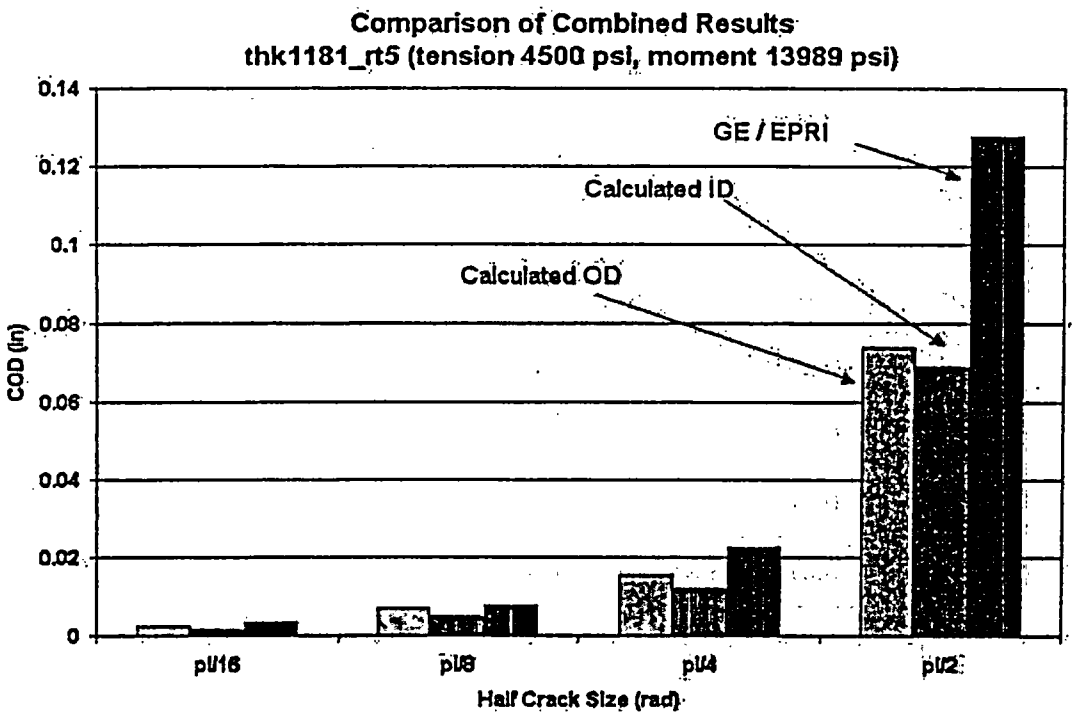

Figure H.16 Comparison of results from combined loading example

H.9 CONCLUSIONS REGARDING WELD RESIDUAL STRESS EFFECTS ON COD

The results found in this study reinforce the previously held belief that circumferential through wall cracks in pipes behave differently when they are located in a weld than when they are located in an area free from residual stresses. Correction functions have been tabulated for use in modifying the GE/EPRI linear elastic crack opening displacement equation to better predict crack opening behavior for pipe cracks in welds. The example used shows one instance in which the modified equation predicts a smaller crack opening displacement than does the GE/EPRI equation. This is significant in the case in which an attempt is made to back-calculate crack length from postulated pipe leakage rates, such as the case in traditional LBB analyses. Crack lengths can be calculated using the known leakage rates, calculated crack opening areas and crack opening displacements, among other factors. If the crack opening area is over predicted, as is the case with the GE/EPRI solution in the example above, the crack length will be under predicted. The equation modification factors provided in Tables H.8 through H.13 can be used to better predict crack opening behavior, which will lead to better LBB evaluations.

This work is also applicable only to type 316 stainless steels. Though it is thought that other materials with similar thermal and strength properties will behave similarly, this hypothesis must be evaluated.

H.10 WELD START-STOP EFFECTS

The previous analyses describing the effects of weld residual stresses on crack opening displacements assumed that the welds were deposited uniformly for the entire circumference of the pipe segments analyzed. The residual stress state of the pipes was developed in an axis-symmetric model. The axis-symmetric results consisting of stresses and plastic strains (if needed) were then transferred to a full three dimensional model. The full three-dimensional model was then in an axis-symmetric state of stress. When the cracks were introduced into the three-dimensional model, the stresses redistributed to eliminate the axis-symmetric nature of the stress. An axis-symmetric analysis of the welding process essentially assumes that

the entire pass is deposited at once along the entire circumference.

In actual pipe welds there is a start and stop point of each weld pass which causes a discontinuity of the stress state in the pipe at this location. While an axis-symmetric analysis is not physically realistic, experience over the years has shown that an axis-symmetric analysis is reasonably accurate for regions away from the start/stop location of an actual pipe weld. This stress discontinuity near the start/stop region of the weld has an effect on crack opening behavior in and near the weld. It is important to know what this effect will be with regard to the results presented from the previous COD analysis. This section of the report will describe a study of crack opening behavior in a pipe model with a full three dimensional weld of seven passes where each pass starts and ends at the same point. An analysis in which the start and stop location of each weld pass is in the same location should be expected to show the most severe example of the start-stop effect on crack opening displacement. In some actual field welds, the passes start and stop at different locations around the circumference, which will lead to a more uniform stress state in the pipe. The following provides a summary of (i) weld start/stop effects on the residual stress state in pipe welds and (ii) the effect on the COD when the crack approaches and grows through a start/stop region of a pipe weld.

H.10.1 The Start/Stop Weld Model

The model used for the analysis is the same as the one described in Appendix G of this report. The model is shown in Figure H.17. The pipe is a bimetallic weld made from several materials, as shown. This represents the geometry of the V. C. Summer bimetallic hot leg pipe weld analyzed in detail in Appendix G. The purpose of the analysis shown in Appendix G was to investigate the growth of pressurized water stress corrosion cracking (PWSCC) in the bimetallic hot leg welds. The welds joined a reactor vessel nozzle to a stainless steel pipe using inconel weld filler metal. The pipe was modeled with a seven-pass weld in which all have the start and stop locations of the weld passes were at the same location around the pipe circumference. Each weld pass traverses 360 degrees of the pipe. The nozzle (made of A508 steel) is 3.22 inches (81.8 mm) thick and has a radius-to-thickness ratio of 5 while the stainless steel pipe is 2.33 inches (59.2 mm) thick with a radius-to-thickness ratio of 6.7. The outer diameter of the nozzle was machined so that the outer diameter of the both the nozzle and stainless steel pipe were equivalent. This machining extended for about 1.5 to 2 thicknesses away from the edge of the weld (see Figure G.19 in Appendix G for more details).

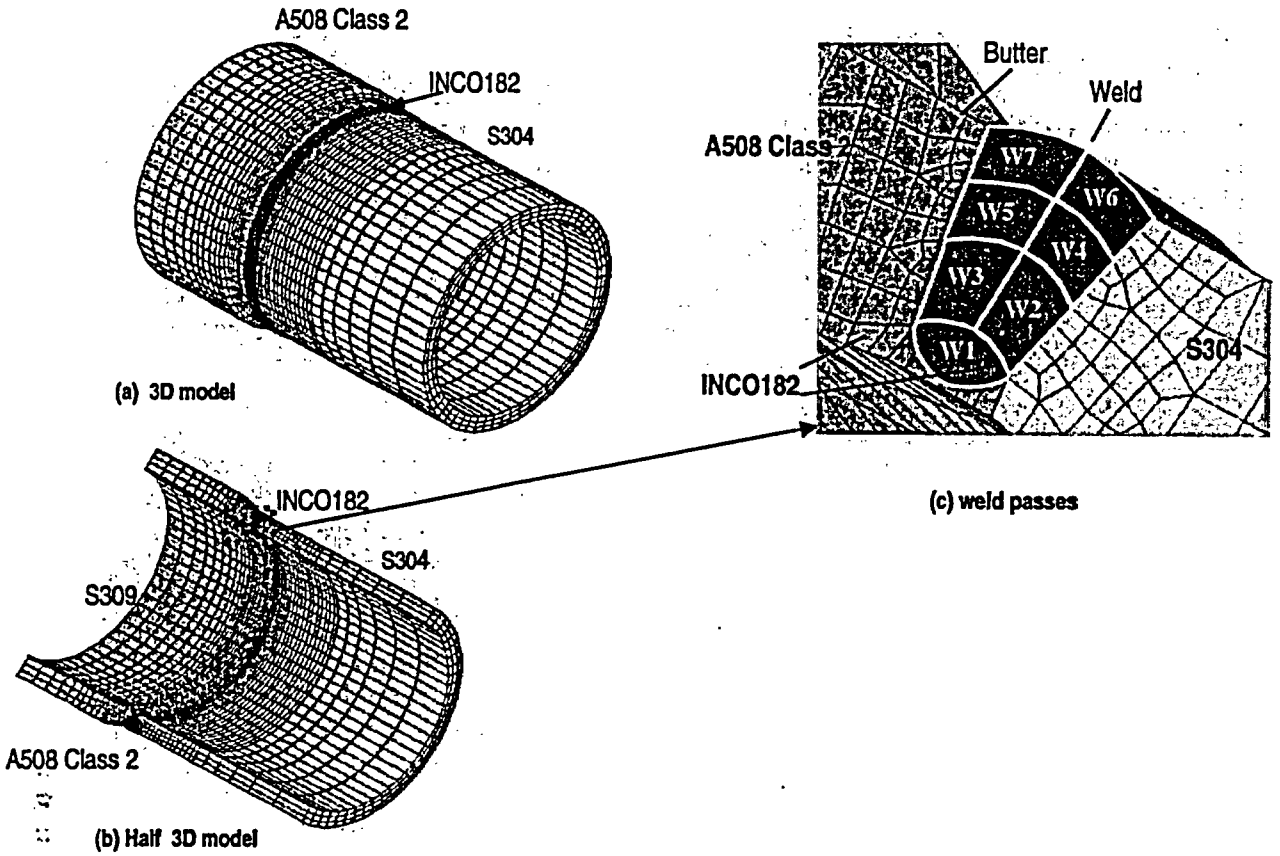

Figure H.17 Start – Stop weld analysis model

One will notice, from examination of Appendix G, that this analysis neglected the effect of the buttering, post weld heat treatment, and weld repair. In addition, the weld passes were lumped to produce seven passes instead of the 21 passes used in the axis-symmetric analysis in Appendix G. By comparing the detailed axis-symmetric solution results to this three dimensional analysis, it is seen that similar trends between the solutions are obtained for regions away from the start/stop locations.

There were two reasons that this bimetallic weld was chosen for this weld start/stop effect study. First, in the actual V. C. Summer hot leg bimetallic weld that experienced field cracking, a significant amount of leaking occurred that was not detected by leak detection equipment, and the crack was not discovered until a scheduled outage. This analysis can provide an estimate of the expected crack opening behavior in similar bimetallic pipe welds to provide understanding of the effects of bimetallic weld residual stress effects on COD (and hence leak rates). Second, the model was readily available and will provide information regarding start/stop effects on generic mono-material as well as bi-material welds.

The materials and geometry of this model are different than those used in the crack opening displacement analyses discussed earlier in this appendix. Hence no direct comparison will be made between the prior and new results presented here. Instead, a qualitative comparison will be made between the crack opening displacements in this pipe model when the cracks are located in the start-stop location, and then in a separate analysis with the crack placed 180 degrees from the start-stop location.

Quarter symmetry models were used in the previous analyses to describe the crack opening displacements. Because of the varying stress field 360 degrees around the circumference of a pipe segment with start-stop weld effects, a full model of the pipe segment was required here. The model is shown in Figure H.17. Node constraints along the weld centerline were used to create the cracks in the previous quarter symmetric models. Node constraints were sequentially released to simulate the growth of the crack. A similar method was used in these full models. The model was split into two halves at the weld centerline. Kinematic nodal constraints were used to join the two halves of the model along the centerline of the weld, and these constraints were released to allow a crack to grow in the pipe segment. As was done previously, four crack lengths were studied with half crack lengths, θ, equal to $\pi / 16$, $\pi / 8$, $\pi / 4$ and $\pi / 2$. A total of eight analyses were performed to find crack surface displacements due only to residual stresses, i.e. with no applied axial load. Analyses were done in which the cracks were centered on the start-stop location of the weld, and also additional cases were examined in which the cracks were placed centered 180 degrees from the start-stop location of the weld. This method allowed a direct comparison of the weld start-stop effects in a pipe segment in the area most affected, and the area least affected by the stress discontinuity that develops at the start/stop location.

H.10.2 Start/Stop Weld Effects on COD – Results

Figures H.18 and H.19 show the baseline axial stresses in the model with no cracks present. In the area of the start and stop of the weld there is a definite difference in the through thickness stress pattern directly before and after the start-stop plane. In the area 180 degrees away from the start stop location, the through thickness axial stress is uniform. Figure H.19 also illustrates the location where the circumferential crack is to be introduced.

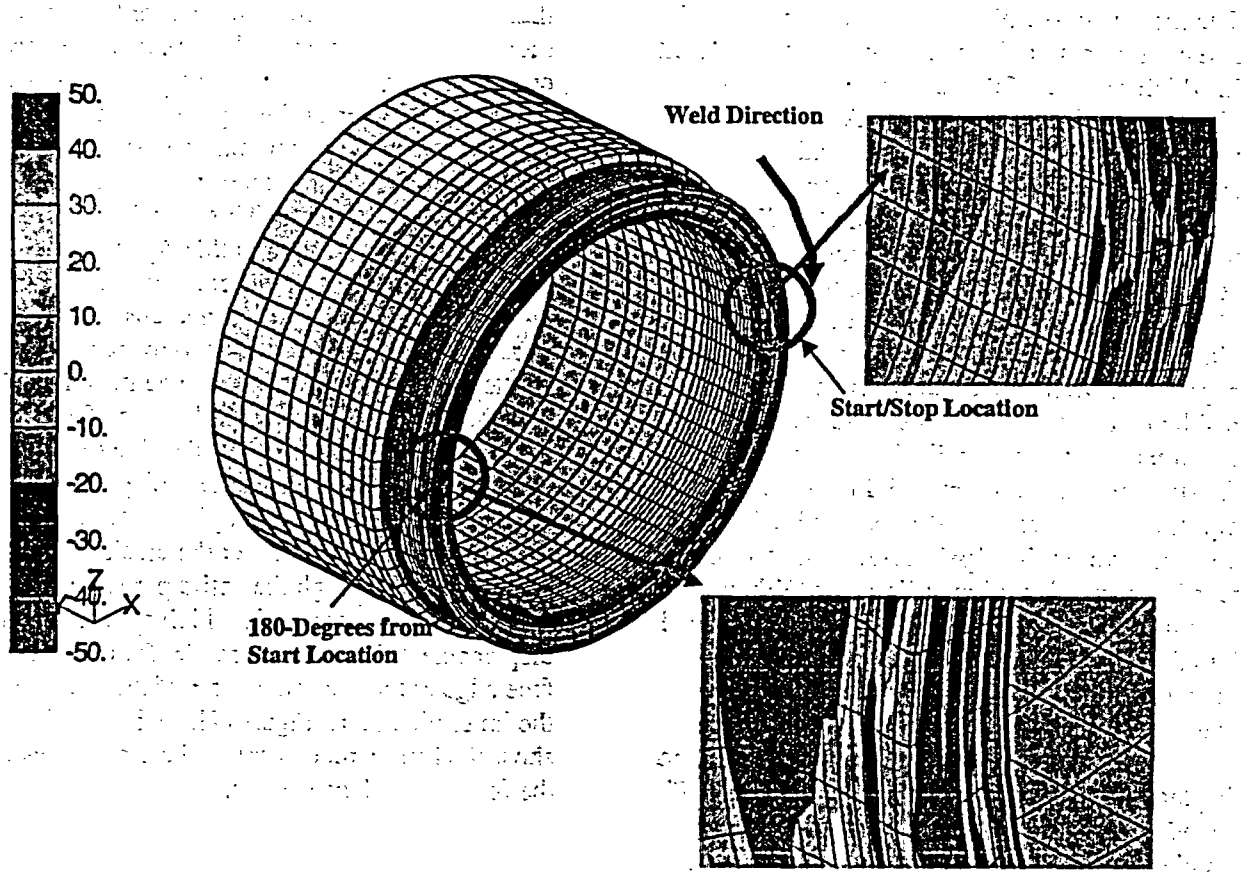

Figure H.18 Baseline weld – axial stresses

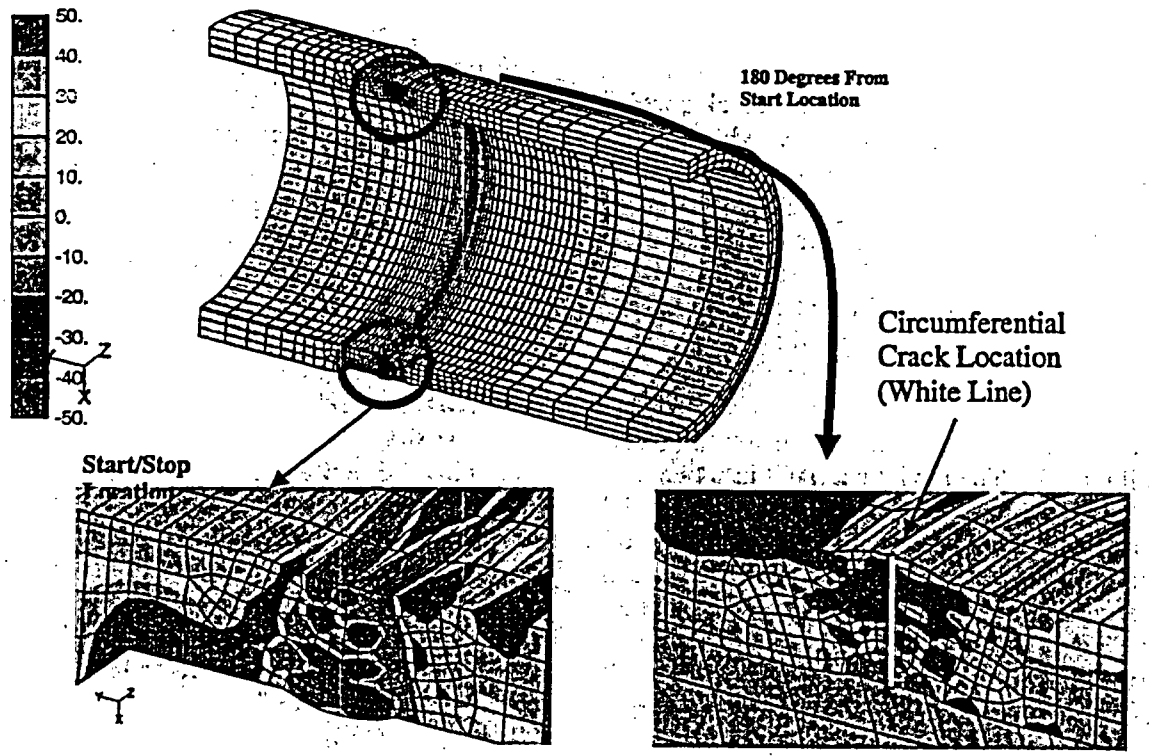

Figure H.19 Baseline weld – axial stresses

The models into which cracks were introduced had constraints on the end of the nozzle segment in which the end of that pipe was fixed in all directions. This represents the A508 steel nozzle-vessel junction. The free end of the smaller diameter Type 304 stainless steel pipe segment was constrained in the radial direction to simulate its connection to a much longer pipe segment, but it was free to move in the axial direction. This set of boundary conditions allowed the crack faces introduced into the pipe segment to freely move due only to the weld residual stresses in the model. As seen in the previous crack opening displacement analyses for stainless steel only material in smaller sized pipes, the weld residual stresses tend to be compressive on the pipe's outer diameter and tensile on the pipe's inner diameter. When a circumferential through wall crack is introduced into this stress field, the crack tends to close at the outer diameter and open on the inner diameter. In reality, the outer diameter crack face would be forced closed (i.e. contact) and no displacement of this crack face would occur. If a model were made in which this effect were simulated, the only crack displacement results that could be obtained would be for the small section of the through wall crack that was forced open due to the tensile stress in the weld toward the inner diameter of the pipe segment. No attempt was made in this case to make a contact model in which the compressive crack faces would meet each other. This was done in the studies described earlier in this Appendix, and including the effect of this contact had a minimal effect on COD when a tensile load is applied of such magnitude as to overcome the contact compressive stresses. The model used here was constructed so that the crack faces would rotate freely on both sides due to the weld residual stresses present. These displacements were examined to get a full picture of how the weld residual stresses affect the crack face displacement through the entire pipe thickness. Results graphs were made which show the full displacement found in the model for the crack face edge at the outer diameter of the pipe and at the inner diameter. Figures H.20 through H.23 show the full displacement of the crack faces for the four crack sizes studied.

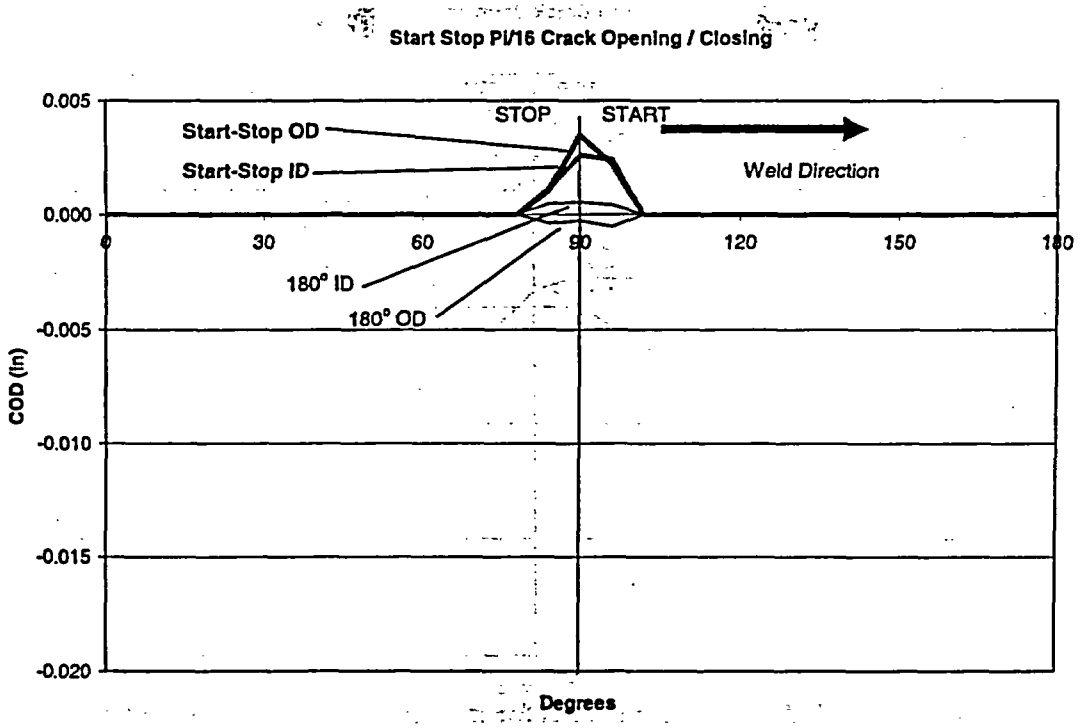

Figure H.20 Crack displacement results for π / 16 crack in start-stop location and 180 degrees away from the start-stop location

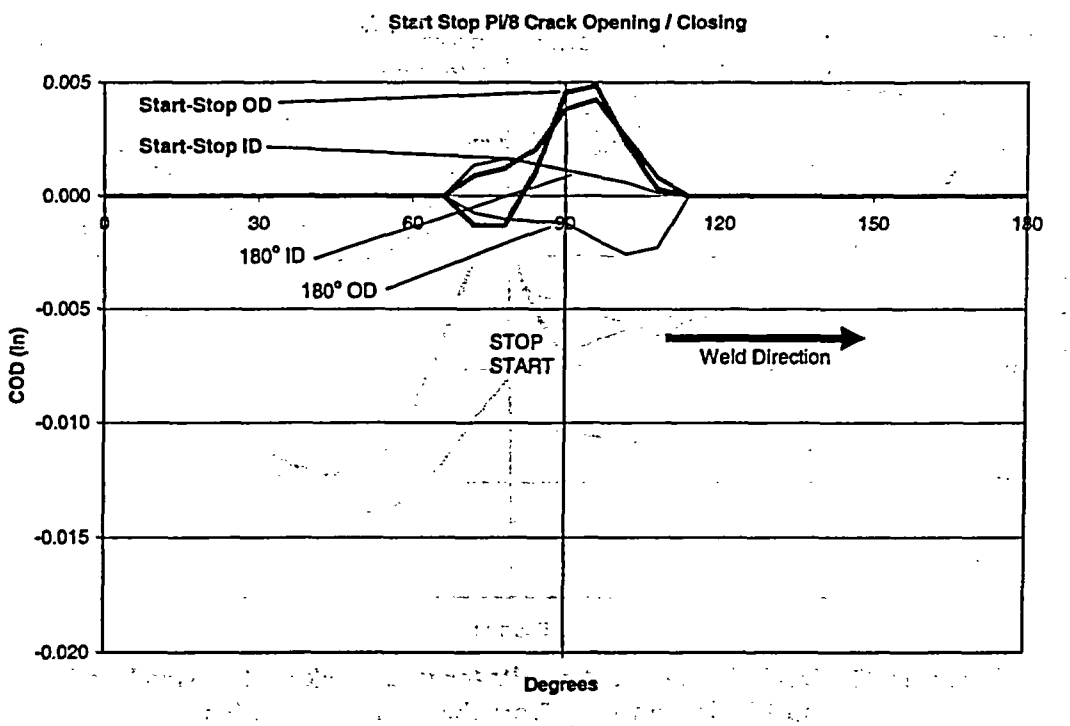

Figure H.21 Crack displacement results for π / 8 crack in start-stop location and 180 degrees away from the start-stop location

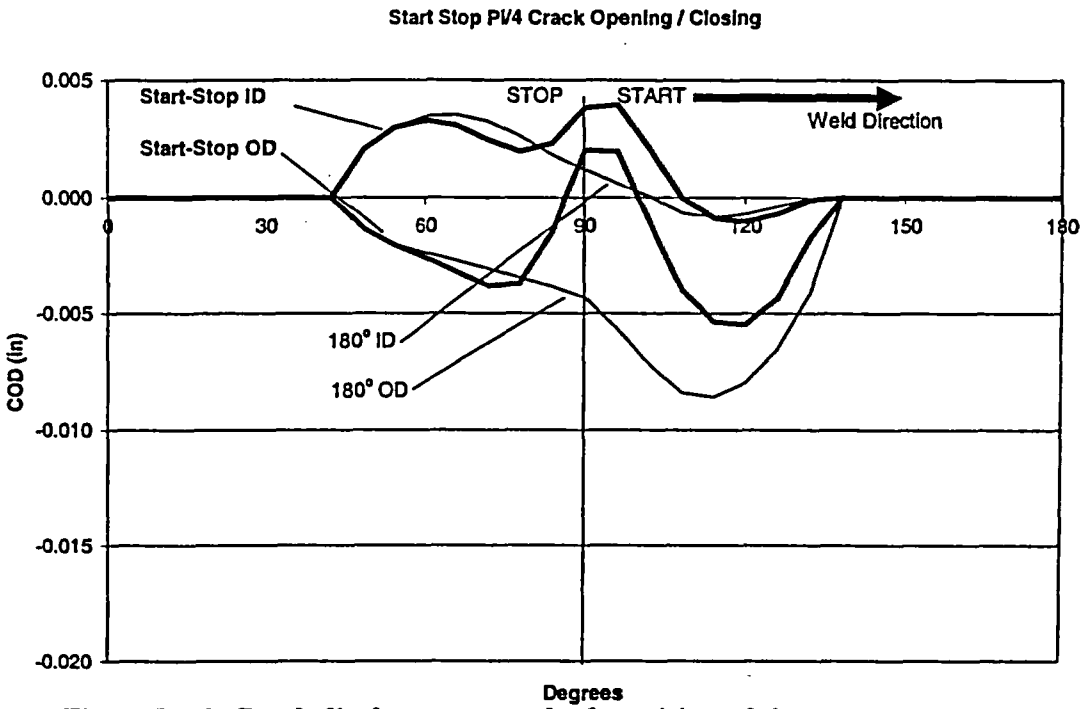

Figure H.22 Crack displacement results for $\pi / 4$ crack in start-stop location and 180 degrees away from the start-stop location

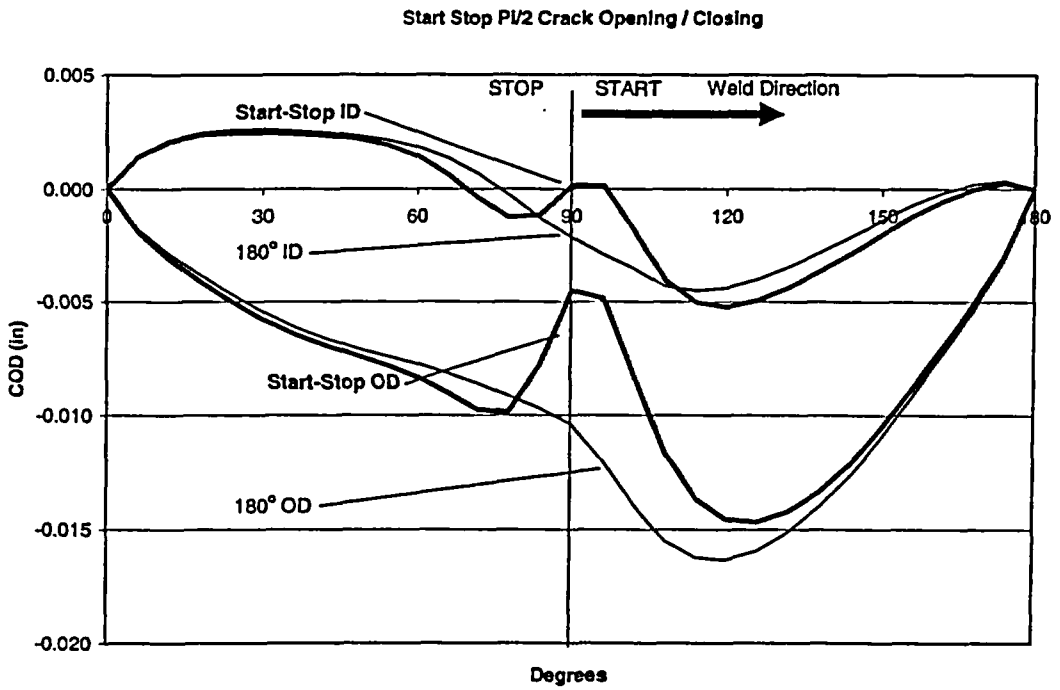

Figure H.23 Crack displacement results for $\pi / 2$ crack in start-stop location and 180 degrees away from the start-stop location

Each of the displacement results graphs represents a different crack size, and they are shown in the order of increasing crack size. Each of the graphs displays the results for a crack placed with its center on the start-stop line of the weld, and also the results for a crack placed 180 degrees away from the start-stop location of the weld. Also, each of the graphs has been made to the same vertical and horizontal scale so that comparisons between the displacements found in cracks of different sizes are easier to make. The horizontal scale in each graph goes from 0 to 180 degrees. The cracks were centered on the location that is designated as 90 degrees in each of the graphs. The weld direction is indicated on each of the graphs. The displacement results for the cracks in the start-stop location are indicated with heavier lines and with notes and leaders. The crack displacements for the locations 180 degrees away from the start-stop location are also indicated with notes and leaders, but with lighter weight lines. The results data are displayed in such a way as to indicate crack opening as a positive displacement, and crack closing as a negative displacement. As discussed earlier, cracks cannot have a negative displacement, but this method is a good way to show variation in the degree of crack closure.

Two things become clear immediately when looking at all of the crack displacement results at once. Firstly, the cracks in the start-stop region are more opened than those placed 180 degrees away from the start-stop region, and secondly, the start-stop effect is important primarily in an area within ± 15 degrees from the start-stop point.

The smallest crack size ($\theta = \pi / 16$) shows the greatest discrepancy between the crack behavior in the start-stop region and the crack 180 degrees away (again, recall that the total crack size is 2θ). The crack in the start-stop area is completely open over the crack's entire length. The total gap, maximum crack opening, between crack faces, is 0.089 mm (0.0035 inches) on the outer diameter of the pipe and 0.066 mm (0.0026 inches) on the inner diameter. The crack 180 degrees away from the start-stop location behaves similarly to the results from the previous non-start/stop crack opening displacement analysis. COD is forced closed on the outer diameter as indicated by the negative displacement value of -0.0137 mm (-0.00054 inches) while the inner diameter is forced open by an almost equal amount of 0.0140 mm (0.00055 inches).

The second smallest crack size ($\pi / 8$) shows similar behavior. The crack in the start-stop location is almost completely open. The outer diameter edge has a maximum crack opening gap of 0.122 mm (0.0048 inches) while the inner diameter has a gap of 0.107 mm (0.0042 inches). The crack in the area opposite the start-stop location has the predicted behavior of a uniform weld stress field. It is closed on the outer diameter and open on the inner diameter. The maximum closure is -0.066 mm (-0.0026 inches) while the maximum crack opening gap is 0.041 mm (0.0016 inches).

The crack with a half crack length of $\pi / 4$ gives an indication of the extent of the area affected by the weld start-stop region. The crack behavior in the start-stop region and the non-start-stop region are almost exactly the same from the left side of the crack to within 15 degrees of the centerline of the crack. The outer diameter of the crack is forced closed, and the inner diameter edge is forced open. Within ± 15 degrees of the start-stop location is where the residual stress effects from the start-stop region have their greatest influence, and the two cracks look completely different in this area. The crack in the start-stop region is completely open in the range of ± 5 degrees from the start-stop point. Once beyond 15 degrees in the weld direction from the start point, the cracks behave similarly again. The inner diameter edge displacements are almost the same for the start-stop crack and for the crack on the opposite side of the pipe. The outer diameter displacements both increase toward zero with a similar slope, but the start-stop crack is less closed on the outer diameter.

The final figure shows the behavior of the crack which has grown to half the circumference of the pipe ($\theta = \pi / 2$). The results look like an expanded version of the previous crack size.

From the left side to within 10 degrees of the start-stop location, both the crack centered in the start-stop area and the one placed 180 degrees away behave almost exactly alike with the inner diameter cracks open and the outer diameter cracks closed. In the start-stop affected region, the crack is more open, but in this case, not completely open. The inner diameter opens a small amount over a 6 degree length, but the outer diameter remains firmly closed, though less so than the crack on the opposite side of the pipe. Once beyond 15 degrees in the weld direction from the weld start point, both cracks behave almost the same again for both the inner diameter and the outer diameter.

General Conclusions. As stated earlier, some general conclusions can be made from the results found in this study. If a crack forms in the start-stop region of a weld, it will be generally more open than one that forms away from this region. The start-stop effect is most pronounced in a range of ± 15 degrees from its center, though there is a pronounced sinusoidal effect which progresses around the circumference and affects axial displacement results in the larger crack sizes. This seems to indicate that the start-stop effect has a more subtle effect on the stress state throughout the weld. The earlier analyses, in which equations were developed to predict crack opening displacements in terms of applied loads, are useful because they can be used as a method to indirectly determine crack lengths from measured leak rates and calculated crack opening displacements. The results of this start-stop analysis show that cracks that form in the start-stop area will be more opened than cracks that form in non-start-stop areas. Thus, ignoring the effect of start/stops would lead to a conservative estimation of the postulated leakage through-wall crack length in a leak-before-break assessment. This is because crack length is back calculated from an assumed crack area for a certain leak rate. The area is based on the crack opening displacement (COD) and the crack length. If the COD were more open in a start-stop area than would be predicted in a non-start-stop area, then the crack length would actually be shorter in the start-stop area than predicted, which is conservative. Of course, only one pipe geometry and size was evaluated in this analysis, and the results should be looked at more qualitatively than quantitatively. A range of pipe sizes and radius to thickness ratios should be studied to get a better understanding of the start-stop effect in a wider range of situations.

H.10.3 Start/Stop Weld Effects on COD – Discussion

There are several interesting general results that were obtained from this study that deserve further discussion. Three subjects are discussed in more detail here.

Bimetallic Welds. The weld start/stop effect study was performed on a bimetallic weld for large diameter, thick pipe, which had the dimensions of the V. C. Summer hot leg pipe that experienced a pin hole sized indication in service. The pinhole emanated from a through-wall axial crack that grew in the IN82/182 weld material driven by hoop residual stresses. This is expected since weld hoop residual stresses are larger, and nearly fully tensile, compared with axial stresses, which alternate between tension and compression through the pipe wall. PWSCC is driven by tensile stresses. In this weld start/stop study we concerned ourselves with circumferential cracks since these are considered more severe than axial cracks since a circumferential crack can rupture the pipe and lead to rapid coolant loss. It is unlikely that a circumferential crack will grow through the pipe wall if driven mainly by weld residual stresses. Rather, a large part through crack can develop, which could potentially lead to a complex crack in service.

This is illustrated in Figure H.24, taken from References H.7 and H.8. This consisted of an analysis of a core shroud weld. This diameter of this shroud is very large but is rather thick (see Figure H.24). The axial residual stress pattern in this vessel is typical of that in thick wall pipe, i.e., tension at the ID, compression in the mid thickness region, and tension again at the OD in the weld region (see References H.7 and H.8). References H.7 and H.8 were concerned with the crack growth behavior of a core shroud where

the main loading is that from the weld induced residual stress field. From an axis-symmetric crack growth solution, where the crack is a full 360 degrees, the results indicate that a crack growing from the inside to the outside vessel surface, or vice versa, would likely stop growing since the K values reduce to negative values for the deeper cracks. This is because the cracks grow into compressive residual stress fields. For a surface crack (Figure H.24) introduced using the finite element alternating method, the position of maximum K shifts from the deepest point of the crack to positions near the intersection of the surface crack and the pipe inner surface as the crack becomes deeper. In fact, for cracks deeper than 0.5 inches, K becomes negative at the deepest point of the crack. This suggests that the cracks, if driven by corrosion mechanisms, which depend on K, will tend to grow long in the angular direction and much slower in the depth direction. Indeed, we expect the tendency for full 360 degree cracks to develop. In many nuclear piping components, 360-degree cracks do develop (see Reference H.9). The potential for this type of crack growth certainly exists in bi-metallic welds of the type considered here.

Stress Redistribution After Introduction of Through-Wall Cracks. The study of residual stress effects on COD's for one material (Type 316 stainless steel) presented earlier in this appendix, suggested that:

- Circumferential cracks will tend to open in regions where tensile weld residual stresses develop for pipe thickness' less than about 0.6-inch. For this size pipe, the axial residual stress field is typical of the bending type, tension on the ID and compression along the OD. As such, the cracks opened at the ID and closed at the OD of the pipe.

- For intermediate thickness pipe (0.89-inch), the COD's also opened at the ID and closed at the OD. For this thickness, the axial residual stress fields were more complicated, typically with tension at the ID, reversing to compression near mid-thickness, back to tension, and finally reversing back to compression near the OD. For this case, the ID tensile field did not reverse to compression until about one quarter of the pipe wall thickness, depending on the R / t ratio.

- For the thick pipe (about 1.2 inches thick), the axial residual stress field started with tension at the ID. However, the stresses very quickly reversed to compression at a distance less than a tenth of an inch through the pipe wall. They then reversed to tension about halfway through the pipe wall, and then back to a low level of compression for a short distance near the OD. For this case, the ID COD closed and the COD on the OD opened – the opposite pattern compared with all other pipe thickness.

All of the above comments can be verified by studying the attachment to this appendix. For the bimetallic weld considered here, which is a very thick pipe of different materials, the stresses are nearly compressive at the ID (see Figure H.19) for nearly half the wall thickness, and become tension for the outer half of the wall thickness. This is a 'bending' type distribution, but opposite in sign to the thin pipe distribution. Of course, the three dimensional analysis case produces a more complicated stress distribution compared with the axis-symmetric distribution considered for the Type 316 stainless steel pipe. From this, one would expect the COD on the pipe ID to close and at the OD to open. However, as seen in Figures H.20 to H.23, the opposite of what is intuitively expected occurs – the ID is open and the OD is closed! The results were double-checked and the analyses were redone using a different crack introduction and analysis scheme, and results validated as correct.

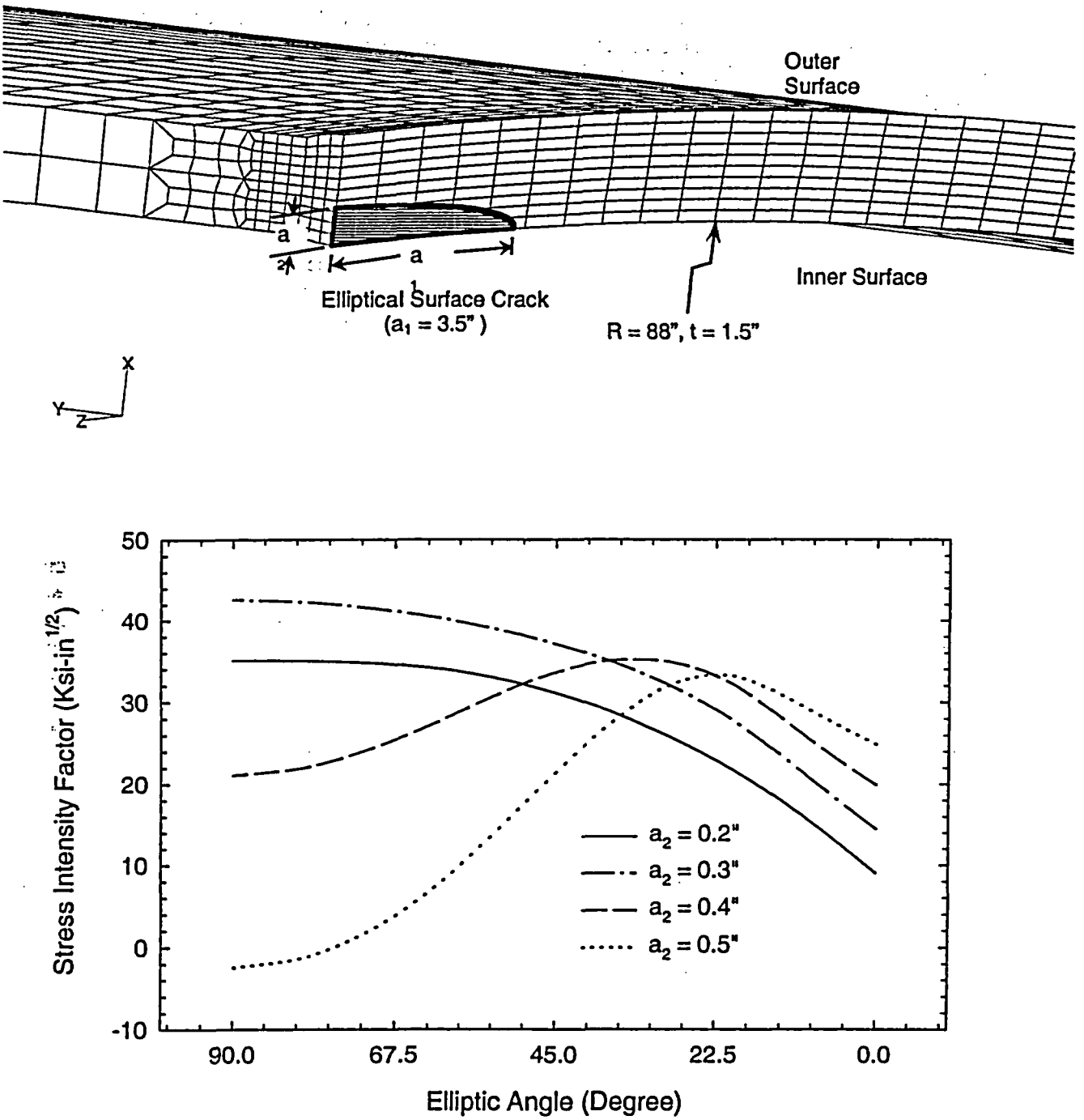

Figure H.24 Stress intensity factors for a surface crack growing through a residual stress field. Crack length, a1, remained constant while the crack depth, a2, increased (Taken from References H.7 and H.8)

There are several possible reasons for this behavior, but it is difficult to suggest which is more plausible. The complicating factors include:

- This is a bimetallic weld, with the A508 nozzle vessel steel being machined down so that, at the weld, the OD is the same as that of the Type 304 stainless steel pipe it is being welded to (see Figures H.17 to H.19). This stiffness difference near the weld region may contribute to the COD's opening and closing in directions contrary to intuition.

- As discussed earlier with regard to the Type 316 stainless steel COD study earlier, hoop residual stresses do indeed play an important role in the crack opening behavior when a crack is introduced. In fact, from Figure G.62 in Appendix G, it is seen that large compressive hoop residual stresses exist over a small region at the pipe weld ID, changing to large tensile values throughout the rest of the pipe thickness. This can introduce crack face rotation as the cracks are introduced. The key point is that it is a more complicated process, especially for thick bimetallic pipe, and analyses may be required on a case by case basis to determine the COD behavior.

- Finally, the three-dimensional nature of the stress field, with the start-stop region reversing the residual stress directions, can contribute to unexpected COD's after introduction of a crack.

Elastic-Plastic Deformation Effects on COD. The analyses included the effect of plastic deformation and strain history during the introduction of the cracks. Another analysis was performed where only the residual stresses were included. For this second analysis case, plasticity was included during the COD introduction into the pipe – but not the history of plastic straining. This second case was performed in part to validate the analysis results (i.e. second case analysis). However, in many cases analyses are performed where only the residual stresses are included (with no plastic strain history) for convenience and because including the entire history is more difficult. Figure H.25 shows the COD's for both cases. The COD patterns are very similar in shape for both cases. However, it is seen that including the history results in larger COD magnitudes.

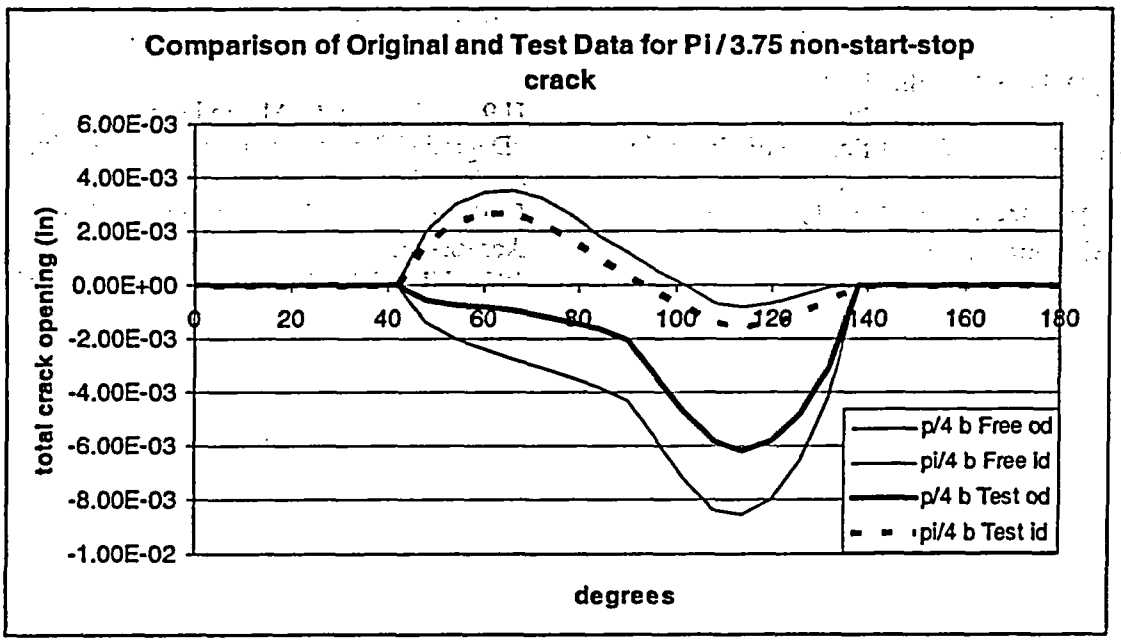

Figure H.25 COD analysis including residual stresses and plastic strain history (thin lines) and only including residual stresses (denoted 'test')

H.11 REFERENCES

H.1 Kumar, V., German, M. D., 1988, "Elastic-Plastic Fracture Analysis of Through-Wall and Surface Flaws in Cylinders," EPRI Report Number NP-5596, Electric Power Research Institute, Palo Alto, Ca.

H.2 VFT™ (Virtual Fabrication Technology) Software, Licensed Caterpillar Product, Distributed by Battelle, 2001, Columbus, OH.

H.3 Barber, T. E., Brust, F. W., Mishler, H.W., 1981, "Controlling Residual Stresses by Heat Sink Welding," EPRI Report Number NP-2159-LD, Electric Power Research Institute, Palo Alto, CA.

H.4 Brust, F. W., Stonesifer, R. B., 1981 "Effect of Weld Parameters on Residual Stresses in BWR Piping Systems," EPRI Report Number NP-1743, Electric Power Research Institute, Palo Alto, CA.

H.5 Paul, D. D., Ghadiali, N., Rahman, S., Krishnaswamy, P., Wilkowski, G., 1994, "SQUIRT – Seepage Quantification of Upsets in Reactor Tubes, User's Manual," NRC Contract Number NRC-04-90-069, Battelle Memorial Institute, Columbus, OH.

H.6 Brust, F. W., Scott, P. Rahman, S., Ghadiali, N., Kilinski, T. Francini, B., Marschall, C. W., Miura, N., Krishnaswamy, P., Wilkowski, G. M., 1995, "Assessment of Short Through Wall Circumferential Cracks in Pipes – Experiments and Analysis," U.S. Nuclear Regulatory Commission Report Number NUREG/CR-6235, U.S. Nuclear Regulatory Commission, Washington D. C.

H.7 F. W. Brust, P. Dong, J. Zhang, "Crack Growth Behavior in Residual Stress Fields of a Core Shroud Girth Weld". Fracture and Fatigue, H. S. Mehta, Ed., PVP-Vol. 350, pp. 391-406, 1997.

H.8 J. Zhang, P. Dong, F. W. Brust, W. J. Shack, M. Mayfield, M. McNeil, "Modeling of Weld Residual Stresses in Core Shroud Structures", International Journal for Nuclear Engineering and Design, Volume 195, pp. 171-187, 2000.

H.9 Wilkowski, G. M., and others (1989): "Degraded Piping Program - Phase II, Summary of Technical Results and Their Significance to Leak-Before-Break and In-Service Flaw Acceptance Criteria", March 1984 - January 1989, NUREG/CR-4082, Volume 8, March.

ATTACHMENT

ANALYSIS RESULTS INCLUDING AXIAL AND CIRCUMFERENTIAL STRESS PLOTS AND FOR ALL PIPE THICKNESS AND R/t RATIO COMBINATIONS

Pipe Thickness .590", R / t = 10

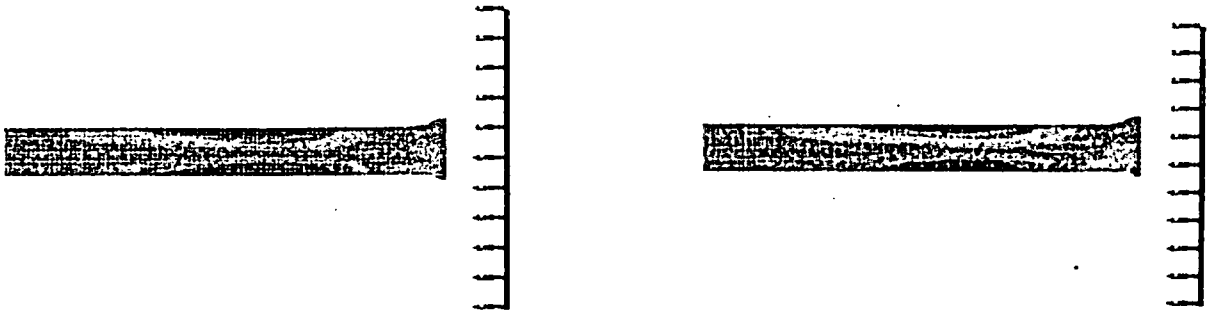

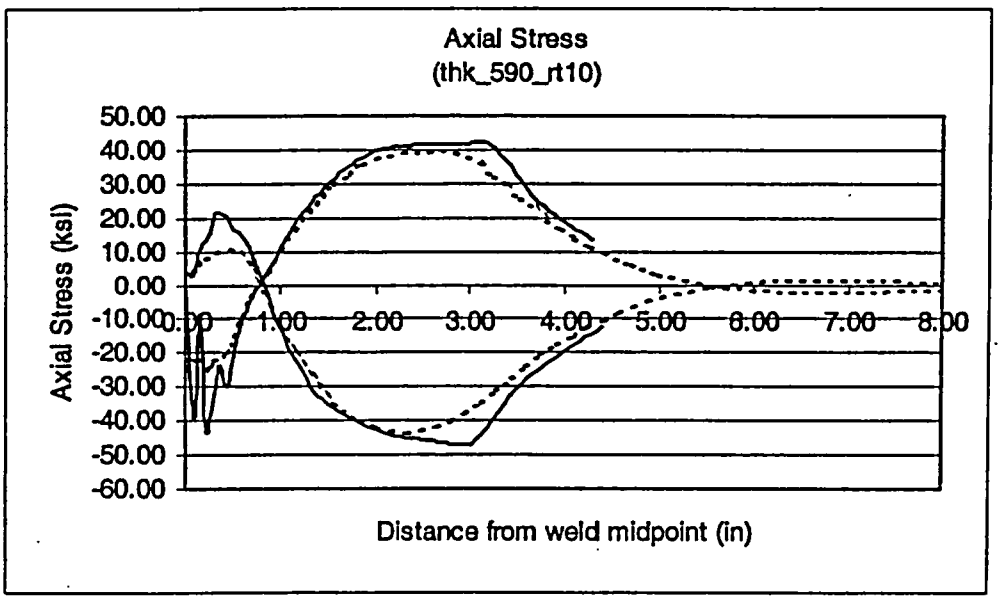

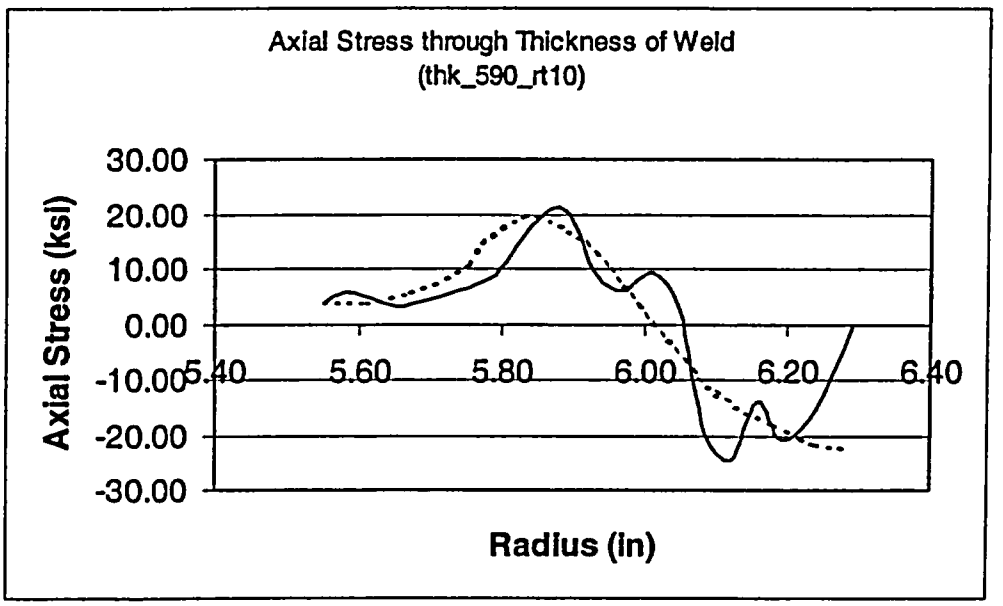

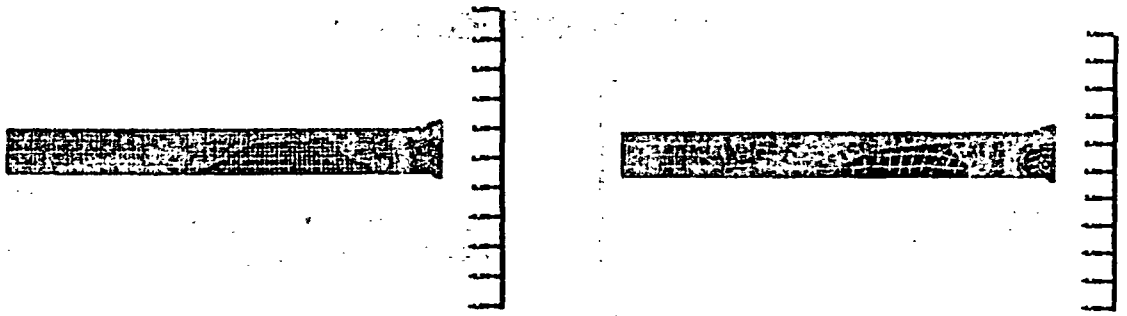

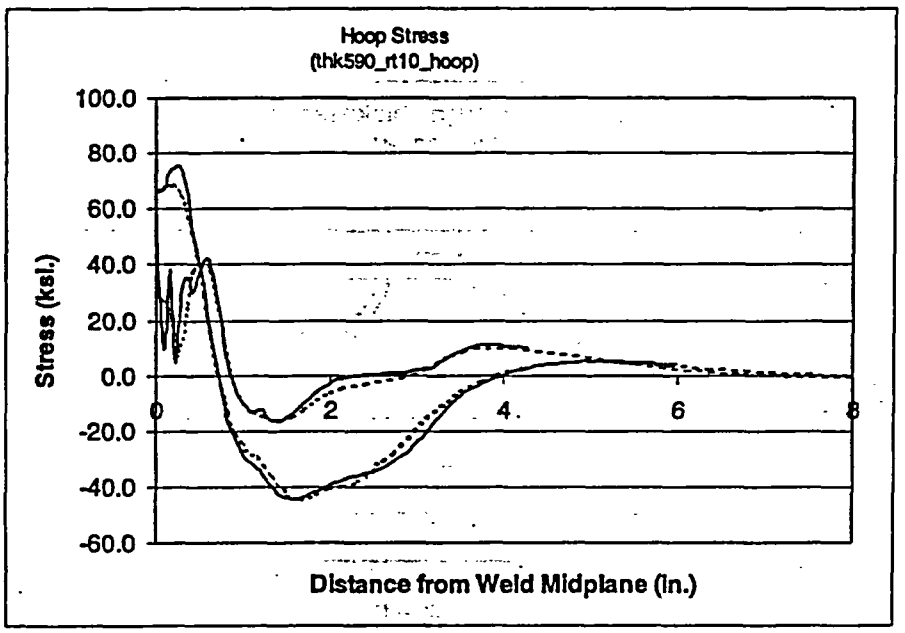
Hoop Stress
(thk590_rt10_hoop)
100.0
80.0
60.0
40.0
20.0
0.0
-20.0
-40.0
-60.0
Stress (ksi.)
0
2
4
6
8
Distance from Weld Midplane (in.)

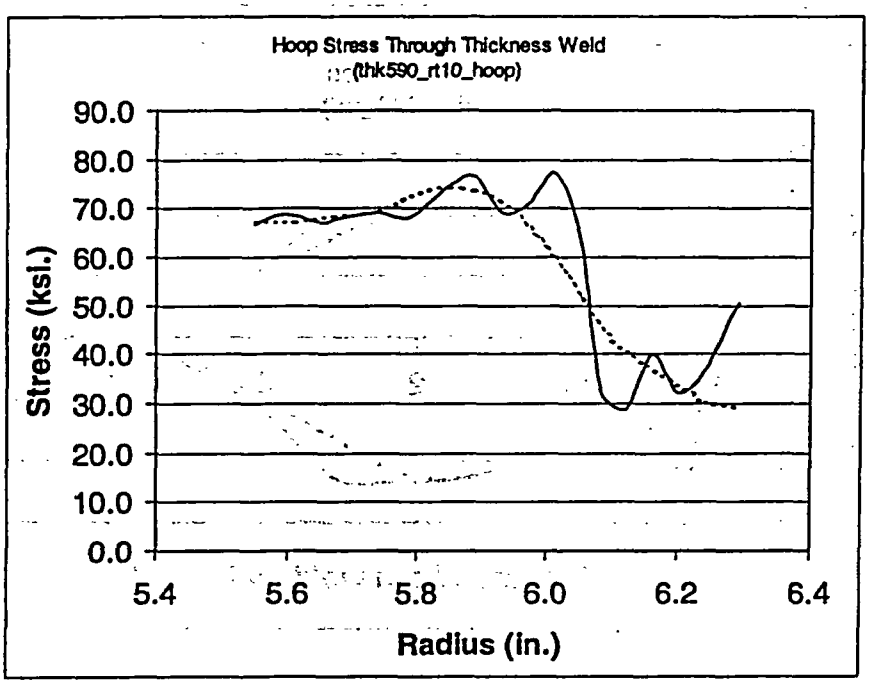
Hoop Stress Through Thickness Weld
(thk590_rt10_hoop)
90.0
80.0
70.0
60.0
50.0
40.0
30.0
20.0
10.0
0.0
Stress (ksi.)
5.4
5.6
5.8
6.0
6.2
6.4
Radius (in.)

Pipe Thickness .590", R / t = 5

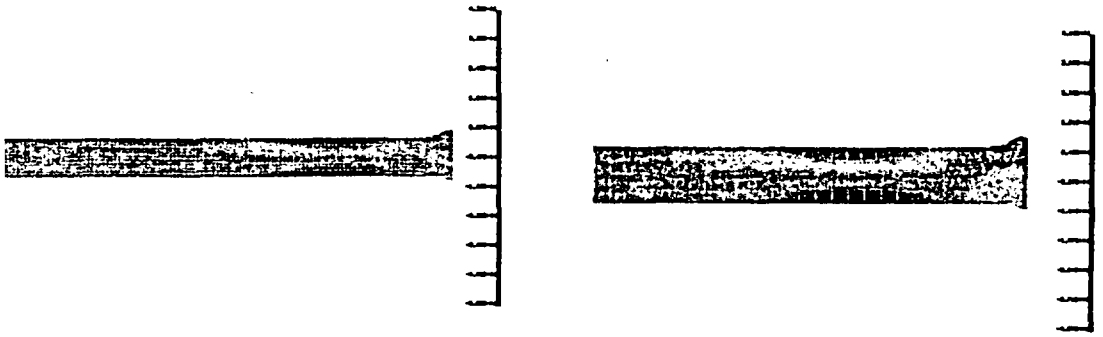

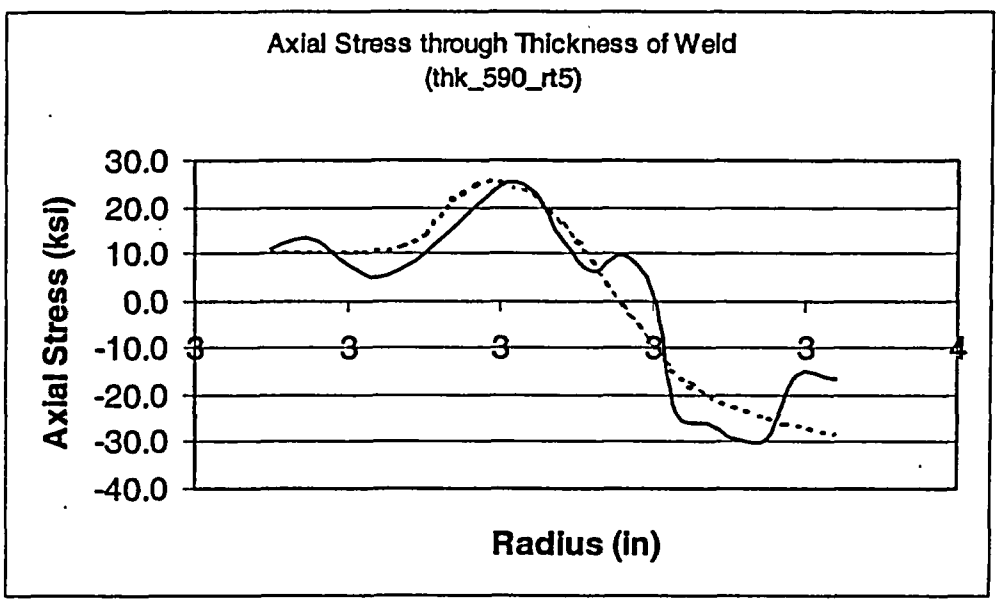

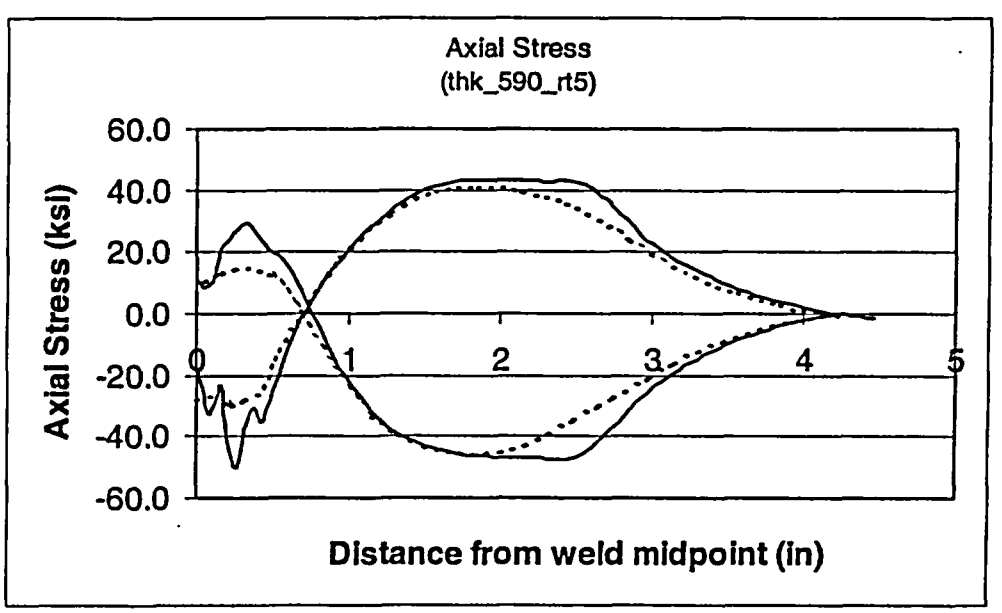

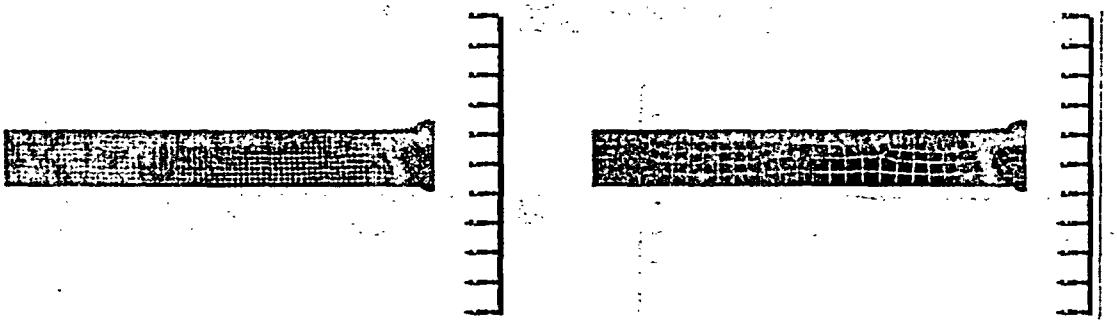

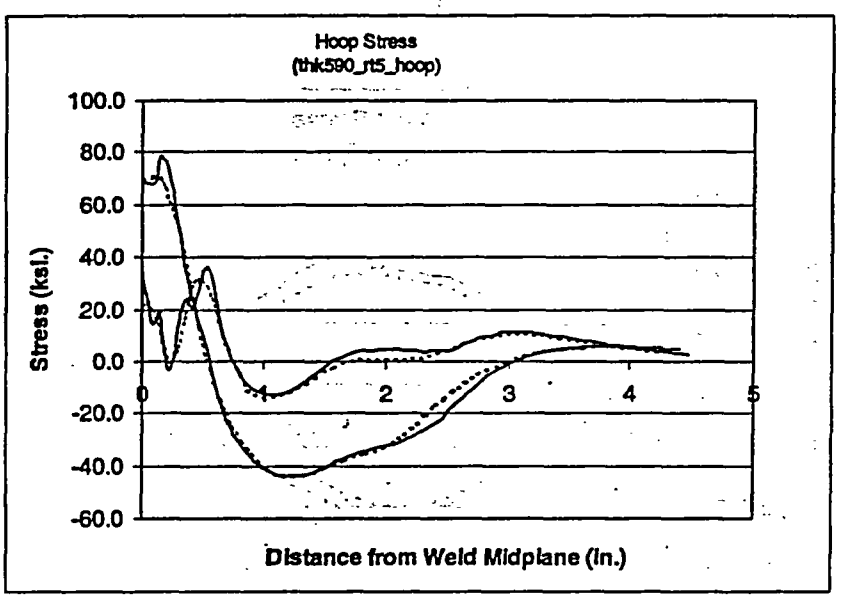
Hoop Stress
(thk590_rt5_hoop)
100.0
80.0
60.0
40.0
20.0
0.0
-20.0
-40.0
-60.0
Stress (ksi.)
0
1
2
3
4
5
Distance from Weld Midplane (in.)

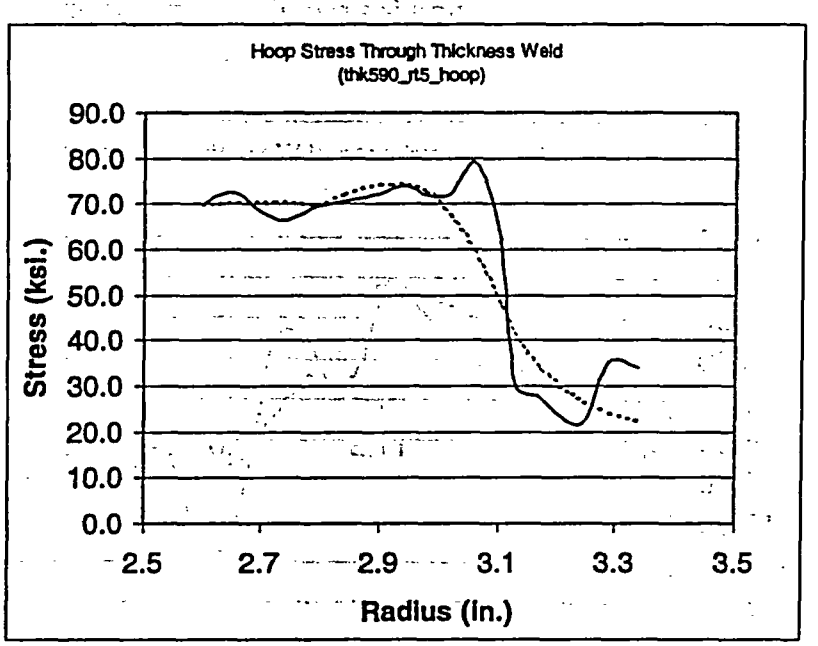
Hoop Stress Through Thickness Weld
(thk590_rt5_hoop)
90.0
80.0
70.0
60.0
50.0
40.0
30.0
20.0
10.0
0.0
Stress (ksi.)
2.5
2.7
2.9
3.1
3.3
3.5
Radius (in.)

Pipe Thickness .590", R / t = 20

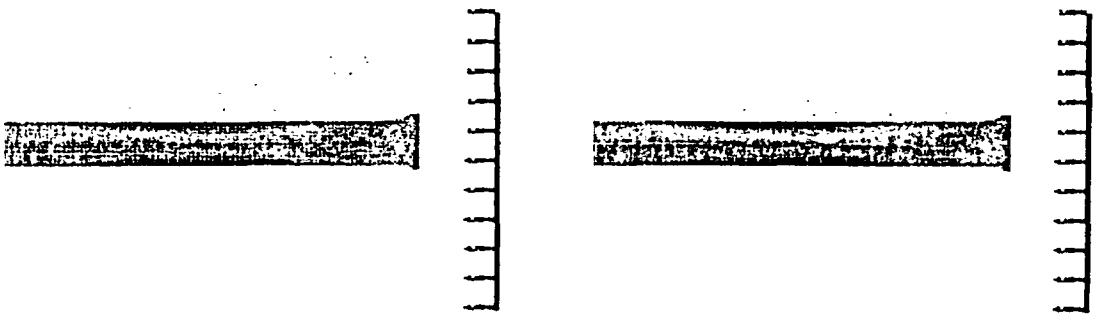

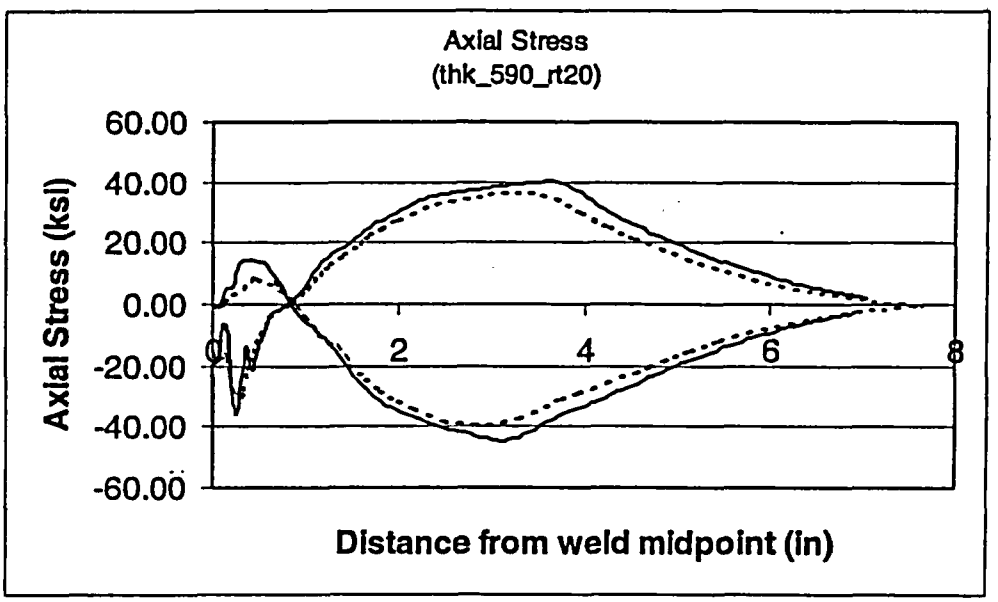

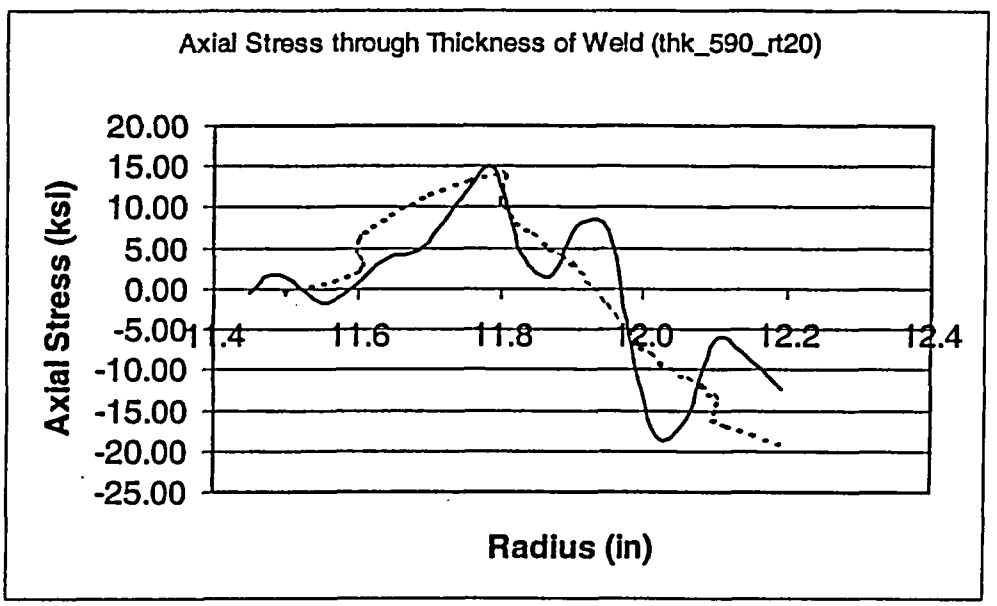

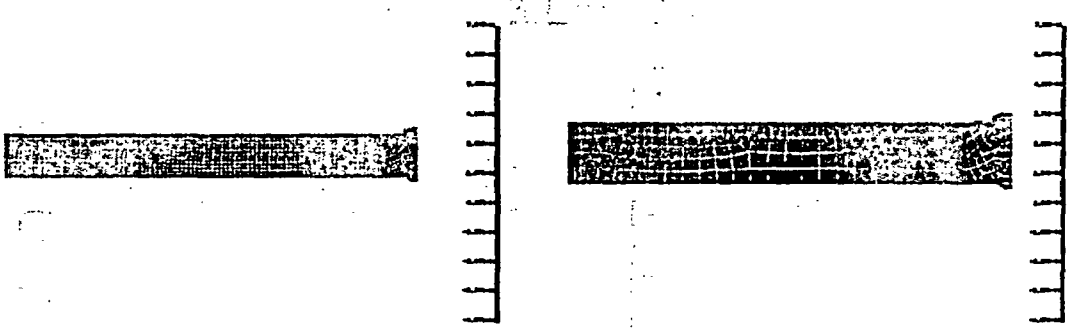

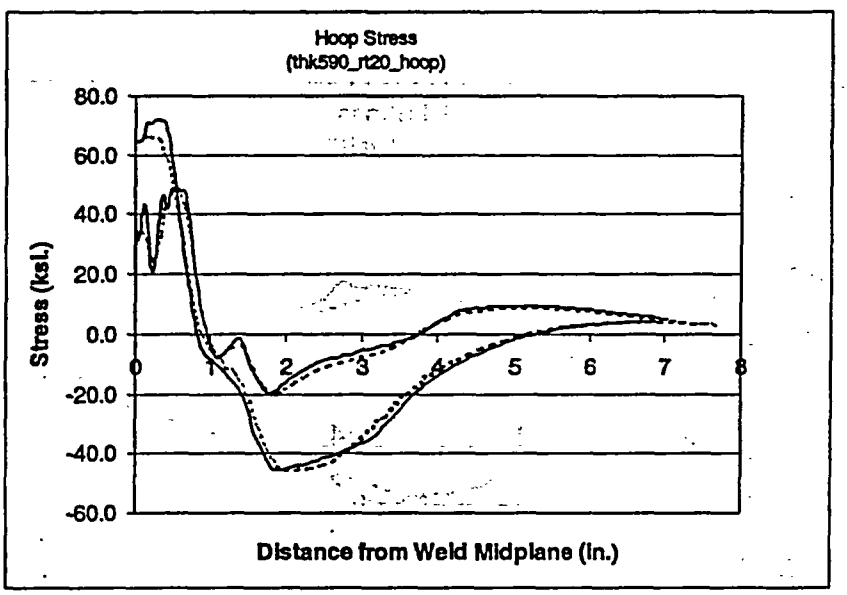
Hoop Stress
(thk590_rt20_hoop)
80.0
60.0
40.0
20.0
0.0
-20.0
-40.0
-60.0
Stress (ksi.)
0
1
2
3
4
5
6
7
8
Distance from Weld Midplane (in.)

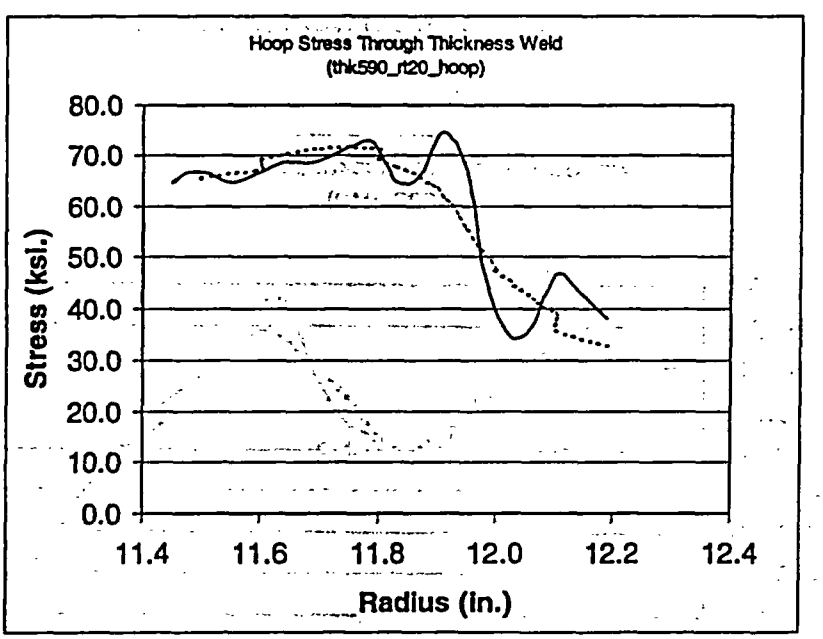
Hoop Stress Through Thickness Weld
(thk590_rt20_hoop)
80.0
70.0
60.0
50.0
40.0
30.0
20.0
10.0
0.0
Stress (ksi.)
11.4
11.6
11.8
12.0
12.2
12.4
Radius (in.)

Pipe Thickness .886", R / t = 10

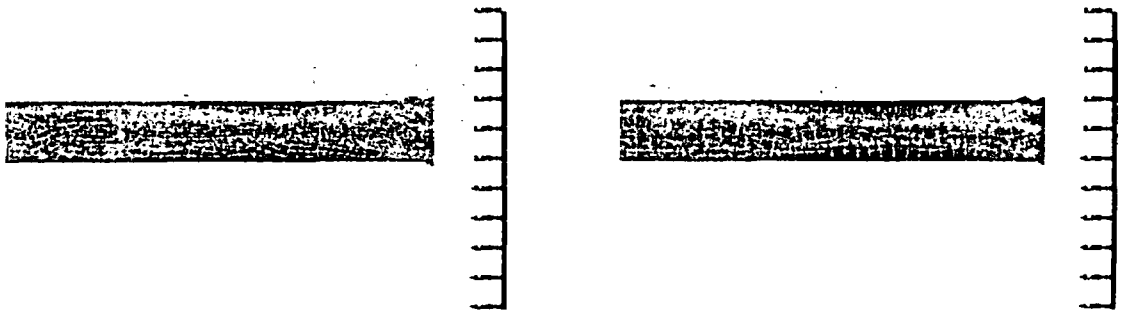

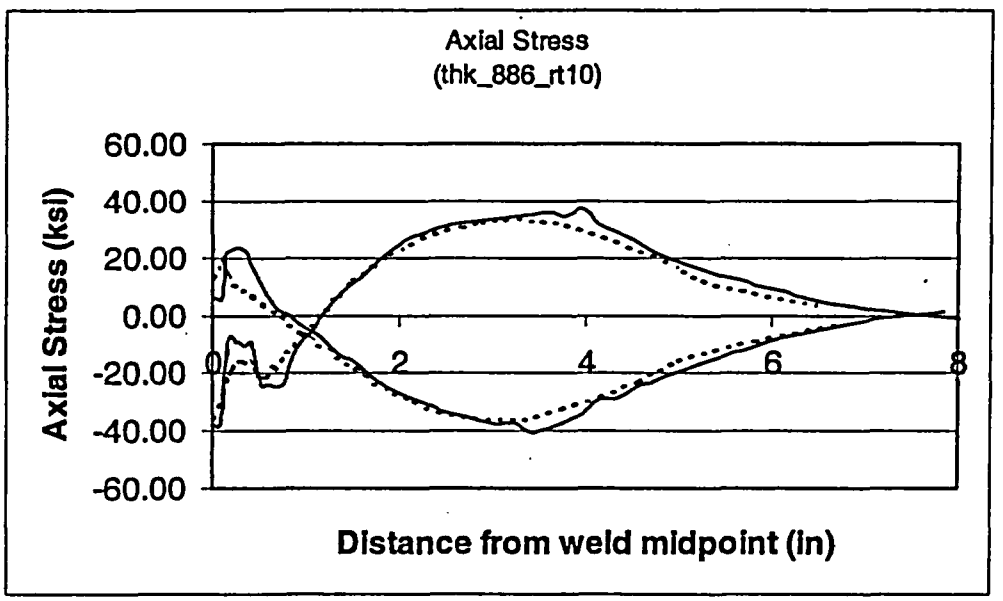

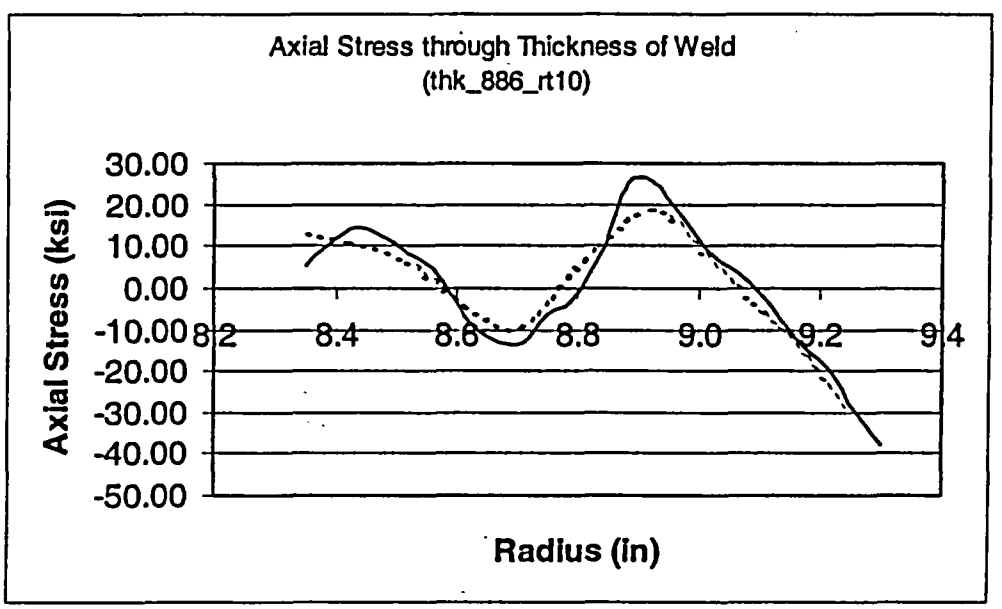

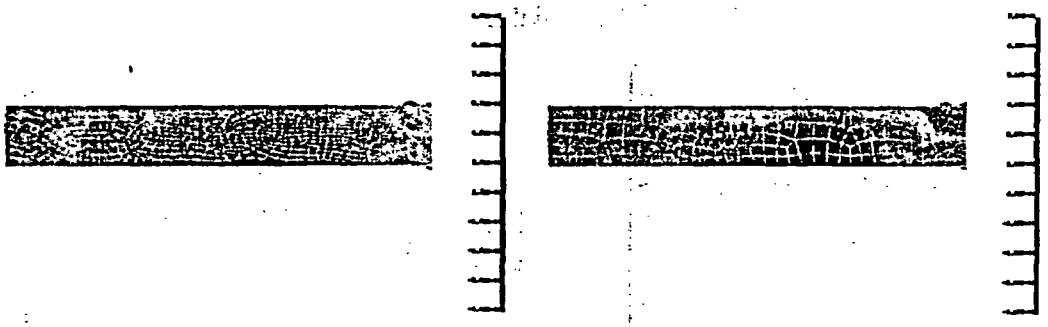

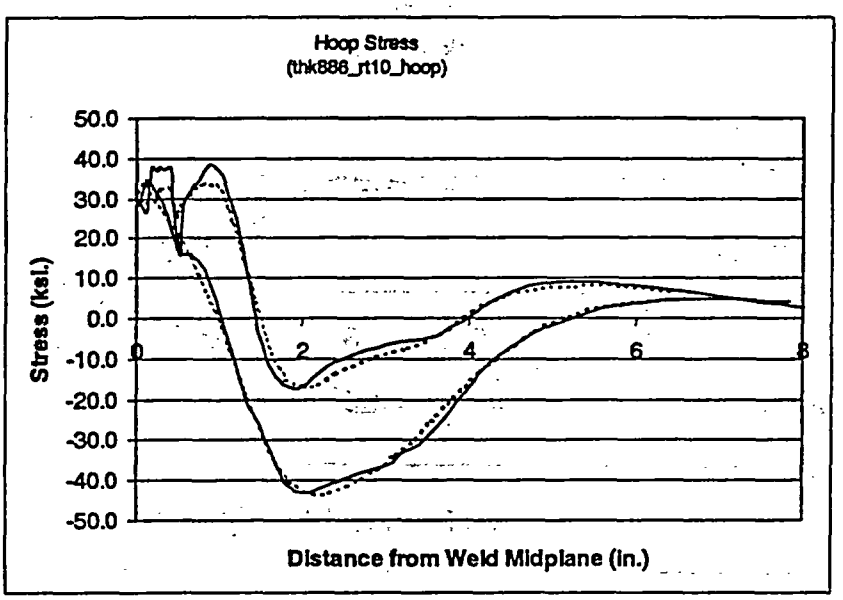
Hoop Stress
(thk886_rt10_hoop)
50.0
40.0
30.0
20.0
10.0
0.0
-10.0
-20.0
-30.0
-40.0
-50.0
Stress (ksi.)
0
2
4
6
8
Distance from Weld Midplane (in.)

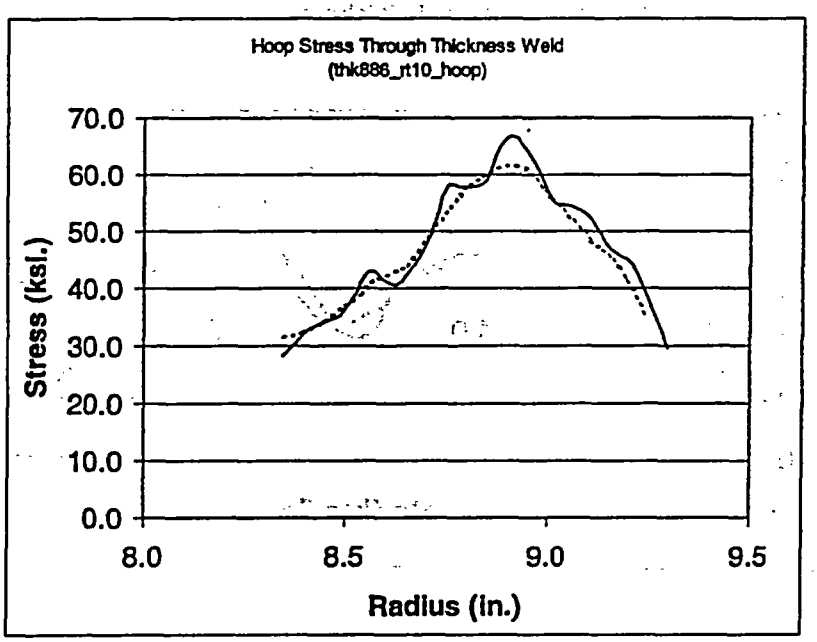
Hoop Stress Through Thickness Weld
(thk886_rt10_hoop)
70.0
60.0
50.0
40.0
30.0
20.0
10.0
0.0
Stress (ksi.)
8.0
8.5
9.0
9.5
Radius (in.)

Pipe Thickness .886", R / t = 5

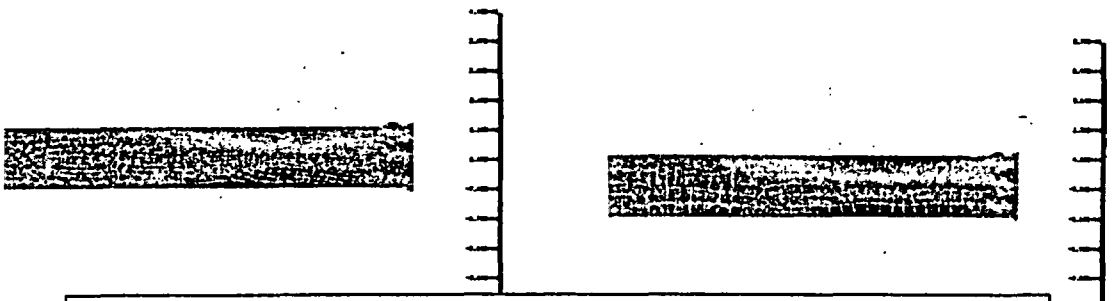

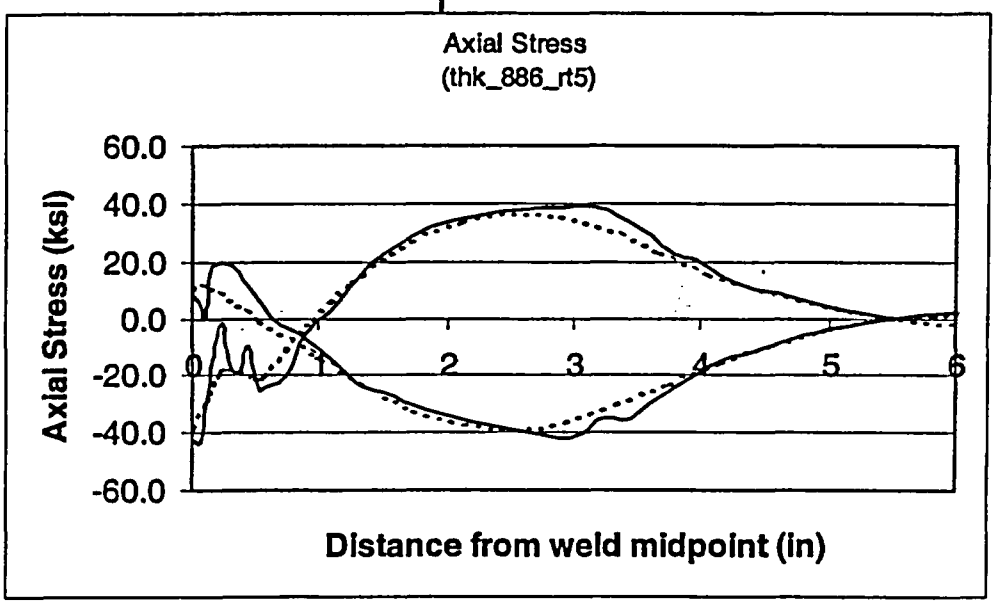

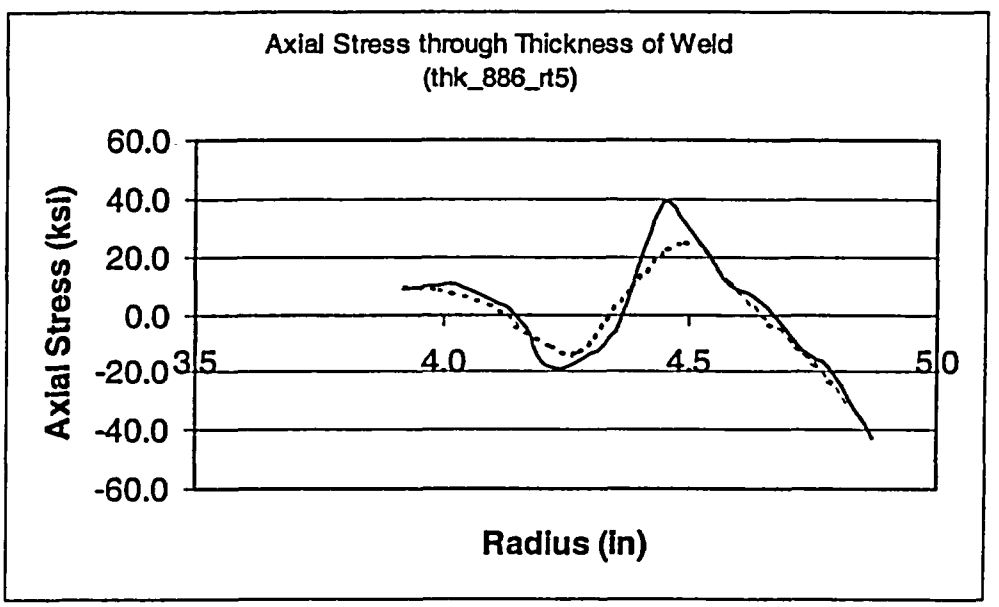

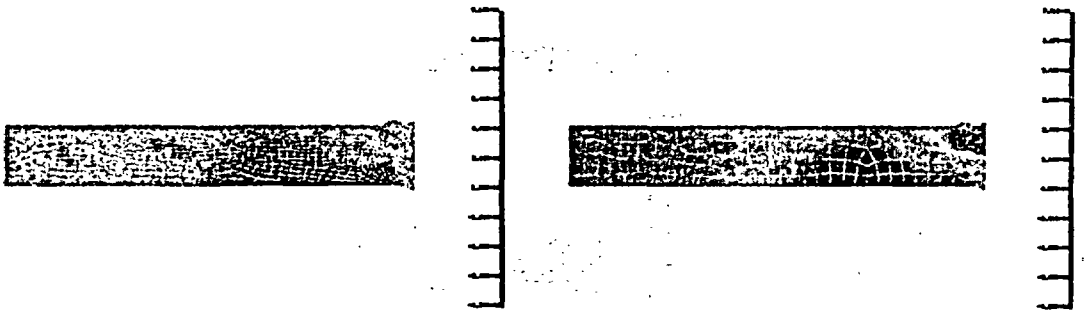

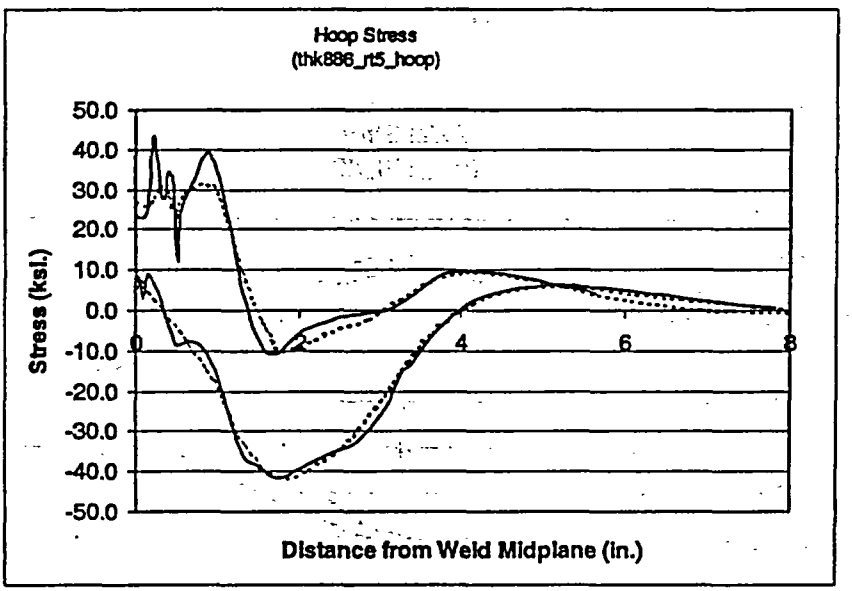
Hoop Stress
(thk886_rt5_hoop)
50.0
40.0
30.0
20.0
10.0
0.0
-10.0
-20.0
-30.0
-40.0
-50.0
Stress (ksi.)
0
4
6
8
Distance from Weld Midplane (in.)

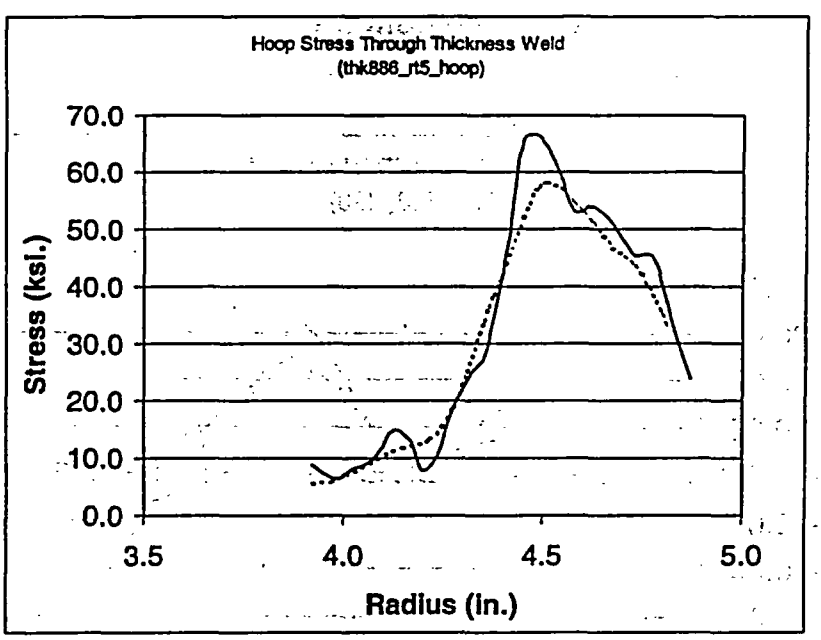
Hoop Stress Through Thickness Weld
(thk886_rt5_hoop)
70.0
60.0
50.0
40.0
30.0
20.0
10.0
0.0
Stress (ksi.)
3.5
4.0
4.5
5.0
Radius (in.)

Pipe Thickness .886", R / t = 20

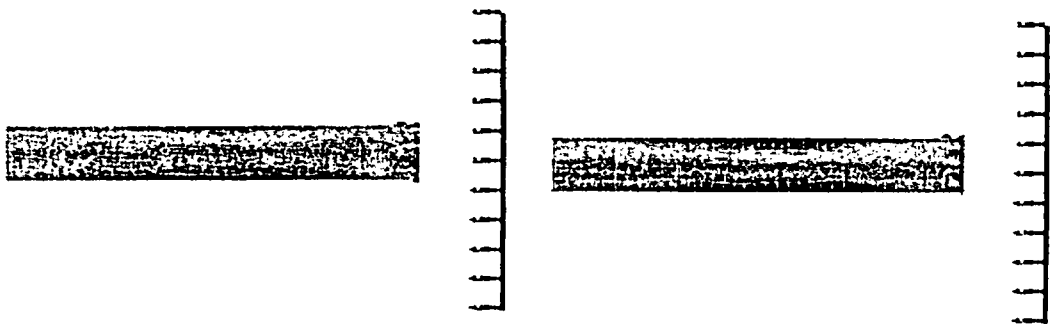

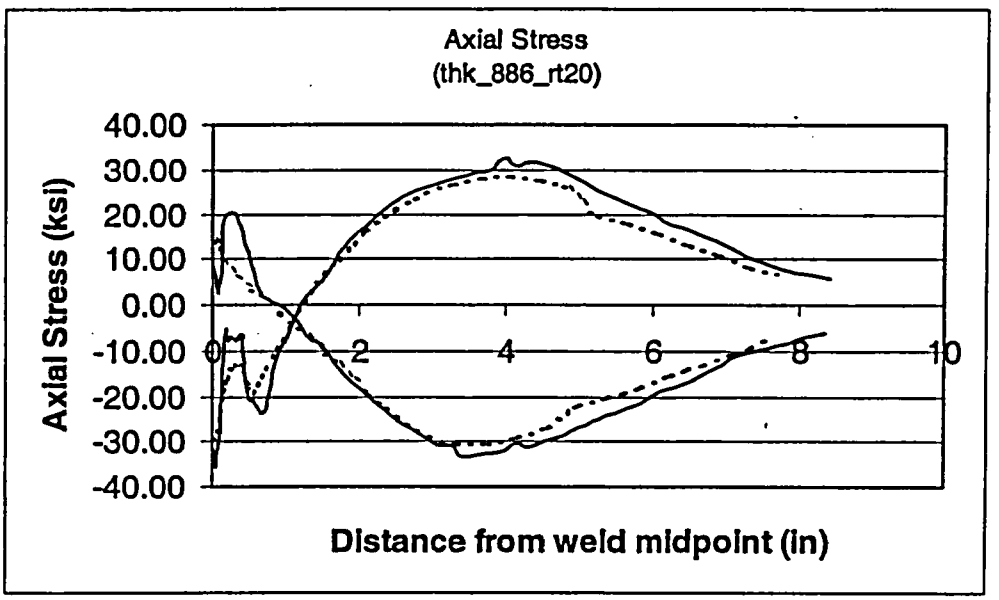

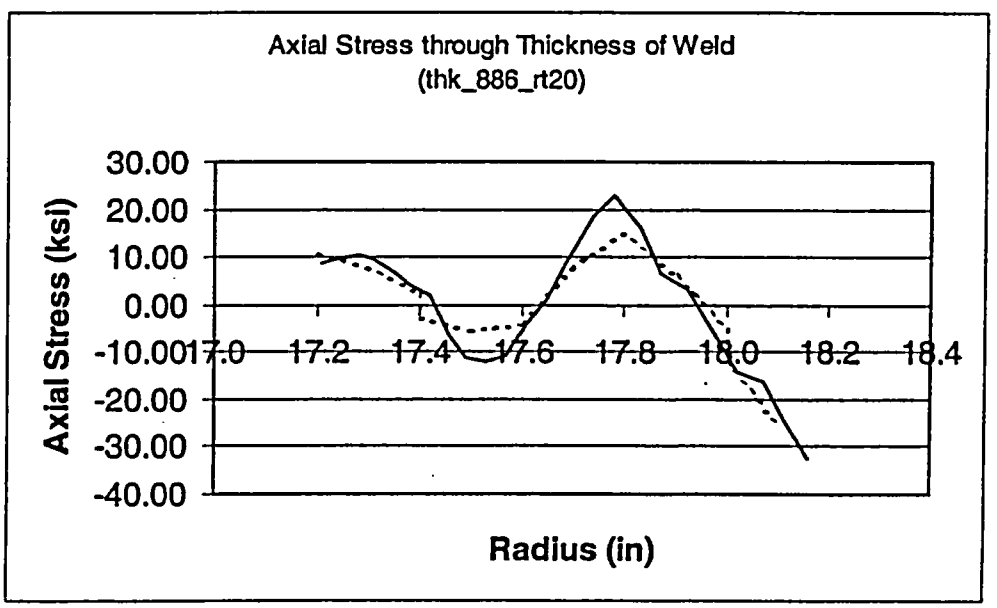

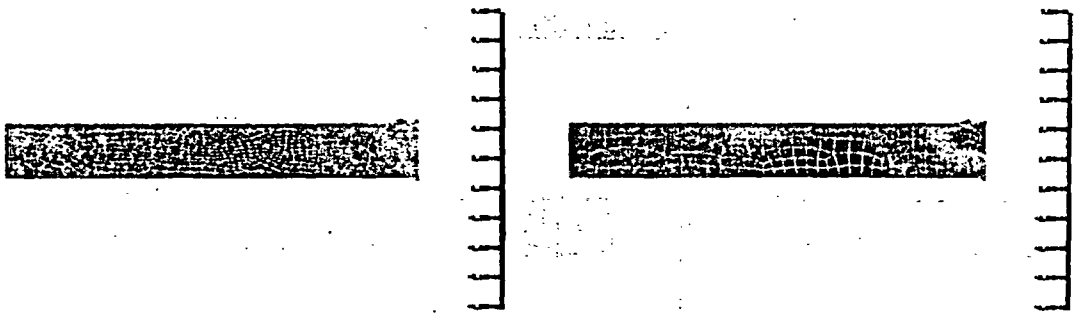

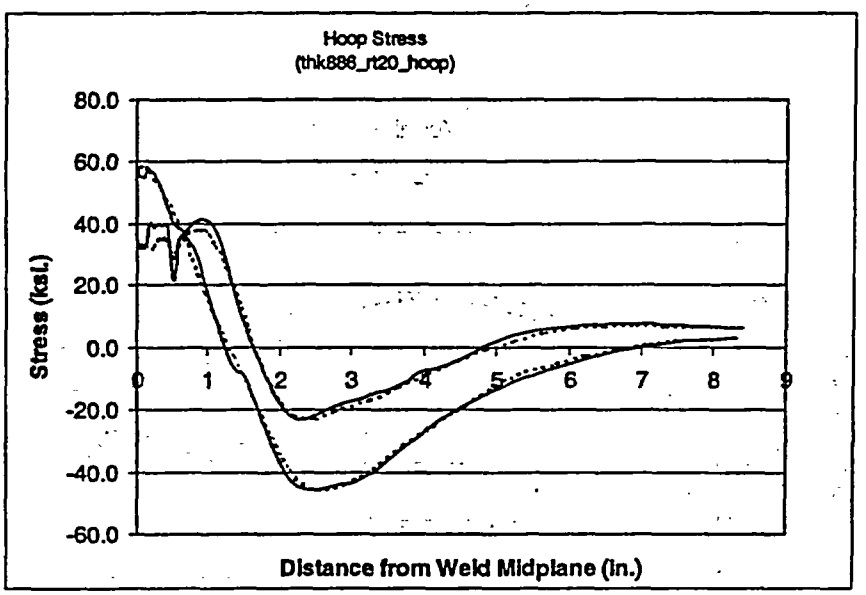
Hoop Stress
(thk886_rt20_hoop)
80.0
60.0
40.0
20.0
0.0
-20.0
-40.0
-60.0
Stress (ksi.)
0
1
2
3
4
5
6
7
8
9
Distance from Weld Midplane (in.)

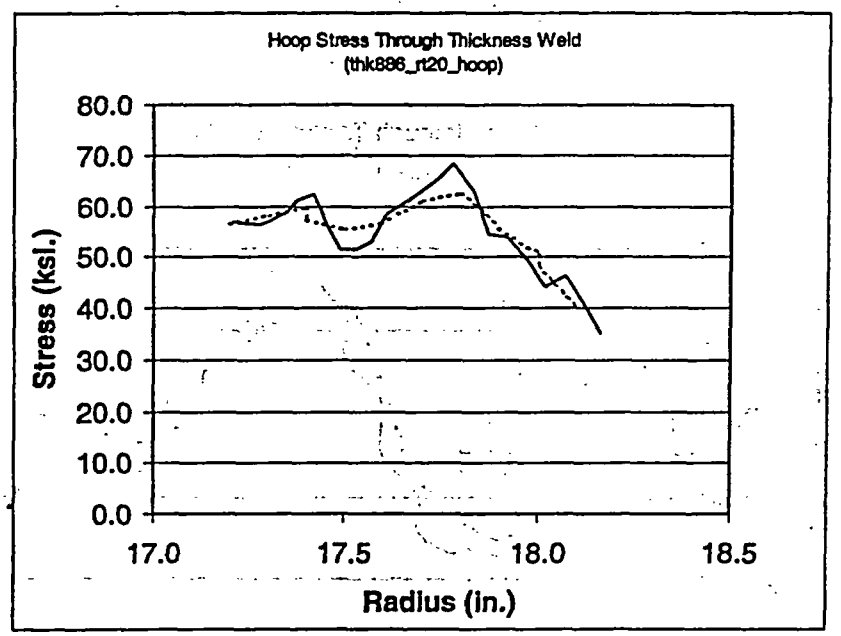
Hoop Stress Through Thickness Weld
(thk886_rt20_hoop)
80.0
70.0
60.0
50.0
40.0
30.0
20.0
10.0
0.0
Stress (ksi.)
17.0
17.5
18.0
18.5
Radius (in.)

Pipe Thickness 1.181", R / t = 10

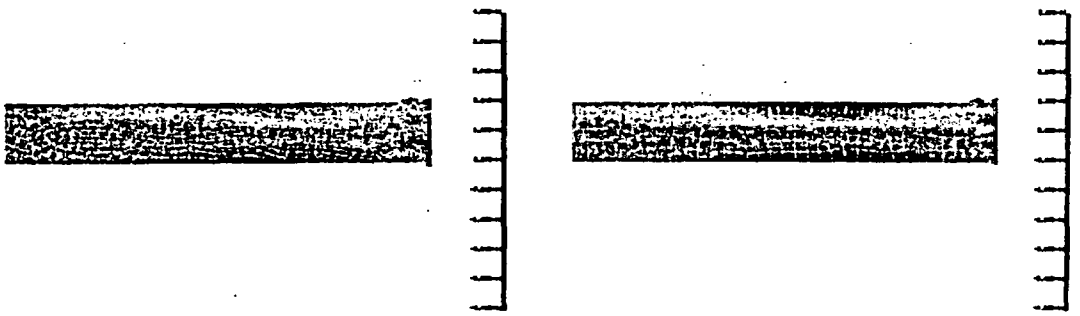

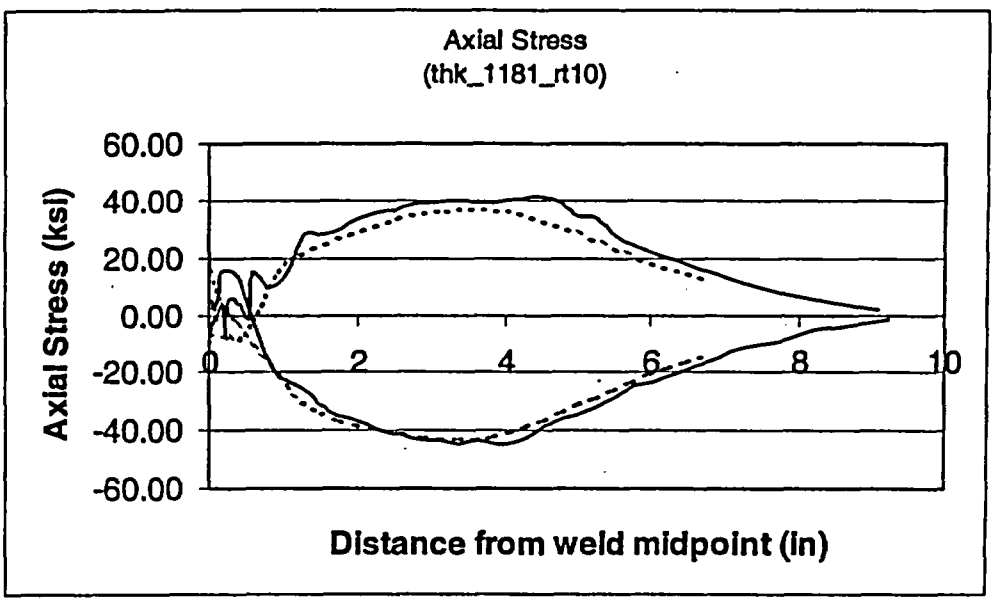

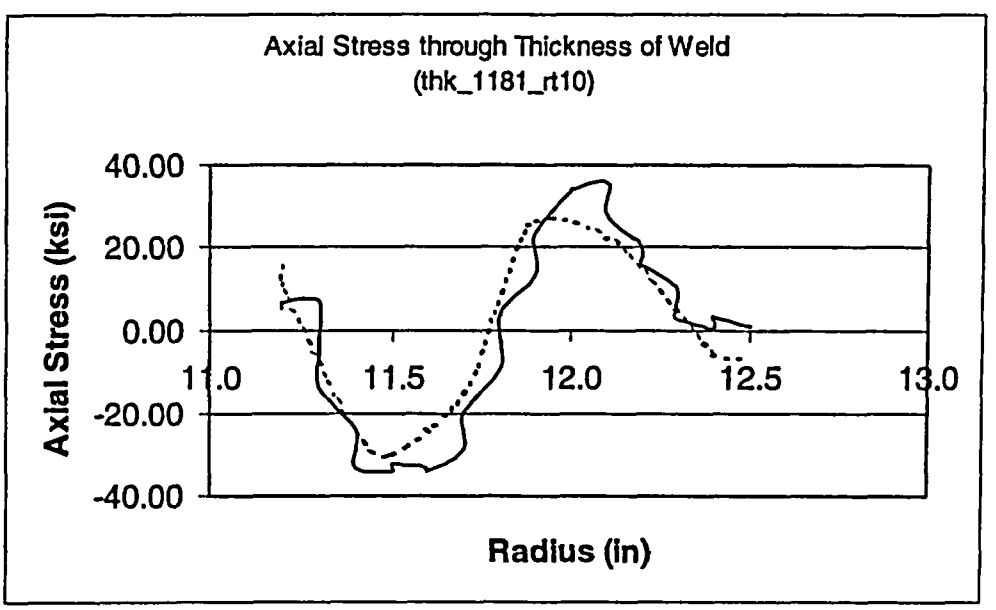

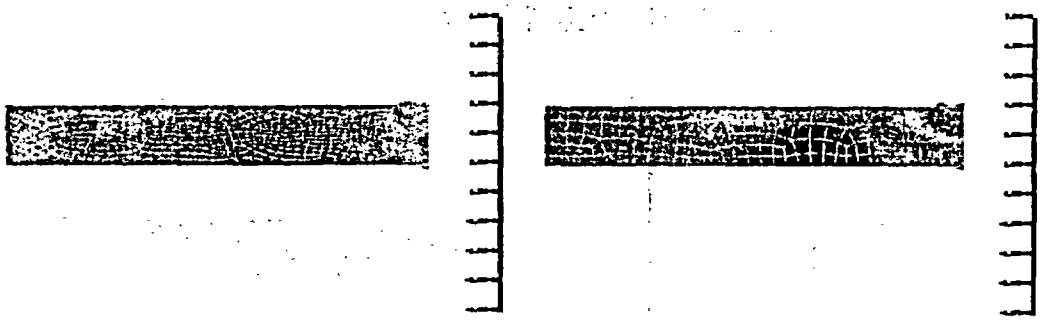

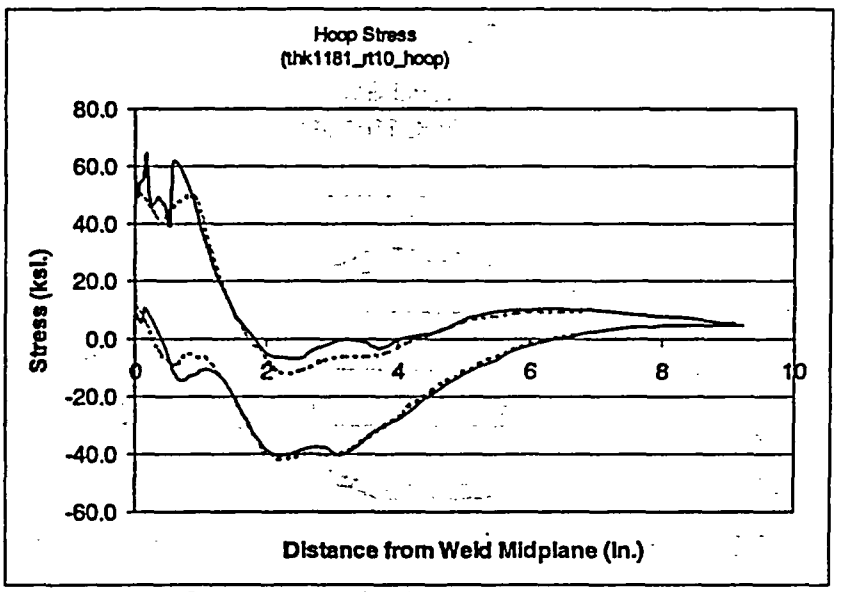
Hoop Stress
(thk1181_rt10_hoop)
80.0
60.0
40.0
20.0
0.0
-20.0
-40.0
-60.0
Stress (ksi.)
0
2
4
6
8
10
Distance from Weld Midplane (in.)

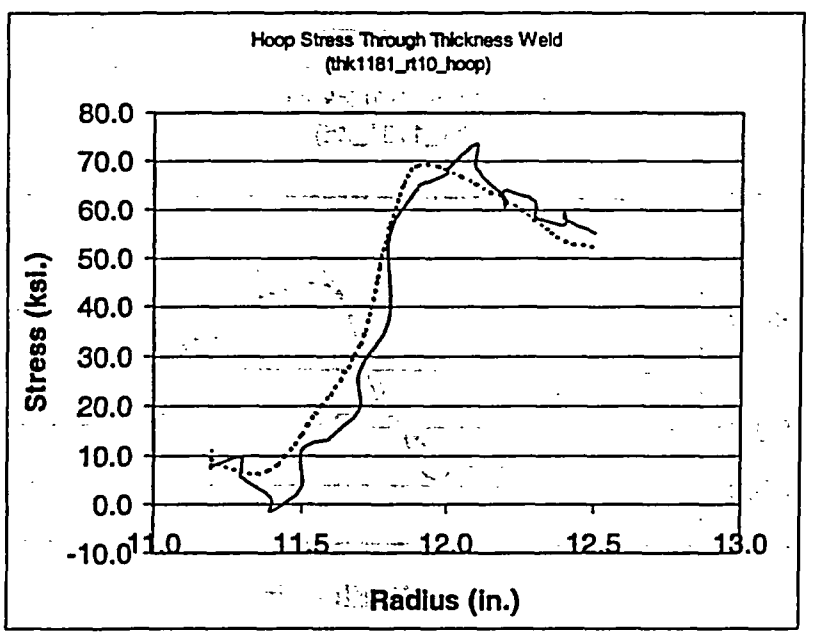
Hoop Stress Through Thickness Weld
(thk1181_rt10_hoop)
80.0
70.0
60.0
50.0
40.0
30.0
20.0
10.0
0.0
-10.0
Stress (ksi.)
11.0
11.5
12.0
12.5
13.0
Radius (in.)

Pipe Thickness 1.181", R / t = 5

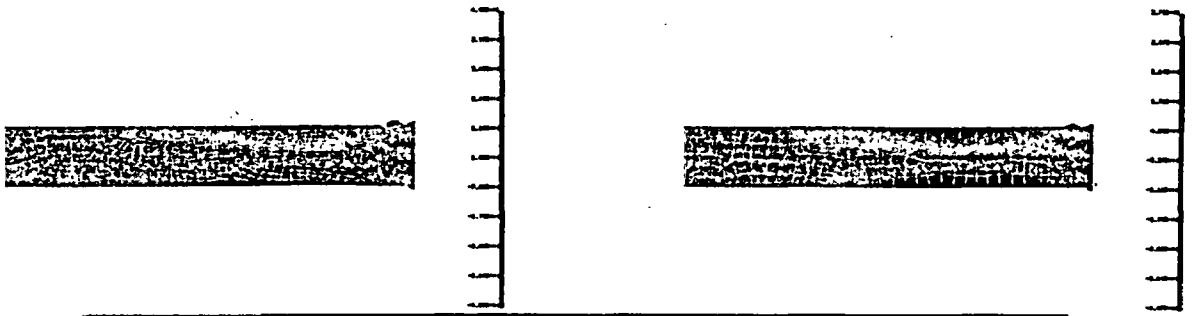

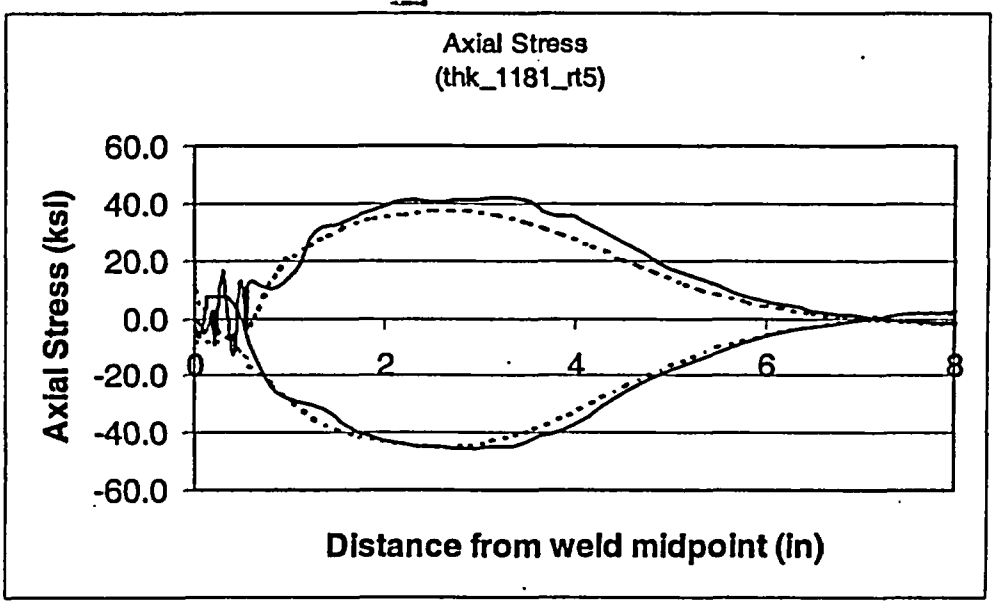

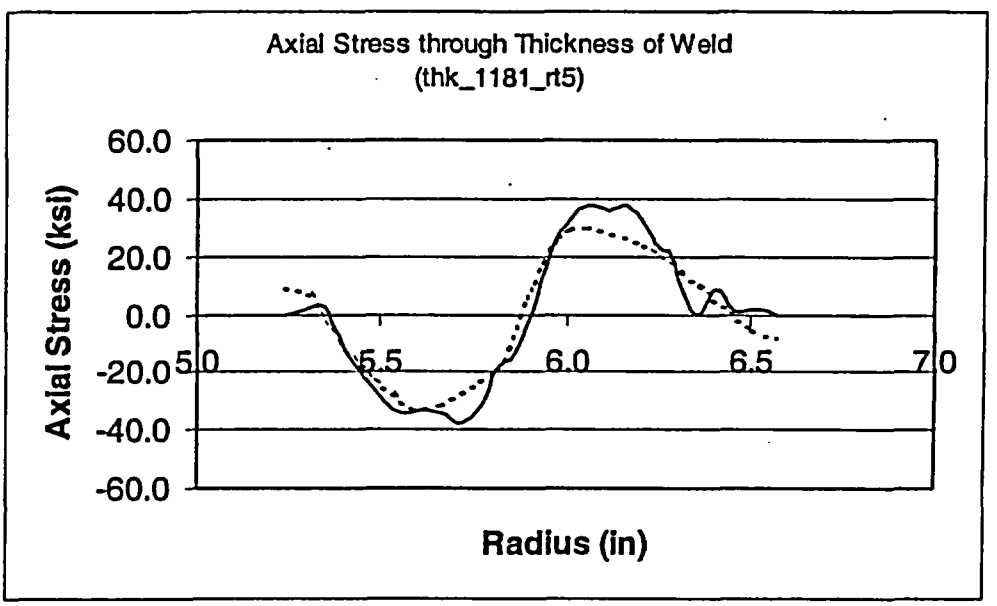

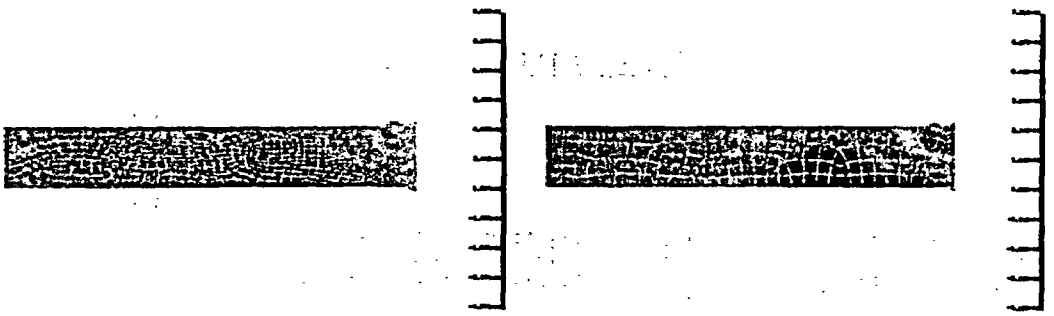

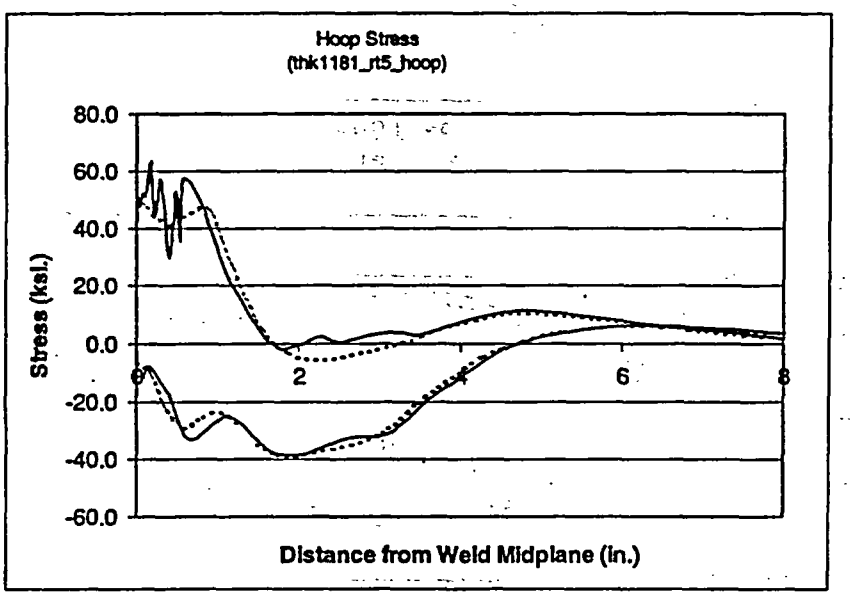
Hoop Stress
(thk1181_rt5_hoop)
80.0
60.0
40.0
20.0
0.0
-20.0
-40.0
-60.0
Stress (ksi.)
0
2
4
6
8
Distance from Weld Midplane (in.)

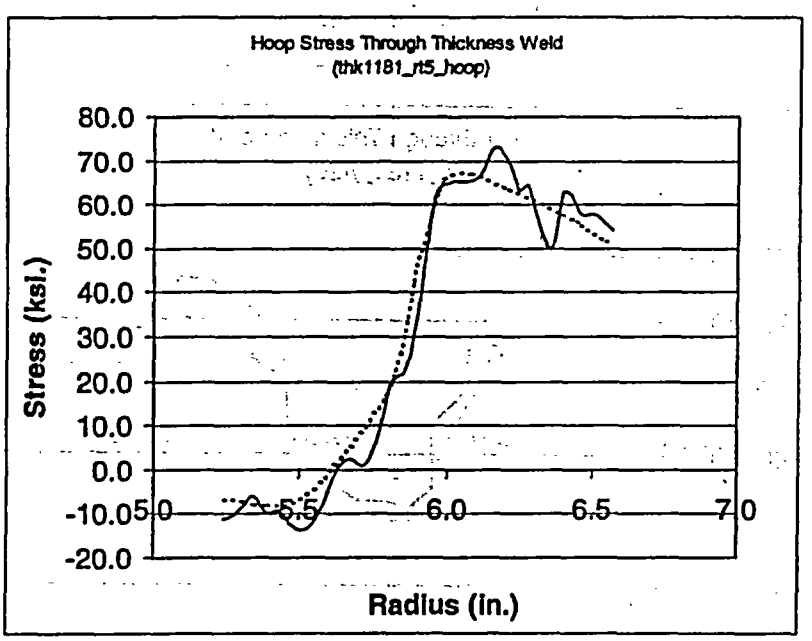
Hoop Stress Through Thickness Weld
(thk1181_rt5_hoop)
80.0
70.0
60.0
50.0
40.0
30.0
20.0
10.0
0.0
-10.0
-20.0
Stress (ksi.)
5.0
5.5
6.0
6.5
7.0
Radius (in.)

Pipe Thickness 1.181", R / t = 20

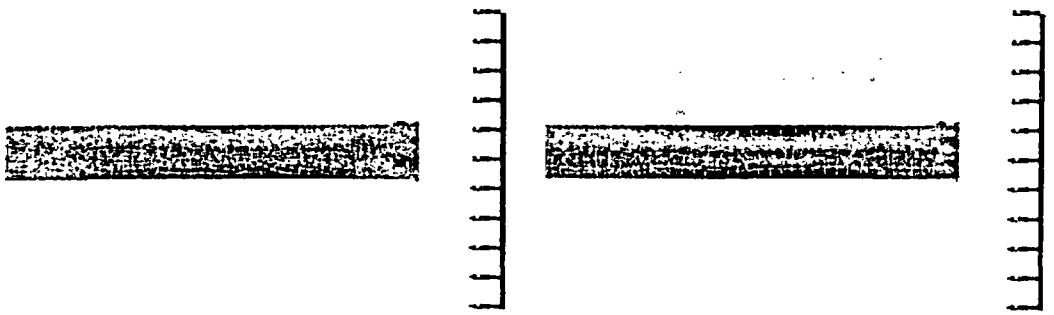

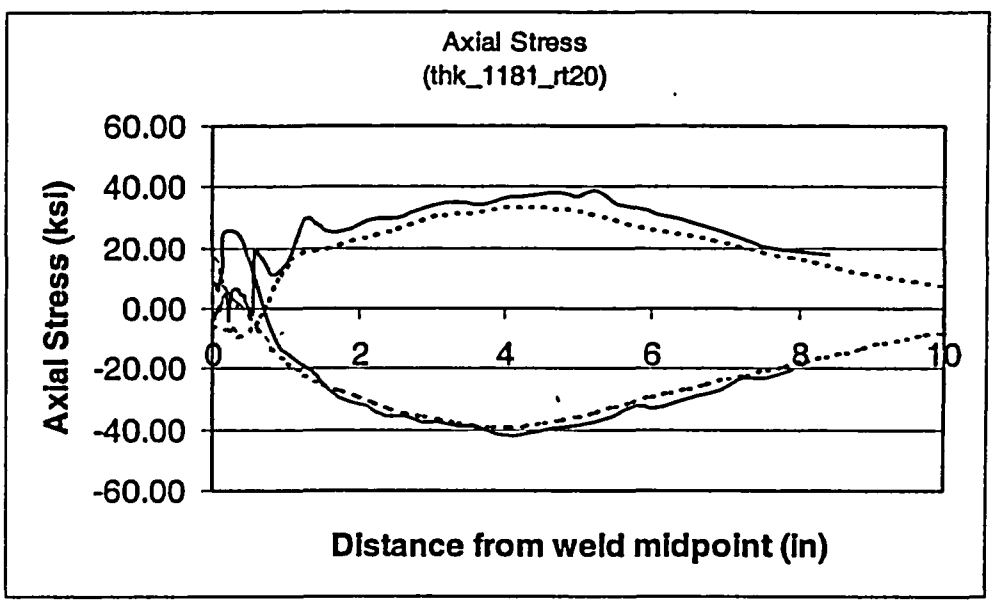

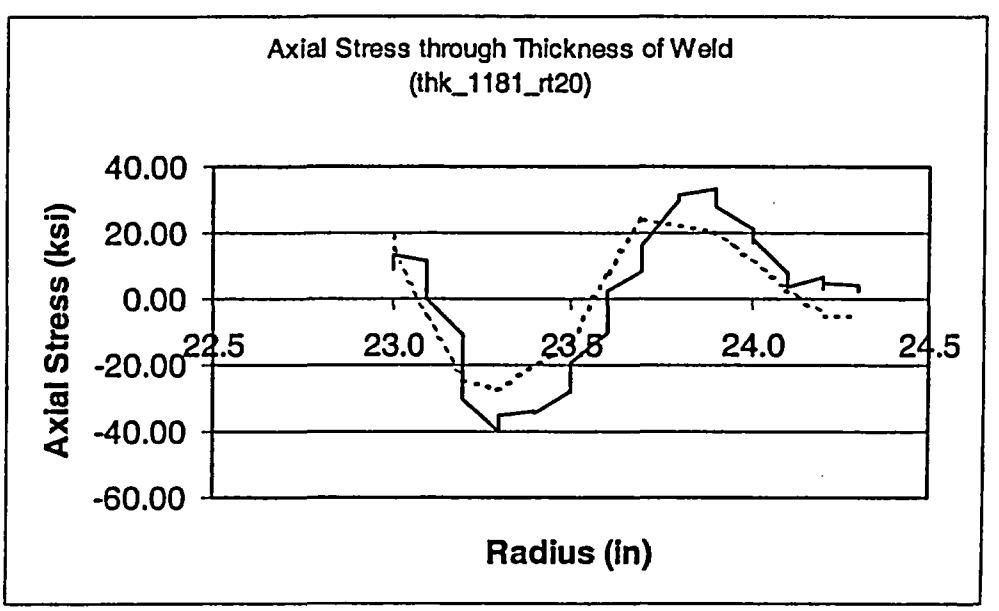

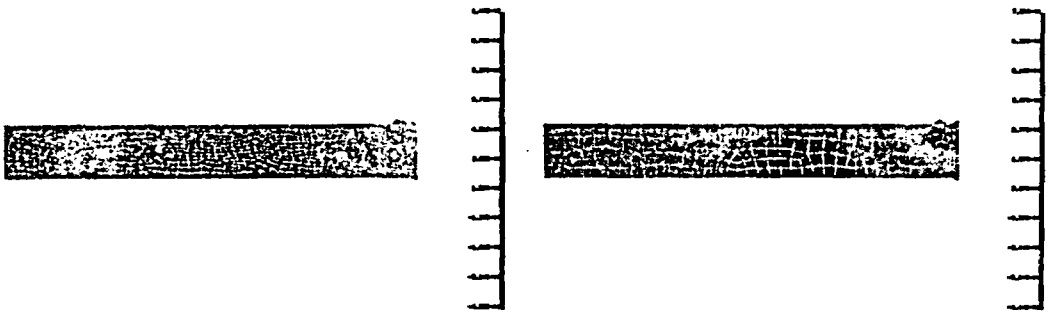

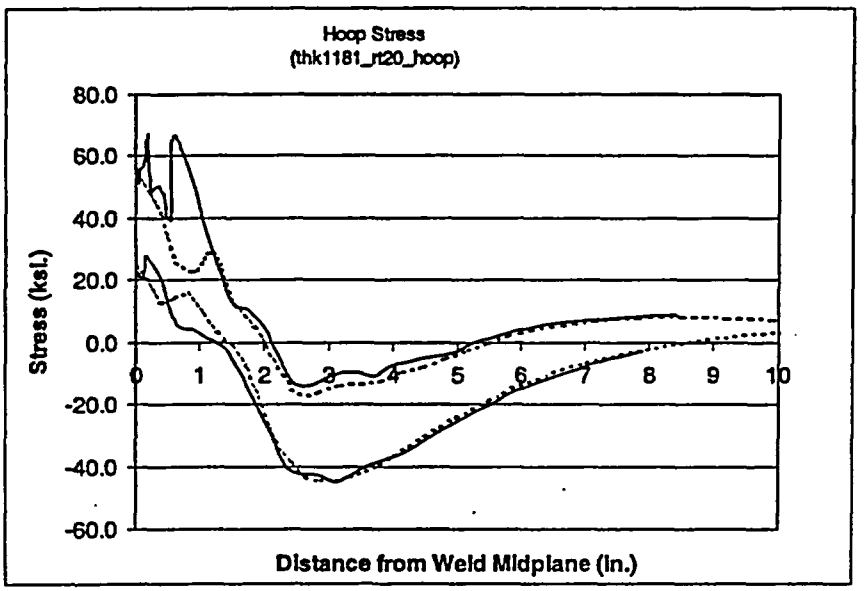
Hoop Stress
(thk1181_rt20_hoop)
80.0
60.0
40.0
20.0
0.0
-20.0
-40.0
-60.0
Stress (ksi.)
0
1
2
3
4
5
6
7
8
9
10
Distance from Weld Midplane (in.)

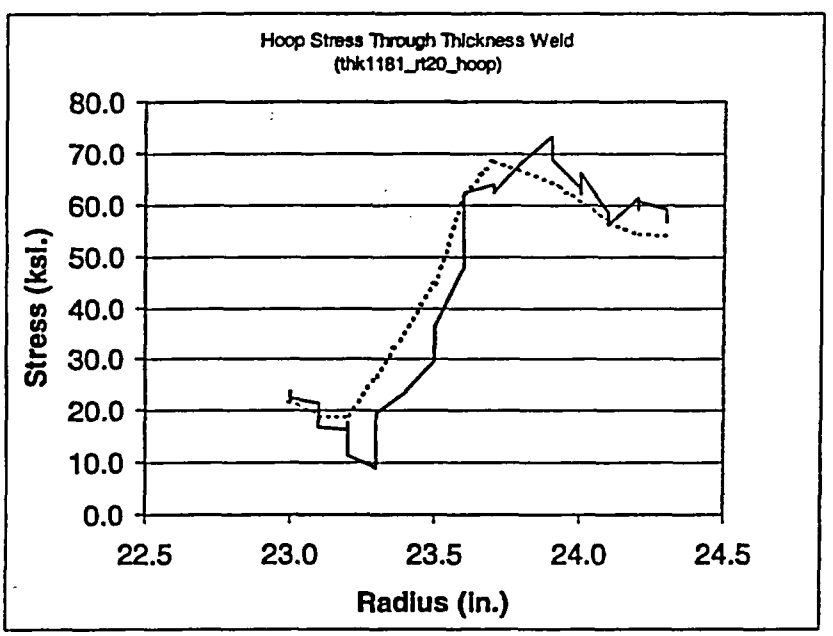
Hoop Stress Through Thickness Weld
(thk1181_rt20_hoop)
80.0
70.0
60.0
50.0
40.0
30.0
20.0
10.0
0.0
Stress (ksi.)
22.5
23.0
23.5
24.0
24.5
Radius (in.)

APPENDIX I

ROUND ROBIN ANALYSES

I.1 INTRODUCTION

As part of the BINP program, the program participants solved two separate round robin problems. Both problems formed the basis for subsequent technical tasks conducted by Battelle and Engineering Mechanics Corporation of Columbus (Emc^2). The first round robin problem involved a series of finite element analyses aimed at developing a matrix of solutions to be used in quantifying the effect of restraint of pressure induced bending on the crack-opening displacements (COD) for leak-before-break (LBB) analyses. The results from this round robin problem then fed into Task 4 of the BINP program where the results from the round robin finite element analyses were curve fit to develop an engineering approximation of the effect of restraint of pressure induced bending on COD values.

The second round robin problem examined the effect of pipe radius-to-thickness (R/t) ratio on elastic-plastic fracture mechanics (EPFM) surface-crack J-estimation scheme analyses. The results from the second round robin then fed into Subtask 7.1 of the BINP program where the effect of R/t ratio on flaw evaluation criteria for Class 2, 3, and Balance of Plant (BOP) piping was studied.

This appendix provides the details of both round robins. The analysis methodologies that were developed in the subsequent BINP tasks are discussed elsewhere in this report.

I.2 FIRST ROUND ROBIN (FINITE ELEMENT ANALYSIS OF CRACK-OPENING DISPLACEMENTS IN AXIALLY LOADED PIPING SYSTEMS FOR LEAK-BEFORE-BREAK APPLICATIONS)

At the end of the Second International Piping Integrity Research Group (IPIRG-2) Program, a study was commissioned to assess the factors that are most critical to leak-before-break (LBB) and in-service flaw evaluation methods (Ref. I.1). One such factor identified was an effect called ***restraint of pressure induced bending on crack-opening displacements***. The existence of a through-wall circumferential crack will result in a bending moment at the crack region for a pipe loaded axially, due to the eccentricity from the neutral axis of the crack plane versus the center of the uncracked pipe. The common analysis practice for LBB is to determine the center crack-opening displacement (COD) by using the solution for an end-capped vessel. The so-called end-capped vessel model, although relatively simple to analyze, allows the ends of the vessel to freely rotate. Furthermore, this model ignores the ovalization restraint at the crack plane from any boundary conditions. Therefore, the end-capped vessel model may over-estimate the crack-opening displacement more than if the pipe is not allowed to rotate.

In a real piping system, the ends of the pipe will be restrained from free rotation. The amount of the restraint will depend on the geometry of the pipe system. In general, the restraint of end rotation will be a function of:

- the magnitude of the load (elastic or plastic effects),
- the pipe R/t ratio,
- the length of the crack (short cracks typical of LBB in primary pipe loops are not affected, but long cracks for smaller-diameter pipe will be effected), and
- the boundary conditions of the pipe either side of the crack location.

For this round robin, six organizations from three countries participated in the finite element round-robin analysis. The objective of this round-robin program was to check the past calculations (Ref. I.1), as well as compare and evaluate the results and modeling approaches from different participants. Each participant was then assigned to solve some additional problems. This resulted in a large matrix of FE results, which would lend themselves to a closed-form analytic expression that was developed later in the BINP program.

The round robin analysis was coordinated by Engineering Mechanics Corporation of Columbus (Emc^2). The other five participating organizations were: Battelle Columbus, Central Research Institute of Electric Power Industry (CRIEPI) of Japan, Korea Electric Power Research Institute (KEPRI), Sungkyunkwan University of Korea (SKKU), and the U.S. Nuclear Regulatory Commission (NRC).

I.2.1 Background on the Effect of Pipe-System Boundary Conditions on Fracture and Leak Rate Analyses

In virtually all nuclear pipe fracture analyses, the pipe-system stress analysis and the fracture analyses are decoupled. That is, typically the stresses in an uncracked-pipe system are determined, and then those stresses are used in an analytical fracture analysis.

Of the effects that are typically decoupled, one of the most stunning results observed came from a pipe-system experiment in the First International Piping Integrity Research Group (IPIRG-1) program. In that experiment, it was experimentally determined that a guillotine break did not occur until the growing through-wall crack was 95 percent around the pipe circumference, see Figure I.1. From pressure loads alone, it was expected that a break would occur once the crack reached 65 percent of the circumference. The crack length of 95-percent of the circumference corresponded to the pressure-induced failure for full restraint of the induced bending moment, see Figure I.2.

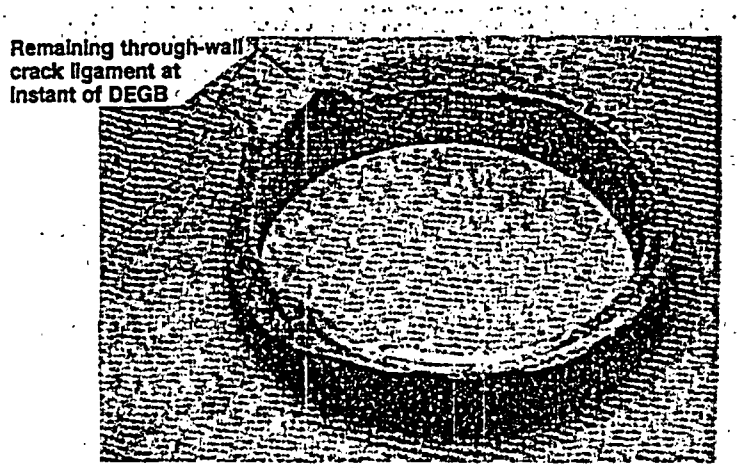

Figure I.1 Photograph of fracture from aged cast stainless experiment (Experiment 1.3-7) from IPIRG-1

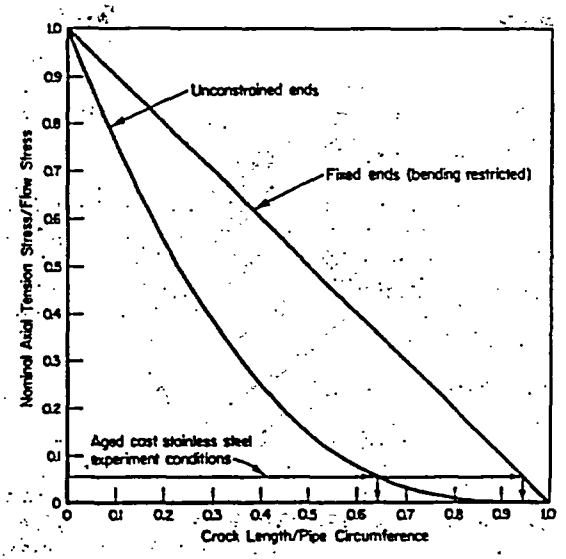

Figure I.2 Net-Section-Collapse analyses predictions, with and without considering induced bending, as a function of the ratio of the through-wall crack length to pipe circumference

The results from this experiment, with the crack located 3.4 pipe diameters from an elbow, provide strong evidence that pipe-system boundary conditions restrain pressure-induced bending, and that this increases the load-carrying capacity of the cracked pipe. Virtually all fracture analyses assume that the pipe is free to rotate due to the pressure-induced bending.

Consequently, the contemporary fracture methods will tend to inaccurately predict the propensity for crack instability because they ignore the restraint that pipe-system boundary conditions provide.

After the excitement subsided concerning the apparent beneficial effects of the restraint of pressure-induced bending on fracture loads, it was later noted, that if the failure loads are increased, then the driving force is reduced, so that the crack-opening displacement in the pipe system will be less than what is typically calculated using current crack-opening-displacement analyses. Hence, the increased load-carrying capacity that is beneficial to LBB is offset by a corresponding decrease in crack-opening displacement that is detrimental to LBB. Because the trade-offs between these two effects were not well understood, some selected case studies were undertaken which are summarized below.

The precise procedure that was originally used by Battelle to assess the effects of restraining the induced bending from pressure loads was defined in NUREG/CR-6300, Section 6.3 on page 6-3 (Ref. I.2). A focused mesh was used at the circumferential crack tip with 20-noded brick elements in ABAQUS. There were 172 elements in the quarter symmetry model with 1,252 nodes, as shown in Figure I.3. Calculations were initially done for a 28-inch diameter pipe with a mean pipe radius to wall thickness ratio (R/t) of 10. Only elastic analyses were conducted.

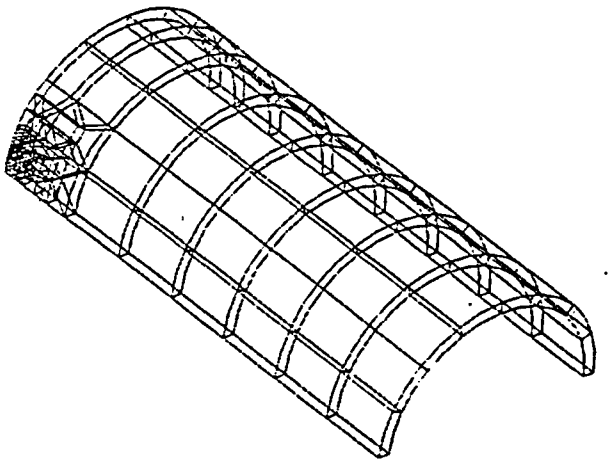

Figure I.3 FE mesh used in past Battelle COD/Restraint effect study

At various distances from the circumferential crack plane, the pipe rotations and ovalizations were restricted in the FE analyses. This distance from the crack to the restraining boundary conditions was called the restraint length. The restraint length was normalized by the pipe diameter for making non-dimensional plots with COD values for different pipe diameters.

In NUREG/CR-6300, the crack length was either 12.5 or 25 percent of the pipe circumference, and the normalized restraint length was 1, 5, 10, and 20. A calculation was also done that would allow free rotation and no ovalization restrictions. This is representative of the fully unrestrained conditions (the end-capped vessel assumption) typically used in all the COD estimation procedures. Since this was an elastic analysis, the COD of the restrained boundary condition analyses could be normalized by the unrestrained COD for any load level. Figure I.4 shows the initial results.

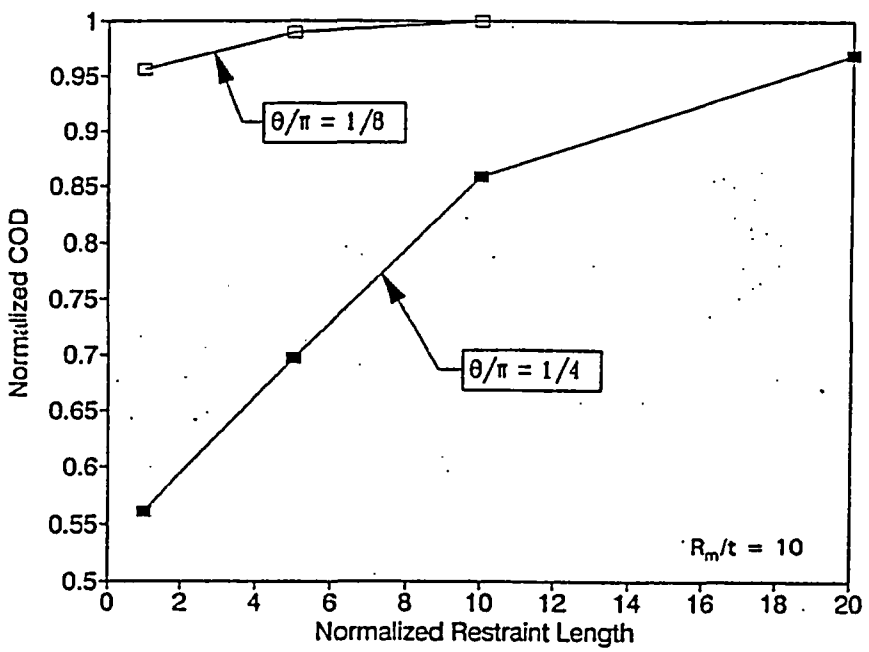

Figure I.4 Normalized graph showing the effects of restraining ovalization and rotations at different distances from the crack plane

Subsequent analyses were conducted for a 4-inch nominal diameter pipe with an R/t of 6. In addition, another crack length of ½ of the pipe circumference (total crack length) was added for both pipe diameters. Figure I.5 shows the results of the both of these analyses together.

The results from the 28-inch diameter pipe FE analysis seem reasonable. The 4-inch nominal diameter pipe results agree with the large pipe results for the large crack, but not for the small or intermediate crack. That may have been due to some problem in the normalization. One would think that the normalized COD should flatten off to a constant value of 1.0. Hence, the small-diameter results are suspicious.

An additional LBB sensitivity study was conducted in NUREG/CR-6443 using the above restrained COD trends. The LBB analysis used the mesh geometry shown in Figure I.3, for a highly restrained condition (L/D = 1) and completely unrestrained conditions applied to 4-inch nominal diameter (R/t of 6) and 28-inch (R/t of 10) diameter pipes under the following conditions:

- a leak rate of 1.89 liters/min (0.5 gpm),
- IGSCC crack morphology parameters,
- a pressure of 15.5 MPa (2,250 psi), and
- a bending stress chosen to give a total pressure plus bending stress of 50-percent of the Service Level A maximum allowable stress from ASME Section III Article NB-3650 for TP304 pipe.

The resulting leakage-size crack was calculated using the SQUIRT Version 2.4 computer code. These results are shown in Table I.1. At this leak rate, the large-diameter pipe is basically unaffected by the restraint condition while the small-diameter pipe is very much affected. The effect of restraint on the COD is strongly controlled by the crack length. It appears to manifest itself as a pipe diameter effect, since a longer normalized crack length is needed in smaller-diameter pipe for LBB to be satisfied.

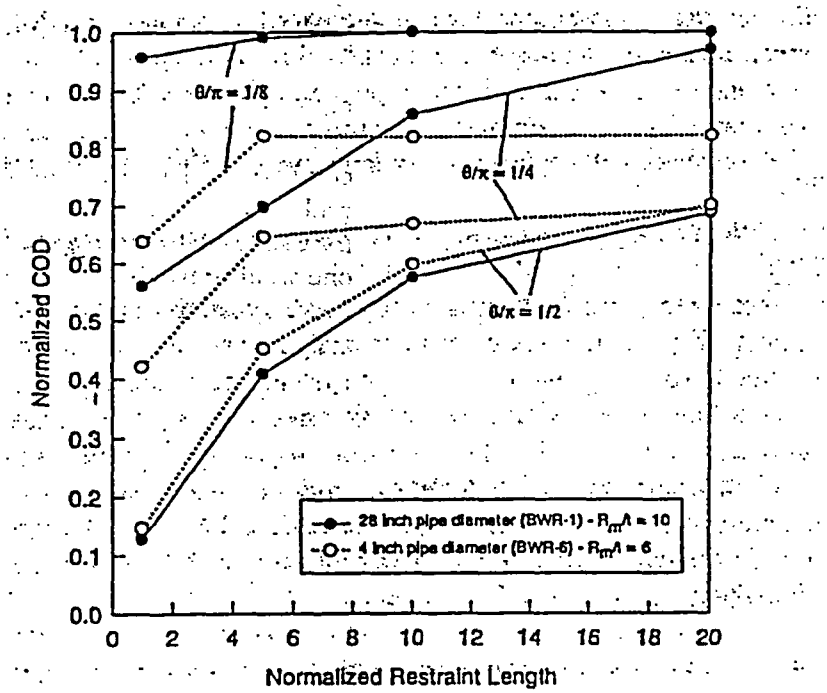

Figure I.5 Normalized COD versus restraint length for two different sets for FE analyses

Table I.1 Differences in leakage flaw sizes due to restraint of pressure-induced bending

Outside Pipe Diameter		Leakage Crack Length, θ/π	
Mm	inches	Restrained	Unrestrained
114.3	4.5	0.7250	0.2360
711.2	28.0	0.0219	0.0219

The corresponding LBB fracture loads were evaluated under the following conditions:

- the crack is centered on the bending plane,
- the average stress-strain curve properties for TP304 stainless steel base metal were used, and
- the crack was assumed to be in the center of the weld, hence the mean minus one standard deviation J-R curve for a stainless steel SAW weld was used.

Using the LBB.ENG2 analysis modified to eliminate the induced bending from the tension component of the axial stress component, the ratio of the unrestrained to restrained failures loads is shown in Figure I.6. This result shows that the effects of the restraint of pipe-system boundary conditions were negligible for the 28-inch diameter pipe. This was because for this leak rate, the crack size was a small percent of the circumference, and hence the beneficial effects on fracture and detrimental effects on COD were negligible. However, the effect on the 4-inch nominal diameter pipe was very large. The unrestrained load is a factor of nine larger than the restrained load. This was a more significant effect than any possible effect from toughness considerations. The reason this occurred was that for this leak rate, under this loading, the normalized crack length in the small pipe for the restrained condition had to be very large when compared with the larger-diameter pipe. The crack, in fact, became so large from this effect, that any benefits on fracture loads were small, especially considering that the additional loads to fracture were all bending loads, not increases in pressure loads. Also, like any LBB analysis, the calculations were made up to maximum load, and were not an actual determination of a DEGB.

The effect seen in this sample calculation suggests that LBB applications need to be assessed carefully for cases where large crack sizes may occur, i.e., small-diameter pipe, or steam-line applications. It also suggests that there may be some concern with LBB applications to intermediate pipe diameters. Fortunately, for large-diameter pipe, where LBB is of greatest benefit, there are no detrimental effects from this phenomenon.

Of practical importance is the fact that the past Battelle analysis assumes symmetric boundary conditions either side of the crack. This would probably never occur in practice. Hence, to make any analysis for this effect a practical tool, one would have to account for the different pipe bending stiffnesses on either side of the proposed crack locations.

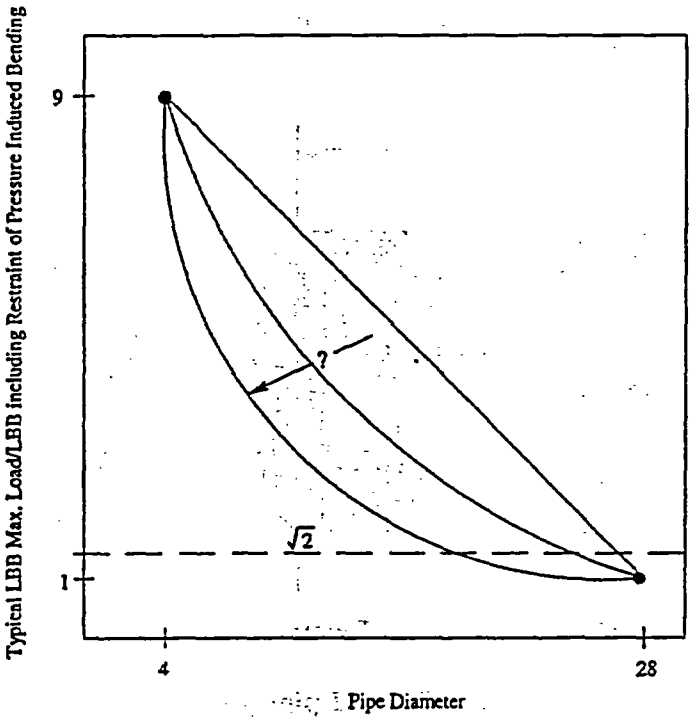

Figure I.6 Calculated maximum loads for LBB with and without restraint of the pressure-induced bending from the pipe system

I.2.2 Problem Statement for First Round Robin Analyses

The objective of this round robin was for the participants to perform linear-elastic finite element analysis to determine the center crack-opening displacement (COD) at the mid-thickness of a through-wall circumferentially-cracked straight pipe restrained at both ends (Figure I.7). The elastic modulus and the Poisson's ratio were assumed to be 200 GPA (29,000 ksi) and 0.3, respectively. The basic variables investigated in the program included the pipe outside diameter (*OD*), pipe mean radius to thickness ratio (R_m/t), half crack length (θ), and the distance between the restraint planes to the crack plane (L_1, L_2).

A total of 144 cases were included in the analysis matrix of the round robin. It covered a wide range of pipe diameters and R_m/t ratios. The effects of different restraint lengths on the two sides of a crack plane (the asymmetric restraint condition) were considered also. The analysis matrix included the cases that were analyzed in NUREG/CR-6300 to evaluate the validity of the prior calculations.

The specifics of each case in the analysis matrix are provided in Table I.2 .and Table I.3. The analysis matrix was grouped into three major case groups, namely, Case 1, Case 2 and Case 3. Case 1 considered the symmetrically restrained pipe with constant R_m/t ratio of 10, but varying pipe diameters. Case 2 was also the symmetric restraint case, but with a constant pipe diameter of 28 inches and varying R_m/t ratios. Case 3 covered the asymmetric restraint case, with a R_m/t ratio of 10 and varying pipe diameters.

Furthermore, the round robin was carried out into two phases. In the first phase all of the participants were required to solve all the cases in Case 1. The modeling approach and COD results from each participant were compared. In the subsequent phase (Phase II), the participants were assigned to solve a different subset of cases in Case 2 and Case 3. This resulted in a COD

database that would be used to develop a closed-form analytical expression in one of the follow-on tasks of the BINP program. Table I.4 summarizes the cases solved by each participant of the program.

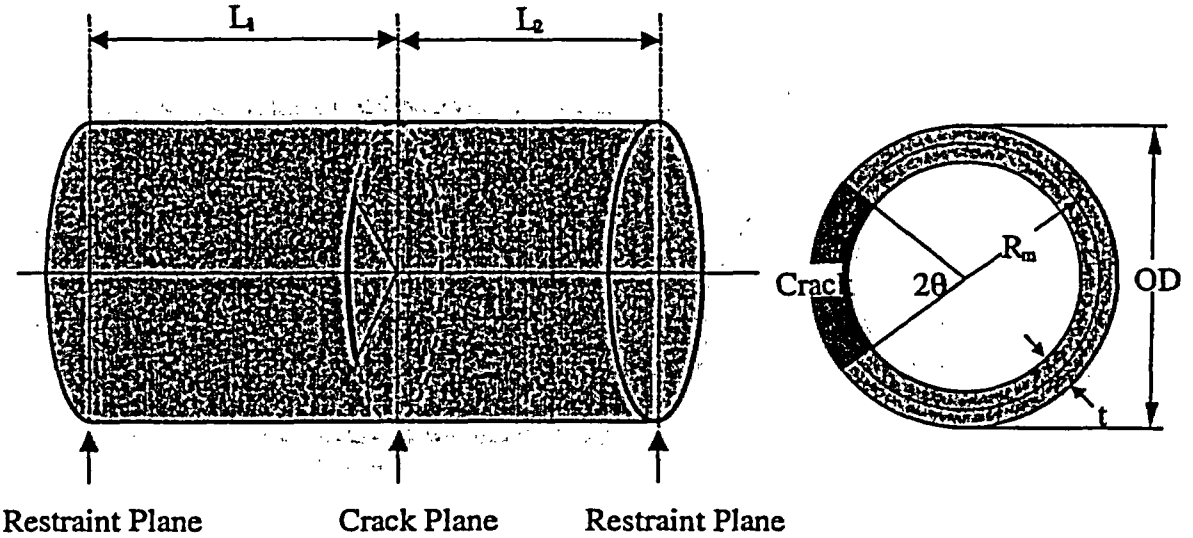

Figure I.7 Cracked-pipe geometry

Table I.2 Symmetric restraint cases

	OD (mm)	R_m/t	Axial Force (kN)	Half Crack Length (radians)			Restraint Length (L/OD)			
Case 1a	711.2	10	50,000	π/8	π/4	π/2	1	5	10	20
Case 1b	323.85	10	5,000	π/8	π/4	π/2	1	5	10	20
Case 1c	114.3	10	500	π/8	π/4	π/2	1	5	10	20
Case 2a	711.2	5	50,000	π/8	π/4	π/2	1	5	10	20
Case 2b	711.2	20	50,000	π/8	π/4	π/2	1	5	10	20
Case 2c	711.2	40	50,000	π/8	π/4	π/2	1	5	10	20

Table I.3 Asymmetric restraint cases

	OD (mm)	R_m/t	Axial Force (kN)	Half Crack Length (radians)			Restraint Length (L_1/OD)			L_2/OD
							5	10	20	
Case 3a	711.2	10	50,000	π/8	π/4	π/2	X	X	X	1
	711.2	10	50,000	π/8	π/4	π/2		X	X	5
	711.2	10	50,000	π/8	π/4	π/2			X	10
Case 3b	323.85	10	5,000	π/8	π/4	π/2	X	X	X	1
	323.85	10	5,000	π/8	π/4	π/2		X	X	5
	323.85	10	5,000	π/8	π/4	π/2			X	10
Case 3c	114.3	10	500	π/8	π/4	π/2	X	X	X	1
	114.3	10	500	π/8	π/4	π/2		X	X	5
	114.3	10	500	π/8	π/4	π/2			X	10

Table I.4 Problems analyzed by the participants

	Participant A	Participant B	Participant C	Participant D	Participant E	Participant F
Case 1a	X	Partial	X	X	X	X
Case 1b	X	X	X	X	X	X
Case 1c	X		X	X	X	X
Case 2a						X
Case 2b					X	
Case 2c			X	X		
Case 3a						X
Case 3b		X			X	
Case 3c			X	X		

It should be noted that, although the problem statement was very specific about other aspects of the problem, it deliberately avoided stipulating how the restraint conditions in a pipe system and the axial load should be applied in the finite element model. This reflects the complex nature of the restraint conditions in various piping systems. The round-robin participants would have to decide on how the restraint and loading conditions would be imposed in their finite element models according to their own interpretations of the piping system. Indeed, different participants imposed the boundary and loading conditions differently, which might be one of the causes for the observed discrepancies of the COD results in the round-robin cases.

The problem statement as distributed to all participants is given below.

Case 1 – Common Problems – All Participants

Case 1a Problem Statement

Using elastic FEM analyses (brick or thick-shell element), calculate the COD at the center of a circumferential through-wall-cracked pipe using the following input parameters:

- Outside diameter of 28-inch,
- The model can be quarter symmetry to give symmetric boundary conditions either side of the crack, see Figure I.3,
- At the crack plane, allow the pipe to move vertically and horizontally (rotation in the crack plane and ovalization are not restricted), but pin any axial displacements in the ligament,
- Do not apply pressure on the crack faces, and no internal pressure,
- Apply an axial force of 50,000 kN, (11,240 pounds)[1] through the center of the uncracked pipe at the end of the model,
- The mean-radius to thickness ratio is 10,
- The total crack lengths (2θ) are 12.5, 25, and 50 percent of the pipe circumference,
- The distances from the crack to the plane of rotation and ovalization restraint should be 1, 5, 10, and 20 outside diameters of the pipe, as well as, unrestrained rotation and ovalization conditions (capped pressure vessel case) for each crack length.

This should be a matrix of 15 FE analyses, where the COD can be given in a table, as well as plotted in a normalized fashion as in Figure I.4.

1 The applied load value is arbitrarily selected since the analysis is linear elastic and will be normalized for restrained versus unrestrained COD values.

Case 1b Problem Statement – all participants

This is similar to Case 1a, but uses a 12-inch nominal diameter pipe with an R_m/t of 10.

This should also result in a matrix of 15 FE analyses, where the COD can be given in a table, as well as plotted in a normalized fashion as in Figure I.4.

Case 1c Problem Statement – all participants

This is a similar problem, but for the 4-inch nominal diameter pipe case shown in Figure I.5.

Again, this should be a matrix of 15 FE analyses, where the COD can be given in a table, as well as plotted in a normalized fashion as in Figure I.4.

Case 2 – Different R_m/t Cases

Case 2a Problem Statement – Selected Participants

Repeat the analysis for Case 1a, but use an R_m/t ratio of 5.

Case 2b Problem Statement – Selected Participants

Repeat the analysis for Case 1a, but use an R_m/t ratio of 20.

Case 2c Problem Statement – Selected Participants

Repeat the analysis for Case 1a, but use an R_m/t ratio of 40.

Case 3 – Nonsymmetrical Restraint Length Cases

Case 3a Problem Statement – Selected Participants

Repeat the analysis for Case 1a for the 28-inch diameter pipe with an R_m/t of 10, but use the following nonsymmetrical restraint lengths. (Half-symmetry pipe FE model needed in these cases.)

1. Restraint length on one side of the crack is equal to one pipe diameter, and the restraint length on the other side of the crack is 5, 10, and 20 pipe diameters from the crack plane.

2. Restraint length on one side of the crack is equal to 5 pipe diameters, and the restraint length on the other side of the crack is 10 and 20 pipe diameters from the crack plane.

3. Restraint length on one side of the crack is equal to 10 pipe diameters, and the restraint length on the other side of the crack is 20 pipe diameters from the crack plane.

This involves six FE calculations for each of the three crack lengths for a total of 18 FE solutions. COD values were to be provided in a table, and normalized by the unrestrained COD values from Case 1a.

Case 3b Problem Statement – Selected Participants

Repeat the analysis for Case 1b for the 12.75-inch diameter pipe with an R_m/t of 10, and using the same nonsymmetrical restraint lengths as for Case 3a. (Again, half-symmetry pipe FE models are needed in these cases.)

This involves six FE calculations for each of the three crack lengths for a total of 18 FE solutions. COD values were to be provided in a table, and normalized by the unrestrained COD values from Case 1b.

Case 3c Problem Statement – Selected Participants

Repeat the analysis for Case 1c for the 4.5-inch outside diameter pipe with an R_m/t of 10, and using the same nonsymmetrical restraint lengths as for Cases 3a and 3b. (Again, half-symmetry pipe FE model are needed in these cases.)

This involves six FE calculations for each of the three crack lengths for a total of 18 FE solutions. COD values were to be provided in a table, and normalized by the unrestrained COD values from Case 1c.

I.2.3 Modeling Approaches

This section compiles the finite element modeling approaches adapted by each of the round-robin participants. The readers should consider the differences in the modeling approaches when comparing the results from all participants.

I.2.3.1 Participant A - As shown in Table I.4, Participant A only participated in the common round-robin cases (i.e., Case 1). Participant A modeled the pipe using 3D 20-node second-order solid-brick elements. All the meshes and models were created using FEMAP Version 6.0, and solved with ABAQUS Version 5.8. Figure I.8 is a hidden view of a typical finite element mesh. One layer of elements was used through the pipe thickness. A regular mesh, refined around the crack tip, was used to discretize the crack-tip region.

At the restrained end of the pipe, the TIE option of the multipoint constraint (MPC) feature in ABAQUS was used to make all corresponding degrees of freedom of the nodes at the restraint plane equal to those of an extra node on the axis of the pipe. This extra node was used for applying a concentrated force in the axial direction as specified in the problem statement. Tables I.5 through Table I.7 summarize the number of elements and nodes used in each of the cases analyzed by Participant A. Notice that the numbers of elements and nodes increase as the restraint length increases. This is due to the fact that the length of the pipe in the finite element model was set to be same as the restraint length.

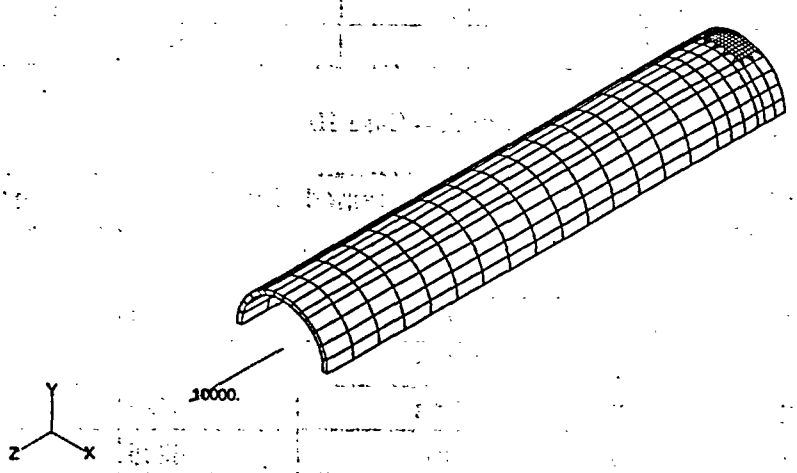

Figure I.8 Representative finite element mesh used by Participant A

Table I.5 Matrix of FE runs by Participant A – Case 1a

Job ID	Half Crack Length	L/D	Constrained	Number Of Nodes	Number Of Elements	Round Robin Case
Pipe3d	π/2	1	Yes	1334	178	Case 1a
Pipe3d1	π/2	5	Yes	2776	374	Case 1a
Pipe3d2	π/2	10	Yes	4630	626	Case 1a
Pipe3d3	π/2	20	Yes	8235	1116	Case 1a
Pipe3d4	π/2	20	No	8235	1116	Case 1a
Pipe3dx	π/4	1	Yes	1334	178	Case 1a
Pipe3dx1	π/4	5	Yes	2776	374	Case 1a
Pipe3dx2	π/4	10	Yes	4630	626	Case 1a
Pipe3dx3	π/4	20	Yes	8235	1116	Case 1a
Pipe3dx4	π/4	20	No	8235	1116	Case 1a
Pipe3dy	π/8	1	Yes	1278	167	Case 1a
Pipe3dy1	π/8	5	Yes	2719	363	Case 1a
Pipe3dy2	π/8	10	Yes	4573	615	Case 1a
Pipe3dy3	π/8	20	Yes	8179	1178	Case 1a
Pipe3dy4	π/8	20	No	8179	1178	Case 1a

Table I.6 Matrix of FE runs by Participant A – Case 1b

Job ID	Half Crack Length	L/D	Constrained	Number Of Nodes	Number Of Elements	Round Robin Case
12Pipe3d	π/2	1	Yes	1334	178	Case 1b
12Pipe3d1	π/2	5	Yes	2776	374	Case 1b
12Pipe3d2	π/2	10	Yes	4630	626	Case 1b
12Pipe3d3	π/2	20	Yes	8235	1116	Case 1b
12Pipe3d4	π/2	20	No	8235	1116	Case 1b
12Pipe3dx	π/4	1	Yes	1334	178	Case 1b
12Pipe3dx1	π/4	5	Yes	2776	374	Case 1b
12Pipe3dx2	π/4	10	Yes	4630	626	Case 1b
12Pipe3dx3	π/4	20	Yes	8235	1116	Case 1b
12Pipe3dx4	π/4	20	No	8235	1116	Case 1b
12Pipe3dy	π/8	1	Yes	1278	167	Case 1b
12Pipe3dy1	π/8	5	Yes	2719	363	Case 1b
12Pipe3dy2	π/8	10	Yes	4573	615	Case 1b
12Pipe3dy3	π/8	20	Yes	8179	1178	Case 1b
12Pipe3dy4	π/8	20	No	8179	1178	Case 1b

Table I.7 Matrix of FE runs by Participant A – Case 1c

Job ID	Half Crack Length	L/D	Constrained	Number Of Nodes	Number Of Elements	Round Robin Case
4Pipe3d	π/2	1	Yes	1334	178	Case 1c
4Pipe3d1	π/2	5	Yes	2776	374	Case 1c
4Pipe3d2	π/2	10	Yes	4630	626	Case 1c
4Pipe3d3	π/2	20	Yes	8235	1116	Case 1c
4Pipe3d4	π/2	20	No	8235	1116	Case 1c
4Pipe3dx	π/4	1	Yes	1334	178	Case 1c
4Pipe3dx1	π/4	5	Yes	2776	374	Case 1c
4Pipe3dx2	π/4	10	Yes	4630	626	Case 1c
4Pipe3dx3	π/4	20	Yes	8235	1116	Case 1c
4Pipe3dx4	π/4	20	No	8235	1116	Case 1c
4Pipe3dy	π/8	1	Yes	1278	167	Case 1c
4Pipe3dy1	π/8	5	Yes	2719	363	Case 1c
4Pipe3dy2	π/8	10	Yes	4573	615	Case 1c
4Pipe3dy3	π/8	20	Yes	8179	1178	Case 1c
4Pipe3dy4	π/8	20	No	8179	1178	Case 1c

I.2.3.2 Participant B - Participant B solved Case 1a (except for the case of L/D=5), Case 1b, and Case 3b. The finite element code used by Participant B was ABAQUS.

For the symmetrically restrained cases, a quarter symmetry model with 776 elements and 4,641 nodes was applied. Regardless of the restraint length, the same FE model with a pipe length of $30D_m$ (pipe mean diameter) was used. Only the location to apply the load and the boundary condition were changed in accordance with the restraint lengths specified for each problem.

For the cases of the asymmetric restraint length, a half symmetry model with 1,160 elements and 6,897 nodes was applied. Similar to the symmetric restraint cases, a single FE model with a pipe length of $50D_m$ was used.

For all the cases, two layers of elements were used for pipe thickness. The crack tip region was discretized with a focused mesh. The 20-noded second-order brick elements were used. Figure I.9 and Figure I.10 show the finite element meshes for the symmetric restraint length and asymmetric restraint length cases, respectively.

The axial load was applied on the cross-section plane at a distance equal to the restraint length from the cracked plane as a uniform tensile stress calculated from the axial force.

Boundary conditions for the unrestraint cases

In the symmetric restraint model, the z-directional symmetry boundary condition was applied to all nodes in the crack ligament and the y-directional displacement at a node on the center of the crack ligament was fixed to prevent the free body motion.

In the asymmetric restraint model, a node on the center of the crack ligament was fixed in the y and z directions to prevent the free body motion. In addition, the tensile stresses were applied on the two planes at the respective restraint lengths from the crack plane.

In both models, the rotations induced by applied axial load was allowed.

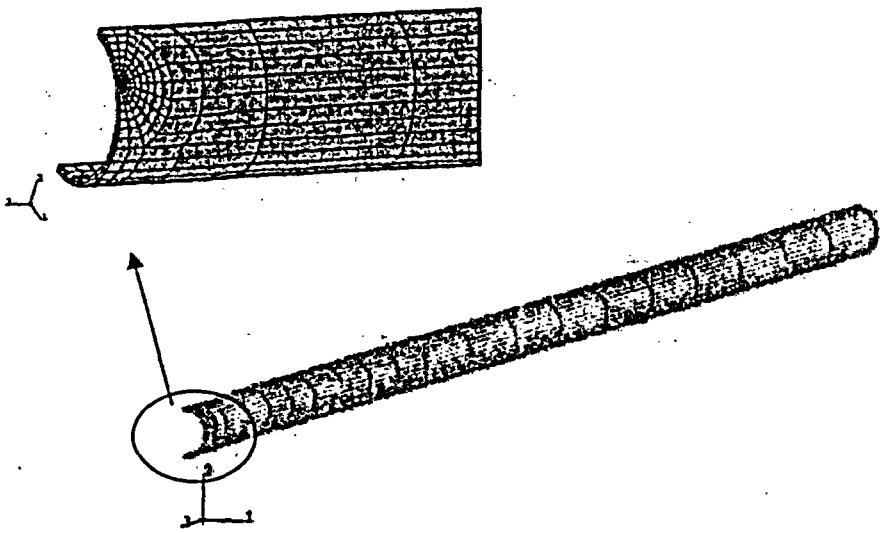

Figure I.9 Finite element mesh used by Participant B for symmetric restraint cases

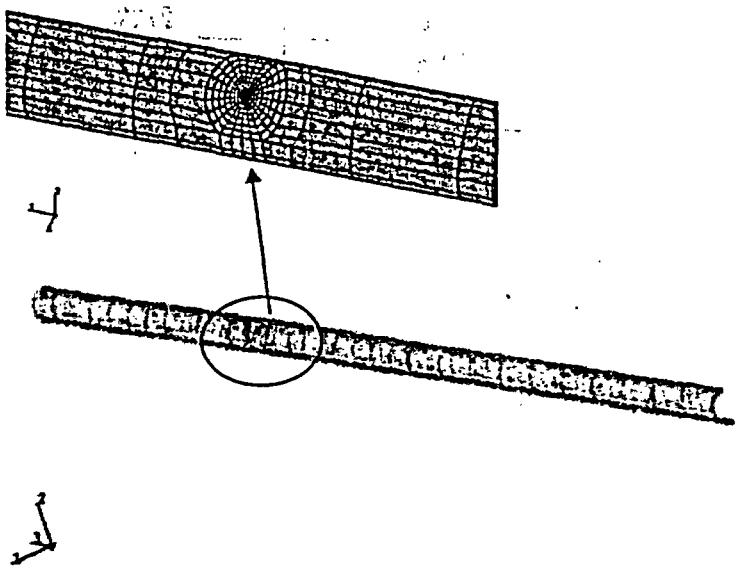

Figure I.10 Finite element mesh used by Participant B for asymmetric restraint cases

Boundary conditions for the restraint cases

The restraint to pressure-induced bending was simulated by constraining the movement in both the radial and circumferential directions, but allowing for the axial movement, for all the nodes beyond the restraint lengths. This is shown in Figure I.11 and Figure I.12.

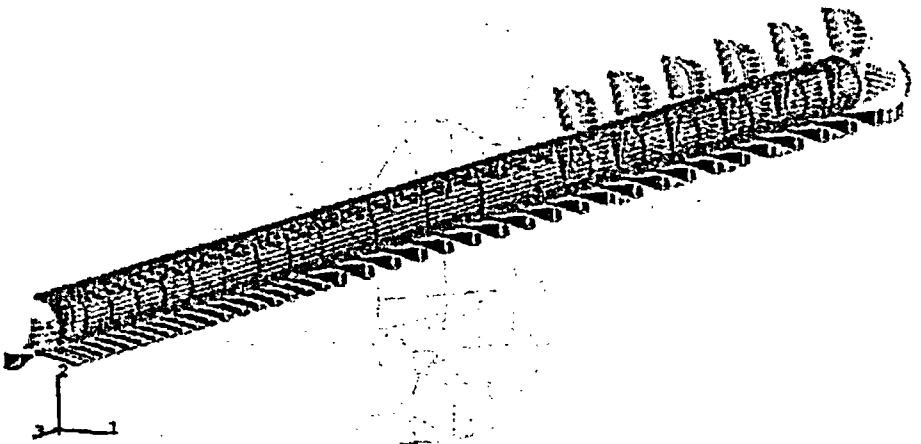

Figure I.11 Boundary conditions for restraining the bending induced tension in the symmetric FE model

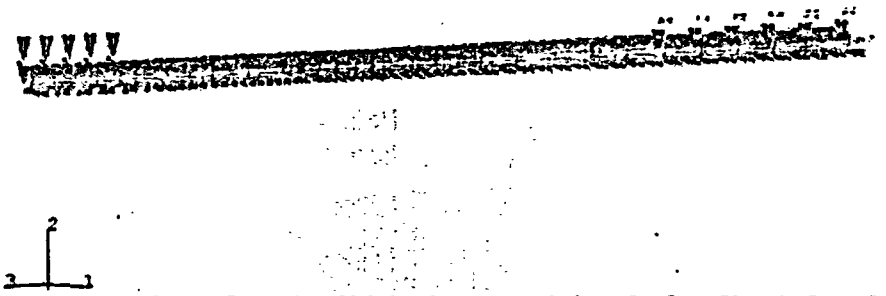

Figure I.12 Boundary conditions for restraining the bending induced tension in the asymmetric FE model

I.2.3.3 Participant C – Participant C used ABAQUS Version 5.8-14 for the COD calculations. 20-noded second-order solid brick elements with reduced integration (ABAQUS element type C3D20R) were used. The pipe length was set to the restraint length for the symmetric restraint cases (quarter-symmetrical model), and the sum of the two restraint lengths for the asymmetric restraint cases (half-symmetrical model). For the unrestraint cases, the length of the pipe was set to $20D_m$. Additional analyses were also performed with pipe lengths up to $100D_m$ to evaluate the effect of pipe length on the unrestraint CODs.

The prescribed axial load was imposed using the "Distributing Coupling Element" feature in ABAQUS as shown in Figure I.13. The distributing coupling element ties all the nodes at the end of the pipe to a single-noded coupling element (Node 1 in Figure I.13) located on the axis of the pipe. The total axial force is applied through the coupling element that then distributes the load to the end of the pipe.

To simulate the pipe restraint effects, the end of the pipe is fixed against the radial and circumferential movement, while allowing for the axial movement. This is shown in Figure I.14 and Figure I.15, respectively, for the symmetric, and asymmetric restraint length cases, respectively.

Figure I.16 shows the axial stress and displacement distributions obtained with the distributing coupling element. It clearly shows that, although the displacement is relatively uniform, the stress varies significantly at the restraint plane.

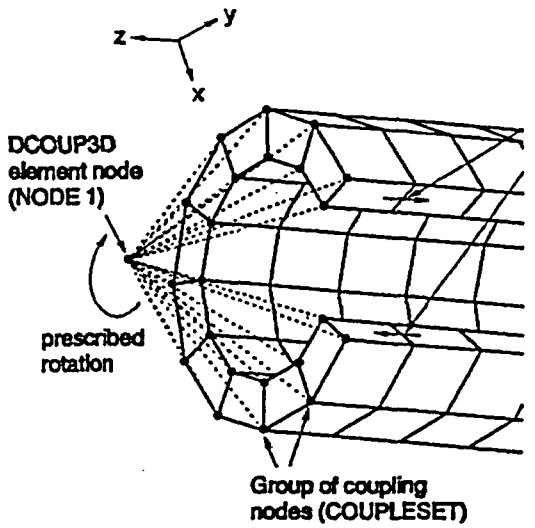

Figure I.13 The "Distributing Coupling Element" in ABAQUS

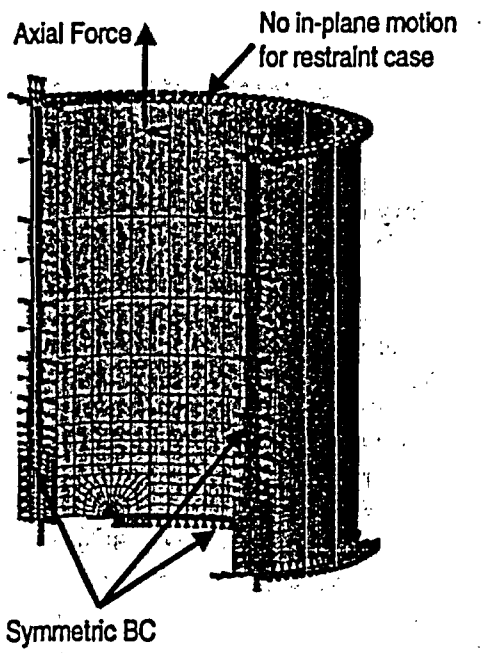

Figure I.14 The finite element mesh and associated boundary conditions used by Participant C for the symmetric restraint cases

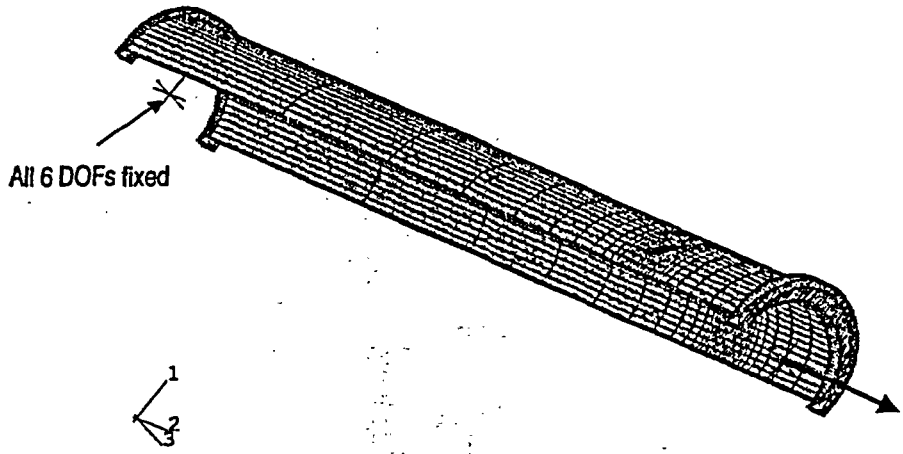

Figure I.15 The finite element mesh and associated boundary conditions used by Participant C for the asymmetric restraint cases

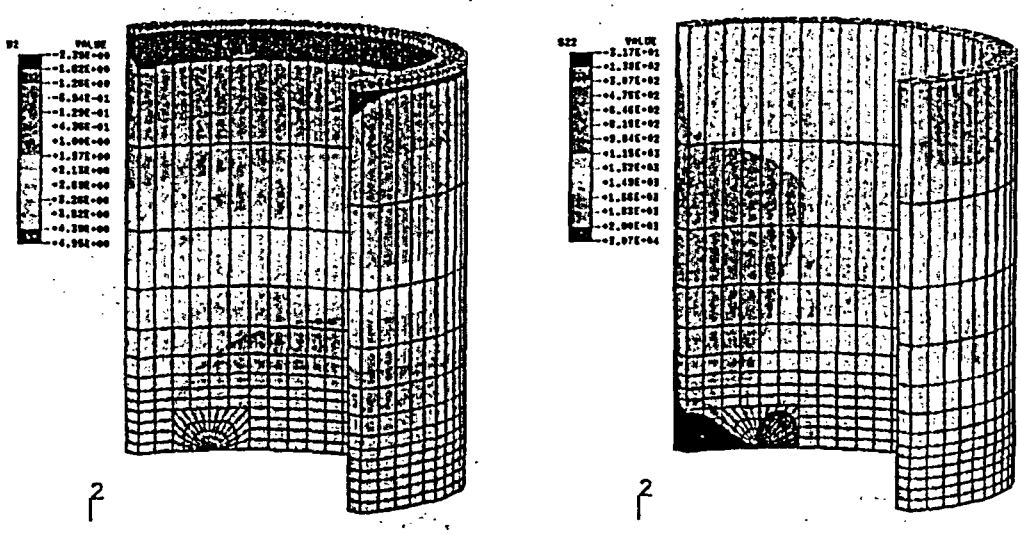

Figure I.16 Axial displacement and stress distributions using the distributing coupling element to impose the axial load (Case 1a, L/D=1, θ/π=1/8, Participant C)

I.2.3.4 Participant D - Participant D used ABAQUS Version 5.8-17 to solve all the cases. 8-noded first-order solid-brick elements with reduced integration (ABAQUS element type C3D8R) were used to discretize the pipe. The number of element layers along the pipe thickness was one. Since there was no node at the mid-thickness, the COD was calculated by averaging the displacements of the nodes on the inner and outer surfaces of the pipe at the crack center.

Similar to Participant B, the pipe length in the finite element model was the same for all the cases analyzed, which is 20D for the symmetric cases, and 30D for the asymmetric cases. The restraint length effect was treated by changing the boundary conditions such that the restrained section of the pipe only allowed for the axial displacement.

Figure I.17 shows the finite element mesh used by Participant D. Focused mesh was not used. The pipe was meshed out evenly in the circumferential direction, but with a finer

element length in the axial direction at the cracked section.

The axial load was applied to the end of the pipe as a uniform tension stress calculated from the axial force.

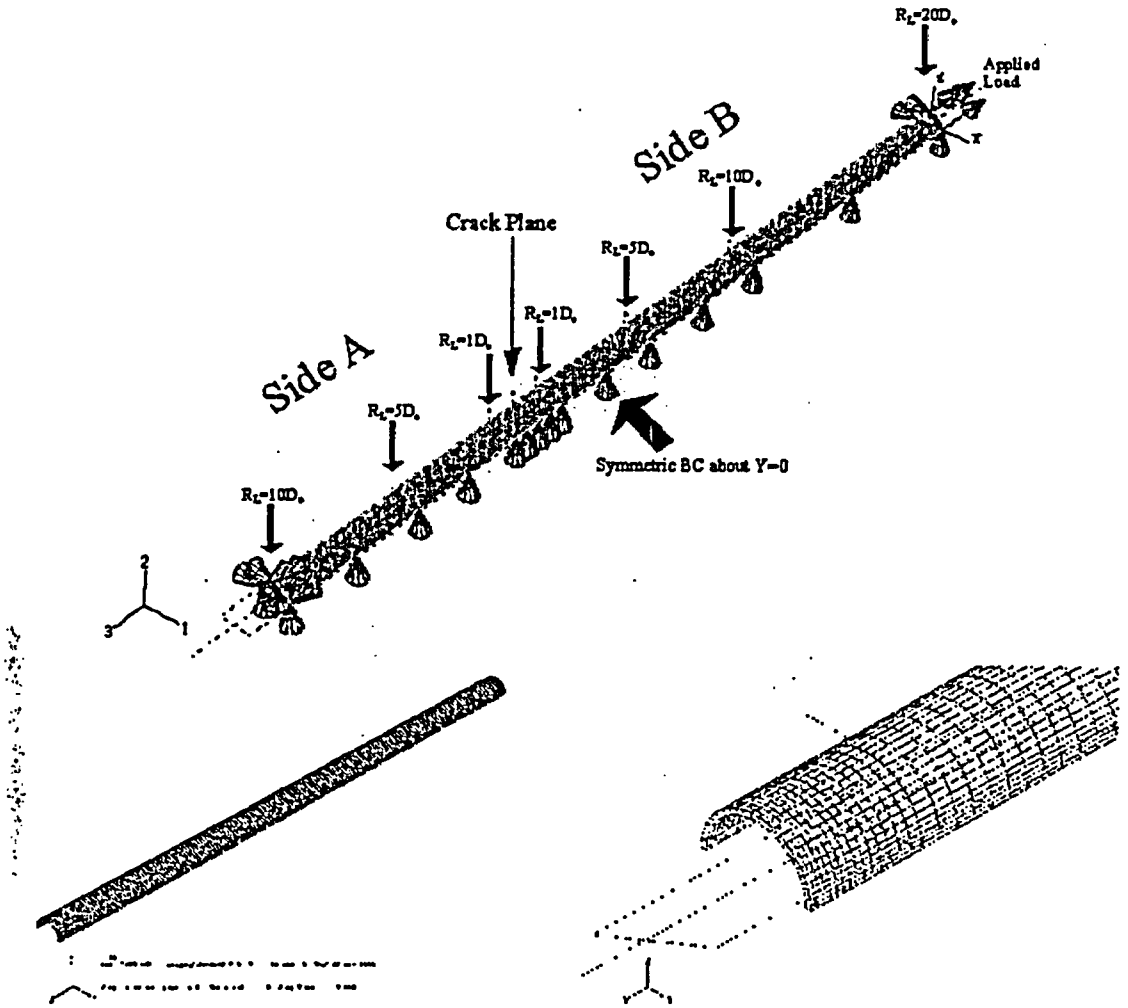

Figure I.17 Boundary conditions and mesh used by Participant D

I.2.3.5 Participant E - Participant E followed the basic steps as described in the NUREG/CR-6300 report, which were:

Step 1: Create a finite element model of a cracked pipe with a total pipe length of twice the restraint length.

Step 2: Apply an arbitrary positive (tensile) displacement loading, Δ, in the axial direction of the pipe to all the nodes in the cross section located at a distance L_R from the cracked plane.

Step 3: Conduct a finite element analysis and determine the COD resulting from the remote displacement, Δ. The stresses at the cross section A-A are not uniform and can be decomposed into a bending component and a tensile component. Denote the COD (unscaled) and the tension stress by δ_{uns} and σ_{ten}, respectively.

Step 4: Compute the scaled COD, $\delta_s = \delta_{uns} \times (\sigma_{ref} / \sigma_{ten})$, where σ_{ref} is reference tensile stress.

Step 5: In the same finite element model apply a

tension stress loading of magnitude σ_{ref} but allowing free rotation. Denote the resultant COD by δ_{∞}.

Step 6: Divide the scaled COD, δ_s, by the reference COD, δ_{∞}, to get the normalized COD, $\delta_{NOR} = \delta_s / \delta_{\infty}$.

Step 7: For a given crack geometry, repeat Steps 1-6 for several values of L_R. Develop a plot of δ_{NOR} versus L_R / D_m and hence, determine the effects of the normalized restraint length, L_R / D_m on the COD.

Figure I.18 shows a typical mesh design for the symmetric restraint case. Linear elastic finite element analyses were performed using the 20-noded 3D brick elements in ABAQUS. A focused mesh was used at the crack tip. The total number of elements was 936. Two layers of elements were used through the thickness. Considering the symmetric condition, only one quarter of the pipe was modeled. The arbitrary applied axial displacement, Δ, was set equal to 2.54 mm (0.1 inches) (Step 2). The applied displacement was applied through a MPC (multi-point constraint in ABAQUS) at the end of the pipe (allow free rotation and no ovalization restrictions). The COD values were estimated at the mean thickness of the center of the crack.

Figure I.19 shows a typical mesh for the asymmetric case, which is a half symmetric FE model. A focused mesh was also used at the crack tip. The total number of elements was 1,552. All displacements and rotations were fixed at one end of the pipe (the right end in Figure I.19), while the other end was subjected to the given applied axial displacement. The COD values were normalized by the unrestrained COD values from Case 1b.

I.2.3.6 Participant F – Participant F calculated the COD values using MARC, a commercial finite element package. 20-noded 3D solid brick elements were used, with a focused mesh near the crack tip. The number of element layers along the pipe thickness was one.

On the restrained section, all the nodes were tied to the node where the rotation around all three axes was fixed (see Figure I.20), so that all the nodes on the restraint plane remained plane during loading. The concentrated axial load was then applied to the tying node.

For the unrestrained cases, the pipe length was set to be equal to 20 times the mean diameters.

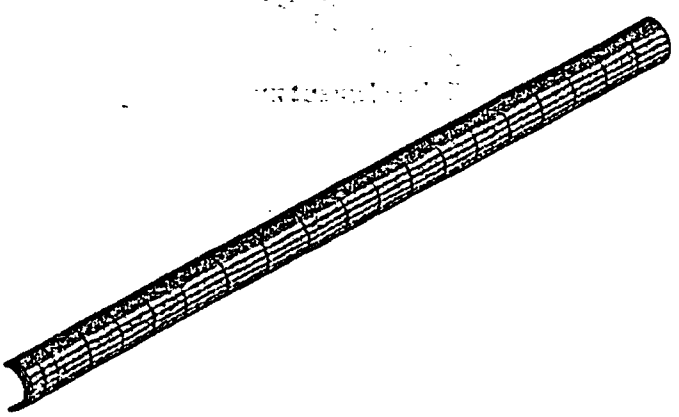

Figure I.18 Typical finite element mesh for the symmetric case by Participant E

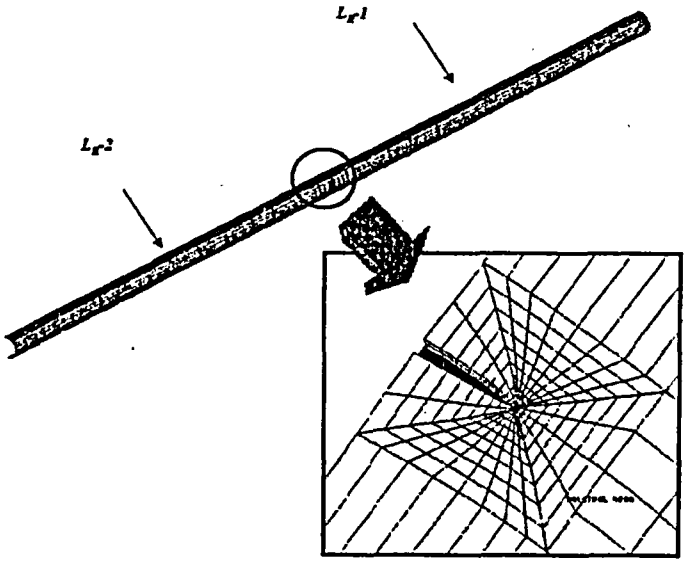

Figure I.19 Typical finite element mesh for the asymmetric case by Participant E

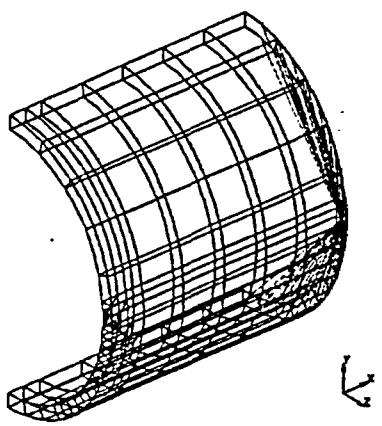

Figure I.20 Typical finite element mesh used by Participant F

Table I.8 Summary of model features

	Participant A	Participant B	Participant C	Participant D	Participant E	Participant F
Pipe length	Restraint length	$30D_m$, $50D_m$ (*)	Restraint length	20D, 30D (*)	Restraint length	Restraint length
Simulation of restraint	At pipe end	On restraint length	At pipe end	On restraint length	At pipe end	At pipe end
Application of axial load	Concentrated force at the TIE node	Uniform stress at restraint plane	Concentrated force at the TIE element	Uniform stress at restraint plane	Uniform displacement at pipe end	Concentrated force at the tying node
Element type	3D 20-node brick	3D 20-node brick	3D 20-node brick with reduced integration	3D 8-node brick with reduced integration	3D 20-node brick	3D 20-node brick
Number of element layer through wall thickness	1	2	1	1	2	1
Mesh refinement	Refined regular mesh at crack tip	Focused mesh at crack tip	Focused mesh at crack tip	Regular mesh	Focused mesh at crack tip	Focused mesh at crack tip
FEM code	ABAQUS	ABAQUS	ABAQUS	ABAQUS	ABAQUS	MARC

(*) for symmetric and asymmetric restraint, respectively.

I.2.4 Remarks On Modeling Approaches

Clearly, there are some marked differences among the modeling approaches used by the six participants. Except for Participant D, all other participants used 20-noded second order solid brick elements and the focused mesh around the crack tip. The number of element layers through the pipe wall thickness was divided: four participants used 1 layer of elements whereas the other 2 participants used 2 layers. Moreover, different approaches were employed to deal with the restraint length and the application of the axial load, reflecting the differences in participants' interpretation of the restraint condition in the actual pipe systems. Table I.8 summaries the major features of each participant's modeling approach.

I.2.5 Results And Discussion

I.2.5.1 Effect of Pipe Length on COD of Unrestraint Pipe - The problem statement did not specify the pipe length for the COD calculation of the unrestrained pipe (i.e., the end-capped vessel). Theoretically, it should be infinitely long. Both Participants C and F investigated the effect of the pipe length on COD of the unrestrained pipe. Figure I.21 shows the results by Participant F for the longest crack length ($\theta=\pi/2$), where θ is half the total crack length. Clearly, pipe lengths greater than $20D_m$, as used for all the participants, are sufficiently long for the COD calculations for the unrestrained pipe.

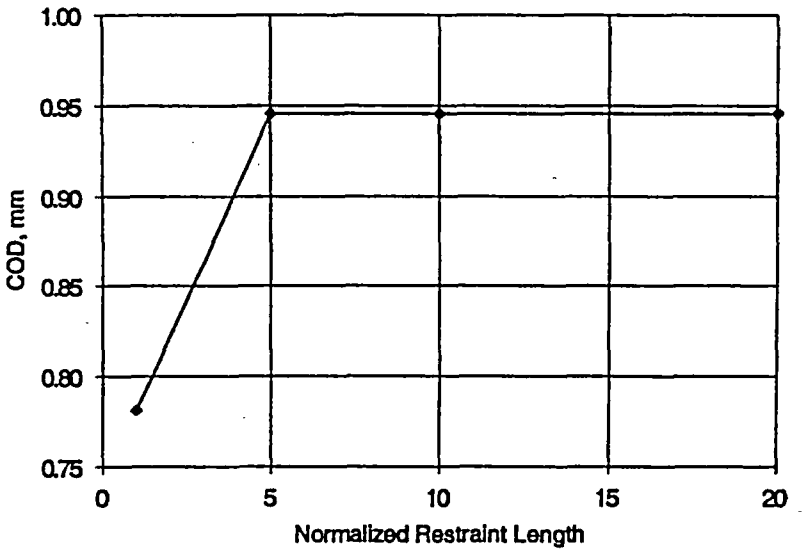

Figure I.21 Effect of pipe length on COD of unrestrained pipe for the longest crack length investigated in this program. Participant F

I.2.6 Comparison of Round-Robin (Case 1) Results

I.2.6.1 Comparison of COD Values in Unrestrained Pipes - Error! Reference source not found.I.22 shows the comparison of the COD values of the unrestrained pipes (the end-capped vessel case) obtained by all participants for the common round-robin cases ($R_m/t = 10$). The COD values are normalized by the mean COD value of all participants for the same case. Overall, the results from Participant C, E, and F are consistent among each other. The discrepancies are within 1% from the mean COD value averaged among these three participants, as shown in Figure I.23.

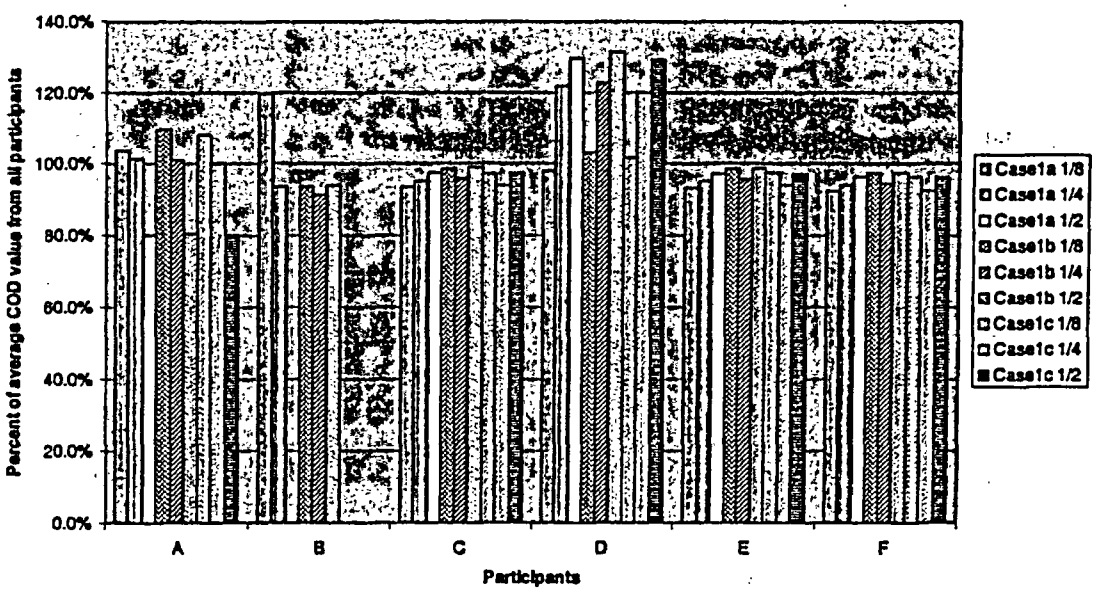

Figure I.22 Comparison of the unrestrained COD values for Cases 1a-1c. The COD values are normalized with respect to the averaged COD value of all participants

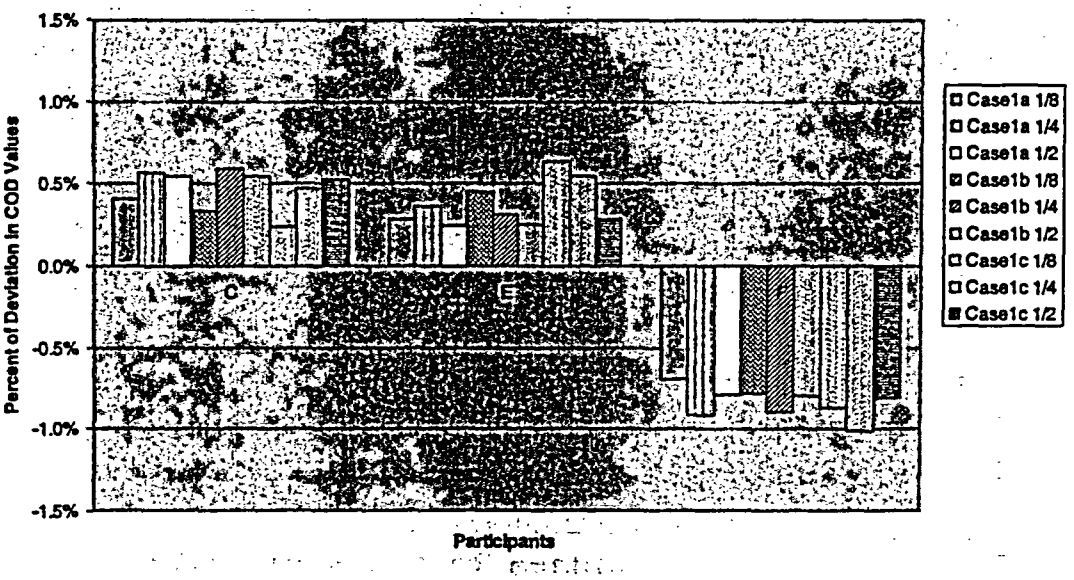

Figure I.23 Comparison of the unrestrained COD values from Participant C, E, and F for Cases 1a-1c. The COD values are normalized by the mean COD value of the three participants of the same case

For the two shorter crack lengths ($\theta=\pi/8$, and $\theta=\pi/4$), the COD values from Participant A were close to the average. However, the CODs of the longest crack length ($\theta=\pi/2$) were only 80% of the averaged values.

Participant B also did reasonably well, expect for one particular case (Case 1a, $\theta=\pi/8$) where the COD was about 120% of the mean value.

The biggest discrepancies were from Participant D for the two long crack cases ($\theta=\pi/4$ and $\theta=\pi/2$). The COD values are over 20 percent higher than the mean values. Table I.9 summarizes the observations on the unrestrained COD comparisons.

Table I.9 Observations on unrestrained pipe case

Participant	Comparison to average from group	Case by case scatter
A	Lower for longest crack length	Significant
B	About the same	One case much higher
C	Very close	Very low
D	Much higher	Significant
E	Very close	Very low
F	Very close	Very low

I.2.6.2 Effect of Pipe Diameter - Despite the fact that the COD values for a specific case could be different, among the different participants all participants reported that the pipe

diameter has no noticeable effect on the ***normalized*** COD values for all the cases in Case 1. The normalized COD only depends on the crack length, R_m/t ratio, and the restraint length. This is illustrated from the data of Participants A and C in Figures I.24 and I.25, respectively. The independence of COD on pipe diameter simplifies the comparison of the round-robin results (Case 1) – it is unnecessary to distinguish the results from different diameter pipes.

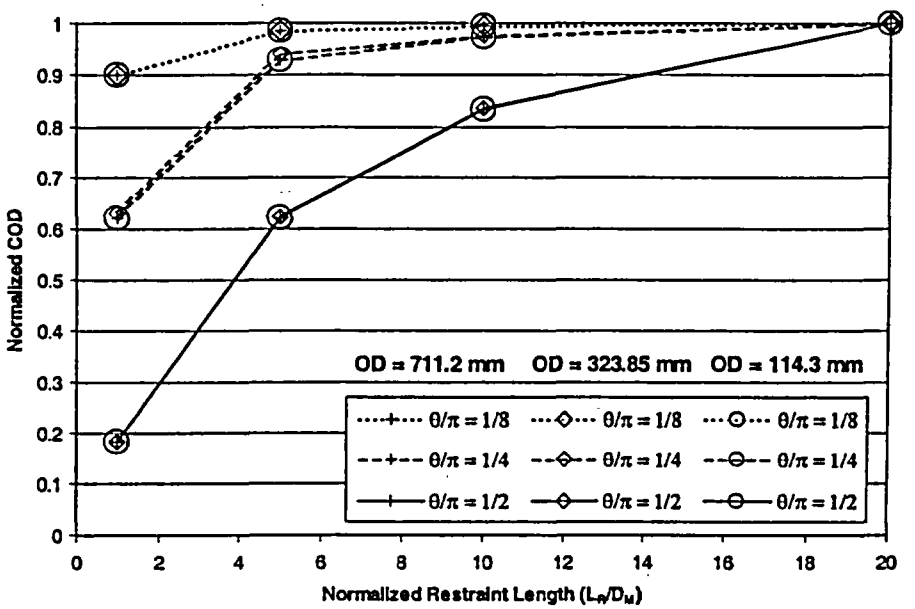

Figure I.24 Normalized COD values for Case 1a-1c from Participant A

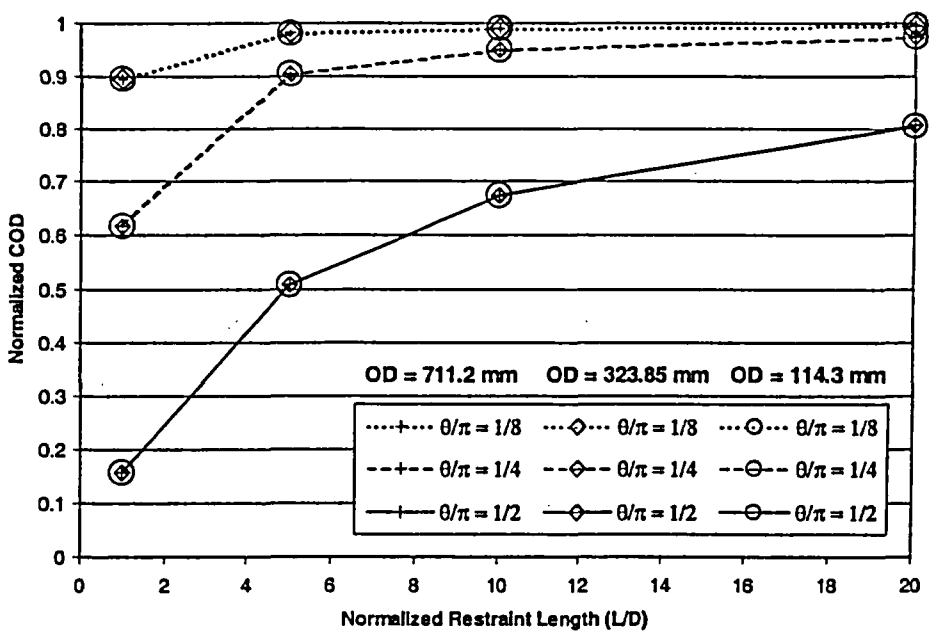

Figure I.25 Normalized COD values for Case 1a-1c from Participant C

I.2.6.3 Comparison of Restraint Cases in Case 1 – Figure I.26 through Figure I.28 show the normalized COD, respectively for each of the crack lengths investigated in the common round-robin cases. Also shown in these figures are the results reported in NUREG/CR-6443 (Ref. I.1). Overall, all participants reported the same trends on the effects of the restraint length and crack length on the normalized COD. The results from Participant C and F are always consistent for all the cases in the round-robin.

The normalized COD calculated by Participant D were consistently lower than those by the other five participants. This might be attributed to the use of the one-layer, first-order elements and the non-focused mesh around the crack tip by Participant D. Also troublesome was the use of uniformed stress to apply the axial load by Participant D. The previous results reported in NUREG/CR-6443 (Ref. I.1) also show noticeable discrepancies when compared with the round-robin results.

Excluding the results from Participant D, the results from all other five round-robin participants are plotted in Figure I.29, for all the round-robin cases. The results are quite consistent for the two short lengths ($\theta=\pi/8$, and $\theta=\pi/4$), with the exception of one data point from Participant B at (L/D=1 and $\theta=\pi/4$). On the other hand, there is noticeable scatter for the cases with the longest crack length ($\theta=\pi/2$).

Table I.10 summarizes the comparison of the round-robin cases among all participants.

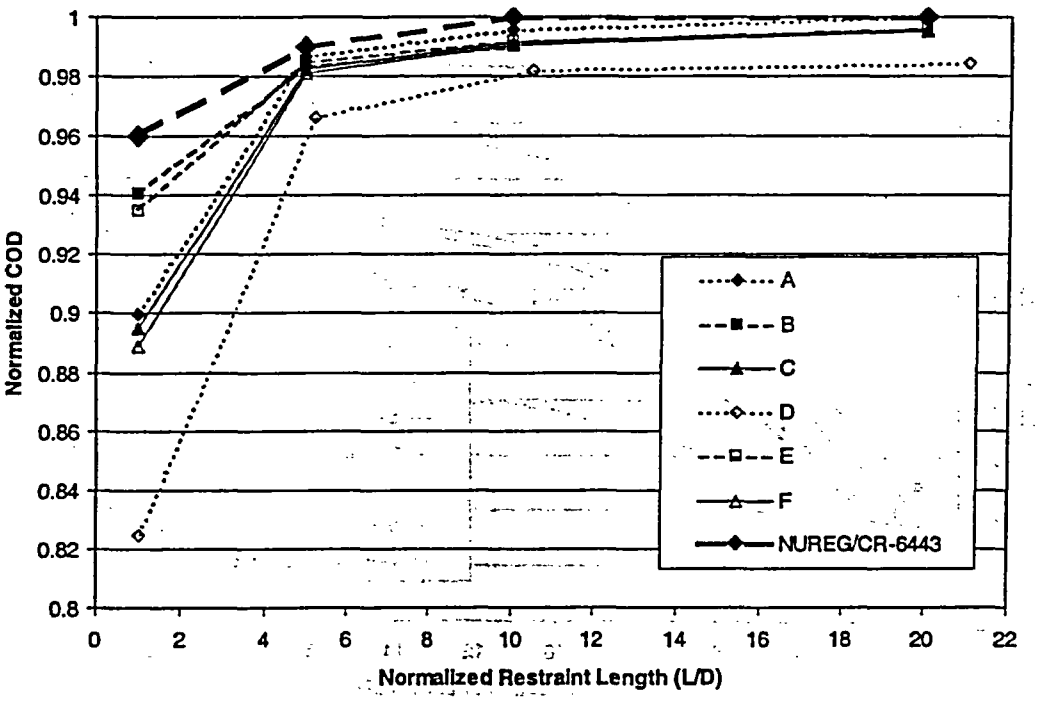

Figure I.26 Comparison of normalized COD in Case 1, half crack length = $\pi/8$

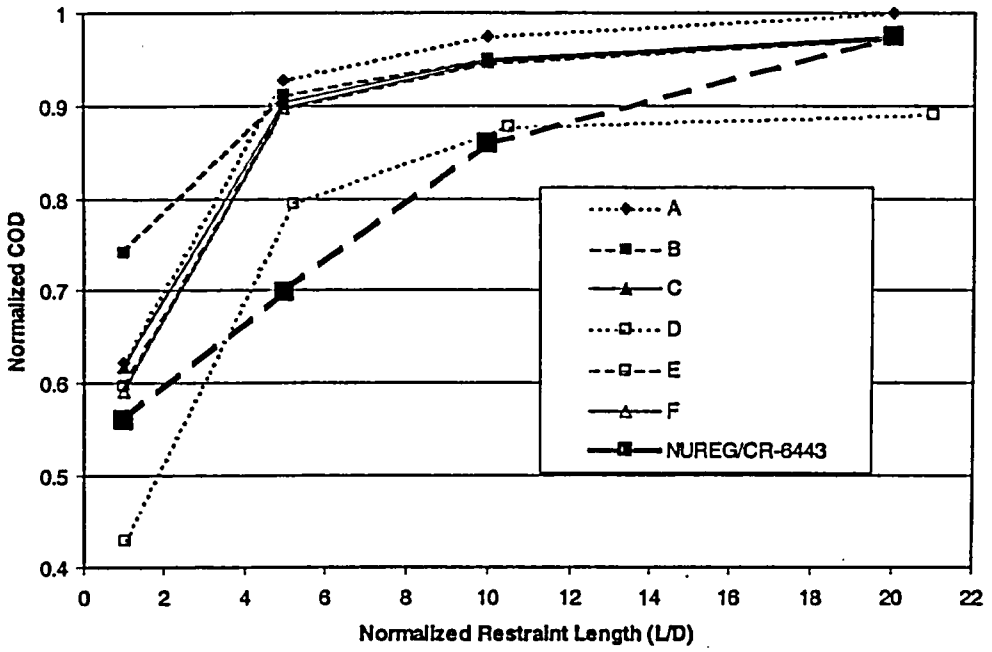

Figure I.27 Comparison of normalized COD in Case 1, half crack length = $\pi/4$

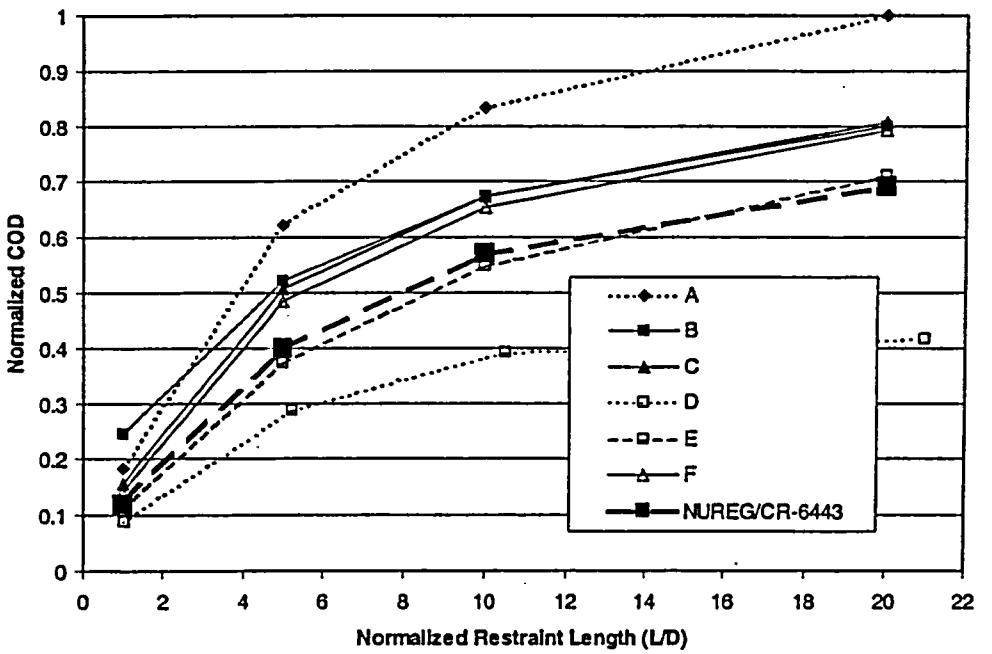

Figure I.28 Comparison of normalized COD in Case 1, half crack length = $\pi/2$

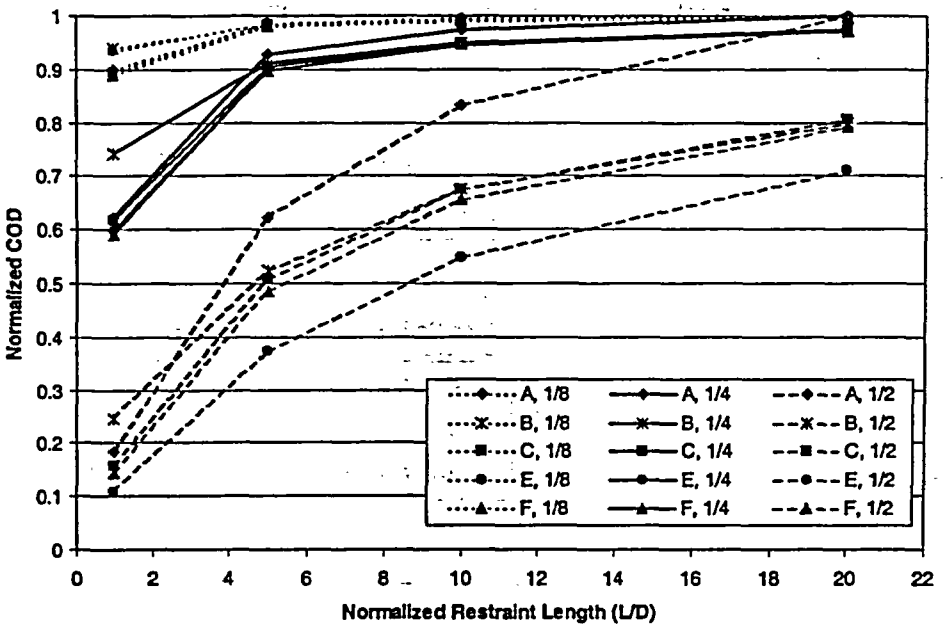

Figure I.29 Comparison of normalized COD for all round-robin cases in Case 1, excluding the results from Participant D and NUREG/CR-6443 (Ref. I.1)

Table I.10 Observations on the round-robin case comparisons

Participant	Comparison to Average from Group
A	Agrees with C, F for $\theta=\pi/8$ and $\pi/4$ but higher for $\theta=\pi/2$
B	Agrees with C, F except for shortest restraint length
C, F	Agree with each other all the time and in the middle of entire group results
D	Generally lower than others
E	Agrees with C, F for $\theta=\pi/8$ and $\pi/4$ but lower for $\theta=\pi/2$
NUREG/CR-6443	Highest for short flaws, lower than C, F for longer flaws

I.2.7 Effect of R_m/t Ratio (Case 2)

The effects of R_m/t ratio on the normalized COD are analyzed by comparing the results in Case 1 and Case 2. As shown in Table I.4, only four participants took part in Case 2, and each participant analyzed a subset of Case 2. The results are presented in Figure I.30 through Figure I.33. The normalized COD increases as R_m/t ratio decreases.

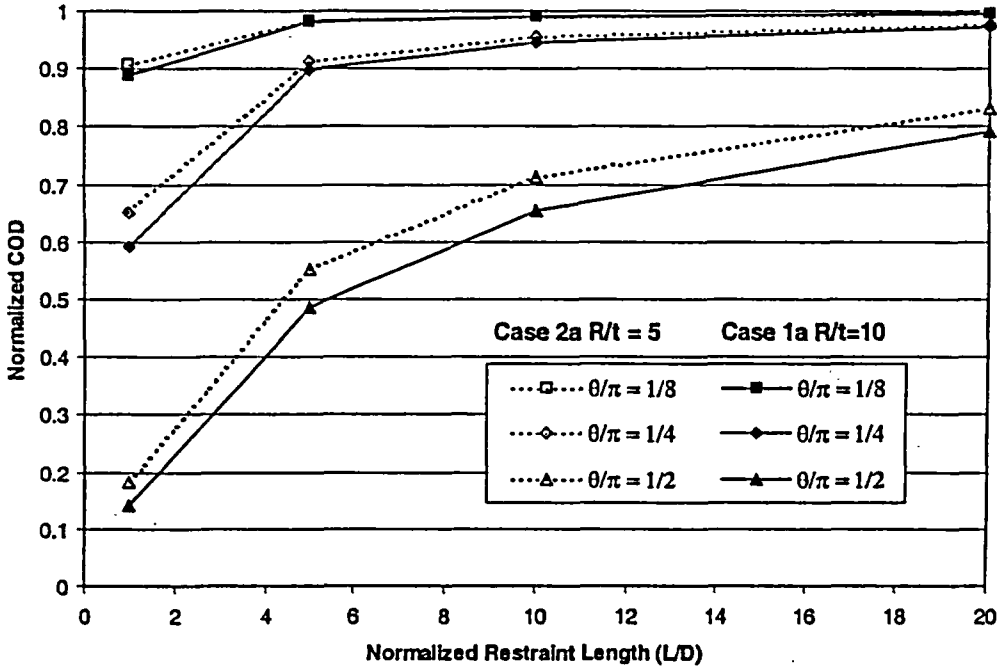

Figure I.30 Effect of R_m/t ratio on normalized COD. Participant F, OD=28-inch

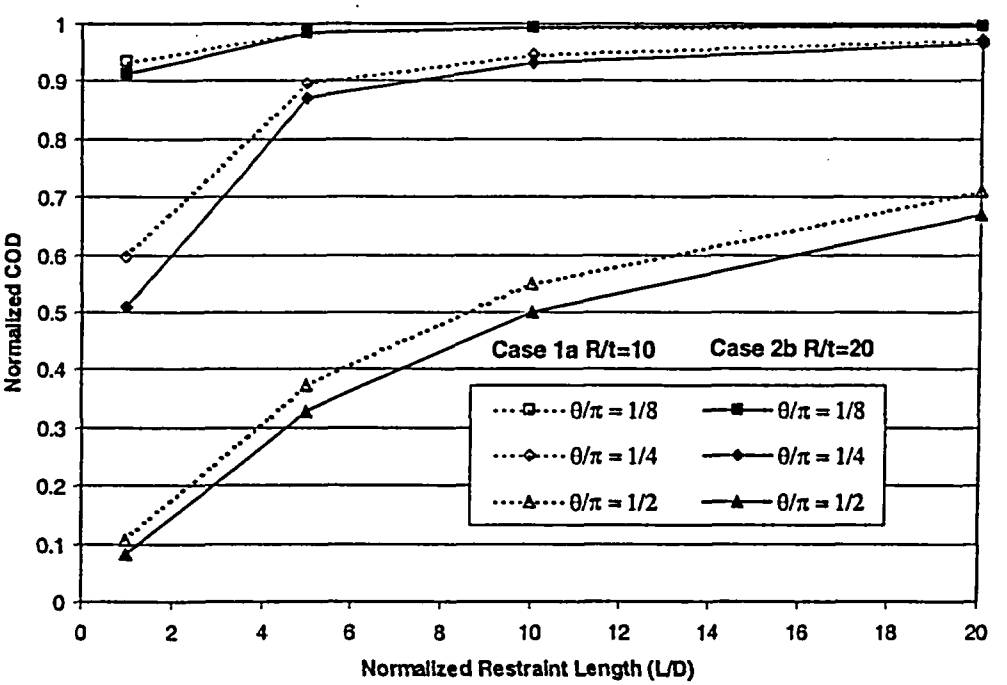

Figure I.31 Effect of R_m/t ratio on normalized COD. Participant E, OD=28-inch

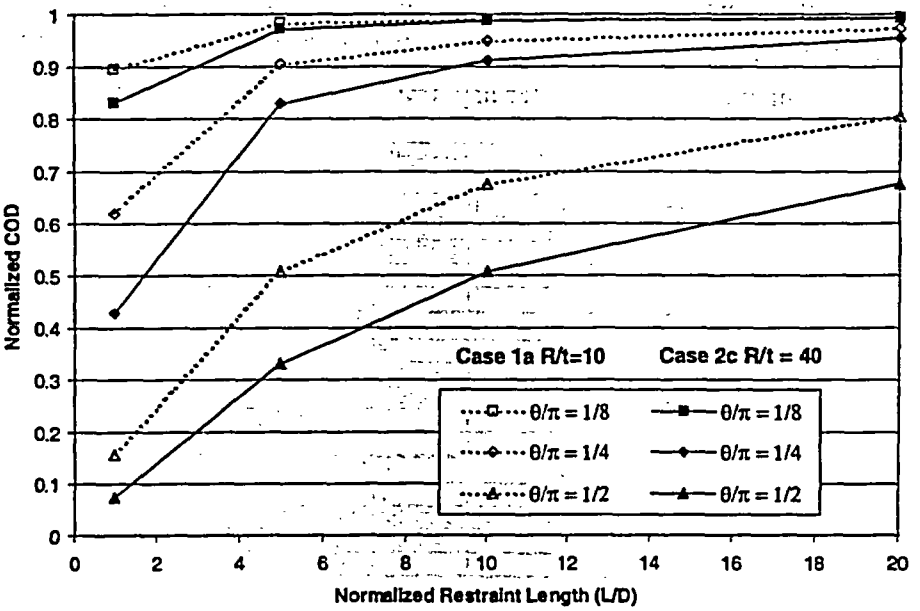

Figure I.32 Effect of R_m/t ratio on normalized COD. Participant C, OD=28-inch

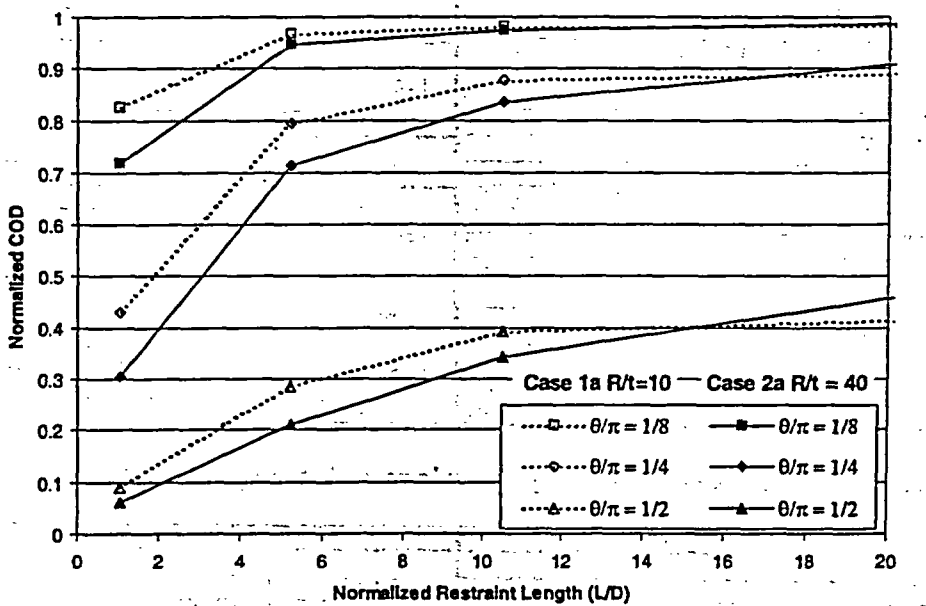

Figure I.33 Effect of R_m/t ratio on normalized COD. Participant D, OD=28-inch

I.2.8 Effect of Asymmetric Restraint Length (Case 3)

Similar to Case 2, each participant was assigned to solve a subset of Case 3. The results are tabulated in Table I.11 to Table I.13. The effects of non-symmetric restraint are depicted in Figure I.34 to Figure I.36, using a subset of the results. Similar to the effect of reducing the symmetric restraint length from both sides of the crack plane, the normalized COD value decreases as the restraint length from one side of the crack plane is shortened. The effect of the asymmetric restraint length is more pronounced as the asymmetry in the restraint length increases. However, significant reductions from

the normalized COD of the symmetrically restrained pipe only exist when the crack length is longest ($\theta=\pi/2$), or the restraint length on one side of the crack plane is very short ($L_2/D=1$).

Table I.11 Normalized COD under asymmetric restraint length, OD=28-inch

Case 3a Participant F					
θ/π = 1/8		L_1/D			
		1	5	10	20
L_2/D	1	0.888915	0.924125	0.93891	0.95639
	5		0.981084	0.983291	0.984323
	10			0.990478	0.991539
	20				0.995292
θ/π = 1/4		L_1/D			
		1	5	10	20
L_2/D	1	0.59183	0.68585	0.736959	0.805576
	5		0.897811	0.908835	0.914071
	10			0.94623	0.952008
	20				0.972409
θ/π = 1/2		L_1/D			
		1	5	10	20
L_2/D	1	0.143176	0.203258	0.251817	0.349994
	5		0.484868	0.516988	0.533301
	10			0.655057	0.681819
	20				0.792594

Table I.12 Normalized COD under asymmetric restraint length, OD=12.75-inch

Case 3b Participant B					
θ/π = 1/8		L_1/D			
		1	5	10	20
L_2/D	1	0.940865	0.950959	0.958131	0.969925
	5		0.983497	0.977444	0.985965
	10			0.991099	0.99199
	20				0.995303
θ/π = 1/4		L_1/D			
		1	5	10	20
L_2/D	1	0.742396	0.774126	0.803464	0.853369
	5		0.910451	0.919498	0.922728
	10			0.950063	0.954941
	20				0.973478
θ/π = 1/2		L_1/D			
		1	5	10	20
L_2/D	1	0.245671	0.275446	0.313982	0.40025
	5		0.522858	0.54151	0.550999
	10			0.673468	0.697404
	20				0.798483

Case 3b Participant E					
θ/π = 1/8		L_1/D			
		1	5	10	20
L_2/D	1	0.935	0.963	0.974	0.979
	5		0.986	0.991	0.995
	10			0.993	0.996
	20				0.997
θ/π = 1/4		L_1/D			
		1	5	10	20
L_2/D	1	0.597	0.8	0.86	0.899
	5		0.896	0.928	0.955
	10			0.945	0.964
	20				0.972
θ/π = 1/2		L_1/D			
		1	5	10	20
L_2/D	1	0.113	0.273	0.404	0.549
	5		0.399	0.502	0.628
	10			0.574	0.669
	20				0.73

Table I.13 Normalized COD under asymmetric restraint length, OD=4.5-inch

Case 3c Participant C					
θ/π = 1/8		L_1/D			
		1	5	10	20
L_2/D	1	0.895167	0.929368	0.944238	0.959108
	5		0.982156	0.98513	0.98513
	10			0.991078	0.992565
	20				0.995539
θ/π = 1/4		L_1/D			
		1	5	10	20
L_2/D	1	0.617438	0.705071	0.756228	0.824066
	5		0.904359	0.914146	0.919706
	10			0.949956	0.955294
	20				0.974199
θ/π = 1/2		L_1/D			
		1	5	10	20
L_2/D	1	0.157449	0.218215	0.270808	0.373945
	5		0.507238	0.539204	0.555338
	10			0.67491	0.700694
	20				0.806393

Case 3c Participant D					
θ/π = 1/8		L_1/D			
		1	5	10	20
L_2/D	1	0.824699	0.869431	0.889782	0.916129
	5		0.966211	0.980468	0.983354
	10			0.98183	0.994099
	20				0.984239
θ/π = 1/4		L_1/D			
		1	5	10	20
L_2/D	1	0.429606	0.49354	0.542892	0.628249
	5		0.79474	0.826453	0.841462
	10			0.877329	0.900642
	20				0.890479
θ/π = 1/2		L_1/D			
		1	5	10	20
L_2/D	1	0.089451	0.12277	0.137155	0.207064
	5		0.286485	0.315024	0.337098
	10			0.391355	0.453497
	20				0.416638

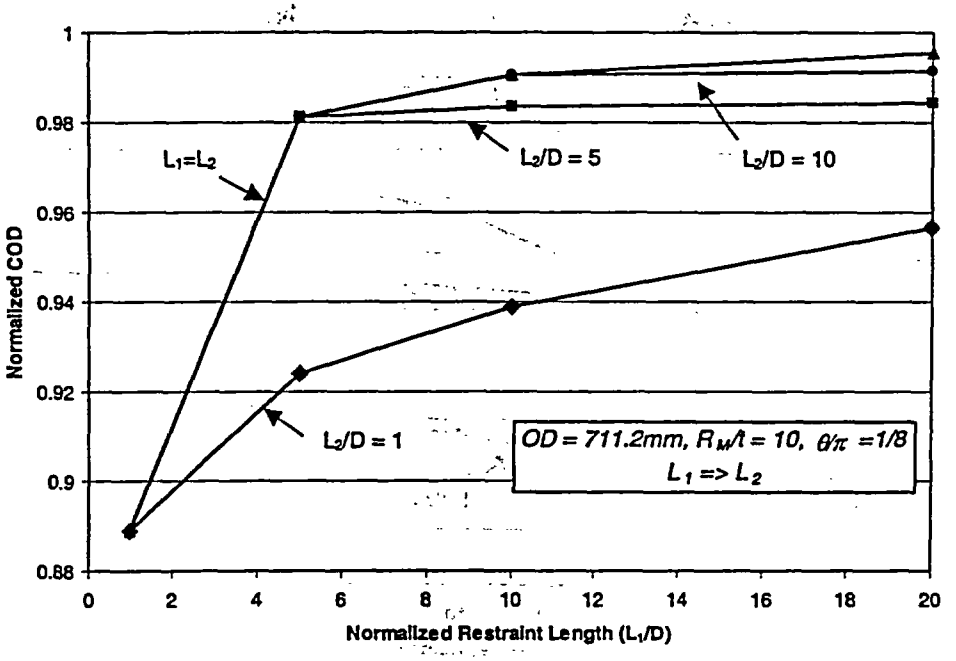

Figure I.34 Normalized COD under asymmetric restraint length from Participant F

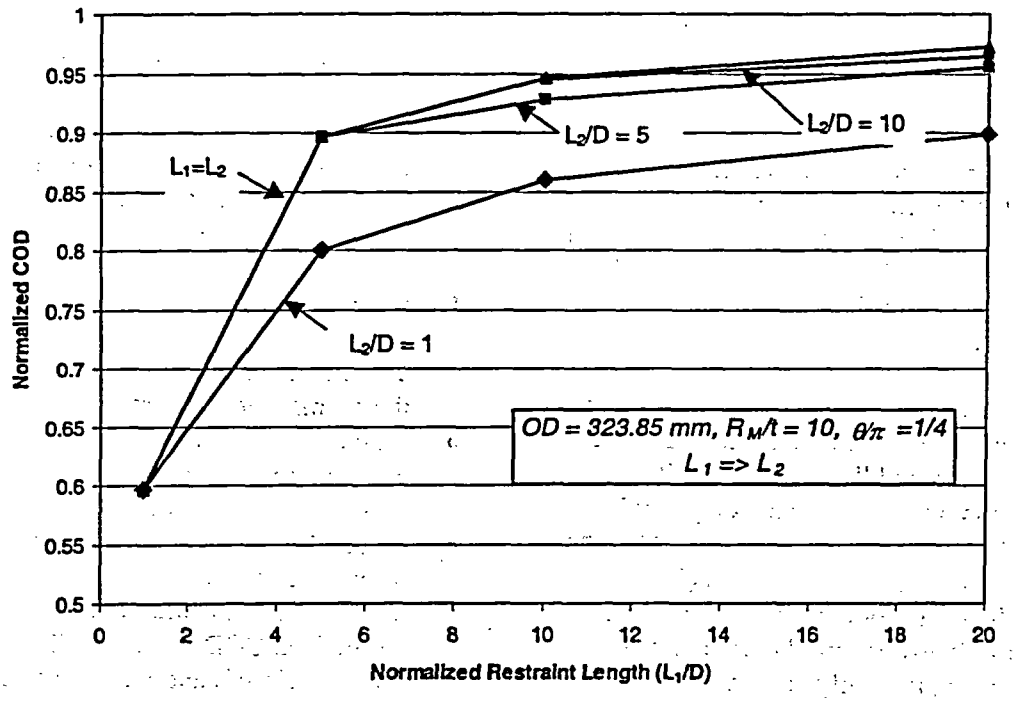

Figure I.35 Normalized COD under asymmetric restraint length from Participant E

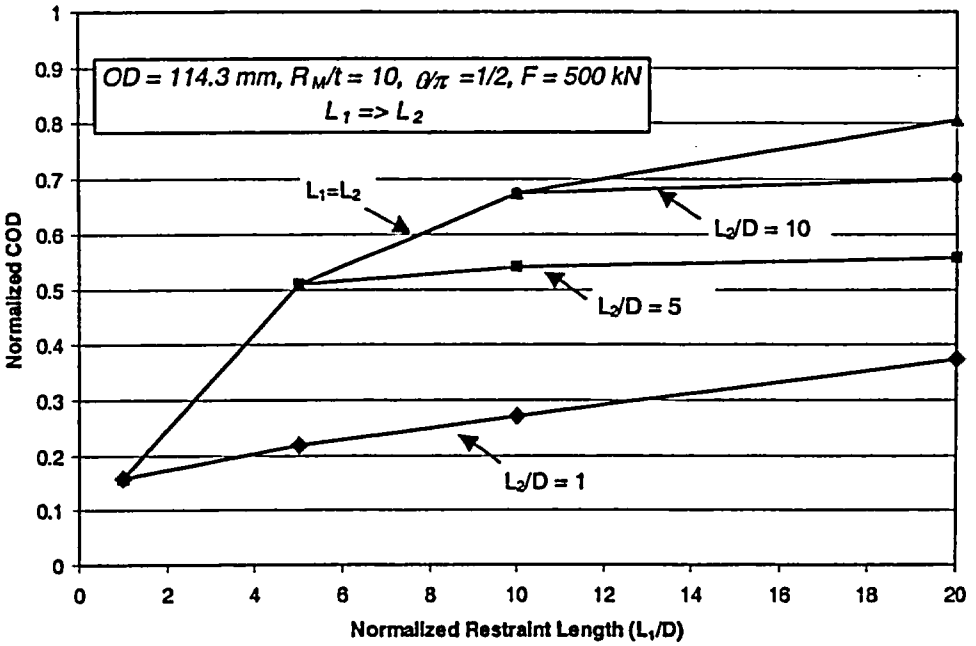

Figure I.36 Normalized COD under asymmetric restraint length from Participant C

I.2.9 Summary of First Round Robin Analyses

Six organizations from three countries participated in this first round robin analysis to investigate the effect of pipe-system restraint on the linear elastic COD values in axially loaded pipe systems. The results from the round-robin cases revealed that:

- The results from Participant C and F agree with each other for all the cases analyzed, and are in the middle of group results.
- The results from Participant A agree with those of Participants C and F, except for the cases of the longest crack length ($\theta=\pi/2$) where the CODs of unrestrained pipe are significantly lower, and the normalized CODs are significantly higher.
- The results from Participant B agree with those of Participants C and F, except for the cases of shortest restraint length (L/D=1).
- The results from Participant D show lower normalized CODs for the restrained pipes and higher CODs for the unrestrained pipes, when compared to those of the other participants. These discrepancies might be attributed to the use of first-order, unfocused elements by Participant D.
- The results from Participant E agree with those of Participants C and F, except that the normalized COD for the longest crack length ($\theta=\pi/2$) are significantly lower.

Other findings from this study include:

- The pipe diameter has negligible effect on the normalized COD results.
- As the R_m/t ratio increases, the restraint effect increases, resulting in lower normalized COD values.
- As the difference in the restraint lengths from the two sides of the crack increases, the asymmetric restraint effect on the normalized COD increases. The effect becomes significant once one of the restraint lengths is reduced to L/D=1, or the crack length is longest ($\theta=\pi/2$).

I.3 SECOND ROUND ROBIN (EFFECT OF R/T RATIO ON SURFACE FLAWED PIPE EPFM ANALYSES)

I.3.1 Background

One of the objectives of the ASME Section XI Working Group on Pipe Flaw Evaluation is to extend the flaw evaluation criteria to other than Class 1 piping. The extension of the in-service flaw evaluation criteria to Class 2, 3, and balance-of-plant (BOP) piping has two aspects that require further development than needed for Class 1 piping. The first is that these piping systems may operate at lower pressures, and hence have higher radius-to-thickness (*R/t*) ratios. The second is the lower operating temperature effects on the fracture behavior of ferritic steels. This round-robin problem focused on the *R/t* effects on the crack-driving force relationships.

I.3.2 Past Round-Robin and FE Efforts

Over the years, there has been many efforts aimed at developing a better solution to the problem of determining an analysis procedure to predict the failure loads of a pipe with a circumferential surface crack under pressure, axial tension, and bending loads. The initial efforts focused on Class 1 pipe that operates at higher temperatures and is generally thicker-walled pipe ($R/t<15$). In the early developmental efforts, there was concern over the accuracy of finite element (FE) solutions, and the ability to use those results to develop or validate simpler closed-form solutions that could lead to a codified procedure.

One of the initial efforts was a 1986 ASME PVP round-robin (RR) analysis of a surface-cracked pipe test (Ref. I.3). This involved a 16-inch diameter schedule 100 A106B pipe, where the crack was 66-percent of the pipe thickness for the entire length of half of the pipe circumference, see Figure I.37.

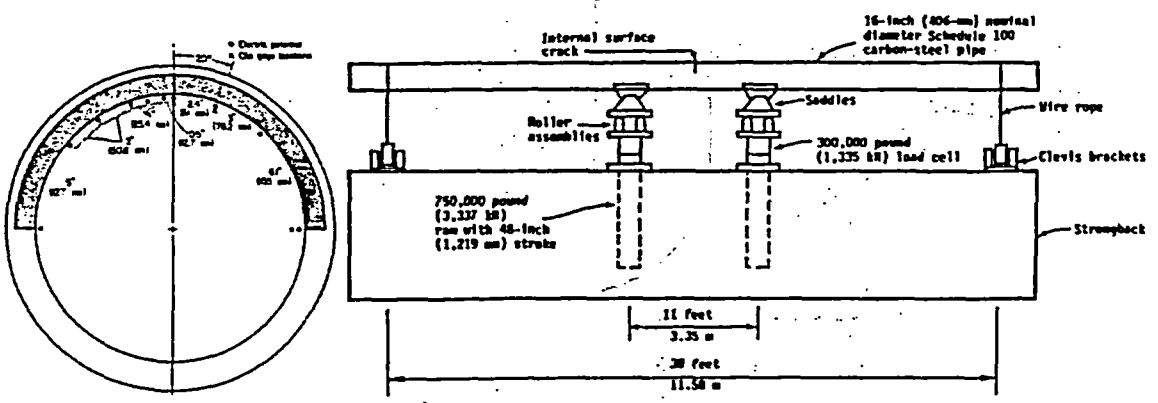

Figure I.37 Pipe test analyzed in 1986 ASME PVP round robin

The *J* versus load-line displacement values from all the 3D analyses at that time are given in 38. There was considerable scatter in the plastic region, and the mesh refinement in the ligament was found to be the major concern, see Figure I.39. Figure I.40 shows the results from that same round robin when the participants used different estimation schemes. The 1986 results showed that FE meshing was important, and that there was considerable scatter in the estimation scheme results.

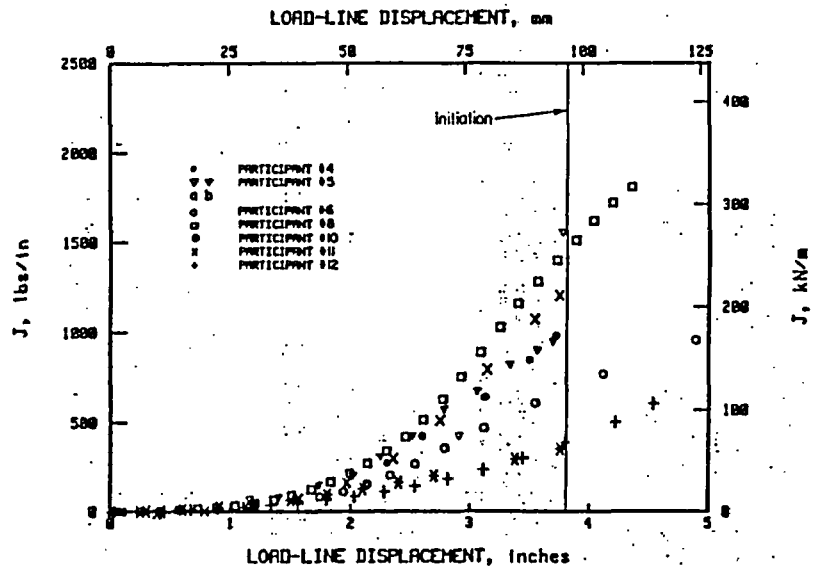

Figure I.38 Results for 3D FE analysis of 1986 ASME PVP round robin - J versus load-line displacement

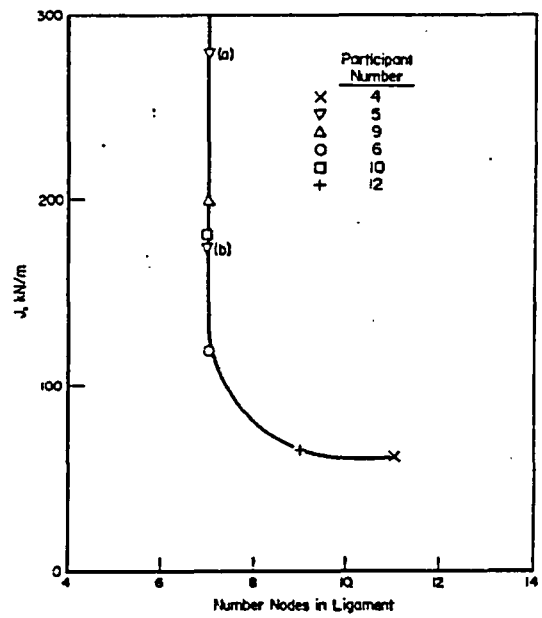

Figure I.39 Results for 3D FE analysis of 1986 ASME PVP round robin - J values at initiation displacement versus number of nodes in ligament of FE model

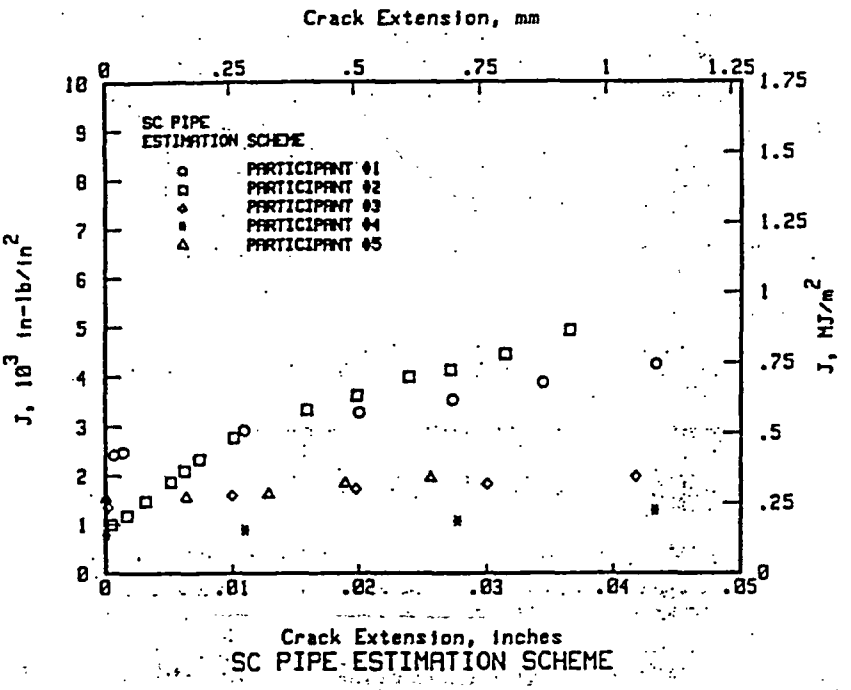

Figure I.40 Results for estimation analysis of 1986 ASME PVP round robin

The work in the 1986 round robin also spurred additional analyses afterwards. For instance, Brickstad conducted analyses using line-spring elements in ABAQUS as part of the Swiss/Swedish Cooperative Program that was presented at 7th IPIRG-1 TAG meeting in November, 1989 (Ref. I.4), Shimakawa and Yagawa (Ref. I.5), Doi et al. (Ref. I.6), Takahashi et al. (Ref. I.7), and Miyoshi (Ref. I.8) also did 3D analyses of the 1986 PVP RR with more refined meshes. Miyoshi had the finest mesh. The results of the J values at the displacement that corresponded to experimentally measured crack initiation are given in Table I.14. Figure I.41 shows that the Brickstad line-spring results compared very closely to the Myoshi 3D analysis with the finest mesh.

Table I.14 Post round-robin analyses of the 1986 ASME round-robin problem

	J at initiation, MJ/m^2
Brickstad (Line-spring)	0.235
Shimakawa and Yagawa, (3D)	0.213
Doi et al., (3D)	0.194
Takahashi et al., (3D)	0.185
Miyoshi (3D – finest mesh)	0.264

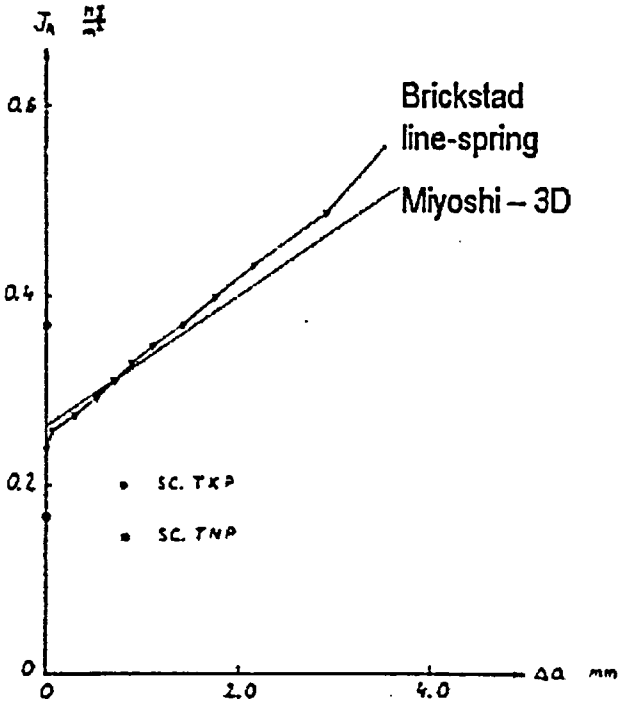

Figure I.41 Comparison of Brickstad and Miyoshi results showing good agreement between line-spring and very refined 3D FE results

Another round-robin effort for circumferential surface cracks was conducted in the IPIRG-1 program, i.e., Round-Robin Problem 2-1. The results of that round robin are summarized in NUREG/CR-6233 Vol. 4 (pg 2-107) (Ref. I.9). This IPIRG-1 round-robin problem involved estimation scheme analyses of an aged cast stainless steel pipe test under pressure and quasi-static bending, i.e., 16-inch diameter, Schedule 100, $R/t = 8$, pressure of 15.5 Mpa (2,250 psi), and test temperature of 288C (550F). Predictions were made of crack initiation and maximum load given an actual tensile stress-strain curve and L-C C(T) specimen *J-R* curves. Table I.15 presents a summary of the initiation load predictions, and the maximum load predictions are given in Table I.16 The difference in the load predictions was much greater than desired, and some participants had significant differences even though they used the same basic analysis procedure.

Another effort that is of value to summarize here is from Mohan, where he compared 3D and line-spring FE results in an IPIRG-2 report for elbow applications (Ref. I.10). Mohan first conducted an analysis to validate the line-spring approach against full 3D FE analyses for straight-pipe with a circumferential surface crack (Ref. I.10). This was done for the same 1986 ASME PVP RR problem, i.e., DP3II Experiment 4112-8. Those results showed that the line-spring analysis gave good agreement with a full 3D brick element analysis when sufficient mesh refinement was used, see Figure I.42. Additionally, Mohan compared full 3D FE results for a surface crack in an elbow to results from using line-spring elements (Ref. I.10). Those results also showed good agreement, see Figure I.43.

Table I.15 Initiation load predictions from IPIRG-1 round-robin using estimation schemes

	Load, kN	Moment, kN-m	Predicted / Experimental
Experimental	319.1	656.6	
Participant A			
R6-Option 1	179.2	368.5	0.56
R6-Option 2	199.7	410.6	0.63
Participant B			
R6-Option 3	301.8		0.95
Participant C			
J_T Analysis	173.1		0.54
Participant D			
R6-Case 1	314.7		0.99
R6-Case 2	285.5		0.89
Participant E			
EPFM (with Press. Corr.)			
SC.TNP1		634.1	0.97
SC.TKP1		465.7	0.71

Table I.16 Maximum load predictions from IPIRG-1 round-robin using estimation schemes

	Load, kN (kip)	Moment, kN-m (in-lb)	Predicted / Experimental
Experimental	326.8 (73.4)	672.5 (5.95x10^6)	
Participant B	301.8 (67.8)		0.92
Participant C			
IWB-3640	259.6 (58.3)		0.79
J_T Analysis	245.7 (55.2)		0.75
J_T Analysis	293.7 (66.0)		0.90
Net-Section-Collapse	366.3 (82.3)		1.12
Participant D			
R6-Case 1	330.5 (74.3)		1.01
R6-Case 2	313.5 (70.4)		0.96
R6-Case 3	323.2 (72.6)		0.99
Participant E Net-Section-Collapse			
1.15 σ-Avg	454.3 (102.1)	934.0 (8.27x10^6)	1.39
σ-Avg	385.0 (86.5)	792.0 (7.01x10^6)	1.18
3 S_m	341.0 (76.7)	702.0 (6.21x10^6)	1.04
IWB-3640 (No Safety Factor)	254.0 (57.0)	522.0 (4.62x10^6)	0.78
DPZP (Best fit for SC)			
1.15 σ-Avg	389.0 (83.6)	799.0 (7.08x10^6)	1.19
σ-Avg	351.0 (78.9)	721.0 (6.39x10^6)	1.08
EPFM (with Press. Corr.)			
SC.TNP1	363.0 (81.4)	745.0 (6.59x10^6)	1.11
SC.TKP1	256.0 (57.4)	525.0 (4.65x10^6)	0.78

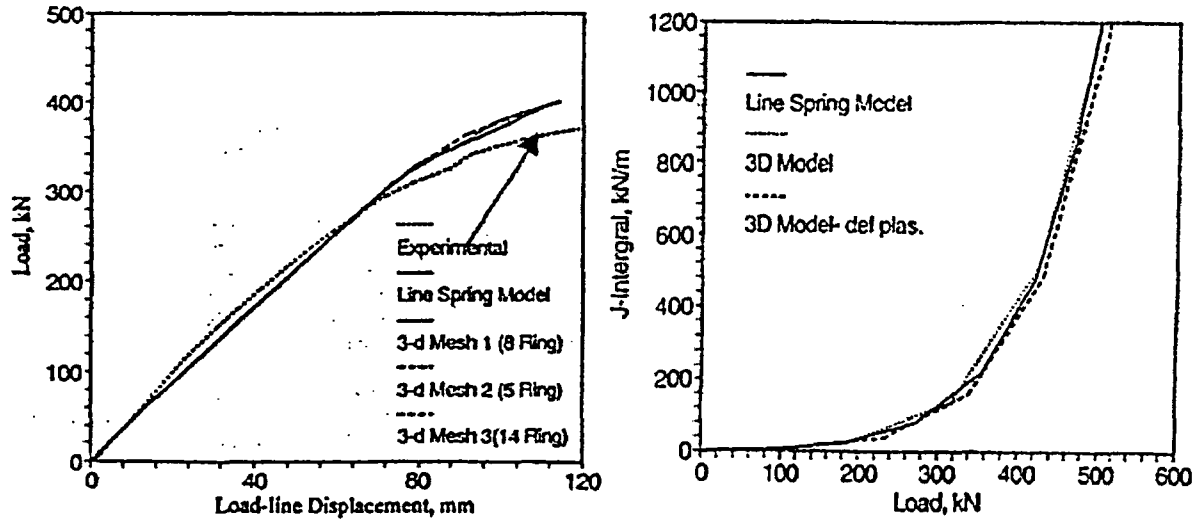

Figure I.42 Comparison of Mohan FE analyses of 1986 ASME PVP round-robin problem

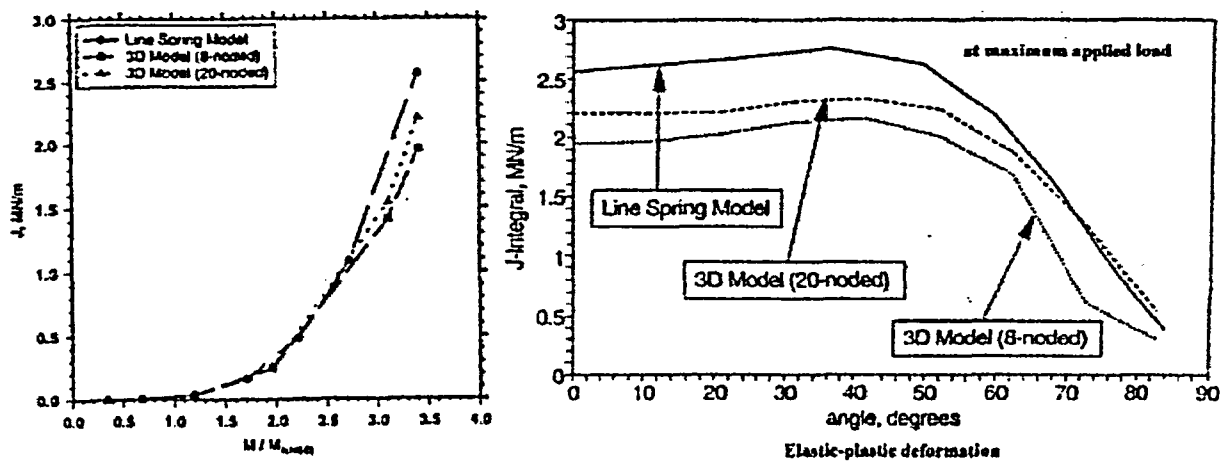

Figure I.43 Comparison of Mohan FE analyses of surface crack in an elbow

I.3.3 *J*-estimation Scheme Development

The *J*-estimation schemes for surface-flawed pipes have elastic and plastic contributions. The elastic contribution is known from tabulated elastic *F*-functions for global bending and axial tension in the open literature.

The elastic-plastic contributions to *J* are more difficult to establish. During past NRC programs on piping, several circumferential surface-cracked-pipe *J*-estimation schemes were developed for Class 1 piping where the *R/t* ratios were less than 15. These estimation schemes are available in the computer code NRCPIPES (Ref. I.11). The available options in NRCPIPES are:

- SC.TNP1 and SC.TNP2,
- SC.TKP1 and SC.TKP2, and
- SC.ENG1 and SC.ENG2.

The differences in these solutions are briefly noted below.

SC.TNP1 is the original SC.TNP solution by Ahmad in NUREG/CR-4872 (Ref. I.12). This analysis used the 360-degree GE/EPRI surface-crack *h*-functions with a *thin*-shell assumption in creating circumferential finite length flaw *h*-functions for pipes in bending.

- SC.TNP2 is a modification by Mohan in NUREG/CR-6298 (Ref. I.13). This was a modification to the Ahmad solution where the distance from the crack plane to the point where the unflawed pipe stress distribution existed was calibrated against numerous finite element (FE) analysis results. The original assumption in the Ahmad SC.TNP solution was that this distance was equal to the pipe thickness. Mohan found that this distance (L) was equal to the pipe thickness (t) times a function of the material strain-hardening exponent (n), i.e., $L=(n\text{-}1)t$. This relation was derived from pipes with only one R/t ratio of approximately 7.5.

- SC.TKP1 is the original SC.TKP solution by Ahmad in NUREG/CR-4872 (Ref. I.12). This analysis used the 360-degree GE/EPRI surface-crack h-functions with a ***thick***-shell assumption in creating circumferential finite length flaw h-functions for pipes in bending.

- SC.TKP2 is a modification by Mohan in NUREG/CR-6298 (Ref. I.13). This was a modification to the Ahmad solution where the distance from the crack plane to the point where the unflawed pipe stress distribution existed was calibrated against numerous finite element analysis results. The original assumption in the Ahmad SC.TKP solution was that this distance was equal to the pipe thickness. Mohan found that this distance (L) was equal to the pipe thickness (t) times a function of the material strain-hardening exponent, i.e., $L=[(n+1)/(2n+1)]t$. This relation was derived from pipes with only one R/t ratio of approximately 7.5.

- SC.ENG1 is an estimation scheme developed by Rahman for circumferential surface flaws that parallels the circumferential through-wall-cracked pipe estimation scheme of Brust in NUREG/CR-4853 and NUREG/CR-6235 (Refs. I.14 and I.15). The Brust circumferential through-wall-cracked pipe estimation scheme was called LBB.ENG. Rahman's SC.ENG1 analysis used the ***original*** net-section-collapse limit-load equations in calculating a parameter $H(a/t)$, which was equal to the thickness of the unflawed pipe, divided by an equivalent thickness to reach limit-load conditions.

- SC.ENG2 is an estimation scheme developed by Rahman for circumferential surface flaws that also parallels the through-wall-cracked pipe estimation scheme of Brust (Refs. I.14 and I.15). Rahman's SC.ENG2 analysis used the ***Kurihara modification of the original*** net-section-collapse limit-load equations in calculating a parameter $H(a/t)$, which was equal to the thickness of the unflawed pipe, divided by an equivalent thickness to reach limit-load conditions. The Kurihara solution modified the net-section collapse equations empirically so that they would work better for short deep flaws (Ref. I.16).

In addition to the results shown above, there is another set of interesting calculations. This was work done by Mohan and others for validation of the ASME FAD curve approach in Code Case N494-2 (Ref. I.17). From the work in that paper, it was shown that several investigators got the same moment versus J values by 3D calculations and line-spring analyses. The results then showed that the Code-Case N494-2 needed a maximum limit of R/t of 15 to avoid under predicting the crack-driving force, see Figure I.44. Mohan also explored the effect of constant depth versus elliptical flaw shapes on the elastic F-function.

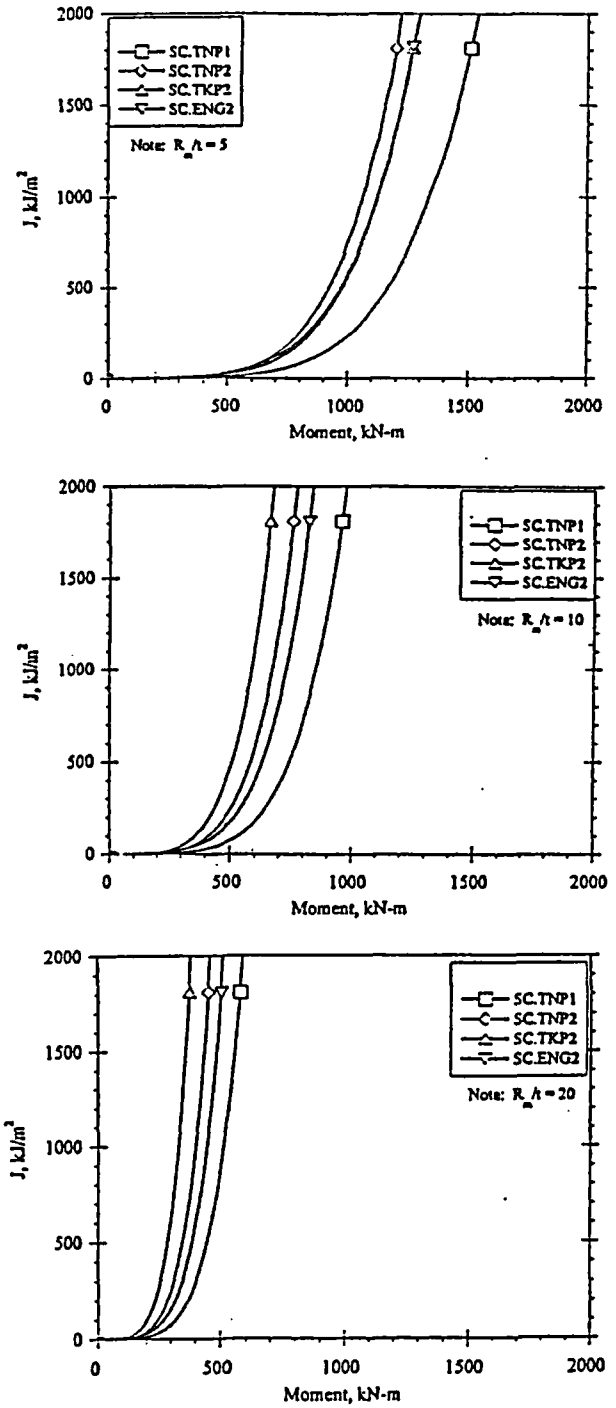

Figure I.44 Differences in *J*-estimation scheme predictions for same diameter pipe with crack dimensions of $\theta/\pi = 0.5$ and $a/t = 0.5$ and $n = 5$

I.3.4 Objective of this Round Robin

The objective of this round robin was to evaluate analysis procedures that were capable of providing consistent crack-driving force for higher *R/t* pipe. The crack driving force solutions were used to

- assess if any of the estimation schemes in NRCPIPES can be used for higher *R/t* pipes, and
- provide procedural basis for the development of *J*-estimation schemes for higher *R/t* pipe in Class 2, 3, and balance-of-plant piping with internal circumferential surface flaws. The actual development of the schemes is being done as part of a separate BINP task.

I.3.5 Problem Statement

There were several parts to this round-robin problem. The Problem Set A contained problems for all participants. The results were to be used to check the computation capabilities of all the participants. The Problem Sets B and C involved cases that would expand the numerical solution database for assessing the *J*-estimation schemes. The five participating organizations are identified as P1, P2, P3, P4, and P5 in this report. P1 and P3 were in Group 1, and the rest in Group 2.

The participating organizations were tasked to generate *J* versus bending moment curves for pipes with internal circumferential surface flaws with or without internal pressure. The surface flaws were centered in the plane of the bending on the tension side of the pipes. The *J* values were taken at the mid-length of the surface cracks, i.e., the location with maximum nominal tension stress. Any analysis approaches deemed appropriate by the individual organization were acceptable. The manner in which the bending moment/displacement was applied was up to the individual participating organization. The end effects from the application of the bending moment/displacement should be minimized.

The stress-strain relation was assumed to obey the generic Ramberg-Osgood power-law hardening relationship,

$$\frac{\varepsilon}{\varepsilon_0} = \frac{\sigma}{\sigma_0} + \alpha\left(\frac{\sigma}{\sigma_0}\right)^n \qquad \text{(I.1)}$$

where σ_0 and $\varepsilon_0 \equiv \sigma_0/E$ are the reference yield stress and strain, respectively, α is a dimensionless parameter, E is the elastic modulus, and n is the strain hardening exponent.

Three sets of problems and associated participating groups are summarized in Table I.17. The overall dimensions of the pipe is determined by its outside diameter (OD) and the pipe wall thickness (t). The size of the flaws is defined by its length (θ), and depth (a). The flat-bottom flaws have a constant depth for the entire length. The flaw shape of semi-elliptical cracks corresponds to semi-elliptical flaws in a flat plate that is then transformed into the pipe curvature. The material parameters that define the Ramberg-Osgood stress-strain relationships and the magnitude of applied internal pressure are given in Table I.17.

Table I.17 Summary of the problem sets and dimensional and material parameters

Case No.	OD	t	θ/π	a/t	Defect Shape	Elastic Modulus	Poisson's Ratio	σ_0	n	α	Internal Pressure	Comments	Participants
	(mm)	(mm)				(GPa)		(MPa)			(MPa)		
A-1	406.4	36.945	0.25	0.500	Flat bottom	182.72	0.30	150.0	5.00	1.00	0.00	Baseline case	Group 1 and Group 2
A-2	406.4	36.945	0.25	0.500	Semi-elliptical	182.72	0.30	150.0	5.00	1.00	0.00	defect shape diff. from A-1	
A-3	406.7	9.500	0.25	0.476	Flat bottom	182.72	0.30	224.0	4.95	5.01	1.55	Pipe experiment 1.2.1.20	
B-1	406.4	9.912	0.25	0.500	Flat bottom	182.72	0.30	150.0	5.00	1.00	0.00	Based on A-1, R_m/t=20	Group 1
B-2	406.4	5.017	0.25	0.500	Flat bottom	182.72	0.30	150.0	5.00	1.00	0.00	Based on A-1, R_m/t=40	
C-1	406.4	36.945	0.25	0.500	Flat bottom	182.72	0.30	150.0	5.00	1.00	27.00	Based on A-1, with pressure	Group 2
C-2	406.4	9.912	0.25	0.500	Flat bottom	182.72	0.30	150.0	5.00	1.00	6.75	Based on B-1, with pressure	
C-3	406.4	5.017	0.25	0.500	Flat bottom	182.72	0.30	150.0	5.00	1.00	3.38	Based on B-2, with pressure	

I.3.6 Analysis Approach

This section describes the analysis approach taken by the five participating organizations. General-purpose FE codes, either ABAQUS® or MARC® were used by the participants.

I.3.7 Geometry Models

The FE models were constructed either by shell and line-spring elements or 3-D solid elements. A typical model using shell and line-spring elements from Participant P1 is shown in Figure I.45 and Figure I.46. Only one quarter of the pipe was modeled due to symmetry conditions. The shell and line-spring elements were of the type S8R5 and LS3S per ABAQUS notation, respectively. There were ten equally-spaced line-spring elements covering the one-half crack front in the model. The 14 shell elements were geometrically-spaced around the circumference, having smaller elements in the region adjacent to the crack. The axial length of the quarter model was $10D_m$, where D_m is the mean diameter of the pipe. A typical FE model using 3-D solid elements (C3D20 in ABAQUS) is shown in Figure I.47 and Figure I.48 from Participant P2. The crack area was modeled using a refined mesh with quarter-point-singularity elements at the crack tip. The 3-D solid element model for Problem A-2 from Participant P3 is shown in Figure I.49 and Figure I.50. The model was made to work with the MARC code.

I.3.8 Loading

Bending loads were imposed on the pipe section by applying a rotation at the far end of the pipe through a kinematic coupling or by four-point bending. In the shell and line-spring element models of Participant P1, the nodes on the far end of the pipe were tied to a reference node through "*KINEMATIC COUPLING" as provided in ABAQUS. The rotational degree of freedom applied to the reference node is then transferred to the end of the pipe through the kinematic coupling. The same coupling mechanism was used in the 3-D solid element

model of Participant P2. The far end of the pipe was sufficiently far from the cracked plane so there was no end effect at the crack of interest.

A four-point bending set up was used by Participant P3, as illustrated in Figure I.51. A similar four-point bending set up was also used by Participant P5.

In cases with internal pressure loading, the internal pressure and the associated axial load were applied first. The magnitude of the axial load represented the end cap load from the internal pressure. The bending loads or displacements were applied subsequently. There was no pressure applied to the crack face in the cases with internal pressure loading.

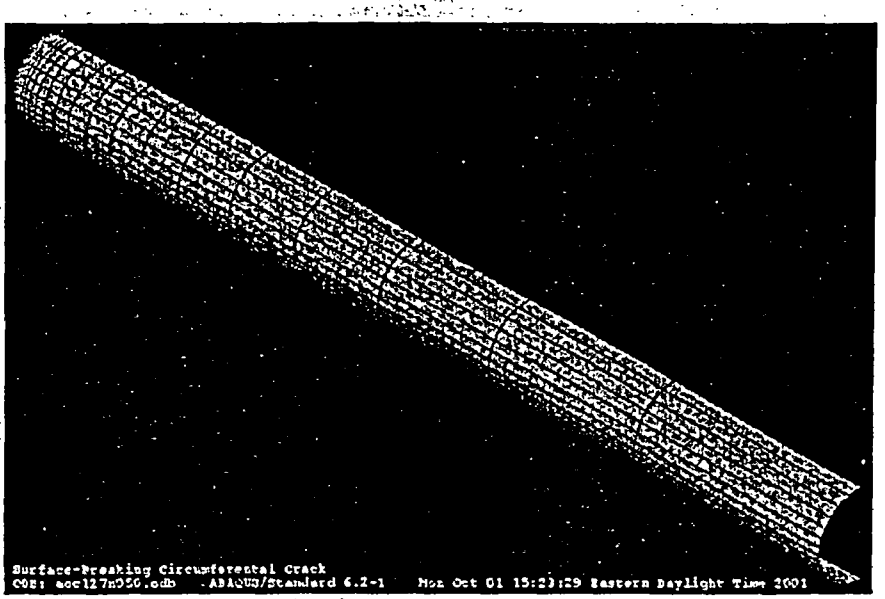

Figure I.45 A typical model using shell and line-spring elements from Participant P1

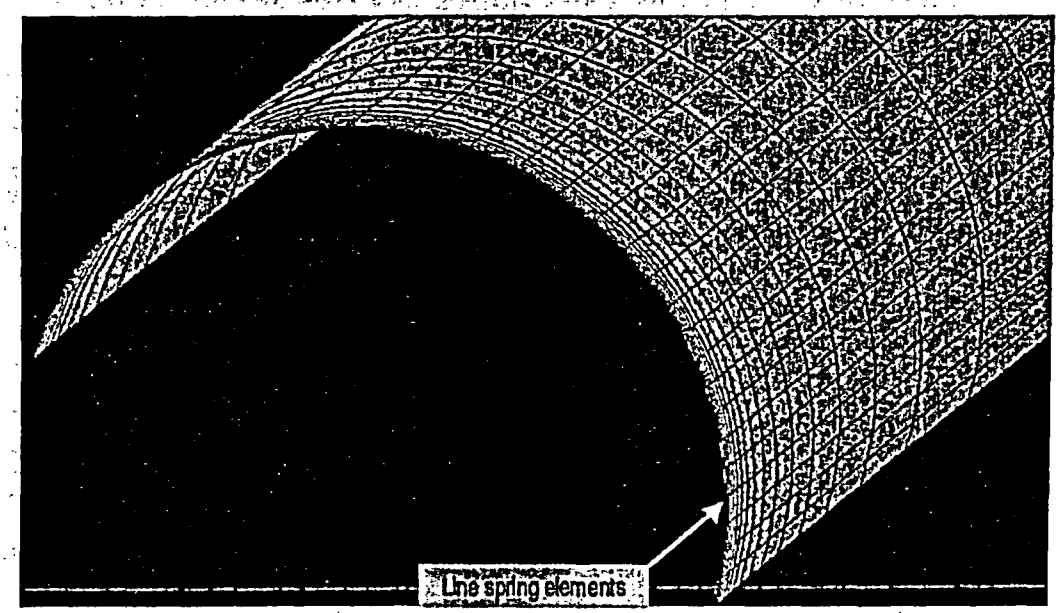

Figure I.46 Focused view of the shell and line-spring model, looking at the cross-sectional plane containing the line-spring elements

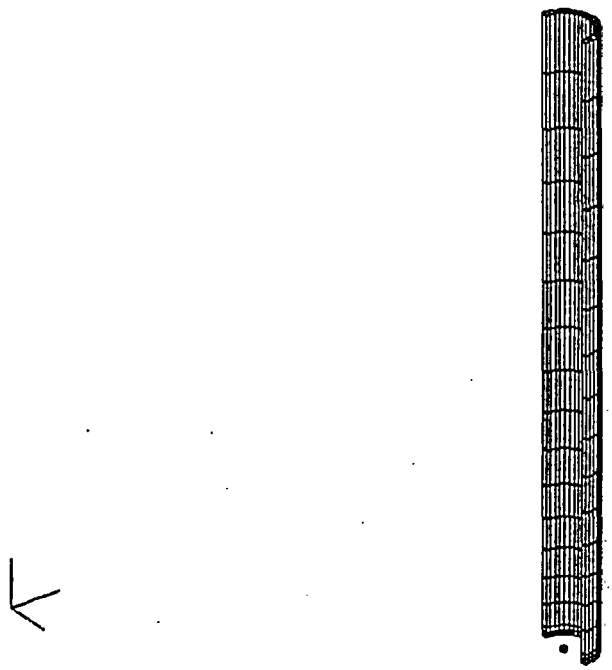

Figure I.47 A typical 3-D solid element model from Participant P2

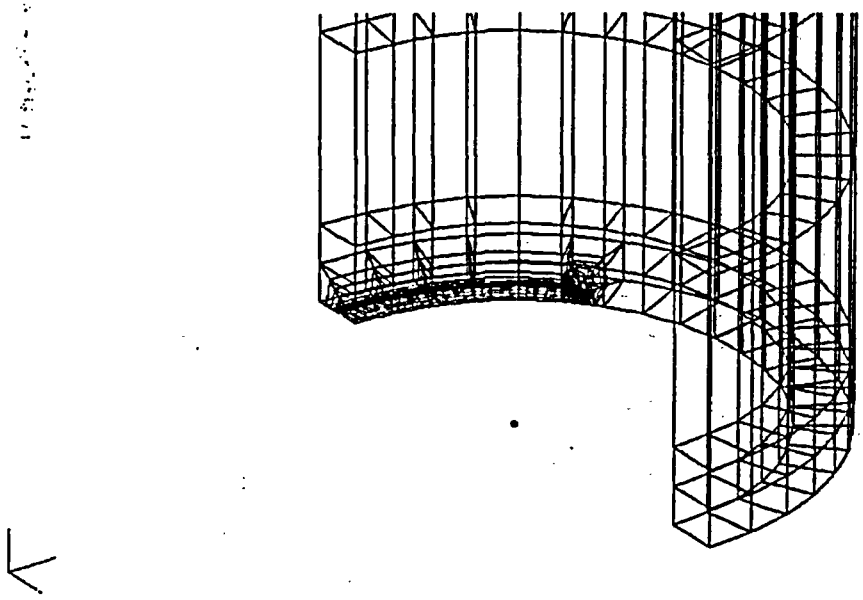

Figure I.48 A focused view of the cracked region of a 3-D solid element model from Participant P2

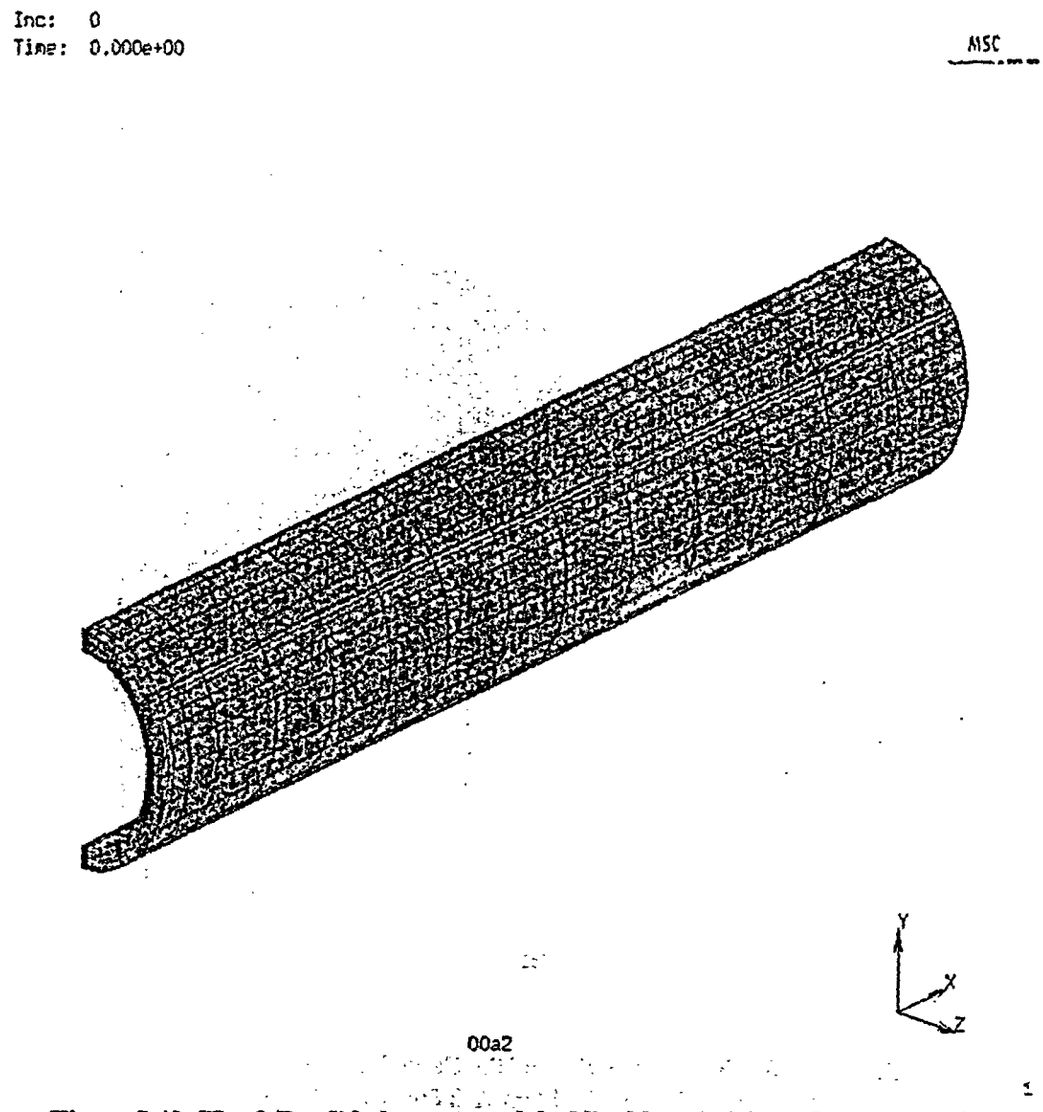

Figure I.49 The 3-D solid element model of Problem A-2 from Participant P3

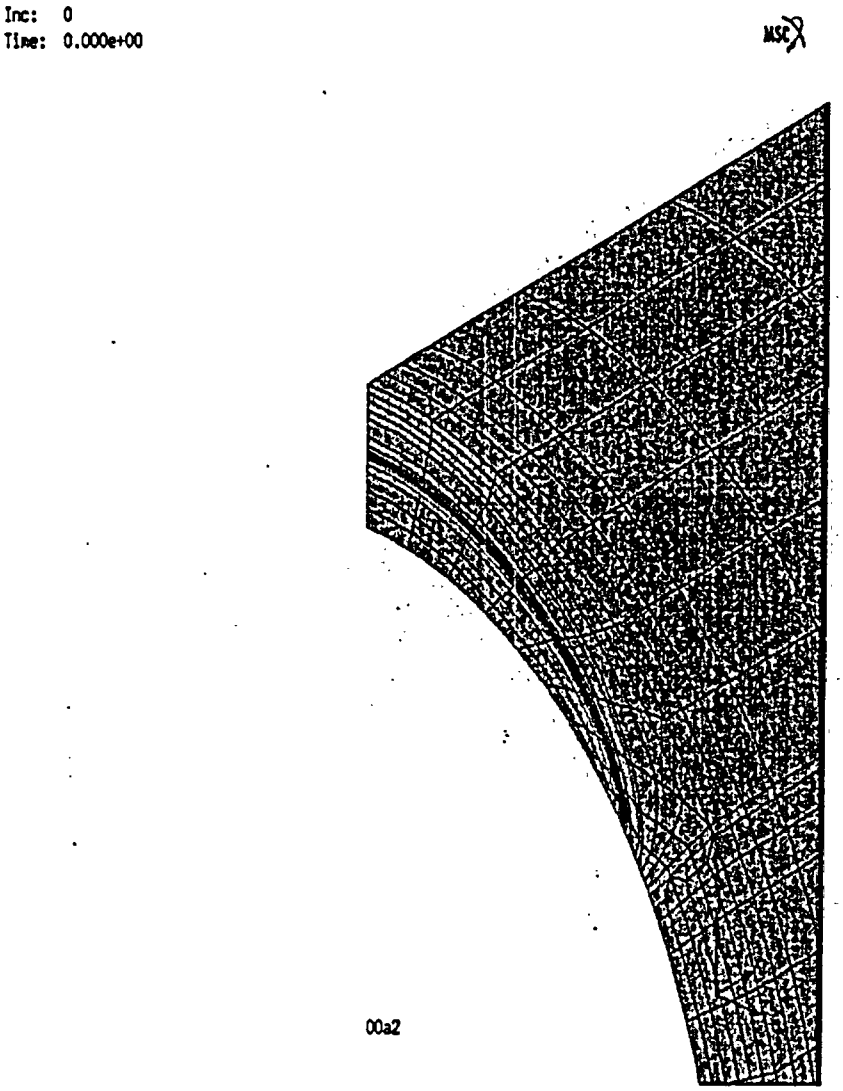

Figure I.50 The focused view of the flawed area of the 3-D solid element model for Problem A-2 from Participant P3

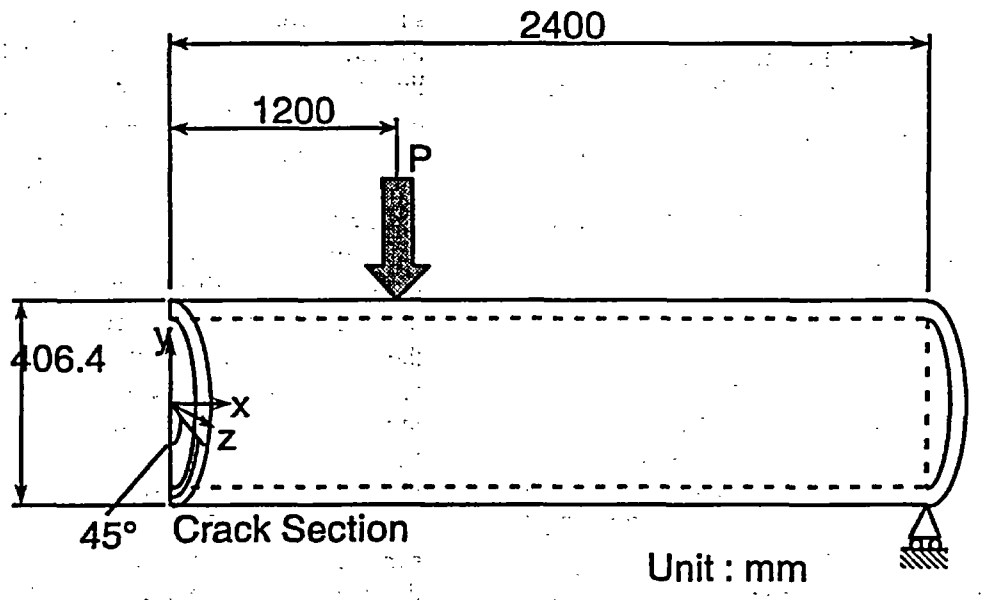

(a) Circumferentially Through-Wall-Cracked Pipe Subjected to 4-Point Bending (Cases A-1, B-1, B-2, and A-2)

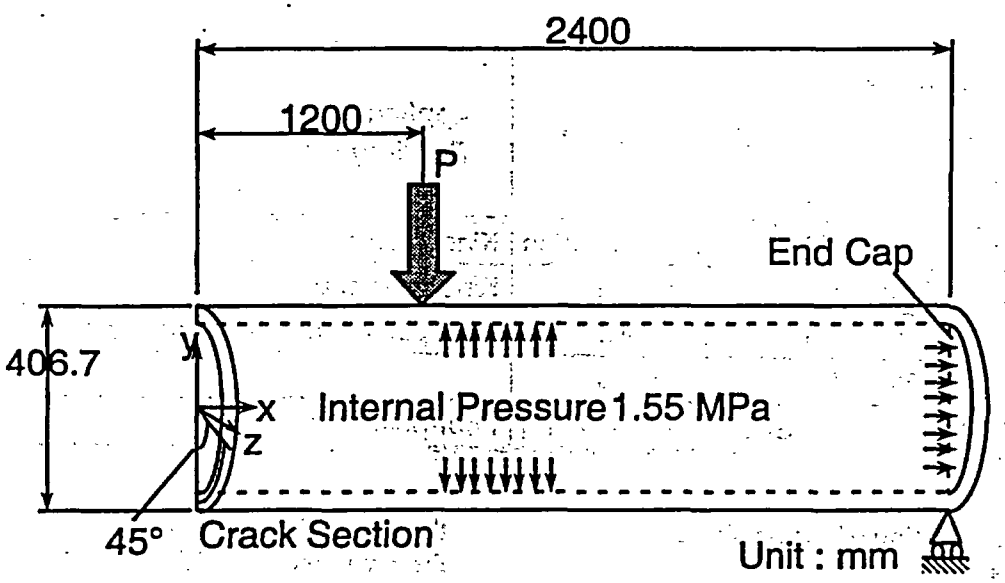

(b) Circumferentially Through-Wall-Cracked Pipe Subjected to 4-Point Bending and Internal Pressure (Case A-3)

Figure 1 Loading Conditions

Figure I.51 Application of bending and internal pressure by Participant P3

I.3.9 FE Procedure Formulation

A small-strain and small-displacement formulation was used by all participants except P3. Participant P3 employed large-strain (LS) and large displacement (LD) formulation for most of its analysis. For comparison, small-strain and small-displacement formulation was tried for some cases by Participant P3. The Ramberg-Osgood stress-strain relation of Equation I.1 conforms to the "*DEFORMATION PLASTICITY" definition of ABAQUS. In the case of 3-D solid models, this definition can be used to precisely represent the power law hardening relationship of Equation I.1. In the case of shell and line-spring models, the "*DEFORMATION PLASTICITY" definition does not work with the line-spring elements. Consequently, the material property has to be defined by the "*ELASTIC" and "*PLASTIC" cards in ABAQUS. The first line of the "*PLASTIC" card defines the plastic flow stress at zero plastic strain. In the case of Ramberg-Osgood stress-strain relation, the non-linearity starts at zero stress. Strictly speaking, the first line of the "*PLASTIC" card would have zero plastic flow stress at zero plastic strain. However, ABAQUS does not allow zero plastic flow stress at zero plastic strain. Consequently, a small, but finite plastic flow stress, has to be given at zero plastic strain. The examination of the analysis results revealed that the magnitude of this finite plastic flow stress at zero plastic strain does not affect the J versus moment relation provided that this initial flow stress was less than one-third of reference yield stress, or σ_0. The analysis procedures and the associated FE codes of all participants are summarized in Table I.18. The blank cells of the table indicate that the corresponding information was not available to the authors.

Table I.18 Summary of the analysis procedures of all participants

Participant	Group	Software Code	Element Type	Application of Bending load	Geometry/Strain Formulation
P1	1	ABAQUS	Shell and line-spring	Kinematic coupling	Small
P2	2	ABAQUS	3-D solid	Kinematic coupling	
P3	1	MARC	3-D solid	Four-point bending	Large and small
P4	2	ABAQUS	3-D solid		
P5	2	ABAQUS	Shell and line-spring	Four-point bending	

I.3.10 Confirmation of the Analysis Procedures

To ensure the quality of the results, it was necessary to verify that the stress and strain state at the cracked plane was not affected by the boundary conditions applied at the far end of the model. The deformed shell and line-spring model from Participant P1, shown in Figure I.52, demonstrates that the cross-section of the pipe at the far end of the pipe remains circular, as if it were a cross section from a very long pipe. Figure I.53 shows that the axial stress has the expected circumferential variation around the circumference of the pipe. This variation is independent of axial position for much of the model, except in the region close to the cracked plane. As expected, the axial stress redistributes in the cracked plane due to the reduced load carrying capability along the length of the surface crack. The deformation and stress patterns of Figure I.52 and Figrue I.53 confirm that the stress and strain state in the cracked plane are free of end effects.

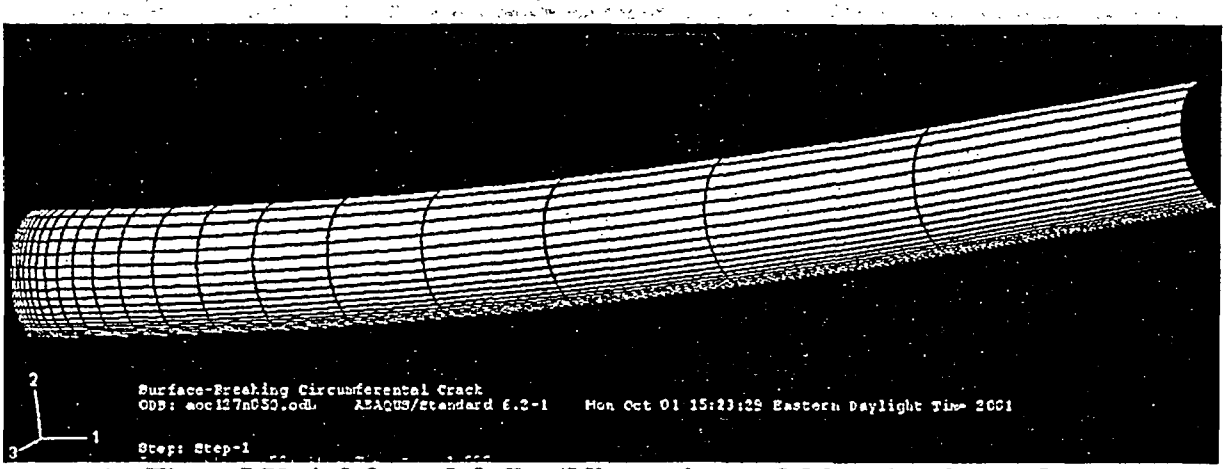

Figure I.52 A deformed shell and line-spring model from Participant P1

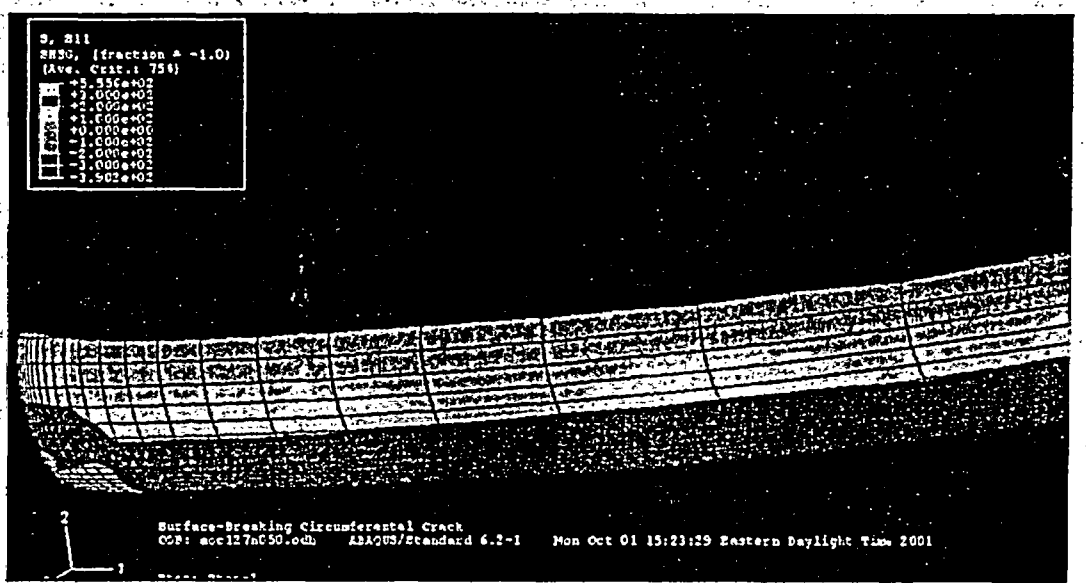

Figure I.53 Contours of axial stress of a deformed shell and line-spring model from Participant P1

I.3.11 Comparison of *J* versus Moment Relations

One of the objectives of this round robin was to provide some baseline *J* versus moment relations so the *J* estimation scheme can be expanded to higher R_m/t ratios than those in the current version of NRCPIPES. This section compares the *J* versus moment relations generated by all the participating organizations.

In the baseline Case A-1, the *J* versus moment relations have generally good agreement, see Figure I.54. At a *J* level of 500 N/mm, the maximum difference in bending moment (between Participants P1 and P2) is approximately 11%. In Case A-2 of Figure I.55, the maximum difference in bending moment (between Participants P1 and P2) is reduced to approximately 8%. The only difference between Case A-1 and A-2 is the flaw shape. Case A-1 has flat-bottom flaw shape, while Case A-2 has semi-elliptical flaw shape. In the line-spring model, the flaw depth is defined as a function of the circumferential position of the nodes that are tied to the line-spring elements. For the flat-bottom flaws, the flaw depth in the entire flaw length covered by the line-spring elements was given as a constant. The sharp transition at the end of the flaw length could not be defined

precisely in the line-spring model. In the case of semi-elliptical flaw shape, the flaw depth was gradually transitioned to a zero depth. The line-spring model can define the gradual transition of flaw depth more precisely. This may have contributed to the reduced difference in Case A-2.

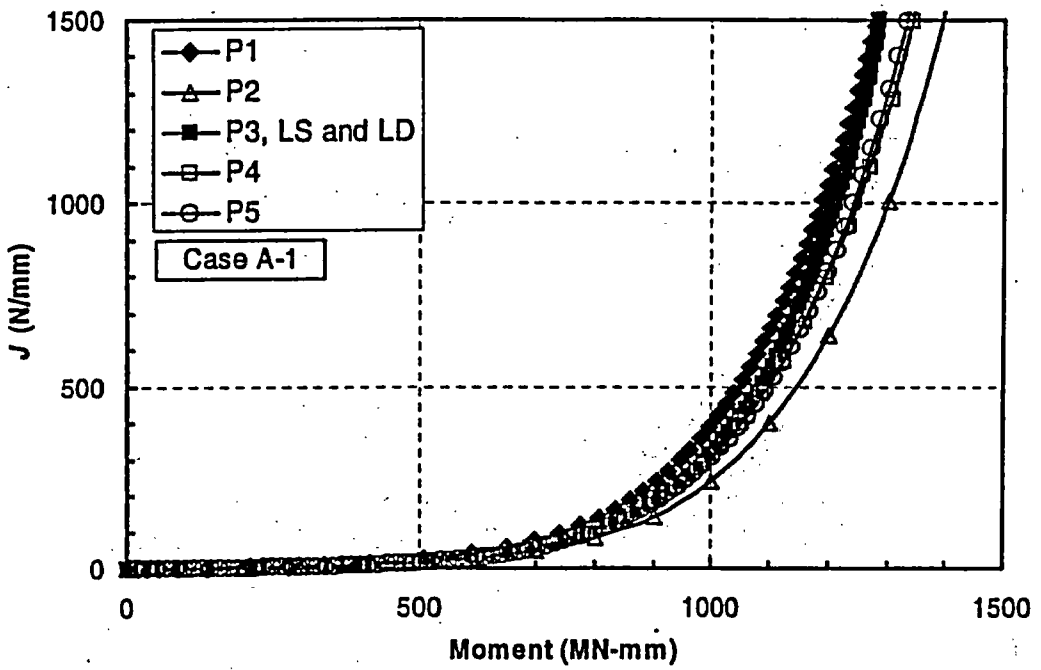

Figure I.54 The *J* versus moment relations of Case A-1. LS and LD stand for large strain and large displacement, respectively

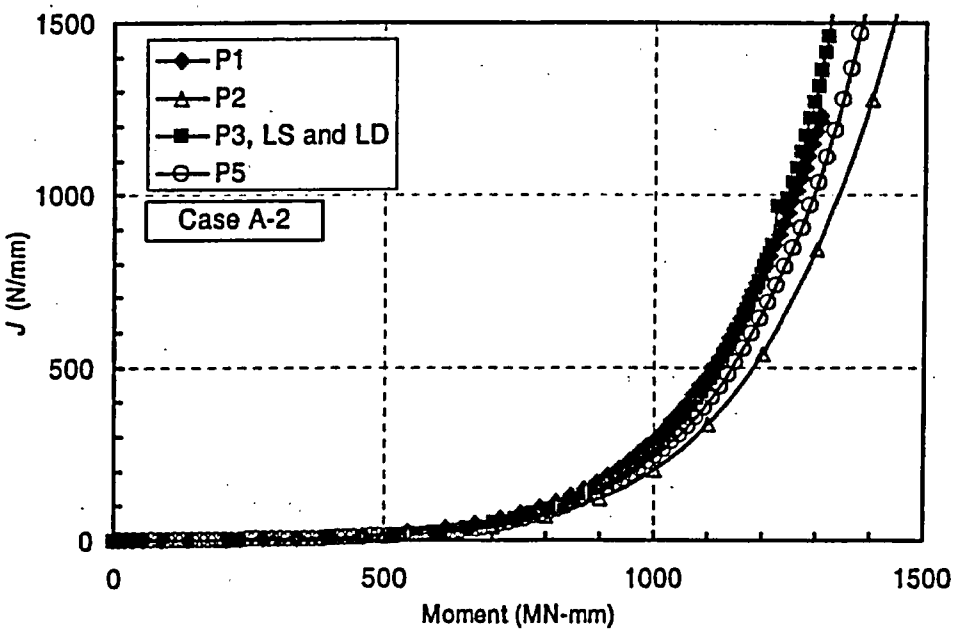

Figure I.55 The *J* versus moment relations of Case A-2

Case A-3 of Figure I.56 was set to simulate pipe Experiment 1.2.1.20. The R_m/t is much greater than Cases A-1 and A-2. Furthermore, there is a small internal pressure. The maximum moment difference at J=500 N/mm is approximately 18%. The results of Participants P1, P2, and P3 are in one group, while the results of Participants P4 and P5 are in another group. This grouping is not consistent with the grouping of modeling approach (shell and line-spring versus 3-D solid elements). For instance, Participant P1 used shell and line-spring elements, while Participants P2 and P3 used 3-D solid elements. Furthermore, Participants P1 and P2 used a small-strain and small-displacement formulation, while P3 used a large-strain and large-displacement formulation. Yet the results of Participants P1, P2, and P3 are in the same group. Similarly, Participants P4 used 3-D solid elements, while Participant P5 used shell and line-spring elements. Yet the results of Participants P4 and P5 are in the same group.

In Case B-1 of Figure I.57, the results of Participants P1 and P3 are close until the large bending moments. The large-strain and large-displacement formulation of Participant P3 captured the effect of cross section change of the pipe. This change eventually resulted in buckling of the pipe. Therefore there is an upper-bound limit of the bending moment, as reflected by the asymptotic increase of the J with little increase of bending moment.

The results of Participant P3 in Case B-2 demonstrate that the effect of buckling is more pronounced for pipes with large R_m/t as compared to Case B-1, see Figure I.58. The upper-bound moment was achieved at a relatively low J of approximately 300 N/mm in the analysis with large-strain and large-displacement formulation. Interestingly, the small-strain and small-displacement results of Participant P3 are closer to its own large-strain and large-displacement results, not the small-strain and small-displacement results of Participant P1.

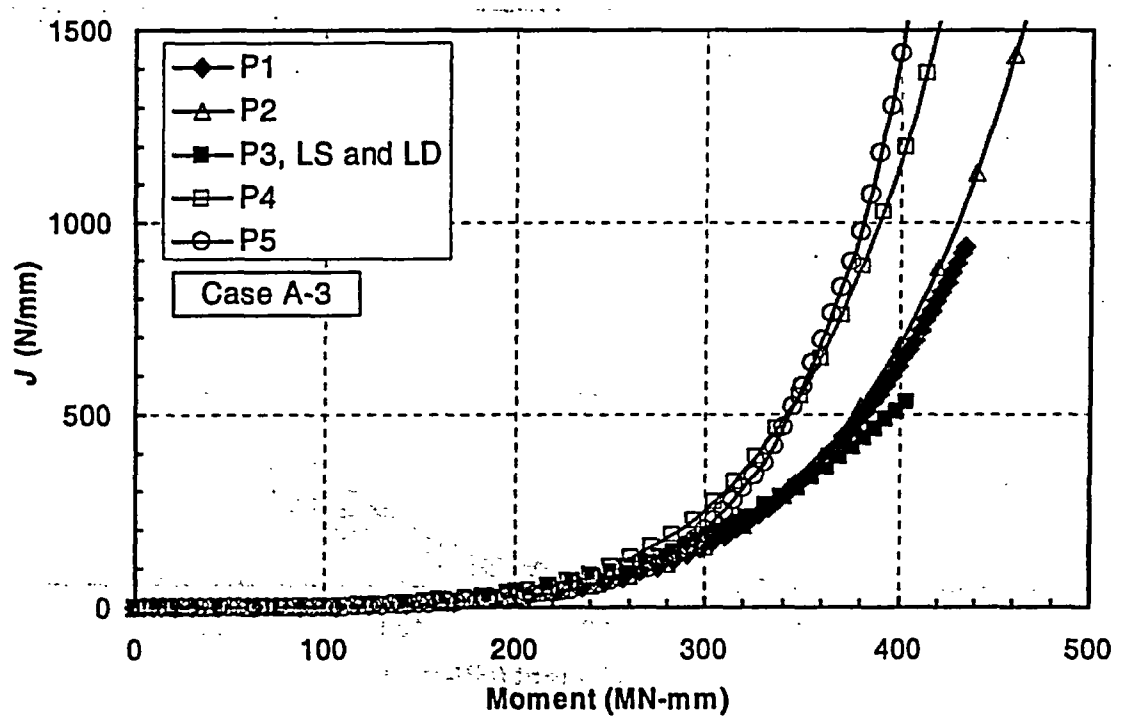

Figure I.56 The J versus moment relations of Case A-3

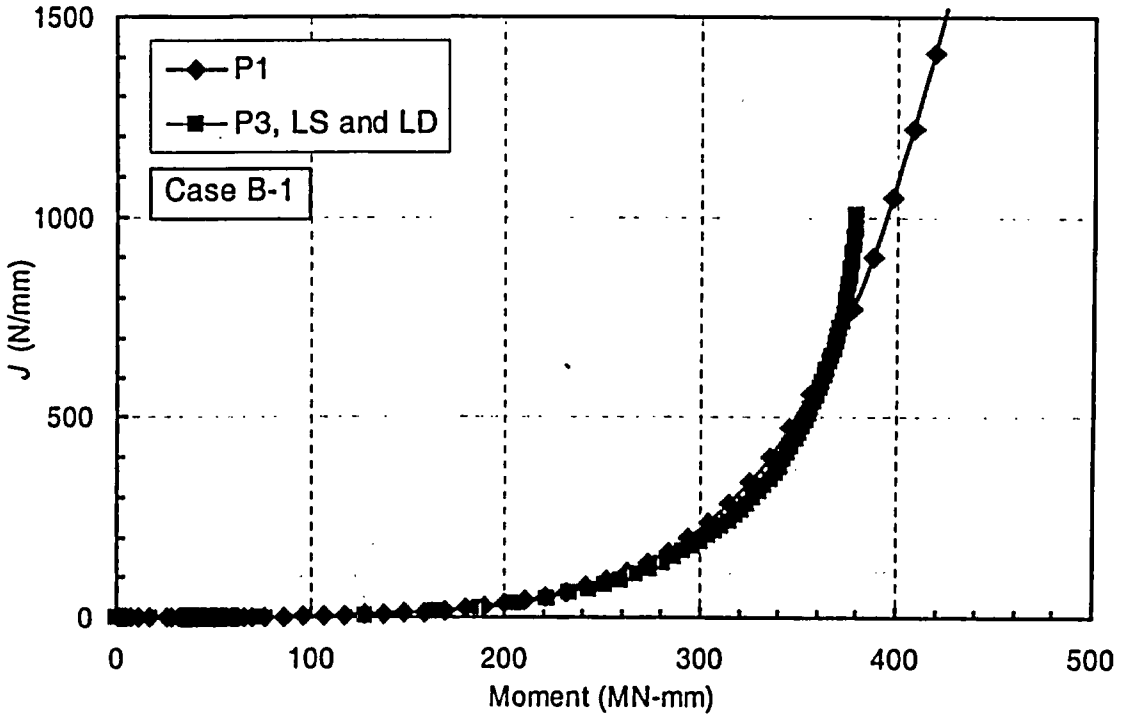

Figure I.57 The *J* versus moment relations of Case B-1

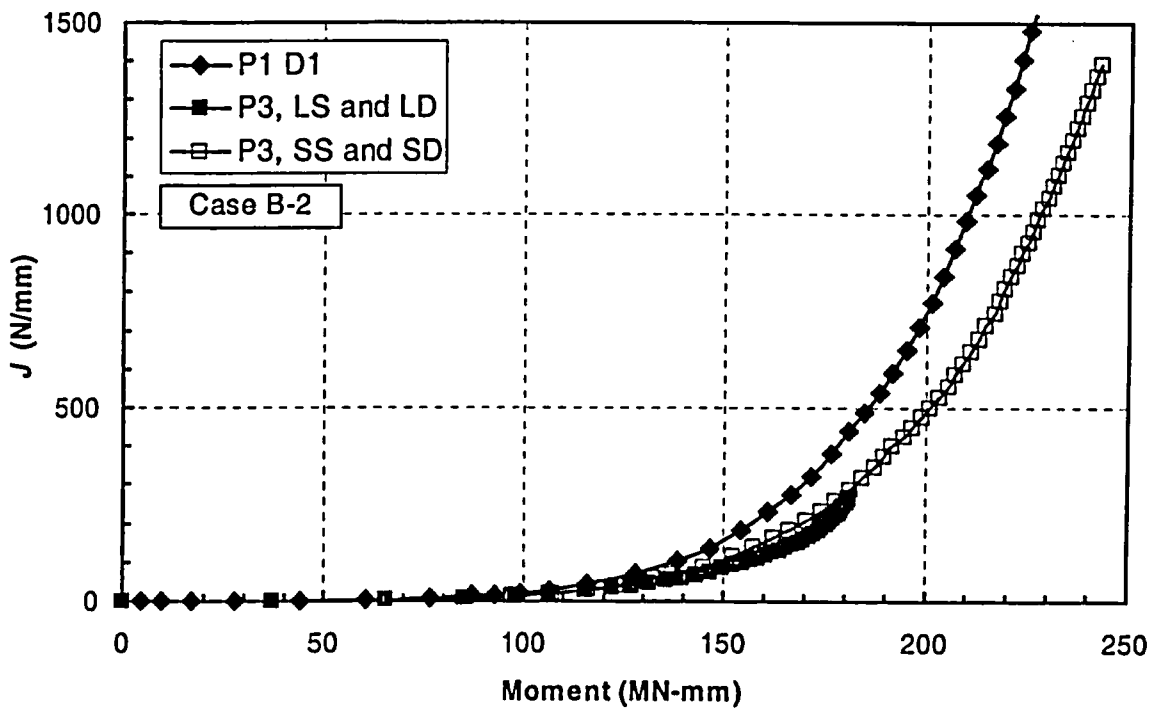

Figure I.58 The *J* versus moment relations of Case B-2. SS and SD stand for small strain and small displacement, respectively

Cases C-1, C-2, and C-3 were designed to examine the effects of R_m/t on the J versus moment relations with internal pressure. The difference in the J versus moment relations increases substantially with the increase of R_m/t, see Figures I.59, I.60, and I.61. The largest difference is in Case C-3 with an 80 percent spread in moment at the J value of 500 N/mm. In Cases C-1 and C2, the results are grouped by the types of FE models. For instance, the results of Participants P1 and P5 are in one group; both used shell and line-spring elements. The results of Participants P2 and P4 are in another group; both used 3-D solid elements. However, such grouping does not exist for Case C-3. The results of Participant P3 are particularly puzzling. The J versus moment curve does not have the asymptotically vertical trend as seen in Cases B-1 and B-2. Instead, the slope of the curve decreases with the increase of moment in the last few load increments. The Case C-3 results of Participant P3 are of large-strain and large-displacement formulation, the same as for Cases B-1 and B-2.

I.3.12 Discussion of Results

The effects of modeling approaches were investigated further. The focus was on the difference between the shell and line-spring model versus the 3-D solid element model. The results of Participants P1 and P2 were the focus of this further investigation. To further simplify the comparison, elastic solutions were generated. The additional benefit of the elastic solution is that the results from open literature can be used for further validation.

The pipe geometry of Case A-1 was selected and first loaded in axial tension. The results of Participant P1, with either flat-bottom or semi-elliptical crack shape, are compared with those of Anderson (Ref. I.18) in Figure I.62. The solution of Anderson was derived using 3-D solid elements with semi-elliptical crack shape. The results of Participant P1 compare very well with those of Anderson for the same crack shape. As expected, the J value of flat-bottom crack is higher than that of the semi-elliptical crack at the same load level.

Similar comparison was conducted for the 3-D solid element results of Participant P2, see Figure I.63. The first impression is that the difference between the flat-bottom and semi-elliptical crack shapes is much smaller than that from the shell and line-spring model. The agreement between the results of Participant P2 and those of Anderson is very good.

Appreciable difference is observed between the line-spring results of Participant P1 and that of Anderson under remote bending, see Figure I.64. Figure I.65 shows that the results of Participant P2 using 3-D solid elements are in better agreement with those of Anderson under the same loading condition. The comparison of Figure I.64 and Figure I.65 suggest that it is possible that the shell and line-spring model may overestimate the elastic J. The same conclusion cannot be drawn from the results of all cases listed in 17. In some of those cases, the shell and line-spring models provided higher J values than those of the 3-D solid models. In other cases, the opposite was true.

Using essentially the same analysis approach as Participant P1, Wang obtained elastic K solutions of internal circumferential cracks of various sizes (Ref. I.19). The line-spring solutions of semi-elliptical shape agreed well with the 3-D solid element solutions with semi-elliptical shape of Chapuloit (Ref. I.20), as shown in Figure I.66. The difference in J versus moment curves among the participating organizations cannot be attributed entirely to the difference in the use of FE elements. It may be deduced that the 3-D solid element solutions of Chapuloit are different from those of Anderson, although a direct comparison of those two solutions was not conducted in this round robin.

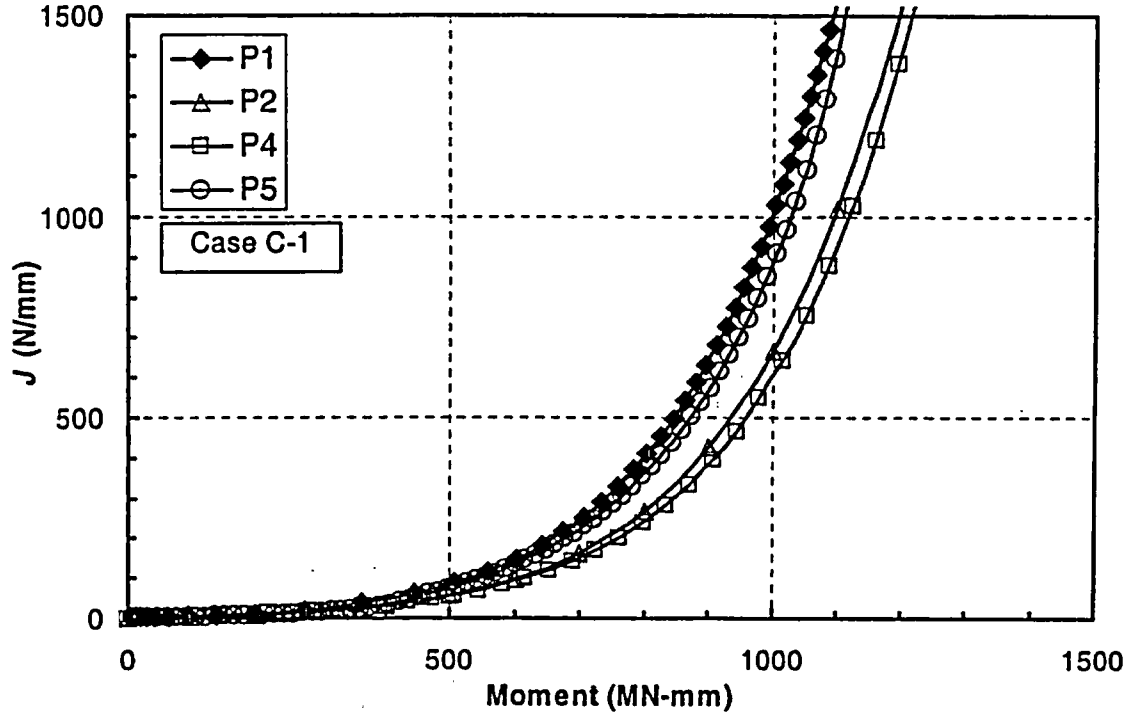

Figure I.59 The J versus moment relations of Case C-1

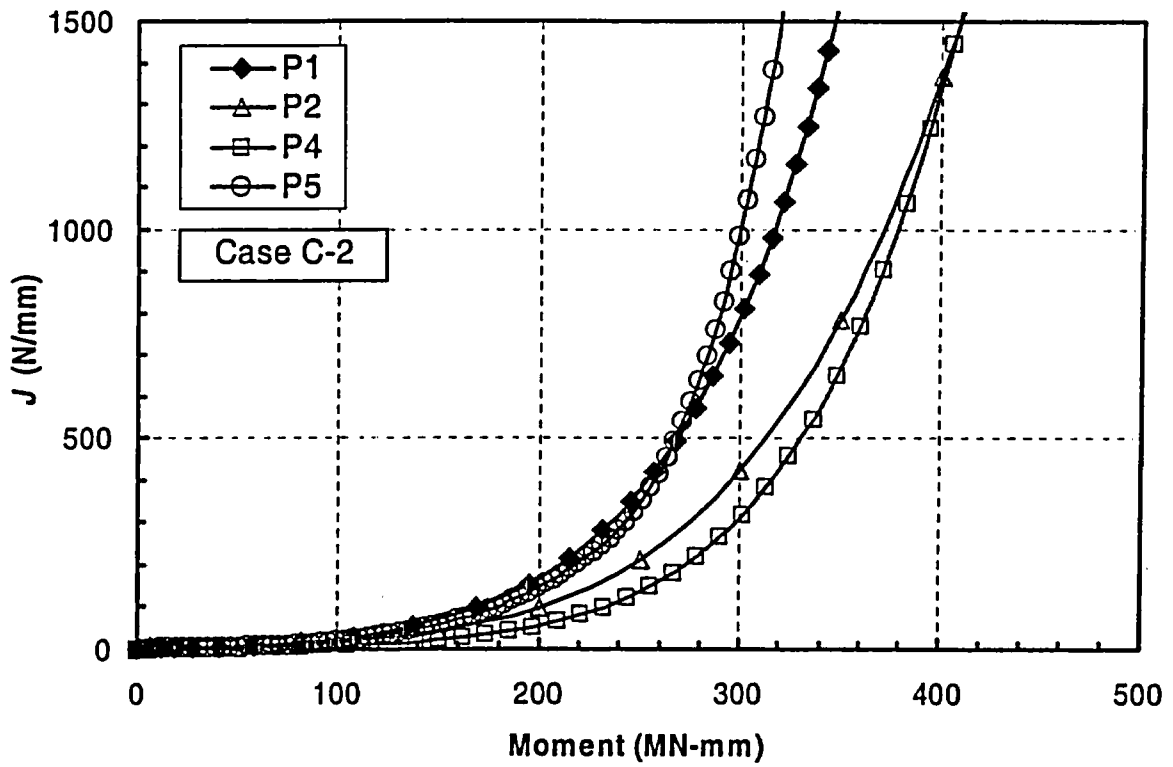

Figure I.60 The J versus moment relations of Case C-2

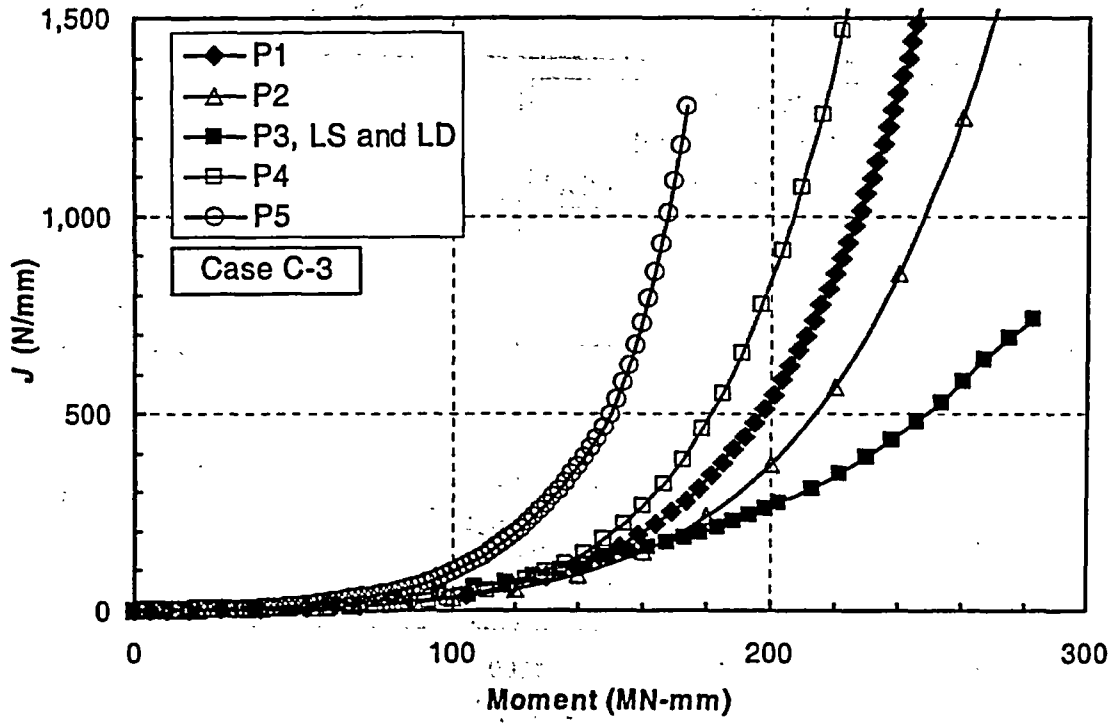

Figure I.61 The *J* versus moment relations of Case C-3

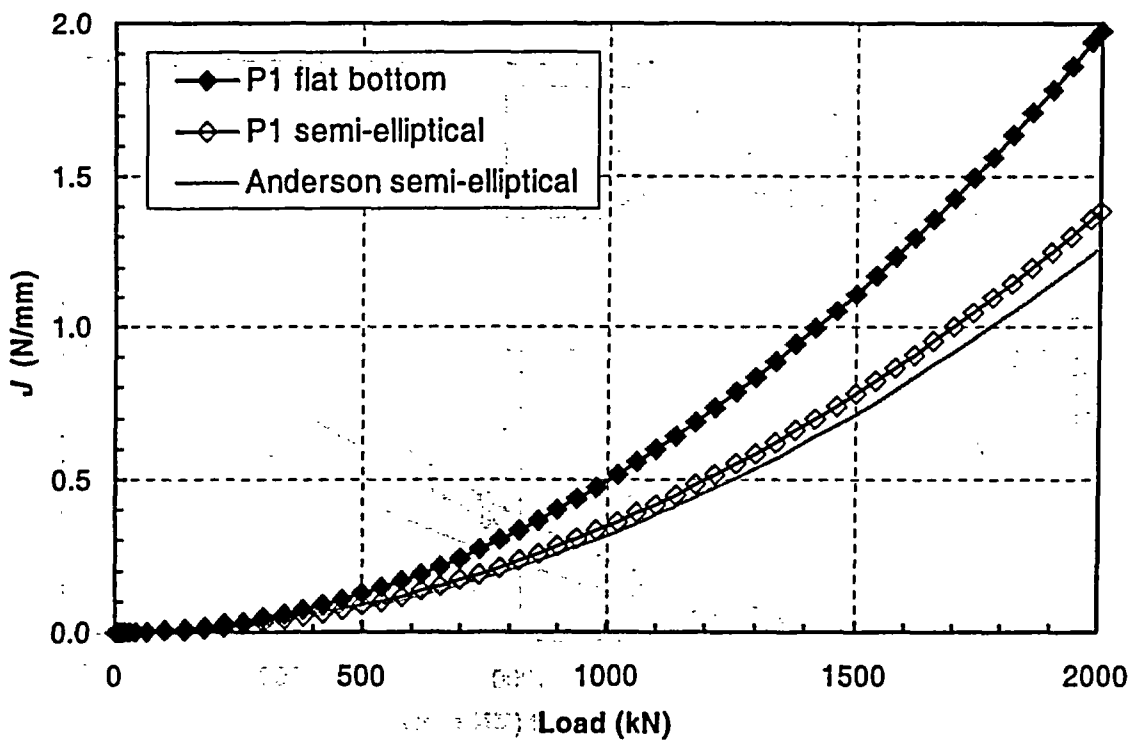

Figure I.62 Comparison of the line-spring results of Participant P1 with the 3-D solid element results of Anderson for a pipe section loaded in tension

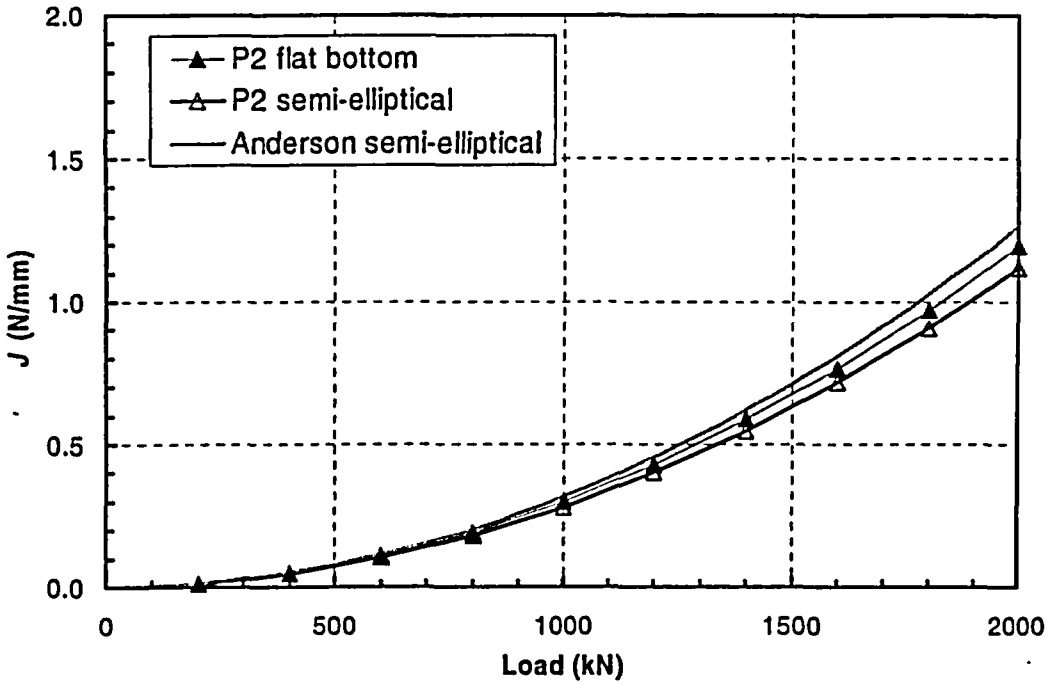

Figure I.63 Comparison of the 3-D solid element results of Participant P2 with the 3-D solid element results of Anderson for a pipe section loaded in tension

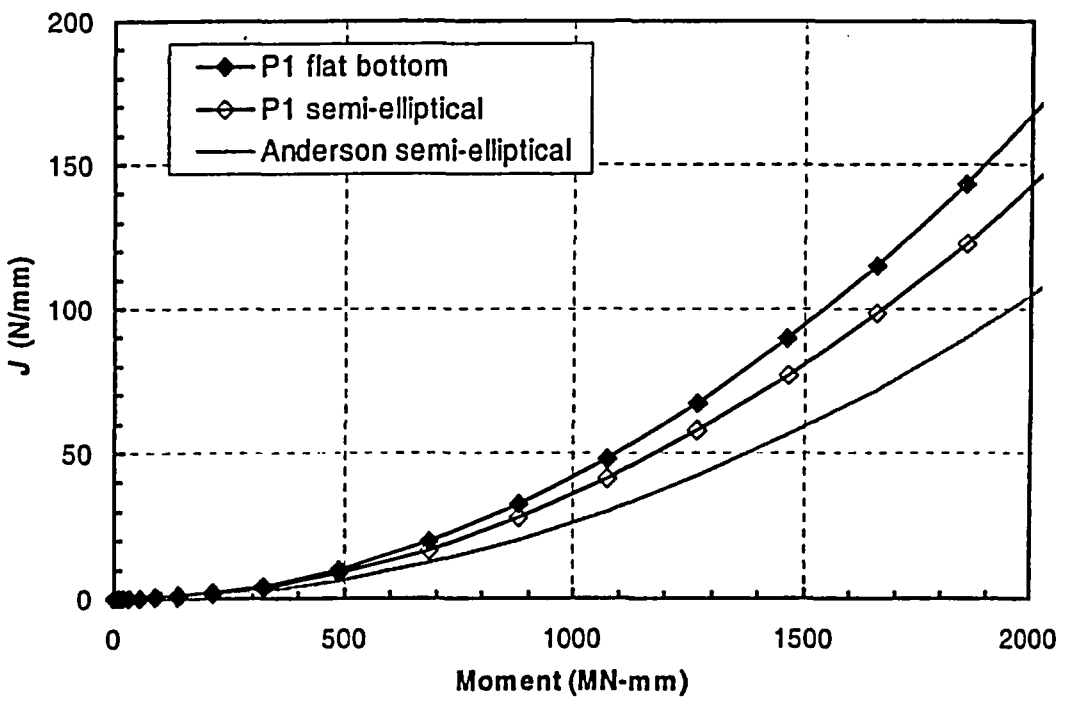

Figure I.64 Comparison of the line-spring results of Participant P1 with the 3-D solid element results of Anderson for a pipe section loaded in bending

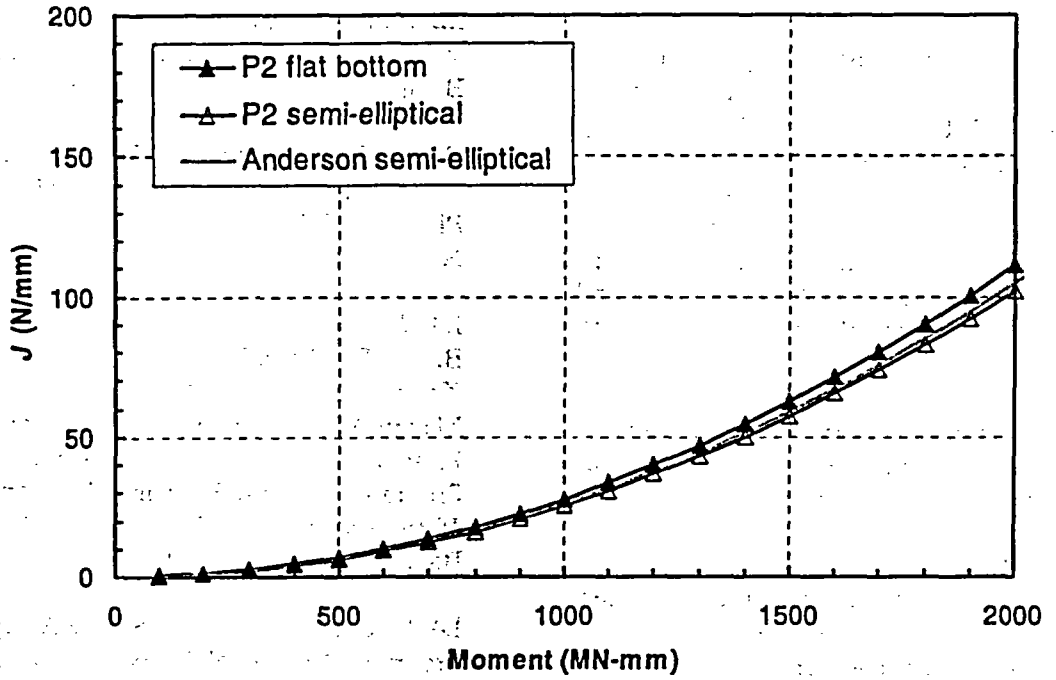

Figure I.65 Comparison of the 3-D solid element results of Participant P2 with the 3-D solid element results of Anderson for a pipe section loaded in bending

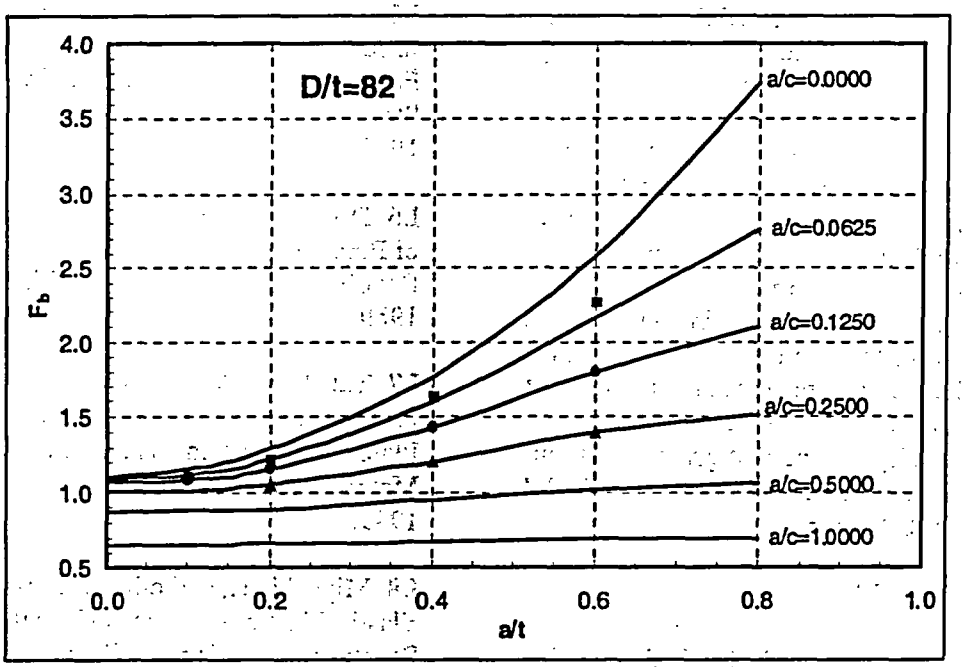

Figure I.66 Comparison of the normalized *K* solutions from the line-spring solution of Wang (Ref. I.19) with the 3-D solid element solution of Chapuloit (Ref. I.20). The lines are from Chapuloit; the symbols are from Wang.

I.3.13 Concluding Remarks

The differences among all participants in bending moment at the J level of interest in Cases A-1, A-2, B-1, B-2, and C-1 are typically less than 10 percent. Larger differences are observed in Cases A-3, C-2, and C-3. By comparison, the cases with internal pressure show larger differences than the cases without internal pressure. Although the use of shell and line-spring versus 3-D solid elements may cause some difference in the J versus moment relations, it cannot possibly be responsible for the large differences observed in some cases. Further investigation is needed to understand the causes of those large differences in some cases.

As indicated earlier, the possibility of local buckling at the surface crack location increases with the increase of R_m/t ratio. The local buckling reduces the load-carrying capability of the pipes. If the J estimation scheme were to extend to large R_m/t ratios, the effect of this local buckling should be considered in the FE analysis by using large-strain and large-displacement formulation. This work showed that sufficient accuracy could be obtained with the line-spring FE approach for the purpose of developing/validating an estimation scheme procedure. However, care should be taken in developing that approach for pipe with R/t of 40 or greater since local buckling at the crack may reduce the pipe's load-carrying capacity more than determined from using the small-strain formulation required for line-spring analyses. A separate effort for the BINP program involves comparing the FE line-spring results to different J-estimation schemes for the purpose of selecting or modifying one that gives consistent agreement with the FE analysis for the applied J versus moment behavior.

I.4 REFERENCES

I.1 Ghadiali, N., Rahman, S., Choi, Y.H., and Wilkowski, G., "Deterministic and Probabilistic Evaluations for Uncertainty in Pipe Fracture Parameters in Leak-Before-Break and In-Service Flaw Evaluations," U.S. Nuclear Regulatory Commission, NUREG/CR-6443, 1996.

I.2 Rahman, S., Brust, F., Ghadiali, N., Choi, Y.H., Krishnaswamy, R., Moberg, F., Brickstad, B., and Wilkowski, G., "Refinement and Evaluation of Crack-Opening-Area Analyses Circumferential Through-Wall Cracks in Pipes for Circumferential Through-Wall Cracks in Pipes," U.S. Nuclear Regulatory Commission, NUREG/CR-6300, 1995.

I.3 Wilkowski, G. M., Ahmad, J., Barnes, C. R., Broek, D., Brust, F., Guerrieri, D., Kiefner, J., Kramer, G., Landow, M., Marschall, C. W., Maxey, W., Nakagaki, M., Papaspyropoulos, V., Pasupathi, V., and Scott, P., "Degraded Piping Program - Phase II Semiannual Report, October 1986-September 1987,' NUREG/CR-4082, BMI-2120, Vol. 6, April, 1988.

I.4 Brickstad, B., "Swiss-Swede Analysis Program: Numerical Analyses of IPIRG Cracked Pipe Experiments with use of Non-Linear Fracture Mechanics," presented at 7th IPIRG-1 TAG meeting Nov. 1989.

I.5 Shimakawa, T., and Yagawa, G., "The Influences of Mesh Subdivisions on Nonlinear Fracture Analysis for Surface Cracked Structures," ASME PVP Vol. 167, pp. 7-14, July 1989.

I.6 Doi, H., and others, "Elasto-Plastic analysis of Pipe with Internal Circumferential Crack in Bending," ASME PVP Vol. 167, pp. 57-62, July 1989.

I.7 Takahashi, Y., and others, "Elastic-Plastic Fracture analysis of Surface Cracks in Pipe and Plates by three-Dimensional Finite Element Method," ASME PVP, Vol. 167, pp. 63-69, July 1989.

I.8 Miyoshi, T., and others, "Finite element Elastic-Plastic Analysis of Growth and Penetration of a Surface Crack," IJPVP, Vol. 33, 1988, pp 15-25.

I.9 Wilkowski, G. M., and others, "International Piping Integrity Research Group (IPIRG) Program," Program Final Report, NUREG/CR-

6233, Vol 4, June 1997, (pg 2-107).

I.10 Mohan, R., and others, "Development of a *J*-Estimation Scheme for Internal Circumferential and Axial Surface Cracks in Elbows," NUREG/CR-6445, BMI-2193, June 1996, see Section 3.0.

I.11 *"NRCPIPES" Windows Version 3.0 - User's Guide*, April 30, 1996, Battelle document to 2nd IPIRG group, Contract NRC-04-91-063.

I.12 Scott, P. M., and Ahmad, J., "Experimental and Analytical Assessment of Circumferentially Surface-Cracked Pipes Under Bending," NUREG/CR-4872, April 1987.

I.13 Krishnaswamy, P., Scott, P., Mohan, R., Rahman, S., Choi, Y. H., Brust F., Kilinski, T., Ghadiali, N., Marschall, C., and Wilkowski, G., "Fracture Behavior of Circumferential Short-Surface-Cracked Pipe," NUREG/CR-6298, November 1995.

I.14 Brust, F. W., "Approximate Methods for Fracture Analyses of Through-Wall Cracked Pipes," NRC Topical Report by Battelle Columbus Division, NUREG/CR-4853, February 1987.

I.15 Brust, F., Scott, P., Rahman, S., Ghadiali, N., Kilinski, T., Francini, R., Marschall, C., Muira, N., Krishnaswamy, P., and Wilkowski, G., "Assessment of Short Through-Wall Circumferential Cracks in Pipes - Experiments and Analyses," NUREG/CR-6235, April 1995.

I.16 Kurihara, R., and others, "Estimation of the Ductile Unstable Fracture of Pipe with a Circumferential Surface Crack Subjected to Bending," *Nuclear Engineering and Design*, Vol. 106, pp. 265-273, 1988.

I.17 Mohan, R., Wilkowski, G. M., Bass, B., and Bloom, J., "Finite Element Analyses to Determine the *R/t* Limits for ASME Code Case N-494 FAD Curve Procedure," ASME PVP Conference, PVP Volume 350, pp. 77-88, July 1997.

I.18 Anderson, T., Thorwald, G., Revelle, D., Lanaud, C., "Stress Intensity Solutions for Surface Cracks and Buried Cracks in Cyclinders, Spheres, and Flat Plates," report to MPC, March 14, 2000.

I.19 Wang, Y.-Y., Rudland, D., and Crompton, J., "Development of Structural Integrity Assessment Procedures and Software for Girth-Welded Pipes and Welded Sleeve Assemblies," draft final report, PRCI PR-185-9831, April, 2001.

I.20 Chapuloit, S., Lacire, M. H., and Le Delliou, P., "Stress Intensity Factors for Internal Circumferential Cracks in Tubes over a Wide Range of Radius over Thickness Ratios," PVP Vol. 365, ASME 1998, pp. 95-106.

NRC FORM 335 (2-89) NRCM 1102, 3201, 3202

U.S. NUCLEAR REGULATORY COMMISSION

BIBLIOGRAPHIC DATA SHEET

(See instructions on the reverse)

1. REPORT NUMBER (Assigned by NRC, Add Vol., Supp., Rev., and Addendum Numbers, If any.)

NUREG/CR-6837, Volume 2

2. TITLE AND SUBTITLE

The Batelle Integrity of Nuclear Piping (BINP) Program Final Report

Volume 2: Appendices

3. DATE REPORT PUBLISHED

MONTH: June YEAR: 2005

4. FIN OR GRANT NUMBER

W6775

5. AUTHOR(S)

P. Scott (1), R. Olson (1), J. Bockbrader (1), M. Wilson (1), B. Gruen (1), R. Morbitzer (1), Y.Yang (1), C. Williams (1), F. Brust (1), L. Fredette (1), N. Ghadiali (1), G. Wilkowski (2), D. Rudland (2), Z. Feng (2), R. Wolterman (2)

6. TYPE OF REPORT

Technical

7. PERIOD COVERED *(Inclusive Dates)*

Nov. 1997 - Sept. 2003

8. PERFORMING ORGANIZATION - NAME AND ADDRESS *(If NRC, provide Division, Office or Region, U.S. Nuclear Regulatory Commission, and mailing address; if contractor, provide name and mailing address.)*

(1) Batelle
505 King Avenue
Columbus, OH 43201

(2) Engineering Mechanics Corporation of Columbus
3518 Riverside Drive, Suite 202
Columbus, OH 43221

9. SPONSORING ORGANIZATION - NAME AND ADDRESS *(If NRC, type "Same as above"; if contractor, provide NRC Division, Office or Region, U.S. Nuclear Regulatory Commission, and mailing address.)*

Division of Engineering Technology
Office of Nuclear Regulatory Research
U.S. Nuclear Regulatory Commission
Washington, DC 20555-0001

10. SUPPLEMENTARY NOTES

C.A. Greene, NRC Project Manager

11. ABSTRACT *(200 words or less)*

Over the past 15 to 20 years, significant research has been conducted aimed at furthering the understanding of the fracture behavior of piping systems in commercial nuclear power plants. While the results from these prior programs have advanced the state-of-the-art understanding, there remained a number of key technical issues still to be resolved.

The BINP program was developed to address what was perceived to be the most critical of these unresolved issues. The program was structured as a series of independent tasks, each focused on one of these issues. After the research was completed, it was found that many of these issues did not have as significant an effect on leak-before-break (LBB) or in-service flaw evaluation criteria as was originally thought. However, one of the areas where significant benefit can be realized for both LBB and in-service flaw evaluations is by using nonlinear stress analysis instead of elastic analysis in the flaw assessments. The additional margin gained by accounting for the energy dissipated by plastic deformation can be significant. Another important advance was the preliminary development of the technical basis for flaw evaluation criteria for Class 2, 3, and balance-of-plant piping.

12. KEY WORDS/DESCRIPTORS *(List words or phrases that will assist researchers in locating the report.)*

Pipe
Fracture Mechanics
Leak-Before-Break
Flaw Evaluation

13. AVAILABILITY STATEMENT

unlimited

14. SECURITY CLASSIFICATION

(This Page) unclassified

(This Report) unclassified

15. NUMBER OF PAGES

16. PRICE

NRC FORM 335 (2-89)

UNITED STATES
NUCLEAR REGULATORY COMMISSION
WASHINGTON, DC 20555-0001

OFFICIAL BUSINESS